

Seismic Design of Nonstructural Building Components: The New Frontier of Earthquake Engineering

A. Filiatrault^{1,2}

1. Professor of Structural Engineering, School for Advanced Studies IUSS Pavia, Palazzo del Broletto, Piazza della Vittoria n.15 - 27100 Pavia, Italy.
Email: andrefiliatrault@iusspavia.it
2. Professor Emeritus, State University of New York at Buffalo, Buffalo, NY 14260, USA. Email: af36@buffalo.edu

Extended Abstract

This keynote address makes the argument that the seismic design of nonstructural components represents the next frontier of earthquake engineering and discusses **WHY** that is, **HOW** this frontier can be crossed and **WHO** should lead the earthquake engineering community in crossing it successfully.

WHY

Nonstructural components and systems are not part of a building's structural load-bearing system but are nonetheless subjected to the same dynamic environment during an earthquake. With the development and implementation of performance-based earthquake engineering, harmonization of seismic performance levels between structural and nonstructural components becomes vital. Even if the structural components of a building achieve a continuous or immediate occupancy performance level after a seismic event, failure of architectural, mechanical or electrical components can lower the performance level of the entire building system. This reduction in performance caused by the vulnerability of nonstructural components has been observed during recent earthquakes worldwide. Moreover, nonstructural damage has limited the functionality of critical facilities, such as hospitals, following major seismic events. The investment in nonstructural components and building contents is far greater than that of structural components and framing (Miranda and Taghavi 2003).

Considering the above and the fact that damage to nonstructural components occurs at seismic intensities much lower than those required to produce structural damage, it is not surprising that in many past earthquakes, losses from damage to nonstructural components have exceeded losses from structural damage. Furthermore, the failure of nonstructural components can become a safety hazard or can hamper the safe movement of occupants evacuating buildings, or of rescue workers entering buildings. In comparison to structural components and systems, there is relatively limited information on the seismic design of nonstructural components. Basic research work in

this area continue to remain sparse, and the available seismic design provisions in codes and guidelines are usually, for the most part, based on past experiences, engineering judgment and intuition, rather than on objective experimental and analytical results. Often, design engineers are forced to start almost from square one after each earthquake event: to observe what went wrong and to try to prevent repetitions. This is a consequence of the empirical nature of current seismic regulations and guidelines for nonstructural components.

HOW

Building codes generally classify nonstructural building components into three broad categories: (1) architectural components; (2) mechanical and electrical equipment; and (3) building contents.

Architectural components are built-in nonstructural components that form part of the building. They include interior partition walls, parapets, chimneys, penthouses, suspended ceilings, appendages and ornamentation, signs and billboards, egress stairways that are independent of the building, cladding systems, window systems and lighting systems.

Mechanical and electrical components are built-in nonstructural components that form part of the building. They include HVAC equipment, engines, turbines, pumps, compressors, pressure vessels, generators, batteries, motors, transformers, panel boards, switch gears, instrumentation cabinets, communication equipment, computers, cooling towers, piping systems, ductwork and electrical conduits.

Building contents are nonstructural components belonging to tenants or occupants of the building. They include filing cabinets, bookshelves and all pieces of furniture found inside buildings.

The most detailed guidelines for the practical seismic assessment and mitigation of nonstructural components are those provided in FEMA E-74 (2012). The document is aimed to assist a wide audience, from the general public and building owners to architects, engineers and facilities and planning personnel. By first reviewing the behaviour of nonstructural components, as observed from past earthquakes, the document provides readers with a clear sense of nonstructural components that typically perform poorly in earthquakes and highlights the potential need for damage mitigation measures. Distinction is made between three broad types of nonstructural components: (i) architectural components, (ii) mechanical, electrical and plumbing (MEP) components, and (iii) furniture, fixtures and equipment (FF&E) and contents. Guidelines are then provided for the survey and assessment of such nonstructural components in existing buildings with the aim to: (i) compile an inventory of nonstructural components, (ii) identify high-risk components, and (iii) identify and prioritize damage mitigation strategies. The creation of an inventory of non-structural components is useful because it clearly identifies the nonstructural components in a facility, provides quantities against which loss measures can be assigned as part of a loss assessment, and will facilitate prioritization of possible interventions. Using a checklist, the surveyor then answers questions about the possible hazard posed by each nonstructural component identified. In compiling the nonstructural inventory, FEMA E-74 also prompts the user to assign a risk rating to the nonstructural component. This is done considering the exposure, gauged from shaking maps (provided in FEMA E-74 for the United States only) and the potential hazard posed by the component. To this

extent, the guidelines prescribe that the risk be assessed as low, medium or high for three different performance factors: (i) life safety, (ii) property loss, and (iii) functional loss. Note that damage to a certain nonstructural component might represent a large potential for monetary (property) loss but low risk to life safety, whereas for other nonstructural components (such as a heavy bookshelf beside a bed) the opposite might be true. By assigning risk ratings to each of the nonstructural components identified during the survey, a prioritized inventory can then be developed, identifying those components that pose the greatest risk for the various performance measures. This prioritized inventory of nonstructural components can be a very useful tool for decision makers aiming to identify the most effective interventions and risk mitigation measures to implement. Chapters 4 and 5 of the FEMA E-74 (2012) document provide general guidelines for the nonstructural risk reduction for existing and new buildings, respectively. Efforts are made to clearly identify what the objectives of retrofit should be and how achieving these objectives will require planning and may require the involvement of various personnel, each having different responsibilities in the retrofit process. A range of design options are identified for potential retrofit, from non-engineered interventions that could be implemented by in-house personnel, to prescriptive and engineered solutions that are developed by a professional engineer and could be required for important facilities such as hospitals and schools. A wide range of informative and practical mitigation strategies for nonstructural components are provided in Chapter 6 of the FEMA E-74 (2012) guidelines. Descriptions, illustrated with photos and drawings, of typical types of failure and retrofit measures for architectural, MEP components and furniture, fixtures, equipment and contents are detailed over some 500 pages, thus providing a very useful resource for risk reduction. For new buildings, the FEMA E-74 guidelines also recommend that a designated nonstructural coordinator develops a specification document containing in one place the aggregate requirements for seismic restraint of nonstructural components and a responsibility matrix for assigning responsibility for design, construction, and inspection of nonstructural installations.

In the last half century, much effort has been devoted to developing rational methods for conducting the seismic analysis of nonstructural building components. The hope was to develop rational analytical methods that could be used in specific seismic design situations. Unfortunately, except for very simple nonstructural building components, none of these proposed seismic analysis methods have found their way into industry standards and seismic provisions. As a consequence, there is currently no general guidance in seismic design provisions on how to consider interactions between primary structural and secondary nonstructural systems. In the vast majority of practical design situations, decoupled analyses are conducted using a “cascading” approach. In this approach, the dynamic properties and the floor responses of the primary structure are estimated without considering the interaction with the nonstructural component. The structural response at the attachment level is then considered as the input motion for the estimation of the response of the nonstructural component. One of the most popular of these cascading methods is the Floor Response Spectrum (FRS) method.

A response spectrum can be obtained not only for a ground motion, but also for the acceleration time-history measured or calculated at any point in a structure. The Floor Response Spectrum (FRS) method consists of first obtaining the response spectrum at the location in the structure where a nonstructural component is attached (the floor response spectrum) and then using this response spectrum to estimate its seismic response. The traditional technique used to calculate a floor response spectrum is first

to conduct a dynamic analysis of the supporting structure by itself under a ground motion to calculate the horizontal acceleration time-history of the floor on which the nonstructural component is attached, and then to compute the response spectrum of this floor acceleration. If a simplified floor design spectrum needs to be constructed for a given structure, then the process needs to be repeated for an ensemble of ground motions representative of the selected design seismic hazard level at the construction site.

Because of the large number of calculations required to generate a design floor response spectrum, alternative methods are often employed. For example, an artificial ground motion that envelops a design ground response spectrum can be used to limit the number of dynamic analyses. However, caution must be exercised in the selection of this artificial ground motion because widely different acceleration time-histories may envelop the same design ground response spectrum, but produce widely different floor response spectrums. Another approach is to generate the floor response spectrum directly using approximate methods such as those recently developed by Sullivan *et al.* (2013), Calvi and Sullivan (2014), Welch (2017), Merino *et al.* (2019), Vukobratović and Fajfar (2015, 2016).

The primary intent of current building code seismic design requirements for nonstructural components in North America, Europe and Australia (ASCE 2016, NRC 2015, CEN 2004, AS 1170.4 2007) is to maintain life-safety. This is attempted by limiting large displacements of nonstructural components by anchoring them to the supporting structure and by minimizing the potential for internal damage to nonstructural components, particularly in critical facilities. Current seismic design requirements are based on the fundamental assumption that nonstructural components can be considered dynamically uncoupled from the structural system to which they are connected, thereby justifying the cascading design approach, discussed earlier.

In current North American, European and Australian design standards, the seismic design of nonstructural components starts by the calculations of equivalent static design forces in the horizontal and/or vertical directions, and applying these forces to the component's centre of mass. The equivalent static design forces are calculated by multiplying the mass of the nonstructural component by the corresponding peak horizontal and/or vertical accelerations anticipated at its centre of mass during the design seismic event. Similar to building structures, the equivalent static forces for the design of essential (critical) nonstructural components are multiplied by an importance factor larger than unity. In addition, to account for the over-strength and nonlinear response of nonstructural components, the equivalent static design forces are divided by a response modification factor larger than unity. The support reactions due to the equivalent static design forces are usually calculated based on the mass distribution of the nonstructural component. Finally, the connections and restraints must be designed to withstand these equivalent static forces. For nonstructural components required for life-safety or continuous operation of important facilities, the components themselves must be designed also for these same equivalent static forces.

In the ASCE 7-16 (ASCE 2016) Standard in the United States, the following special certification requirements are included for Seismic Design Category C to F (ASCE 2016) to ensure that nonstructural components designated as seismic systems will perform as intended: 1) Essential active mechanical and electrical equipment is required to demonstrate and certify compliance by either shake table testing or experience data;

and 2) Components containing hazardous material are required to demonstrate and certify compliance by shake table testing, experience data or analysis. In practice, most certification compliances of nonstructural components designated as seismic systems are conducted through shake table testing. For this purpose, special seismic qualification testing procedures have been developed for nonstructural building components (ICC-ES 2012).

Finally, the incorporation of nonstructural components within the framework of performance-based earthquake engineering and seismic loss estimation requires the development of scientifically-based fragility curves, relating proper engineering demand parameters with the probabilities of entering certain damage stages, and consequence functions, relating each assessed damage state to possible consequences (e.g. dollars, downtime, deaths). Recently, scientifically-based fragility curves for sprinkler piping systems have been developed (Tian *et al.* 2014, 2015a, 2015b, Soroushian *et al.* 2015) through the following five steps: 1) Cyclic testing of sprinkler piping joints; 2) Hysteretic modelling of sprinkler piping joints; 3) Seismic testing of sprinkler piping subsystems; 4) Numerical modelling of sprinkler piping subsystems; and 5) Fragility analysis of sprinkler piping systems.

WHO

Close collaboration between architects and structural engineers understood to be highly desirable has now become practice within Europe, North America and Australia. Unfortunately, this collaboration has not been successful for the design and installation of nonstructural components. The seismic design and installation of nonstructural components remains a controversial issue in terms of expertise and responsibility. Often the question arises during the course of a construction project as to who should be responsible for the integration of structural and nonstructural seismic designs and installations. Within current construction practices, the answer to this question is not always clear. The main stakeholders in a construction project that could be involved in the seismic design and proper installation of the nonstructural components are the building owner, the architect, the structural, mechanical and electrical engineers and a variety of specialty contractors. Looking at the specific competences of each stakeholder, one can argue that architects, mechanical and electrical engineers in many cases do not have sufficient specific knowledge to seismically design and properly install nonstructural components or are not sufficiently trained in that role. At the same time, structural engineers are often not interested in the design of nonstructural components and believe this issue is not inherent with their responsibility and fee structures. The architects often entrust the task to subcontractors that apply the codes and standards seismic prescriptions to the best of their abilities but often do not have adequate expertise, particularly if some engineering design calculations are required. It seems to be necessary that a new professional discipline of “nonstructural coordinator” be introduced within the building professions to ensure that the nonstructural components achieve the level of system reliability in meeting the demands caused by a design earthquake. The nonstructural coordinator should be familiar with the basic principles of structural design and earthquake engineering. At the same time, a good background regarding the architectural aspects involved in the design process is required (MEP systems, furniture, architectural components, etc.). The knowledge of the applicable codes and standards providing prescriptions for the seismic protection of nonstructural components as well as the ability to quantify and optimize the costs involved in the design process is also of paramount importance for a nonstructural coordinator. The author believes that structural engineers, familiar with the seismic

provisions for the various typologies of nonstructural components, would be the most suited professionals to serve as nonstructural coordinators in a construction project.

The advancements in Building Information Modelling (BIM) technology have significantly enhanced several aspects of the planning, design and construction processes along with numerous aspects of the project management. To assess building performance in the early design stage, access to a comprehensive set of data regarding a building's geometry, contents, use, and mechanical equipment allows improving the accuracy of information to be incorporated throughout the design process. The combination of sustainable design strategies (e.g. performance-based seismic design) and BIM technology has the potential to change the traditional design practices and to efficiently produce a high-performance facility design. The capability of BIM to organize and export information to external software could greatly increase the feasibility of conducting comprehensive and automatic seismic design and risk assessment. The development of seismic assessment/design software for specific nonstructural component typologies that are able to read the data provided by Building Information Models and provide output files that can be uploaded in the original Building Information Models could represent a new frontier in the seismic design of nonstructural components.

Building Information Models could be very useful in the seismic design of buildings to identify performance targets both, for structural and nonstructural components. The integration of structural and nonstructural components in Building Information Models would allow identifying optimum seismic design solutions. Nonstructural components can be sensitive to story drifts and/or floor accelerations. By increasing the strength of the structure, the story drift demand may be decreased but, at the same time, the floor accelerations along the height of the building may be increased. The integration of the structural and nonstructural components in the same Building Information Model and the clear understanding of all components present in the building are very useful in order to improve the seismic performance of the building. The seismic design can be optimized in order to limit drift or acceleration based on the nonstructural components intended for the building. A correct application of performance-based seismic design by integrating structural and nonstructural components not only allows the definition of a single serviceability limit state, but the assessment of various performance levels. This strategy permits to take into account a range of possible seismic demands and to investigate the damage consequences related to structural and nonstructural components for various limit states. The accuracy of Building Information Models in terms of details and quantities is also of paramount importance to perform accurate seismic loss estimation analyses or to develop detailed models in external software in order to perform more sophisticated analyses. The nonstructural coordinator in collaboration with BIM software developers could be responsible to verify the accuracy of Building Information Models. If the details required for the analysis of nonstructural components are not available in the Building Information Models, the nonstructural coordinator should ask the particular BIM software developer to improve their models or should be able to directly improve the Building Information Model by introducing the information that are considered essential for the seismic analysis.

Recently, Perrone and Filiatrault (2017) developed a conceptual framework to perform the automatic seismic design of nonstructural components using information available in Building Information Models. The use of the framework was illustrated through a proof-of-concept case study on the automatic seismic design of sway braces for

pressurized fire suppressant sprinkler piping systems using a Building Information Model.

REFERENCES

- ASCE 2016. Minimum Design Loads and Associated Criteria for Buildings and Other Buildings. ASCE 7-16, American Society of Civil Engineers Reston, Virginia.
- AS 1170.4. 2007. Australian Standard – Structural Design Actions Part 4: Earthquake Actions in Australia. Standards Australia, Sydney, AU.
- Calvi PM, Sullivan TJ. 2014. Estimating floor spectra in multiple degree of freedom systems, *Earthquake and Structures*. 7(1), 17-38.
- CEN. 2004. EN-1998-1 :2004: E : Eurocode 8 – Design Provisions for Earthquake Resistant Structures, Comité Européen de Normalization, Brussels, Belgium.
- FEMA E-74. 2012. Reducing the Risks of Nonstructural Earthquake Damage – A Practical Guide,” FEMA E-74 Document, Federal Emergency Management Agency, Washington, DC.
- ICC-ES. 2012. Acceptance Criteria for Seismic Qualification by Shake-Table Testing of Nonstructural Components and Systems. International Code Council Evaluation Service, International Code Council AC156. Whittier, CA, 10 p.
- Miranda E and Taghavi S. 2003. Estimation of Seismic Demands on Acceleration-sensitive Nonstructural Components in Critical Facilities. Proceedings of the Seminar on Seismic Design, Performance, and Retrofit of Nonstructural Components in Critical Facilities, ATC 29-2, Newport Beach, CA, 347–360.
- Merino, R.J., Perrone, D. and Filiatrault, A. 2019. “Consistent Floor Response Spectra for Performance-Based Seismic Design of Nonstructural components,” *Earthquake Engineering & Structural Dynamics*, 49(3), 261-284, DOI: <https://doi.org/10.1002/eqe.3236>.
- NRC. 2015. National Building Code of Canada, National Research Council, Ottawa, Canada, 708 pp.
- Perrone, D. and Filiatrault, A. 2017. Use of Building Information Modelling for the Automated Seismic Design of Nonstructural components. *Journal of Automation in Construction*, 84, 166-175, DOI: <http://dx.doi.org/10.1016/j.autcon.2017.09.002>.
- Soroushian, S., Zaghi, A. E., Maragakis, E. M., Echevarria, A., Tian, Y., Filiatrault, A. 2015. Seismic Fragility Study of Fire Sprinkler Piping Systems with Grooved Fit Joints. *ASCE Journal of Structural Engineering*, 141(6), 1-15. DOI: [https://doi.org/10.1061/\(ASCE\)ST.1943-541X.0001122](https://doi.org/10.1061/(ASCE)ST.1943-541X.0001122).
- Sullivan TJ, Calvi PM, Nascimbene R. Towards improved floor spectra estimates for seismic design, *Earthquakes and Structures* 2013; 4(1):109-132.
- Tian, Y., Filiatrault, A. and Mosqueda, G. 2014. Experimental Seismic Fragility of Pressurized Fire Suppression Sprinkler Piping Joints,” *Earthquake Spectra*, 30(4), 1733-1748.
- Tian, Y., Filiatrault, A. and Mosqueda, G. 2015a. Seismic Response of Pressurized Fire Sprinkler Piping Systems I: Experimental Study. *Journal of Earthquake Engineering*, 19(4), 649-673.
- Tian, Y., Filiatrault, A. and Mosqueda, G. 2015b. Seismic Response of Pressurized Fire Sprinkler Piping Systems II: Numerical Study. *Journal of Earthquake Engineering*, 19(4), 674-699.
- Vukobratović, V, Fajfar, P. A method for the direct determination of approximate floor response spectra for SDOF inelastic structures. *Bull Earthq Eng* 2015; 13(5):1405–1424.

Vukobratović, V, Fajfar, P. A method for the direct estimation of floor acceleration spectra for elastic and inelastic MDOF structures. *Earthq Eng Struct Dyn* 2016; 45(15):2495–2511.

Welch DP, Sullivan TJ. Illustrating a New Possibility for the Estimation of Floor Spectra in Nonlinear Multi-Degree of Freedom Systems. *Proceedings of the 16th World Conference on Earthquake, 16WCEE*, Paper N° 2632, Santiago, Chile, 2017.

Keywords: Nonstructural Building Components; Performance-Based Earthquake Engineering; Seismic Design and Analysis, Building Information Modelling.

Modelling Techniques for Seismic Analysis of Limited Ductility RC Buildings

Raneem Alazem^{1,5}, Elisa Lumantarna^{2,5}, Nelson T. K. Lam^{3,5}, and Scott Menegon^{4,5}

1. Corresponding Author. PhD Candidate, Department of Infrastructure Engineering, the University of Melbourne, Parkville, VIC 3052, Australia
Email: ralazem@student.unimelb.edu.au
2. Lecturer, Department of Infrastructure Engineering, the University of Melbourne, Parkville, VIC 3052, Australia
Email: elu@unimelb.edu.au
3. Professor, Department of Infrastructure Engineering, the University of Melbourne, Parkville, VIC 3052, Australia
Email: ntkl@unimelb.edu.au
4. Research Fellow, Centre for Sustainable Infrastructure, Swinburne University of Technology, Hawthorn, VIC 3122, Australia
Email: smenegon@swin.edu.au
5. Bushfire and Natural Hazard Cooperative Research Centre, East Melbourne, VIC 3002, Australia

Abstract

This paper is aimed at evaluating the seismic performance of representative limited ductile Australian RC buildings for considerations of applying cost effective retrofitting measures. The structural performance of a case study RC building was analysed to study the behaviour under time history loading. SeismoStruct software has been employed for performing nonlinear analysis of the structure. Modelling of limited ductility structures is not straightforward, thus the modelling techniques and material properties used for the limited ductile RC buildings have been heavily verified using experimental test results from literature, with modelling recommendations presented in this paper. The overall research aim of this paper was to determine if the behaviour predictions of such building match with the analysis results.

Keywords: existing structures; seismic evaluation; limited ductility buildings; performance validation; non-linear time history analysis

1. INTRODUCTION

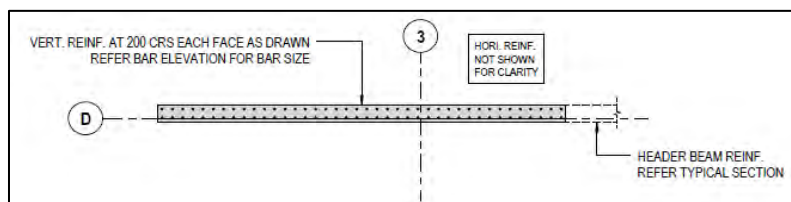
Due to the lack of historical perspective on seismic design, existing Australian reinforced concrete (RC) buildings can be extremely vulnerable and brittle. That is due to lack of adequate structural design and detailing for those buildings designed prior to the publishing of the earthquake loading standard in 1995. Several existing literatures has touched on this topic in more detail, specifically for structures in Australia, such as Amirsardari et al. (2020) and Menegon (2018). Thus, the first step towards making calculated risk mitigation decisions regarding those structures is to undertake seismic analysis and identify the specific vulnerabilities in representative structures. This current paper aims to further that research by undertaking seismic analysis, nonlinear time history analysis, on a case study building with several vulnerable features, with the aim of confirming whether the behavior displayed by the structure matches the predicted behavior at failure. This leads to the focus on reliable modelling techniques for these vulnerable criteria of structures. Recommendations of modelling techniques, which have been validated, are provided to act as a modelling framework for limited ductile RC structures.

2. CASE STUDY BUILDING

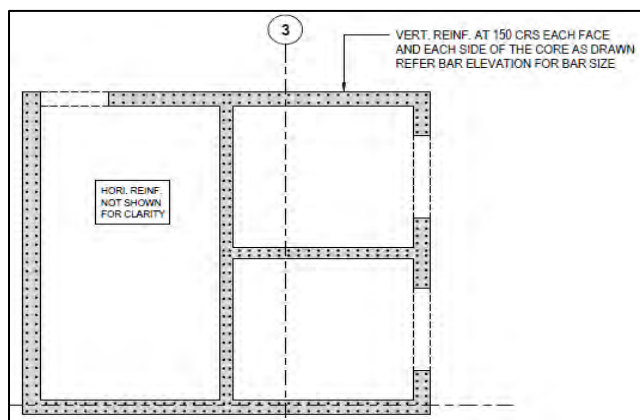
Before the methodology and modelling techniques are approached, it is important to understand the features and properties of a building that these modelling recommendations are applicable to i.e. limited ductile buildings. Weak column-strong beam, inadequate confinement, poor anchorage and lap splices, low reinforcement percentages, torsional eccentricity and other features of these buildings have been covered by Amirsardari (2018) in detail. In a paper published by Menegon et al. (2019), limited ductility buildings are categorized into 3 general categories: Soft-storey buildings, vertically irregular buildings, and horizontally irregular buildings. Based on these categories, different case study buildings, which are simplified adaptations of real buildings, were developed for more clarity. These include RC wall buildings with symmetrical & asymmetrical wall configurations, RC Wall buildings with high strength columns not designed for drift, RC wall building with ground storey transfer columns, and RC frame dominated building. One of these buildings, Case Study Building 3, is adopted for the analysis in this paper. Case study building 3 is a 6-story RC wall building with asymmetric wall configuration (torsionally eccentric). The proposed building analysed in this paper was assumed to be:

- Located in Melbourne, on a shallow soil site (Class C)
- Typical importance level (level 2)
- Designed and detailed in accordance with AS3600 (Standards Australia, 2009) and AS1170.4 (Standards Australia, 2007), based on industry standards (rather than more advanced analysis and design methods)
- The critical elements of the lateral load resisting system were deemed to be close to the minimum required design actions
- Earthquake actions were the critical load scenario

As a result of the torsional eccentricity of this building, the exterior perimeter columns are expected to have larger inter-story drifts than the walls, and the cores are expected to have large magnitudes of torsional actions. Note that the interior gravity system was not modelled since it was expected that the perimeter frames fail prior to the interior gravity system. Some of the design properties



(a) Shear Wall (Right side is mirror image of left)



(b) Core Wall (Right side is mirror image of left)

Figure 3: Typical design and detailing of (a) Shear Wall (b) Core Wall (Menegon ,2019)

2. METHODOLOGY AND MODELLING

SeismoStruct software was utilised for the seismic assessment of the case study building. SeismoStruct (Seismosoft, 2020a) is a finite element software that is capable of predicting displacement behaviour of structures under static/dynamic loading, as well as allowing the visualisation of the extent of damage under seismic events and excitations. The program has been used in a range of previous research investigating the seismic performance of RC buildings (Almeida et al., 2016; Bolea, 2016; Carvalho et al., 2013; Hoult, (2017), Dias-Oliveira et al., 2016; Belejo et al., 2012).

For this paper, a nonlinear time history analysis was performed on the structures. The initial modelling techniques adapted were based on literature (Martini,2007; Beyer et al., 2008; Seismosoft, 2020a; Seismosoft, 2020b; Yu, 2006) that analysed similar structures, i.e., existing RC buildings. From there, using experimental data from literature, the modelling parameters were refined and calibrated to provide the best results for typical Australian limited ductile structures.

Consistency in the modelling, especially in highly nonlinear analysis such as the buildings being considered, is very important. This is because those structures have a stiffness that is close to zero, making them very sensitive to even the smallest changes in the inputs, or even project settings, and possibly causing large differences in the results.

2.1. MATERIAL PROPERTIES

Both material properties chosen were previously recommended for use by Belejo et al. (2012) limited ductility buildings. For the concrete, the Mander et al. (1988) nonlinear concrete model - con_ma was utilised. It is a unified stress-strain model for confined concrete member subjected to uniaxial cyclic loading. However, the model does have a few shortcomings which include: (1) shows a uniform degree of strength degradation which may not always be the case (depends on magnitude of strain reversal) (2) the initial stiffness of the unloading branches predicted is overestimated (as shown in the verification section of this paper). Nonetheless, it is accurate enough for the purpose of this research, also recommended for use by Amirsardari (2018) for limited ductile buildings. The definition of this material is straightforward as it depends on the concrete properties of the elements to be modelled. It is important to note that SeismoStruct does not model column shear degradation unless a code-based capacity check is applied in the software. Thus, the required residual strength was specified to the corresponding limit state in the code checks.

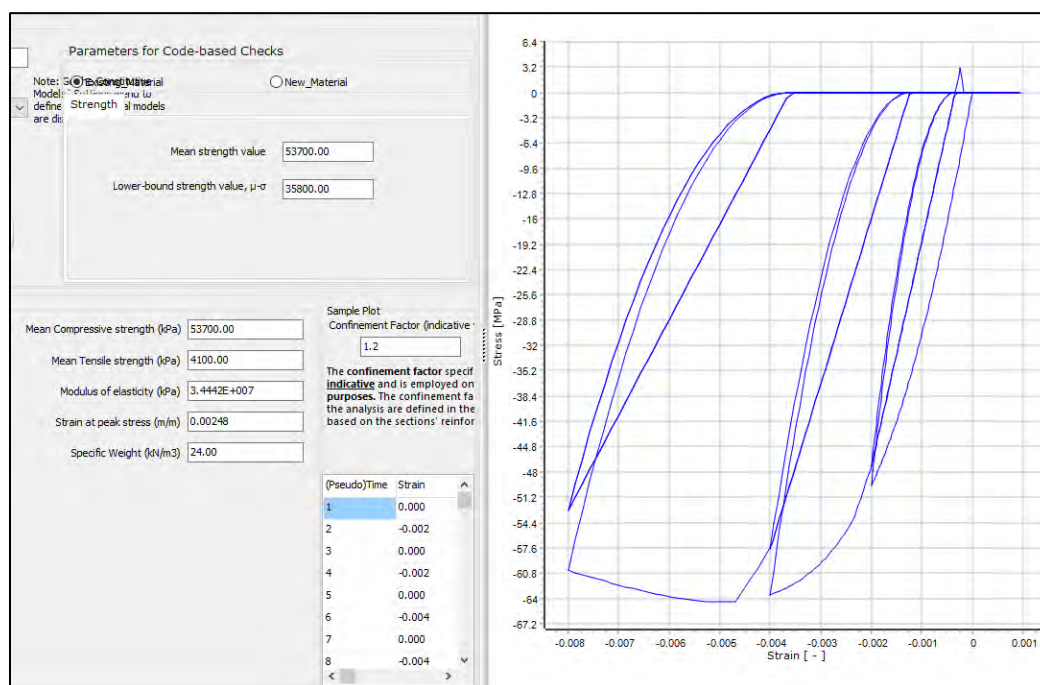


Figure 4: Concrete model input screen in SeismoStruct

For the steel, the Menegotto-Pinto steel model - stl_mp was applied, as shown in Figure 5. The Menegotto model with isotropic hardening enhancement is based on a relatively simple formulation and its efficiency has been verified experimentally.

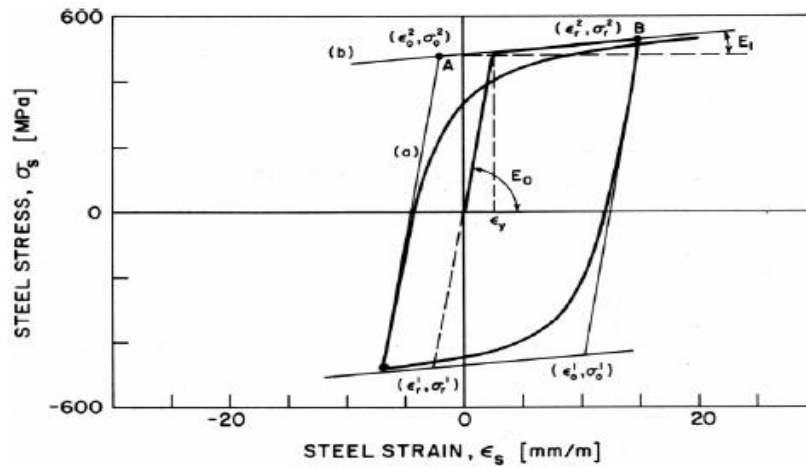


Figure 5: Menegotto-Pinto Steel Model

For this model, a few parameters must be specified. The curvature parameter R is considered dependent on the strain difference between the current asymptote intersection point and the previous load reversal point with maximum or minimum strain depending on the corresponding steel stress. R_0 is the value of the parameter R during the first loading, and a_1 , a_2 are experimentally determined parameters to be defined together with R_0 . R influences the shape of the transition curve, as shown in Figure 6, and allows a good representation of the Bauschinger effect and pinching of the hysteretic loop (Yu, 2006). As R increases, the curve becomes sharper, whereas a smoother curve is obtained with a lower R value.

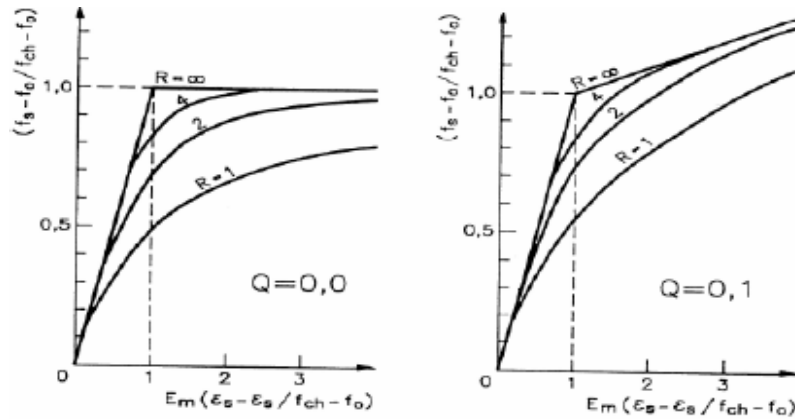


Figure 6: Influence of R on the shape of the curve

a_3 defines the isotropic hardening and a_4 defines the value beyond which isotropic hardening occurs, and these values can also be experimentally evaluated and calibrated. However, the contribution of isotropic hardening is significantly smaller than that of kinematic and thus the values adopted would not considerably alter the response. This agrees with a sensitivity study done as part of the modelling research for this paper, in which the set of values for those coefficients that has been proposed by Monti et al. (1996), shown in Table 1, was used as a starting set of data and then refined. Each coefficient value was varied while the others remained constant to study the effect of the change on the hysteresis curve. The findings showed that altering the values of a_2 , a_3 , and a_4 had a negligible effect, at least on the low ductility elements and buildings being

considered in this study, and thus they were kept the same. The coefficient a_1 had the most significant effect, in which increasing it to a value close to R increased the pinching of the hysteresis significantly, whereas reducing that value reduced the pinching. Limited ductile elements usually experience high pinching, so the recommend coefficients proposed in Table 1 reflect that.

Table 1: Recommended coefficients for stl_mp model

	R_0	a_1	a_2	a_3	a_4
Monti et al. (1996) Recommendation	20	18.5	0.15	0.025	2
Refined and Calibrated Set	20	20	0.15	0.025	2

The inputs for strain hardening parameter ($e_{sh} = 0.01$) and fracture buckling strain ($e_{su} = 0.05$) were utilised based on mean values for steel bars tested by Menegon et al (2015), also utilised by Hoult (2017).

2.2. ELEMENT CLASSES

The element class deemed to be most suitable for this analysis is the $infrmFBPH$ - fibre based plastic hinge model. This is used to model column, beams, and wall elements. This model features a distributed inelasticity displacement- and forced-based formulation but concentrating such inelasticity within a fixed length of the element. The advantages of this include reduced analysis time (since fibre integration is carried out for the two-member end section only), as well as full control/calibration of the plastic hinge length (or spread of inelasticity), which allows the overcoming of localisation issues. (SeismoSoft, 2020a).

A plastic hinge length, in terms of percentage of wall/column height or beam length also needs to be specified. The plastic hinge length equation was adopted from Priestley et al. (2007) with a minor adaptation as suggested by Hoult (2017). The adaptations based on Hoult (2017) include adding an additional term to allow for effects of tension shifts ($0.1l_w$), as well as considering the effective height ($L_c = 0.7H$). Thus, the plastic hinge equation used is as show in Equation 1 (refer to Priestly et al. , 2007 for parameter definitions). This equation was used to calculate all the plastic hinge lengths for the columns, walls, and beams.

$$L_p = kL_c + 0.1l_w + L_{SP} \quad \text{Equation 1}$$

2.3. WALL MODELLING

The walls have been modelled using the Wide-Column Model (WCM) proposed by Beyer et al. (2008). This method utilises modelling of each planar component of the wall with an individual line element, assigned to rectangular-fibre wall section. Then, these individual components are joined using horizontal links. It is advisable to apply structural nodes at the corners of the wall so that all the nodes can be joined by the links, which are to be applied at every half storey height. Note that the images in Figure 7 are that of a C section, however, this method has been applied for other wall shapes, such as the rectangular and block shape. When applying this concept in SeismoStruct, an elastic frame element with a stiffness of $1E+008$ kN and torsional rigidity of 9893.58 kNm² should be created, as recommended by Hoult (2017). Then, this element should be

used to connect the structural nodes of the wall, as opposed to using links in the constraint part of SeismoStruct to link the wall. The usage of a rigid elfrm element ensures that the model is sufficiently constrained.

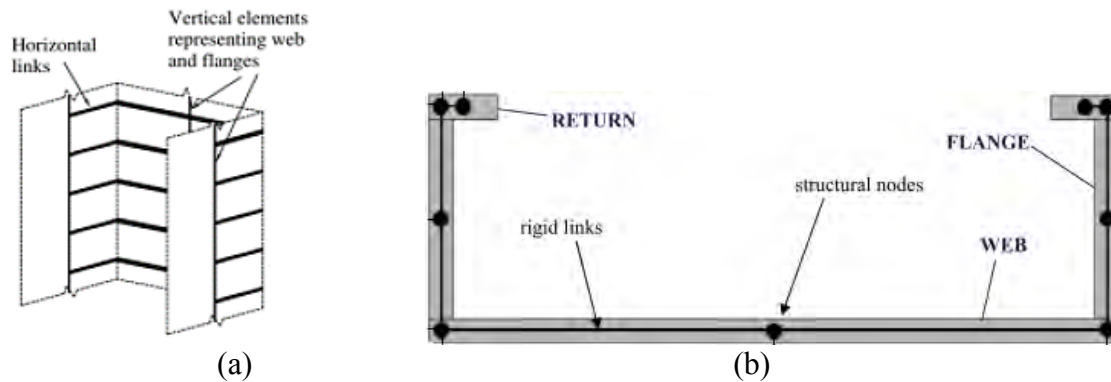
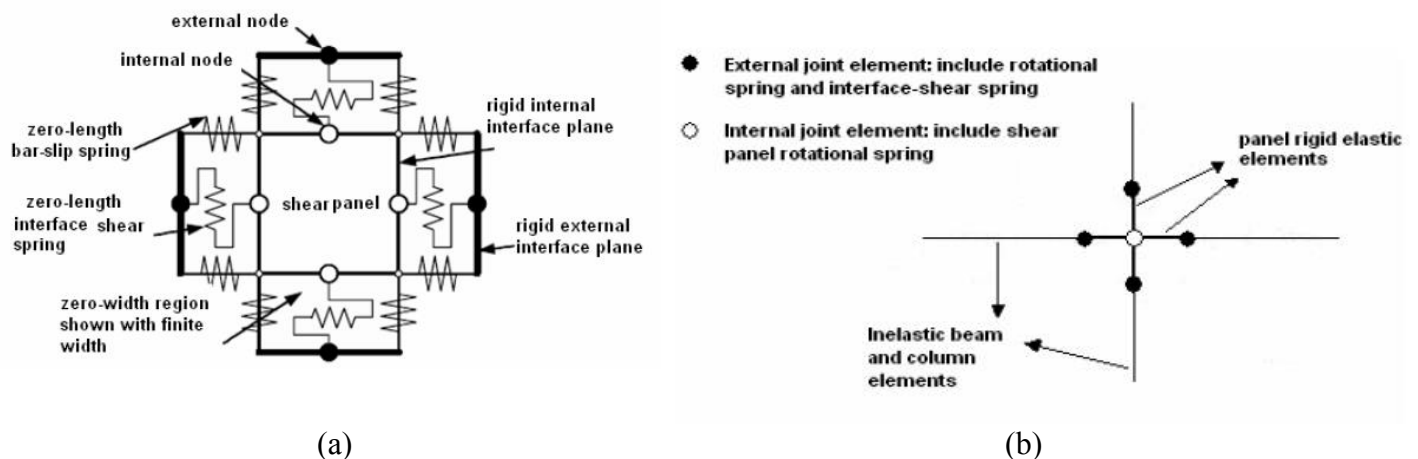


Figure 7: (a) Wide Column Model (Beyer et al., 2008) (b) Rigid Horizontal links on C shaped wall (Hoult, 2017)

2.4. JOINT MODELING

It is common in the design of RC frames to assume rigid joints. However, this assumption cannot be applied for limited ductile buildings due to their detailing deficiencies, such as inadequate confinement. Thus, they are susceptible to joint shear failure or bond failure (brittle failure mechanisms), this can lead to joint failure at low displacement demands and may be followed by global collapse of the frame (Amirsardari, 2018). Thus, accurate modelling of the joint inelastic behaviour is crucial, especially if the global cause of failure is related to the joints. In these instances, the Lowes et. Al (2003) model, as shown in figure 8, is recommend, also utilized by Yu (2006) and Amirsardari (2018) to model limited ductile RC joints.



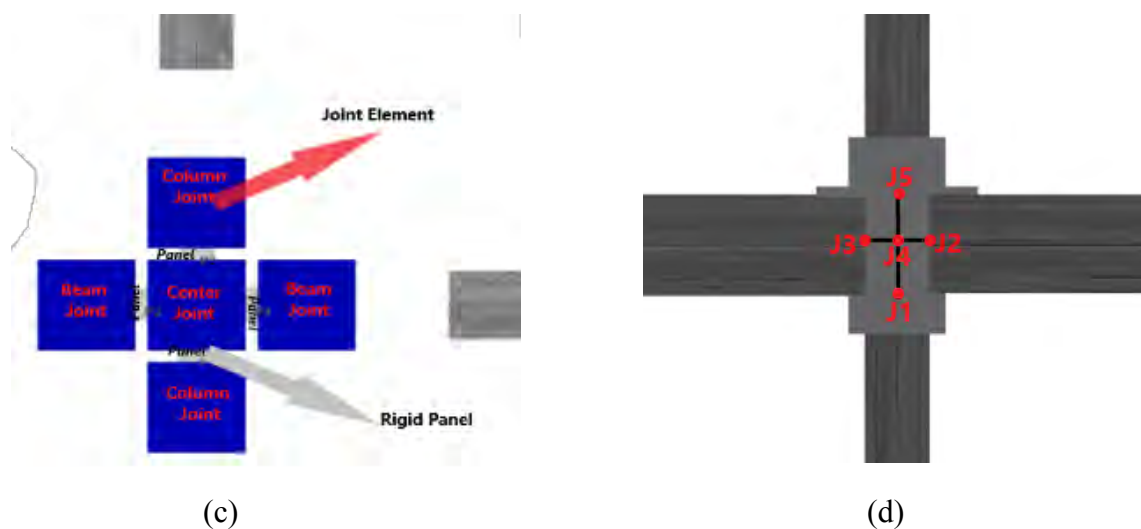


Figure 8: (a) Beam-Column Joint Model (Lowes et al., 2003) (b) Proposed SeismoStruct Joint Model (c) Joint model in SeismoStruct (d) Joint model in SeismoStruct showing how it connects to the beams and columns

In SeismoStruct, all kinds of springs are modelled by defining a Joint Element. The Joint Element is a 3D element with uncoupled axial, shear and moment actions that can be used to model, for instance, pinned or flexible beam-column connections (Seismosoft, 2020a). The joint element connects two initially coincident structural nodes, and require the definition of an independent force-displacement (or moment-rotation) response curve for each of its local six degrees-of-freedom ($F1, F2, F3, M1, M2, M3$). The proposed element incorporates a shear panel component, bar-slip, and interface-shear components, as shown in Figure 8(a). The Takeda curve is adopted to model the force-deformation response of the springs for the link element. This method was also adapted and verified by Yu (2006) and Seismosoft (2020b). The calibration of the moment-rotation relationships for the bar-slip mechanism is based on empirical methods, which were extensively described by Yu (2006), by defining the bar slip and spring force and then converting that to moment-rotation. The joint shear strength is defined using another empirical approach used by Amirsardari (2018). The interface-shear spring is derived from a shear stress vs. slip response curve, defined by Walraven (1994) at a crack width of 0.1mm (the effect of varying crack width during loading will follow the hysteretic rules of the Takeda curve). This is then multiplied by the cross-sectional area of the beam and column to convert the relation to shear force vs. slip relationship (Yu, 2006; Walraven, 1994). The joint panels are modelled as elastic frame elements (elfrm) with very high stiffness ($EA, EI, \text{ and } GJ$ of $1E+19$), to model the panels as rigid, based on the verification done by Seismosoft (2018b). Thus, the 3 link elements defined using the calibrated properties (Beam, Column and Center), as shown in figure 8(c), can now connect the inelastic frame elements (infrmFBPH) to the elastic panel zone. Note that joint J4 is usually where the beams and columns would be directly connected if the joint is not modelled explicitly. J3 and J2 are offset half the width of column, and J1 and J5 are offset half the width of the beam, and then each of those joints are connected to the center joint, J4, via the rigid panel. Then the link elements are connected as shown in Figure 8 (c), which is an expanded view of Figure 8(d). The final input into the software, inclusive of all parameters defined is represented in Figure 9.

Help

Element Class: Joint_BM

Ok

Cancel

Curve Types

F1

lin_sym

F2

lin_sym

F3

Takeda

M1

lin_sym

M2

Takeda

M3

lin_sym

Yielding strength F_y

1.6200E+006

Initial stiffness K_y

4.8000E+006

Post yielding to initial stiffness ratio

1.000000E-006

Outer loop stiffness degradation factor

1.000000E-005

Inner loop stiffness degradation factor

1.00

Curve Parameters

F1 Parameter(s)

1.0000E+016

F2 Parameter(s)

1.0000E+016

F3 Parameter(s)

1.6200E+006 4.8000E+006 1.000000E-006 1.000000E-005 1.00

M1 Parameter(s)

1.0000E+016

M2 Parameter(s)

1.6200E+006 3.1240E+011 0.01741953 0.10 0.90

M3 Parameter(s)

1.0000E+016

Represents bar-slip of beam

Represents interface-shear spring

(a)

Help

Element Class: Joint_COL(1-2)

Ok

Cancel

Curve Types

F1

Takeda

F2

lin_sym

F3

lin_sym

M1

lin_sym

M2

Takeda

M3

lin_sym

Yielding strength F_y

720000.00

Initial stiffness K_y

4.8000E+006

Post yielding to initial stiffness ratio

1.000000E-006

Outer loop stiffness degradation factor

1.000000E-005

Inner loop stiffness degradation factor

1.00

Curve Parameters

F1 Parameter(s)

720000.00 4.8000E+006 1.000000E-006 1.000000E-005 1.00

F2 Parameter(s)

1.0000E+016

F3 Parameter(s)

1.0000E+016

M1 Parameter(s)

1.0000E+016

M2 Parameter(s)

2.4940E+008 2.7711E+011 0.01902065 0.10 0.90

M3 Parameter(s)

1.0000E+016

Represents bar-slip of Column

Represents Interface shear spring

(b)

Help

Element Class: Joint_Int_Cen

Ok

Cancel

Element Type: link: Link element

Curve Types

F1

lin_sym

F2

lin_sym

F3

lin_sym

M1

lin_sym

M2

Takeda

M3

lin_sym

Yielding strength F_y

8.0304E+007

Initial stiffness K_y

6.1773E+010

Post yielding to initial stiffness ratio

0.03019744

Outer loop stiffness degradation factor

1.000000E-005

Inner loop stiffness degradation factor

1.00

Curve Parameters

F1 Parameter(s)

1.0000E+016

F2 Parameter(s)

1.0000E+016

F3 Parameter(s)

1.0000E+016

M1 Parameter(s)

1.0000E+016

M2 Parameter(s)

8.0304E+007 6.1773E+010 0.03019744 1.000000E-005 1.00

M3 Parameter(s)

1.0000E+016

Represents the shear panel rotational spring

(c)

Figure 9: Definition of Link element in SeismoStruct, showing what each parameter represents, for (a) Beam Joint (b) Column Joint (c) Centre Joint

3. MODELLING VALIDATION

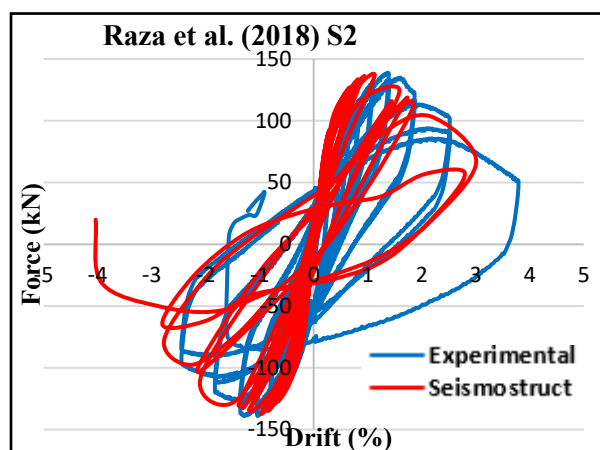
To ensure that the proposed modelling methodology model the limited ductile and inelastic behaviour, it was verified against experimental data of different wall, columns, and joint specimens, sharing the same inelastic behaviour that was expected of these existing Australian buildings. Their material properties can be seen in Tables 2 and 3. The comparison between the experimental results and the results from analyses using SeismoStruct are shown in Figures 10-12. Most of them display a reasonably accurate match in terms of backbone curve and maximum force reached, as well as displacement at collapse. The software is consistently seen to provide slightly more conservative results. Note that some elements with single layer of reinforcement faced convergence issues, so the element was modelled with 2 layers instead of one, while maintaining the same reinforcement ratio. It is also noted that decreasing the timesteps for time-history analyses can help with any convergence issues that may arise with these limited ductility models. The software is not capable of truly capturing the gradual decrease in cyclic loading; thus, the hysteresis usually displays a sudden degradation whereas experimental results show a more controlled gradual decrease, but overall, it is matching with the experimental results.

Table 2: Material Properties of Verified Columns and Walls

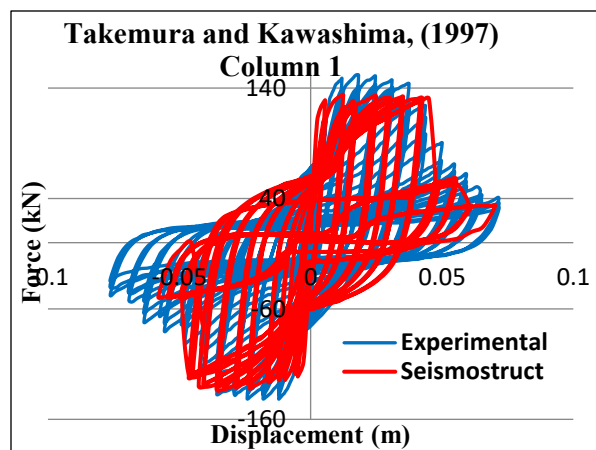
ID								Longitudinal		Transverse	
		b	h	L	N	f'_c	f_y	#bars	d	d	s
		(mm)	(mm)	(m)	(kN)	(MPa)	(MPa)		(mm)	(mm)	(mm)
Raza et al. (2018)	S2	250	300	2.55	1485	65	565	6	16	10	150
Takemura and Kawashima (1997)	1	400	400	1.25	157	35.9	363	20	12.7	6	70
Altheeb (2016)	Wall1	120	0.9	2.75	190	35.2	500	5	10	10	200
Menegon (2018)	S01	400	1.2	2.6	585	41.9	532	14	20	12	250

Table 3: Material Properties of Verified Joints

Joints	Joint Type	f'_c (MPa)	Beam		Column		Joint Aspect Ratio (h_b/h_c)
			ρ_l	f_y (MPa)	ρ_l	f_y (MPa)	
Panteledis et al. (2002) Unit 3	Exterior	34	0.032	468	0.024	468	1
Shafaei et al. (2014) J2	Exterior	24.7	0.02	460	0.02	460	1

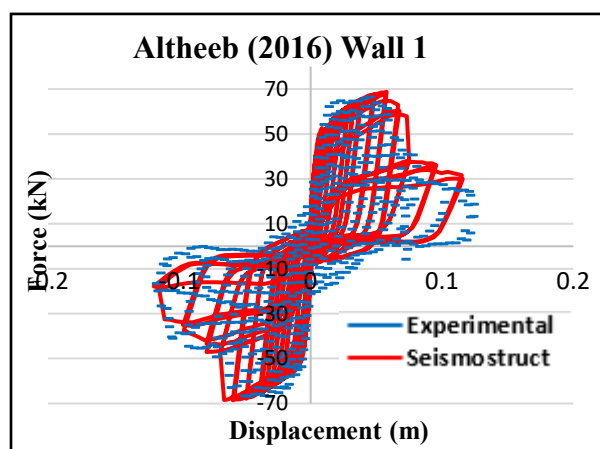


(a)

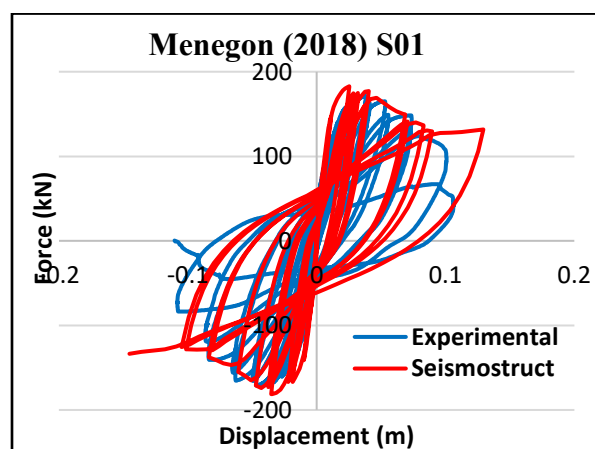


(b)

Figure 10: **Columns** Hysteresis Loop Experimental data versus SeismoStruct results (a) Raza et al. (2018) S2 (b) Takemura and Kawashima, (1997) Column 1

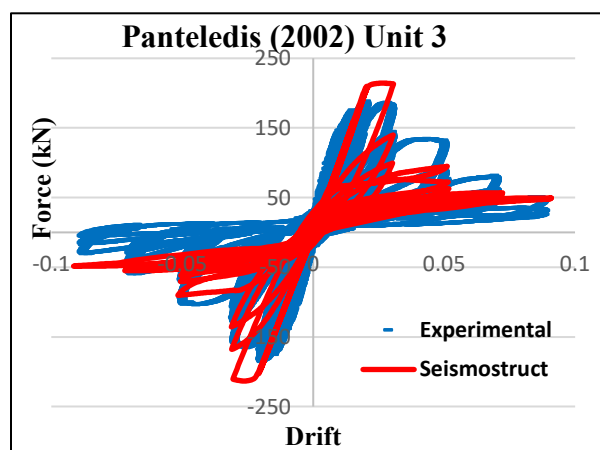


(a)

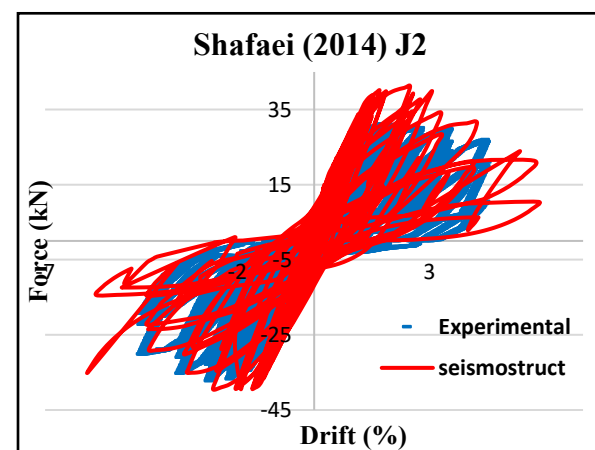


(b)

Figure 11: **Walls** Hysteresis Loop Experimental data versus SeismoStruct results (a) Altheeb (2016) wall 1 (b) Menegon (2018) Wall 1



(a)



(b)

Figure 12: **Joints** Hysteresis Loop Experimental data versus SeismoStruct results (a) Panteledis (2002) Unit 3 (b) Shafaei (2014) J2

4. ACCELEROGRAMS

Time history analyses are only informative and relevant if the accelerograms chosen suitable for the scenario, i.e. an accurate representation of a real-life earthquake that is likely to happen in the region of the analysed building, which is Melbourne, Australia, which has a low-to-moderate seismicity. This method for predicting these ground motions was developed by Hu et al. (2019) in which the Conditional Mean Spectrum(CMS) methodology is applied , by using a diverse range ground motion prediction equations (GMPes) along with a component attenuation model (CAM) (Lam et al., 2010; Hu et al., 2018). This results in accelerograms for bedrock conditions being retrieved from global ground motion database, followed by scaling to optimize the match with the respective CMS as target spectra. Moreover, soil amplification affect is analysed with soil profiles generated from borehole records taken from capital cities in South East Australia. 12 accelerograms are generated for a 2500-year return period, 4 accelerograms each for three boreholes from different sites, as shown in Table 4. Table 5 shows the earthquakes that were used as a basis for the generation of the used accelerograms. The earthquake loading is applied in the y-direction, as shown in Figure 13.

Table 4: Borehole information for accelerogram generation

Borehole	City	Site Class	Natural Period (s)	Soil Depth (m)	Average Shear Wave Velocity (m/s)
1	Melbourne	C	0.52	31.5	244.5
2	Melbourne	C	0.40	30.6	303.8
3	Melbourne	D	1.05	60	228.2

Table 5: Earthquakes used to generate required accelerograms

Earthquake Name	Year	Station Name	Magnitude	Mechanism	R_{rup} (km)	V_{s30} (m/s)	Scaling Factor
San Fernando	1971	Fairmont Dam	6.61	Reverse	30.19	634.33	1.29
Coalinga-01	1983	Parkfield - Gold Hill 3W	6.36	Reverse	39.12	510.92	0.73
Whittier Narrows-02	1987	Mt Wilson - CIT Seis Sta	5.27	Reverse Oblique	19.78	680.37	0.99
Loma Prieta	1989	Hayward City Hall - North	6.93	Reverse Oblique	55.11	735.44	1.28

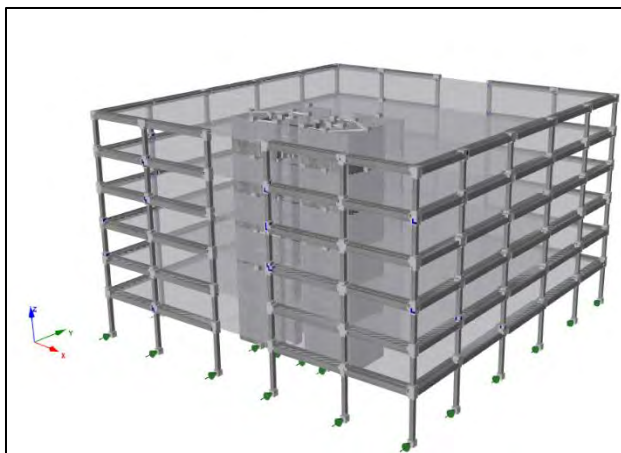


Figure 13: Earthquake loading applied in the Y-direction on the case study building

5. PERFORMANCE LEVELS

Seismic assessment of the case study building was evaluated by studying its response with respect to specified performance levels. Performance levels define the extent of damage considered to be acceptable for different limit states. The same performance levels adapted in the AlAzem (2019) paper are utilized in this study. The choice of these levels has been based on the recommendations in Amirsardari et al. (2020) and Menegon et al. (2019). When the first component of the building reaches a specific structural damage limit or when the inter-storey drift limit has been exceeded, the structure was considered to be at that performance level. Figure 6 demonstrates how the performance levels are displayed in SeismoStruct.

Table 6: Summary of Performance levels selected (Amirsardari, 2020 and Menegon, 2019)

Performance Level	Damage State	Description	Force-Displacement Behaviour	Concrete Strain	Steel Strain	Inter-Storey Drift (%)
Immediate Occupancy	Slight	<ul style="list-style-type: none"> Minimal Damage. Hairline cracks. 	Point of First Yield	0.0015	0.005	0.2
Damage Control	Moderate (Repairable)	<ul style="list-style-type: none"> Concrete reaches maximum strength Minimal reinforcement inelastic strains 	Effective Yield	0.002	0.01	0.5
Life Safety	Extensive (Severe)	<ul style="list-style-type: none"> Large cracks and spalled concrete Partial collapse of some elements 	Lateral Load Failure (20% reduction from peak strength)	0.006	0.05	1

Collapse Prevention (confined)	Complete (Partial Collapse)	<ul style="list-style-type: none"> • Loss of stability • Imminent danger of collapse 	Ultimate drift (50% reduction from peak strength)	0.008	0.1	2
--	--------------------------------	--	--	-------	-----	---

6. RESULTS

Table 7 shows the performance levels reached, and for which limits (Concrete/steel strain, drifts) for the 12-time history analyses run. It also shows the number and type of elements that have reached those limits, for each respective level of the building. This will help illustrate a clearer idea of the most vulnerable parts of the structure.

Table 7: Results of each Accelerogram Scenario

Performance level reached			Number of Element failures and Failure Type																					
			Borehole 1- Class C							Borehole 2- Class C							Borehole 3- Class D						Drift Exceeded	No. Walls
			No. Columns						Drift Exceeded	No. Columns						No. Columns								
			L1	L2	L3	L4	L5	L6		L1	L2	L3	L4	L5	L6	L1	L2	L3	L4	L5	L6			
Acc 1	Slight Damage	Concrete Strain Reached	10	18	20	20	20	14	At L2, L3, L4,L5,L6	7	12	18	14	12	4	9	20	20	20	17	8	At L2, L3, L4,L5,L6	2 walls @ reinforcement strain	
	Moderate Damage		5	12	17	15	12	1			7	12	10	1		5	11	14	14	8				
Acc 2	Slight Damage	Concrete Strain Reached	4	11	12	11	3	At L2	3	8	11	8	2		10	16	20	17	12	5				
	Moderate Damage			2	4						1				3	11	12	11	4					
Acc 3	Slight Damage	Concrete Strain Reached		4	4	1				3	4	1				2	3							
	Moderate Damage										7	12	10	1										
Acc 4	Slight Damage	Concrete Strain Reached	7	12	12	11	3	1		2	7	9	4	1		6	10	12	9	2				
	Moderate Damage			7	7	2										2	4							



Figure 14: Vulnerable elements reaching specified performance limit states (Slight Damage-Yellow, Moderate Damage-Orange) shown on the case study building for Acc 2 of Borehole 3- Class D soil

The case study building being studied has been designed and detailed in accordance with AS3600 and AS1170.4, with a design return period of 500 years. It is also interesting to note the individual elements that reach specific performance criteria, as that would indicate what would fail in the case of an earthquake of a high intensity.

Under the 12 accelerograms scenarios, the case study building remained at either slight or moderate damage, with the columns, across a few levels, reaching concrete yield, as observed from Table 7. Levels 2 and 4 specifically had the highest number of columns reaching these performance criteria compared to the other floors. No beams reached any of the performance criteria, 2 of the smaller wall sections reached slight damage due to reinforcement strain being reached, and only in three scenarios did the building exceed the slight damage inter-story drift of 0.2%. In some of the cases where the building has reached moderate damage state, it was due to only a few columns having surpassed the point of first yield, such as Acc 1 of Borehole 1. Figure 14 shows a scenario where some columns are at slight and moderate damage.

Overall, the results obtained by these analyses show that buildings designed according to AS1170.4, for earthquake action, provides a satisfactory performance under earthquake loading, even though it is limited ductile. When compared to the buildings analysed in Alazem et al. (2019) and Amirsardari et al. (2020), which were Australian representative buildings designed prior 1995 and had all of the features of a limited ductile building (weak confinement, low reinforcement levels, weak column-strong beam, poor anchorage), it becomes clear that this case study building has a much better performance. This can be attributed to a better design when compared to those designed prior 1995 i.e., higher reinforcement content, two layers of reinforcement, better confinement, and higher concrete material strengths. Furthermore, this case study building only had columns, and only one wall section in one scenario, reached the maximum of moderate damage performance levels whereas the buildings analysed by Alazem and Amirsardari had several of their elements (columns, beams, walls and joints) reach the collapse prevention performance limit.

7. CONCLUSION

In this study, a case study building representative of Melbourne structures, designed in accordance with AS3600 and AS1170.4, was analysed under time-history analysis. Accelerograms for the time-history analysis were generated used CAM based on the work of Hu et al. (2019), for soil classes C and D. All the elements that have the potential of inelasticity and causing failure in the structure have been included in the model, such as shear degradation and joint modelling that takes into account bar-slip, interface shear and shear panels. Thus, the structure has been modelled with techniques that have been verified from literature and experimental results and calibrated to ensure the most accurate behavior representation. Furthermore, performance limits have been defined to be able to describe the behavior of the structure and its elements in terms of damage levels, strains, and drifts. The results obtained showed that the structure, under several earthquake scenarios, remains fully functional, and thus it can be said that buildings designed to withstand earthquake loading behave much better than those that are not. Even if this case study building was somewhat vulnerable, it still provided a satisfactory performance under earthquake loading.

8. ACKNOWLEDGMENTS

Special thanks to the Bushfire and Natural Hazards CRC, for funding and supporting this research, as a part of a larger initiative aimed at making existing Australian buildings safer.

9. REFERENCES

- Almeida, J. P., Tarquini, D., & Beyer, K. (2016). Modelling Approaches for Inelastic Behaviour of RC Walls: Multi-level Assessment and Dependability of Results. *Archives of Computational Methods in Engineering*, 23(1), 69-100.
- Altheeb, A. H. (2016). Seismic drift capacity of lightly reinforced concrete shear walls. (PhD Thesis), Department of Infrastructure Engineering, The University of Melbourne.
- Amirsardari, A., Lumantarna, E., Rajeev, P., Goldsworthy, H.M. (2020): Seismic Fragility Assessment of Non-ductile Reinforced Concrete Buildings in Australia, *Journal of Earthquake Engineering*, DOI: 10.1080/13632469.2020.1750508
- Amirsardari, A. (2018), *Seismic assessment of reinforced concrete buildings in Australia including the response of gravity frames*, PhD Thesis, Department of Infrastructure Engineering, The University of Melbourne.
- Amirsardari, A., Goldsworthy, H. M., & Lumantarna, E. (2017). Seismic site response analysis leading to revised design response spectra for Australia. *Journal of Earthquake Engineering*, 21(6), 861-890. doi: 10.1080/13632469.2016.1210058
- Belejo, A., Bento, R., & Bhatt, C. (2012). Comparison of different computer programs to predict the seismic performance of SPEAR building by means of the SPEAR building Pushover by means Analysis of Pushover Analysis. 15 WCEE Lisboa 2012.
- Beyer, K., Dazio, A., & Priestley, M. J. N. (2008). Inelastic Wide-Column Models for U-Shaped Reinforced Concrete Walls. *Journal of Earthquake Engineering*, 12(sup1), 1- 33. doi: 10.1080/13632460801922571
- Bolea, O. (2016). The Seismic Behaviour of Reinforced Concrete Frame Structures with Infill Masonry in the Bucharest Area. *Energy Procedia*, 85, 60-76.
- Carvalho, G., Bento, R., & Bhatt, C. (2013). Nonlinear static and dynamic analyses of reinforced concrete buildings—comparison of different modelling approaches. *earthquake and structures (EAS)*, An International Journal, Techno-Press, Editors-in-Chief: Stavros A. Anagnostopoulos (European ed.), Izuru Takewaki (Asia-Pacific ed.), Jerome P. Lynch (American ed.), 4(5), 451-470.
- Caterino, N. & Cosenza, E. (2018). A multi-criteria approach for selecting the seismic retrofit intervention for an existing structure accounting for expected losses and tax incentives in Italy. *Engineering Structures*. 174. 840-850. 10.1016/j.engstruct.2018.07.090.
- Dias-Oliveira, J., Rodrigues, H., & Varum, H. (2016). Seismic assessment of low ductile RC structures: buildings from before the modern seismic codes. *Engineering Computations*, 33(4), 1282-1307.
- Hoult, R. (2017), *Seismic Assessment of Reinforced Concrete Walls in Australia*, PhD thesis, University of Melbourne, Melbourne.
- Hoult, R., Goldsworthy H.M., and Lumantarna, E. (2015). *Improvements and difficulties associated with seismic assessment of infrastructure in Australia*. Paper presented at the Bushfire and Natural Hazards CRC & AFAC conference, Adelaide, Australia.
- Hu, Y., Lumantarna, E., Lam, N., Menegon, S., Wilson, J. (2018). Development of a soil site ground motion database for Australian seismic structural design. In *Proceedings of the 2018 Australian Earthquake Engineering Society Conference in Perth*.

- Hu, Y., Lam, N.T.K., Menegon, S. (2019) . ‘Ground Motion Accelerograms for Nonlinear Time History Analysis in Low-to-Moderate Seismicity Regions’ Australian Earthquake Engineering Society, Newcastle, New South Wales, Nov 29- Dec 1, viewed 13 October, 2020, <https://aees.org.au/wp-content/uploads/2019/12/26-Yiwei-Hu.pdf>
- Lam, N., Wilson, J., & Tsang, H. H. (2010). Modelling earthquake ground motions by stochastic method. *Stochastic control*, 475-492.
- Lowes, L.N., Mitra, N., Altoontash, A. [2003] “A beam-column joint model for simulating the earthquake response of reinforced concrete frames,” Pacific Earthquake Engineering Research Center, University of California, Berkeley.
- Martini, S. (2007). Design Verification of a Force- and Displacement-Based Designed Torsionally Unbalanced Wall Building. (Masters of Earthquake Engineering), Rose School, Pavia, Italy.
- Mander J.B., Priestley M.J.N., Park R. (1988) "Theoretical stress-strain model for confined concrete," *Journal of Structural Engineering*, Vol. 114, No. 8, pp. 1804-1826
- Menegon, S. J., Tsang, H. H., & Wilson, J. L. (2015). *Overstrength and ductility of limited ductile RC walls: from the design engineers perspective*. Paper presented at the Proceedings of the Tenth Pacific Conference on Earthquake Engineering, Sydney, Australia
- Menegon, S.J. (2018), *Displacement Behaviour of Reinforced Concrete Walls in Regions of Lower Seismicity*, PhD Thesis, Department of Infrastructure Engineering, The University of Melbourne.
- Menegon, S.J., Tsang, H.H., & Lumantarna, E et al. (2019) Framework for seismic vulnerability assessment of reinforced concrete buildings in Australia, *Australian Journal of Structural Engineering*, 20:2, 143-158.
- Monti, G., Filippou, F.C., Spacone, E. [1996] “Analysis of hysteretic behaviour of anchored reinforcing bars,” *ACI Structural Journal*, Vol. 94, No. 3, pp. 248-261.
- Pantelides, C. P., Hansen, J., Nadeau, H., & Reaveley, L. D. (2002). Assessment of reinforced concrete building exterior joints with substandard details *PEER 2002/18*: Pacific Earthquake Engineering Center, University of California, Berkeley.
- Priestley, M. J. N., Calvi, G. M., & Kowalsky, M. J. (2007). Displacement-based seismic design of structures. Pavia, Italy, IUSS Press.
- Alazem R., Lumantarna E., Lam N.T.K., Menegon, S. (2019). ‘Development of Cost-Effective Mitigation Strategy for Limited Ductile Reinforced Concrete Buildings’ Australian Earthquake Engineering Society, Newcastle, New South Wales, Nov 29- Dec 1, viewed 13 October, 2020, <https://aees.org.au/wp-content/uploads/2019/12/55-Raneem-Alazem.pdf>
- Raza S., Menegon S.J., Tsang H.H., Wilson J.L. (2018) Experimental Testing Program to Investigate the Collapse Drift Capacity of Limited Ductile High-Strength RC Columns. In: Wang C., Ho J., Kitipornchai S. (eds) *ACMSM25. Lecture Notes in Civil Engineering*, vol 37. Springer, Singapore
- SeismoSoft. (2020a). SeismoStruct User Manual 2020 (Release: 3 Build: 1). Retrieved from https://seismosoft.com/wp-content/uploads/prods/lib/SeismoStruct-2018-User-Manual_ENG.pdf
- SeismoSoft. (2020b). SeismoStruct Verification Report 2020 (Release: 3 Build: 1). Retrieved from <https://seismosoft.com/wp-content/uploads/prods/lib/SeismoStruct-2020-Verification-Report.pdf>

- Standards Australia. (2007). AS 1170.4-2007: Structural design actions, Part 4: Earthquake actions in Australia. Sydney, NSW: SAI Global
- Standards Australia. (2009). AS 3600-2009 Concrete Structures. Sydney, NSW: SAI Global
- Takemura, H., and Kawashima, K., "Effect of loading hysteresis on ductility capacity of reinforced concrete bridge piers", *Journal of Structural Engineering* 43 1997, pp. 849-858.
- Walraven, J.C. [1994] "Rough Cracks Subjected to Earthquake Loading," *Journal of Structure Engineering, ASCE*, Vol.120, No. 5, pp. 1510-1524.
- Xiao, Y., and Martirosyan, A., "Seismic Performance of High-Strength Concrete Columns", *Journal of Structural Engineering*, March, 1998, pp. 241-251.
- Yu, W. (2006) *Inelastic modeling of reinforcing bars and blind analysis of the benchmark tests on beamcolumn joints under cyclic loading*, Thesis, European school for advanced studies in reduction of seismic risk.

An Atlas of Earthquake Scenarios for Australian Localities

Joanne Stephenson², Trevor Allen^{1,2}, Dan Clark², Kaya Wilson² and Richelle Spry²

1. Corresponding Author. Email: trevor.allen@ga.gov.au
2. Geoscience Australia, Canberra, Australia

Abstract: Geoscience Australia has produced an Atlas of Australian earthquake scenarios (the Atlas) to support planning and preparedness operations for emergency management agencies. The Atlas provides earthquake scenarios represent realistic “worst-case” events that may impact population centres around Australia. Such scenarios may also support seismic risk assessments for critical infrastructure assets to inform remediation actions that could be taken to improve resilience to rare seismic events in Australia. The Atlas of seismic scenarios uses the underlying science and data of the 2018 National Seismic Hazard Assessment (NSHA18) to identify the magnitudes and epicentre locations of these hypothetical earthquakes.

Locations and magnitudes of earthquake scenarios are based upon deaggregation of the NSHA18 hazard model. The USGS ShakeMap software is used to produce ground motion intensity fields with the shaking levels being modified by seismic site conditions mapped at a national scale. Fault sources are incorporated into the Atlas where the magnitude of a given scenario exceeds a threshold magnitude of 6.0 and where the rupture length is likely to be longer than 10 km. If a scenario earthquake is located near a known fault within the Australian Neotectonic Features database, a partial or full-length rupture is modelled along the mapped fault.

The Atlas generated two scenarios for each of the 160 localities across Australia. The scenarios are based on some of the most likely earthquake magnitude-distance combinations estimated at each site. Output products include shaking contours for a range of intensity measures, including peak acceleration and velocity, as well as response spectral acceleration for 0.3, 1.0 and 3.0 seconds. Also included are raster images and the associated metadata used for generating the scenarios.

Keywords: emergency planning and preparedness, earthquake scenario, ShakeMap

INTRODUCTION

Geoscience Australia receives regular requests from local and state emergency services for realistic “worst-case” earthquake scenarios to be created for population centres and/or locations of high-importance infrastructure. Deterministic scenarios, such as these, are also now desired by guidelines for the design and maintenance of major infrastructure assets throughout Australia (e.g., Australian National Committee on Large Dams, 2019). To date there is no comprehensive catalogue of earthquake scenarios for Australia, so the scenarios are provided on a needs, and often *ad hoc*, basis. The Atlas of Earthquake Scenarios presented here, aims to streamline the production of hypothetical earthquake events and allow relevant stakeholders to self-serve information they require. The earthquake scenarios represent realistic “worst-case” events to support planning operations for emergency management agencies.

Often during seismic risk assessment, extreme magnitudes are chosen for planning purposes. However, such events may not be scientifically plausible in the region and may lead to significant misinterpretation of the potential risk. Alternatively, previous well-known events can be used for future planning purposes; for example, the Newcastle earthquake of 1989 which resulted in 13 fatalities and over 160 reported injuries (Daniell and Love, 2010; Walker, 2010). Using events such as these is a popular approach as they lend credibility to the chosen scenario with the impacts of such historical events being well documented. Therefore, emergency managers can benchmark planning scenarios based on historical analogues (e.g., Chesnais *et al.*, 2019). However, planning and preparedness must also focus on emergency management and the general public being ready for earthquake events that have not yet occurred in historic times – those with a low probability but with extreme consequences.

One-hundred and sixty localities across Australia were identified to develop earthquake scenarios (Figure 1). These localities were chosen principally because they are moderate-to-large population centres and thus represent a societal risk, or are sites that have strategic value to the Australian economy, such as liquefied natural gas and port facilities (e.g., Chesnais *et al.*, 2019).

The following document outlines the: 1) process of breaking down the 2018 National Seismic Hazard Assessment (NSHA18; Allen *et al.*, 2018; 2020) into the key contributors to the seismic risk for a location via deaggregation (e.g., McGuire, 1995; Bazzurro and Cornell, 1999); 2) scientific considerations and limitations of the deaggregation processes; and 3) creation of the scenarios using the United States Geological Survey’s (USGS) ShakeMap software (Wald *et al.*, 1999; Worden *et al.*, 2017).

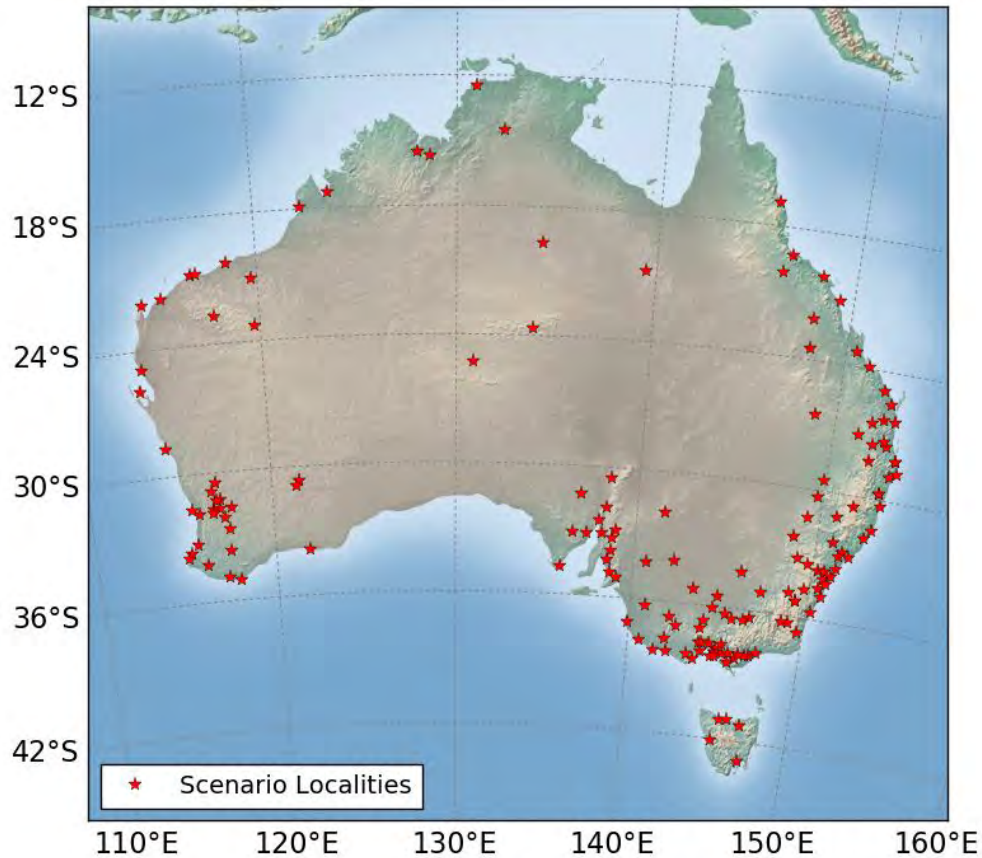


Figure 1: A map showing the 160 localities across Australia for which earthquake scenarios are generated.

HAZARD DEAGGREGATION

Deaggregation (or disaggregation) of seismic hazard can assist with understanding the hazard posed to communities from earthquakes (McGuire, 1995; Bazzurro and Cornell, 1999) by taking a seismic hazard model (i.e., the source rate model and ground-motion characterisation model; e.g., Gerstenberger *et al.*, 2020) and returning the predominant earthquake sources that contribute to the seismic hazard at any location. The key contributors are provided in terms of magnitude (M) and distance (R) from the chosen location (e.g., Figure 2). The hazard can also be broken down into the components of the parameter, ε – the number of standard deviations that the logarithmic spectral acceleration differs from the mean (McGuire, 1995; Bazzurro and Cornell, 1999). Spatial deaggregations (e.g., Harmsen and Frankel, 2001) can also be returned to identify the location of earthquake sources on a 2D longitude-latitude grid (e.g., Figure 3).

Deaggregation of the NSHA18 was performed on the National Computational Infrastructure (NCI; nci.org.au) using the OpenQuake-engine (Version 3.7; Pagani *et al.*, 2014). After comprehensive testing, deaggregation parameters were chosen to provide an optimal trade-off between computational expense and deaggregation resolution. The chosen parameters were longitude-latitude bins of 0.2 degrees (approximately 20 km). Magnitude bins were also set to 0.2 units. Therefore, the location and magnitudes of earthquake scenarios contributing to the seismic hazard at any one locality are dependent on this discretisation level. For the deaggregation process, a response spectral acceleration S_a (0.2 s) was chosen. A period of

0.2 s was chosen rather than peak ground acceleration (PGA) because it was considered that this intensity measure was representative of the shortest effective period of buildings and structures that are designed using the standard (Building Seismic Safety Council, 2009), and that this reflects the ground-motion intensity measure to which a large proportion of structures in Australia would be sensitive. A 1/10,000 annual exceedance probability (AEP) was chosen as a low enough exceedance probability to produce scenarios that could be considered realistic worst case, or “black swan” events. However, it is worth noting that the ground-motions characterised at the locality from the chosen scenarios do not correspond to the probabilistic 1/10,000 AEP ground-motions – it is merely a method to draw upon a broader range of potential scenario magnitudes. The output from deaggregation consists of a list of longitude-latitude pairs, magnitudes and probabilities. The scenarios were selected from these lists as explained in the following section.

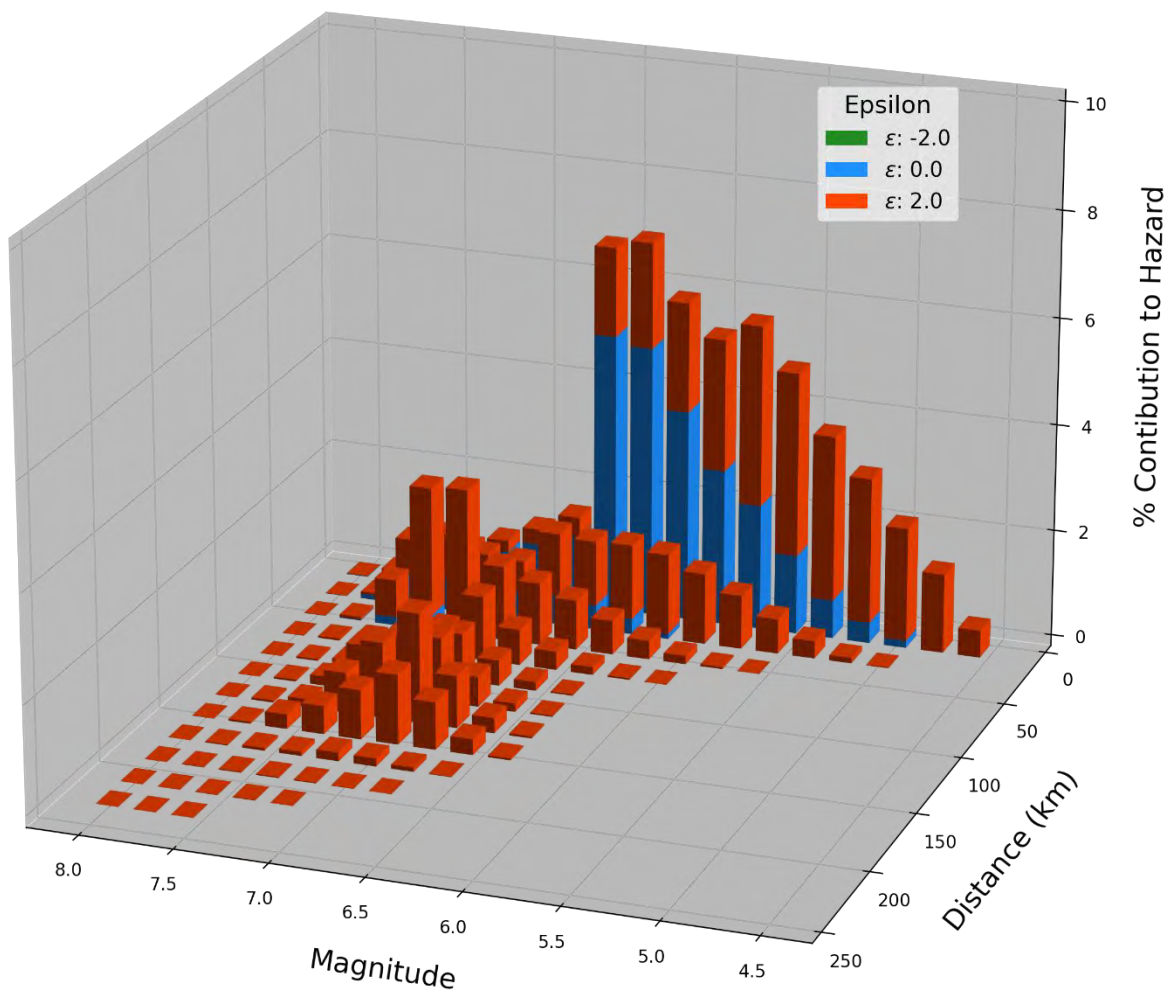


Figure 2: 3D Magnitude-distance-epsilon deaggregation for the city of Melbourne for $S_a = 0.2$ s at the 0.5% in 50 year exceedance.

SCENARIO SELECTION

The selection of ShakeMap scenarios was guided by deaggregation of the NSHA18 using the OpenQuake-engine (Pagani *et al.*, 2014). Two scenarios at each location were chosen for

inclusion in the Atlas of Earthquake Scenarios. In the first instance, the location with the highest total contribution to the S_a (0.2 s) seismic hazard at the 1/10,000 AEP was selected from the magnitude, longitude, latitude deaggregation by summing the probabilities in each location bin and picking the modal location. Secondly, the magnitude which has the largest contribution to the hazard is selected at the modal location. For the second scenario, further logic was applied to allow for magnitude diversity in scenarios at the same location. For example, if the second chosen scenario is less than 0.5 units above or below the initial scenario, another value will be selected recursively until the magnitudes are suitably different and exceed the ± 0.5 magnitude unit threshold. The second scenario may be either of higher or lower magnitude relative to the primary scenario.

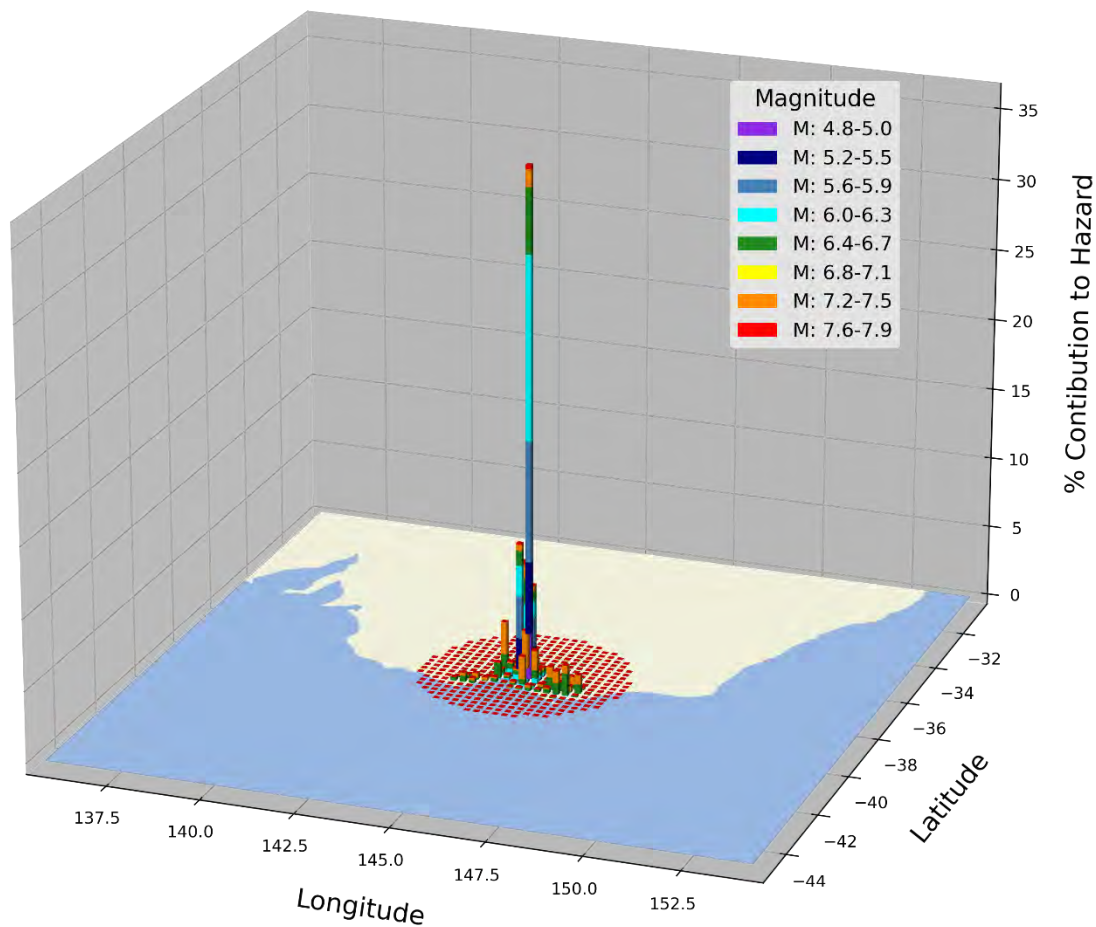


Figure 3: Magnitude-longitude-latitude deaggregation for the city of Melbourne performed for $S_a = 0.2$ s for 0.5% in 50 year probability of exceedance.

It is important to note that the magnitude of the scenarios may not necessarily be reflective of the absolute hazard level. For regions where the hazard is affected by fault sources, larger-magnitude earthquakes might be selected for scenarios given the faults' increased influence on hazard calculations at lower exceedance probabilities. Further, while the magnitude of the scenarios may be comparable between regions, the average return period for each of these earthquakes might vary significantly.

SHAKEMAP

ShakeMap is a software package developed and maintained by the USGS primarily to provide situational awareness on earthquake impacts and information on ground motion intensities in near-real-time (Wald *et al.*, 1999; Worden *et al.*, 2017). Although the primary purpose of ShakeMap is to generate maps for ground motion in the real time following a significant earthquake, it can also be used to generate ground motions following hypothetical earthquake events, or scenarios. Such scenarios can be assigned a magnitude, hypocentre depth, location and/or fault rupture geometry. This allows the tool to be used for preparedness and disaster planning exercises, as well as post-earthquake response and recovery.

Using ShakeMap V4.0 (Worden *et al.*, 2017), ground motions are calculated relative to the modelled point or fault source using four equally weighted ground-motion models (GMMs) as used for non-cratonic regions in the NSHA18 (Allen *et al.*, 2020). These GMMs, a subset of those used in the NSHA18, include two models based on Australian crustal conditions (Somerville *et al.*, 2009; Allen, 2012), one model developed for eastern North America (Atkinson and Boore, 2006) and one shallow active crustal model (Boore *et al.*, 2014). The calculated shaking intensities were modified using time-averaged shear wave velocity values in the upper 30 m (V_{S30}) estimated from the site-specific Australian Seismic Site Conditions Map (ASSCM; McPherson, 2017), combined with weighted amplification factors embedded within two of the selected GMMs (Atkinson and Boore, 2006; Boore *et al.*, 2014).

Conversion to macroseismic intensity uses the conversion equations of Worden *et al.* (2012).

USE OF FINITE-FAULT SOURCES

As the magnitude of the selected scenario increases, it follows that the rupture dimensions of the host fault will also increase (e.g., Wells and Coppersmith, 1994; Leonard, 2014). When estimating the ground-motion field from an earthquake scenario, the shaking intensities are dependent upon the closest distance to the fault rupture. Consequently, for scenarios of larger magnitude, source finiteness is important in order to constrain the ground shaking field. Following the approach of Allen *et al.* (2008), finite-fault sources are assigned for scenarios of $M \geq 6.0$.

If the selected earthquake scenario met the magnitude criteria, the preferred scenario location was manually assessed relative to the simplified neotectonic features as used within the NSHA18 (Clark *et al.*, 2016). Once a feature was selected, a fault source was traced along the surface projection of the feature for a rupture length determined by the Leonard (2014) magnitude-length scaling relationship for stable continental region ruptures. For dipping features, the dip angles were assigned based on those in the Neotectonic Features database (Clark, 2012). Where a dip value and direction were not present in the database, dip angles and directions were assumed to be consistent with those in the surrounding region. The assumed dip angles vary by neotectonic domain (Clark *et al.*, 2012), but 40 ± 10 degrees would be a typical range. Figure 4 shows a comparison of the ground motion intensity fields caused by a point source compared to a fault-source scenario of the same magnitude. The greater intensity levels for the scenario with the finite-fault are a consequence of the

presumed up-dip rupture (and thus shorter source-to-site distance) of the earthquake from the rupture centroid at the preferred focal depth of 10 km.

In instances where there is no record of a nearby neotectonic feature, yet the highest contributor to the hazard is an event over M 6.0, fault geometries have been inferred based on current understanding of the geology and horizontal crustal stress field of the region (e.g., Rajabi *et al.*, 2017).

Table 1 outlines the data products available for download from the Atlas of Earthquake scenarios. More detail concerning output files from USGS ShakeMap can be found at: http://usgs.github.io/shakemap/manual4_0/ug_products.html#sec-products-4.

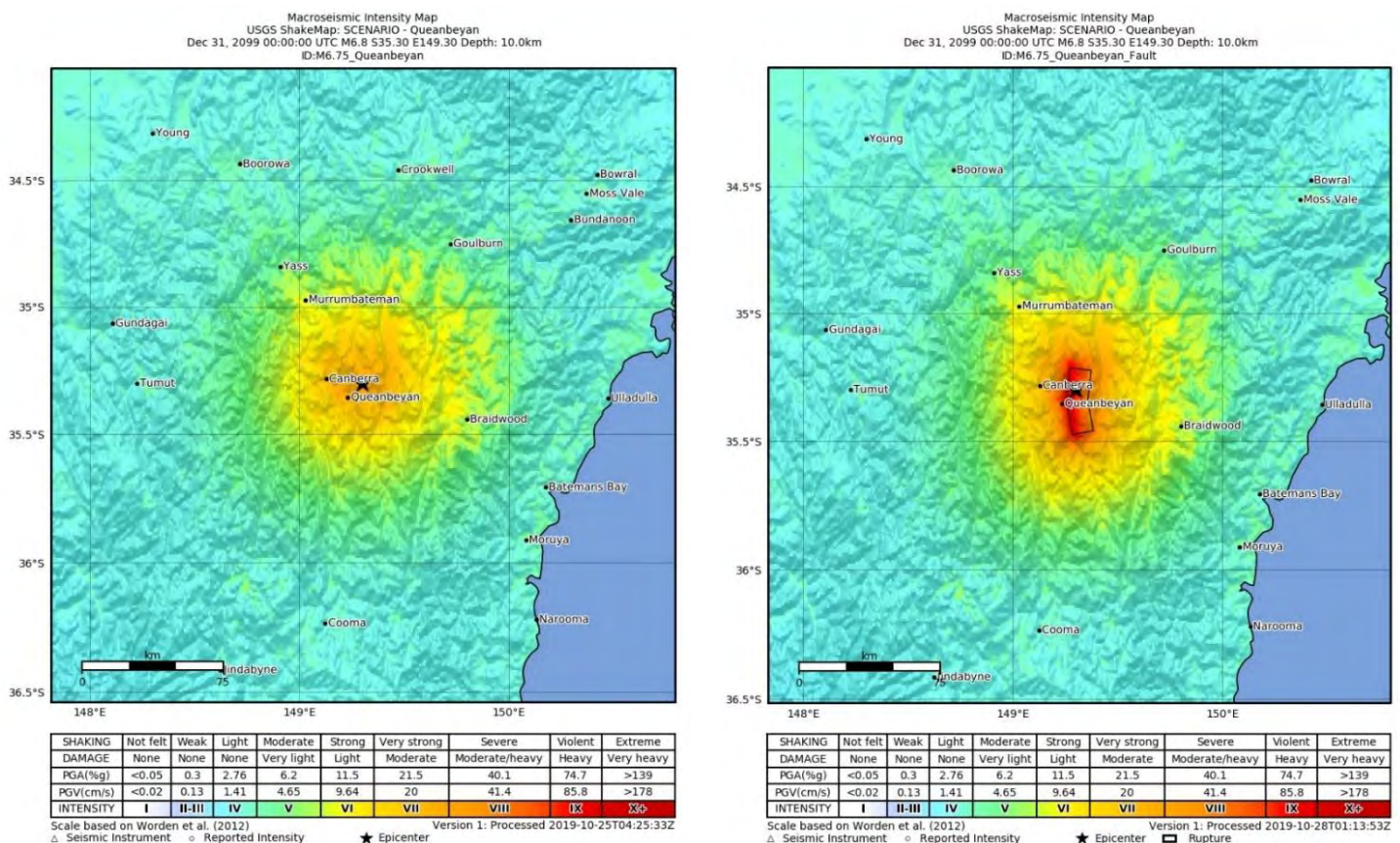


Figure 4 Two ShakeMaps showing macroseismic intensity for two M 6.75 earthquakes near Queanbeyan, NSW. Left: using a point source at a depth of 10 km. Right: Using a finite source on the Queanbeyan Fault.

CONCLUSION

Geoscience Australia has produced an Atlas of Australian earthquake scenarios (the Atlas) to support planning and preparedness operations for emergency management agencies. The Atlas provides earthquake scenarios which represent realistic “worst-case” events for locations and magnitudes based up on deaggregation of the NSHA18 at the 1 in 10,000 AEP. USGS ShakeMap (Wald *et al.*, 1999; Worden *et al.*, 2017) is used to produce ground motion intensity fields for each region of interest, with the rock reference site condition being modified by the Australian Seismic Site Class Model (McPherson, 2017). Fault sources are

incorporated into the Atlas where the magnitude exceeds a threshold magnitude of 6.0, where the rupture length is likely to be longer than 10 km.

The Atlas contains two scenarios for each of the 160 selected localities across Australia with a range of formats and ground-motion intensity measure types. The scenarios will support planning and preparedness operations for emergency management agencies, as well as provide guidance for deterministic seismic hazard assessments.

Table 1: List of data products available for download within the Atlas of Seismic Scenarios.

Data format	Purpose/Information
pga.pdf or pga.jpg	PDF or JPEG format showing a peak ground acceleration contours in units of %g.
pgv.pdf or pgv.jpg	PDF or JPEG format showing a peak ground velocity contours in units of cm/s.
intensity.pdf or intensity.jpg	Macroseismic intensity map reporting likely seismic intensity for the given scenario.
shape.zip	ZIP folder containing all contours as shape files for use in GIS software.
cont_<IM>.json	Ground-motion contours for different intensity measures (IMs) in json format
psa0p3.pdf or psa1p0.jpg	0.3 second peak acceleration map in units of %g
psa1p0.pdf or psa1p0.jpg	1.0 second peak acceleration map in units of %g
psa3p0.pdf or psa1p0.jpg	3.0 second peak acceleration map in units of %g
grid.xml	Extensible Markup Language (xml) files that contain gridded data for all intensity measures, and V_{S30} values extracted from the ASSCM
uncertainty.xml	Extensible Markup Language (xml) files that contain an estimate of the ShakeMap uncertainty field (Wald <i>et al.</i> , 2008)
info.json	Metadata for ShakeMap calculation, including GMMs used.
*Mag_Lon_Lat.csv and * Mag_Dist_Eps.csv	Spatial and magnitude-distance-epsilon deaggregation outputs in csv format for a 0.5% probability of exceedance in 50 years
<CITY>_Mag_Lon_Lat.png and * <CITY>_Mag_Dist_Eps.png	Spatial and magnitude-distance-epsilon deaggregation 3D plots in png format for a 0.5% probability of exceedance in 50 years

ACKNOWLEDGMENTS

The authors thank Tanja Pejić and Sharmin Shamsalsadati and two anonymous reviewers of this manuscript. We publish with the permission of the Chief Executive Officer of Geoscience Australia.

REFERENCES

- Allen, T., Griffin, J., Leonard, M., Clark, D., and Ghasemi, H. (2018). The 2018 National Seismic Hazard Assessment for Australia: model overview, *Geoscience Australia Record 2018/27*, Canberra, 126 pp, doi: 10.11636/Record.2018.027.
- Allen, T. I. (2012). Stochastic ground-motion prediction equations for southeastern Australian earthquakes using updated source and attenuation parameters, *Geoscience Australia Record 2012/69*, Canberra, 55 pp.
- Allen, T. I., Griffin, J. D., Leonard, M., Clark, D. J., and Ghasemi, H. (2020). The 2018 National Seismic Hazard Assessment of Australia: quantifying hazard changes and model uncertainties, *Earthq. Spectra* Vol 36, No S1, pp 5-43, doi: 10.1177/8755293019900777.
- Allen, T. I., Wald, D. J., Hotovec, A. J., Lin, K., Earle, P. S., and Marano, K. D. (2008). An Atlas of ShakeMaps for selected global earthquakes, *U.S. Geological Survey Open-File Report 2008-1236*, Golden, CO, 35 pp.
- Atkinson, G. M., and Boore, D. M. (2006). Earthquake ground-motion prediction equations for eastern North America, *Bull. Seismol. Soc. Am.* Vol 96, pp 2181-2205, doi: 10.1785/0120050245.
- Australian National Committee on Large Dams (2019). Guidelines for design of dams and appurtenant structures for earthquake, *Australian National Committee on Large Dams*, 136 pp.
- Bazzurro, P., and Cornell, C. A. (1999). Disaggregation of seismic hazard, *Bull. Seismol. Soc. Am.* Vol 89, No 2, pp 501-520.
- Boore, D. M., Stewart, J. P., Seyhan, E., and Atkinson, G. M. (2014). NGA-West 2 equations for predicting PGA, PGV, and 5%-damped PSA for shallow crustal earthquakes, *Earthq. Spectra* Vol 30, No 3, pp 1057-1085, doi: 10.1193/070113EQS184M.
- Building Seismic Safety Council (2009). NEHRP recommended seismic provisions for new buildings and other structures, *FEMA P-750*, Washington, D.C., 388 pp.
- Chesnais, M., Green, A., Phillips, B., Allen, T., Edwards, M., Sexton, J., and Weatherley, D. (2019). Queensland state earthquake risk assessment, *Queensland Fire and Emergency Services*, 39 pp.
- Clark, D. (2012). *Neotectonic Features Database*, Retrieved 2 October, 2020, from <http://pid.geoscience.gov.au/dataset/ga/74056>.
- Clark, D., Leonard, M., Griffin, J., Stirling, M., and Volti, T. (2016). Incorporating fault sources into the Australian National Seismic Hazard Assessment (NSHA) 2018, *Australian Earthquake Engineering Society 2016 Conference*, Melbourne, Victoria.
- Clark, D., McPherson, A., and Van Dissen, R. (2012). Long-term behaviour of Australian stable continental region (SCR) faults, *Tectonophysics*. Vol 566-567, pp 1-30, doi: 10.1016/j.tecto.2012.07.004.
- Daniell, J. E., and Love, D. (2010). The socio-economic impact of historic Australian earthquakes, *Australian Earthquake Engineering Society 2010 Conference*, Perth, Western Australia, pp 18.
- Gerstenberger, M. C., Marzocchi, W., Allen, T., Pagani, M., Adams, J., Danciu, L., Field, E., Fujiwara, H., Luco, N., Ma, K.-F., Meletti, C., and Petersen, M. (2020). Probabilistic seismic hazard analysis at regional and national scale: state of the art and future challenges, *Rev. Geophys.* Vol 58, pp e2019RG000653, doi: 10.1029/2019RG000653.

Harmsen, S., and Frankel, A. (2001). Geographic deaggregation of seismic hazard in the United States, *Bull. Seismol. Soc. Am.* Vol 91, No 1, pp 13–26, doi: 10.1785/0120000007.

Leonard, M. (2014). Self-consistent earthquake fault-scaling relations: update and extension to stable continental strike-slip faults, *Bull. Seismol. Soc. Am.* Vol 104, No 6, pp 2953–2965, doi: 10.1785/0120140087.

McGuire, R. K. (1995). Probabilistic seismic hazard analysis and design earthquakes: closing the loop, *Bull. Seismol. Soc. Am.* Vol 85, No 5, pp 1275-1284.

McPherson, A. A. (2017). A revised seismic site conditions map for Australia, *Geoscience Australia Record 2017/12*, Canberra, doi: 10.11636/Record.2017.012.

Pagani, M., Monelli, D., Weatherill, G., Danciu, L., Crowley, H., Silva, V., Henshaw, P., Butler, R., Nastasi, M., Panzeri, L., Simionato, M., and Vigano, D. (2014). OpenQuake Engine: An open hazard (and risk) software for the Global Earthquake Model, *Seismol. Res. Lett.* Vol 85, No 3, pp 692–702, doi: 10.1785/0220130087.

Rajabi, M., Tingay, M., Heidbach, O., Hillis, R., and Reynolds, S. (2017). The present-day stress field of Australia, *Earth-Sci. Rev.* Vol 168, pp 165-189, doi: 10.1016/j.earscirev.2017.04.003.

Somerville, P., Graves, R., Collins, N., Song, S.-G., Ni, S., and Cummins, P. (2009). Source and ground motion models for Australian earthquakes, *Australian Earthquake Engineering Society 2009 Conference*, Newcastle, New South Wales.

Wald, D. J., Lin, K.-W., and Quitoriano, V. (2008). Quantifying and qualifying ShakeMap uncertainty, *U.S. Geological Survey Open-File Report 2008-1238*, 27 pp.

Wald, D. J., Quitoriano, V., Heaton, T. H., Kanamori, H., Scrivner, C. W., and Worden, C. B. (1999). TriNet "ShakeMaps": Rapid generation of peak ground-motion and intensity maps for earthquakes in southern California, *Earthq. Spectra* Vol 15, No 3, pp 537-556, doi: 10.1193/1.1586057.

Walker, G. (2010). Comparison of the impacts of Cyclone Tracy and the Newcastle earthquake on the Australian building and insurance industries, *Aust. J. Struct. Eng.* Vol 11, No 3, pp 283-293, doi: 10.1080/13287982.2010.11465073.

Wells, D. L., and Coppersmith, K. J. (1994). New empirical relationships among magnitude, rupture length, rupture width, rupture area, and surface displacement, *Bull. Seismol. Soc. Am.* Vol 84, No 4, pp 974-1002.

Worden, C. B., Gerstenberger, M. C., Rhoades, D. A., and Wald, D. J. (2012). Probabilistic relationships between ground-motion parameters and Modified Mercalli Intensity in California, *Bull. Seismol. Soc. Am.* Vol 102, No 1, pp 204-221, doi: 10.1785/0120110156.

Worden, C. B., Thompson, E. M., Hearne, M., and Wald, D. J. (2017). ShakeMap V4 Manual: technical manual, user's guide, and software guide, *U. S. Geological Survey*, <https://usgs.github.io/shakemap/>.

Seismic performance categories for post-installed fasteners in Australia

Anita Amirsardari¹, Tilak Pokharel², Jessey Lee³ and Emad Gad⁴

1. Corresponding Author. Research Fellow, Faculty of Science, Engineering and Technology, Swinburne University of Technology, VIC 3122.
Email: aamirsardari@swin.edu.au
2. National Technical Manager, Australian Engineered Fasteners and Anchors Council (AEFAC), Swinburne University of Technology, VIC 3122.
Email: tilakpokharel@swin.edu.au
3. Training and Development Manager, Australian Engineered Fasteners and Anchors Council (AEFAC); Lecturer, Faculty of Science, Engineering and Technology, Swinburne University of Technology, VIC 3122.
Email: jesseylee@swin.edu.au
4. Professor and Dean of School of Engineering, Faculty of Science, Engineering and Technology, Swinburne University of Technology, Swinburne University of Technology, VIC 3122. Email: egad@swin.edu.au

Abstract

Post-installed fasteners in concrete require prequalification which involves tests and assessment procedures to define their performance. Under seismic actions the prequalification requirements and hence the selection of suitable seismic performance categories for fasteners is highly dependent on the damage conditions of the concrete substrate. This study provides an overview of the work that is currently being undertaken to develop recommendations for selecting seismic performance categories for post-installed fasteners in Australia. Firstly, a summary of international practice is presented. Then, a rapid assessment of reinforced concrete buildings is conducted to determine the expected extent of damage to building components for various conditions. Based on the findings two forms of criteria are recommended for selecting seismic performance categories for fasteners.

Keywords: Prequalification requirements, fastening, anchors, seismic assessment, reinforced concrete buildings.

1. INTRODUCTION

Post-installed fasteners in concrete do not have predictable capacities for all possible failure mechanisms and require prequalification which involves tests and assessment procedures to define their performance. Significant research has been conducted internationally (e.g., Europe and USA) to develop prequalification requirements for fasteners which has resulted in different levels of prequalification based on the application of the fasteners. Under seismic actions it has been highlighted that the performance of post-installed fasteners is highly dependent on the damage state of the concrete substrate which is related to expected crack widths and the opening and closing nature of the crack.

In Australia work is being instigated by the Australian Engineered Fasteners and Anchors Council (AEFAC) to develop provisions for seismic prequalification requirements and design of fasteners. AEFAC was formed in 2012 to improve the quality and safety of the Australian fastener industry. It initiated the first deemed-to-comply design provisions for safety-critical fastenings to concrete which was published in 2015 as a technical specification, SA TS 101 (Standards Australia, 2015) and in 2018 as the Australian standard for the design of post-installed and cast-in fastenings in concrete, AS 5216 (Standards Australia, 2018). The provisions in AS 5216 are based on the European prequalification requirements and design methodology. Previous work has been undertaken to investigate the direct adoption of the European specification for selecting seismic performance categories for fasteners which defines the necessary level of prequalification (Heath et al., 2016; Lee et al., 2018; Pokharel et al., 2019). It has been highlighted that a direct adoption may not be applicable for Australia due to the difference in seismicity, detailing and construction practice.

This study provides an overview of the work that is currently being undertaken to develop recommendations for selecting seismic performance categories for post-installed fasteners in Australia. An overview of international seismic prequalification requirements and specification criteria for selecting seismic performance categories is provided. This is then followed by a rapid assessment of reinforced concrete (RC) buildings in Australia to evaluate the expected extent of damage to building components at various intensities of earthquakes. The findings are used to develop a simple specification for Australia which is similar to European practice. A comparison of the different approaches adopted by standards/codes is presented and finally, recommendations and conclusions are provided for Australia.

2. REVIEW OF INTERNATIONAL PRACTICE

The following subsections provide an overview of the prequalification requirements for fasteners and the design specifications for selecting the level of prequalification required for seismic applications. The prequalification requirements discussed in this paper assume that the fasteners will be located outside of regions where yielding of reinforcement and spalling of concrete may occur, i.e., the plastic hinge regions for flexural RC members. This is reflected in the prequalification testing conditions under which the fasteners' performance is examined, namely the limits for the crack widths of the concrete substrate. The crack widths within the plastic hinge region can be significantly larger as seismic energy is dissipated through yielding of reinforcement

and spalling of concrete. Hence, special design of connections needs to be considered in these regions.

2.1 Europe

In Europe, the prequalification requirements for fasteners are published by the European Organisation for Technical Assessment (EOTA) and are stated in European Assessment Documents (EAD) or Technical Reports (TR). For static and quasi-static actions, the prequalification requirements are dependent on whether the fasteners are to be used in cracked or uncracked concrete (e.g., EAD 330232 (EOTA, 2016a) for mechanical fasteners and EAD 330499 (EOTA, 2017) for chemical fasteners). For cracked concrete, the fasteners are tested in crack widths of approximately 0.3 mm which generally corresponds to the maximum crack widths recommended for serviceability requirements. For seismic actions, two performance categories are specified: C1 and C2 (EOTA, 2016b). The tests conducted for C1 involve pulsating tension and alternating shear loading of the fastener in a static crack with a maximum width of 0.5 mm. For C2, similar tests are conducted for a static crack with a maximum width of 0.8 mm and the fastener is also loaded in tension in crack cycling conditions to simulate the opening and closing nature of cracks during seismic loading. The maximum crack width of 0.8 mm is representative of the upper-bound crack width for a member at initial yield which is the maximum expected stress in the reinforcement bars outside of the hinge region (Hoeler, 2006; Mahrenholtz et al., 2017).

EN 1992-4:2018 (European Committee for Standardization (CEN), 2018) sets the provisions for the design of fastenings for use in concrete structures, however each member state can set their own requirements. The recommended performance categories are provided in Table 1, they are dependent on: the design ground acceleration on rock ground conditions (a_g), the soil factor (S), and the building importance class.

Table 1: Recommended seismic performance categories for fasteners in accordance with EN 1992-4:2018

Seismicity class	$a_g S$	Importance class			
		I	II	III	IV
Very low	$a_g S \leq 0.05g$	No seismic performance category required			
Low	$0.05g < a_g S \leq 0.1g$	C1	C1 ¹ or C2 ²	C1 ¹ or C2 ²	C2
> Low	$a_g S > 0.1g$	C1	C2	C2	C2

1: For connecting non-structural components to structures | 2: For connecting structural components to structures

2.2 Germany

In Germany, the specification of the prequalification requirement for fasteners is provided in the National Annex to EN 1992-4, DIN EN 1992-4/NA:2019-04 (German Institute for Standardization (DIN), 2019). The seismic performance category is specified based on the permissible crack width of the concrete substrate under seismic load conditions. In addition, it is suggested that the behaviour factor (q) (i.e., seismic force reduction factor to account for inelastic behaviour) adopted in the design of the structure may be used to estimate the crack widths outside of the plastic hinge regions and discontinuity areas. A summary of the minimum requirements is provided in Table 2.

Table 2: Minimum seismic performance categories required for fasteners in accordance with DIN EN 1992-4/NA:2019-04

Crack width under earthquake design load	Prequalification requirement	Behaviour factor used to estimate crack widths
$w_k \leq 0.3 \text{ mm}$	No seismic performance category required	$q = 1.0$
$w_k \leq 0.5 \text{ mm}$	C1	$1.0 < q \leq 1.5$
$w_k \leq 0.8 \text{ mm}$	C2	$1.5 < q \leq 3.0$
$w_k > 0.8 \text{ mm}$	Fastenings in plastic hinge regions not covered by DIN EN 1992-4	

w_k : is the characteristic crack width (95 percentile) in accordance with DIN EN 1992-1-1 and DIN 1992-1-1NA

2.3 USA

The USA provisions for the prequalification of fasteners in concrete are provided in American Concrete Institute standards (ACI) or Acceptance Criteria published by the International Code Council Evaluation Service (ICC-ES). In general, they are similar to the European requirements for non-seismic applications and C1 for seismic performance category (e.g. ACI 355.2 (2007) and ACI 355.4 (2011) for mechanical and chemical fasteners, respectively). The USA is also in the process of introducing a second seismic performance category which will be similar to the C2 category in Europe (ICC-ES, 2020). Furthermore, the USA has seismic prequalification requirements for anchor channels corresponding to C1 category (ICC-ES, 2019). Similar requirements are yet to be developed by Europe.

The seismic design provisions are provided in ASCE/SEI 7 (2016), which sets the minimum design loads and associated criteria for buildings and other structures. ACI 318M-14 (2014) provides the building code requirements for structural concrete, including anchoring into concrete. Seismic design and prequalification requirements are necessary for fasteners in structures which are assigned to Seismic Design Category (SDC) C, D, E, or F. The assignment of SDC is based on seismic demand and risk category of the structure, where seismic demand is defined by the spectral acceleration response in the short period range and at one second. The risk category is similar to the importance level of buildings adopted in the European and Australian codes. It is expected that with the introduction of the second seismic performance specifications will be extended to consider the structural ductility demand or to include a performance based approach (ICC-ES, 2020).

2.4 Australia

The Australian earthquake loading standard, AS 1170.4:2007 (R2018) (Standards Australia, 2007, Reconfirmed 2018) defines the level of seismic demand for a site via: (i) the probability factor (k_p), (ii) the earthquake hazard design factor (Z), and (iii) the spectral shape factor as a function of period ($C_h(T)$) which incorporate the effects of local site conditions for sites varying from hard rock conditions (Class A) to very soft soil conditions (Class E). Currently, there are no provisions for the seismic prequalification or design of fasteners. The provisions in AS 5216:2018 are relevant for service-load conditions of the structure and the fasteners are required to be prequalified in accordance with relevant EADs. Work is being conducted to extend the scope of AS 5216 to include prequalification and design provisions for seismic applications. In addition, research is being undertaken at Swinburne University of Technology to further investigate the performance of fasteners under seismic actions (Neupane et al., 2020).

3. RAPID ASSESSMENT OF AUSTRALIAN RC BUILDINGS

The review of international practice demonstrated that each nation/region has provided specifications for selecting seismic performance categories based on their own seismicity, design and construction practice. To assist with the development of specifications for Australia a rapid assessment is conducted to evaluate the seismic performance of a wide range of buildings.

3.1 Seismic demand - interstorey drift

The maximum interstorey drift is approximated for buildings which have walls or combined wall and frame as the seismic force resisting system with plan-asymmetry. This type of construction is very typical in Australia and particularly vulnerable under seismic actions. The method discussed in Tsang et al. (2009) is adopted to estimate the maximum interstorey drift which assumes plan and vertical regularity. The prediction uses the displacement response spectrum (RSD), building height and estimated effective natural periods of the building. It also incorporates the contribution of the second mode. The effect of plan-asymmetry is incorporated by using the amplification factors recommended in Lumantarna et al. (2019) based on an extensive parametric study of typical Australian buildings with uni-axial and bi-axial plan-asymmetry. The equation for calculating the maximum interstorey drift is provided in Eq. 1.

$$\text{Maximum interstorey drift} = \theta = \lambda_{avg} \lambda_1 \lambda_2 \lambda_3 \frac{RSD(T_{1,eff})}{h_n} \quad \text{Eq. 1}$$

Where λ_{avg}	is the drift multiplier based on taking the reciprocal of the participation factor for the fundamental mode of vibration; it is recommended that $\lambda_{avg} = 1.5$.
λ_1	is the drift multiplier factor based on the shape of a parabola; it is recommended $\lambda_1 = 1.5$.
λ_2	is the drift multiplier to account for higher mode effects; the contribution of the second is particularly significant. $\lambda_2 = 0.35 + 2.0 \left(\frac{RSD(T_{2,eff})}{RSD(T_{1,eff})} \right) \geq 1.0$
λ_3	Plan-asymmetry amplification factors taken as 2.7, 2.1, and 1.6 in the acceleration-, velocity, and displacement-controlled regions of the response spectrum as suggested in Lumantarna et al. (2019).
$RSD(T_{1,eff})$	is the spectral displacement response at the effective fundamental modal period which is approximated as $1.5T_1$ (suitable for limited ductile buildings).
$RSD(T_{2,eff})$	is the spectral displacement response at the effective second modal period (approximated as $0.25T_{1,eff}$).
T_1	is the first fundamental building period calculated in accordance with AS 1170.4:2007 (R2018)
h_n	is the building height.

As an example, the predicted maximum interstorey drift versus the fundamental building period for $k_p Z$ of 0.08 g for various site classes is provided in Figure 1. It is noted that AS 1170.4:2007 (R2018) requires the interstorey drift to not exceed 1.5 % for buildings, however the results from the assessment approach show that the interstorey drifts can exceed 1.5 %. The discrepancy is due to the difference in the method to calculate interstorey drift and the rapid and conservative nature of the adopted approach to predict maximum interstorey drift demand.

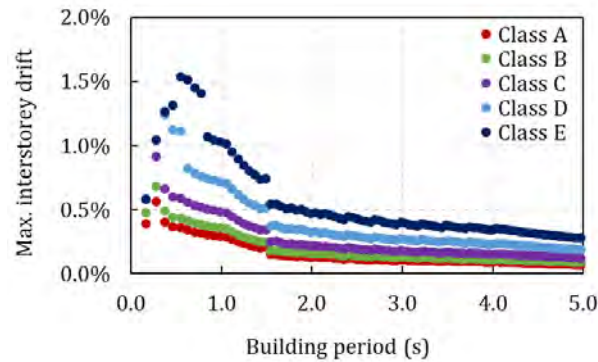


Figure 1: Maximum interstorey drift estimations for buildings for $k_p Z = 0.08$ g

Furthermore, the predicted maximum interstorey drifts may be related to simple parameters used to define seismic demand, namely the level of seismicity ($k_p Z$) and local site conditions. This will assist to develop a specification criterion for selecting fastener performance categories based on parameters that are similar to Eurocode (Table 1). It is noted that in AS 1170.4, the response spectra is defined using site amplification factors in the acceleration-controlled (F_a) and velocity-controlled (F_v) region of the spectra, the values are provided in Table 3. The relation between $k_p Z F_v$ is selected rather than $k_p Z F_a$ as it better distinguishes the estimated maximum interstorey drifts for different site conditions and different intensities of earthquakes. As an example, the maximum drift for a 5-storey building plotted against $k_p Z F_v$ is provided in Figure 2

Table 3: Site amplification factors in the acceleration- and velocity-controlled region of the spectra in accordance with AS 1170.4:2007 (R2018)

	Class A	Class B	Class C	Class D	Class E
F_a	0.80	1.00	1.25	1.25	1.25
F_v	0.80	1.00	1.42	2.25	3.50

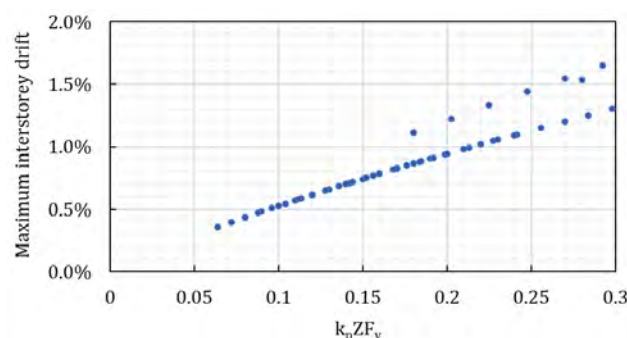


Figure 2: Maximum interstorey drift plotted against $k_p Z F_v$ for a 5-storey building

3.2 Recommended fastener performance categories

By assessing the expected level of damage to building components at different interstorey drifts, it is possible to specify the required seismic performance categories for fasteners. The suggested interstorey drift and corresponding fastener performance categories which is considered to be suitable for Australian building practice is provided in Table 4.

Table 4: Suggested fastener seismic performance category for maximum predicted interstorey drifts

Interstorey drift	Building component damage state	Fastener seismic performance category
$\leq 0.5\%$	Less than yield in plastic hinge regions.	Seismic prequalification of fasteners is not required for drift demands less than the component's yield capacity. This is because the element is essentially responding within its linear range and the stresses outside of the plastic hinge region will be significantly less than yield and therefore minimum damage is expected (i.e., small crack widths).
$< 0.5\% \text{ to } \leq 1.0\%$	Yield is reached in some building components, but the drift demand is significantly less than ultimate capacity.	C1 is recommended for deformation demands that may lead to yielding of some building components, however the drift demand is still significantly less than their ultimate capacity and hence significant damage outside of the plastic hinge region is not expected.
$\geq 1.0\%$	Full plastic hinges developing in some building components.	C2 is suggested for higher deformation demands as it is expected that yield limit will be reached just outside of the plastic hinge region and multiple moment reversals exceeding yield capacity may take place.

The interstorey drift limits in Table 4 are used to develop a criterion for selecting seismic performance categories for fasteners based on k_pZF_v . The maximum interstorey drift response for buildings ranging from 1- to 30-storeys are considered as they represent a common range of the building heights in Australia (the response of a 5-storey building has been provided in Figure 2). The 95th percentile is then used to determine the limits for k_pZF_v , the corresponding values for 0.5 % and 1.0 % interstorey drifts are approximately 0.09 g and 0.18 g, respectively. For the purpose of setting limits for standard/code application, 0.1 g and 0.18 g are the limiting values selected to directly define the seismic performance categories for Importance Level 2 buildings. In addition, the minimum requirement for Importance Level 3 and 4 are set to C1 and C2, respectively as failure of connections in these buildings will have significantly greater consequence. A summary of the recommendations for each site class is provided in Table 5. 'Not applicable' has been written for cases for which a seismic performance category is not suitable for a certain site sub-soil class and/or k_pZ values. For example, C2 category is required for buildings located on site Class E for all k_pZ values (i.e., $k_pZ \geq 0.08g$).

Table 5: Minimum recommended seismic performance categories for fasteners.

Importance level	$(k_p Z)$ for site sub-soil class					Seismic performance category
	E	D	C	B	A	
2	Not applicable	Not applicable	Not applicable	≤ 0.1	≤ 0.12	Seismic prequalification is not required
	Not applicable	0.08	≤ 0.12	< 0.1 to ≤ 0.18	< 0.12 to ≤ 0.22	C1
	≥ 0.08	> 0.08	> 0.12	> 0.18	> 0.22	C2
3	Not applicable	0.08	≤ 0.12	≤ 0.18	≤ 0.22	C1
	≥ 0.08	> 0.08	> 0.12	> 0.18	> 0.22	C2
4	≥ 0.08					C2

4. COMPARISON BETWEEN DIFFERENT RECOMMENDATIONS

To provide comparison between the different international specifications, the required fastener performance categories for buildings with Importance Level 2 have been determined using: the proposal for Australia (Table 5), Eurocode, ACI, and the simplified approach of using the behaviour factor in the German Annex. It's noted that the $a_g S$ in Eurocode is considered to be equivalent to $k_p Z F_a$, the behaviour factor q is equivalent to μ/S_p where μ is the structural ductility factors and S_p is the structural performance factor in accordance with AS 1170.4, and SDCs in accordance with ASCE/SEI 7 (2016) are determined by using $k_p Z C_h(\text{short period})$ and $k_p Z C_h(1.0)$. The results are obtained for various site classes assuming that the buildings are located on a site with a hazard (Z) value of 0.08 g and have been designed with a ductility factor of 2 and hence have a μ/S_p value of 2.6. The summary of the results is presented in Figure 3. C0 represents the cases for which seismic prequalification is not necessary, C1/C2 represents requirements in EN 1992-4 when a distinction is made between structural and non-structural connections.

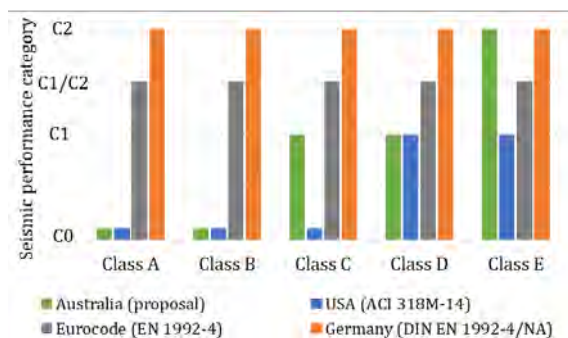


Figure 3: Comparison of fastener performance category requirement for an Importance Level 2 building in accordance with proposal for Australia, ACI (USA), EN 1992-4, and German Annex.

5. RECOMMENDATIONS AND CONCLUSIONS

The aim of this study is to provide recommendations for selecting seismic performance categories for post-installed fasteners in Australia. The following are recommended:

- Based on a rapid assessment approach a specification criterion has been developed using simple parameters which is comparable with international

approaches. It is suggested that the specification outlined in Table 5 to be provided as a guide for designers when selecting seismic performance categories for fasteners without requiring detailed structural analysis. Further research is required to refine the specifications. The recommendations are predominantly based on limited-ductile detailing and flexural response of building components assuming that fasteners will be located outside of plastic hinge regions.

- (ii) It is also recommended that designers are given the option to conduct detailed analysis of the structure to assess the expected level of damage to the concrete in which the fasteners are to be installed. This can be achieved by calculating the expected crack widths under seismic actions and considering the opening and closing nature of the crack. The requirements are consistent with the specifications in the German Annex which are widely accepted and are in line with the European prequalification requirements. The expected crack widths may be calculated by using the equation for maximum crack width (w) in accordance with AS 3600:2018. It's noted that outside of plastic hinge regions the stress in the reinforcement is not expected to exceed yield. The specified fastener performance category based on expected crack width is provided in Table 6.

Table 6: Minimum required seismic performance categories for fasteners

Crack width under design earthquake	Fastener seismic performance category
$w \leq 0.3mm$	Seismic prequalification is not required
$w \leq 0.5mm$	C1
$w \leq 0.8mm$	C2
$w > 0.8mm$ (plastic hinge region)	Not covered ¹

¹ For crack widths greater than 0.8 mm special design and alternative solutions may be required.

ACKNOWLEDGEMENT

The authors would like to acknowledge the technical input and ongoing financial support from the AEFAC Founding Members: Ancon Building Products, Hilti (Australia), Hobson Engineering, ramsetreid, Stanley Black and Decker (Powers) and Würth Australia, and Supporting Members: Allthread Industries, Icons, Simpson Strong-Tie (Australia), and United Fasteners. The authors would also like to acknowledge Professor Nelson Lam from the University of Melbourne for reviewing various aspects of this study and Associate Professor Hing-Ho Tsang from Swinburne University of Technology for providing guidance for the assessment component of this study.

REFERENCE

- American Concrete Institute. (2007). ACI 355.2-07: Qualification of post-installed mechanical fasteners in concrete. ACI
- American Concrete Institute. (2011). ACI 355.4-11: Qualification of post-installed mechanical fasteners in concrete. ACI
- American Concrete Institute. (2014). ACI 318M-14: Building code requirements for structural concrete (ACI 318M-14) and commentary (ACI 318RM-14). Michigan, United States of America: ACI

- American Society of Civil Engineers. (2016). ASCE/SEI 7-16: Minimum design loads and associated criteria for building and other structures. Virginia, United States of America: ASCE
- European Committee for Standardization (CEN). (2018). EN 1992-4: Eurocode 2: Design of concrete structures - Part 4: Design of fastenings for use in concrete.
- European Organisation for Technical Assessment. (2016a). EAD 330232-00-0601: Mechanical fasteners for use in concrete.
- European Organisation for Technical Assessment. (2016b). TR 049: Post-installed fasteners in concrete under seismic action.
- European Organisation for Technical Assessment. (2017). EAD 330499-00-0601: Bonded fasteners for use in concrete.
- German Institute for Standardization (DIN). (2019). DIN EN 1992-4/NA: National Annex - Nationally determined parameters - Eurocode: Design of concrete structures - Part 4: Designing of fastenings for use in concrete, English translation of DIN EN 1992-4/NA:2019-04. Berlin, Germany: Beuth Verlag GmbH
- Heath, D. J., Tsang, H.-H., Lee, J., & Gad, E. F. (2016). Seismic design provisions for fastenings to concrete in Australia. Paper presented at the Australian Structural Engineering Conference (ASEC), Brisbane, Australia.
- Hoeler, M. S. (2006). Behavior and testing of fastenings to concrete for use in seismic applications. (Doctor of Philosophy Thesis). University of Stuttgart, Stuttgart, Germany.
- International Code Council Evaluation Service. (2019). AC 232: Acceptance criteria for anchor channels in concrete elements.
- International Code Council Evaluation Service. (2020). AC510-0620-R2: Proposed New Acceptance Criteria for Steel Seismic Qualification of Post-installed Anchors in Concrete. California, United States of America: <https://icc-es.org/wp-content/uploads/2020/04/7-AC510-0620-pre.pdf>
- Lee, J., Pokharel, T., Tsang, H.-H., & Gad, E. F. (2018). Requirement for seismic performance of post-installed fastenings in Australia. Paper presented at the Australian Structural Engineering Conference (ASEC), Adelaide, Australia.
- Lumantarna, E., Lam, N., & Wilson, J. (2019). Predicting maximum displacement demand of asymmetric reinforced concrete buildings. Paper presented at the Australian Earthquake Engineering Society 2019 Conference, Newcastle, Australia.
- Mahrenholtz, P., Wood, R. L., Elgehausen, R., Hutchinson, T. C., & Hoehler, M. S. (2017). Development and validation of European guidelines for seismic qualification of post-installed anchors. *Engineering Structures*, 148, 497-508. doi:<http://dx.doi.org/10.1016/j.engstruct.2017.06.048>
- Neupane, C. C., Lee, J., Pokharel, T., Tsang, H.-H., & Gad, E. F. (2020). Development of seismic test set-up for fasteners in Australia. Paper to be presented at the Australian Earthquake Engineering Society Virtual Conference.
- Pokharel, T., Lee, J., Amirsardari, A., Tsang, H.-H., & Gad, E. (2019). Seismic prequalification and design of fasteners in Australia. Paper presented at the Concrete 2019, Sydney, Australia.
- Standards Australia. (2007). AS 1170.4-2007 (R2018): Structural design actions - Part 4: Earthquake actions in Australia. Sydney, Australia: SAI Global
- Standards Australia. (2015). SA TS 101: Design of post-installed and cast-in fastenings for use in concrete. Sydney, Australia: SAI Global
- Standards Australia. (2018). AS 5216: Design of post-installed and cast-in fastenings in concrete. Sydney, Australia: SAI Global
- Tsang, H.-H., Su, R. K. L., Lam, N. T. K., & Lo, S. H. (2009). Rapid assessment of seismic demand in existing building structures. *The Structural Design of Tall and Special Buildings*, 18, 427-439. doi:10.1002/tal.444

Seismic vulnerability analysis of highly populated building

Behnam Beheshtian¹, Hing-Ho Tsang², Javad Hashemi³

1. Ph.D. student, Department of Civil and Construction Engineering, Swinburne University of Technology, Melbourne, Australia
2. Corresponding Author. Associate Professor, Department of Civil and Construction Engineering, Swinburne University of Technology, Melbourne, Australia
3. Senior Lecturer, Department of Civil and Construction Engineering, Swinburne University of Technology, Melbourne, Australia

Seismic vulnerability analysis of highly populated buildings has attracted minimal attention in the literature. This type of buildings ranges from the entertainment arena and stadium to religious and community buildings, and often house a massive number of people. Highly populated buildings are of critical importance as a damaging earthquake can potentially cause considerable casualties and economic losses. It is stipulated in IBC-2012 and ASCE/SEI 7-10 that the collapse probability of highly populated buildings, Category III and IV structures, has to be limited to less than 1% in a 50-year life-span. This study aims to develop an understanding of the seismic vulnerability of this type of buildings that are located in regions of low-to-moderate seismicity. For this purpose, the main building of the AsiaWorld-Expo in Hong Kong, with a maximum capacity of over 30,000 people is investigated as a case study. A 3D numerical model of the structure is created using OpenSees, and a suite of hazard consistent earthquake scenarios are utilized for evaluating the seismic vulnerability of the building. The results show that the studied building could be moderately damaged at peak ground velocity (PGV) more than 0.6 m/s and extensively damaged at PGV exceeding 0.8 m/s.

Keywords: seismic vulnerability, highly populated buildings, nonlinear analysis, earthquake ground motion, limit state

1) Introduction

The seismic vulnerability assessment of highly populated buildings has attracted minimal attention in the literature. This type of buildings, ranging from the entertainment arena and stadium to religious and community buildings, can house a massive number of people. They are of critical importance as a damaging earthquake can potentially cause considerable casualties and repair/reconstruction costs and downtime. These structures, which are mainly the engineering symbols in a megacity, are categorized as high importance level and are designed based on higher load intensities in comparison to ordinary buildings.

Structural failure as a limit state can be defined based on various criteria, among those are individual risks or group risk or a combination of them (Steenbergen et al. 2015). For individual fatality risk, a value between 10^{-6} and 10^{-5} is deemed tolerable (Joint Committee on Structural Safety 1981; Melchers and Beck 2018; Tsang and Wenzel 2016). Based on IBC-2012 and ASCE/SEI 7-10 and considering collapse as a limit state, the 50-year life span collapse probability for Risk Category I and II structures is required to be 1%, and for category III and IV structures is advised to be less than 1% (HH Tsang 2016; Tsang et al. 2020).

The earthquake engineering community has mostly neglected the seismic vulnerability of highly populated buildings. Among the few publications, Gkologiannis et al. (2010) has analyzed the new football stadium of Panathinaikos F.C. in Votanikos, Athens, Greece, with an emphasis on the steel roof and its interaction with the underlying reinforced concrete structures. They realized that the steel roof should be designed so that its interaction with the underlying structures is minimized. After four significant earthquakes in Posočje, Uranjek et al. (2011) has presented the necessary strengthening procedures for churches of this region. Similarly, Cakir et al. (2015) has done seismic assessment of historical masonry mosques and specified the most critical parts of these structures. Dogangun and Sezen (2012) have investigated the seismic vulnerability of historical masonry buildings and presented the most common factors contributing to the deterioration of historical buildings. Sezen (2012) reported collapse of approximately 70% of masonry minarets and 10% of mosques in the cities of Düzce and Bolu after the 1999 earthquakes.

Consequence-based engineering and vulnerability analysis are relatively new approaches toward seismic risk reduction of structures (Abrams 2002). In these approaches, which incorporate probabilistic seismic analysis (PSA) concept, the performance of structure is investigated under a range of ground motion intensities. Cost-benefit analysis (CBA) is a tool for understanding the financial consequences of hazards, which can also be used for risk-informed decision making (Liel and Deierlein 2013). To this end, incremental dynamic analysis (IDA) and realistic ground motion records covering a wide range of return periods are employed to develop seismic fragility functions, which are the essential input for CBA. The ground motions could be chosen from a ground motion database or synthetically simulated for various scenarios (Menegon et al. 2019).

This study aims to develop an understanding of the seismic vulnerability of highly populated buildings that are located in regions of low-to-moderate seismicity. For this purpose, as a case study, the main building of the AsiaWorld-Expo located in Hong Kong, with a maximum capacity of over 30,000 people, is investigated. This structure is analysed for a suite of excitations with increasing intensities; thus, the building's vulnerability to various earthquake scenarios is realized.

2) Modeling of case study building

The AsiaWorld-Expo is a regular and symmetric structure that was originally designed and approved based on the Hong Kong Building (Construction) Regulations 1990 and the British Standards. The “Typical Hall Building” which is the main building of the AsiaWorld-Expo in Hong Kong has around 70,000 square meters area with a length of 360 meters and a width of 192 meters. The length of the building has columns spaced at 8.3 meters, and the width of the building has two main bays, each around 77 meters long. The roof-truss consists of two Mono Cap type trusses and some out of plan elements for providing lateral stability. Figure 1 illustrates some of the key geometrical features of this structure.

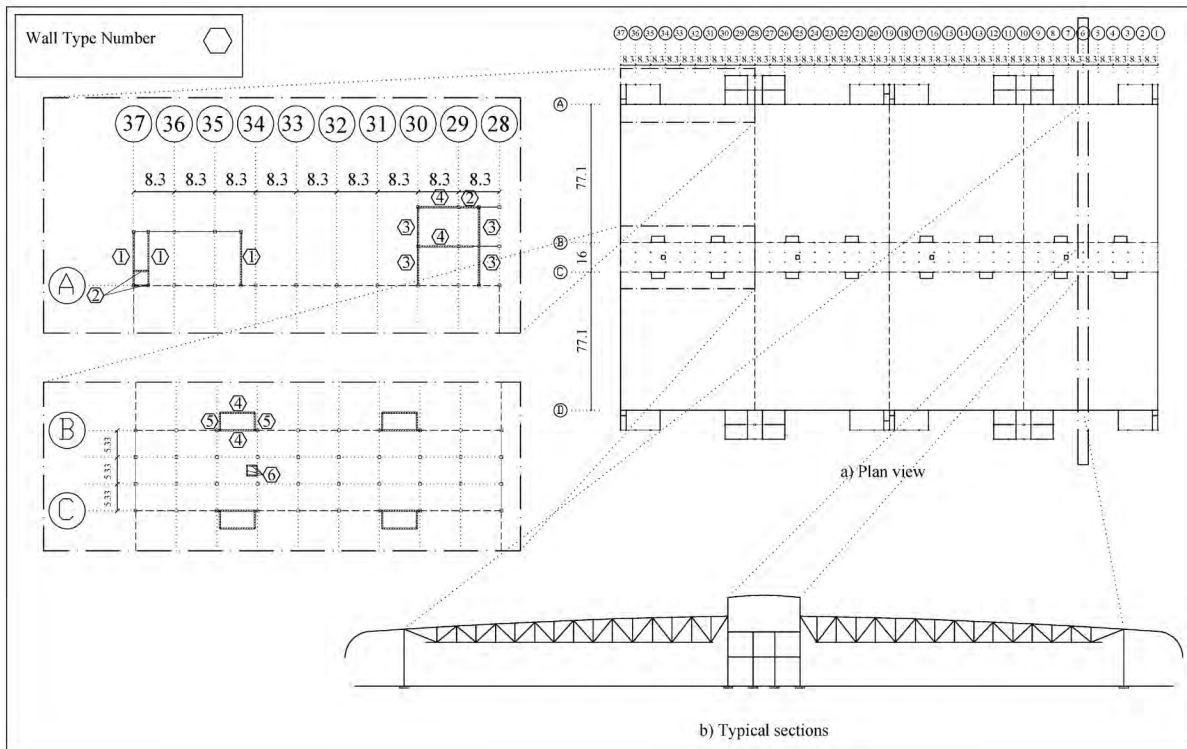


Figure 1: Plan and section view of the Typical Hall Building, including shear walls, beams, and columns.

This structure is loaded based on the available instructions of the drawing. Thus, for each floor, the self-weight, live load and dead load of 15.7 kN/m^2 , 5 kN/m^2 and 2.2 kN/m^2 are respectively considered. The self-weight and the utility loads of the roof create a dead load of 0.85 kN/m^2 . In addition to the vertical gravitational loads, the structure is subjected to the lateral seismic loads, and the seismic participation mass is calculated as the dead load plus 30% of the live load. The concrete used in this building had a characteristic compressive strength of 40 MPa, complying to CS1:1990 (characteristic compressive strength at 28 days = 40 MPa). The utilized steel rebars have a characteristic tensile strength of 460 MPa conforming to CS2:1995.

To perform vulnerability analysis of the case-study structure, an FE numerical model was constructed in OpenSees (Mazzoni et al. 2006). As 3D nonlinear modelling of the selected megastructure is computationally expensive, the High-Performance Computer at Swinburne University of Technology is utilized for running the analysis. The OpenSeesSP 3.2.0 was used on the Linux machine to reduce the computation time of the analysis to a practical range. The post-processing of the analysis results was handled by developing a Matlab® (MATLAB 2019)

framework. This framework is designed to collect and sort the ground motion analysis results obtained from the supercomputer, and to create the fragility functions.

In order to provide maximum consistency to the real structure, six column types and three beam types are adopted in the numerical model. The modelled beams and columns are deemed to be based on the grouping of the actual structural elements, and assigning the closest section to each beam and column. The nonlinear cyclic behaviour of the beam-column elements is modelled using distributed plasticity. For this reason, frame elements are modelled using *forceBeamColumn* elements. The core and cover concrete are modelled using *concrete02* material and the steel rebars are modelled using *steel02* material. Figure 2 schematically represents the modelled element, distributed plasticity, defined sections and the utilized material.

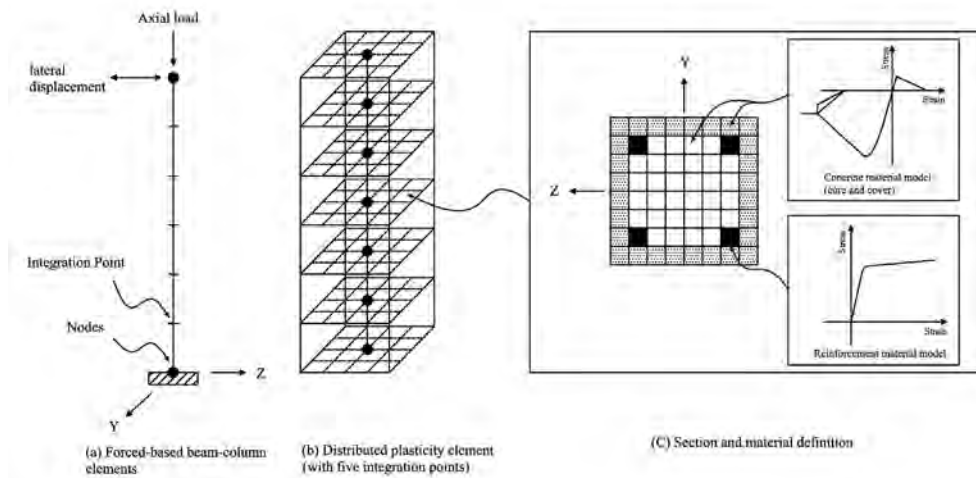


Figure 2: Schematic representations of (a) Forced-based beam-column element, (b) Distributed plasticity element (with five integration points), (c) Section and material definition

The required parameters for both the steel and concrete materials are calculated based on the suggestions made by Cordova (2005), which are shown in Tables 1 and 2. The damping is modelled using the Rayleigh damping (mass- and stiffness-proportional damping) corresponding to the critical-damping ratio of 5% for the first and third modes.

Table 1: Opensees input for the definition of Concrete02 material*

Variable Name	Core concrete (confined)	Cover concrete (unconfined)
f'_{c0}	$K(0.85 f'_c)$	$0.85 f'_c$
ε_{c0}	$0.002 K$	0.002
f'_{cu}	$0.2 K (0.85 f'_c)$	0
ε_{cu}	$\frac{0.8}{Z_m} + 0.002 K$	0.01
λ	0.1	0.1
f_t	$0.94 \sqrt{0.85 f'_c} \text{ (MPa)}$	0
E_{ts}	$f_t/0.002$	0

* In this table f'_c is the nominal compressive strength of concrete, and Z_m is the variables defined by Equations (1).

$$Z_m = \frac{0.5}{\frac{3 + 0.29 (0.85 f'_c)}{145 f'_c - 1000} + 0.75 \rho_s \left(\frac{h''}{S_h}\right)^{0.5} - 0.002 K} \quad \text{Equation (1)}$$

In these equations, K is the factor defined by $K = 1 + \rho_s f_{yh}/f'_c$, ρ_s is the volumetric ratio of transverse steel to core concrete, f_{yh} is the yield stress of the transverse reinforcement (MPa), f'_c is the concrete compressive strength (MPa), h'' is the width of confined concrete measured to the outside of the perimeter hoop and S_h is the centre to centre spacing between hoop reinforcement sets.

Table 2: Opensees input for the definition of reinforcements using Steel02 material#

Variable Name	Reinforcements
f_y	$1.25 f_{y,nominal}$
E	$2.0 \times 10^{11} \text{ N/m}^2$
b	0.02
R_0	18.5
CR_1	0.925
CR_2	0.15

In this table f_y is the yield strength, E is the initial elastic tangent, b is the strain-hardening ratio (ratio between post-yield tangent and initial elastic tangent), and R_0 , CR_1 and CR_2 are parameters to control the transition from elastic to plastic branches.

The shear walls are modelled using SFI MLVEM element in OpenSees. The SFI MLVEM element developed by Kolozvari et al. (Kolozvari et al. 2015a; Kolozvari et al. 2015b) is a novel analytical model for the RC walls, which incorporates the coupling of axial and shear responses. This model utilizes the fixed-strut-angle panel formulation, that couples the axial and shear responses at the panel (microfiber) level, and the flexural and shear responses at the model element level. In this way, the SFI MLVEM model for 6 shear wall types is created. The SFI MLVEM elements are 2D elements; hence, they cannot be utilized in a 3D OpenSees model. For overcoming this hurdle, an equivalent spring model is calibrated to each wall using the Modified IMK hysteresis model. Thus, the properties of the calibrated IMK elements can be placed into the 3D model and act as a reliable substitution of the wall (C.K. Gulec 2009). The calibration of the IMK spring was an iterative procedure that was performed by minimization of a mean square error loss function. The result of this procedure and its associated equivalent column-spring model for the Wall Type 6 is shown in Figure 3. This calibration has taken more than 10,000 cycles of loss minimization.

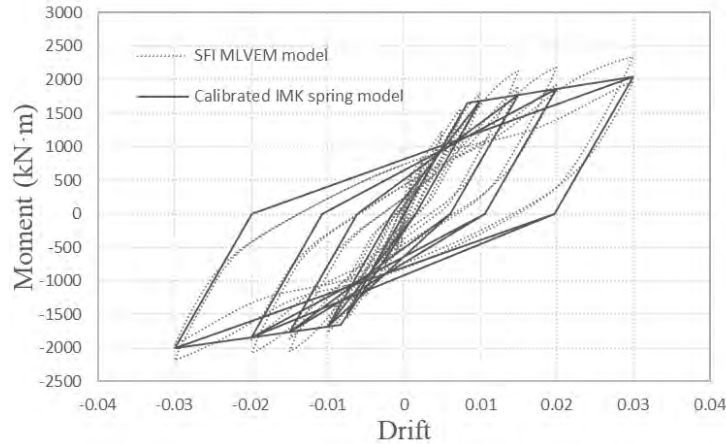


Figure 3: Calibration of IMK hysteresis model to SFI MLVEM model (both correspond to the Wall Type 6)

3) Ground motion inputs

The assessment of the seismic structural fragility is a crucial ingredient of vulnerability assessment. The fragility of a structure is a conditional probability that predicts the damage state of a structure, given the occurrence of a seismic demand. Incremental dynamic analysis (IDA) would typically result in the realization of various structural responses due to a range of seismic hazards. In this project, the ground motion simulation uses a suite of hazard consistent earthquake scenarios, which encompasses various magnitude-distance (M-R) pairs. Thus, more geological information such as the locations and geometries of the significant faults of the studied region have been included (Menegon et al. 2019). A suite of 300 ground motions is used for the time history analysis. The suite consists of ground motions developed for 15 levels of peak ground velocities (PGV), four M-R combinations for each PGV, and five simulated ground motions for each M-R. This suite of synthetic ground motions is produced based on stochastic simulation of the seismological model using the program GENQKE (Lam et al. 2010) and by calibration of the Atkinson and Boore (2006) intraplate source model to the crustal properties of Melbourne (Lam et al. 2006). The M-R combinations were derived by a study conducted on the relationship of the PGV, magnitude, and distance parameters, presented in Figure 4. Moreover, based on the work of Tsang et al. (2018), the major faults of the Greater Melbourne area are considered in the process of M-R selection.

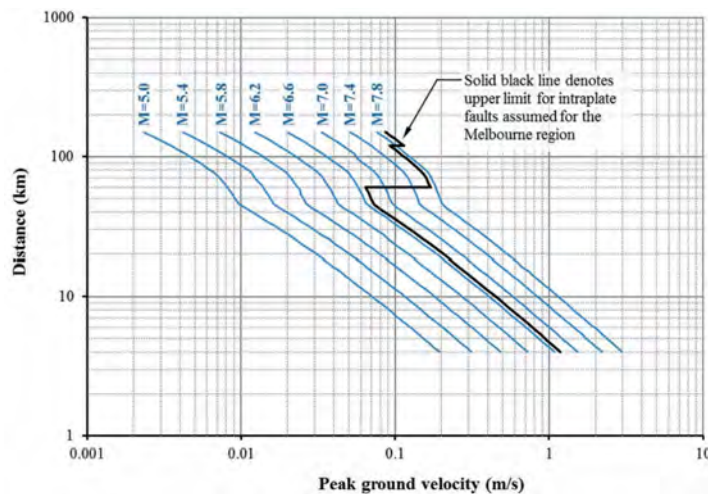


Figure 4: Peak ground velocity (PGV), moment magnitude (M) and source-site distance (R) relationship for the Greater Melbourne Region (Menegon et al. 2019).

4) Vulnerability assessment

4-1) Damage states

Damage states are an integral part of the vulnerability analysis of structures. Damage states link the occurrences of an engineering demand parameter (EDP) to various physical damage levels. D'Ayala et al. (2015) has provided a comprehensive review of relevant studies so that structural engineers are able to create a simple nonlinear structural model and obtain the structural vulnerability functions.

Structural damage states are typically differentiated by four damage states, based on HAZUS (2012) Technical Manual, namely, Slight, Moderate, Extensive, and Complete. These damage states and their detailed descriptions are restated in other seismic guidelines and design codes of practice such as SEAOC (1995), ATC (2003).

The damage states are mainly defined based on drift and material strain limits. The later for the concrete structures include specifying concrete compressive strain limits and reinforcement tensile strain limits. In this research, as shown in Table 1, four damage states are adopted based on the proposed framework in Menegon et al. (2019), which are deemed to be consistent with Australia's National Construction Code (NCC). In this table, the permanent drift is selected with reference to the works of Wibowo et al. (2014), Wilson et al. (2015), and Raza et al. (2018) where they have done a comparative study using a database of 190 columns and investigated the post-peak drift of reinforced concrete columns. Also, the material strains are proposed based on Calvi et al. (2007), Calvi and Sullivan (2009) and the work of Menegon (2018), where he experimentally tested reinforced concrete walls, which were designed and detailed based on AS 1170.4 and AS 3600.

Table 3. Proposed inter-storey drift and material strain limits associated with different performance levels and damage states (Menegon et al. 2019).

Performance Level	Damage State	Damage Index (DI)*	Transient Drift Limit (%)	Permanent Drift Limit (%)	Concrete Strain ϵ_c	Steel Strain ϵ_s
1	Slight Damage	15% ($\leq 17\%$)	0.5 (not specified) 0.4 (brittle NSC [†]) 0.7 (ductile NSC [†])	0.2	0.0015	ϵ_{sy}
2	Moderate Damage	30% (10–33%)	1.0	0.5	0.002	$2\epsilon_{sy}$
3	Extensive Damage	100% ($> 30\%$)	2.5 if axial load ratio [‡] is less than 0.20, otherwise 1.5 in accordance with AS 1170.4	Varying with axial load ratio [‡] , 1.0 if not specified	0.006	0.05
4	Complete Damage	100% ($> 60\%$)	Depending on types of elements, and varying with axial load ratio [‡]	NA	NA	NA

* Damage Index (DI) is defined as the repair to replacement cost ratio. Structural and non-structural damage are included. A single value is recommended for each performance level, whilst the typical range, as reported in the literature, is given in the brackets for reference.

[†] NSC = non-structural components.

[‡] Axial load ratio is taken as $N^*/(f'_c A_g)$, where: N^* is the axial load on the wall due to gravity actions in accordance with AS 1170.4, which is typically taken as $G + 0.3Q$; f'_c is the maximum compressive strength of the concrete (it should be noted that the mean strength, rather than the characteristic strength, should be taken for assessment purposes); and A_g is the gross cross-sectional area of the wall.

4-2) Vulnerability results

After performing response time series analysis for all the 300 simulated input ground motions, the roof drifts of the studied frame were recorded. As shown in Figure 5, the analysis results coupled with the transient drift limits for slight, moderate, and extensive damage states are plotted. In this way, by comparing the drifts, the building's possible damage induced by each ground motion can be inferred. The results indicate that the building's response is mainly within the slight to moderate damage range and in very few cases surpasses the extensive damage threshold.

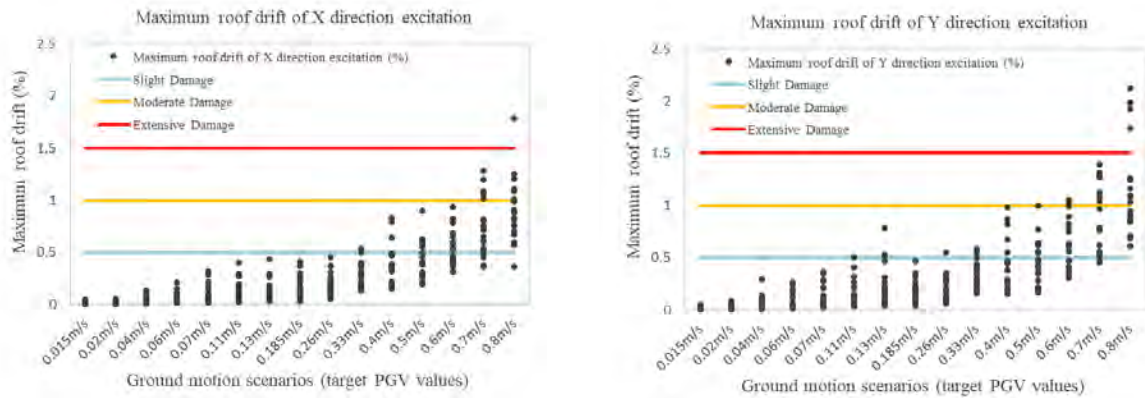


Figure 5: The response analysis results for 300 simulated ground motions

As previously discussed, there are five simulated ground motions for each M-R combination and four M-R pairs for each PGV level; hence there are 20 GMs for each PGV level. The average values of these twenty ground motions are calculated, and then sorted based on increasing peak ground velocity values. The results, as shown in Figure 6, are representing the average structural drift response at various PGV levels.

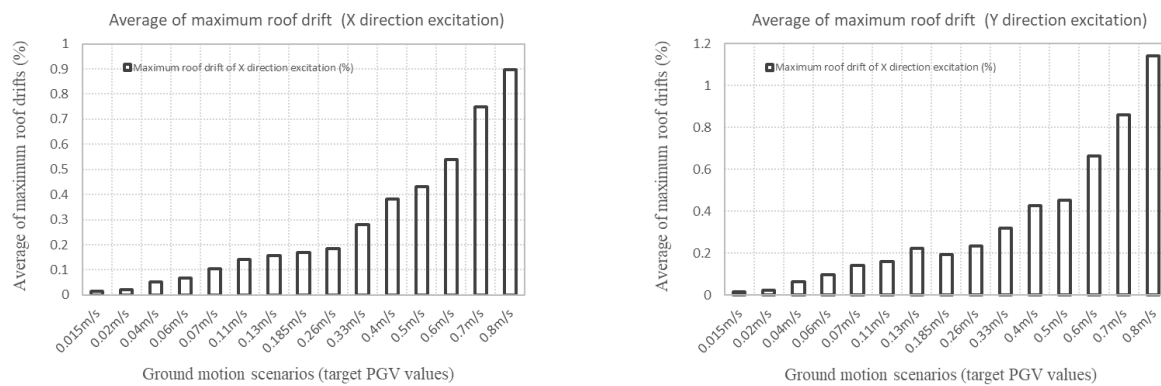


Figure 6: Average of maximum structural drift response at various PGV levels

5- Conclusions

This paper studies the structural vulnerability of a highly populated building located in a low to moderate seismic region. As a case study, the main building of the AsiaWorld-Expo in Hong Kong, with a maximum capacity of over 30,000 people, is investigated. A suite of 300 ground motions is used to evaluate its seismic performance based on a nonlinear 3D model of the building structure. The ground motions were simulated for four magnitude-distance combinations at each of the fifteen PGV levels. The results show that the studied building could be moderately damaged at PGVs more than 0.6 m/s and extensively damaged at PGVs exceeding 0.8 m/s. The results of this study contribute to a better understanding of the seismic performance of highly populated buildings, which are hugely neglected in the literature.

6- References

- Abrams DP (2002) Consequence-based engineering approaches for reducing loss in mid-America, Conference on Apr; Citeseer
- Atkinson GM, Boore DM (2006) Earthquake Ground-Motion Prediction Equations for Eastern North America Bulletin of the Seismological Society of America 96:2181-2205 doi:10.1785/0120050245
- Gulec C.K, Whittaker A.S (2009) Performance-Based Assessment and Design of Squat Reinforced Concrete Shear Walls. University at Buffalo, MCEER: Earthquake Engineering to Extreme Events
- Cakir F, Seker BS, Durmus A, Dogangun A, Uysal H (2015) Seismic assessment of a historical masonry mosque by experimental tests and finite element analyses KSCE Journal of Civil Engineering 19:158-164 doi:10.1007/s12205-014-0468-4
- Calvi G, Priestley M, Kowalsky M (2007) Displacement-based seismic design of structures Earthquake spectra 24:1-24
- Calvi G, Sullivan T (2009) A model code for the displacement based seismic design of structures: DBD09 draft subject to public enquiry. Iuss Press
- Code P (2005) Eurocode 8: Design of structures for earthquake resistance-part 1: general rules, seismic actions and rules for buildings Brussels: European Committee for Standardization
- Cordova PP, Deierlein GG (2005) Validation of the Seismic Performance of Composite RCS Frames: Full-Scale Testing, Analytical Modeling, and Seismic Design. John A. Blume Earthquake Engineering Center Technical Report 155. Stanford Digital Repository. Available at: <http://purl.stanford.edu/zd207gv1593>
- Council AT (2003) Preliminary Evaluation of Methods for Defining Performance, ATC-58-2.
- D'Ayala D, Meslem A, Vamvatsikos D, Porter K, Rossetto T, Silva V (2015) Guidelines for analytical vulnerability assessment of low/mid-rise buildings, vulnerability global component project Global Earthquake Model
- Dogangun A, Sezen H (2012) Seismic vulnerability and preservation of historical masonry monumental structures Earthquakes and Structures 3:83-95 doi:10.12989/eas.2012.3.1.083
- Gkologiannis C, Gantes C, Athanasiadis A, Majowiecki M, Zoulas F, Schmidt H (2010) Structural Design of the New Football Stadium of Panathinaikos F.C. in Votanikos, Greece IABSE Symposium Report 97:63-70 doi:10.2749/222137810796024097
- HAZUS F (2012) 2.1 technical manual. Technical report, Federal Emergency Management Agency
- Joint Committee on Structural General principles on quality assurance for structures and General principles on reliability for structural design, report, 1981
- Kolozvari K, Orakcal K, Wallace JW (2015a) Modeling of Cyclic Shear-Flexure Interaction in Reinforced Concrete Structural Walls. I: Theory Journal of Structural Engineering 141 doi:10.1061/(asce)st.1943-541x.0001059

- Kolozvari K, Tran TA, Orakcal K, Wallace JW (2015b) Modeling of Cyclic Shear-Flexure Interaction in Reinforced Concrete Structural Walls. II: Experimental Validation *Journal of Structural Engineering* 141:04014136 doi:10.1061/(asce)st.1943-541x.0001083
- Lam N, Venkatesan S, Wilson J, Asten M, Roberts J, Chandler A, Tsang HH (2006) Generic Approach for Modelling Earthquake Hazard *Advances in Structural Engineering* 9:67-82 doi:10.1260/136943306776232963
- Lam N, Wilson J, Tsang HH (2010) Modelling Earthquake Ground Motions by Stochastic Method. In. *Sciyo*. doi:10.5772/9745
- Liel AB, Deierlein GG (2013) Cost-Benefit Evaluation of Seismic Risk Mitigation Alternatives for Older Concrete Frame Buildings *Earthquake Spectra* 29:1391-1411 doi:10.1193/030911eqs040m
- MATLAB (2019) MATLAB:2019a. The MathWorks Inc.
- Mazzoni S, McKenna F, Scott MH, Fenves GL (2006) OpenSees command language manual Pacific Earthquake Engineering Research (PEER) Center
- Melchers RE, Beck AT (2018) Structural reliability analysis and prediction. John Wiley & sons
- Menegon S (2018) Displacement behaviour of reinforced concrete walls in regions of lower seismicity Doctor of Philosophy thesis, Department of Civil and Construction Engineering, Swinburne University of Technology
- Menegon SJ, Tsang HH, Lumantarna E, Lam NTK, Wilson JL, Gad EF (2019) Framework for seismic vulnerability assessment of reinforced concrete buildings in Australia *Australian Journal of Structural Engineering* 20:143-158 doi:10.1080/13287982.2019.1611034
- Raza S, Tsang HH, Wilson JL (2018) Unified models for post-peak failure drifts of normal- and high-strength RC columns *Magazine of Concrete Research* 70:1081-1101
- SEAOC V (1995) Performance based seismic engineering of buildings Sacramento (CA): Structural Engineers Association of California, USA
- Sezen H (2012) Earthquake Engineering. BoD–Books on Demand. doi:10.5772/1608
- Steenbergen RDJM, Sýkora M, Diamantidis D, Holický M, Vrouwenvelder T (2015) Economic and human safety reliability levels for existing structures *Structural Concrete* 16:323-332 doi:10.1002/suco.201500022
- Tsang HH, Lumantarn E, Lam N, Wilson JL, Gad EF (2016) Annualised collapse risk of soft-storey building with precast RC columns in Australia. In: *Mechanics of Structures and Materials: Advancements and Challenges - Proceedings of the 24th Australasian Conference on the Mechanics of Structures and Materials*. CRC Press (Taylor & Francis Group)
- Tsang HH, Daniell JE, Wenzel F, Werner AC (2018) A semi-probabilistic procedure for developing societal risk function *Natural Hazards* 92:943-969 doi:10.1007/s11069-018-3233-z

- Tsang HH, Daniell JE, Wenzel F, Wilson JL (2020) A universal approach for evaluating earthquake safety level based on societal fatality risk *Bulletin of Earthquake Engineering* 18:273-296 doi:10.1007/s10518-019-00727-9
- Tsang HH, Wenzel F (2016) Setting structural safety requirement for controlling earthquake mortality risk *Safety Science* 86:174-183
doi:https://doi.org/10.1016/j.ssci.2016.02.028
- Uranjek M, Dolinšek B, Gostič S (2011) Seismic strengthening of churches as a part of earthquake renewal in the Posočje region, Slovenia. WIT Press.
doi:10.2495/eres110201
- Wibowo A, Wilson JL, Lam N, Gad EF (2014) Drift performance of lightly reinforced concrete columns 59:522-535 doi:10.1016/j.engstruct.2013.11.016
- Wilson J, Wibowo A, Lam N, Gad EF (2015) Drift behaviour of lightly reinforced concrete columns and structural walls for seismic design applications *Australian Journal of Structural Engineering* 16:62-74

A Novel Self-centring Slip Friction Brace for Mitigating the Seismic Responses of a RC Double-column Bridge Bent

Kaiming Bi¹, Xunyi Pan², Hong Hao³

1. Corresponding author. Senior Lecturer, School of Civil and Mechanical Engineering, Curtin University, Bentley, WA 6102, Australia. kaiming.bi@curtin.edu.au
2. Master student, School of Civil and Mechanical Engineering, Curtin University, Bentley, WA 6102, Australia. Xunyi.pan@postgrad.curtin.edu.au
3. John Curtin Distinguished Professor, School of Civil and Mechanical Engineering, Curtin University, Bentley, WA 6102, Australia. Email: hong.hao@curtin.edu.au

Abstract

Bridges may suffer large residual displacements after a severe earthquake, which significantly impedes the post-quake rescue activities. It is imperative to minimize the residual deformations of bridge structures. In the present study, a novel self-centring slip friction (SCSF) brace is developed to dissipate seismic energy and reduce the residual displacement of bridges. Different from the conventional self-centring energy dissipation (SCED) device where the energy dissipation and self-centring components work separately, the energy dissipation component in this device simultaneously helps to provide the self-centring capability to the device by adopting a delicate design, i.e. this device can provide the energy dissipation and self-centring capabilities all in one compact package. In the present study, the mechanism of the device is firstly introduced, and experimental studies were carried out to examine the behaviour of the device.

Keywords: self-centring slip friction brace, double-column bridge bent, seismic behaviour, residual displacement

1. INTRODUCTION

In current engineering practices, reinforced concrete (RC) bridge columns are normally designed according to the ductility based philosophy. Under this design philosophy, the collapse of the bridge generally can be avoided when it is subjected to a severe earthquake. However, in order to dissipate seismic energy, plastic hinges are allowed to be formed in the bridge columns. Large residual deformations are therefore unavoidably formed and repeatedly observed in the bridge columns in many previous major earthquakes.

Extensive research efforts have been made to reduce the adverse residual displacement of bridge structures. These methods might be roughly divided into two classes. The first class is by adopting the novel structural system such as rocking column (e.g. [1, 2]) or segmental column (e.g. [3, 6]). The second class is based on the structural fuse concept [11]. In this concept, sacrificial element is designed to yield before the yielding of the more important structural members (e.g. the bridge column in bridge structures) to dissipate seismic energy. The more important structural members are therefore protected. Buckling restrained braces (BRBs) might be the most widely used structural fuse. However, it should be noted that, BRBs cannot reduce the residual displacement of bridge column though the seismic energy can be stably dissipated. To overcome this problem, self-centering energy dissipation (SCED) devices

have been proposed and developed.

A SCED device normally includes an energy dissipation component and a self-centering component. The commonly used energy dissipation mechanism such as through the buckling of steel core (in BRB), the yielding of metallic components (in the metallic damper), the friction (in the friction damper), and the deformation of viscoelastic material can be used to form the energy dissipation system [5]. For the self-centering component, shape-memory alloy (SMA) wires, bars, plates and rings were adopted by some researchers due to its unique superelasticity [6]. High-strength pre-stressed tendon is another candidate to provide self-centering force [7]. Prepressed normal [8] and disc [9] springs have also been used to provide self-centering force by some researchers. However, it should be noted that, certain limitations also exist in these devices. For example, SMA is quite expensive, which will significantly increase the costs of the project; a large portion (can be up to 20% or even more as reported in [10]) of the pre-stress in the tendon can be lost during the service life of the structure, which therefore decreases the effectiveness of the device.

Recently, Hashemi et al. [11] proposed an innovative resilient slip friction (RSF) joint to improve the seismic performance of a rocking steel-timber wall system. This RSF joint in essence is a SCED device. However, different from the conventional SCED device where the energy dissipation and self-centering components work separately, the energy dissipation component in this joint simultaneously helps to provide self-centering capability to the device by adopting a delicate design, i.e. this joint can provide the energy dissipation and self-centering capabilities all in one compact package [11]. In particular, this joint consists of two wedge-shaped centre slotted plates (or centre plates) and two cap plates (or cover plates). Each centre plate is connected to the two cover plates by the pre-compressed disc springs. When relative movement occurs between the two ends of the centre plates and the two cover plates, energy can be dissipated through friction between the contacting surfaces of these plates. Moreover, the angle of the wedge-shaped core plate is delicately designed to make sure that, in the unloading phase, the reversing force provided by the disc springs is larger than the resisting friction force between the plate surfaces, so that the joint can go back to its original position after unloading, and the self-centring capability is thus achieved. Inspired by this RSF joint, a novel self-centering slip friction (SCSF) brace is developed in the present study. The design, working mechanism and performance are introduced in this paper.

2. SELF-CENTERING SLIP FRICTION BRACE

2.1 Brace configuration, working mechanism and advantages

Fig. 1(a) shows the three-dimensional (3D) sketch of the brace. It can be seen that this brace includes 9 parts, namely: (1) the wedge-shaped inner core, (2) two outer sleeves, (3) disc springs, (4) cushion blocks, (5) nuts, (6) high-strength bolts, (7) four ear plates, (8) stiffeners and (9) two end plates. As shown in Fig. 1(b), two grooves are reserved in the inner side of the upper and lower outer sleeves respectively, and the two wedge-shaped inner cores are installed in the two grooves. The brace also includes four ear plates that are rigidly welded onto the outer sleeves, and disc springs are installed onto the ear plates to connect the inner core and outer sleeves together by using a number of bolts. Each bolt includes a high-strength rod, a nut, a cushion block and couple of disc springs as shown in Fig. 1(a). To avoid the possible local deformation of the ear plates, stiffeners are used to strength the ear plates.

Fig. 2 shows the working principle of the brace. At the beginning, the disc springs are pre-compressed by tightening the nuts. First, consider the brace is under axial tension load. When the axial tension load applied to the brace (Fig. 2(a)) is less than the static friction force between the inner cores and the outer sleeves, no relative movement occurs between the inner cores and

the outer sleeves; When the tension load is larger than the friction force at the contacting surfaces, relative movement starts to occur at these surfaces (Fig. 2(b)), and the brace starts to dissipate energy. Due to the relative movement, the gap (s_2) between the upper and lower outer sleeves also increases, the disc springs are further compressed (Fig. 2(b)) and the compressive forces in the disc springs increase as well. During the unloading process, the compressive forces in the disc springs will make the inner cores go back to their original positions automatically due to the delicately designed wedge-shaped inner cores, and the self-centering capability of the brace is thus achieved. The condition to achieve the self-centering capability will be introduced in Section 2.2. Under compression, the same mechanism applies. To avoid repetition, they are not introduced in detail.

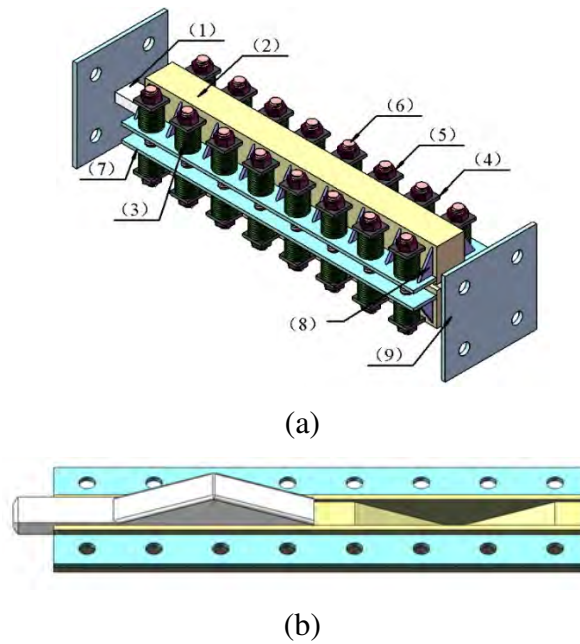


Fig. 1. (a) 3D sketch of the brace, and (b) outer sleeve and inner core.

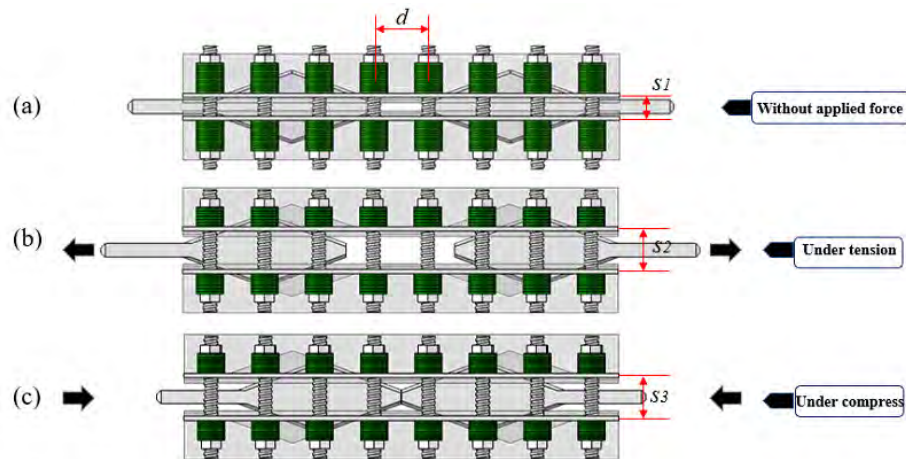


Fig. 2. Working mechanism of the SCSF brace: (a) original position, (b) under tension, (c) under compression.

2.2 Analytical model

The working mechanism of the brace is the same when it is under tension or compression as discussed above. To simplify the analysis, only the analytical model of the brace under tension is discussed herein. Fig. 3(a) shows the free body diagram of the inner core when the pre-

compressive force provided by the disc springs at each bolt is $F_{b,pr}$. It is obvious that a compressive force F_τ will be applied to the contacting surface of the inner core, which further introduces a friction force F_f at the contacting surface, and

$$F_f = \mu_s \cdot F_\tau \quad (1)$$

in which μ_s is the static friction coefficient.

Based on the force equilibrium in the vertical direction of Fig. 3(a), it can be seen that $F_{b,pr}$, F_τ and F_f have the following relationship

$$F_{b,pr} = F_\tau \cdot \cos \theta - F_f \cdot \sin \theta \quad (2)$$

where θ is the angle of the wedge-shaped inner core.

The slip force therefore can be calculated as follows if the brace includes n bolts by considering the equilibrium in the horizontal direction

$$F_{slip} = n \cdot (F_\tau \cdot \sin \theta + F_f \cdot \cos \theta) \quad (3)$$

Substituting Eqs. (1) and (2) into Eq. (3), the slip force can be re-written as

$$F_{slip} = n \frac{F_{b,pr}(\sin \theta + \mu_s \cos \theta)}{\cos \theta - \mu_s \sin \theta} \quad (4)$$

When the axial force is larger than the slip force, relative movement between the inner cores and outer sleeves will occur. At this time, the disc springs are further compressed as discussed. The compressive force provided by the disc springs at each bolt is

$$F_{b,u} = F_{b,pr} + k_s \Delta_s \quad (5)$$

where Δ_s is the deformation of disc springs, and k_s is the stiffness of the disc springs, which is almost linear elastic based on the experimental study as will be introduced in section 3.

When the disc springs deforms Δ_s , the deformation of the brace is

$$\Delta_m = 2 \frac{\Delta_s}{\tan \theta} \quad (6)$$

and the force provided by the brace thus can be calculated as follows based on Eq. (4)

$$F_{ult} = n \frac{F_{b,u}(\sin \theta + \mu_k \cos \theta)}{\cos \theta - \mu_k \sin \theta} \quad (7)$$

It should be noted that the static friction coefficient μ_s is replaced by the kinematic friction coefficient μ_k in the above equation.

During the unloading process, the restoring force can be similarly obtained by reversing the direction of F_f in Fig. 3(a), and it has the following form

$$F_{restoring} = n \frac{F_{b,u}(\sin \theta - \mu_s \cos \theta)}{\mu_s \sin \theta + \cos \theta} \quad (8)$$

Similarly, when the brace goes back to its initial location, the residual force in the brace can be obtained based on Eq. (8) by changing the force of the disc springs into the preload and the static friction coefficient into the kinetic friction coefficient, i.e.

$$F_{residual} = n \frac{F_{b,pr}(\sin \theta - \mu_k \cos \theta)}{\mu_k \sin \theta + \cos \theta} \quad (9)$$

Based on Eqs. (1-12), the force-deformation relation of the brace can be determined, and it is shown in Fig. 3(b). It can be seen that the brace presents a flag-shaped hysteretic behaviour with an excellent self-centering capability. It is obvious that, in order to ensure that the brace

can go back to its original position, both $F_{residual}$ and $F_{restoring}$ should be large than zero. According to Eqs. (8) and 9, the following condition should be satisfied, namely $\mu_k < \tan\theta$ and $\mu_s < \tan\theta$. Based on this condition, the lubricating oil can be selected once the angle θ is determined.

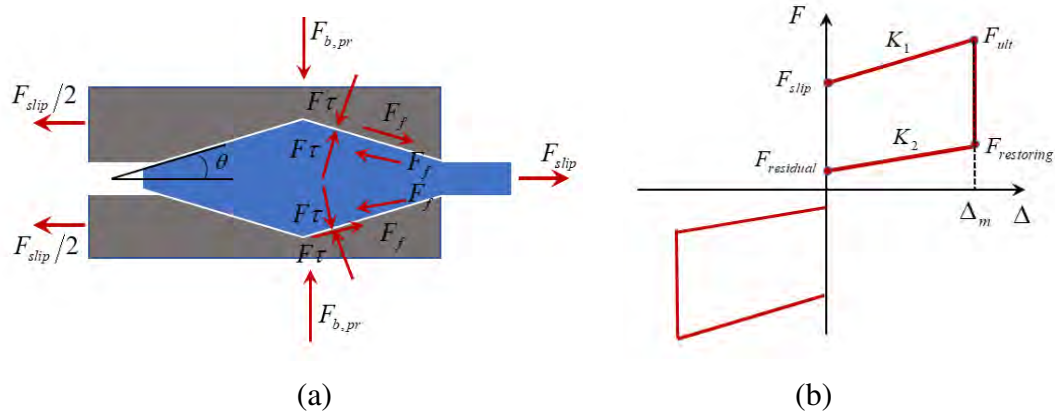


Fig. 3. (a) Free body diagram of the brace when it is under an axial tensile force; (b) hysteretic behaviour of the brace.

3. EXPERIMENTAL STUDY

A prototype of the brace was designed and manufactured. It is obvious that to obtain the behaviour of the damper, the friction coefficient between the inner cores and outer sleeves, and also the stiffness of the disc springs should be known. Friction and disc spring tests were therefore performed to obtain these parameters. Due to the page limit, they are not introduced in detail, only the results are reported herein. It was found that after applying the Molykote (Dow Corning) BR2 Plus High Performance Grease to the contact surface, the friction coefficient was found to be about 0.07. For the disc spring stiffness, when 12 pieces of disc springs were used (with the parameters of each disc spring shown in Fig. 4 and Table 1, the combined disc spring (i.e. with 12 pieces) stiffness was 4.85kN/mm.

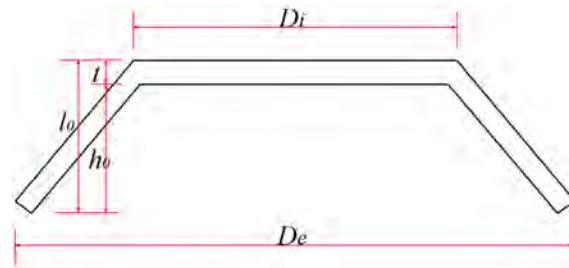


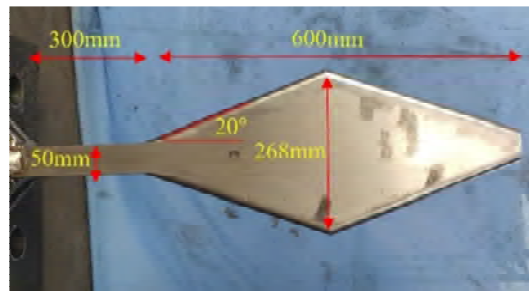
Fig. 4. Dimensions of one disc spring

Table 1 Parameters of one disc spring

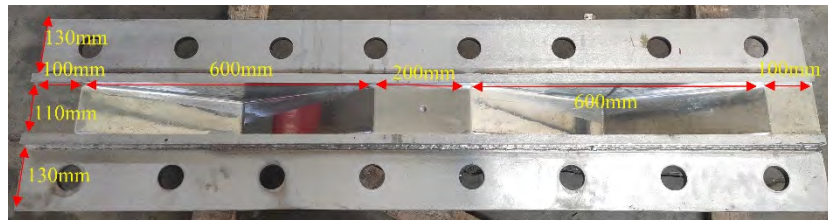
Parameter	Value
Outer diameter (D_e)	100 mm
Inner diameter (D_i)	51 mm
Thickness (t)	7 mm
Overall height (l_0)	9.2 mm
Internal height (h_0)	2.2 mm

The whole brace was then manufactured and tested. The components of the brace has been shown in Fig. 1. Except the disc springs and high strength bolts, all the other components are made from the Q345 steel. Fig. 5(a) shows the parameters of the inner core. As shown, the

angle of the inner core was 20 degrees, and the length of the wedged shape was 600 mm. The thickness of the inner core was 110 mm, and the height at the end and middle of the core was 50 and 268 mm respectively. The edges of the inner core were rounded to avoid the direct contact with the outer sleeves. The grooves in the outer sleeve were carefully manufactured to host the inner cores. A gap of 200 mm was reserved between the two inner ends of the inner cores to ensure the deformation capacity of the brace. The total length of the outer sleeve was 1600 mm, and the thickness of the outer sleeves and ear plates were 60 mm and 16 mm, respectively. The brace included 16 high strength bolts and the diameter of each bolt was 50 mm. On each bolt, 2 groups of disc springs were installed and each group consisted of 12 pieces of disc springs. Each group of disc springs was loaded a compressive force of 28 kN by using a torque wrench. Fig. 6 shows the whole brace after assembling. The assembled brace was then installed to a 2000 kN servo hydraulic testing system to obtain its hysteretic behaviour. Fig. 6 shows the testing setup, and the brace was subjected to a cyclic loading protocol shown in Fig. 7.



(a)



(b)

Fig. 5. Dimensions of the (a) inner core and (b) outer sleeve.

The black line in Fig. 8 shows the force-displacement relationship of the brace obtained in the test. It can be seen that the brace exhibited stable energy dissipation capacity and excellent self-centering capability with almost no residual displacement. This is because the friction coefficient of the lubricating oil was about $\mu = 0.07$ as obtained in the friction test, while the angle of the inner core was $\theta = 20^\circ$ ($\tan \theta = 0.364$), the condition $\mu < \tan \theta$ was satisfied. The theoretical results obtained from the analytical analyses are also shown in the figure (the red curve). The comparison shows that the two curves match well with each other except when the brace was under a relative large negative displacement (under compression), under which the restoring force was slightly larger than the analytical results. These results validate the analytical derivations on the one hand, on the other hand, they also show the brace test was successful. When the brace is applied to the double-column bridge bent, it is expected that the seismic performance of the RC double-column bridge bent can be significantly improved. Due to the page limit, this part is not presented in the paper.

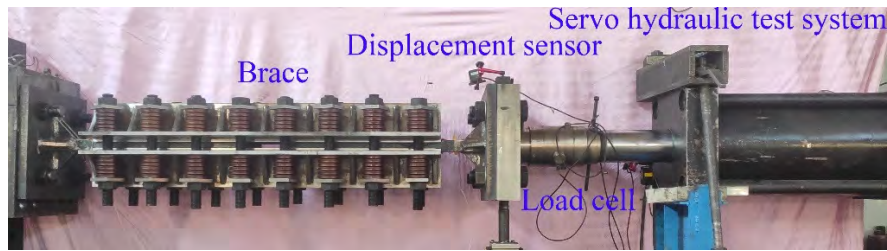


Fig. 6. Test setup.

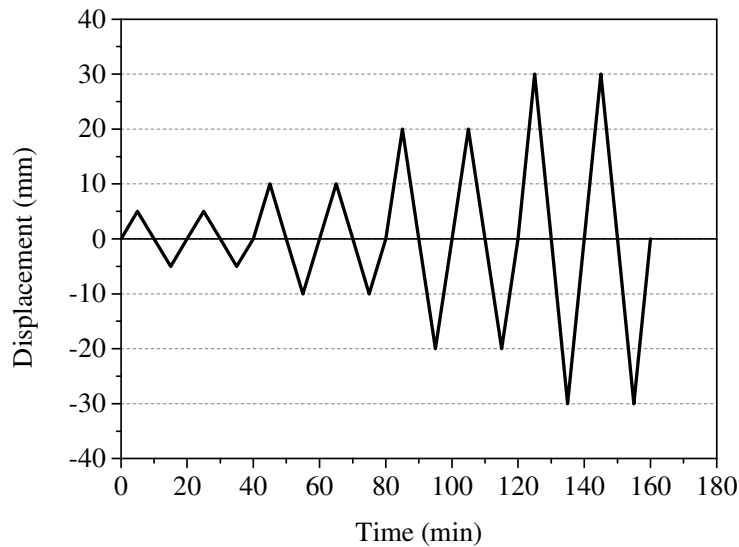


Fig. 7. Loading protocol for the whole damper

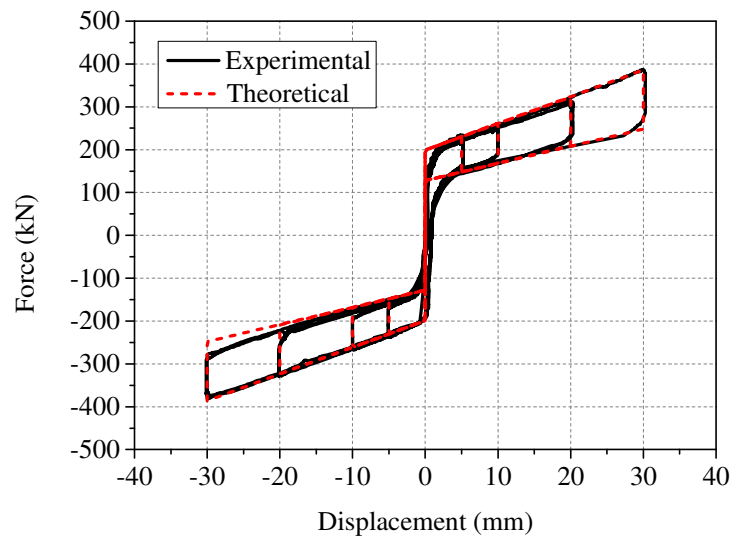


Fig. 8. Hysteretic behaviours of the brace obtained from the analytical, experimental and numerical studies

4. CONCLUSIONS

A novel self-centering slip friction brace (SCSF), which provides energy dissipation and self-centering capabilities in a compact package, is proposed in the present study to dissipate seismic energy and reduce the residual displacement of RC double-column bridge bents. The

mechanism of the brace is introduced, and its energy dissipation and self-centering capabilities are examined through analytical and experimental studies. It can be found that the brace has a flag-shaped hysteretic curve with excellent energy dissipation and self-centering capabilities. The analytical and experimental results match well with each other, demonstrating the accuracy of the corresponding analyses.

REFERENCES:

- [1] Han Q, Jia ZL, Xu K, Zhou YL, Du XL. Hysteretic behavior investigation of self-centering double-column rocking piers for seismic resilience. *Eng Struct* 2019;188: 218-232.
- [2] Zhou YL, Han Q, Du XL, Jia ZL. Shaking table tests of post-tensioned rocking bridge with double-column bents. *J Bridge Eng* 2019; 24(8):04019080.
- [3] Li C, Hao H, Bi K. Numerical study on the seismic performance of precast segmental concrete columns under cyclic loading. *Eng Struct* 2017; 148:373-386.
- [4] Li C, Bi K, Hao H, Zhang XH, Tin DV. Cyclic test and numerical study of precast segmental concrete columns with BFRP and TEED. *B Earthq Eng* 2019; 17:3475–3494.
- [5] Symans MD, Charney EA, Whittaker AS, et al. Energy dissipation systems for seismic applications: current practice and recent developments. *J Struct Eng* 2008; 134(1):3-21.
- [6] Wang W, Fang C, Zhang A, Liu XS. Manufacturing and performance of a novel self-centring damper with shape memory alloy ring springs for seismic resilience. *Struct Control Health Monit* 2019: e2337.
- [7] Hassanli R, Youssf O, Mills JE. Seismic performance of precast posttensioned segmental FRP-confined and unconfined crumb rubber concrete columns. *J Compos Constr* 2017; 21(4):04017006.
- [8] Ma H, Yam MCH. Modelling of a self-centring damper and its application in structural control. *J Constr Steel Res* 2011; 67(4):656-666.
- [9] Xu LH, Liu JL, Li ZX. Cyclic behaviors of steel plate shear wall with self-centering energy dissipation braces. *J Constr Steel Res* 2019; 153:19-30.
- [10] Maji AK, Negret I. Smart prestressing with shape-memory alloy. *J Eng Mech* 1998; 124(10):1121-1128.
- [11] Hashemi A, Zarnani P, Masoudnia R, Quenneville P. Seismic resistant rocking coupled walls with innovative resilient slip friction (RSF) joints. *J Constr Steel Res* 2019; 129:215-226.

In-situ and laboratory investigation of chemical anchor performance under quasi-static and seismic loading in masonry.

Burton, C.¹, Vaculik, J.², Visintin, P.³, Griffith, M.⁴, Sheikh, A.⁵

1. Corresponding Author. PhD student, School of Civil, Environmental and Mining Engineering, University of Adelaide, SA 5000, Australia.
Email: chris.burton@adelaide.edu.au
2. Research Fellow, School of Civil, Environmental and Mining Engineering, University of Adelaide, SA 5000, Australia.
Email: jaroslav.vaculik@adelaide.edu.au
3. Associate Professor, School of Civil, Environmental and Mining Engineering, University of Adelaide, SA 5000, Australia.
Email: phillip.visintin@adelaide.edu.au
4. Professor, School of Civil, Environmental and Mining Engineering, University of Adelaide, SA 5000, Australia.
Email: michael.griffith@adelaide.edu.au
5. Associate Professor, School of Civil, Environmental and Mining Engineering, University of Adelaide, SA 5000, Australia.
Email: abdul.sheikh@adelaide.edu.au

Keywords: Unreinforced masonry, seismic retrofit, anchor testing, material testing, in-situ testing, laboratory testing

Extended Abstract

Seismic retrofitting of existing unreinforced masonry structures relies particularly on the strength of the anchorage of the retrofit structural components to the supported masonry. Quasi-static testing of chemical anchors in masonry frequently results in anchor pull out capacities exceeding manufacturer's recommended characteristic capacities for design. However, investigations following the earthquakes in Christchurch in New Zealand in 2011 (Dizhur et al. 2016) reported that in many situations, the anchorages performed well below the expected capacity. This difference between real world observations and test results suggests that there is an interaction between static and dynamic loading of chemical anchors in masonry that is not captured in the anchor strength models being used by design engineers. This paper reports on in-situ and laboratory anchor and material strength testing undertaken by the authors to identify possible interactions that explain this difference.

To improve the understanding of performance of chemical anchors in varying loading scenarios, a series of material tests and anchor strength tests have been conducted under laboratory conditions to enable comparison with field results to facilitate better understanding of the observed anchor performance. These tests were performed on "old" masonry units recovered from three separate houses as well as "new" bricks sourced for this investigation. The old bricks were either plain or frogged recovered from houses in Croydon Park reported

on by Burton et al. (2019) and the new bricks were specifically sourced as moulded (sandstock) rather than extruded units to be similar to the site-won old bricks. Neither cored, drilled or extruded bricks were used as due to their geometry and the manufacturing process, they are not representative of vintage masonry units.

The material tests undertaken cover tension and compression tests on both the old and new masonry units, with the tensile strength being measured for both flexural (lateral modulus of rupture) in accordance with Australian standard AS4456.15 - *Masonry units, segmental pavers and flags— Methods of test Method 15: Determining lateral modulus of rupture* (Standards Australia 2003) and direct tensile strength using “dog bone” test specimens, rather than using the indirect splitting test discussed in AS4456.18 - *Masonry units, segmental pavers and flags— Methods of test Method 18: Determining tensile strength of masonry units and segmental pavers* (Standards Australia 2003). Compression strength was determined using masonry prisms with a length to width ratio of approximately 3.5:1, and all the material tests were loaded at approximately 2kN/minute.

Adhesive anchors in masonry typically fail as a result of (a) cone/wedge type failure, (b) the anchor pulling out of the hole (slipping) or (c) the brick being extracted from the surrounding masonry. A fourth failure mode which involves splitting of the brick if the anchor is located close to an edge can also occur (Arifovic and Nielsen 2006) as can failure of the anchor shaft. To investigate how deficiencies in installation practices and loading rates impact these failure modes, a series of quasi-static anchor pull out capacity tests were undertaken using Hilti M12 zinc plated and galvanised Class 5.8 anchor rods with Hilti HIT-HY 170 injection mortar (a hybrid injection mortar) with all anchors being installed into solid clay masonry without sieves. A hand operated worm gear drive horizontally orientated loading machine was used applying the load at approximately 2kN/minute with the masonry unit being simply supported. The quasi-static anchor pull out tests covered anchors installed correctly in accordance with manufacturers recommendations (Hilti 2019) on old and new bricks and a range of incorrect installations in new bricks including the drilled hole being too shallow, cleaning not being done correctly, or at all, and inadequate quantity of adhesive. Impact tests on correctly installed chemical anchors in new bricks were also undertaken using a swinging hammer machine that was manufactured for this project.

A further installation deficiency is over tightening of anchors at installation. Anecdotal evidence suggests that the tightening torque specified in anchor manufacturers documentation (eg Powers 2017, Hilti 2019, Ramset 2019) is rarely if ever measured during installation on site, but rather the anchors are tightened by “feel”. Tests to determine typical tightening torques were undertaken to obtain an understanding of how much torque and consequently tension was being applied to anchors at initial tightening in addition to the tests on the anchorages.

Overall, the tests have demonstrated that the rate of loading and deficiency in the quality of installation (other than over tightening) of the anchors seem to have only minimal impact on overall anchor capacity. This effectively removes these aspects from consideration of anchor performance, allowing the focus of investigations to move to more site specific aspects including the effects of over tightening of the anchors at installation and the nature of the retrofit structure and how it interfaces with the masonry.

Acknowledgements

The authors gratefully acknowledge the financial support of the Australian Research Council (through grant no. DP190100797) and the Bushfire and Natural Hazards CRC for the work presented in this paper. The conclusion and opinions expressed herein are those of the authors and not necessarily of the sponsors.

References

Arifovic, F. and M. P. Nielsen (2006). Strength of anchors in masonry.

Burton, C., J. Vaculik, P. Visintin, M. Griffith and A. Sheikh (2019). Pull out capacity of chemical and mechanical anchors in clay masonry under quasi-static, cyclic and impact loading. Australian Earthquake Engineering Society 2019 Conference. Newcastle, NSW.

Dizhur, D., A. Schultz and J. Ingham (2016). "Pull-out behavior of adhesive connections in unreinforced masonry walls." Earthquake Spectra **32**(4): 2357-2375.

Hilti (2019). Hilti Anchor Fastening Technology manual.

Powers (2017). "ANCHORING & FASTENING SYSTEMS Technical Manual for the Design Professional."

Ramset (2019). "Specifiers Anchoring Resource Book ANZ Edition 2."

Standards Australia (2003). AS/NZS 4456.15:2003 - Masonry units, segmental pavers and flags—Methods of test. Method 15: Determining lateral modulus of rupture.

Standards Australia (2003). AS/NZS 4456.18:2003 - Masonry units, segmental pavers and flags—Methods of test. Method 18: Determining tensile strength of masonry units and segmental pavers.

Towards an Australian Earthquake Ground-Motion Database

Chaitra Chandra Mouli¹, Alan Wu², Gaurang Sharma³, Zhijun Chen⁴, Ryan D. Hoult⁵, Hadi Ghasemi⁶, Trevor Allen⁷

1. Master of Data Science, The University of Melbourne, Parkville, VIC 3010.
Email: chaitracmoul@student.unimelb.edu.au
2. Master of Data Science, The University of Melbourne, Parkville, VIC 3010.
Email: chaoxinw@student.unimelb.edu.au
3. Master of Data Science, The University of Melbourne, Parkville, VIC 3010.
Email: gaurangs@student.unimelb.edu.au
4. Master of Data Science, The University of Melbourne, Parkville, VIC 3010.
Email: zhijunc1@student.unimelb.edu.au
5. Department of Infrastructure Engineering, The University of Melbourne, Parkville, VIC 3010.
Email: ryan.hoult@unimelb.edu.au
6. Seismologist, Geoscience Australia, Symonston, ACT 2609.
Email: Hadi.Ghasemi@ga.gov.au
7. Seismologist, Geoscience Australia, Symonston, ACT 2609.
Email: Trevor.Allen@ga.gov.au

Abstract

A vital component of any seismic hazard analysis is Ground Motion Models (GMMs) that predict the expected ground motions at a site for specific earthquake scenarios. Due to the limited nature of ground-motion datasets from which to assess or develop new GMMs, particularly for stable tectonic regions like Australia, multiple GMMs must be used to capture the epistemic uncertainty in ground-motion prediction. This research reports on a project aimed at developing a data pipeline (a series of data processing steps, that moves raw data to a database in a processed format) for ground-motion data recorded from Australian earthquakes. The data pipeline will accept raw seismic data in different file formats, processes the data into meaningful information (such as ground-motion intensity measures and instrument metadata), and stores this information into a suitably structured database. The OpenQuake Engine and the Ground Motion Prediction Equations Strong Motion Modeller's Toolkit (GMPE-SMTK) is used here for the purpose of analysing the performance of existing GMMs using visualisation techniques. The outcomes from the visualisations of this study could then be used to provide further advice on the applicability of GMMs for seismic hazard studies in Australia. This will be significant in selecting and developing GMMs, and thus, producing more accurate seismic hazard results in the future.

Keywords: Ground Motion Model (GMMs), Data Pipeline, Database, Visualisation

1. INTRODUCTION

Seismic hazard can be determined by understanding the rate of seismicity near a given locality, as well as knowledge on how the propagation of ground-shaking energy varies across Australia in order to determine the level of ground-shaking that has a given probability of exceedance (Cornell, 1968; McGuire, 1995). These studies allow for mitigation strategies to be developed and so that communities are more resilient to earthquake events (Allen *et al.*, 2018).

A vital component of any seismic hazard analysis is a model for predicting the expected distribution of ground motions (the phenomenon of the shaking of Earth's crust after an earthquake), at a site due to possible earthquake scenarios (Cotton *et al.*, 2006). More recent studies by seismologists have given rise to developments of predictive models to explore the expected distribution of ground motions for an earthquake of a given magnitude at a given distance from the rupture. These predictive models are referred to as Ground Motion Models (GMMs). Often called attenuation relations, these models describe the probability distribution function of ground motions. The main input parameters in GMMs are magnitude, distance, site classifications, style-of-faulting, hanging-wall/foot-wall, depth to top of rupture, dip and depth of soil (Abrahamson, 2007).

However, there are epistemic uncertainties involved in the development of GMMs because of the limited nature of datasets, especially for stable tectonic regions like Australia. Therefore, multiple GMMs are often used to capture these uncertainties in seismic hazard studies. In order to assist the selection and development of GMMs for hazard studies, a comprehensive database of earthquake ground motions is required. Therefore, the goals of the project are:

- To develop a database of Australian earthquake ground motions, complete with earthquake time series data, spectral data, and instrument and event metadata.
- To explore the proximity of GMMs using high-dimensional visualisation techniques, and augmentation of these methods (e.g., Scherbaum *et al.*, 2010).
- To visualise earthquake data relative to sampled models and provide advice on ground-motion model performance.

1.1 Related Work

Since the advent of seismology, the quest to delve deep into the study of the prediction of ground motions has come a long way. With the underlying conceptual knowledge, common to all studies, ample journals and articles have been published related to GMMs (Douglas, 2018). Ghasemi & Allen, 2018 discussed the selection and ranking of GMM for the seismic assessment in Australia. Both qualitative and quantitative ranking techniques were considered. For instance, high dimensional model representation matrices were used in the research to study characteristics of the models. In terms of database systems, Shanker *et al.*, 2008 provides a summary of distributed real time database systems (DRTDBS). It is a technique to access and operate the data in distributed database systems (DDBS) with time limitations. Although this technology (DRTDBS) is not a mandatory solution for GMM databases, it is still an ideal and powerful alternative.

2. DATA

The earthquake data in this project was recorded for earthquakes in western and central Australia on permanent and temporary networks operated by Geoscience Australia. The data provided by Geoscience Australia consists of several different types of files, which are waveform data, station metadata, PAZ data (poles and zeros) and earthquake event data (e.g., magnitudes and locations). Some of the data provided by Geoscience Australia was accessed from Incorporated Research Institutions for Seismology (IRIS), a non-profit organisation that collects, processes, curates and manages geoscience data, archives and distributes data to support the seismological research community.

2.1 Waveform Data

The waveform data are in MiniSEED (Mini Standard for the Exchange of Earthquake Data) format and can be imported into an ObsPy Stream object using ObsPy's *read()* function (Megies *et al.*, 2011). Each Stream contains multiple Trace objects, which contain gap-less continuous time series and related header/meta information. Each trace can be plotted to show the waveform. For example, the waveform data collected by AU.CARL.00.HHE (i.e., station at the Carlisle Urban Monitoring Site in Perth, Western Australia) from the 8th November 2018 M_w 5.2 Lake Muir earthquake is plotted in Figure 1. The data illustrated in Figure 1 represents the raw digital counts on the vertical axis from the channel HHE (i.e., first letter specifies the general sampling rate and response band of the instrument, with H as High Broad Band, second letter specifies the family to which the sensor belongs, with H as High Gain Seismometer and the third is the orientation code, with E implying East) in station CARL in Geoscience Australia's network ("AU").

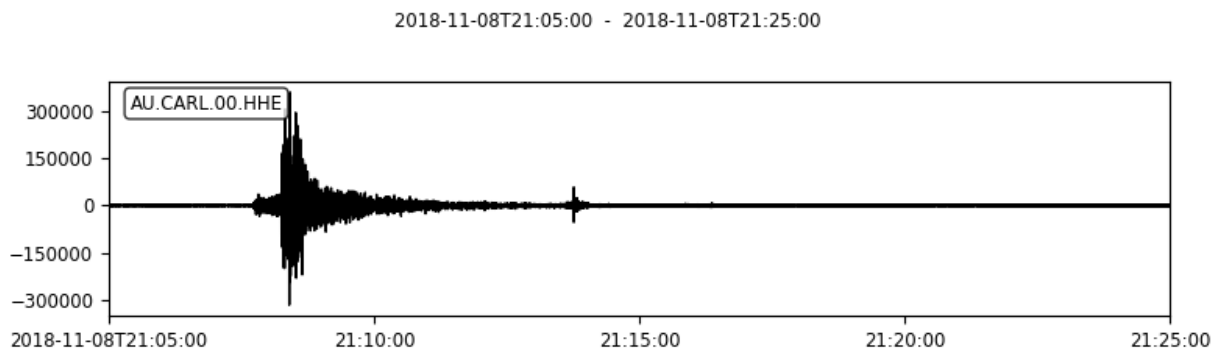


Figure 1: Time series data that shows ground motion recorded at the Carlisle Urban Monitoring Site in Perth, Western Australia from the 8th November 2018 MW 5.2 Lake Muir earthquake.

2.2 Station Metadata

Station metadata files contain attributes and characteristics for each earthquake recording station. They come in several different formats. The two formats considered here are, raw data format (e.g., instrument sensitivity and PAZ information) and Dataless SEED format. They should be processed and used to generate the station XML file, which is an appropriate format to store station metadata. In order to generate the station XML file, an ObsPy inventory object should be obtained. An inventory object has a hierarchical structure, starting with a list of Networks, each containing a list of Stations which again each contain a list of Channels (Figure 2). The Responses are attached

to the channels as an attribute. This structure is shown in Figure 2 (Creating stationxml file from scratch ObsPy). In the end, a station XML file can be created easily from an Inventory object. Figure 3 shows a sample of the station xml file, displaying the inventory details of the Australian site at CARL station.

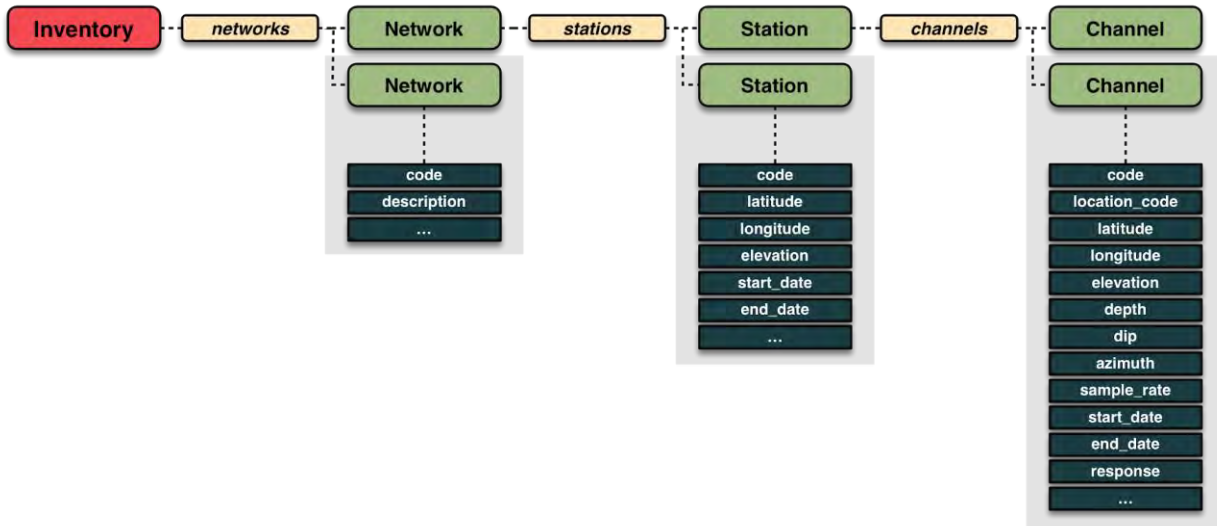


Figure 2: Obspy Inventory Object structure

```

<?xml version="1.0" encoding="UTF-8" standalone="yes">
<Inventory>
  <Network code="AU" startDate="2020-05-05T00:00:00.000000Z">
    <Description>A test stations.</Description>
    <Station code="CARL">
      <Latitude unit="DEGREES">-31.9835</Latitude>
      <Longitude unit="DEGREES">115.9267</Longitude>
      <Elevation unit="METERS">345.0</Elevation>
      <Site>
        <Name/>
      </Site>
      <CreationDate>2009-08-02T00:00:00.000000Z</CreationDate>
    </Station>
    <Channel code="HHE" locationCode="">
      <Latitude unit="DEGREES">-31.9835</Latitude>
      <Longitude unit="DEGREES">115.9267</Longitude>
      <Elevation unit="METERS">345.0</Elevation>
      <Depth unit="METERS">10.0</Depth>
      <SampleRate>200.0</SampleRate>
      <Response>
        <InstrumentSensitivity>
          <Value>174652949.554</Value>
          <Frequency>1.0</Frequency>
          <InputUnits/>
          <OutputUnits/>
        </InstrumentSensitivity>
        <Stage number="1">
          <PolesZeros/>
          <StageGain/>
        </Stage>
      </Response>
    </Channel>
  </Network>
</Inventory>
    
```

Figure 3: Sample of generated station.xml file

2.3 PAZ (Poles and Zeros) Data

Since the response of recording stations is frequency dependent, they require PAZ information in order to calculate the frequency responses for each station.

3. DATABASE OUTLINE

3.1 The Choice of Database

Since the database will keep running for a long time, the operation cost of business software such as Oracle will be a negative feature. Therefore, the two main candidates are MySQL and CouchDB, which the former is a typical relational database and the latter is a non-relational database. A general comparison between MySQL (a relational database that organises data into tables and the data is queried/accessed using SQL (Structured Query Language) and CouchDB (a non-relational NoSQL (Not Only SQL) database that stores data in JSON (JavaScript Object Notation)) for this project is provided in Table 1.

Database	Pro	Con
MySQL	<ul style="list-style-type: none"> Well tabulated and formatted Easily query data ITACA uses MySQL so can be a reference Reference in terms of MySQL is sufficient 	<ul style="list-style-type: none"> As a relational database, MySQL will not be suitable for unformatted data Worse performance than non-relational database with big data
CouchDB	<ul style="list-style-type: none"> Be able to handle missing features Suitable for the data formats available Friendly to distributed system 	<ul style="list-style-type: none"> Not so popular as MySQL, the amount of reference is less

Table 1: Comparison between MySQL and CouchDB

Both the database platforms support the virtual environment such as Docker, so the deployment should not be a problem. The main consideration is data format, current demands and the advantages/disadvantages between relational databases and non-relational databases. In the perspective of data, xml files and json objects (JavaScript Object Notation, a text based structured data format) are more suitable for non-relational databases rather than relational databases.

Considering the possible missing features (such as sampling rates of some channels) and the flexibility of the structure, CouchDB is chosen as the preferred platform for the project. Another requirement of the database is to consider the scalability. The realistic solution may not be a distributed format, but the consideration of the increment of data in future is necessary. Non-relational databases have natural advantages when compared with relational databases in terms of distributed systems, so it is another important reason to support CouchDB.

3.2 Design of the Database

The data in the project will contain waveform data, station metadata, earthquake intensity measures and earthquake event data. Since CouchDB, compatible with json format, is the final choice, the design of the database is that all file formats are converted to dictionary objects which are Python equivalent for json objects in CouchDB. It allows to maintain a balance between the convenience of reading/writing the database and the usage of powerful data analysis tools. And as the content discussed above, these three kinds of data files are quite easily converted to the required format.

Figure 4 shows the database system architecture.

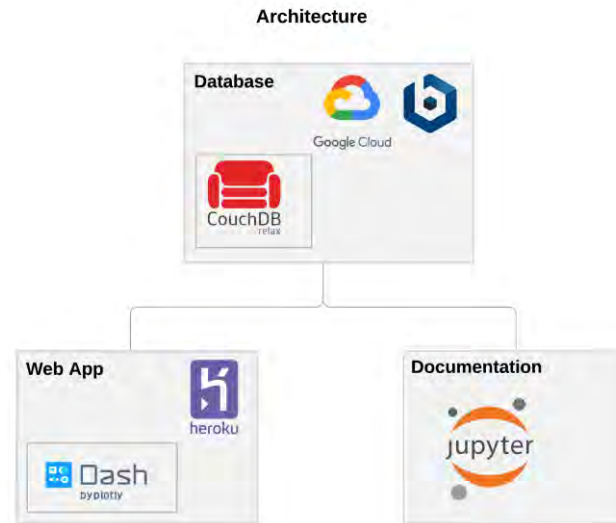


Figure 4: Database System architecture

4. DATABASE DEPLOYMENT

The different data files can be deployed into the database as described below. The data once deployed into the database is retrieved for further analysis and visualisation.

4.1 Station Metadata in the CouchDB

The station metadata available as a station xml file can be processed into dict objects by Python scripts, which are converted into json files once deployed into the CouchDB. The station xml file can also be converted to json dumps for the CouchDB.

4.2 Waveform Data in the CouchDB

The waveform data, available as mseed files, is processed by Python scripts into dictionary objects, and written into the CouchDB json files. Each MSEED file contains traces, where each trace has time series data along with metadata information about the network, station, location, channel, start and end times, sampling rates along with other mseed attributes. The data types of the different values are standardised and saved as dictionary objects. A database is created (if it doesn't exist) in the CouchDB for each waveform data source (event), containing multiple mseed files and the dictionary objects are deployed into the database as json files. Figure 5 displays the database storage structure for the waveform dataset in the Couchdb server.

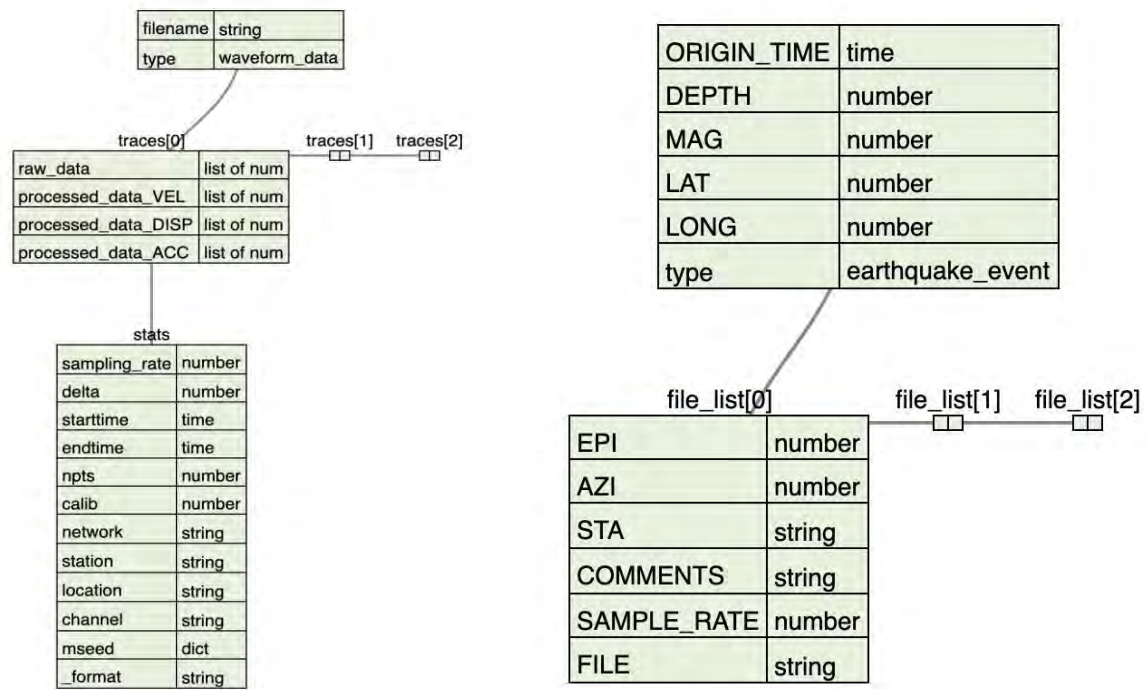


Figure 5: Database storage structure for waveform data and earthquake event data

4.3 Earthquake Events Data in CouchDB

Earthquake event information is originally stored in a CSV (Comma separated Values) file, and each event associates with several mseed files. Each earthquake event will need to be stored as a single document in CouchDB. We will retain all the columns in the CSV file as the schema for the event data. Figure 5 displays the database storage structure for the earthquake event data in the Couchdb server.

5. DATA VISUALISATION

The data can be used for visualising the instrument responses and the time series waveform data, as shown in Figure 1. The instrument response for each earthquake record station can be plotted, Figure 6 shows the instrument response for AU.PIG2.EHE. Additionally, the instrument response can be attached to their corresponding waveform and then subsequently removed as shown in Figure 7.

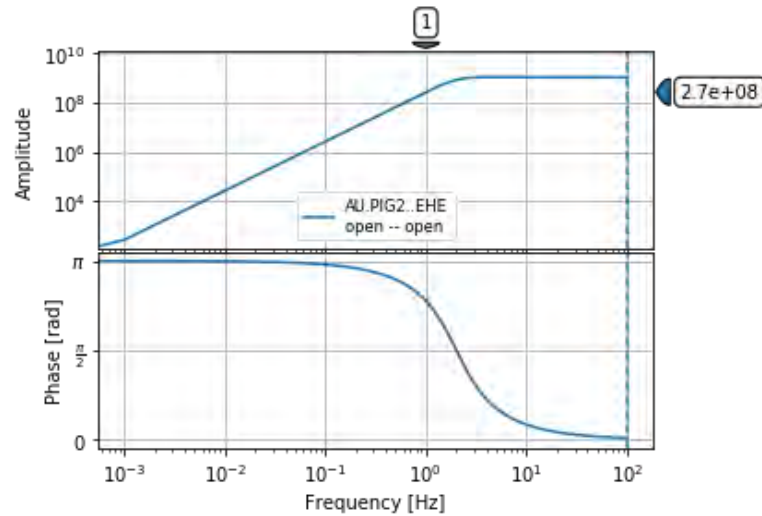


Figure 6: Instrument Response for AU.PIG2.EHE

AU.PIG2.EHE | 2001-12-28T16:31:38.460000Z - 2001-12-28T16:32:17.980000Z | 100.0 Hz, 3953 samples

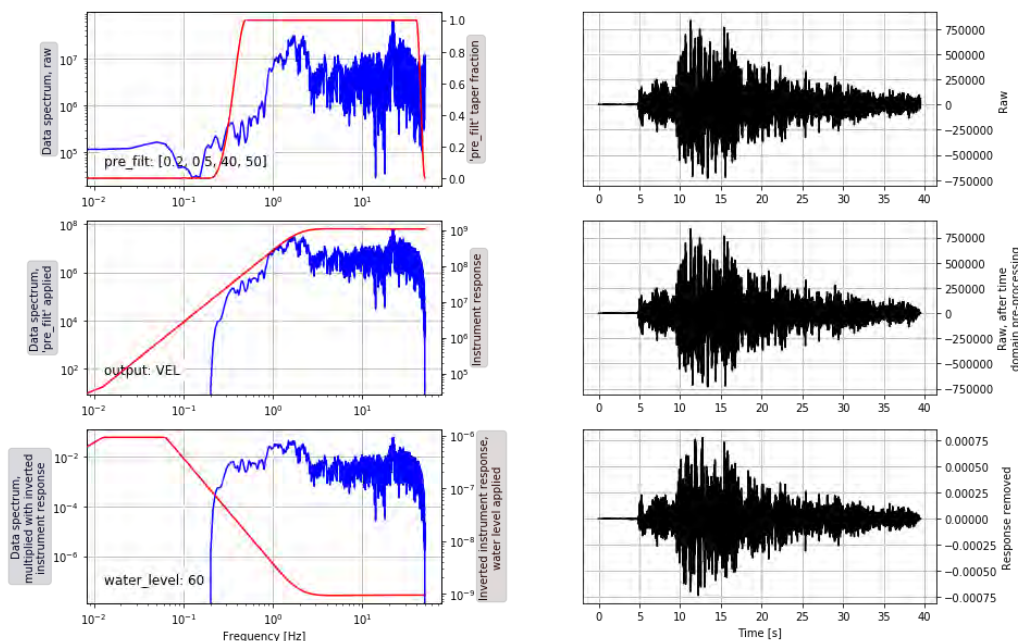


Figure 7: Visuals during response removal in the frequency domain for AU.PIG2.EHE for an earthquake of magnitude 4.5 on 28-12-2001 recorded during the Burakin, WA earthquake sequence (Allen *et al.*, 2006)

Figure 8 shows the web app dashboard that enables the client to query by earthquake events. Waveform data and station meta data will be retrieved according to users' inputs. Some of the important numbers will also be shown on the dashboard, such as Peak Ground Velocity (PGV), Peak Ground Acceleration (PGA) and so on. The dashboard system will greatly reduce the work needed for querying and visualizing results, assisting in downstream analysis.

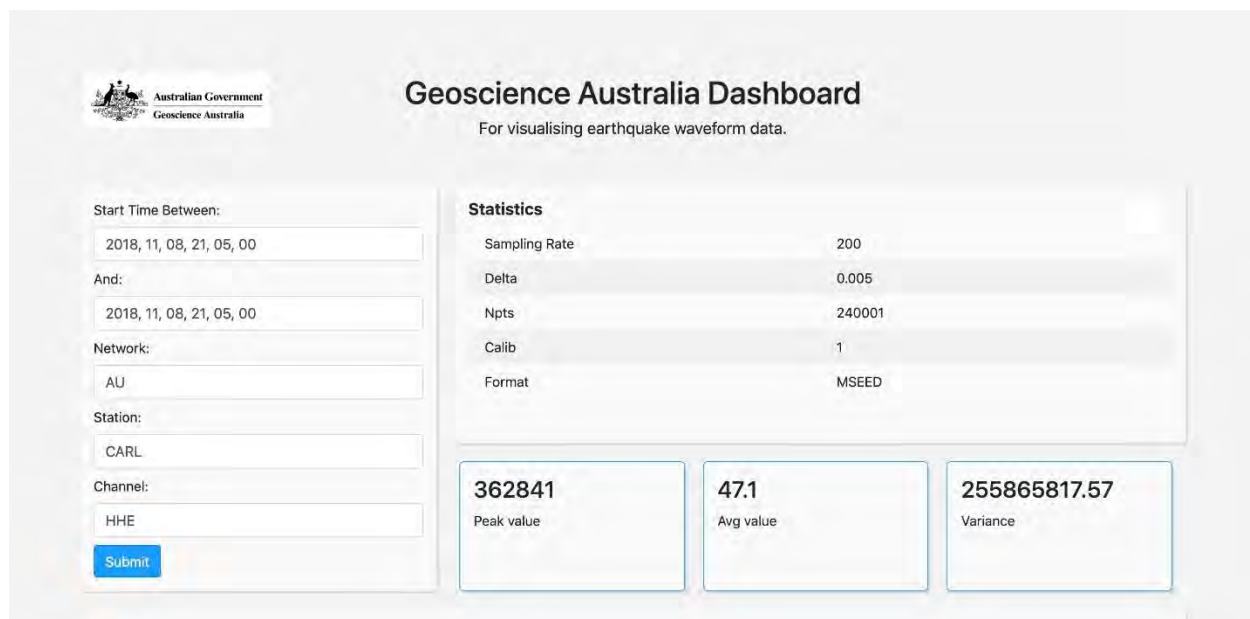


Figure 8: Geoscience Australia Database Dashboard

6. CONCLUSIONS

The objective of the project is to develop a data pipeline to process raw seismic data into processed earthquake ground-motion data and metadata and to store the data in a CouchDB database. Once the database is populated with data in the CouchDB server, data can be retrieved using python scripts for analysis and visualisation. The pipeline is powered and operated by python scripts. Deploying the data pipeline (CouchDB and interactive python scripts) into a cloud based virtual machine, Google Cloud Platform (GCP) handles the increasing size of the database over time, making the database scalable. Secure access can be provided to the database and the python scripts for querying, based on the user access and purpose by the designated database administrator.

The data from the database can be retrieved for use with various toolkits like the OpenQuake engine and the Ground Motion Prediction Equations Strong Motion Modeller's Toolkit (GMPE-SMTK) for the purpose of analysing the performance of various GMMs (Weatherill, 2014).

By aggregating and storing the different earthquake data files (waveform data, station metadata, PAZ data (poles and zeros) and earthquake event data) available into a CouchDB database, this project aims to benefit the seismologists at Geoscience Australia and the earthquake engineering

community by providing a python powered NoSQL database (CouchDB) for analysis of GMMs and data visualisations.

REFERENCES

- Abrahamson. (2007). *Ground motion models no. 3*. Retrieved from http://www.ce.memphis.edu/7137/PDFs/Abrahamson/C07_v2_part1.pdf
- Allen, T. I., T. Dhu, P. R., & Schneider, J. F. (2006). Empirical attenuation of ground-motion spectral amplitudes in southwestern Western Australia. *Bull. Seismol. Soc. Am*, 96, 572–585, doi: 10.1785/0120040238.
- Allen, T., Griffin, J., Leonard, M., Clark, D., & Ghasemi, H. (2018). The 2018 National Seismic Hazard Assessment: Model Overview (GA Record 2018/27). Canberra, Australia.: Geoscience Australia, Commonwealth of Australia.
- Cornell, C. A. (1968). Engineering seismic risk analysis. *Bull. Seismol. Soc. Am*, 58, 1583-1606.
- Cotton, F., Scherbaum, F., Bommer, J. J., & Bungum, H. (2006). Criteria for selecting and adjusting ground-motion models for specific target regions. *Application to central Europe and rock sites. Journal of Seismology*, 10(2), 137.
- Creating stationxml file from scratch obspy*. (n.d.). Retrieved from https://docs.obspy.org/tutorial/code_snippets/stationxml_file_from_scratch.html
- Douglas, J. (2018). *Ground motion prediction equations 1964-2018, Department of Civil and Environmental Engineering, University of Strathclyde July 2018*, pp 624.
- Ghasemi, H., & Allen, T. (2018). Selection and ranking of ground-motion models for the 2018 National Seismic Hazard Assessment of Australia: summary of ground-motion data, methodology and outcomes. *Geoscience Australia Record 2018/29, Canberra*, pp 29,.
- IRIS*. (n.d.). Retrieved from <https://www.iris.edu/hq/>
- McGuire, R. K. (1995). Probabilistic seismic hazard analysis and design earthquakes: closing the loop. *Bull. Seismol. Soc. Am.*, 85, 1275-1284.
- Megies, T., Beyreuther, M., Barsch, R., Krischer, L., & Wassermann, J. (2011). ObsPy – What can it do for data centers and observatories? *Annals Geophys*, 54, 47-58, doi: 10.4401/ag-4838.
- Scherbaum, F., Kuehn, N. M., Ohrnberger, M., & Koehler, A. (2010). Exploring the proximity of ground-motion models using high-dimensional visualization techniques. *Earthquake Spectra*, 26(4), 1117-1138.
- Shanker, U., Misra, M., & Sarje, A. K. (2008). Distributed real time database systems: background and literature review. *Distributed and parallel databases*, 23(2), 127-149.
- Weatherill, G. A. (2014). OpenQuake Ground Motion Toolkit - User Guide. *Global Earthquake Model (GEM) Technical Report*, pp 87, <https://github.com/GEMScienceTools/gmpe-smtk-docs>.

using additional phase data, and the proximity of events within groups becomes more apparent.

Leonard (2008) conducted a major review of Australian seismicity and defined the “South West Australia (SWA) seismic zone” (Figure 1). This was divided by Dent (2016) into eight zones by latitude, A-H (see Figure 1). Two of these zones were subdivided in Dent (2017), creating new zones L and M. In this paper, a new zone, (zone I), is appended to the east of the region to accommodate seismicity north of Ravensthorpe, and some other events which occurred during this study period. Also, zone A is extended northwards to include seismicity near Latham (Figure 1). Earthquake cluster groups within those zones have been named alphanumerically according to the zone in which they fall.

Table 1 The most significant clusters - ie. containing events Magnitude ML 4.0 and above.

Place	Name	Max ML	Date largest event
W of Burakin	A2	5.2	30/3/2002
N of Koorda	C1	4.4	24/11/2004
N of Kalannie	A5	4.1	22/9/2005
Bonnie Rock	L2	4.2	3/1/2017
N of Beacon	B1	4.6	31/1/2009
Yorkrakine	D1	4.6	31/8/1997

The seismicity of the 2017-2020 period is dominated by a sequence near Lake Muir, in the south of the SWA region, that occurred between September 2017 and January 2018. This sequence included two ML 5 events, about 7 km apart. They were described in detail by Dent et al. (2019) and Clark et al. (2020). Each event had its own aftershock sequence, and they are treated as two normal MSAS sequences and therefore will not be discussed in further detail here.

2. Cluster review technique

Clusters were reviewed by relocating the larger events, and other events which seemed peripheral to the groups. They were relocated using the EQLOCL earthquake location program (SRC, Melbourne) and the WA2 earth model. Original GA phase picks were used, but additional data from the PSN (Public Seismic Network, Dent et al., 2010) were usually included. The magnitudes assigned by GA have been carried over.

In all cases, a lower RMS of residuals was achieved. Data from the more remote stations ($> \sim 200$ km) may have been omitted from the calculation if data from closer stations, at approximately the same azimuth, were available. Over 100 relocations were made, and these are being forwarded to the International Seismological Centre in the U.K. identified as CUPWA locations (Curtin University Perth WA).

3. Seismicity June 2017 – June 2020

All GA-located events in southwestern Australia, between June 2017 and June 2020, are plotted on Figure 2A and Figure 2B. These maps include some sub-ML 2.0 events (from ML 1.4) up until August 2019, when GA discontinued putting such events in the catalogue (Glanville, pers. comm., 2020). This may be to address any assumption that the catalogue may be complete to these low magnitude levels.

Cluster centres identified as active prior to June 2017 are shown on these figures (and Figure 1) as green hexagons. A number of studies have already identified several cluster centres within this three-year 2017-2020 period (e.g. Dent & Collins, 2018; Dent & Love, 2018; Dent & Love, 2019), and this will be expanded upon below.

Other potential cluster locations may be identified from the plot of earthquake locations for June 2017 to June 2020 in Figure 2 (A, B). These locations are from the GA online earthquake database (Geoscience Australia, 2020). The central areas of Figure 2 (A, B) are expanded in Figures 3 and 4 for greater detail. Some of the cluster centres identified coincide with centres which were active prior to this study (shown as green hexagons), and are listed in Table 2. The overall seismicity of this three-year period is divided in this report into three categories:

- 1) activity at cluster centres which were also active prior to 2017
- 2) activity at cluster centres not (yet) known to be active prior to 2017
- 3) all other seismicity.

3.1. Category 1: Continuing or renewed activity at cluster centres noted prior to June 2017

This category contains clusters active between June 2017 and June 2020, but which were also active in the years before this (and recognised and defined in previous reports, as listed in Table 2). There are 14 clusters in this category. These clusters are significant in that they appear to demonstrate that some cluster locations may be relatively long lived. Activity at B1 (Figure 4) was first noted in 2009 (Dent, 2009; Dent, 2012), and events from the Morbinning location (F3 – Figure 5) may go back to the 1960s (Dent & Collins, 2016). The cluster locations in Category 1 were discussed in the reports cited in Table 2, but extra points of interest for some of them are given below.

B1 (north of Beacon – Figure 3):

There are seven events (the largest being ML 2.9) most of which occurred on 17 September 2018. These events, although not well located, appear to be co-located. No other activity has been noted at this centre since then. This was the site of six ML 4 events and over 250 smaller events in early 2009 (Dent, 2009), and is noted in Table 1.

B2 (NW of Beacon – Figure 2A):

About 100 events are shown in the figure, including five ML 3 events (largest ML 3.4). These are in a region where three cluster centres have already been defined (B1, B2 & B4); but the events seem dispersed, and the relationship to the three cluster centres (if any) is not clear. The area is expanded in Figure 3. Several events have been re-located, using additional data from the PSN network and are plotted in Figure 4. The relocations (with smaller RMS of residuals) bring many events close to location B2. The findings suggest that most of the other events could also be relocated to this location. B2 was a site of significant activity in 2012, and data from some field stations that operated at that time was used to relocate the events and better define the cluster location (Dent, 2018).

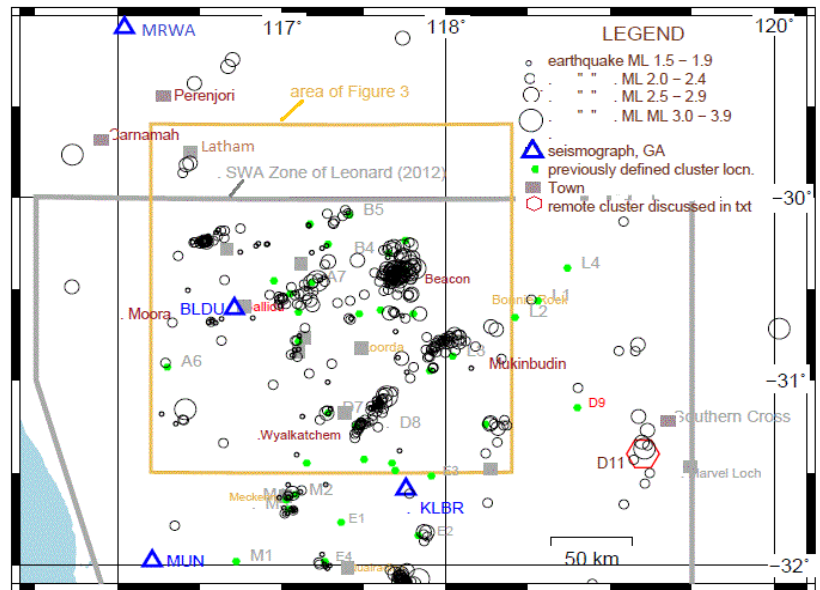


Figure 2A Earthquakes 2017-2020 in SWA (Northern region).

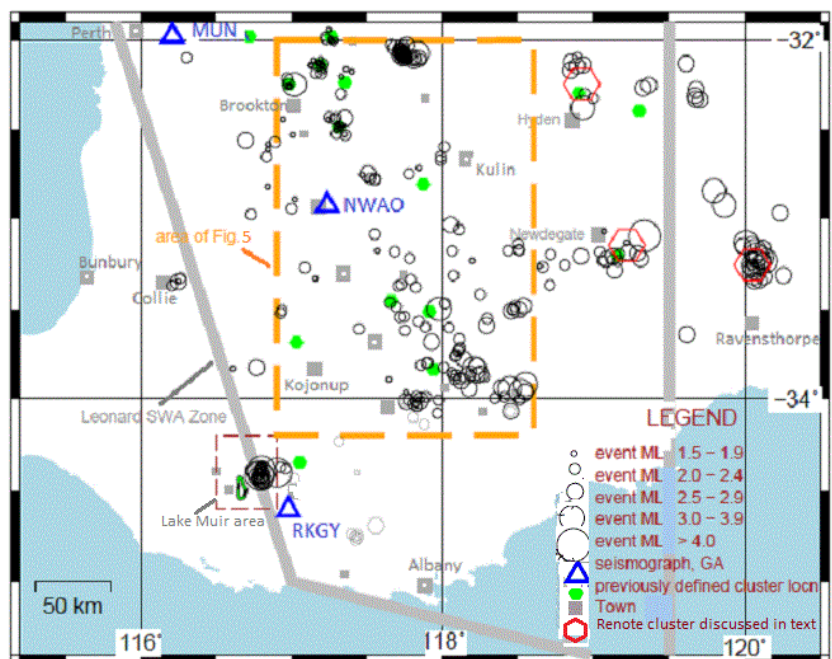


Figure 2B Earthquakes 2017-2020 in SWA (Southern region).

It is estimated that approximately 75 events may have come from the B2 location in 2019. In 2012, the same region produced about 80 located events; the largest at that time was ML 3.5, suggesting a similarity in the levels of activity in 2019 and 2012.

D2 (ESE of Wyalkatchem – Figure 3): This cluster was originally defined in Dent (2012), based on a small group of events that occurred in 2011. Events at that time showed a NE-SW lineation, as do the events in Figure 3. Figure 3 shows a similar lineation in the events to the north, near Yelbeni, about 20 km NE of Wyalkatchem (Dent & Love, 2018). However, as shown in Dent & Love (2018), the lineation largely disappears when events are relocated using additional data. This is consistent with an investigation by Dent (2010) which suggested a similar orientation for events near Koorda was introduced by the poor azimuthal distribution of the recording stations.

E2 (West of Bruce Rock – Figure 2A): This group of 5 events, between 13 and 15 June 2020 (largest event ML 2.6), is at the same location as a group of 6 events in 2013-2014 (largest ML 2.4).

G1 (SW of Dumbleyung – Figure 5): A group of ~ 20 events (including three ML 2.9 events) occurred in the area in 2013 and 2014. The end of the cluster was monitored by temporary field instruments (Dent 2014), and a probable origin point defined (G1- Dent 2017). The 2020 events are not well located, but seem to come from the same location.

G3 (south of Newdegate – Figure 2B): This centre was defined in Dent (2017) on the basis of an ML 3.1 event in May 2017, and several smaller events earlier in that year. About another six events occurred in 2019, including a magnitude ML 4.3 event in June 2019.

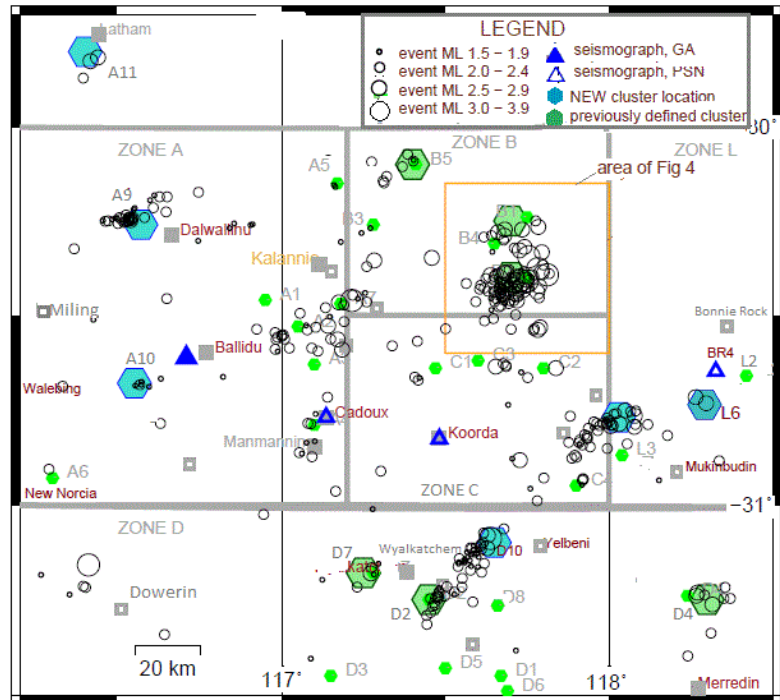


Figure 3. Expanded view of Figure 2A. Legend as in Figure 2A, blue hexagons are new clusters.

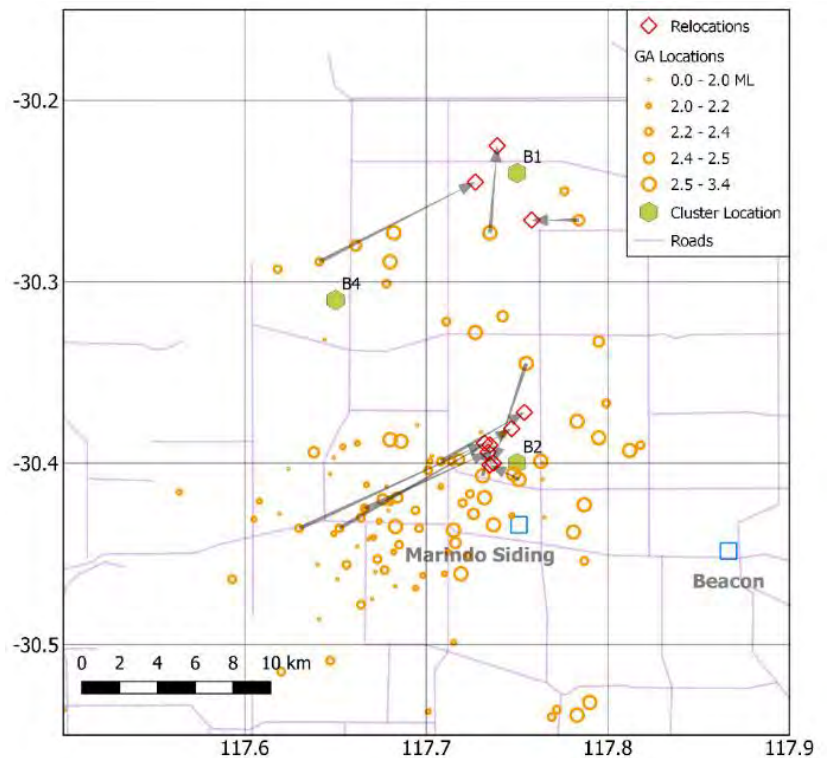


Figure 4. Earthquakes and relocations near Beacon, 2017-2020

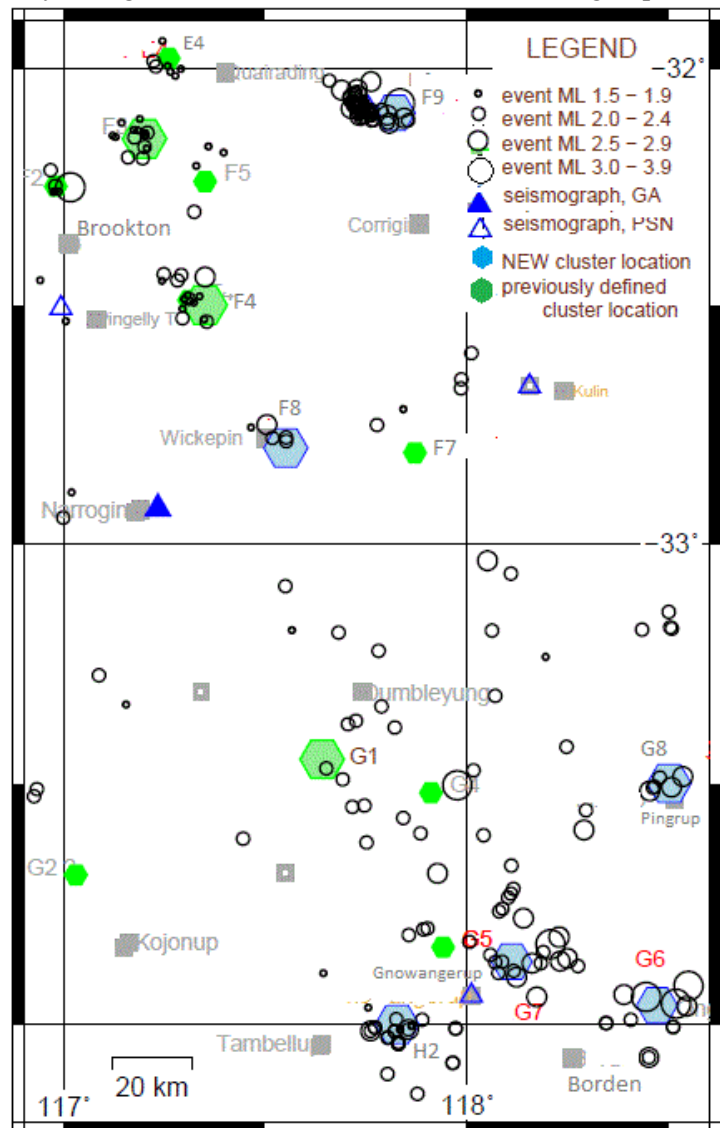
Table 2 Category 1 Clusters which were also active (and identified) prior to June 2017.

Name	Place Name	Number of Events	Active Period	Maximum Magnitude	Latitude	Longitude	Reference
B1	N of Beacon	7	Sep 2018	2.9	-30.24	117.75	Dent (2012)
B2	NW of Beacon	109	Jun 2019	3.4	-30.40	117.75	Dent (2014)
B5	NE of Kalannie	10	Apr-May 2018	2.4	-30.10	117.41	Dent (2017)
D2	SE of Wyalkatchem	20	Dec 2019	2.3	-31.25	117.45	Dent (2012)
D4	N of Merredin	7	Oct-Nov 2017	2.6	-31.24	118.24	Dent (2015)
D7	W of Wyalkatchem	4	Jun 2019	2.6	-31.18	117.28	Dent (2017)
E2	W of Bruce Rock	5	Jun 2020	2.9	-31.84	117.84	Dent (2016)
E4	W of Quairading	6	Jun 2020	2.3	-31.90	117.24	Dent & Collins (2018)
F1	N of Hyden	5	Jun 2018	2.9	-32.30	118.90	Dent (2014)
F2	N of Brookton	6	Mar 2019	3.1	-32.25	116.98	Dent (2014)
F3	Morbinning	15	Apr-May 2018	2.4	-32.14	117.19	Dent (2014)
F4	East of Pingelly	15	June 2018	2.9	-32.49	117.31	Dent (2014)
G1	SW of Dumbleyung	5	Feb 2020	2.4	-33.46	117.66	Dent (2014)
G3	Sth of Newdegate	16	Jun 2019	4.3	-33.21	119.16	Dent (2016)

F1 (north of Hyden – Figure 2B): There are about 15 events in this area, which is about 30 km west of a 30 km long palaeo-scarp investigated by Clark et al., (2008). Events in this area need further examination as they are hard to locate accurately, being remote from most seismic stations. A group of five events occurred north of location F1 in June 2018 (largest ML 2.9), and a relatively solitary ML 3.1 event about 30 km south of this in December 2019. The events are all provisionally allocated to location F1, which has been a source of significant intermittent activity since about 2012.

3.2. Category 2: Newly noted clusters active in 2017 – 2020

The clusters in this category were active between June 2017 and June 2020 but were not identified in studies of earlier seismicity. Some recent studies of the seismicity within this period identified new cluster locations, but they have not yet been named according to the zonal convention used here. These clusters are listed and named in Table 3 along with the references to the reports that described them. Their locations are shown in Figures 2 to 5 (filled blue hexagons in Figure 5). Other cluster centres are noted for the first time in this report and are also listed in Table 3 (indicated as ‘new’) and shown in Figures 2 to 5 (blue hexagons in Figure 5). A brief description of each of these new cluster groups is given below. The major event in each group has been relocated using additional Public Seismic Network (PSN) phase data, and sometimes smaller events have also been relocated. The clusters have been assigned names according to the zonal convention used

**Figure 5 Seismicity in northern regions of SWA, 2017- Expanded view of Figure 2B**

above. The locations of the clusters were strongly influenced by the relocation of selected events, but the general distribution of the GA-determined epicentres in the groups is also considered.

A9 (west of Dalwallinu – Figure 3): The largest event in this group was ML 2.4. The GA locations show an east-west lineation over about 25 km. The largest events seem to plot to the NE of the cluster area, but the relocations move them to the main group. The east-west trend is probably a function of poor seismograph distribution.

A10 (SW of Ballidu – Figure 3): The largest event was ML 2.3 and its relocation confirms the GA location. There were about 6 events in this group.

Table 3 Category 2 Newly identified cluster centres (active June 2017- June 2020).

Name	Place Name	Number of Events	Active Period	Maximum Magnitude	Latitude	Longitude	Reference (or new)
L5	NW of Welbungin	~40	Jun 2017	2.9	-30.75	118.02	Dent & Collins (2017)
L6	N of Mukinbudin	3	25 Jan. 2019	2.6	-30.73	118.30	new
D10	NW of Yelbeni	36	Dec 2017	2.4	-31.12	117.61	Dent & Love (2017)
F9	N of Corrigin	46	Jul 2017	3.3	-32.05	117.82	Dent & Judge (2017)
G6	N of Ongerup	9	Jan 2019	3.6	-33.96	118.47	Dent & Love (2019)
G7	NE Gnowangerup	20	Mar 2019	3.5	-33.87	118.11	Dent & Love (2019)
A11	S of Latham	3	Apr 2020	2.9	-29.80	116.40	new
A9	W of Dalwallinu	15	Jun 2018	2.4	-30.23	116.57	new
A10	SW of Ballidu	6	May 2018	2.3	-30.68	116.55	new
D11	NW of Marvel Loch	5	Jul-Oct 2017	3.1	-31.37	119.21	new
F8	W of Wickepin	5	Dec 2017	2.6	-32.84	117.59	new
G8	N of Pingrup	6	Dec 2019 - Jan 2020	2.6	-33.50	118.50	new
H2	NE of Tambellup	8	March 2018	2.8	34.00	117.826	new
I1	N of Ravensthorpe	24	Sep 2017	3.5	-33.19	119.98	new

A11 (south of Latham – Figure 3): This is a small cluster of three events (ML 2.5, 2.9 and 2.2) occurring in March, April and May of 2020. D10 (NW of Yelbeni): First described in Dent & Love (2018), more events have occurred at this location since that report.

D11 (NW of Marvel Loch – Figure 2A): This group is about 30 km south of Southern Cross, and contains at least 5 earthquakes, which occurred between July and October 2017, with MLs between 2.4 and 3.1. The events are outside of the optimal area for locations, and so location uncertainties are relatively large.

F8 (SE of Wickepin – Figure 5): There were five events in December 2017, the largest being ML 2.6. The gap angle is large (there are no GA stations to the east of the events), meaning larger epicentral uncertainties. Relocations suggest the true location is about 10 km SE of the GA locations.

F9 (north of Corrigin – Figure 5): A group of nearly 50 events, which followed an ML 3.3 event on 19 July 2018. Most of the events (~30) were in the first 3 days, but some late aftershocks were well recorded by a field station placed less than 10 km from the epicentre, allowing a good estimate of the cluster location to be made. The cluster is described in more detail in Dent & Judge (2017).

G6 (north of Ongerup – Figure 5): This group includes three ML 3+ events between January and August 2019, the first of which was the largest (ML 3.6). The group is described in more detail by Dent & Love (2019).

G7 (NE of Gnowangerup – Figure 5): This group contains about 30 events, mostly in March 2019. The largest event was ML 3.5 on 11 March 2019. It is described in more detail in Dent & Love (2019). It is approximately contemporaneous with the nearby Ongerup cluster described above.

G8 (north of Pingrup – Figure 5): A group of six relatively small events (largest ML 2.6) between December 2019 and January 2020.

H2 (east of Tambellup – Figure 5): This group of approximately eight events is scattered through 2018, 2019 and 2020. Three of them were in March 2018 (largest ML 2.8). Another five events occurred in late 2019-early 2020. These events seem to be at the same location as a group which occurred between 1999 and 2000, the largest of these being ML 2.5 (10 October 1999).

I1 (N of Ravensthorpe – Figure 2B): This group was active between August and September 2017 and may be the most significant cluster group in southwest Australia in the 2017-2020 period. It began with an ML 3.1 event on 24 August 2017, followed by three more events in the next three days. Stronger activity returned on 9 September 2017 with another ML 3.1 event, and high levels of activity continued until an ML 3.5 event occurred on 11 September 2017. The last recorded event was on 16 September (ML 2.5). In all there were 24 located events of which eight were $ML \geq 3.0$, but there were almost certainly more unlocated events of lesser magnitudes. A temporary station installed at Ravensthorpe in late September 2017 did not detect any aftershocks.

L5 (NW of Welbungin – Figure 3): Originally described in Dent & Collins (2017), but the number of events at this location has approximately doubled in the two years since that report, bringing the total number of events to about 40. The largest of these more recent events was ML 2.9 (22 February 2020) – the same magnitude as the largest of the earlier group.

L6 (north of Mukinbudin – Figure 3): Three events were located by GA between 1700 and 1705 UTC on 25 January 2019, the largest being ML 2.6. The smallest (ML 2.1) was located by GA about 20 km SW of the other two, but reference to the nearby PSN station (BR4) indicates they all had the same S-P time (1.5 sec) and therefore came from the same location. Another 10 smaller events from the same location can also be identified on BR4. The location is named L6, and reference to Figure 6 shows that it occurs within a NE trending zone of cluster locations, named as the “Bonnie Rock seismic lineament” in Dent & Collins (2018).

3.3. Category 3: All other seismicity, 2017 to 2020

This represents the seismicity remaining after the above cluster groups are removed from the catalogue. They consist mainly of mainshock/aftershock (MSAS) sequences, and other apparently independent events. These remaining events, or groups of events, are divided into two categories:

- large (ML 3.0 and above), of which there are six groups, the details of which are discussed below (they are indicated as red circles on Figure 6)
- small (less than ML 3.0).

3.3.1 Large events and groups of events (see red circles, in Figure 6)

1) Lake Muir. The Lake Muir seismicity (September 2018 to February 2019) consisted of an ML 5.7 event (September 2018) and an ML 5.2 event (November 2018), each with its own group of many aftershocks (Dent et al., 2019; Clark et al., 2020). In all, there were 13 events of ML 3.0 or more, and about 800 smaller events in the sequence.

Table 4 Category 3- larger solitary or MSAS sequences (ML 3.0 and above).

Location	Date	ML	Comment
West of Burakin	31/8/2017	3.9	Solitary
Dumbleyung	23/5/2018	3.1	Solitary
Lake Muir	16/9/2018	5.3	Many aftershocks
Calingiri	29/9/2018	3.2	1 small aftershock
SW of Carnamah	29/12/2018	3.0	Solitary
NE of Southern C.	23/6/2019	3.8	Solitary
N of Denmark	01/8/2019	3.8	4 small aftershocks

2) Burakin. August 2017, ML 3.9. This event occurred about 10 km northeast of Burakin, and there were no nearby events in the week leading up to the event, or after it. A relocation of this event has confirmed its location, but some other events in the area between 2017 and 2020 probably represent continuing activity from the important swarm about 12 km west of Burakin, noted in Table 1, and shown as Location A2 on Figure 3. This was mostly active between September 2001 and May 2002, (Leonard, 2002) and included three ML 5 events. Relocation of an ML 2.9 event on 30 August 2018 moves it about 10 km westwards to a location suggested by Dent & Collins (2020) to be the source of all three magnitude 5 events.

3) North of Denmark. The events of 1 August 2019, the largest event being ML 3.8. This group was studied by Dent & Love (2019). The main event is about 15 km NE of a group of aftershocks, but relocates close to the other events. This group is classed as a normal main shock/aftershock (MSAS) sequence.

4) Calingiri. The main event was ML 3.2 on 29 September 2018, and there was an ML 2.0 foreshock on 10 September. The pair are classed as an MSAS sequence, and they are about 10 km southwest of the ~ 3km surface rupture produced by the ML 5.7 event of March 1970 (Gordon & Lewis, 1980).

5) Dumbleyung. The events of 28 May 2018, the largest event being ML 3.1. This event appears isolated, but an ML 2.1 event 10 km to the southeast which occurred two hours later is a probable aftershock. The event is here termed *isolated*, but it locates close to cluster G4 (Nyabing), which was defined on the basis of a group of events in December 2015, the largest being ML 2.9 (Dent, 2016); this event may be related to that location.

6) SW of Carnamah. The event of 29 December 2018, magnitude ML 3.0. There were no other events near this earthquake. It is an isolated event.

3.3.2. Remaining seismicity events smaller than ML 3.0

A concentration of events is noted near Cadoux and Burakin. Burakin was the site of intense seismicity in 2001 to 2002 (Leonard, 2002; Dent & Collins, in prep.), and Cadoux has seen periods of activity since the magnitude ML 6.1 event in 1979 (Lewis et al., 1981). A concentration of events is also seen near Meckering, site of a magnitude ML 6.9 event in 1968 (Gordon & Lewis, 1980). The events in these areas are not particularly clustered in time, and locations are not good enough to say confidently that many are co-located, so no new cluster locations have been defined.

Many of the remaining unassociated events are relatively small (e.g. ML 2.0 or less) and have relatively large epicentral uncertainties (e.g. greater than about 10 km), and this makes interpretation of associations difficult. Some may belong to some of the groups already discussed above. Others may belong to minor cluster groups that have not yet been identified. A minority of the remainder may be genuinely *isolated* or *independent* events.

4. Discussion

In this report, 28 earthquake cluster groups active between June 2017 and June 2020 are identified. Fourteen are centres identified from activity prior to June 2017, and 14 are identified for the first time in this report. It seems likely that some or all of these 14 may also be found to be represented in the earlier seismic record – i.e., from 1959, when seismic monitoring in SWA began, to ~2010, which is about the time a systematic search for earthquake clusters began.

A problem with the analysis is the (variable) uncertainty in epicentral locations, which is largely a function of the number and positioning of the recording seismographs. GA has used five seismographs in the region for the location of most of the events discussed here. The number of seismographs in the

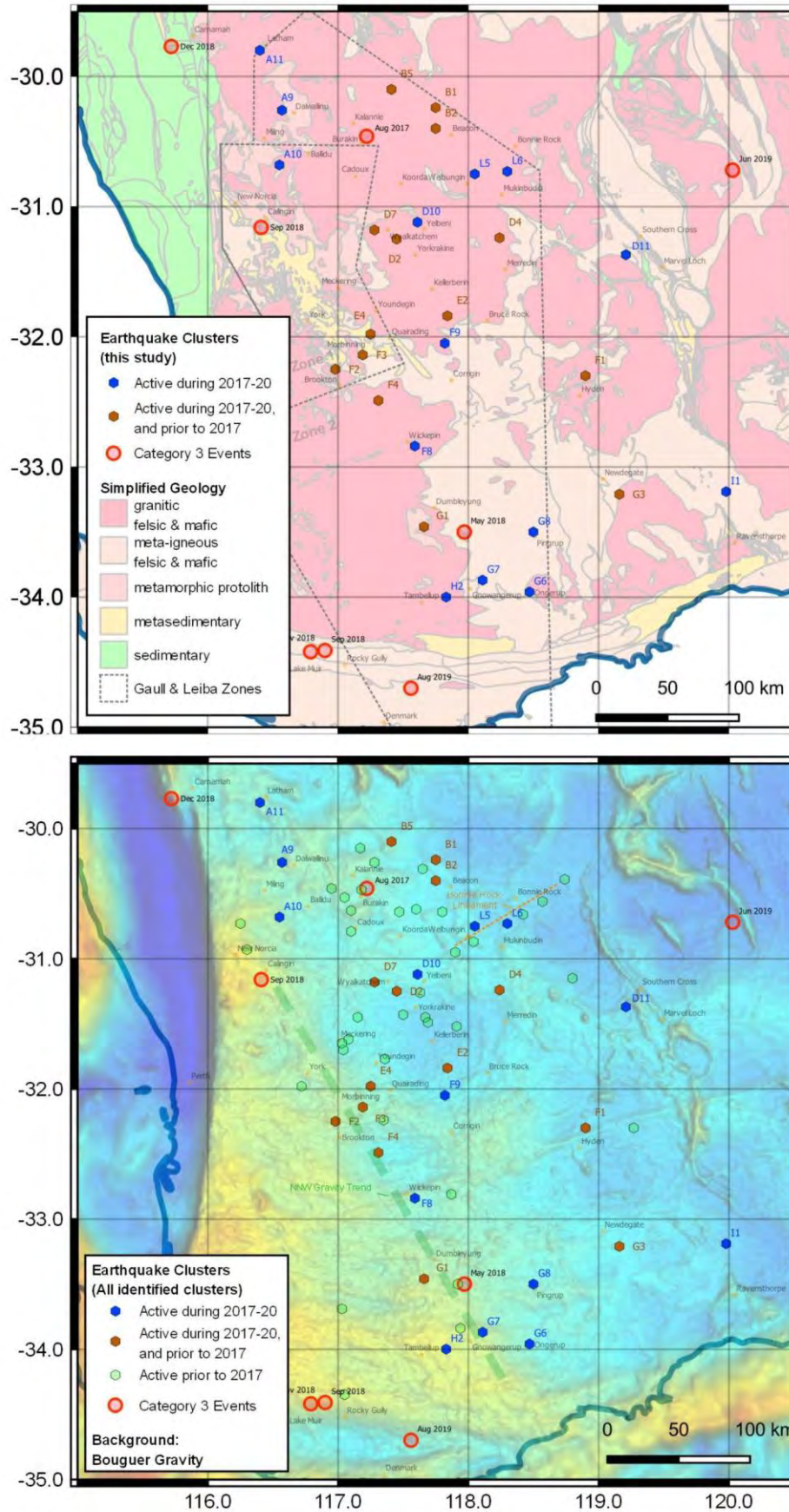


Figure 6. A) Clusters active during 2017-2020; background is simplified interpreted bedrock geology. B) All identified earthquake clusters; background is Bouguer gravity.

area increased in mid-2020, when the Geological Survey of WA installed four new seismographs (near Koorda, Beacon, Mukinbudin and Ongerup), and it is expected that future earthquakes in the region will be located with increased precision, and that the clustering of earthquakes will consequently be more obvious.

Figure 6 summarises the seismicity during 2017-2020, simplified by reducing groups of earthquakes to cluster points as discussed above. Clusters which were identified as active only during this period are shown in blue; those which were also active prior to June 2017 are shown in brown. Some larger events during this period are not considered to belong to a cluster (i.e. defined here as Category 3 events) and are shown as red circles in Figure 6. In all, 14 new clusters are added to the previous total of 51. Note that uncertainties remain in the location of these cluster centres, particularly for those remote from the centre of the region in Figure 1 (i.e. outside the optimum location region of the seismograph network). It is possible that future seismicity may help to refine the locations, particularly if closer stations are installed.

The geological elements of the region, simplified from the 1:500,000 map of interpreted bedrock geology of Western Australia (Geological Survey of Western Australia, 2020a), are shown in Figure 6A. The cluster locations define a NNW trend, and follows a trend observable in the Bouguer Gravity Anomaly map of the region (Geological Survey of Western Australia, 2020b) shown in Figure 6B. This association was noted by Everingham (1968), and it can be seen that the majority of clusters are found within the igneous granitic regions of the South West Terrane of the Yilgarn Block. The meta-igneous and meta-sedimentary areas host few clusters and have a lower overall seismicity. Many of the isolated events occur to the southwest of the majority of the seismicity. The Lake Muir events are on the southern border of the Yilgarn craton with the Albany-Fraser Orogen, or possibly within the orogen.

The majority of clusters so far defined are distributed throughout two zones identified by Gaull & Michael-Leiba (1987), as shown on Figure 6. However, some significant clusters (eg, the “north of Ravensthorpe” cluster, 11, are to the east of these zones. Gaull and Michael-Leiba (1987) assigned a higher hazard rating to zone 1 as it contained the two major earthquakes in the catalogue at that time - i.e. Meckering (1968) and Cadoux (1979). Many of the clusters noted in the southern regions of Figure 6 were active after 2018, which may indicate increased seismicity levels in the south following the two magnitude ML 5 events at Lake Muir in late 2018.

4. Acknowledgements

Many thanks to Clive Collins for his extensive comments and edits. The constructive comments by Trevor Allen, Virginia Ward Mike Turnbull and Ruth Murdie are also much appreciated.

5. References

- Clark, D., Dentith, M., Wyrwoll, K.H., Yanchou, L., Dent, V. & Featherstone, W., 2008. The Hyden fault scarp, Western Australia: paleoseismic evidence for repeated Quaternary displacement in an intracratonic setting. *Aust. J. Earth Sci.*, V 55
- Clark, D. J., Brennand S., Brenn G., Garthwaite M. C., Dimech J., Allen T. I., and Standen S., 2020. Surface deformation relating to the 2018 Lake Muir earthquake sequence, southwest Western Australia: new insight into stable continental region earthquakes. *EGU Solid Earth*, 11, 691–717.
- Denham, D., Alexander, L., Everingham, I., Gregson, P., R McCaffrey, & Enever J., 1987. The 1979 Cadoux earthquake and intraplate stress in Western Australia, *Aust. J. Earth Sci.*, 34, 507-521.
- Dent, V. F., 2010. A NE lineation of epicentres northeast of Perth – fact or fiction? A review of earthquake hypocentres in the region, 2005. In: Proc. AEES 2010, Conference, Perth.

- Dent, V. F., Harris, P, and Hardy, D., 2010. A new seismograph network in the southwest seismic zone of Western Australia. In: *Proc. AEES 2010, Conference, Perth, WA.*
- Dent, V.F., 2011. The Yorkrakine, W.A. seismic deployment, April – May 1996. In: *Proc. AEES 2010 Conference, Barossa Valley.*
- Dent, V. F., 2012. Evidence for shallow focal depths and denser locations for three southwest seismic zone earthquake clusters, 2011. In: *Proc. AEES 2012 Conference, Gold Coast, Qld.*
- Dent, V.F., 2016. Clustered seismicity in the Southwest Australia seismic zone, 2015-2016. In: *Proc. AEES 2026 Conference, Melbourne.*
- Dent, V.F., 2017 Earthquake clusters in the southwest Australia seismic zone, June 2016-May 2017. In: *Proc. AEES 2017, Conference, Canberra.*
- Dent, V.F., & Judge, A., 2017. Investigation of an earthquake cluster near Corrigin, southwestern Australia, July 2017. In: *Proc. AEES 2017, Conference, Canberra.*
- Dent V.F., & Collins, C., 2017. A new interpretation of the seismicity of the Mukinbudin/Bonnie Rock area of Western Australia. In: *Proc. AEES 2017 Conference, Canberra.*
- Dent, V. F. & Love, D., 2018. An earthquake cluster east of Wyalkatchem, Western Australia, in late 2017. In: *Proc. AEES 2018, Conference, Perth.*
- Dent, V.F. & Collins, C.D.N., 2018. Seismicity of the Quairading area, Western Australia, with special reference to an earthquake cluster in 1992. In: *Proc. AEES 2018, Conference, Perth.*
- Dent, V.F. & Collins, C.D.N., 2018. Clustered seismicity in southwest Australia, June 2012 – May 2013. In: *Proc. AEES 2018, Conference, Perth*
- Dent, V. F. & Love, D., 2019. Seismicity in 2019 in the Great Southern region of Western Australia. In: *Proc. AEES 2019, Conference, Newcastle.*
- Dent, V. F., Love, D. & Collins, C., 2019. Possible clustering in space and time of aftershocks of the ML 5.7 Lake Muir earthquake, southwest Australia, 16 September 2018. In: *Proc. AEES 2019, Conference, Newcastle.*
- Dent, V. F., & Collins, C., 2020. The extent of the epicentral zone for events associated with two ML 5 events in March 2002 near Burakin, Western Australia - a review of field and epicentral data. In: *Proc. AEES 2020, Conference.*
- Everingham, I.B., 1968. The seismicity of Western Australia, *Bureau of Mineral Resources, Geology and Geophysics*, Report 132.
- Gaull, B. A. and Michael-Leiba, M., 1987. Probabilistic earthquake risk maps of southwest Western Australia, *BMR Journal of Australian Geology and Geophysics* 10, 145-151.
- Geoscience Australia, 2020. *Online Earthquake Database*. Available at <https://earthquakes.ga.gov.au/>. Accessed 01 June 2020.
- Gordon, F.R. and Lewis, J.D., 1980. The Meckering and Calingiri earthquakes: October 1968 and March 1970. *Geological Survey of Western Australia Bulletin* 126.

Leonard, M., 2002. The Burakin WA earthquake sequence Sep 2000 – June 2002. In: *Proc. AEES 2002 Conference*, Adelaide.

Leonard, M., 2008. One Hundred Years of Earthquake Recording in Australia. *Bull. Seismol. Soc. Am.* 98, 1458–1470.

Lewis, J.D., Daetwyler, N.A., Bunting, J.A. and Moncreiff, J.S., 1981. The Cadoux Earthquake 2 June 1979. Geological Survey of Western Australia, Report 11, pp 69.

Geological Survey of Western Australia, 2020a. 1:500 000 State interpreted bedrock geology of Western Australia, 2020: Geological Survey of Western Australia, digital data layer, www.dmirs.wa.gov.au/datacentre.

Geological Survey of Western Australia, 2020b. WA Gravity - Version 1 - 2016: Geological Survey of Western Australia, digital data layer, www.dmirs.wa.gov.au/datacentre.

The extent of the epicentral zone for events associated with two ML 5 events in March 2002 near Burakin, Western Australia - a review of field and epicentral data

V. F. Dent[#] & C.D.N. Collins^{##}

[#]University Associate, Curtin University, Perth, W.A.; Honorary Research Associate, The UWA Institute of Agriculture, UWA, Perth: Email: vic_dent@yahoo.com

^{##}G.P.O. Box 2972 Canberra ACT 2601: Email: cdncollins@inet.net.au

Abstract

A significant series of earthquakes occurred near Burakin in the northern WA wheat belt between September 2001 and June 2002, including three ML 5 events. Geoscience Australia (GA) deployed up to 15 field seismographs in the area at various times in that period to provide better earthquake locations, but a detailed review of the data has not been performed. The larger events in March 2002 are relocated here by giving most weight to the closer field stations and using a velocity model with lower velocities. The seismic activity from 20 March 2002 onwards (10 days before the largest event, ML 5.2) was higher than that from 1 – 20 March. The relocations have resulted in most GA locations shifting 1 – 2 km, and some larger events by up to 5 km. In particular, the ML 5.0 event of 5 March was relocated about 4 km southwest. The relocations effectively reduce the epicentral spread, suggesting the origin of the seismicity is confined to a single fault, or a system of faults of limited extent.

1 Introduction

The Burakin region is about 250 km north-northeast of Perth (**Error! Reference source not found.**), and in the north of a seismically active region known as the Southwest Seismic Zone (SWSZ), (Doyle, 1971). The SWSZ hosted the very damaging 1968 Meckering earthquake (Gordon & Lewis, 1980). Burakin is only about 40 km north of the 1979 Cadoux earthquakes (Lewis et al., 1981), which also caused surface rupturing (**Error! Reference source not found.**). The Burakin area was seismically active from September 2001 to June 2002, with about 500 events located by GA, including an ML 5.2 event on 28 September 2001, and two more ML 5 events in March 2002. Leonard (2003) noted other peaks in activity on 28 December 2001 and 4 February 2002. Lesser sporadic activity has continued to the present day. Epicentres with magnitudes of 3.0 and above that were determined by Geoscience Australia (GA) for the 12-month period July 2001 - June 2002 are shown on **Error! Reference source not found.**.

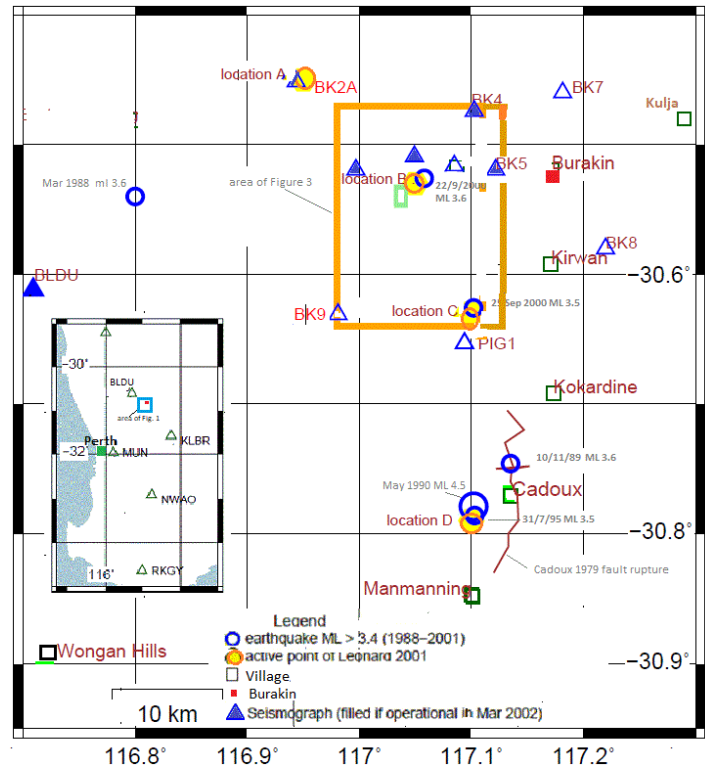


Figure 1: Location map.

The previous magnitude 5 event in the SWSZ occurred 11 years earlier (ML 5.5 near Meckering, January 1990), and the next magnitude 5 event following the Burakin events occurred 17 years later (magnitude Mw 5.3 near Lake Muir, September 2019). The Lake Muir sequence is probably one of the best-studied earthquake sequences in Australia, but the epicentre plots (in Dent et al., 2019, Clark et al., 2020) only vaguely followed the 5 km surface rupture that the earthquake produced.

GA deployed field recorders at approximately 15 different locations between September 2001 and June 2002, but for much of this period the number of stations contributing data was much less than this. Unfortunately, the quality of the locations (as indicated by the locations of the stations used, the RMS of residuals, the number of defining phases, etc.) is not recorded for events in the GA earthquake database before 2011. However, GA has kindly provided much of the original data to the authors (digital seismograms and computer location files) and these data have been used in this study.

The Burakin region seismicity was initially discussed by Leonard (2002, 2003), but has not yet been described in detail. As stated by Leonard (2002) there are estimated to be over 16,000 earthquakes in the Burakin sequence from September 2001 to June 2002, and a full review of available data is not attempted here. In this report, only March 2002 events are reviewed, but this period includes two of the three ML 5 events. Other periods may be discussed in following reports. **Error! Reference source not found.** suggests the Burakin events within this period are relatively dispersed and no trends in the data have previously been proposed. The object of this paper is to present improved earthquake locations, and to try to clarify any trends in epicentral distribution.

Given that many of the more recent ML 5+ events in the WA wheat belt area have caused measurable ground rupturing or displacement, e.g. Kalannie in 2005 and Katanning in 2007 (Dawson et al., 2008); and Lake Muir, in 2018 (Clark et al., 2020) it may be that there was some ground displacement associated with this group of events, but it escaped detection at the time (Interferometric Synthetic Aperture Radar (InSAR) measurements were not available) and would by now be too eroded to observe.

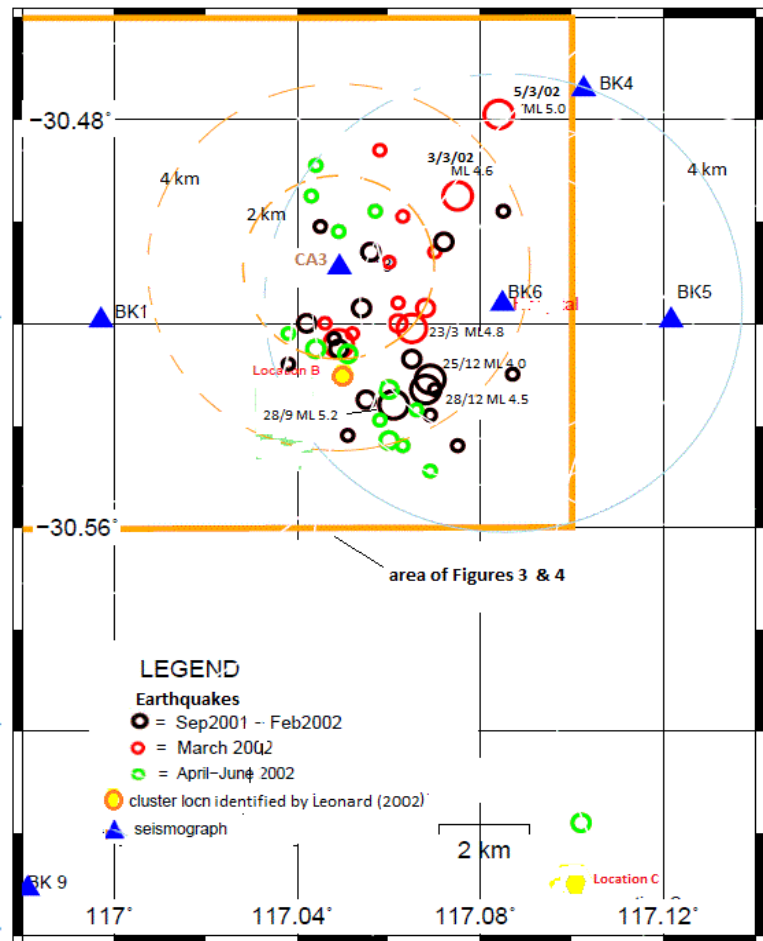


Figure 2: Events near Burakin, ML 3 and above September 2001 – June 2002

The field station CA3 (**Error! Reference source not found.**) was the closest to the seismic activity with most events less than 5 km from it. Fortunately, CA3 operated throughout most of the active period, with only minor periods of downtime. The use of CA3 data is essential if any credence is to be given to the computed focal depths. For good depth control, at least one recording station is needed at an epicentral distance similar to the focal depth of the earthquake. For most of March 2002, BK1 (**Error! Reference source not found.**) was the only other field station in operation.

2 Comments on epicentral locations and relocations

GA generally uses all available data to locate an event, and this usually includes data from relatively remote seismographs (distance greater than about 150 km) of the Australian National Seismograph Network (ANSN), in this case Ballidu, Kellerberrin, Mundaring and Morawa. To these data, data from field network were added where available. The GA determinations for the two ML 5 events in March 2002 are reproduced in Appendix B, and they show that the data used by GA is dominated by the remote data. The inclusion of such data, even if given a low weighting, usually results in a location where the residuals for the closer field stations are of the order of 0.3 secs. or more. However, the near-field data are often of high quality (because of the relative closeness and higher sampling rate), and the residuals for these stations should be low (less than about 0.1 s). In the relocations plotted in this report, the close stations are given maximum weight (resulting in residuals < 0.1 s), and relatively distant stations (distance > 100 km) are given little or no weight. This often results in the epicentres moving 1-2 km, and sometimes much more (up to 5 km in the case of the ML 5.0 event of 5 March 2002).

Another potential problem with the GA epicentre locations is the earth velocity model used in the computations. The model WA2 (Dent, 1989) was used by the Mundaring Geophysical Observatory (MGO) for WA earthquake solutions from 1991 until its closure in April 2000. GA continued to use the WA2 model until 2014. However, as mentioned by Bathgate (2010) there are concerns that the velocities this model uses are overestimates of the true velocities. In relocations of Lake Muir events (Dent et al., 2019) it was found that the VIC5A model (Gibson et al., 1981; Wesson & Gibson, pers.comm., 1986) as used in Central Victoria, with overall lower velocities, appeared to give better results for solutions where near-field data (less than about 100 km) were used. Trials of the model on the Burakin data provided by GA suggested that it would give better results for this data set as well, and it was adopted for solutions in this report. The authors suspect that the lower velocities fit solutions using direct waves (Pg, Sg) well, but for refracted waves, (observed only at distances > ~ 200 km), the Pn and Sn velocities of the WA2 model may be more appropriate.

Some of the more significant relocations used in this study are shown in Appendix A. The RMS of residuals, using the VIC5A model is shown, as is the RMS that would be achieved if the WA2 model was used. In the majority of cases, the VIC5A model produces the lower RMS. The depth computed by the two models, using the same data set, is also shown. Most solutions using the VIC5A model are between 0.5 and 2 km depth, whereas for WA2, the majority are < 0 km (average about -0.5 km). On the basis of these results, the VIC5A model is considered the superior model.

The number of phases and stations used in the solutions is also shown in Appendix A, including the data used in the original GA solutions. The GA RMS is also shown. The GA solutions use more data, but the RMS of residuals is much higher (averaging about 0.35 secs.).

EQLOCL outputs suggest the average GA solution has an uncertainty of about ± 2 km. The relocations have an average RMS of < 0.1 secs, which suggests more accurate solutions. However, the uncertainties computed by the location program are relatively high (about ± 5 km) because the amount of data used is low (usually about 6 - 8 phase arrivals).

3 An overview of March 2002 activity

There were 155 events located by GA in the Burakin area during March 2002 and the distribution of magnitude vs time is shown in Figure A. Figure B shows the number of events located by GA on each day during March. Also shown is the number of triggerings on field stations CA3 (1-7 March) and BK1 (8-31 March) derived by the authors from data supplied by GA. As indicated earlier, many more events were detected than were located.

Initially, the activity in March 2002 was relatively low, with 6 events located by GA in the first 4 days (largest ML 3.1 on 1 March).

An ML 5.0 event occurred at 0147 UTC on 5 March 2002, and an ML 4.6 event 2 hours later. Altogether, GA located 36 events on 5 March. In the period 5-19 March GA located 110 events, the majority of which (87) were quite small (ML < 2.0).

On 20 March 2002 the seismicity increased markedly, with nearly 20 events of ML 2.3+ in the four days after, the largest being an ML 4.8 event on 23 March. The activity culminated in an ML 5.2 event on 30 March 2002. GA located only 3 events on 30 March (ML 2.8, 5.2 and 2.4), and two on 31 March (ML 3.3 and 2.2). In total, GA located 38 events during 20-31 March, and all were relatively large (only 5 were less than ML 2.0). It seems probable that due to the large numbers of events, GA may have ceased locating small events in the second half of the month, i.e. ignoring the smaller events types that may have been located in the first half of the month.

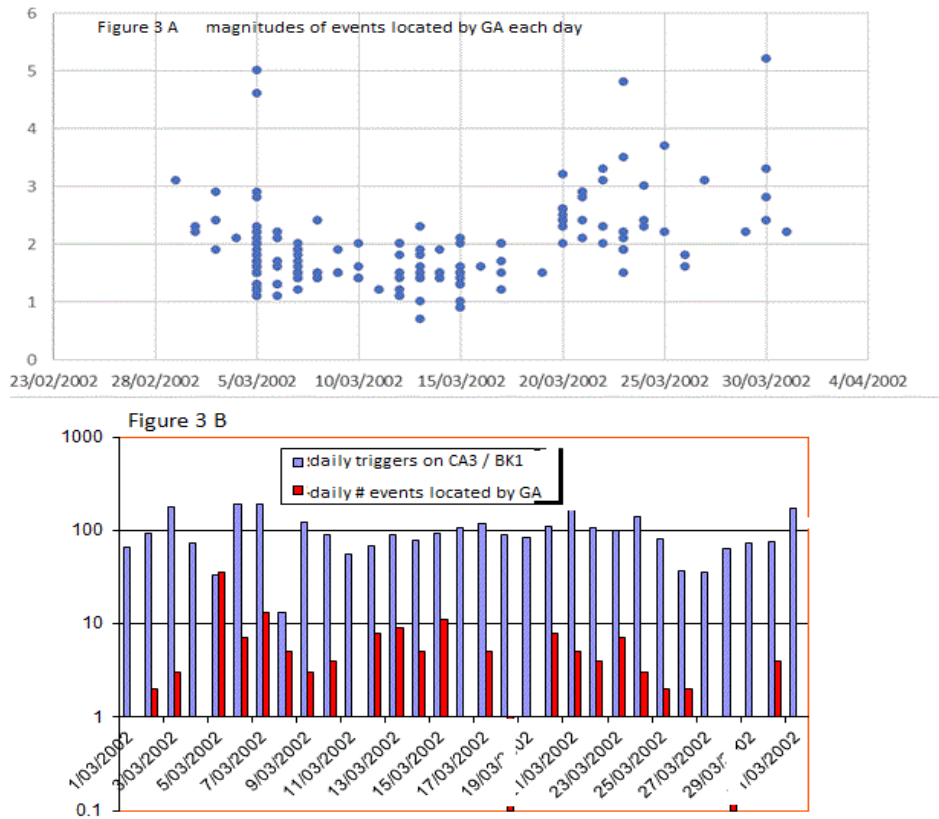


Figure 3: A) Magnitude vs Time, B) Frequency of events.

Figure B shows that although GA located about 155 events in March, the field data (recorded by CA3 and BK1) indicates about 100 triggers per day for most of March, and about 200 per day on 30 and 31 March 2002 following

the ML 5.2 event. Typical recordings from CA3 and BK1 are shown in **Error! Reference source not found.**(A & B). The vast majority of these were probably of magnitudes less than ML 1.5 and probably not recorded at BLDU or KLBR, and hence not located by GA. Future work could significantly increase the number of epicentres available for this period, although their uncertainties would be large due to their low magnitudes.

In the process of reviewing the data, it was noted that CA3 was not operating for most of 5 March, and therefore locations of some events occurring on that day will be poorer. Also note that most locations for events of magnitudes less than ML 1.5 were quite poor, (with large RMS of residual times) and attempts to relocate these events did not result in lessening the location uncertainties.

Results of relocations

About 30 of the 155 events initially located by GA have been relocated by the authors using the methodology discussed above, i.e. using only field station data, and data from BLDU, KLBR and MUN where available. Analysis of the data is presented in two parts, corresponding to the time periods: 1 – 19 March and 20 – 31 March 2002

CA3 and BK1 provided data for most of March 2002. BK4 and BK5 provided some data in the last few days of March, and solutions using these data have reduced uncertainties.

The field stations operated at 100 samples per second, which, while faster than the other ANSN stations (e.g. BLDU, KLBR) which recorded at 50 samples per second, is still less than would be desirable for such short epicentral distances. Also, at CA3 (i.e. epicentral distance about 3 km or less), the precise onset of S phase arrivals is often hard to establish (see **Error! Reference source not found.**A), and so the weighting of S arrivals at CA3 should be low.

4.1 Relocations 1 to 19 March

Figure shows the 116 GA locations for this period (including 36 on 5 March 2002), and the 15 relocations presented here. Locations which are assumed to have relatively low precision (i.e. do not use CA3) which

includes most of the events on 5 March, or that rely on low quality data, are shown with fainter symbols. The GA locations for the two largest events (ML 4.6, ML 5.0 - filled symbols) are about 5 and 3 km NE of CA3; the most

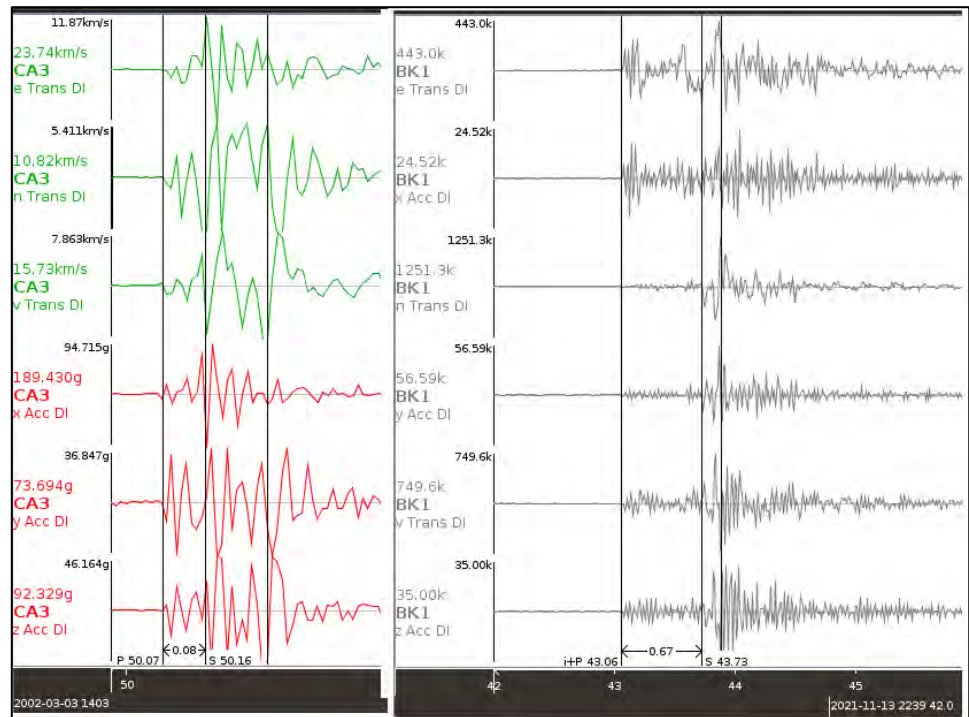


Figure 4: Typical recording from CA3 (4A) and BK1 (4B)

significant feature is that both of these events have been moved much closer to CA3. Many of the other events have also been shifted towards CA3, and there seems to be a concentration of epicentres to the S and SW of CA3. The average shift is about 2 km, and locations mostly move to the south or southwest.

3.2 Relocations 20 to 31 March 2002

Fifteen of the 38 GA locations in this period have been relocated, as shown on Figure . The average shift is much smaller than in the previous period, and the main events (ML 4.8, ML 5.2 - filled symbols) have only been shifted by about 1 km.

Discussion

The activity west of Burakin in March 2002 represents a significant surge in activity which was initiated by an ML 5.1 event in September 2001. Leonard (2002) suggests the sequence could have begun in September 2000 with a swarm of about 1700 earthquakes, including an ML 3.6 event, near this location.

Overall, relocations of the epicentres in March 2002 have resulted in a general shift towards station CA3. There seems to be a concentration of events at about 2 km south to southwest of CA3, and there may be a group at a similar distance to the north of CA3. Considering the uncertainties in the locations, it is possible that the events are more closely grouped than Figure and Figure suggest. Closer examination of the many small events recorded by CA3 and BK1, but not yet located, may help to clarify the epicentral distributions. However, two-station locations are unreliable, and a third close station is required. This requirement may be met if other periods of the deployment are investigated at a later date.

The focal depths determined by GA (using the WA2 model) are often constrained to 2 km depth, because allowing an unconstrained depth to be calculated from the data often results in negative depths. The relocations presented here frequently have computed depths of between 2 and 3 km. While these depths appear to be reasonable, not too much confidence can be given to them because there was only one close seismograph (CA3). However, the fact that most if not all of the recordings at CA3 have S-P times of less than 0.3 seconds means that the events necessarily have focal depths of less than 4km.

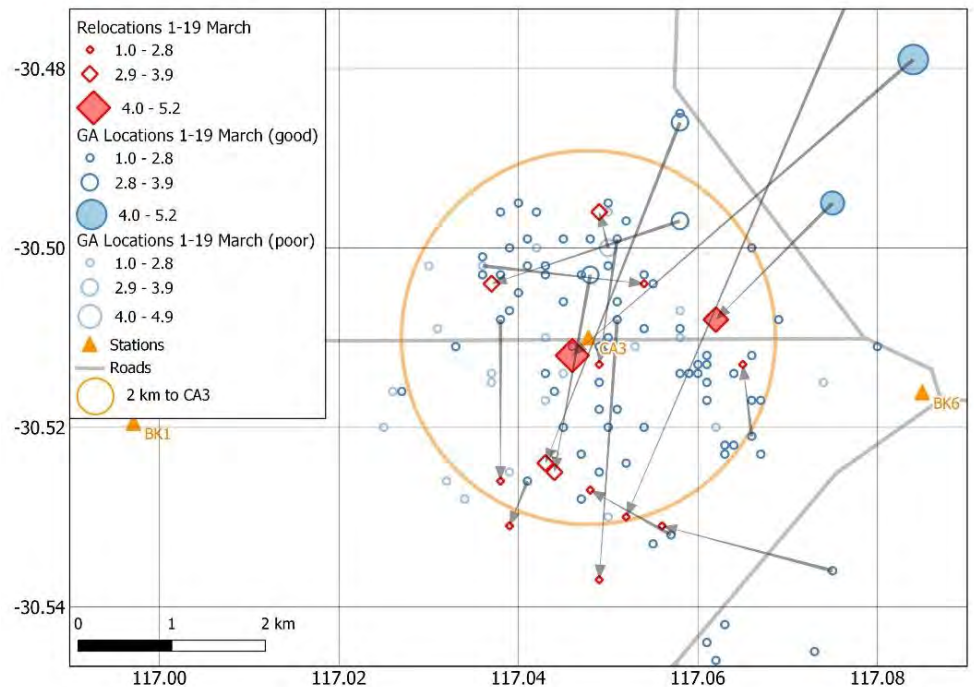


Figure 5: Relocations of events for the period 1 to 19 March

The plot of ML 3.0 & above epicentres in April and May 2002 (see **Error! Reference source not found.**) shows continued activity near CA3, but there is a group of epicentres a little further SSE. This may suggest that the Burakin epicentres have an overall SSE trend. Ongoing work on the overall sequence of events will hopefully clarify any trends present.

Error! Reference source not found.

shows an ML 3.5 event located about 15 km SE of CA3. This event was the largest of a group of five events between 26 and 29 April 2002. This is the same location as a swarm north of Cadoux of approximately 1700 events about 18 months earlier, between September and October 2000 (at Location C of Leonard & Boldra, 2001). The largest event in this sequence was ML 3.5 on 25 September 2000 (**Error! Reference source not found.**), and their plot suggests a NNE trend to the sequence. Location C, was the most active (at the time) of 4 points they identified (A, B, C and D) which defined an arcuate group extending from just west of Cadoux (location D) to about 40 km NW of Cadoux (location A, **Error! Reference source not found.**). Their location B, about 15 km to the NW of location C, was the location of an ML 3.6 event on 22 September 2000. It turns out, but was not recognised in Leonard & Boldra (2001), that this point is the location of the 2001-2002 Burakin swarm discussed in this paper. Leonard (2002) has suggested that the brief activity at Location B, in September 2000, marks the beginning of the greater Burakin sequence.

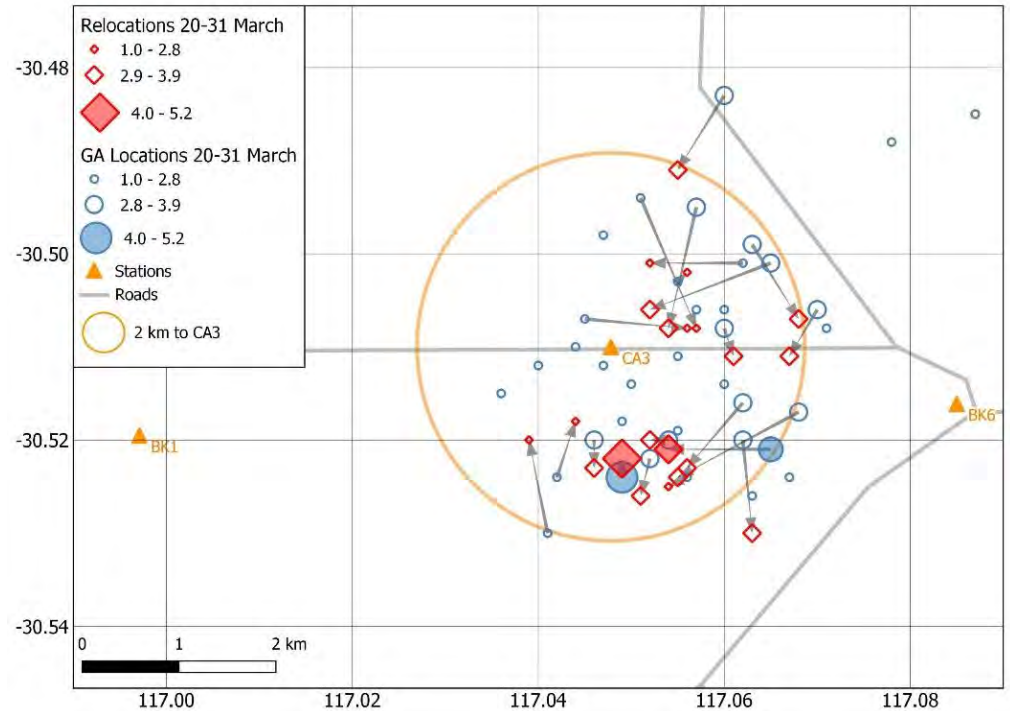


Figure 6: Relocations of events for the period 20 to 31 March

The number of well-monitored large earthquakes in Australia, with follow-up publications, is small. Some examples would be Tennant Creek (1988, ML 6.8; Bowman et al., 1990), Kalgoorlie (2010, ML 5.0; Bathgate et al., 2010), and Lake Muir (2018 ML 5.7; Clark et al., 2020). Other large earthquakes in Western Australia (Meckering, 1968, ML 6.7; Gordon & Lewis, 1980) and Cadoux (1979, ML 6.3; Lewis et al., 1981) were poorly monitored. The seismic deployments around the Tennant Creek events were critical in defining the causative faults. Another classic deployment, revealing the structure of the fault plane, was the Eugowra deployment around the relatively small ML 4.3 Eugowra earthquake of 1994 (Gibson et al., 1994).

The Burakin events were relatively well monitored, and it is hoped that any findings regarding this sequence might help to give insights into other major events or sequences of events, in the region. Although many stations were deployed over the time span of the sequence, only four have contributed to this study of March 2002 events and the

resultant locations are still considered relatively poor. It is planned to study other periods in the sequence which may have been better monitored, and perhaps more insights into epicentral distribution will emerge.

5 Conclusions

A large number of earthquakes were detected in the Burakin area during the period from 2001 to 2002. The events located by GA were mainly the largest ones recorded by the regional and temporary networks. The 28 September 2001 and 5 March 2002 ML 5 events are both poorly located, and are possibly much closer to the relatively well-located 30 March 2002 ML 5.2 event than the GA locations suggest. The completeness of the catalogue for events less than ML 2 is far from uniform. However, the temporary network, which varied in distribution and coverage between September 2001 and June 2002, allowed the intermittent location of relatively small events (down to ML 1.4) which would not otherwise have been located.

The relocations presented here suggest that the geographical spread of epicentres is substantially less than indicated by the GA data. Some relatively large events are moved by up to 5 km, and the relocations indicate that the activity was mostly within 2 km of CA3. The two magnitude 5 events in March 2002 appear to come from this location. There is a possible NNW-SSE trend to events in the greater Burakin sequence (September 2000 – June 2002). Focal depths seem to be consistently around 2 km. These values are dependent to some degree on the earth velocity model used, but are generally deeper than values given by solutions using the WA2 model, which are often less than 0.5 km deep.

5 Acknowledgements

The assistance of GA staff in providing data and information is much appreciated, and Dan Clark, Mike Turnbull and Virginia Ward are thanked for their comments and editing on the manuscript.

References

- Bowman, J.R, Gibson, G. and Jones, T., 1990. Aftershocks of the 1988 January 22 Tennant Creek, Australia Intraplate Earthquakes: Evidence for a Complex Thrust-Fault Geometry. *Geophysical Journal International*, 100 (1), 87–97.
- Bathgate J., Glanville H. and Collins C., 2010. *The Kalgoorlie Earthquake of 20 April 2010 and its Aftershock Sequence*. In Proc. AEES 2010, Conference, Perth.
- Clark, D. J., Brennand S., Brenn G., Garthwaite M. C., Dimech J., Allen T. I., and Standen S., 2020. *Surface deformation relating to the 2018 Lake Muir earthquake sequence, southwest Western Australia: new insight into stable continental region earthquakes*. EGU Solid Earth, 11, 691–717.
- Dawson, D, Cummins, P., Tregoning, P. and Leonard, M., 2018. *Shallow intraplate earthquakes in Western Australia observed by Interferometric Synthetic Aperture Radar*. Journal of Geophysical Research. 113, B11408, doi:10.1029/2008JB005807.

- Dent V.F., 1989. *Computer generated crustal models for the southwest seismic zone, Western Australia*. Bur. Min. Res. Aust. Report 1989/43.
- Dent V., Love D. & Collins C., 2019. *Possible clustering in space and time of aftershocks of the ML 5.7 Lake Muir earthquake, southwest Australia, 16 September 2018*. In Proc. AEES 2019 Conference, Newcastle, NSW.
- Doyle H. A., 1971. *Seismicity and structure in Australia*. Bulletin of the Royal Society of New Zealand, 9, 149-152.
- Gibson, G., Wesson, V. & Cuthbertson, R., 1981. Seismicity of Victoria to 1980. *Journal of the Geological Society of Australia*, 28:3-4, 341-356.
- Gibson, G., Wesson, V., & Jones, T., 1994. The Eugowra NSW Earthquake Swarm of 1994. In Proc. AEES 1994 Conference, Canberra. pp 71-80.
- Gordon F.R. and Lewis J.D., 1980. *The Meckering and Calingiri earthquakes: October 1968 and March 1970*. Geological Survey of Western Australia Bulletin 126.
- Leonard M., 2003. *Respite leave Burakin quaking in anticipation*. AusGeo News 70, June 2003.
- Leonard M. & Boldra P., 2001. *Cadoux swarm September 2000 – an indication of rapid stress transfer?* In Proc. AEES 2001 Conference, Canberra.
- Leonard M., 2002. *The Burakin WA earthquake sequence Sep 2000 – June 2002*. In Proc. AEES 2002 Conference, Adelaide.
- Lewis J.D., Daetwyler N.A., Bunting J.A. and Moncrieff J.S. 1981. *The Cadoux earthquake, 2 June 1979*. Geological Survey of Western Australia, Report 11.

Appendix A. Comparison of rms values and depths for GA solutions, and relocations using WA2 and VIC5A velocity models.

			Relocations							Original GA Locations	
Date	Time	ML	Lon	Lat	Vic5		WA2		Times/ Stns*	rms	Times/ Stns*
					dep	rms	dep	rms			
01-Mar-02	1847 45.4	3.1	117.043	-30.524	0.50	0.095	0.03	0.160	6t4s	0.352	24t13s
03-Mar-02	0944 28.0	2.9	117.044	-30.035	-0.10	0.155	-0.40	0.186	7t4s	0.394	17t10s
05-Mar-02	0147 39.1	5.0	117.049	-30.499	2.00	0.146	0.40	0.181	6t4s	0.481	25t14s
05-Mar-02	03 29 57.1	4.6	117.062	-30.508	-0.40	0.051	-0.40	0.162	6t4s	0.640	22t14s
07-Mar-02	0308 21.6	1.6	117.039	-30.532	-0.05	0.104	-0.30	0.193	7t4s	0.232	10t5s
08-Mar-02	1654 17.3	2.4	117.065	-30.513	2.20	0.06	0.50	0.007	6t4s	0.274	15t8s
14-Mar-02	1501 33.7	1.9	117.067	-30.515	2.10	0.053	-0.40	0.017	6t4s	0.254	10t5s
20-Mar-02	1147 04.0	3.2	117.061	-30.511	1.90	0.074	-0.40	0.027	6t4s	0.313	18t10s
20-Mar-02	2116 35.9	2.4	117.057	-30.508	2.10	0.032	-0.40	0.020	6t4s	0.384	16t10s
20-Mar-20	2215 34.9	2.5	117.056	-30.508	2.10	0.027	-0.40	0.025	6t4s	0.340	16t9
21-Mar-20	0144 59.3	2.9	117.054	-30.508	2.20	0.046	-0.40	0.070	7t4s	0.275	20t11s
22-Mar-02	0325 45.7	3.1	117.068	-30.507	2.10	0.024	-0.40	0.079	6t3s	0.181	10t6s
23-Mar-02	1316 22.5	4.8	117.054	-30.521	3.10	0.036	1.90	0.049	8t6s	0.365	23t14s
23-Mar-02	1420 47.1	3.5	117.063	-30.53	1.90	0.026	1.60	0.052	7t5s	0.328	29t16s
23-Mar-02	1636 03.3	1.9	117.063	-30.529	2.00	0.054	1.60	0.020	8t5s	0.385	18t10s
24-Mar-02	1955 54.1	2.4	117.054	-30.525	2.00	0.048	1.50	0.063	7t4s	0.444	19t10s
26-Mar-02	1215 24.4	1.8	117.052	-30.481	1.90	0.069	-0.30	0.015	5t4s	0.459	16t8s
26-Mar-02	1230 13.7	1.6	117.065	-30.513	2.10	0.031	-0.40	0.056	7t4s	0.450	14t7s
29-Mar-02	1650 30.6	2.2	117.044	-30.518	1.30	0.042	-0.40	0.049	8t4s	0.256	16t9s
30-Mar-02	0558 20.0	2.8	117.052	-30.52	1.90	0.018	0.40	0.047	8t4s	0.271	20t11s
30-Mar-02	2115 45.8	5.2	117.049	-30.519	2.10	0.047	0.80	0.075	6t4s	0.428	29t18s

* Time/Stns = Number of Phases and Stations used in the analysis

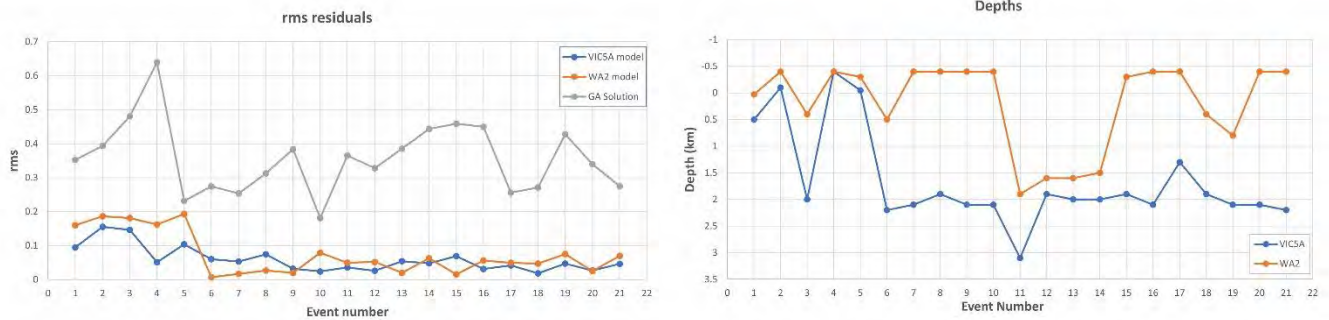


Figure: Comparison between GA solutions and relocated solutions using WA2 and VIC5A models.

Appendix B: Various EQLOCL solutions for the two major earthquakes

Date	2002-03-05			GA Location, first ML 5 event			
Origin Time	0147 38.85	+-	1.67				
Zone	50						
Easting	508.37	+-	6.93	Longitude	117.087		
Northing	6628.34	+-	6.26	Latitude	-30.477		
Depth	0.26	+-	16.68				
Arrival times = 25 S.D. = 0.481 Seismographs = 14							
Nearest recorder = 5.1 km		Gap = 79.5 deg		Accuracy = A			
Effects Code = F		Imax = 4		Fault =			
1 km W (257 deg) of BK4							
WESTERN AUSTRALIA							
201 km NE (36 deg) of PERTH							
9 km NW (301 deg) of Burakin							
MAGNITUDES							
Code	R	ML	MD	MB	MS	MW MN	
FITZ	1615	4.9					
FORT	1050	5.4					
MEEK	450	4.7					
RKGY	458	4.9					
Mean 5.0 Assign ML 5.0							
DATA USED							
Code	Wave	AT	+-	WT	CT	DT Dist Azim Ad Ae	
CA3	i-P	39.82	0.10	1.56	39.69	0.13	5.1 225 7.2 7.2
CA3	i S	40.00	12.00	0.54	40.27	-0.27	5.1 225 7.2 7.2
BK1	i-P	40.16	0.10	1.50	40.46	-0.30	9.8 241 3.6 3.6
BK1	i S	41.15	0.10	1.35	41.58	-0.43	9.8 241 3.6 3.6
CMC	i-P	44.89	0.10	1.37	44.53	0.36	34.8 178 1.0 1.0
CMC	i S	48.82	0.10	1.24	48.47	0.35	34.8 178 1.0 1.0
BLDU	i-P	45.45	0.10	1.36	45.25	0.20	39.2 247 0.9 0.9
KLBR	i-P	61.90	0.10	1.22	61.50	0.40	139.0 153 -30.8 30.8
KLBR	e S	77.10	0.10	0.77	77.24	-0.14	139.0 153 0.2 0.2
PIG4	i-P	65.13	0.10	1.21	65.27	-0.14	165.9 211 -30.8 30.8
PIG4	i S	84.31	0.10	1.09	84.70	-0.39	165.9 211 0.2 0.2
MORW	i-P	68.88	0.10	1.19	68.00	0.88	186.1 326 -42.2 42.2
MORW	e S	90.30	0.10	0.75	89.72	0.58	186.1 326 -40.3 40.3
MUN	i-P	68.07	0.10	1.19	68.01	0.06	186.3 206 -42.2 42.2
MUN	i S	89.50	0.10	1.07	89.74	-0.24	186.3 206 -40.3 40.3
NNAO	e PN	78.06	0.10	0.56	78.36	-0.30	271.9 177 -42.2 42.2
MEEK	e P	100.86	0.10	0.77	100.03	0.83	450.8 19 -42.2 42.2
MEEK	e S	144.73	0.10	0.69	145.48	-0.75	450.8 19 -40.3 40.3
RKGY	i-P	101.50	0.10	1.10	100.90	0.60	458.2 181 -42.2 42.2
KMBL	i-P	102.14	0.10	1.09	102.31	-0.17	469.8 103 -42.2 42.2
KMBL	e S	149.00	0.10	0.69	149.46	-0.46	469.8 103 -40.3 40.3
FORT	i-P	172.50	0.10	1.01	173.22	-0.72	1056.5 94 -42.2 42.2
FORT	e S	273.00	0.10	0.63	272.93	0.07	1056.5 94 -40.3 40.3
FITZ	i-P	241.05	0.10	1.00	242.08	-1.03	1626.0 34 -42.2 42.2
FITZ	e S	392.63	0.10	0.63	392.81	-0.18	1626.0 34 -40.3 40.3
25 times used, S = 0.481							
Deferred Data							
NNAO	i SN	112.31	0.10	0.69	107.77	4.54	271.9 177 -40.3 40.3
RKGY	e S	161.10	0.10	0.69	147.00	14.10	458.2 181 -40.3 40.3
GIRL	e P	158.30	0.10	0.71	155.89	2.41	913.2 341 -42.2 42.2
GIRL	e S	241.30	0.10	0.64	242.75	-1.45	913.2 341 -40.3 40.3
BBOO	i-P	263.45	0.10	1.00	267.83	-4.38	1838.7 103 -42.2 42.2
BBOO	e S	434.70	0.10	0.63	437.63	-2.93	1838.7 103 -40.3 40.3
STKA	i-P	321.76	0.10	1.00	327.30	-5.54	2342.5 100 -55.3 55.2
STKA	e S	545.26	0.10	0.63	556.11	-10.85	2342.5 100 -51.9 51.3
ARPS	e P	327.66	0.10	0.70	331.76	-4.10	2394.3 113 -56.2 56.1
ARPS	e S	588.13	0.10	0.63	565.96	22.17	2394.3 113 -52.8 52.1
KAKA	i-P	339.88	0.10	1.00	342.98	-3.10	2520.6 41 -57.4 56.9
KAKA	e S	584.26	0.10	0.63	587.19	-2.93	2520.6 41 -54.4 53.9
CMSA	i-P	358.67	0.10	1.00	361.00	-2.33	2726.1 99 -57.9 57.6
CMSA	e S	629.60	0.10	0.63	619.60	10.00	2726.1 99 -56.4 56.4

Date	2002-03-05			RELOCATION			
Origin Time	0147 39.32	+-	32.86				
Zone	50						
Easting	504.40	+-	104.80	Longitude	117.046		
Northing	6624.42	+-	504.61	Latitude	-30.512		
Depth	1.75	+-	209.00				
Arrival times = 6 S.D. = 0.154 Seismographs = 4							
Nearest recorder = 0.5 km		Gap = 138.9 deg		Accuracy = B			
Effects Code = F		Imax = 4		Fault =			
0 km SW (219 deg) of CA3							
WESTERN AUSTRALIA							
196 km NE (36 deg) of PERTH							
12 km W (274 deg) of Burakin							
DATA USED							
Code	Wave	AT	+-	WT	CT	DT Dist Azim Ad Ae	
CA3	i-P	39.82	0.10	1.71	39.78	0.04	0.5 39 77.0 77.0
CA3	i S	40.00	12.00	0.59	40.02	-0.02	0.5 39 77.0 77.0
BK1	i-P	40.16	0.10	1.57	40.40	-0.24	4.8 260 23.8 23.8
BK1	i S	41.15	0.10	1.41	40.99	0.16	4.8 260 23.8 23.8
CMC	i-P	44.89	0.10	1.38	44.89	-0.00	31.2 171 -36.7 36.7
BLDU	i-P	45.45	0.10	1.37	45.37	0.08	34.1 250 -36.7 36.7
6 times used, S = 0.154							
Deferred Data							
CMC	i S	48.82	0.10	1.24	48.64	0.18	31.2 171 -27.7 27.7
KLBR	i-P	61.90	0.10	1.22	62.33	-0.43	137.4 150 -38.8 38.8
KLBR	e S	77.10	0.10	0.77	78.68	-1.58	137.4 150 -29.4 29.4
PIG4	i-P	65.13	0.10	1.21	66.07	-0.94	160.5 211 -38.8 38.8
PIG4	i S	84.31	0.10	1.09	85.14	-0.83	160.5 211 -29.4 29.4
MUN	i-P	68.07	0.10	1.19	69.38	-1.31	181.0 205 -52.0 52.0
MUN	i S	89.50	0.10	1.08	90.87	-1.37	181.0 205 -29.4 29.4
MORW	i-P	68.88	0.10	1.19	70.19	-1.31	187.3 328 -52.0 52.0
MORW	e S	90.30	0.10	0.75	92.64	-2.34	187.3 328 -29.4 29.4
NNAO	e PN	78.06	0.10	0.56	80.54	-2.48	268.2 176 -52.0 52.0
NNAO	i SN	112.31	0.10	0.69	110.85	1.46	268.2 176 -45.7 45.7
RKGY	i-P	101.50	0.10	1.10	104.36	-2.86	454.2 180 -52.0 52.0
RKGY	e S	161.10	0.10	0.69	152.57	8.53	454.2 180 -45.7 45.7
MEEK	e P	100.86	0.10	0.77	104.61	-3.75	455.8 19 -52.0 52.0
MEEK	e S	144.73	0.10	0.69	152.98	-8.25	455.8 19 -45.7 45.7
KMBL	i-P	102.14	0.10	1.09	106.75	-4.61	472.8 102 -52.0 52.0
KMBL	e S	149.00	0.10	0.69	156.75	-7.75	472.8 102 -45.7 45.7
GIRL	e P	158.30	0.10	0.72	162.68	-4.38	915.0 341 -42.0 53.0
GIRL	e S	241.30	0.10	0.64	257.26	-15.96	915.0 341 -37.8 45.7
FORT	i-P	172.50	0.10	1.01	180.16	-7.66	1055.5 94 -41.3 53.3
FORT	e S	273.00	0.10	0.63	288.76	-15.76	1055.5 94 -37.4 46.2
FITZ	i-P	241.05	0.10	1.00	249.11	-8.06	1625.1 34 -44.3 55.5
FITZ	e S	392.63	0.10	0.63	412.77	-20.14	1625.1 34 -40.1 48.6
BBOO	i-P	263.45	0.10	1.00	271.60	-8.15	1818.2 103 -46.2 57.0
BBOO	e S	434.70	0.10	0.63	453.63	-18.93	1818.2 103 -42.1 49.6
STKA	i-P	321.76	0.10	1.00	326.92	-5.16	2339.5 100 -56.6 64.4
STKA	e S	545.26	0.10	0.63	557.16	-11.90	2339.5 100 -53.1 58.4
ARPS	e P	327.66	0.10	0.70	331.90	-4.24	2394.7 113 -56.6 64.4
ARPS	e S	588.13	0.10	0.63	566.50	21.63	2394.7 113 -53.1 58.4
KAKA	i-P	339.88	0.10	1.00	343.73	-3.85	2526.1 41 -57.4 64.6
KAKA	e S	584.26	0.10	0.63	588.22	-3.96	2526.1 41 -54.4 59.5
CMSA	i-P	358.67	0.10	1.00	361.55	-2.88	2729.3 99 -57.9 65.2
CMSA	e S	629.60	0.10	0.63	620.22	9.38	2729.3 99 -56.4 61.5

Date	2002-03-30	GA Location	2 nd event
Origin Time	2115 46.14 +- 0.27		
Zone	50		
Easting	504.72 +- 1.84	Longitude	117.049
Northing	6623.14 +- 1.40	Latitude	-30.524
Depth	0.81 +- 3.01		
Arrival times	= 29	S.D. = 0.428	Seismographs = 18
Nearest recorder	= 1.7 km	Gap = 61.4 deg	Accuracy = A
Effects Code	= F	Imax = 4	Fault =
1 km S (179 deg) of CA3			
WESTERN AUSTRALIA			
195 km NE (36 deg) of PERTH			
12 km W (268 deg) of Burakin			
MAGNITUDES			
Code	R	ML	MD
BB00	1811	5.4	
CM5A	2707	5.5	
FITZ	1621	3.9	
FORT	1053	5.6	
GIRL	915	5.2	
KAKA	2510	5.4	
KMBL	472	4.6	
MEEK	456	4.5	
QIS	2497	5.7	
STKA	2325	5.4	
QLP	2668	5.6	
Mean	5.2		Assign ML 5.2
DATA USED			
Code	Wave	AT	+-
CA3	i+PG	46.33	0.10
CA3	i SG	46.63	0.10
BK1	e PG	46.82	0.10
BK1	e SG	47.64	0.10
BK5	i-PG	47.32	0.10
BK5	i SG	48.32	0.10
BK4	i+PG	47.36	0.10
BK4	i SG	48.39	0.10
CMC	i-P	51.15	0.10
CMC	e S	54.72	0.10
PIG2	e PG	53.28	0.10
PIG2	e SG	58.56	0.10
PIG3	i PG	63.01	0.10
PIG3	e SG	74.94	0.10
KLBR	i-P	68.41	0.10
PIG4	i PG	71.48	0.10
MUN	i+P	74.40	0.10
MUN	e S	95.71	0.10
MORW	i+P	75.71	0.10
MORW	e S	97.35	0.10
MORW	i-P	84.77	0.10
MEEK	e P	107.84	0.10
KMBL	e S	156.15	0.10
GIRL	i-P	164.86	0.10
FORT	e P	180.00	0.10
FORT	e S	281.82	0.10
FITZ	e S	400.15	0.10
BB00	e S	445.95	0.10
Deferred Data			
NMAO	e S	118.08	0.10
MEEK	e S	157.04	0.10
GIRL	e S	257.12	0.10
FITZ	i+P	247.49	0.10
BB00	i+P	270.07	0.10
ASPA	e P	270.50	0.10
ASPA	e S	439.65	0.10
STKA	i-P	328.21	0.10
STKA	i-P	328.21	0.10
QIS	e S	345.79	0.10
QIS	e S	583.41	0.10
KAKA	e P	346.29	0.10
KAKA	e S	590.11	0.10
QLP	i+P	361.82	0.10
QLP	e S	627.52	0.10
CM5A	i-P	364.97	0.10
CM5A	e S	635.24	0.10
RMQ	i-P	397.89	0.10
CTA	e P	402.03	0.10
Velocity Ratios			
CMC	MUN	MORW	KMBL
1.71	1.76	1.74	1.76
0.06	0.02	0.02	0.01
MUN	1.76	1.75	0.00
0.02	0.01	0.00	0.02
MORW	1.74	0.00	1.73
0.02	0.00	0.01	0.02
KMBL	1.76	1.75	1.77
0.01	0.02	0.02	0.00
FORT	1.76	1.76	1.77
0.00	0.01	0.01	0.01

Date	2002-03-30	Origin Time	2115 45.73 +- 0.33	Zone	50	Easting	504.67 +- 1.99	Longitude	117.049
Northing	6623.38 +- 7.56	Latitude	-30.522	Depth	2.15 +- 5.54	Arrival times	= 7	S.D. = 0.051	Seismographs = 5
Nearest recorder	= 1.4 km	Gap	= 126.2 deg	Accuracy	= A	Effects Code	= F	Imax	= 4
1 km S (181 deg) of CA3									
WESTERN AUSTRALIA									
195 km NE (36 deg) of PERTH									
12 km W (269 deg) of Burakin									
DATA USED									
Code	Wave	AT	+-	WT	CT	DT	Dist	Azim	Ad
CA3	i+PG	46.33	0.10	1.66	46.33	-0.00	1.4	1	60.8
CA3	i SG	46.63	0.10	1.49	46.66	-0.03	1.4	1	60.8
BK1	e PG	46.82	0.10	1.10	46.88	-0.06	5.0	273	26.7
BK1	e SG	47.64	0.10	0.99	47.51	0.13	5.0	273	26.7
BK5	i-PG	47.32	0.10	1.53	47.28	0.04	7.0	87	19.4
BK4	i+PG	47.36	0.10	1.53	47.35	0.01	7.4	44	18.6
PIG2	P	53.28	0.05	1.55	53.32	-0.04	43.7	214	-36.7
Deferred Data									
BK5	i SG	48.32	0.10	1.38	48.12	0.20	7.0	87	19.4
BK4	i SG	48.39	0.10	1.38	48.23	0.16	7.4	44	18.6
CMC	i-P	51.15	0.10	1.39	51.07	0.08	30.2	171	-36.7
CMC	e S	54.72	0.10	0.87	54.68	0.04	30.2	171	-27.7
PIG2	S	58.56	0.30	0.97	58.52	0.04	43.7	214	-27.7
PIG3	P	63.01	0.10	1.26	63.12	-0.11	103.2	211	-38.8
PIG3	S	74.94	0.50	0.82	75.42	-0.48	103.2	211	-27.7
KLBR	i-P	68.41	0.10	1.23	68.51	-0.10	136.4	150	-38.8
PIG4	i PG	71.48	0.10	1.21	78.97	-7.49	159.8	211	0.9
MUN	i+P	74.40	0.10	1.20	75.61	-1.21	180.2	206	-38.8
MUN	e S	95.71	0.10	0.75	96.98	-1.27	180.2	206	-29.4
MORW	i+P	75.71	0.10	1.19	76.66	-0.95	188.3	328	-52.0
MORW	e S	97.35	0.10	0.75	99.26	-1.91	188.3	328	-45.7
NMAO	i-P	84.77	0.10	1.15	86.74	-1.97	267.1	176	-52.0
NMAO	e S	118.08	0.10	0.73	116.92	1.16	267.1	176	-45.7
MEEK	e P	107.84	0.10	0.77	111.06	-3.22	456.7	19	-52.0
MEEK	e S	157.04	0.10	0.69	159.49	-2.45	456.7	19	-45.7
KMBL	e P	108.84	0.10	0.76	113.03	-4.19	472.3	102	-52.0
KMBL	e S	156.15	0.10	0.69	162.95	-6.80	472.3	102	-45.7
GIRL	i-P	164.86	0.10	1.02	169.17	-4.31	916.0	341	-42.0
GIRL	e S	257.12	0.10	0.64	263.83	-6.71	916.0	341	-37.8
FORT	e P	180.00	0.10	0.70	186.48	-6.48	1055.1	94	-41.3
FORT	e S	281.82	0.10	0.63	295.02	-13.20	1055.1	94	-37.4
FITZ	i+P	247.49	0.10	1.00	255.55	-8.06	1625.8	34	-44.3
FITZ	e S	400.15	0.10	0.63	419.25	-19.10	1625.8	34	-40.1
BB00	i+P	270.07	0.10	1.00	277.90	-7.83	1817.7	103	-46.2
BB00	e S	445.95	0.10	0.63	459.86	-13.91	1817.7	103	-42.1
ASPA	e P	270.50	0.10	0.70	279.49	-8.99	1831.4	69	-46.2
ASPA	e S	439.65	0.10	0.63	462.75	-23.10	1831.4	69	-42.1
STKA	i-P	328.21	0.10	1.00	333.24	-5.03	2339.1	100	-56.6
STKA	e S	550.80	0.10	0.63	563.40	-12.60	2339.1	100	-53.1
QIS	i+P	345.79	0.10	1.00	348.98	-3.19	2513.4	69	-57.4
QIS	e S	583.41	0.10	0.63	592.53	-9.12	2513.4	69	-54.4
KAKA	e P	346.29	0.10	0.70	350.13	-3.84	2526.7	41	-57.4
KAKA	e S	590.11	0.10	0.63	594.63	-4.52	2526.7	41	-54.4
QLP	i+P	361.82	0.10	1.00	364.32	-2.50	2688.5	87	-57.9
QLP	e S	627.52	0.10	0.63	620.27	7.25	2688.5	87	-56.4
CM5A	i-P	364.97	0.10	1.00	367.86	-2.89	2728.9	99	-57.9
CM5A	e S	635.24	0.10	0.63	626.47	8.77	2728.9	99	-56.4
RMQ	i-P	397.89	0.10	1.00	400.91	-3.02	3125.0	89	-60.1
CTA	e P	402.03	0.10	0.70	402.64	-0.61	3146.6	75	-60.1

NO VELOCITY RATIOS

A Review of Experimental and Analytical Studies on Masonry Infilled-Frames Subjected to Lateral Loads

Sonam Dorji¹, Hossein Derakhshan², Tatheer Zahra³, David P Thambiratnam⁴ and Alireza Mohyeddin⁵

1. Corresponding Author. PhD Student, Science and Engineering Faculty, Queensland University of Technology, Brisbane, QLD 4000. Email: s5.dorji@hdr.qut.edu.au
2. Lecturer, Science and Engineering Faculty, Queensland University of Technology, Brisbane, QLD 4000. Email: hossein.derakhshan@qut.edu.au
3. Lecturer, Science and Engineering Faculty, Queensland University of Technology, Brisbane, QLD 4000. Email: t.zahra@qut.edu.au
4. Professor, Science and Engineering Faculty, Queensland University of Technology, Brisbane, QLD 4000. Email: d.thambiratnam@qut.edu.au
5. Senior Lecturer, School of Engineering, Edith Cowan University, Perth, WA 6027. Email: a.mohyeddin@ecu.edu.au

Abstract

This paper presents a review of the literature on masonry-infilled frame structures subjected to lateral loads. A database of 167 experimental studies on the parameters that influence the response of masonry infill are first discussed. It is shown that there are far too many geometrical and material parameters that affect the behaviour and that the experimental results are not consistent. Masonry infill is in general analysed using an equivalent strut modelling method, which is also briefly described. It is demonstrated that despite rigorous studies across many years, researchers have not been able to find a generic model. Finally, finite element concepts introduced by different researchers are discussed which confirm that further research is required to obtain realistic structural performance of masonry-infilled frames. A future research direction is also provided.

Keywords: masonry-infilled, equivalent strut, masonry, parametric analysis, finite element modelling

1 INTRODUCTION

A masonry-infilled frame (MIF) structural system consists of frame members confining a masonry wall (Figure 1). According to an American standard developed by The Masonry Society TMS 402/602-16 (TMS, 2017) such structures have been in use for nearly a century. Masonry is in most cases produced using local materials and labour and therefore can provide an economical construction (Kaushik et al., 2006). In addition, brick walls have good sound, heat and waterproofing properties. These composite structures also allow for efficient dissipation of seismic forces and have potential to reduce the overall cost of building construction (Crisafulli, 1997). However, the structural behaviour of MIF is considered complex and yet to be adequately formulated in design standards (Alwashali et al., 2019; Wijaya et al., 2020).

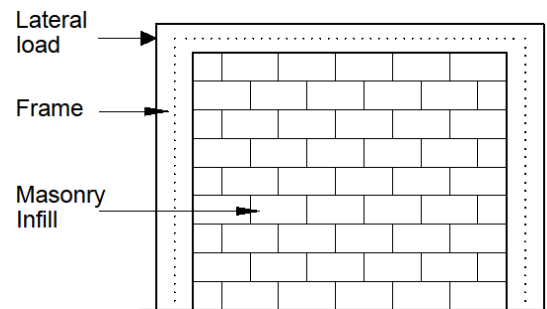


Figure 1: Components of MIF

Structurally, masonry-infills have relatively high initial stiffness and low deformability and their presence between the frame members alter the behaviour of MIF from that of initially designed to a complex mechanism (Mohyeddin, 2011). Despite the complexity, the research in the field of MIF had begun as early as 1930s and continues to evolve for the reasons stated in Table 1.

Table 1: Comments from past researchers on analysing MIF

Blackard et al. (2009)	MIF is a complex and composite structure to model
Asteris et al. (2011)	MIF does not have the simplicity and accuracy necessary for design engineers
Chrysostomou and Asteris (2012)	Uncertainties in defining strength properties and modelling exist in both with and without openings in MIF
Sipos et al. (2013)	Conflicting views of MIF modelling have resulted in the ‘deconstruction’ of the masonry-infill structures
Sigmund and Penava (2014)	While some researchers showed that infill walls led to the failure of the building, others have suggested that the walls were beneficial
Huang et al. (2016)	The interaction between the frame and the wall is complicated
Mohyeddin et al. (2017)	There cannot be a single model to represent MIF; instead the models need to vary from one structure to the other
Alwashali et al. (2019)	Large variations in the literature and codes cause confusion to practicing engineers
Madiawati et al. (2019)	The response of MIF is highly nonlinear
Wijaya et al. (2020)	Further studies are required to provide clear guidelines on analysing MIF

The objective of the present research is to explore the reasons for the complexities in analysing MIF through a review of experimental investigations, related modelling techniques, and finally finite element (FE) studies and provide a clear direction for future research. The MIFs considered

here are all unreinforced masonry subjected to in-plane loading. Reinforced masonry and out-of-plane loadings have overall different behaviours to MIF and are therefore not considered. Few studies (Almusallam & Al-Salloum, 2007; Yuksel & Teymur, 2011; Koutas et al., 2015; Basha & Kaushik, 2016; Dautaj et al., 2018) that included the use of polymers, textiles and retrofitted frames to improve the performance of MIF are also omitted from this research. Previous experimental studies that focused on parametric studies of MIFs are discussed in Section 2. The modelling concepts including single and multi-strut modelling techniques are explained in Section 3, and finally, the FE studies in the area of MIF are reviewed in Section 4.

2 PARAMETRIC EXPERIMENTAL STUDIES ON MIFS

A summary of 167 experiments along with the behaviour-influencing parameters that have been included in each study are listed in Table 2. The parameters are classified into four categories - strength of frame members, masonry material properties and aspect ratio (height to length), presence of openings, and the number of storeys and bays and loading. Effects of each of the parameters on the overall behaviour of MIF is discussed herein. The percentage of experiments carried out in different countries is represented in Figure 2(a). Almost one-third of the experiments were conducted in the US. The European countries account for 38% of the tests. Among the Asian countries, China, India and Japan have almost equal share of the experiments. Figure 2(b) illustrates the scale of the specimen employed. Half-scale is more common with more than 76 tests out of 167. One-eighth scale experimental program is the second-highest which is closely followed by full scale experiments.

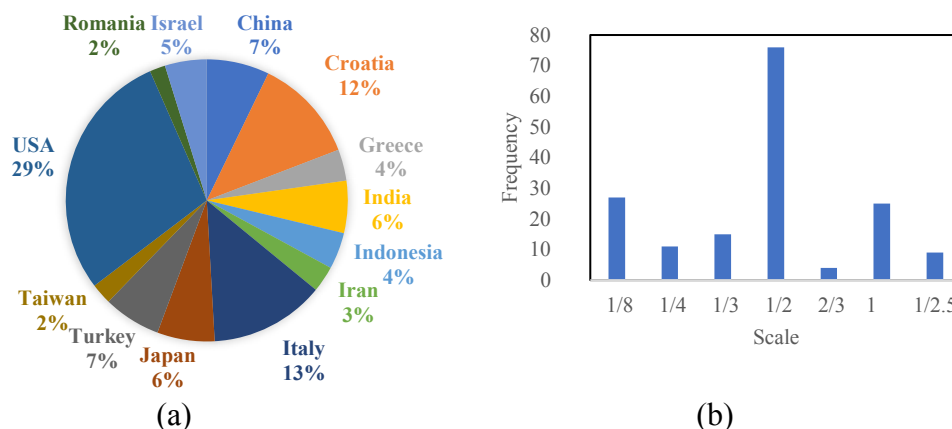


Figure 2: (a) Distribution of experiments by region (b) Scaling factors used in the experiments

2.1 STRENGTH OF FRAME MEMBERS

Mehrabi (1994) and Alwashali et al. (2019) tested MIFs that were designated as ‘strong’ and ‘weak’ frames. In the study of Mehrabi (1994), only those frames designed using equivalent static forces as per the Uniform Building Code (1991) were considered strong. Alwashali et al. (2019) used an index, β , defined as a ratio of the lateral strength of the column to the lateral strength of the infill and tested three MIFs with $\beta = 0.4, 0.6$ and 1.5 in which the MIFs with $\beta > 1$ were termed strong and the rest were called weak. Mehrabi (1994) testified that the strength of MIF was, on an average, as high as 83% with stronger frames than those with the weaker frames; however, the increase in stiffness of MIF was recorded to be just 14%. By increasing the value of β from 0.4 to 0.6, Alwashali et al. (2019) observed that there was just a slight improvement in the stiffness (13%) of MIF. For $\beta = 1.5$, which was a substantially stronger frame, the stiffness of MIF enhanced also by just 14% compared to the MIF with $\beta = 0.6$; whereas the corresponding

Table 2: Parameters influencing MIF behaviour as investigated in different studies

Authors	Strength of frame members			Masonry and aspect ratio				Openings	Number of storeys and bays and loading		
	Strength of column	Strength of beam	Reinforcement in frames	Type of masonry material	Compressive strength of masonry	Aspect ratio of panel	Strength of mortar		Number of storeys	Number of bays	Vertical loading
Fiorato et. al. (1970)			✓					✓	✓	✓	✓
Mehrabi (1994)	✓	✓			✓	✓				✓	✓
Al-Chaar et. al. (2002)				✓						✓	
Kakaletsis & Karayannis (2008)					✓			✓			
Blackard et. al. (2009)								✓			
Mansouri et. al. (2013)								✓			
Di Trapani (2014)					✓						
Sigmund & Penava (2014)								✓			
Chiou & Hwang (2015)						✓	✓				
Schwarz et. al. (2015)						✓		✓			✓
Bob et. al. (2016)				✓							
Gazic & Sigmund (2016)	✓		✓								
Huang et. al. (2016)				✓		✓					
Jin et. al. (2016)		✓									
Tekeli & Aydin (2016)								✓			
Zhai et. al. (2016)						✓		✓			
Suzuki et. al. (2017)									✓	✓	
Su et. al. (2017)								✓			
Teguh (2017)				✓							
Morandi et. al. (2018)								✓			
Alwashali et. al. (2019)	✓	✓					✓				
Cai & Su (2019)				✓							
Madiawati et. al. (2019)								✓			

rise in strength was 101.9%.

Gazic and Sigmund (2016) conducted a parametric research of MIFs by changing the cross-sectional area of the column. The study found that by increasing the cross-sectional area by 67%, the MIF had become at least 1.37 times stronger. Gazic and Sigmund (2016) and Fiorato et al. (1970) studied the influence of different percentages of reinforcement in columns on MIF. While Fiorato et al. (1970) showed a dramatic growth (almost tripled) in the strength of the MIF on addition of reinforcement ratio on frame members from 0.011 to 0.034, no significant difference in strength was observed on varying the amount of reinforcement in column in Gazic and Sigmund (2016). These two studies are the only two that had been undertaken to identify the effect of the reinforcement on the performance of MIF and unfortunately the results are not comprehensive. Alwashali et al. (2019) and Jin et al. (2016) investigated the effect of the cross-sectional area of the beam on MIF. Both studies confirmed that the higher cross-sectional area of the beam provided better lateral strength of the MIF. The rise was 13.5% and 23% due to 5-times and 4.2-times increase in the cross-sectional area of the beam in the studies of Alwashali et al. (2019) and Jin et al. (2016) respectively. This enhanced strength of MIF due to the increase in beam strength is substantially lower compared to the rise in MIF strength caused by the increase in column strength discussed earlier. This finding once again confirms the importance of having stronger column in MIF.

Essentially, there are two methods through which the researchers have attempted to quantify the effect of frame members on MIF. In the first method, the frame members were made relatively stronger than the masonry panel and the second method was to investigate the effect of geometrical configuration of the frame members which included the change of cross-section and the amount of reinforcement in them. The number of experiments using these methods are very limited to perform any major statistical comparisons. Furthermore, no parametric studies have been undertaken to investigate the effect of some important mechanical factors including characteristic compressive strength of concrete and yield strength of reinforcement. For developing a viable analysis and design techniques for MIF structures, a large number of parametric analysis using the two methods mentioned above and the associated mechanical factors is necessary.

2.2 MASONRY MATERIAL AND ASPECT RATIO OF PANEL

Figure 3a illustrates the different types of masonry materials employed as an infill panel. Clay bricks and concrete blocks are the most common infill, while fly-ash constitutes 6% of infill panels. Other categories include gypsum, calcarenite and ceramic tiles which together form 4% of the infill panels. Al-Chaar et al. (2002) and Teguh (2017) compared the performance of two MIFs – one with clay bricks and the other with concrete blocks, and observed no significant difference in the force-displacement response between the two MIFs. Huang et al. (2016) also tested the same type of infill material, i.e. clay and concrete masonry, but found that the MIFs with clay brick was 1.34 times stronger and 1.70 times stiffer than the MIFs with concrete blocks. Di Trapani (2014) investigated the effect of having clay brick and calcarenite blocks as infill materials on MIF along with a bare frame. Comparing the stiffness to a bare frame, the study found that the clay brick MIF was 11.4 times stiffer, while the calcarenite MIF was 8.3 times stiffer. In addition to clay brick and concrete block MIF, Cai and Su (2019) and Bob et al. (2016) both conducted experiments on one more type of infill –

gypsum blocks in the study of Cai & Su (2019) and ceramic tiles in the study of Bob et al. (2016). Cai and Su (2019) reported that the clay brick MIF was, respectively, 2.4-fold and 2.2-fold stronger. The initial stiffness of the clay brick MIF was also found to be much higher at 4 times and 1.8 times than that of the MIFs with concrete blocks and gypsum blocks respectively. Similarly, Bob et. al. (2016) observed that the MIF with clay brick was stronger, on an average, by a factor of 1.32 compared to the concrete block MIF. The results from the above studies clearly show that the clay brick MIFs have superior structural ability than MIFs with other infill materials when subjected to lateral loads which verify the widely use of this material as an infill.

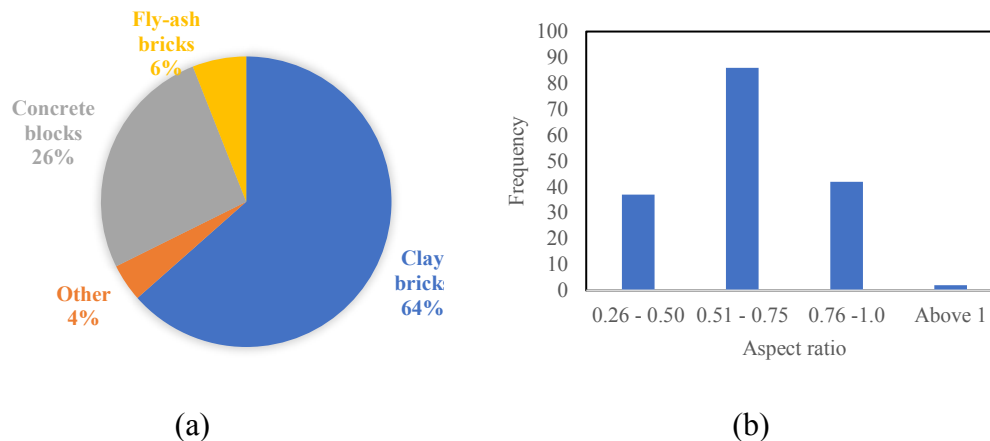


Figure 3: a) Type of masonry materials and b) Aspect ratio used in the experiments

Mehrabi (1994) examined the effect of compressive strength of masonry on MIF and remarked that there was a 54% enhancement of MIF strength when the masonry strength was increased from 9.52 MPa to 14.2 MPa. However, the weaker infill was made of hollow blocks while the higher strength infill was made of solid blocks which corresponded to the effective masonry thicknesses of 46.6 mm and 92.1 mm respectively. Kakaletsis and Karayannis (2008) observed completely different behaviour where the study found similar stiffness of MIF in having either strong infill that had 16.43 MPa mean compressive strength or weak infill that had 3.87 MPa mean compressive strength; and, the weaker infill produced 1.1 times higher lateral strength of MIF compared to the stronger infill. Chiou and Hwang (2015) and Alwashali et al. (2019) assessed the effects of mortar strength. Alwashali et al. (2019) found that weak mortar produced relatively equal structural performance of MIF in comparison to the strong mortar. This comparable behaviour was described in terms of the relative strengths of the frame and the infill by the parameter β defined earlier, where weak mortar led to higher β and therefore better performance. However, Chiou and Hwang (2015) found that stronger mortar resulted in stronger MIF where the lateral strength with a mortar compressive strength of 7 MPa was found to be 1.27 times weaker than the MIF with a mortar strength of 13 MPa. Not only are the results inconsistent but the studies are inadequate to draw any conclusion.

A number of researchers also varied the aspect ratio (height/length) of the masonry panel (Figure 3(b)) in order to understand its influence on the overall behaviour of MIF. Huang et al. (2016) reported that on increasing the aspect ratio from 0.5 to 0.67, the strength and stiffness dropped by 22.9% and 11.8% respectively. A similar result but of lower magnitude was also published by Zhai et al. (2016) where a 29% increase in aspect ratio caused a 6.5% reduction in strength. Conducting a similar experiment, however, Chiou and Hwang (2015) recorded a significant rise in strength by a factor of

1.76 when the aspect ratio was approximately doubled. Adding to these conflicting results, Mehrabi (1994) and Schwarz et al. (2015) reported that the aspect ratio had ‘minimal’ impact. Therefore, when it comes to the effect of masonry material on MIF, except that the clay brick had produced at least equal or better performance compared to other infill materials, no other agreeable investigation results have been obtained until now.

2.3 OPENINGS

Fiorato et al. (1970) conducted one of the early studies to investigate the effect of openings on MIF behaviour. The opening area in the experiment varied between 2.89% to 50% and the research observed that the strength of the MIF with opening was less than the strength of the solid MIF but the variation was not proportional to the ratio of opening. Su et al. (2017) tested MIFs with different opening areas (0%, 25.7% and 100%) and found that the increase in the opening area led to a huge drop in the lateral resistance and stiffness where the MIF with 25.7% opening area had, respectively, 1.70 times and 2 times lesser strength and stiffness than the fully infilled MIF. However, the ductility factor of MIF with 25.7% opening area was almost twice the ductility of fully infilled MIF. Providing similar conclusions through the testing of six different kinds of MIF (four with openings and two solid) and a bare frame, Kakaletsis and Karayannis (2008) stated that the openings had ‘increased the ductility factor of frames’ which ranged from 3.20 – 6.77. However, this conclusion is ambiguous because the ductility factors for solid MIFs were equally high at 4.24 and 6.31, unless the comparison was made with respect to the bare frame which had a ductility factor of 3.97. In terms of strength and stiffness, the study observed an average reduction of 17% and 26% compared to solid MIFs. Morandi et al. (2018) also provided results to demonstrate that a door opening led to a drop in the strength by almost half due to the presence of 34% opening area in MIF. Mansouri et al. (2014) by experimenting on one solid and four MIFs with different opening sizes and locations reported (8 – 40)% reductions in strength and stiffness of MIFs. It is the only study which concluded that the ductility of the MIF with opening had reduced compared to solid MIF. The difference in the average ductility factors was calculated to be 19%; however, the data is not comprehensive. Tekeli and Aydin (2017) tested MIFs with different opening areas of 4, 9, 16 and 25% and reported that the MIFs had a decline in strength of 1, 10, 20 and 30% respectively when compared with full MIF. Two studies (Blackard et al., 2009; Tekeli & Aydin, 2017) focussed on the effect due to location of the openings. Openings that were placed at the centre of the infill panel were termed concentric, and those that were placed at some distance from the centre were called eccentric openings. While Blackard et al. (2009) did not observe any major difference in response of having concentric or eccentric openings, Tekeli and Aydin (2017) stated that the MIFs with concentric openings performed better than the eccentrically placed openings; but there are no data to compare. Although it can be inferred that the presence of openings causes a degradation of strength and stiffness but increase in ductility of MIF, these effects are not completely formulated. From the location point of view, the research results are too fewer to make any judgement.

2.4 NUMBER OF STOREYS AND BAYS

Fiorato et al. (1970) constructed scaled multi-storey MIF structures and found more flexibility in structures with higher storeys. This was attributed to the overturning moment induced from upper storeys on the first storey. Mehrabi (1994) observed that

there was no notable difference in applying the vertical loads either on columns or beams. However, on raising the magnitude of the load on the column by 50%, the stiffness improved by 33% and strength by 25%. Suzuki et al. (2017) compared one storey one bay MIF and two storey one bay MIF and found ‘similar’ behaviour. Several studies (Fiorato et al., 1970; Mehrabi, 1994; Al-Chaar et al., 2002; Suzuki et al., 2017) examined the effect of increasing the number of bays on MIF lateral behaviour. All of these studies confirmed that an addition of even a single bay resulted in a better performance with Mehrabi (1994) and Suzuki et al. (2017) reporting a multi-bay strength and stiffness of almost two times that of a single bay MIF. The effect due to number of storeys is too less to investigate which, therefore, needs further investigation.

Of the parameters, the effect of having openings on MIF has been studied the most. Moderately studied parameters include the type of masonry material, aspect ratio of masonry panel and the number of bays and their outcomes show that further exploration is required. Rest of the parameters have been sparingly studied. In carrying out the parametric analysis, it required interpretation of large body of literature. Extracting meaningful comparisons among the experimental studies was difficult as the experiments were constrained by their own scope of studies. This difficulty can be the reason why there are limited studies on the parametric analysis of MIF. The authors, as far as possible, limited the variation of other parameters when one of them was being studied.

3 EQUIVALENT STRUT MODELLING OF MIF

Strut modelling concept is based on the assumption that the infill panel is equivalent to a diagonal strut running from the top the of the windward column to the bottom of the leeward column (Figure 4). According to Mohyeddin (2011) one of the early works in developing this method was Polyakov (1939) who carried out extensive field observations and conducted 57 experiments on structural models with solid and perforated bricks subjected to wind load. Since the beams and columns were connected using hinge connections, the experiment had drawn criticism of not being able to replicate the actual behaviour.

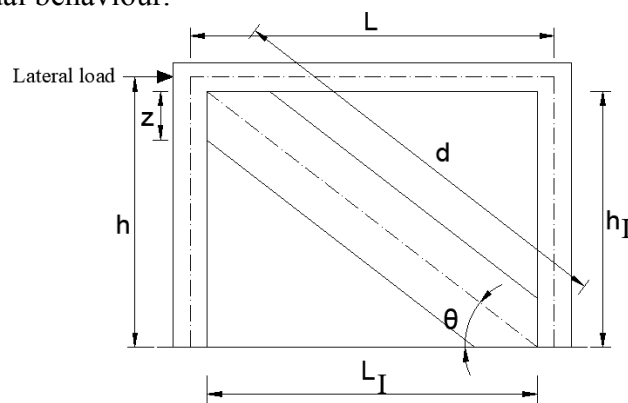


Figure 4: Equivalent strut

Extensive research in MIF followed thereafter with a focus on developing a generic strut that is suitable for all types of MIFs. Most of the studies estimated the strut width, w , using a relative stiffness ratio of the masonry and the frame, $\lambda_h h$, proposed by Stafford-Smith (1962) as:

$$\lambda_h h = \sqrt[4]{\frac{E_m t \sin 2\theta}{4 E_f I_c h_I}} h \quad (3.1)$$

where h is the height of the column from the base/foundation to the centreline of the beam, E_m and t are the modulus of elasticity and thickness of the masonry, θ is the angle formed between the diagonal of the infill and the horizontal line, E_f is the modulus of elasticity of the frame material, I_c is the moment of inertia of the column and h_I is the height of the infill panel. Although single strut modelling is widely used, a major drawback of this technique is that it cannot completely describe MIF's inherent nature of having highly variable material and nonlinear properties. Such limitations have given rise to multi strut modelling techniques (Crisafulli, 1997; El-Dakhakhni et al., 2003; Crisafulli & Carr, 2007; Burton & Deierlein, 2014;) and proposing of MIF models continue even today as in Kumar et al. (2018), Baloevic et al. (2019) and Basha et al. (2020). This review will not discuss in detail the various strut models and readers are directed to Mohyeddin et al. (2017) for extensive investigations on strut modelling.

4 PARAMETRIC FE MODELLING OF MIF

There are two ways of performing FE analysis of MIF – macro and micro modelling. Macro modelling is no different than equivalent strut modelling discussed in Section 3. In micro modelling, however, each of the materials and the interface between the brick and mortar, and the masonry and frame members are considered as separate elements. Although micro modelling involves enormous runtime, effort, and are often expensive, many researchers have employed this method to understand the behaviour of MIFs.

Durrani and Luo (1994) conducted an FE analysis to investigate the effect of the infill thickness, column and beam stiffness, the presence of opening and the aspect ratio of the infill panel. Unlike the moment-resisting frames utilized in other studies, flat-slab structures with low lateral stiffness were used. Such structures are highly susceptible to seismic loads according to the survey carried out after the 22 February, 2011 Christchurch earthquake (Kam et al., 2011). A major finding by Durrani and Luo (1994) was that the strut widths were 'quite different' at initial and ultimate strengths. This relationship was also observed by Mohyeddin (2011) and Stafford-Smith and Carter (1969). The research developed a series of curves to indicate how the strut width reduced with increase in the thickness of masonry and made the following conclusions (only the ones relevant to this review are mentioned):

- Aspect ratio had the most impact with the square panels having a large strut width
- MIF depended more on column stiffness than the stiffness of beam which was also observed in few of the experimental studies discussed in Section 2
- Openings reduced strut width and a reduction factor, $k = 1 - \left(\frac{A_{op}}{A_I} \right)^2$ was proposed where A_{op} is the area of opening and A_I is the area of infill.

Hammoudah et al. (2017) analysed the impact of opening, vertical loads and aspect ratio through nonlinear analysis of reinforced concrete frame with masonry brick wall. It must be noted that the aspect ratio in this study was defined as L/h and the values

varied from 0.5 to 2. Internal actions such as stress, bending moment and displacement were initially found to reduce with the increase in L/h ratio from 0.5 to 1.5. However, a reverse trend of decrease in the magnitude of internal actions was observed when the ratio was further raised to 2 and therefore, an aspect ratio of 1.5 was defined as ‘optimum’ for MIF. For specimens subjected to vertical loads, a similar pattern was illustrated where a uniformly distributed load of 7.5 kN/m was found ‘optimum’. In other words, MIF with aspect ratio of 1.5 and vertical loading of 7.5 kN/m was recommended. Further parametric analysis based on the location of the opening was also performed and it was inferred that the openings placed at the upper left and the bottom corner of the infill had the maximum implication on MIF partially verifying the experimental results of Tekeli and Aydin (2017).

Sipos et al. (2018) validated a numerical model with the experimental data from the literature to explore the outcomes of having multi storeys and bays, masonry compressive strength and peak ground acceleration in MIF. Measuring the response in terms of drift ratio, the study recorded that there was minimal impact due to an extension in bay length from 4 m to 6 m, contradicting the experimental observations discussed earlier where an additional bay resulted in much greater performance of MIF. The drift, however, doubled when the building height was increased from 6 to 9 storeys and this response was explained as an accumulation of mass being more dominant than the improvement in the stiffness in increasing the height of the structure thereby attracting greater seismic loads. By raising the masonry compressive strength from 1.17 MPa to 2.29 MPa and finally to 5.01 MPa, the drift ratio reduced by 19% and 32% respectively in comparison to the weakest masonry. This study also suggested that the model effectiveness is dependent on the type of analysis and the amount of lateral load applied.

Ahani et al. (2019) conducted an experiment on a single bay, single storey MIF and subsequent FE sensitivity analyses were performed on the infill opening. The openings in the FE analysis were located on the top left, centre and bottom right of the infill and each of these positions were placed with different sizes of opening - 9.5%, 19%, 29.5% and 39.5% of the infill area. In general, it was observed that the MIF with opening positioned at the top left had become weaker compared to the other MIFs (e.g. for 9.5% opening area, there was a 11% and 22% strength reductions in relation to the MIFs with opening in the centre and bottom right respectively) contradicting the findings of Hammoudah et al. (2017). Another conclusion from the study was that if the opening area exceeded 40% of the infill area, the strength contribution from the masonry wall can be neglected.

Despite the advancement in developing powerful FE packages, only few parameters were investigated ignoring some important parameters including the percentage of reinforcement in frame members and strength of concrete. Considering that there are many other factors that could potentially affect the lateral behaviour of MIF, significant investigation is required.

5 CONCLUDING REMARKS AND FUTURE RESEARCH

The parameters affecting the overall behaviour of MIF can be broadly classified into two categories – material and geometry. From material perspective, the type of masonry

(clay, concrete, ceramic, gypsum) and compressive strength of frame, masonry and mortar have been studied in the literature. Geometrical factors include the cross-section of frame members, percentage of longitudinal and transverse reinforcements, number of storeys and bays, aspect ratio of panel, openings and vertical loadings. The effect of openings on MIF has been studied adequately. Moderately studied parameters include the type of masonry material, aspect ratio of masonry panel and the number of bays and their outcomes show that further exploration is required. Rest of the parameters have been sparingly studied.

Although MIF has been studied since the 1930s, no consensus on the modelling has been achieved. The difficulty in the FE modelling of MIF can be attributed for two reasons: 1) The interaction between frame and masonry panel has a highly nonlinear response and 2) There are large number and variability of material, geometric and contact properties involved in the behaviour. The nonlinear response of the MIFs has given rise to computation complications and mathematical modelling. Despite the ongoing research in the area of MIF for a long period of time, there are limited studies being performed to understand the effect of each parameter. The available results are also very scattered and contradicting. Therefore, a large parametric study of the factors affecting the overall behaviour of MIF is necessary in order to fully understand its behaviour when subjected to lateral loads.

6 ACKNOWLEDGEMENT

The authors thank the Concrete Masonry Association of Australia for funding the project.

REFERENCES

- Ahani, E., Mousavi, M., Ahani, A., & Kheirollahi, M. (2019). The Effects of Amount and Location of Openings on Lateral Behavior of Masonry Infilled RC Frames. *Journal Of Civil Engineering*, 23(5), 2175-2187. <https://doi.org/10.1007/s12205-019-0714-x>.
- Al-Chaar, G., Issa, M., & Sweeney, S. (2002, 08/01). Behavior of Masonry-Infilled Nonductile Reinforced Concrete Frames. *Journal of Structural Engineering-asce - J STRUCT ENG-ASCE*, 128. [https://doi.org/10.1061/\(ASCE\)0733-9445\(2002\)128:8\(1055\)](https://doi.org/10.1061/(ASCE)0733-9445(2002)128:8(1055)).
- Almusallam, T. H., & Al-Salloum, Y. A. (2007). Behavior of FRP Strengthened Infill Walls under In-Plane Seismic Loading. *Journal of Composites for Construction*, 11(3), 308-318. [https://doi.org/10.1061/\(ASCE\)1090-0268\(2007\)11:3\(308\)](https://doi.org/10.1061/(ASCE)1090-0268(2007)11:3(308)).
- Alwashali, H., Sen, D., Jin, K., & Maeda, M. (2019, 03/26). Experimental investigation of influences of several parameters on seismic capacity of masonry infilled reinforced concrete frame. *Engineering Structures, Volume 189*, Pages 11-24.
- Asteris, P. G., Antoniou, S. T., Sophianopoulos, D. S., & Chrysostomou, C. Z. (2011). Mathematical Macromodeling of Infilled Frames: State of the Art. *Journal of Structural Engineering*, 137(12), 1508-1517.
- Baloevic, G., Radnic, J., & Grgic, N. (2019). Numerical model for dynamic analysis of masonry-infilled steel and concrete frames. *Materialwissenschaft und Werkstofftechnik*, 50(5), 519-532. <https://doi.org/10.1002/mawe.201900006>.

- Basha, S., Surendran, S., & Kaushik, H. B. (2020). Empirical Models for Lateral Stiffness and Strength of Masonry-Infilled RC Frames Considering the Influence of Openings. *Journal of Structural Engineering*, 146(4).
- Basha, S. H., & Kaushik, H. B. (2016). Behavior and failure mechanisms of masonry-infilled RC frames (in low-rise buildings) subject to lateral loading. *Engineering Structures*, 111, 233-245. <https://doi.org/10.1016/j.engstruct.2015.12.034>.
- Blackard, B., Willam, K., & Sivaselvan, M. (2009, 01/01). Experimental observations of masonry infilled reinforced concrete frames with openings. *American Concrete Institute, ACI Special Publication*, 199-221.
- Bob, C., Marginean, S., & Scurt, A. (2016, 05/27). Theoretical/experimental study of reinforced-concrete frame with masonry infill. *Proceedings of the Institution of Civil Engineers - Structures and Buildings*, 169, 1-15.
- Burton, H., & Deierlein, G. (2014, 08/01). Simulation of Seismic Collapse in Nonductile Reinforced Concrete Frame Buildings with Masonry Infills. *Journal of Structural Engineering*, 140, A4014016.
- Cai, G., & Su, Q. (2019, 2019/10/21). Effect of Infills on Seismic Performance of Reinforced Concrete Frame structures—A Full-Scale Experimental Study. *Journal of Earthquake Engineering*, 23(9), 1531-1559. <https://doi.org/10.1080/13632469.2017.1387194>.
- Chiou, T., & Hwang, S. J. (2015, 02/01). Tests on cyclic behavior of reinforced concrete frames with brick infill. *Earthquake Engineering & Structural Dynamics*, 44.
- Chrysostomou, C., & Asteris, P. (2012, 08/01). On the in-plane properties and capacities of infilled frames. *Engineering Structures*, 41, 385-402.
- Crisafulli, F. (1997). Seismic behaviour of reinforced concrete structures with masonry infills.
- Crisafulli, F., & Carr, A. (2007, 06/01). Proposed macro-model for the analysis of infilled frame structures. *Bulletin of the New Zealand Society for Earthquake Engineering*, 40, 69-77.
- Dautaj, A. D., Krasniqi, C., Sadikaj, A., Shatri, B., & Kabashi, N. (2018). Experimental study on strengthening effects of glass fibre-reinforced polymers on masonry infilled reinforced concrete frames. *European Journal of Environmental and Civil Engineering*. <https://doi.org/10.1080/19648189.2018.1528893>.
- Di Trapani, F. (2014). *Masonry infilled RC frames: Experimental results and development of predictive techniques for the assessment of seismic response*.
- Durrani, A. J., & Luo, Y. H. (1994). Seismic retrofit of flat-slab buildings with masonry infills.
- El-Dakhakhni, W., Elgaaly, M., & Hamid, A. (2003, 02/01). Three-Strut Model for Concrete Masonry-Infilled Steel Frames. *Journal of Structural Engineering*, 129, 177-185.
- Fiorato, A. E., Sozen, M. A., & Gamble, W. L. (1970). An Investigation of the Interaction of Reinforced Concrete Frames with Masonry Filler Walls.
- Gazic, G., & Sigmund, V. (2016, 09/01). Cyclic testing of single-span weak frames with masonry infill. *Grđevinar*, 68, 617-633. <https://doi.org/10.14256/JCE.1614.2016>.

- Hammoudah, S. M., Chaudhary, M. T. A., & Essawy, A. S. (2017). Analytical and parametric study on masonry infilled reinforced concrete frames using finite element method. *Advances in Structural Engineering*, 20(12), 1891-1906.
- Holmes, M. (1961). Steel Frames With Brickwork And Concrete Infilling. *Proceedings of the Institution of Civil Engineers*, 19(4), 473-478.
- Huang, Q., Guo, Z., & Kuang, J. S. (2016, 09/01). Designing infilled reinforced concrete frames with the 'strong frame-weak infill' principle. *Engineering Structures*, 123, 341-353.
- Jin, K., Choi, H., & Nakano, Y. (2016, 02/29). Experimental Study on Lateral Strength Evaluation of Unreinforced Masonry-Infilled RC Frame. *Earthquake Spectra*, 32.
- Kakaletsis, D. J., & Karayannis, C. G. (2008, 2008/02/13). Influence of Masonry Strength and Openings on Infilled R/C Frames Under Cycling Loading. *Journal of Earthquake Engineering*, 12(2), 197-221. <https://doi.org/10.1080/13632460701299138>.
- Kam, W. Y., Pampanin, S., & Elwood, K. (2011). Seismic performance of reinforced concrete buildings in the 22 February Christchurch (Lyttelton) earthquake. *Bulletin of the New Zealand Society for Earthquake Engineering*, 44(4), 239-278.
- Kaushik, H., Rai, D. C., & Jain, S. (2006). Code approaches to seismic design of masonry-infilled reinforced concrete frames: A state-of-the-art review. *Earthquake Spectra*, 22(4), 961-983. <https://doi.org/10.1193/1.2360907>.
- Koutas, L., Bousias, S. N., & Triantafillou, T. C. (2015). Seismic Strengthening of Masonry-Infilled RC Frames with TRM: Experimental Study. *Journal of Composites for Construction*, 19(2). [https://doi.org/10.1061/\(ASCE\)CC.1943-5614.0000507](https://doi.org/10.1061/(ASCE)CC.1943-5614.0000507).
- Kumar, M., Khalid, F., & Ahmad, N. (2018). Macro-Modelling Of Reinforced Concrete Frame Infilled With Weak Masonry For Seismic Action. *NED University Journal of Research*, 15(1), 15-38.
- Madiawati, M., Tanjung, J., Hayati, Y., Agus, A., & Medriosa, H. (2019, 05/01). Experimental investigation of seismic performance of reinforced brick masonry infilled reinforced concrete frames with a central opening. *International Journal of GEOMATE*, 16, 35-41. <https://doi.org/10.21660/2019.57.4592>.
- Mainstone, R. J. (1971). *On the stiffnesses and strengths of infilled frames*. Building Research Station. [//catalog.hathitrust.org/Record/009615980](http://catalog.hathitrust.org/Record/009615980).
- Mansouri, A., Marefat, M., & Khanmohammadi, M. (2014). Experimental evaluation of seismic performance of low-shear strength masonry infills with openings in reinforced concrete frames with deficient seismic details. *The Structural Design of Tall and Special Buildings*, 23. <https://doi.org/10.1002/tal.1115>.
- Mehrabi, A. B. (1994). *Behavior of Masonry-infilled Reinforced Concrete Frames Subjected to Lateral Loadings*. University of Colorado.
- Mohyeddin, A. (2011). *Modelling and Performance of RC Frames with Masonry Infill under In-Plane and Out-of-Plane Loading*.
- Mohyeddin, A., Dorji, S., Gad, E. F., & Goldsworthy, H. M. (2017). Inherent limitations and alternative to conventional equivalent strut models for masonry infill-frames. *Engineering Structures*, 141, 666-675.

- Morandi, P., Hak, S., & Magenes, G. (2018). Performance-based interpretation of in-plane cyclic tests on RC frames with strong masonry infills. *Engineering Structures*, 156, 503–521. <https://doi.org/10.1016/j.engstruct.2017.11.058>.
- Schwarz, S., Hanaor, A., & Yankelevsky, D. (2015). Experimental Response of Reinforced Concrete Frames with AAC Masonry Infill Walls to In-Plane Cyclic Loading. *Structures*, 3. <https://doi.org/10.1016/j.istruc.2015.06.005>.
- Sigmund, V., & Penava, D. (2014, 2014/01/02). Influence of Openings, With and Without Confinement, on Cyclic Response of Infilled R-C Frames — An Experimental Study. *Journal of Earthquake Engineering*, 18(1), 113-146.
- Sipos, T. K., Rodrigues, H., & Grubišić, M. (2018). Simple design of masonry infilled reinforced concrete frames for earthquake resistance. *Engineering Structures*, 171, 961-981. <https://doi.org/https://doi.org/10.1016/j.engstruct.2018.02.072>.
- Sipos, T. K., Sigmund, V., & Hadzima-Nyarko, M. (2013). Earthquake performance of infilled frames using neural networks and experimental database. *Engineering Structures*, 51, 113-127. <https://doi.org/10.1016/j.engstruct.2012.12.038>.
- Stafford-Smith. (1962). Lateral Stiffness of Infilled Frames. *Journal of the Structural Divison*, 88(6).
- Stafford-Smith, B., & Carter, C. W. (1969). A Method Of Analysis For Infilled Frames.
- Su, Q., Cai, G., & Cai, H. (2017). Seismic behaviour of full-scale hollow bricks-infilled RC frames under cyclic loads. *Bulletin of Earthquake Engineering*, 15(7), 2981-3012.
- Suzuki, T., Choi, H., Sanada, Y., Nakano, Y., Matsukawa, K., Paul, D., Gülkan, P., & Binici, B. (2017). Experimental evaluation of the in-plane behaviour of masonry wall infilled RC frames. *Bulletin of Earthquake Engineering*, 15(10), 4245-4267.
- Teguh, M. (2017, 12/31). Experimental Evaluation of Masonry Infill Walls of RC Frame Buildings Subjected to Cyclic Loads. *Procedia Engineering*, 171, 191-200.
- Tekeli, H., & Aydin, A. (2017, 08/13). An experimental study of the seismic behavior of Infilled RC frames with opening. *Scientia Iranica*, 24. <https://doi.org/10.24200/sci.2017.4150>.
- TMS. (2017). TMS 402/602 Building Code Requirements and Specifications for Masonry Structures, 2016. *Concrete International*, 39(2), 11.
- Uniform Building Code (1991). California, USA.
- Wijaya, H., Rajeev, P., Gad, E., & Amirsardari, A. (2020). Effect of Infill-Wall Material Types and Modeling Techniques on the Seismic Response of Reinforced Concrete Buildings. *Natural hazards review*, 21(3).
- Yuksel, E., & Teymur, P. (2011). Earthquake performance improvement of low rise RC buildings using high strength clay brick walls. *Bulletin of Earthquake Engineering*, 9(4), 1157-1181. <https://doi.org/10.1007/s10518-010-9242-2>.
- Zhai, C., Kong, J., Wang, X., & Chen, Z. (2016). Experimental and Finite Element Analytical Investigation of Seismic Behavior of Full-Scale Masonry Infilled RC Frames. *Journal of Earthquake Engineering*, 20(7), 1171-1198.

Torsional Performance of RC U-shaped Walls: Recent Experimental and Numerical Findings

Ryan D. Hoult¹

1. Corresponding Author. Lecturer, Department of Infrastructure Engineering, University of Melbourne (UoM), Parkville, VIC 3010, Australia.
Email: ryan.hoult@unimelb.edu.au

ABSTRACT:

Reinforced concrete U-shaped walls are embedded within the building stock internationally and provide the primary lateral resistance for many of these structures in the events of high winds or earthquakes. In such events, these types of walls are not only expected to deform laterally but have the potential to twist. There is a paucity of research that has focused on the torsional resistance of reinforced concrete walls and the current methods for the design for torsion in building codes cannot be applied to an open section. This paper explores the recent experimental and numerical research that has focused on the torsional performance of reinforced concrete U-shaped walls. The torsional stiffness of these walls has been found to degrade at a similar rate as the translational stiffness of the walls. A simple mechanical model is programmed that can readily determine the torsional capacity of RC U-shaped walls. Using the mechanical model, a large-scale parametric study is performed, which finds a correlation between the moment capacity of the section and torsional capacity of the wall.

Keywords: torsion, flexure, torque, twist, cores, C-shaped

1. Introduction

Reinforced concrete (RC) U-shaped walls (Figure 1a) are one of the most geometrically popular structural elements used in building construction practice. They form the “backbone” structural system in millions of RC buildings internationally, primarily bracing the structure against lateral loads (e.g., wind and earthquakes). Due to the increasing demand for more efficient use of the building area, the wall is sometimes placed on the perimeter of the building (Figure 1b). Furthermore, one of the primary methods of strengthening older buildings is to add RC walls to the periphery (Lombard *et al.*, 2000). The RC wall is typically much stiffer than any other structural elements in the building, which creates plan asymmetry due to offset of stiffness from the centre of mass. Thus, these building configurations have the potential to create a torsional response (i.e., twist) when subjected to earthquake ground motions. In fact, even for symmetric structures, accidental loading and mass eccentricities are inevitable and can trigger critical, unforeseen torsional responses. Furthermore, in low-to-moderate seismic regions, it is common to find just a single, peripheral U-shaped wall, which alone needs to resist the twisting of the building. In these regions, it is possible that the additional stresses induced in the wall from the twisting actions (Figure 1a) will result in a premature and brittle failure. However, even in regions of high seismicity, building codes do not cater for the design of open-section walls (e.g., U-shaped) subjected to torsion. Importantly, if the U-shaped core walls do not have the required reinforcement detailing for the torsional demand, extensive damage will occur to structural (and non-structural) elements. This damage will result in large post-earthquake retrofit costs or more often requires demolition of the entire building, assuming that the worst-case scenario of catastrophic building collapse did not occur. This research investigates experimentally and numerically the torsional performance and capacity of RC U-shaped walls.

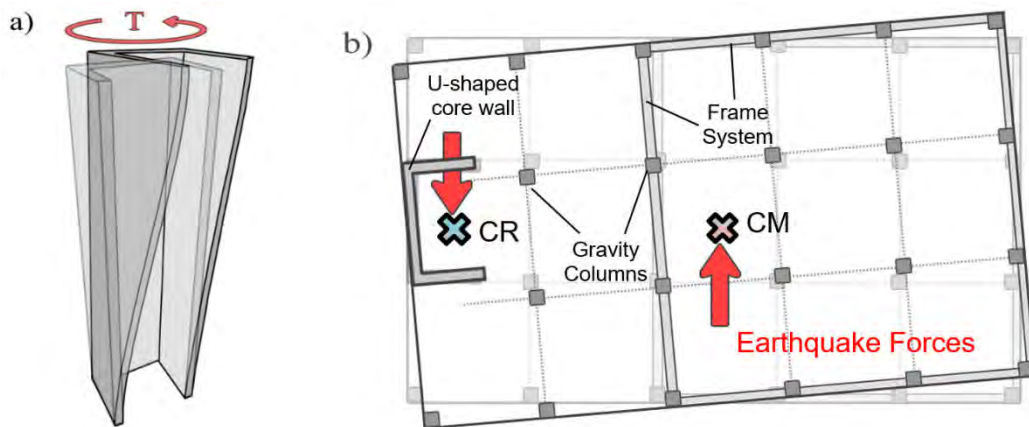


Figure 1 (a) U-shaped core wall subjected to torsion (T), and (b) floor layout of asymmetric building with peripheral U-shaped core wall (centre of rigidity [CR], or stiffness, is offset from the centre of mass [CM])

There is a very limited amount of research that has focused on the torsional performance of RC walls. Some torsion related experimental research has been conducted on RC U-shaped beams due to the wide application of these types of elements in rail viaduct engineering (Krpan & Collins, 1981b; Xu *et al.*, 2018a). However, the experimental results from beam specimens cannot be extrapolated to determine the expected performance on walls given the differences in (i) boundary conditions and restraints, (ii) reinforcement detailing, (iii) axial load, and (iv) loading conditions. To the knowledge of the author, only two experimental campaigns have ever focused on the torsional capacity of RC walls. The first consisted in testing eight half-scale wall units for torsion (Peng & Wong, 2011). However, these specimens were all rectangular in cross-section, whereas RC core walls typically have non-planar sections (i.e., U-shaped). In the second test programme, core wall specimens with H-shaped

cross-sections were tested for torsion (Maruta *et al.*, 2000), but a highly-contentious scale factor of 1:12 was employed.

Recent experimental and numerical research was conducted by the author to better understanding the torsional performance of RC U-shaped walls. This paper summarises some of this work and addresses some of the future research being proposed by the author.

2. Shear centre distance

Beyer *et al.* (2008) investigated the seismic performance and inelastic behaviour of two RC U-shaped wall specimens denoted TUA and TUB, with cross-sections and reinforcement detailing shown in Figure 2.

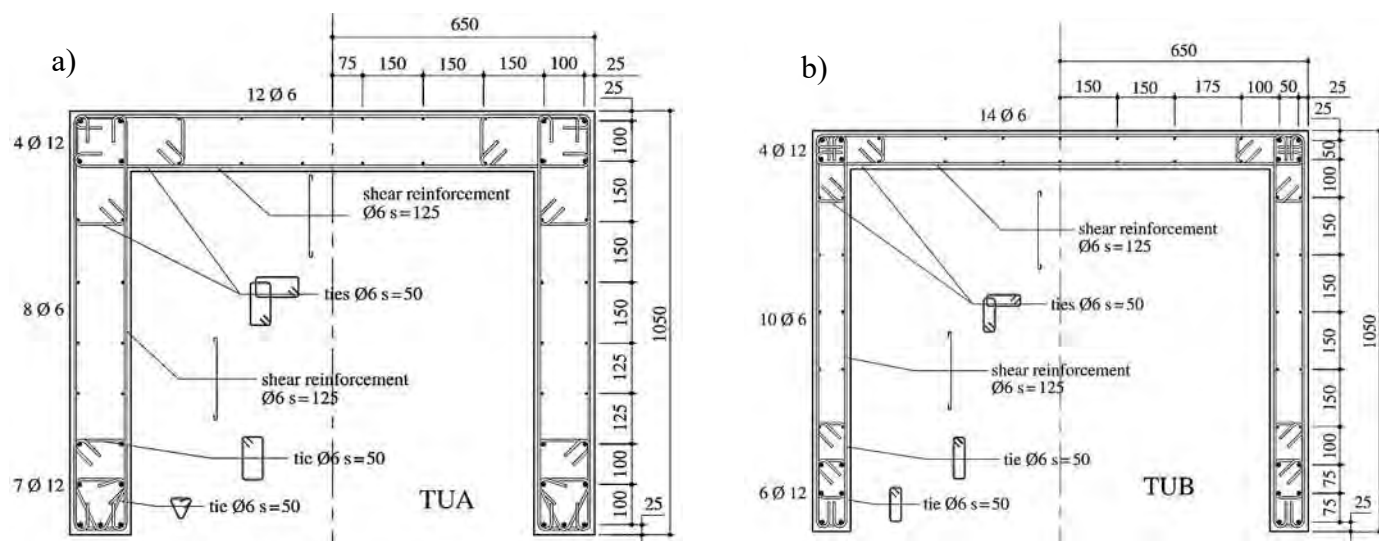


Figure 2 Cross-sections of specimens (a) TUA and (b) TUB (Beyer *et al.*, 2008)

As was briefly discussed in Beyer *et al.* (2008), when loading the wall in the east-west direction, the north-south actuators were used to restrain the collar of the wall from twisting. The forces, and the corresponding torsional moment that was applied by the north-south actuators, were necessary since the shear centre of the U-shaped wall was located outside of the section and the force applied in the east-west direction did not pass through the location of the shear centre. The distance of the shear centre (d_{sc}) from the web of the wall is depicted in Figure 3. The torsional moment required to restrain the collar from twisting reduces as the wall is subjected to greater displacement demands in the east-west direction. The torsional moment decreases because with increasing ductility the flanges are more and more damaged and therefore the shear centre moves closer to the centre of the web of the wall (Pegon *et al.*, 2000), and thus the magnitude of the required force couple reduces (Beyer *et al.*, 2008).

The elastic shear centre distance ($d_{sc,elastic}$) from the centre line of the web can be calculated using the expression from Vlasov (1961) for thin-walled U-shaped sections:

$$d_{sc,elastic} = \frac{\left(\left(L_f - \frac{t_w}{2} \right)^2 t_w \right)}{\left(2 \left(L_f - \frac{t_w}{2} \right) t_w \right) + \frac{(L_w - t_w)t_w}{3}}$$

1

where L_f is the outer dimensional length of the flange, L_w is the outer dimensional length of the web and t_w is the thickness of the wall.

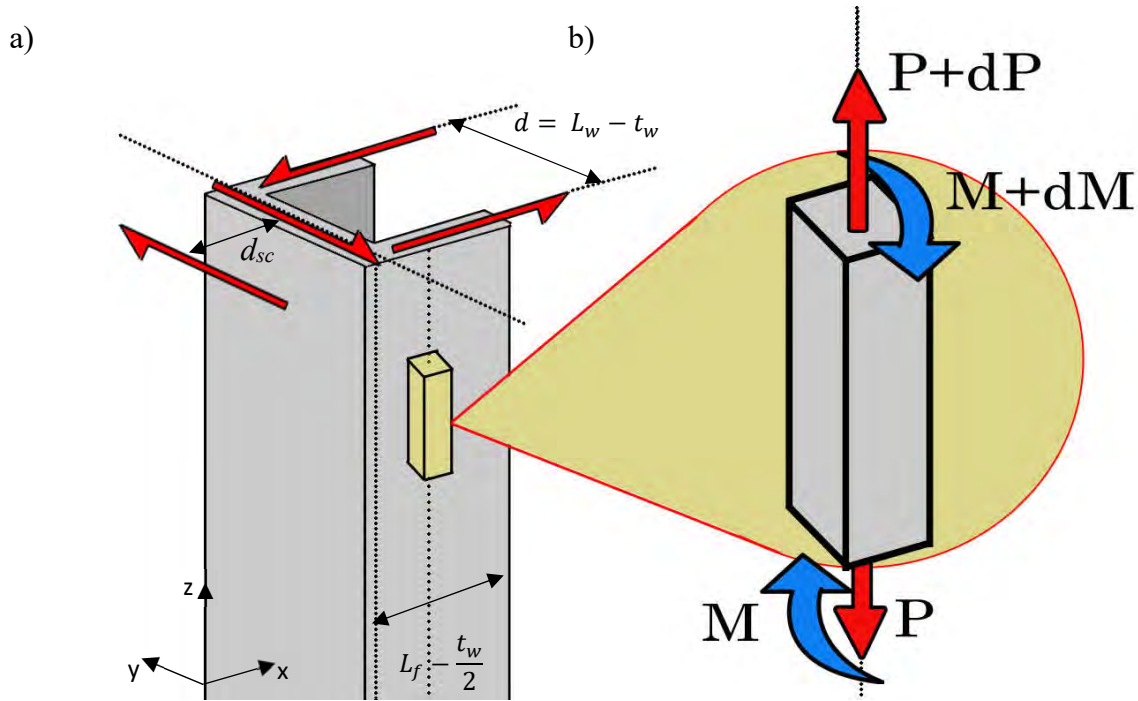


Figure 3 (a) U-shaped wall with (b) a section of the flange depicted with moments and longitudinal forces

The magnitude of the shear centre distance (d_{sc}) from the centre of the web can be calculated at several different drift levels from the experimental data using Equation 2:

$$d_{sc} = \frac{\left(\left(\frac{F_{NS_E} - F_{NS_W}}{2} \right) L_w \right)}{F_{EW}} + \frac{t_w}{2}$$

2

where F_{NS_E} , F_{NS_W} and F_{EW} correspond to the force applied by the actuators experimentally in the north-south (east) side, north-south (west) side and east-west side respectively.

Figure 4(a) plots the shear centre distance (d_{sc}) found experimentally as a function of the wall drift in the east-west direction. The $d_{sc,elastic}$ values are also illustrated in Figure 4(a) (dotted lines), which were calculated using Equation 1 for both TUA and TUB (corresponding to 407 mm and 417 mm respectively). Figure 4(a) shows that the value of SC decreases from the elastic estimate as a function of the drift (or displacement) demand of the wall in the east-west direction. This corroborates the observations by Ile and Reynouard (2005) who found that for RC U-shaped walls the location of the shear centre moved from its initial position, ‘which was very close to the

theoretical position for an elastic homogenous wall', closer to the web and centroid as the wall achieved higher displacements and endured more damage. Figure 4(b) shows a function for calculating the distance of the shear center (d_{sc}) as a function of absolute drift (δ), which was found to fit the data best ($R^2 = 0.94$). It should be noted that the value of the shear center distance, d_{sc} , in Figure 4(b) has been normalized to the elastic shear center distance, $d_{sc,elastic}$. Thus, to calculate d_{sc} as a function of drift, Equation 3 can be used.

$$d_{sc} = (-0.206 \ln \delta - 0.36)d_{sc,elastic}$$

3

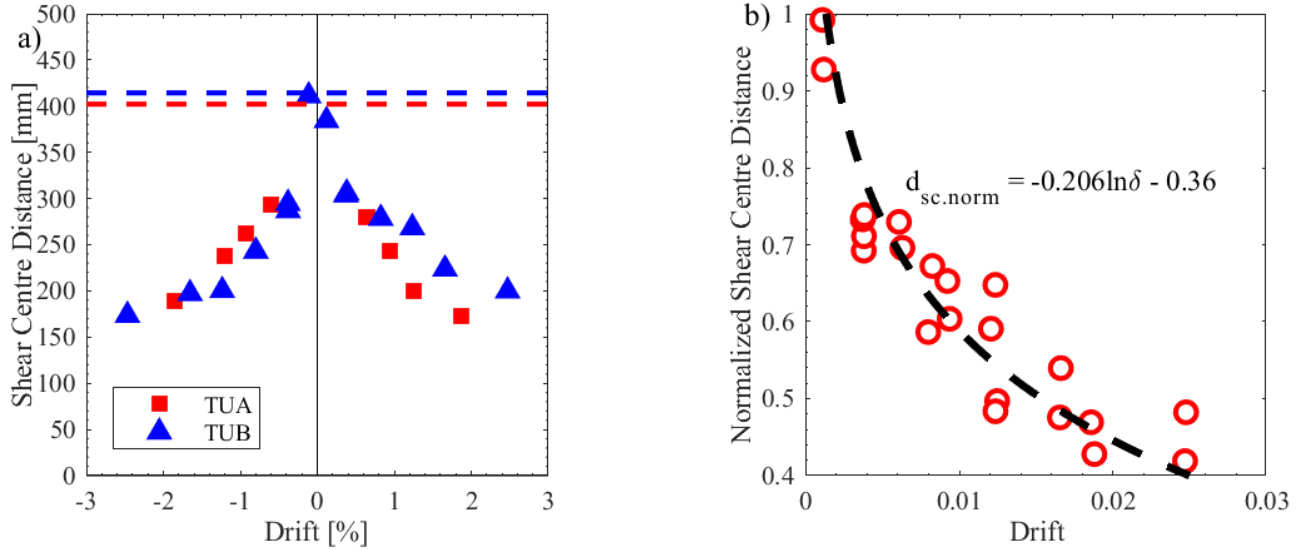


Figure 4 Shear centre distance calculated from experimental results for specimens TUA and TUB (a) as a function of drift and (b) line-of-best fit

The experimental data from RC specimen CW1 from Behrouzi *et al.* (2019) provides an opportunity to test Equation 3. Specimen CW1, with cross-section of the wall given in Figure 5a, was tested to investigate the performance of RC U-shaped walls under strong-axis bending. It is important to note that the cross-section, detailing, and shear-span ratio of CW1 is vastly different to that of TUA and TUB. An axial load ratio of 5% was held constant during testing and an overturning moment was applied to the wall to increase the shear-span-ratio such that effective height (H_e) was approximately 8,600 mm. During testing, the head of the wall was restraint from moving out-of-plane. Using the available dataset from Birely *et al.* (2014), the recorded moment resisting the wall head from movement and the force applied parallel to the web of the wall was used to calculate the shear center distance (d_{sc}) from the web. The experimental value of d_{sc} was estimated at several different cyclic displacements (or drifts) achieve by the wall. Figure 5b illustrates the estimated values of d_{sc} as a function of drift. Furthermore, Equation 1 is used to calculate the $d_{sc,elastic}$ of 401 mm. Thus, using Equation 3, the predicted d_{sc} as a function of drift is presented in Figure 5b, which compares well to the experimental data of CW1.

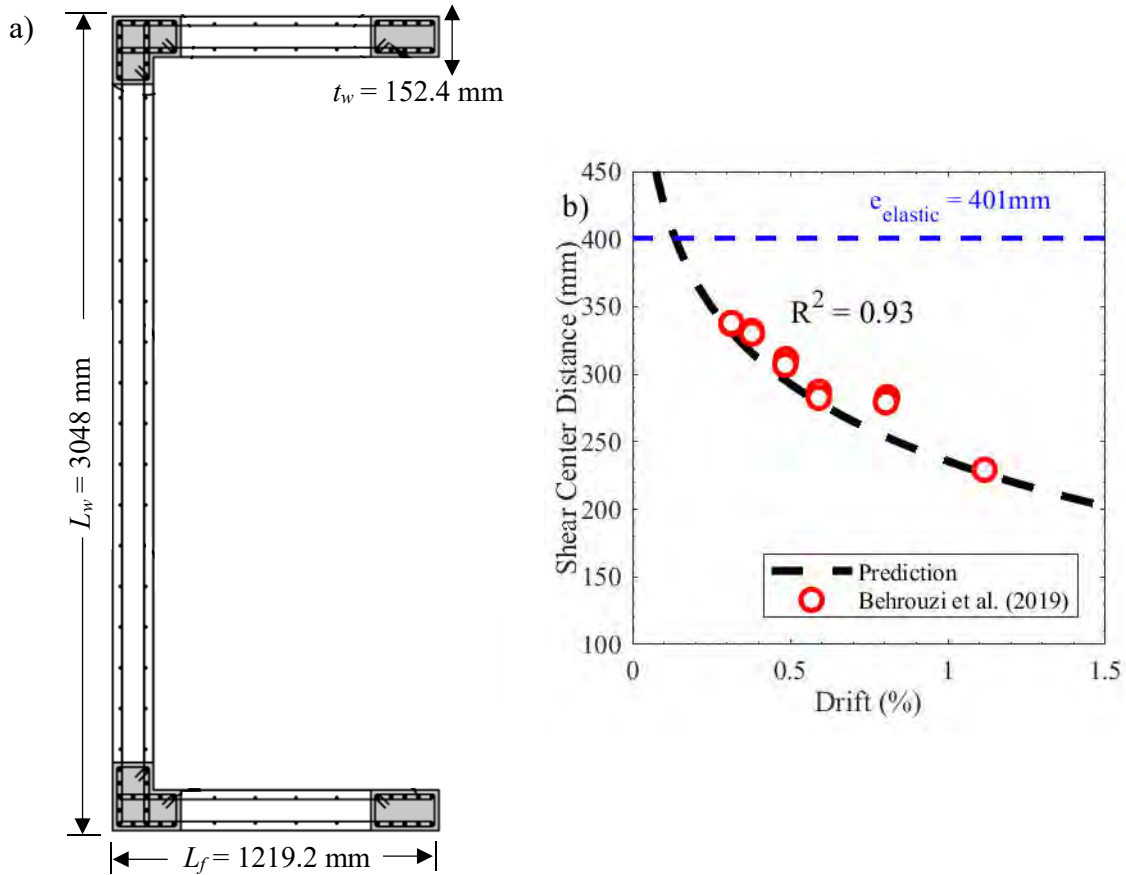


Figure 5 (a) W6 specimen from Lowes *et al.* (2013) (b) shear centre prediction with drift compared to W6 results

The results here on the shear centre distance can ultimately help future research that focuses on mechanical models in estimating the torsional stiffness, performance, and capacity of these types of walls.

3. Decay of Torsional Stiffness

Three experimental RC U-shaped walls have been tested under quasi-static loading, where a small twist was subjected at different flexural positions: specimens TUA and TUB in (Beyer *et al.*, 2008) (discussed briefly in the previous section) and specimen TUF in (Hoult *et al.*, 2020). Specimen TUF had the same cross-sectional dimensions as TUB but had a larger shear span ratio and was detailed with a single layer of longitudinal reinforcement.

In Hoult and Beyer (2020a), the author investigated the torsional stiffness of the U-shaped wall on the translational displacement demands using some experimental results. The two wall specimens TUA and TUB were subjected to a small twist at different flexural positions (A, B, C, D, and O) and at ductility (μ) values of 1.0 and 4.0, which is illustrated in Figure 6(a). Similarly, a small twist was applied to specimen TUF at diagonal positions (Figure 6b) and at drift levels of 0%, 0.4%, 1.0%, 1.5%, 2.0% and 2.5%.

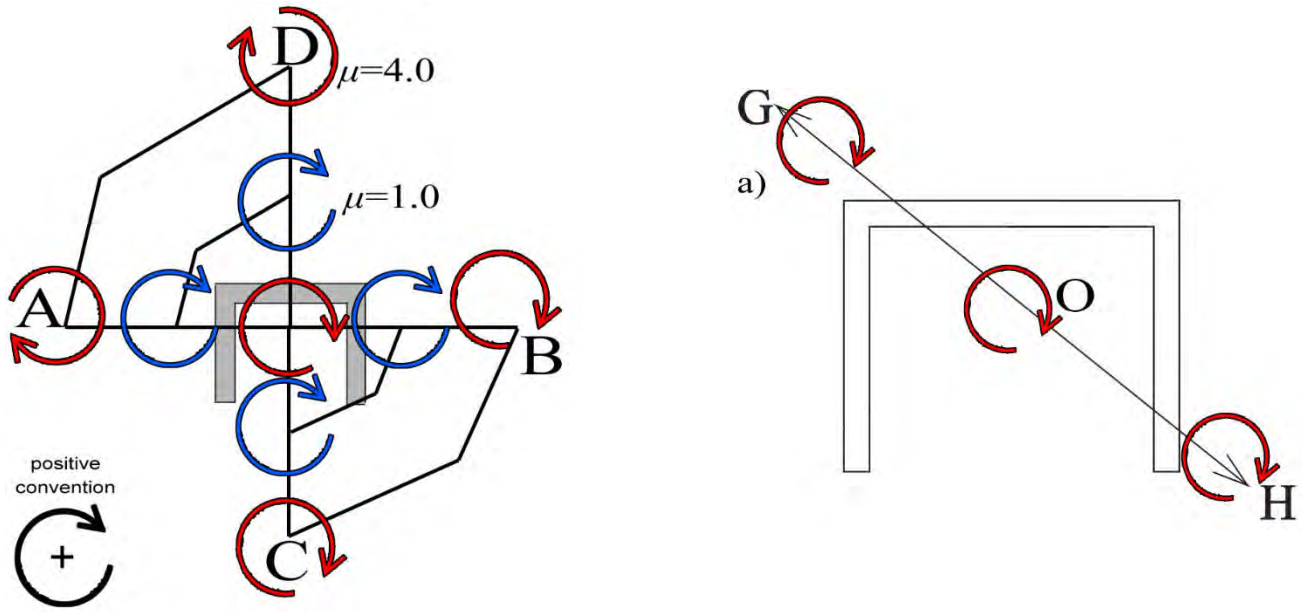


Figure 6 (a) Displacement pattern with rotations for TUA and TUB (blue arrows for $\mu = 1$, red arrows for $\mu = 4$), and (b) positions of wall TUF at which the twist was applied at different drift levels

For the sake of brevity, only some of the results are presented here, where the interested reader can find more details in Hoult and Beyer (2020a) and Hoult *et al.* (2020). Experimental torque-rotation results for specimens TUA, TUB, and TUF are given in Figure 7 for some loaded positions and for different levels of μ or δ . The rotations (in milliradian) and the torque (in kNm) were calculated using Equation 4 and 5:

$$\theta = \frac{\Delta_{NS-E} - \Delta_{NS-W}}{1.3 \text{ m}} \quad 4$$

$$T = \frac{F_{NS-E} - F_{NS-W}}{2} \cdot 1.3 \text{ m} \quad 5$$

where Δ_{NS-E} and Δ_{NS-W} are the displacements (in mm) in the NS direction experienced at the east and west side of the web and measured at a height of 2.95 m and 4.25 m above the foundation for TUA/TUB and TUF respectively. The 1.3 m in the denominator of Equation 4a is the distance between the NS actuators and also between the LVDTs measuring the displacements Δ_{NS-E} and Δ_{NS-W} (in meters). The applied torque was simply calculated as the difference between the actuator forces in the NS direction multiplied by the lever arm.

As originally hypothesized in Hoult and Beyer (2020a), Figure 7 shows that the torsional stiffness decreases as a function of ductility (or in-plane translational displacement/drift), which can be observed for all specimens and for all flexural positions. This is clearly illustrated in Figure 7(c) for TUF at position O, where the drift (δ) level indicated in the legend is that achieved by the wall prior to subjecting a small twist when centred (i.e., at position O). For TUF at position G (Figure 7d), residual rotations can be observed on return to a force-couple of zero; compare the curves for drifts of 0.4% and 1.0%, for example, with the same applied force-couple of 30 kN. Hoult *et al.* (2020) believe that this behaviour was observed primarily due to no axial load being applied, where the flange in tension is able to rotate more freely in comparison to the flange in compression for the same applied

force. This type of behaviour was also observed with the numerical finite element modelling results in Hoult and Beyer (2020a) for walls with no axial load.

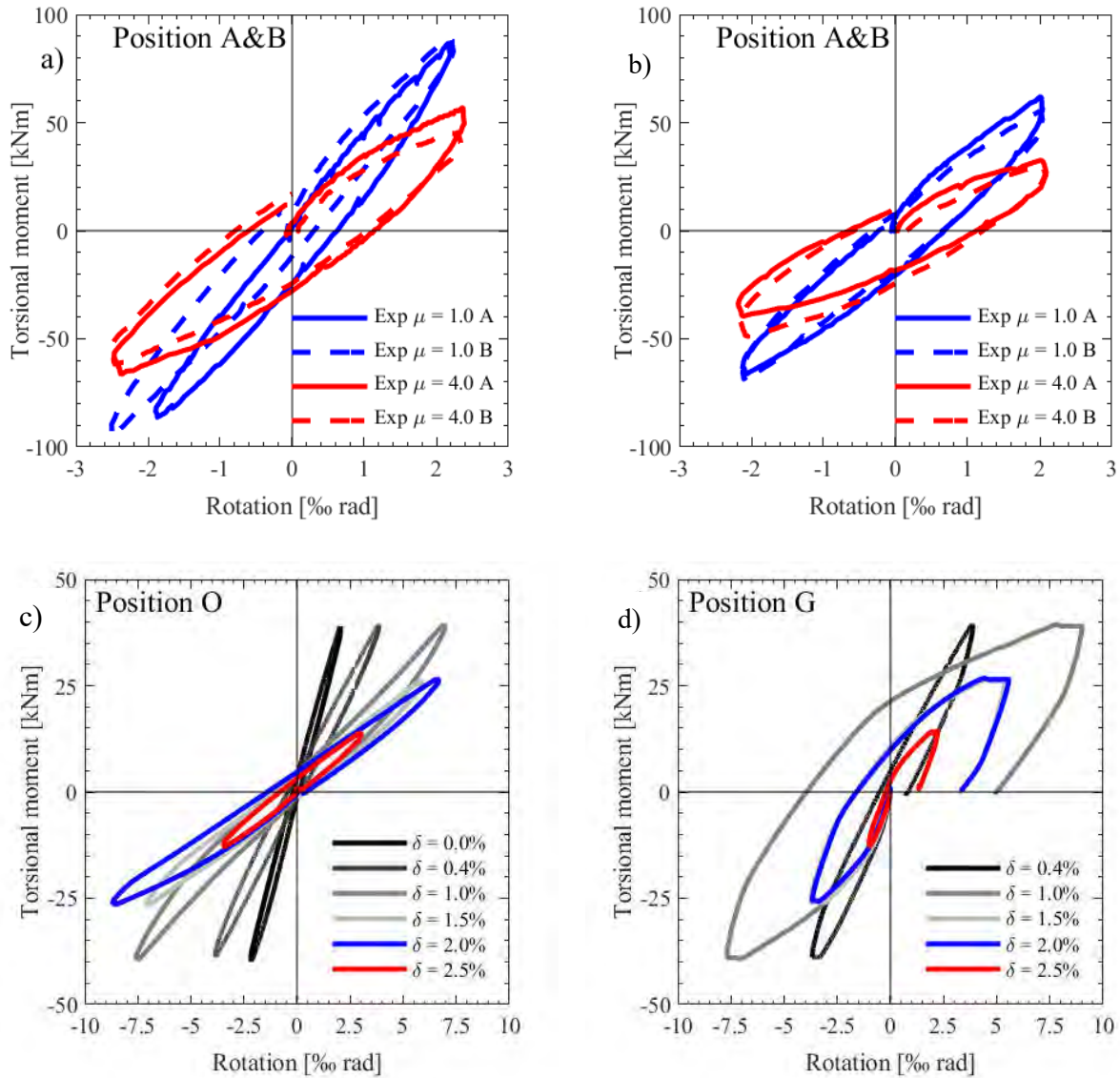


Figure 7 Torque-rotation results for (a) TUA at positions A & B, (b) TUB at positions A & B, (c) TUF at position O, and (d) TUF at position H

In Figure 8, the torsional stiffness (J_R) values of TUF are normalized to the elastic, uncracked torsional stiffness and plotted as a function of ductility (μ). It should be noted that the J_R is defined here as the secant stiffness connecting the maximum and minimum torque moment (Hoult & Beyer, 2020a). Superimposed in Figure 8 are the normalized torsional stiffness values of the experimental and numerical results from Hoult and Beyer (2020a) of TUA and TUB and the normalized translational stiffness (K_x) values. The K_x has been normalized to the elastic translational stiffness of the uncracked wall as determined in Hoult and Beyer (2020). The secant stiffness is computed assuming the wall behaves as an ideal elastoplastic system.

Overall, the decay in torsional stiffness follows the decay in translational stiffness. These results substantiate the theory that at position O, when the wall is centred and not subjected to any translational displacements (Figure

8a), the decay in torsional stiffness is greater in comparison to the wall loaded at a translational displacement (Figure 8b). Furthermore, the experimental results of TUA, TUB, and TUF have confirmed that the decay of the torsional stiffness for loading in the diagonal direction is similar for loading along the principal axes (Hoult *et al.*, 2020). For a more in-depth discussion on the decay of the torsional stiffness the reader is therefore referred to Hoult and Beyer (2020a).

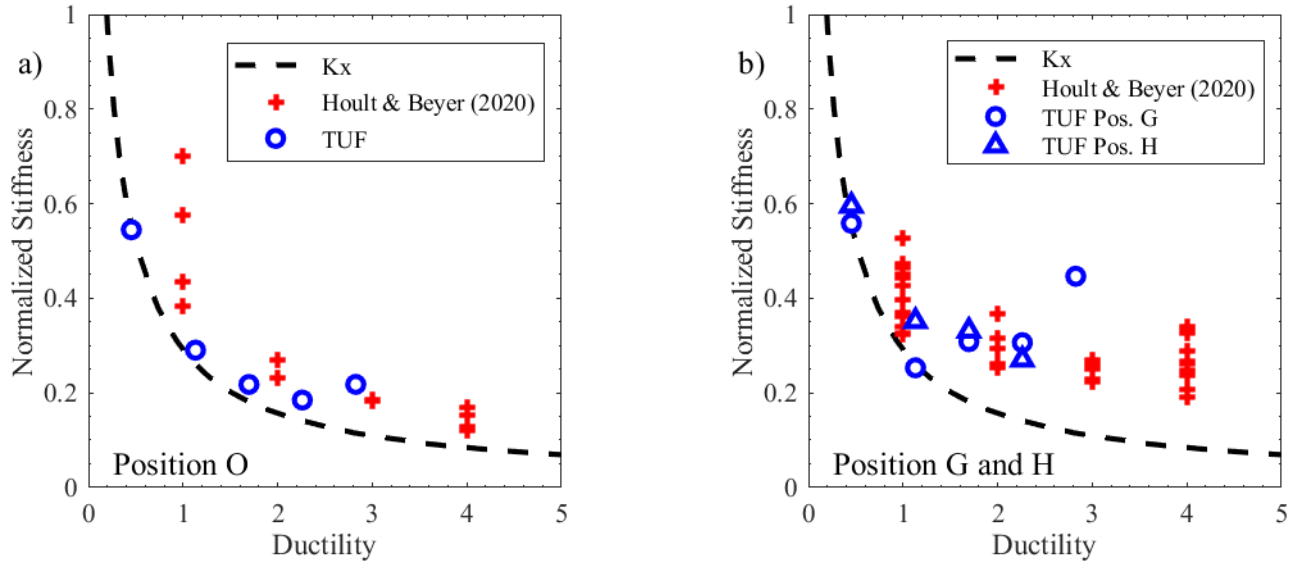


Figure 8 Normalized rotational stiffness results compared to the normalized translational stiffness (K_x) for (a) position O and (b) positions G and H (Hoult *et al.*, 2020)

The experimental and numerical results here can help future building codes. For example, the flexural effective stiffness values that are recommended in PEER (2017) for service and maximum considered earthquake (MCE) levels correspond to 0.75 and 0.2 respectively. These values appear to underestimate the degradation of stiffness observed here for torsion. Furthermore, the effective stiffness values recommended for shear behaviour of structural walls for service and MCE level events correspond to 0.4 and 0.2 (PEER, 2017), which appear to provide better estimates of the corresponding degradation of stiffness of these walls subjected to torsional actions. However, the normalised torsional stiffness values when the wall is centred (i.e., Figure 8a) show that an effective stiffness coefficient as low as 0.10 could be used as a lower-bound value for MCE design purposes (i.e., a ductility greater than 2).

4. Torsional Capacity of RC U-shaped walls

As stated in the introduction, there is a paucity of research on the torsional performance of RC walls, particularly for post-cracked, inelastic behaviour. Current mechanical models that predict the torsional capacity of RC U-shaped sections (Chen *et al.*, 2016; Krpan & Collins, 1981a; Xu *et al.*, 2018a; Xu *et al.*, 2018b) have been specifically derived for beams, the conditions of which are dissimilar to that experienced by a wall. More specifically, the current mechanical models do not account for cantilever-wall restraint conditions, axial load, and potential confinement of the concrete in boundary regions of the wall. A mechanical model that was originally developed by Krpan and Collins (1981a) for open section U-shaped beams was modified by the author for application to RC U-shaped walls (Hoult, 2020). For the sake of brevity, the reader is redirected to Hoult (2020)

for a full description of the program and the expressions that were either adopted or derived by the author. A simple, computationally-inexpensive mechanical model to derive the torque-rotation curve is warranted in order to conduct a parametric study using a large range of design parameters. An illustrative example of the results from this mechanical model procedure are given in Figure 9: uncracked (elastic) stage (Figure 9a), cracked (elastic) stage (Figure 9b), and inelastic stage (Figure 9c).

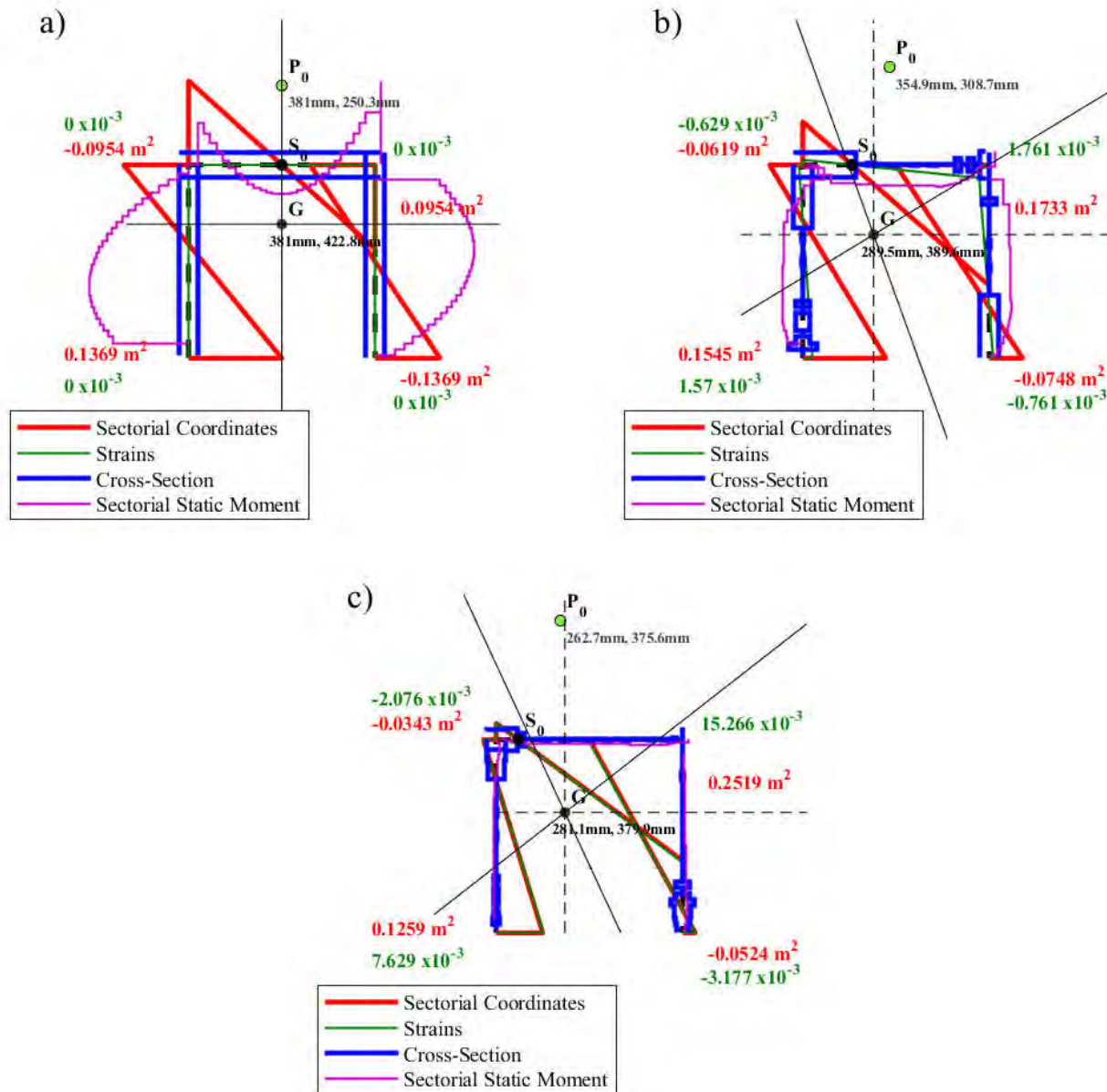


Figure 9 Cross-sectional properties of specimen MEM-C for (a) uncracked-elastic stage, (b) cracked-elastic stage and (c) inelastic stage ($1 \text{ mm} = 0.039 \text{ in}$, $1 \text{ m}^2 = 1550 \text{ inch}^2$)

These types of wall sections are primarily controlled by warping torsion, where the longitudinal strains (and stresses) will ultimately govern the capacity of the wall section under torque. Similarly, when a wall is subjected to flexural loading, the moment capacity of the wall will be governed by the compressive and tensile strains. These idealised strain distributions at the ultimate capacity for the two different loading cases are illustrated in

Figure 10, which show the wall section failing due to the ultimate compressive strains (ϵ_{cu}) being reached at the ends of the flange for both cases. It is reasonably assumed here that, at this ultimate capacity state, the largest tensile strains (ϵ_t) in the section given in Figure 10 are greater than yield (ϵ_y).

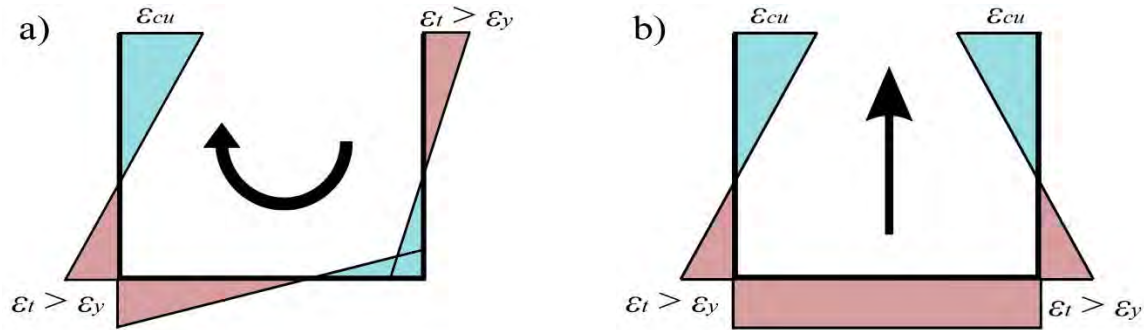


Figure 10 Idealised strain distributions at ultimate for a U-shaped thin-walled section subjected to (a) torsion and (b) flexure about the minor axis (with web in tension)

Until recently, the idealised strain distributions illustrated in Figure 10a for a RC U-shaped wall section under torsion was only hypothesised. The recent experimental testing in Hoult *et al.* (2020) used state-of-the-art instrumentation to collect data, including digital image correlation techniques. This data was analysed in Hoult and Beyer (2020b), which showed the strains at the base of the wall when centred (i.e., position O) and subjected to the torque. Figure 11 clearly shows that the experimentally observed strain distributions match well to that hypothesised in Figure 10a.

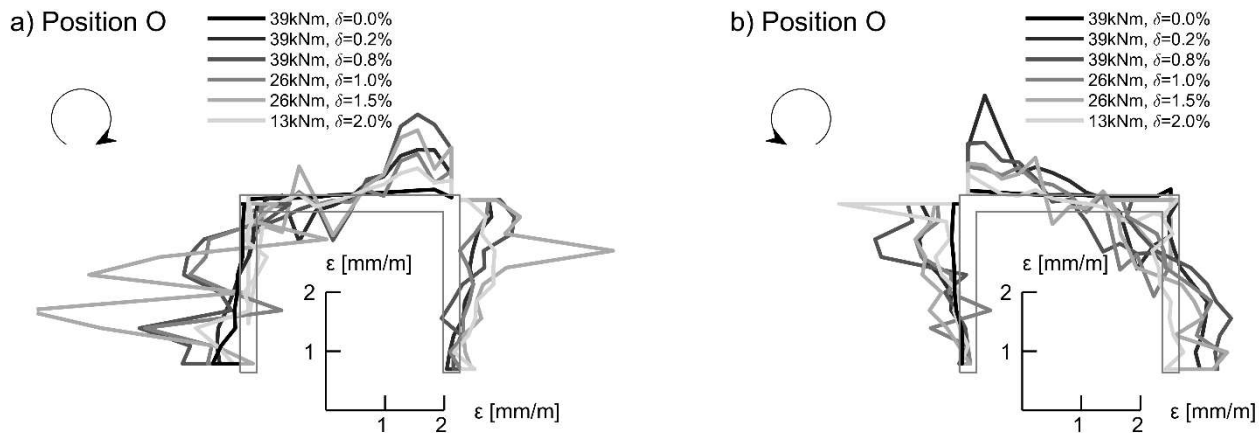


Figure 11 Longitudinal strains at the base of TUF subjected to torsion (a) at position O, clockwise torque (b) position O, counter clockwise torque

A large parametric study was conducted using the mechanical model first developed in Krpan & Collins (1981a) for beams and modified in Hoult (2020) for RC U-shaped walls. In total, 70 RC U-shaped walls were analysed with a varied range of typical design parameters, including the web length, flange length, wall thickness, concrete strength, and axial load ratio (*ALR*). The results of the parametric study showed that a positive correlation could be found for most of these parameters with respect to the ultimate torque capacity of the wall, whereas a negative correlation was found with respect to the thickness of the wall and the ultimate torque. This is illustrated in Figure 12, which shows that a power function best fits the increasing concrete strength with respect to the ultimate torque

of the wall (Figure 12a), whereas the torque capacity increases exponentially as a function of the web length (Figure 12b). Furthermore, an increase in the ultimate torque of the wall can be observed with increasing ALR . Using the results of the parametric study, a nonlinear regression analysis was undertaken to find a relationship between the ultimate torque of the wall and the design parameters discussed above. The interested reader is referred to Hoult (2020) for the corresponding expression that can be used for assessment and design purposes.

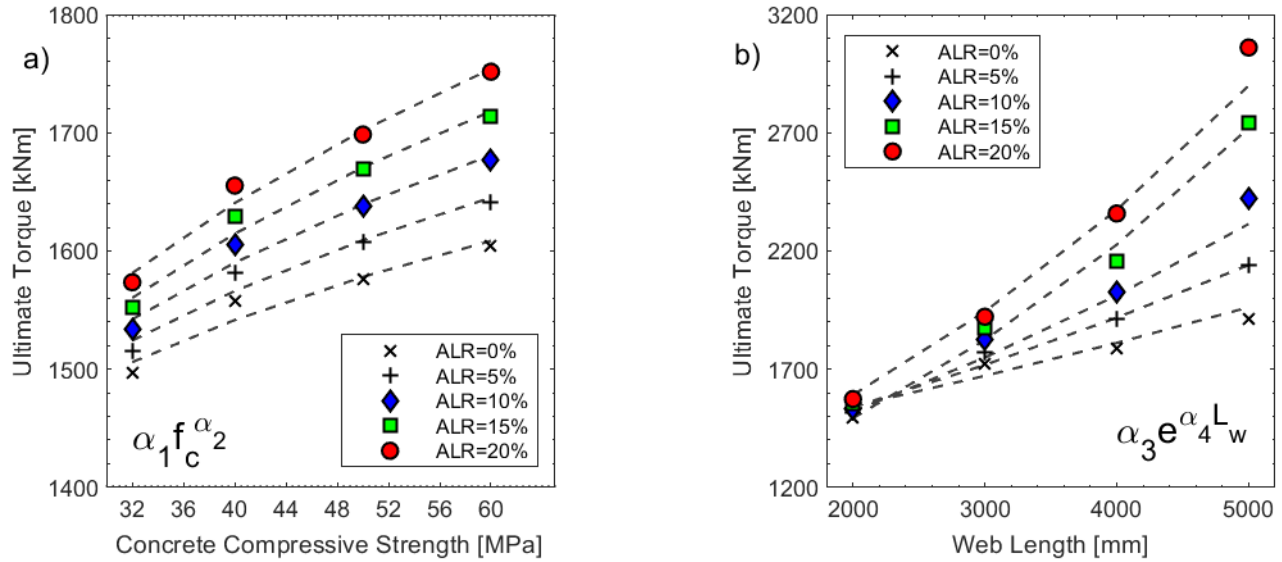


Figure 12 Ultimate torque of RC U-shaped wall as a function of (a) web length (L_w) and (b) wall thickness (t_w)

5. Conclusions

This paper provided an overview of the some of the latest research results by the author investigating the torsional performance of RC U-shaped walls (Hoult *et al.*, 2020; Hoult & Beyer, 2020a; Hoult & Beyer, 2020b; Hoult, 2020). In summary, some of the research findings include:

- The shear centre of RC U-shaped walls was shown move closer to the web of the wall as a function of ductility (or drift). A simple expression was derived using some experimental results, which can be used to calculate the shear centre as a function of drift.
- The torsional stiffness of RC U-shaped walls was shown to degrade with in-plane or diagonal flexural loading. Furthermore, the decay in torsional stiffness was shown to degrade at approximately the same rate as the translational stiffness of the wall, particularly when centred.
- Effective stiffness values were recommended for future building codes for service and MCE and for structural elements under torsion.
- Residual rotations were observed in RC U-shaped walls with no axial load after loading to a flexural position and applying a twist. This type of behaviour is thought to be due to the flange in tension being able to rotate more freely in comparison to the flange in compression for the same applied force.
- Digital image correlation techniques were used to derive the strain at the base of RC U-shaped wall specimen TUF. These results showed that the strain distribution when the wall was subjected to a twist correlated well to that hypothesised for an open section governed by warping.

- The results from a large parametric study showed correlations between several design parameters and the ultimate torque of RC U-shaped walls. The results were subsequently used in a nonlinear regression analyses to derive an expression for the ultimate torque of RC U-shaped walls.

Previous experimental testing of RC walls with simpler geometries (e.g., rectangular) and simpler loadings (e.g., lateral force, flexural loading) have repeatedly showed how unconfirmed, non-validated models often grossly fail to predict the displacement capacity of structural members. Thus, experimental research on the torsional performance and capacity of RC U-shaped walls is necessary and recommended, given the abundant use of these elements in the RC building stock internationally and the paucity of evidence that exists.

6. References

- Behrouzi, A., Mock, A., Lehman, D., Lowes, L., & Kuchma, D. (2019). Impact of Bi-Directional Loading on the Seismic Performance of C-Shaped Piers of Core Walls. *Submitted to the Journal of Engineering Structures*.
- Beyer, K., Dazio, A., & Priestley, M. J. N. (2008). Quasi-Static Cyclic Tests of Two U-Shaped Reinforced Concrete Walls. *Journal of Earthquake Engineering*, 12(7), 1023-1053. doi:10.1080/13632460802003272
- Birely, A., Mock, A., Behrouzi, A., Kuchma, D., Lehman, D., & Lowes, L. (2014). Seismic Behavior of Modern Reinforced Concrete C-Shaped Walls (Specimen UW6). *Network for Earthquake Engineering Simulation*. doi:10.4231/D3C24QP0D
- Chen, S., Ye, Y., Guo, Q., Cheng, S., & Diao, B. (2016). Nonlinear model to predict the torsional response of U-shaped thin-walled RC members. *Structural Engineering and Mechanics*, 60(6), 1039-1061.
- Hoult, R., Appelle, A., Almeida, J., & Beyer, K. (2020). Seismic performance of slender RC U-shaped walls with a single-layer of reinforcement. *Engineering Structures*, 225. doi:10.1016/j.engstruct.2020.111257
- Hoult, R., & Beyer, K. (2020a). Decay of Torsional Stiffness in RC U-Shaped Walls. *Journal of Structural Engineering*, 146(9). doi:10.1061/(ASCE)ST.1943-541X.0002733
- Hoult, R., & Beyer, K. (2020b). RC U-shaped walls subjected to in-plane, diagonal, and torsional loading: new experimental findings. *Submitted to Engineering Structures*.
- Hoult, R., Goldsworthy, H., & Lumantarna, E. (2019). Fragility Functions for RC Shear Wall Buildings in Australia. *Earthquake Spectra*, 35(1), 333-360. doi:10.1193/120717eqs251m
- Hoult, R. D. (2020). Torsional Capacity of Reinforced Concrete U-Shaped Walls. *Submitted to Thin-walled Structures*.
- Ile, N., & Reynouard, J. M. (2005). Behaviour of U-shaped Walls Subjected to Uniaxial and Biaxial Cyclic Lateral Loading. *Journal of Earthquake Engineering*, 09(01), 67-94.
- Krpan, P., & Collins, M. P. (1981a). Predicting Torsional Response of Thin-Walled Open RC Members. *Journal of the Structural Division*, 107(6), 1107-1127.
- Krpan, P., & Collins, M. P. (1981b). Testing thin-walled open RC structure in torsion. *Journal of the Structural Division*, 107(6), 1129-1140.
- Lombard, J., Lau, D. T., Humar, J. L., Foo, S., & Cheung, M. S. (2000). *Seismic strengthening and repair of reinforced concrete shear walls*. Paper presented at the Proceedings of the 12th World Conference on Earthquake Engineering.
- Lowes, L., Lehman, D., Kuchma, D., Mock, A., & Behrouzi, A. (2013). Large-Scale Tests of C-shaped Reinforced Concrete Walls. from NEES Project Warehouse <https://www.designsafe-ci.org/data/browser/public/nees.public/NEES-2005-0104.groups>
- Maruta, M., Suzuki, N., Miyashita, T., & Nishioka, T. (2000). *Structural capacities of H-shaped RC core wall subjected to lateral load and torsion*. Paper presented at the Proceedings of the 12th WCEE. New Zealand: The New Zealand Society for Earthquake Engineering.

- PEER. (2017). Tall buildings initiative: Guidelines for performance-based seismic design of tall buildings (Version 2.03).
- Pegon, P., Plumier, C., Pinto, A., Molina, J., Gonzalez, P., Tognoli, P., & Hubert, O. (2000). U-shaped-wall: Quasi-static biaxial test in the X and Y direction - test report. In *TMR-ICONS-TOPIC5* (pp. 23): JRC Ispra.
- Peng, X.-N., & Wong, Y.-L. (2011). Behavior of reinforced concrete walls subjected to monotonic pure torsion—An experimental study. *Engineering Structures*, 33(9), 2495-2508. doi:10.1016/j.engstruct.2011.04.022
- Vlasov, V. Z. (1961). *Thin-walled elastic beams* (Second Edition ed.). Jerusalem: Israel Program for Scientific Translations.
- Xu, J., Chen, S., Guo, Q., Ye, Y., Diao, B., & Mo, Y. L. (2018a). Experimental and Analytical Studies of U-Shaped Thin-Walled RC Beams Under Combined Actions of Torsion, Flexure and Shear. *International Journal of Concrete Structures and Materials*, 12(1), 33. doi:10.1186/s40069-018-0245-8
- Xu, J., Diao, B., Guo, Q., Ye, Y., Mo, Y. L., & Zhou, T. (2018b). Parametric Study on Mixed Torsional Behavior of U-Shaped Thin-Walled RC Girders. *Advances in Civil Engineering*, 2018, 18. doi:10.1155/2018/3497390

A Cost-Effective Approach for Seismic Structural Health Monitoring

Ryan D. Hoult¹, Adam Pascale², Tommy H.T. Chan³

1. Corresponding Author. Postdoctoral Researcher, Department of Infrastructure Engineering, University of Melbourne (UoM), Parkville, VIC 3010, Australia.
Email: ryan.hoult@unimelb.edu.au
2. Chief Scientist, Seismology Research Centre, Richmond, VIC, 3121. Email: adam.pascale@src.com.au
3. President of the Australian Network of Structural Health Monitoring, Professor of Civil Engineering, Science and Engineering Faculty, School of Civil & Environmental Engineering, Queensland University of Technology (QUT), Australia. Email: tommy.chan@qut.edu.au

ABSTRACT:

A rapid estimate of the damage state of a building after an earthquake event is of crucial importance, having the potential to save lives, reduce injuries, and mitigate costs associated with structural damage and economic downtime. Visually determining the damage state accurately is often difficult, and so instrumentation can be installed to estimate the extent and locations of damage. However, the current minimum requirements of industry standard instrumentation are costly and have been shown to provide an insufficient amount of information. This paper investigates a simple, computationally inexpensive method for determining the displacement profile of a building (with time) using minimal instrumentation. The preliminary results in this paper show some potential for the method to be used in seismic health monitoring applications. Further research is proposed by the authors, where inexpensive and new technologies can be employed to determine the displacements of a structure in near-real time.

Keywords: monitoring, structural, health, seismic, earthquake, instruments

1. Introduction

The global population boom of recent decades has consequentially resulted in the expansion of urban areas that have created densely-populated cities in close proximity to large, active faults, significantly increasing the exposure of people to the risk of seismic events (D'Alessandro *et al.*, 2014). For example, the United States Geological Survey (USGS) has predicted that there is an approximate 30 percent chance of a magnitude (M) 7.5+ earthquake occurring in Los Angeles County, California, within the next 30 years (Field *et al.*, 2014). A M 7.8 earthquake scenario rupturing from the southern San Andreas fault in California is estimated to cause 1,800 deaths, 53,000 injuries and economic losses of around USD \$213 billion (Porter *et al.*, 2011), the majority of which results from 'shake-related building and content damage'. Another example is the Philippines, which is located in one of the most seismically active regions in Asia. Recent studies have reportedly warned that an earthquake of up to M 7.2 is overdue for the West Valley Fault in the Philippines, which could damage up to 1.3 million residential structures and cause approximately 34,000 deaths, leaving more than 100,000 people injured (MMEIRS, 2004). To mitigate the amount of deaths and injuries caused, a swift and accurate estimate of the performance and amount of damage of a building is of crucial importance to city officials, stakeholders, and rescue teams who are concerned with the safety of building inhabitants (Çelebi, 2008). Rapidly evaluating a building visually is difficult to do, as the presence of structural finishes and fireproofing often hide the extent of damage. This lack of uncertainty will typically result in a conservative decision to re-occupy the building, corresponding to significant economic losses (Çelebi, 2008). In an attempt to overcome this, building codes in some high seismic regions require accelerometers to record the building response and provide, in near real-time, the health of the structure, which would reduce an inspection program. For example, the Uniform Building Code (UBC, 1997) recommends that for some buildings in high seismic regions (e.g., California) a minimum of three tri-axial accelerometers be installed. Adopted from the initial UBC recommendations, the National Code of the Philippines now requires some buildings, such as those that are over fifty meters tall and located in seismic zone 4 (e.g., Manila), to be equipped with a minimum of three accelerometers (Figure 1a), which should be located at the ground floor, middle floor and floor below roof (DPWH, 2015). While it is emphasized that these requirements were developed to help reduce deaths, injuries, and economic losses, it is unclear how this instrumentation layout (i.e., Figure 1a) will aid in rapidly indicating the extent and location of damage of a building without a prescribed methodology. In fact, past earthquake events have shown that this minimum of three accelerometers does not provide a sufficient amount of meaningful information to indicate the health of a building or the damage locations in the structure (Çelebi, 2006). Instead, many accelerometers are currently required, which must be strategically placed at specific locations and on several floors, such as that in Figure 1b. The deployment of multiple accelerometers on all floors and in every direction is not feasible due to costs involved in instrumentation and installation as well as the difficulty in installing (Çelebi, 2008).

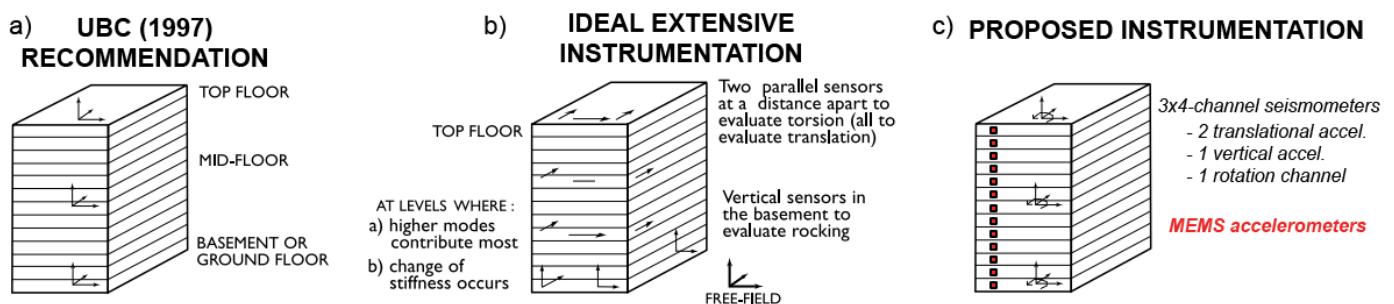


Figure 1 Seismic health monitoring layouts (a) UBC recommendations (b) ideal instrumentation setup and (c) proposal

There has been some recent research in the area of seismic health monitoring. For example, Limongelli (2003) investigated the ideal location of a limited number of sensors for multistorey structures, while an additional paper by the author investigated an interpolation method for seismic health monitoring densely instrumented multistorey structures (Limongelli, 2014). Ulusoy *et al.* (2012) discuss the design and implementation strategy for seismic health monitoring of hospital buildings in the United States. More recently, Erazo & Hernandez (2016) developed a method for determining lateral displacements, accelerations, strains, base shear and overturning moment of structures that are partially instrumented. There is still a paucity of research that has focused on the derivation of a simple method for determining the health and damage state of a structure with a minimal amount of instrumentation.

This research undertaken here focuses on a simple method to readily determine the elastic displacement profile of a high-rise building using the minimal instrumentation requirements. Data from a real building is obtained that was recently subjected to a large magnitude earthquake event. Using the equations of dynamics equilibrium and the first 3 modes of translation of the building, an estimate of the displacement time history of all the floors of the building can be calculated, so as to estimate the seismic health of the building. This paper presents some of the preliminary results of the work that has been undertaken.

2. Methodology

The method that will be used here to predict the displacement profile of a building with time uses a model analysis procedure and the equations of dynamic equilibrium. The dynamic response behaviour of a multi-storey structure can be resolved into the different modes of vibration. These different modes of vibration and the corresponding mode shapes can be found from the accelerations recorded by the sensors in the building and using a Fourier transformation. After identifying the dynamic characteristics of the first three modes of the structures, i.e. the mode shape vectors ($\phi_{j=1,2,3}$) and modal natural periods ($T_{j=1,2,3}$) (or frequencies, $f_{j=1,2,3}$), an estimate of the mass distribution on each floor could be considered. As this study is limited to focusing on the accelerations (and corresponding displacements) in the North-South (NS) direction of the building (Figure 1a), so the first three modes of translation in the NS direction will be determined. Furthermore, in this research, the mass (m) is assumed to be equal on each floor. However, a refined mass matrix is ultimately determined using an iterative procedure that uses random numbers as mass floor factors and compares the calculated displacements at mid- and full-height of the structure to that recorded by the accelerometers. The excitation (L) and generalised mass (M) factors can be found, and subsequently the participation factors (L/M) can be determined using Equation 1 and 2 for each of the mode shapes:

$$L_j = \{\phi_{j,n}\}\{r\} \quad 1$$

where j is the mode of vibration considered (i.e., 1, 2, and 3 in this study) and n is the floor number, and r is a vertical array of the normalised mass factors.

$$M_j = \{\phi_{j,n}\}^T \{m\} \{\phi_{j,n}\} \quad 2$$

The modal displacement coefficients ($\eta_{j=n}$) for each building floor (n) and for each mode shape (j) can thus be calculated:

$$\eta_{j,n} = \frac{L_j}{M_j} \phi_{j,n} \quad 3$$

Displacement (u_j) of a single-degree of freedom (SDOF) system can be generated for each time step (t) using the acceleration (\ddot{u}_j) captured by the accelerometer at the base a building as input and for the three vibration modes.

$$u_{j,t} = (-\ddot{u}_{j,t-1} + A_j u_{j,t-1} + B_j u_{j,t-2}) / C_j \quad 4$$

where the constants A , B , and C in Equation 4 can be calculated with:

$$A_j = -(\omega_j^2) + \left(\frac{2}{dt^2}\right) \quad 5$$

where ω_j is the angular frequency ($= 2\pi f_j$) of the j^{th} mode of vibration and dt is the time step (in seconds).

$$B_j = \omega_j \left(\frac{\zeta}{dt}\right) - \left(\frac{1}{dt^2}\right) \quad 6$$

where ζ is coefficient of damping (assumed to be 2.5% in the research here).

$$C_j = \left(\frac{1}{dt^2}\right) + \left(\omega_j \frac{\zeta}{dt}\right) \quad 7$$

The displacement of the building on floor n can then be found as a function of time (t) (i.e., displacement time history):

$$d_{n,t} = u_{1,t}\eta_{1,n} + u_{2,t}\eta_{2,n} + u_{3,t}\eta_{3,n} \quad 8$$

It should be noted that this method is currently limited to elastic behaviour, as the research that is conducted here.

3. Atwood Building Data

Figure 2a shows a schematic of the Atwood Building, which is a 1980s structure located in the highly seismic region of Anchorage (Figure 2b), Alaska (Çelebi, 2006). The 20-story building is a steel moment-resisting framed structure that is 39.6 m x 39.6 m in plan and 80.5 m tall. This building was selected for a seismic monitoring system, comprising of 31 accelerometers deployed throughout the superstructure and foundation (see Figure 2a). The seismic monitoring system configuration was designed to assess (a) translational motion, (b) torsional motion, (c) interstory drift (i.e., displacement between selected two consecutive floors), and (d) rocking of the building (Çelebi, 2006). Since the sensor arrays were deployed in 2003, numerous small, medium, and large-sized earthquakes from near and far sources have been recorded. The extensive instrumentation layout used in the Atwood Building presents an opportunity to use the methods described in the previous section in an attempt to derive the displacement profile of the building with time.

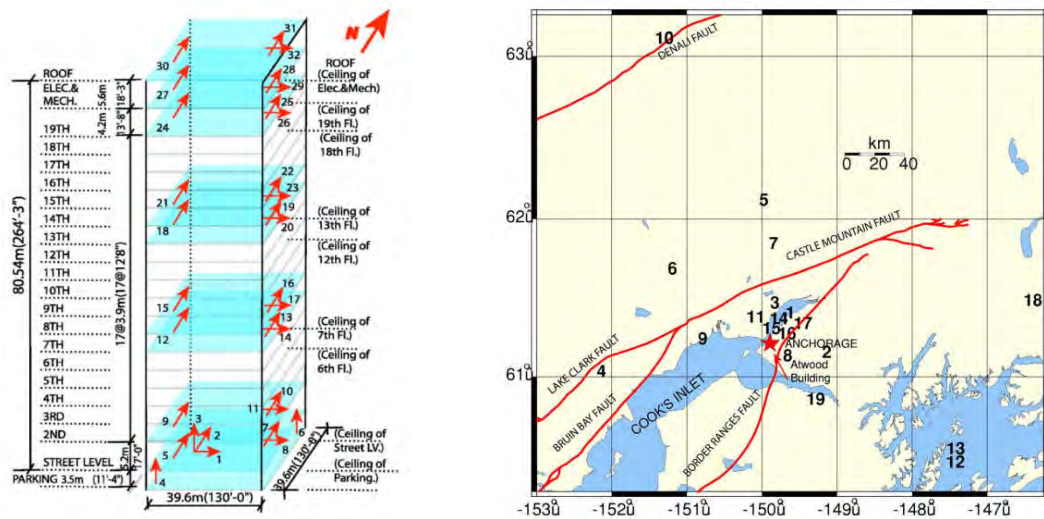


Figure 2 (a) Three-dimensional schematic of the Atwood Building showing accelerometers deployed within the structure (b) location of Atwood Building in Anchorage, Alaska with major faults in the region (Çelebi, 2006)

One earthquake recording will be used for this study: a moment magnitude (M_W) 7.1 occurred approximately 12 km to the North of the Atwood building site on November 30, 2018. This event was the largest in Anchorage, Alaska since the great 1964 earthquake of M_W 9.2 (Liu *et al.*, 2019). However, relatively little structural damage occurred in the 2018 event, most likely as a result of the improved building codes that have occurred in the past half a century or so (Liu *et al.*, 2019).

For this research exercise, it is assumed that the Atwood building has only three accelerometers deployed in the building, which corresponds to the current minimum standard (Figure 1a): accelerometers A5, A18, and A30 shown in Figure 2a. Ultimately, the displacement profile of the building in the NS direction, derived using the methods described in the previous section, will be compared to the recordings from the accelerometers on all levels of the Atwood building located to the West of the floor plate and facing in the NS direction (i.e., accelerometers A5, A9, A12, A15, A18, A21, A24, A27, and A30 in Figure 2a).

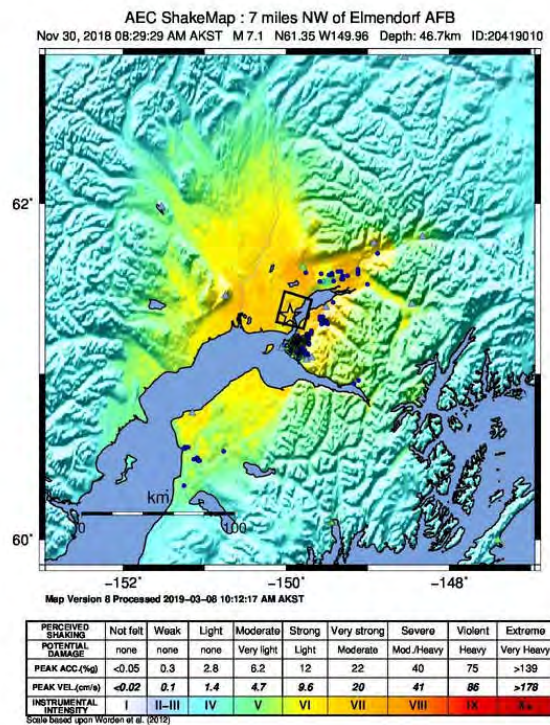


Figure 3 Shake Map from AEC (2018) of the M_W 7.1 on November 30, 2018 in Alaska

The acceleration-time history for the M_W 7.1 event as captured by the accelerometer at the base of the Atwood building in the NS direction (i.e., A5) is shown in Figure 4a. Using a Fourier transformation of the acceleration time histories of the accelerometers at mid-height and roof of the Atwood building (i.e., A18 and A30 respectively), the amplitude Fourier spectrum in Figure 4b shows the natural frequencies in the NS of 0.43 Hz, 1.59 Hz, and 3.00 Hz. These natural frequencies correspond well to those calculated in Çelebi (2006) for the same building subjected to different earthquake ground motions.

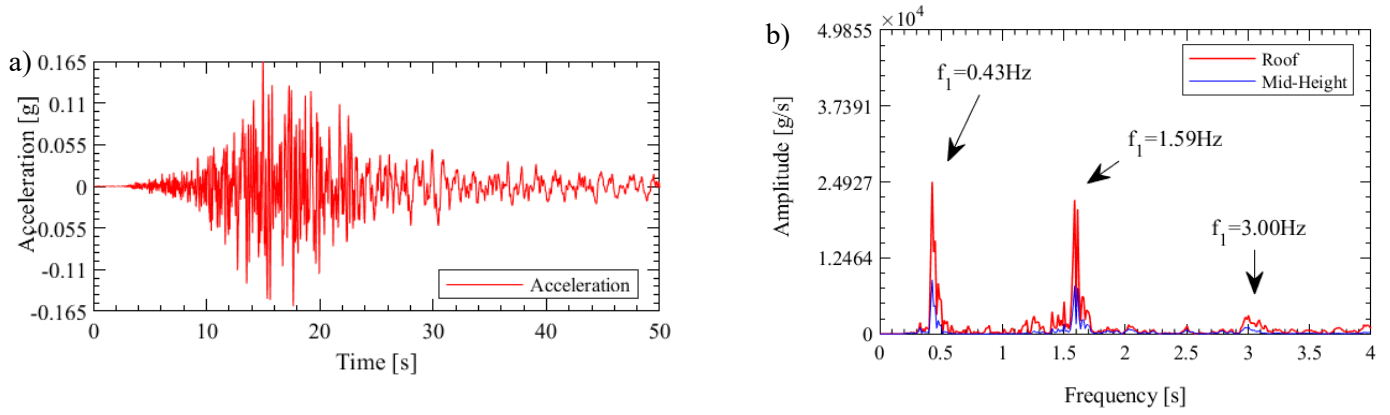


Figure 4 M_w 7.1 event (a) acceleration-time history (b) amplitude spectra in North-South with indicated natural frequencies using A18 and A30

Three polynomial functions were derived by the authors to approximate the modes shapes (MS) of the first 3 mode responses of the structure:

$$MS_1 = \left(\frac{1.20}{H_n^2} \right) H_i^2 - \left(\frac{0.20}{H_n} \right) H_i \quad 9$$

$$MS_2 = \left(\frac{3.53}{H_n^3} \right) H_i^3 - \left(\frac{9.35}{H_n^2} \right) H_i^2 + \left(\frac{4.82}{H_n} \right) H_i \quad 10$$

$$MS_3 = \left(\frac{20.26}{H_n^3} \right) H_i^3 - \left(\frac{27.40}{H_n^2} \right) H_i^2 + \left(\frac{8.13}{H_n} \right) H_i \quad 11$$

where H_n is the full height (i.e., roof height) of the structure and H_i is the height of the structure at level i .

The corresponding mode shapes of the Atwood building using Equations 9 to 11 are illustrated in Figure 5. Superimposed in Figure 5 are the mode shape factors using amplitudes obtained from a Fourier Transformation of eight accelerometers located to the West of the floor plate of the Atwood building. The estimated mode shapes correlate reasonably well to the observed mode shape factors recorded from the Atwood building.

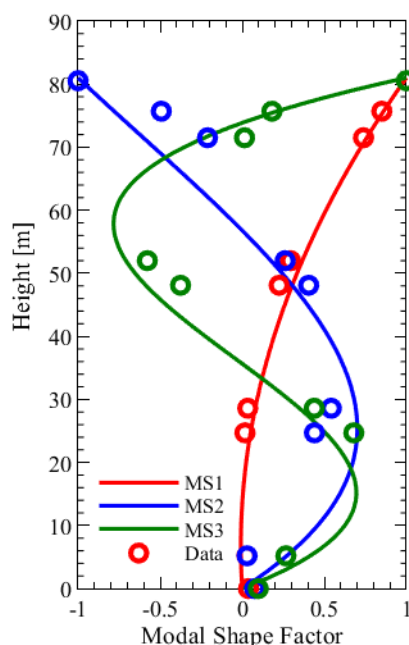


Figure 5 Estimated modal shapes with data points from the observed accelerations of the Atwood building in NS

Using the method and expression discussed in Section 2, the displacement time histories of all floors of the Atwood building were estimated for motion in the NS direction, using the acceleration recorded at street level (A5) as input. It is worth emphasising here again that this method attempts to derive the displacement profile of the building (with time) only using three accelerometers (A5, A18, and A30), which would correspond to the current minimal requirements as outlined in Section 1. Figure 6 plots the resulting displacement time histories of the roof level and approximate mid-height level, comparing the simulated response to the recorded responses from A18 and A30. The first observation from Figure 6 is the relatively good estimation of the simulated cycles of displacement of the structure in comparison to what was recorded. However, the amplitude and peak responses do not match, and appear to worsen in lower stories of the structure. For example, compare the simulated to recorded displacement amplitudes in Figure 6b with Figure 6a. Assuming the building is performing elastically during this earthquake event, there are several possible reasons for this lack of accuracy regarding the estimated amplitudes of displacement: (i) the assumed mass distribution needs further refinement, (ii) better estimates of the mode shapes could be calculated, (iii) the assumed damping coefficient needs refinement, and (iv) contributions of torsional displacements of the building.

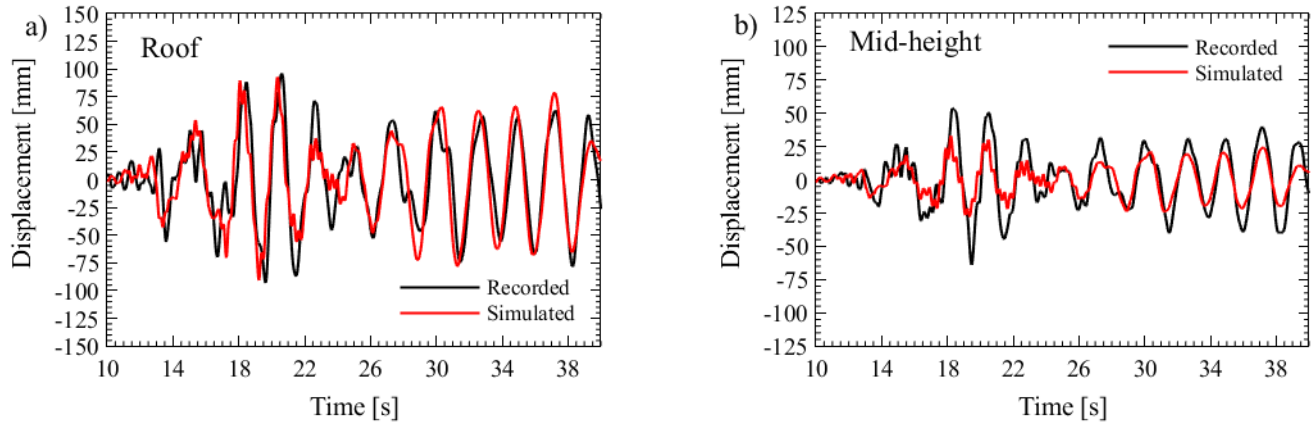


Figure 6 recorded versus simulated displacement time-history of the building (a) roof (A30) (b) mid-height (A18)

The former of these possibilities, the torsional displacement of a building, can be tested, as there is another accelerometer placed on the East side of the floor plate recording the NS direction of motion. For example, accelerometers A18 and A19 in Figure 2a are located on the same floor, but at different edges of the building periphery. Figure 7 shows the relative displacement (δ) of the floor plan in the NS at a single moment in time using the recorded displacement from A18 and A19. Figure 7 shows that torsion was present in this structure, where the relative displacement (δ) and corresponding angle (θ) has been scaled up for illustration purposes. This finding could account for some of the difference in displacement simulated using the methods described in Section 2 in comparison to that recorded. It is possible to simultaneously simulate the translational and torsional displacement of the building using similar methods as that used here (Hoult *et al.*, 2015). However, this is out of the scope of the investigation undertaken here but will be the focus of future research conducted by the authors.

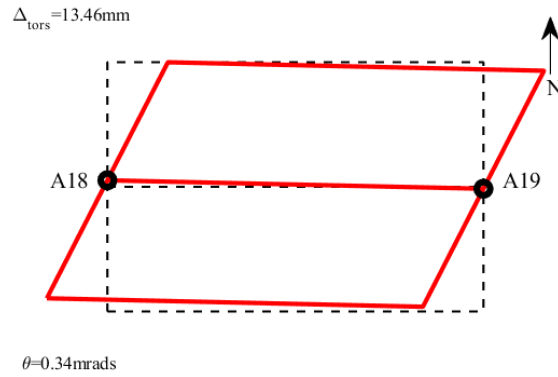


Figure 7 Displacement differential in the North-South of the Atwood building at approximate mid-height (accelerometer A18 and A19) with indicated torsional displacement (δ) and rotation (θ) at $t=39.83s$

The methods used here to simulate the displacement profile of the Atwood building show some potential in providing a rapid estimate of the seismic health of a building, equipped with the minimum required instrumentation, subjected to a large earthquake, and in near real-time.

4. Conclusions

The equations of dynamical equilibrium were used here in an attempt to simulate the displacement time history of the Atwood building subjected to a M_W 7.1 earthquake. This method is simple, computational inexpensive, and

can provide estimates of displacement (and drifts) of the building in near-real time in the event of an earthquake, which can be used as an indicator of the seismic health of the building. The simulations here were compared to some of the recorded displacements in the building, which were found to underestimate the displacement amplitudes in some cases. It was found that the torsional response of the building could be responsible for some of the underestimation of the displacement. The authors plan to conduct a more thorough investigation to assess whether this method is robust in providing accurate estimations of the elastic displacement profile of a building during an earthquake, with one of the aims to evaluate the robustness of the method presented here for determining interstory drifts of a building subjected to large earthquake ground motions. The findings will be reported in the future.

5. References

- AEC. (2018). *Alaska Earthquake Center, 'Magnitude 7.1 - 7 miles NW of Elmendorf AFB'*. Retrieved from <https://earthquake.alaska.edu/event/20419010>.
- Algan, B. B. (1982). *Drift and damage considerations in earthquake-resistant design of reinforced concrete buildings*. (Ph.D.), University of Illinois at Urbana-Champaign.
- Çelebi, M. (2006). Recorded Earthquake Responses from the Integrated Seismic Monitoring Network of the Atwood Building, Anchorage, Alaska. *Earthquake Spectra*, 22(4), 847-864. doi:10.1193/1.2359702.
- Çelebi, M. (2008). *Real-time monitoring of drift for occupancy resumption*. Paper presented at the Proc. 14th World Conference on Earthquake Engineering (14WCEE).
- D'Alessandro, A., Luzio, D., & D'Anna, G. (2014). Urban MEMS based seismic network for post-earthquakes rapid disaster assessment. *Adv. Geosci.*, 40, 1-9. doi:10.5194/adgeo-40-1-2014.
- DPWH. (2015). *Guidelines and Implementing Rules on Earthquake Recording Instrumentation for Buildings*.
- Erazo, K., & Hernandez, E. M. (2016). High-resolution seismic monitoring of instrumented buildings using a model-based state observer. *Earthquake Engineering & Structural Dynamics*, 45(15), 2513-2531.
- Field, E. H., Arrowsmith, R. J., Biasi, G. P., Bird, P., Dawson, T. E., Felzer, K. R., Jackson, D. D., Johnson, K. M., Jordan, T. H., Madden, C., Michael, A. J., Milner, K. R., Page, M. T., Parsons, T., Powers, P. M., Shaw, B. E., Thatcher, W. R., Weldon, R. J., II, & Zeng, Y. (2014). Uniform California Earthquake Rupture Forecast, Version 3 (UCERF3)—The Time-Independent Model. *Bulletin of the Seismological Society of America*, 104(3), 1122-1180. doi:10.1785/0120130164 %J Bulletin of the Seismological Society of America.
- Hou, S., Zeng, C., Zhang, H., & Ou, J. (2018). Monitoring interstory drift in buildings under seismic loading using MEMS inclinometers. *Construction and Building Materials*, 185, 453-467. doi:10.1016/j.conbuildmat.2018.07.087.
- Hoult, R. D., Lumantarna, E., & Goldsworthy, H. M. (2015, 6-8 November, 2015). *Torsional Displacement for Asymmetric Low-Rise Buildings with RC C-shaped Cores*. Paper presented at the Proceedings of the Tenth Pacific Conference on Earthquake Engineering, Sydney, Australia.
- Krüger, M., Grosse, C. U., & Marrón, P. J. (2005). Wireless Structural Health Monitoring Using MEMS. *Key Engineering Materials, Trans Tech Publications, Ltd.*, 293-294, 625-634. doi:10.4028/www.scientific.net/kem.293-294.625.
- Limongelli, M. P. (2003). Optimal location of sensors for reconstruction of seismic responses through spline function interpolation. 32(7), 1055-1074. doi:10.1002/eqe.262.
- Limongelli, M. P. (2014). Seismic health monitoring of an instrumented multistory building using the interpolation method. 43(11), 1581-1602. doi:10.1002/eqe.2411.
- Liu, C., Lay, T., Xie, Z., & Xiong, X. (2019). Intralab Deformation in the 30 November 2018 Anchorage, Alaska, MW 7.1 Earthquake. *Geophysical Research Letters*, 46(5), 2449-2457. doi:10.1029/2019GL082041.

- MMEIRS. (2004). *Earthquake Impact Reducation Study for Metropolitan Manila, Republic of the Philippines: Final Report, Volume 1, Executive Summary*. Retrieved from http://ndrrmc.gov.ph/attachments/article/1472/Earthquake_Impact_Reduction_Study_Volume_1.PDF.
- Porter, K., Jones, L., Cox, D., Goltz, J., Hudnut, K., Mileti, D., Perry, S., Ponti, D., Reichle, M., Rose, A. Z., Scawthorn, C. R., Seligson, H. A., Shoaf, K. I., Treiman, J., & Wein, A. (2011). The ShakeOut Scenario: A Hypothetical Mw7.8 Earthquake on the Southern San Andreas Fault. 27(2), 239-261. doi:10.1193/1.3563624.
- UBC. (1997). *Uniform Building Code*. Retrieved from Whittier, California.
- Ulusoy, H. S., Kalkan, E., Fletcher, J. P. B., Friberg, P. A., Leith, W., & Banga, K. (2012). *Design and implementation of a structural health monitoring and alerting system for hospital buildings in the United States*. Paper presented at the 15th World Conference on Earthquake Engineering, Lisboa, Portugal.
- Zou, X., & Seshia, A. A. (2015, 21-25 June 2015). *A high-resolution resonant MEMS accelerometer*. Paper presented at the 2015 Transducers - 2015 18th International Conference on Solid-State Sensors, Actuators and Microsystems (TRANSDUCERS).
- Zou, X., Thiruvengathanathan, P., & Seshia, A. A. (2014). A Seismic-Grade Resonant MEMS Accelerometer. *Journal of Microelectromechanical Systems*, 23(4), 768-770. doi:10.1109/JMEMS.2014.2319196.

Ground Motion Accelerogram Dataset for Nonlinear Time History Analysis in Southeastern Australia

Yiwei Hu^{1,4}, Nelson Lam^{2,4}, Scott Menegon^{3,4}

1. Corresponding Author. PhD candidate, Department of Infrastructure Engineering, The University of Melbourne, Parkville, VIC 3010, Australia. Email: huyh1@student.unimelb.edu.au
2. Professor, Department of Infrastructure Engineering, The University of Melbourne, Parkville, VIC 3010, Australia. Email: ntkl@unimelb.edu.au
3. Research Fellow, Department of Civil and Construction Engineering, Swinburne University of Technology, Melbourne, Australia. Email: smenegon@swin.edu.au
4. Bushfire and Natural Hazard Cooperative Research Centre, Melbourne, Australia

Abstract

This paper is aimed at demonstrating the application of the Conditional Mean Spectra (CMS) methodology for sourcing accelerogram records for use in dynamic analyses of structures in regions away from tectonic boundaries. The main challenges with deriving CMS for selecting and scaling accelerograms stem from the paucity of representative strong motion data and event recurrence data. The CMS constructed in this study have been employed for retrieving and scaling accelerograms from international strong motion databases. Four suites of bedrock accelerograms for Southeastern Australia have been selected and scaled, corresponding to four hazard levels (hazard design factor of 0.08, 0.10, 0.12 and 0.15 g). Each suite contains 24 pairs of scaled accelerograms to represent ground motion excitations in the primary direction and the orthogonal direction. Soil surface ground motion accelerograms to represent the conditions of 20 example soil sites have been generated accordingly for engineering research and for supporting the design and assessment of critical infrastructure and heritage structures.

Keywords: Australian Ground Motion Selection, Component Attenuation Model, Conditional Mean Spectra, Ground Motion Database

1. INTRODUCTION

Potentially destructive intraplate earthquakes can occur anywhere away from tectonic plate boundaries despite historical precedence (Bird, Kreemer & Holt, 2010). Strong ground motion accelerograms are sought in intraplate regions for constructing site-specific response spectra or for supporting the design of critical facilities. The lack of strong indigenous records in stable continental regions (SCRs), for example Southeastern Australia (SEA), requires selecting and scaling accelerograms from international ground motion databases. The Pacific Earthquake Engineering Research (PEER, 2014) ground motion database based at University of California, Berkeley, provides online resources for downloading accelerograms for use in research or engineering practices. To select and scale accelerograms using the database, a target elastic response spectrum needs to be specified. To serve for this purpose, the Conditional Mean Spectrum (CMS) methodology was developed in the past decades (Baker, 2011; Baker and Cornell, 2006; Jayaram, Lin & Baker, 2011) to compute an event-specific response spectrum which is more realistic than the commonly employed uniform hazard spectrum or code spectrum.

Adopting the CMS methodology in regions of lower seismicity is not straightforward due to the paucity of available strong motion records and associated recurrence data. The uncertainties over ground motion modelling and identification of dominating earthquake scenarios were studied in SEA regions by a comparison study with five shortlisted Ground Motion Prediction Expressions (GMPEs) and three sets of weighting schemes (Hu, Lam & Menegon, 2019). The CMS derived from the three schemes of weighting parameters demonstrate good consistency, and the modelling outcome is robust for ground motion selection and scaling purposes. In this study, following the work by Hu and co-workers (2019), CMS were constructed at four reference periods of 0.2, 0.5, 1 and 2 seconds with an equal weight assigned to each GMPE. Six bedrock ground motion records were selected and scaled for each CMS (Section 2). The 24 selected ground motions were recorded from more than 20 different seismic events to achieve diversity in the dataset. The same procedure was repeated for four hazard levels to accommodate the needs in different engineering situations. The four hazard levels correspond to the hazard design factor of 0.08, 0.1, 0.12 and 0.15 g.

The presence of soils and extremely weathered rocks can modify the amplitude and shape of ground motion excitations. In contrast to the tightly-packed bedrock, the relatively loose surficial materials have decreasing soil density and shear wave velocity, which amplifies ground motion through an impedance. The bedrock accelerograms sourced in Section 2 were processed through soil sediment based on equivalent-linear one-dimensional analysis to generate soil surface accelerograms. The soil site properties (including soil density, shear wave velocity and dynamic properties) were retrieved and analysed from geotechnical borehole records from capital cities in the SEA region (Section 3). 20 Soil site profiles were selected to constitute a diverse set of site conditions. A case study is presented in Section 4 to provide a preliminary guide on how to generate soil surface accelerograms that are suitable for nonlinear time history analysis for engineering practitioners in SEA.

2. BEDROCK ACCELEROGRAMS

In this section, the process of selecting and scaling bedrock ground motions using the Conditional Mean Spectrum (CMS) methodology is briefly described. Detailed procedures and comparison studies can be found in Hu, Lam & Menegon (2019). The outcome from the ground motion selection study includes four suites of bedrock accelerograms for SEA, corresponding to four hazard levels (hazard design factor of 0.08, 0.10, 0.12 and 0.15 g). Each suite contains 24 pairs of scaled accelerograms to represent ground motion excitations in the primary direction and the orthogonal direction. Each pair was scaled with one scaling factor to ensure the response spectrum in the primary direction movement matches well with the target CMS.

An outline of the procedure for constructing the CMS is provided here.

- (1) Decide on the reference natural period of vibration (T^*) and identify the target code spectral acceleration $Sa(T^*)$;
- (2) Determine the Ground Motion Prediction Expressions (GMPEs) and weighting factors to apply for predicting median response spectral value $\mu(T)$ and standard deviation $\sigma(T)$;
- (3) Identify dominant earthquake scenarios expressed in magnitude-distance (M-R) combinations corresponding to the selected value of T^* by disaggregation analysis;
- (4) Calculate epsilon $\epsilon(T^*)$ which is the number of standard deviations from $\mu(T^*)$ to match with the target response spectral value $Sa(T^*)$ in logarithmic scale;
- (5) Construct the conditional mean spectrum by applying correlation coefficients $\rho(T, T^*)$.

Details of the various components of the CMS construction process as outlined in the above are to be described in the rest of this section. The bedrock ground motion selection and the scaling process is to be introduced in this section as well.

2.1 Ground Motion Modelling

Ground Motion Prediction Expressions (GMPEs) are used to predict earthquake intensities expressed in different forms such as response spectral accelerations, peak ground acceleration and peak ground velocity for a given M-R combination, site class, and faulting mechanism. Five GMPEs were employed in this study to represent SEA conditions. The five GMPEs consists of two generic empirical GMPEs that were developed in Western North America (WNA); two locally developed GMPEs in SEA that were recommended for use by Geoscience Australia; and the adaptive stochastic model of CAM. The CAM model serves to fast track predictions from the seismological model using algebraic expressions for use by engineers in a transparent manner and is capable of capturing intra-regional variability of shear wave velocity kilometres deep into bedrock (Lam et al. 2000; Tang et al. 2020).

Equal weight of 20% was assigned to each of the GMPE model (Table 1) to predict response spectral values and standard deviation. The response spectra accelerations (RSA) from all five GMPEs were cross-compared in Figure 1 to demonstrate good consistency. Importantly, the selection of GMPEs is generally consistent with that adopted in the PSHA assessment of the Australian continent (Leonard et al., 2014), and the weighting parameters were validated in Hu, Lam & Menegon (2019).

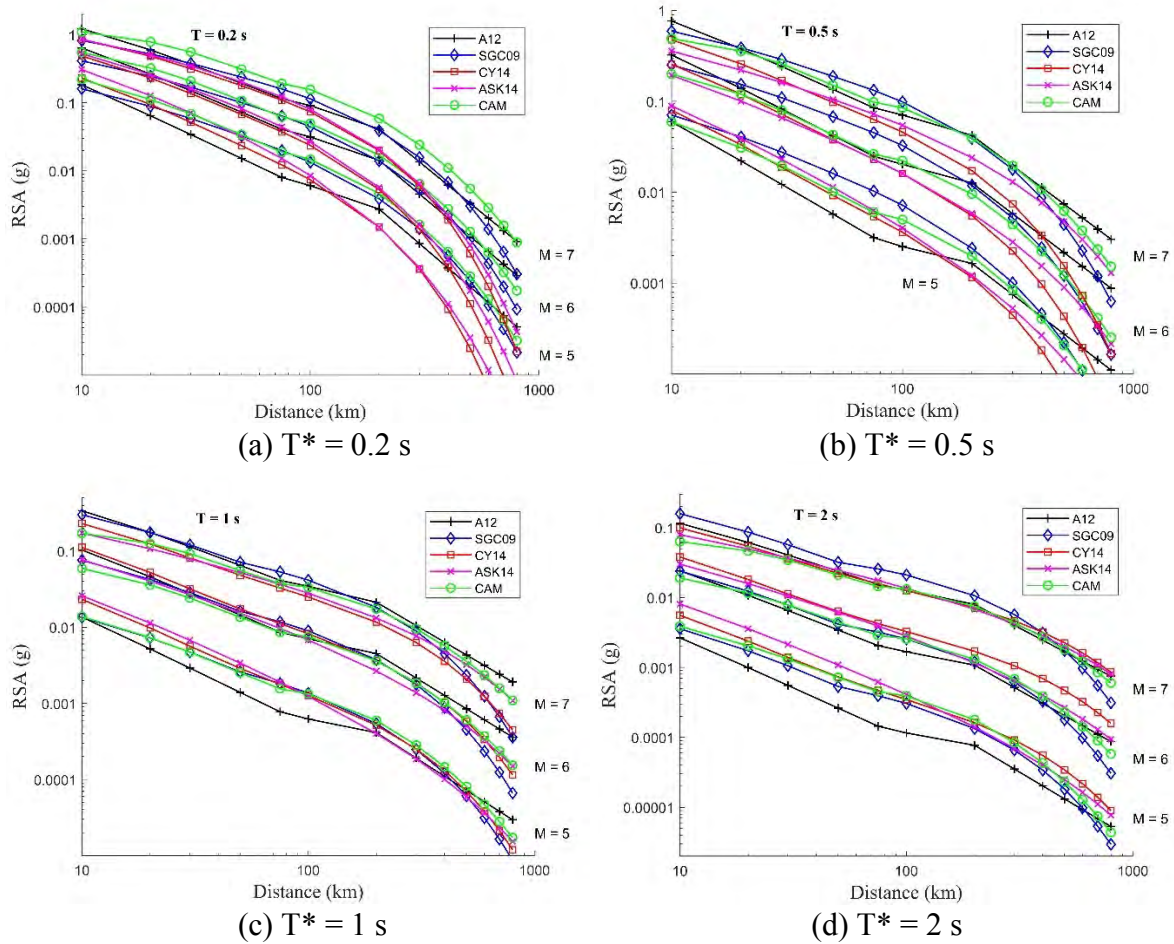


Figure 1. Comparison among predictions by the 5 selected GMPEs at period 0.2, 0.5, 1 and 2 seconds

Table 1. Selected GMPEs and weighting factors

GMPEs	Reference	Weighting Factor
<i>ASK14</i>	Abrahamson, Silva & Kamai, 2014	20%
<i>CY14</i>	Chiou and Young, 2014	20%
<i>A12</i>	Allen, 2012	20%
<i>SGC09</i>	Somerville et al. 2009	20%
<i>CAM</i>	Tang et al. 2020	20%

2.2 Dominant Earthquake Scenarios

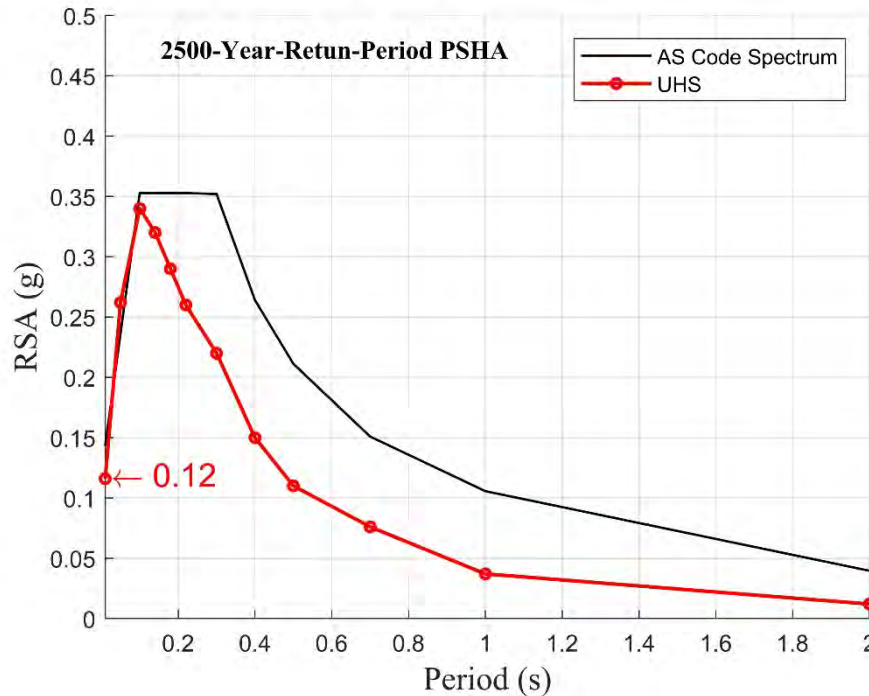
In regions of lower seismicity, to completely rely on previous event data to predict future earthquake recurrence is inaccurate because of the very limited time-window in existing event databases. Alternatively, the uniform seismicity approach was employed that assumes a uniform distribution of seismic activities within 200 km from the site. The recurrence rate was determined from a macro approach of recurrence modelling from a large event database sourced around the

world (Lam et al., 2016). The number of $M > 5$ events in a 50-year period was found between 5 to 10 in an area of 1 million km in intraplate regions. Considering a hazard design factor of 0.12 g, the rate of recurrence can be translated into the Gutenberg-Richter relationship of Eq. (1).

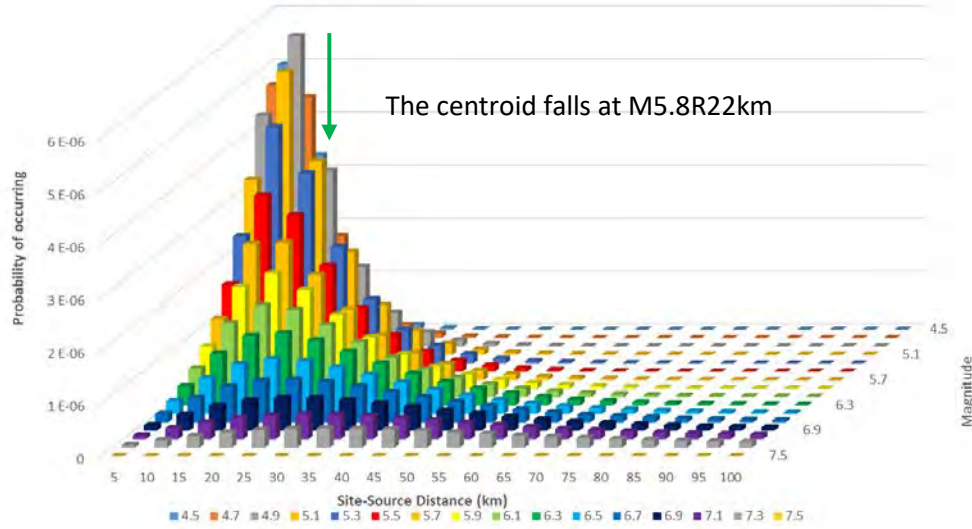
$$\log_{10} N(M) = 5.5 - 0.9M \quad (1)$$

where M is moment magnitude; $N(M)$ is number of events with magnitude exceeding M .

The uniform hazard spectrum calculated from the probabilistic analysis with the proposed GMPEs and uniform hazard approach was plotted in Figure 2(a) against the code spectrum stipulated by AS1170.4 for rock sites (Class B_e). Results from disaggregation analyses are presented in the 3D bar chart of Figure 2(b) for a natural period of 0.2 seconds. No distinct dominating earthquake scenario can be observed in the bar chart, and the mean scenario was determined from the centroid, which reads $M5.8$ and $R22$ km. As the probability contribution mainly comes from small magnitude event ($4.5 \leq M \leq 6$) in close distance ($10 \text{ km} \leq R \leq 25 \text{ km}$) at $T^* = 0.2$ seconds, the averaged controlling scenario is normalised to a controlling magnitude of $M5.5$ at a period of 0.2 seconds. The controlling distance is back calculated in order that the median predicted spectral acceleration at 0.2s equals to that predicted by the mean scenario of $M5.8$ and $R22$ km as stated above. The averaged controlling M-R combinations for the four hazard design factors that will be of interest to engineering practitioners in Australia (i.e. 0.08, 0.10, 0.12 and 0.15) are summarised in Table 2.



(a) Uniform Hazard Response Spectrum

(b) Disaggregation Analysis and the Probability Distribution Bars at $T^* = 0.2$ seconds**Figure 2. Probabilistic seismic hazard analysis****Table 2. Averaged controlling scenarios**

Hazard value (g)	Period of Interest (s)			
	0.2	0.5	1	2
0.08	M5.5R25 $\epsilon=0.94$	M6R39 $\epsilon=1.31$	M6.5R56 $\epsilon=1.39$	M7R148 $\epsilon=1.21$
0.10	M5.5R21 $\epsilon=0.98$	M6R33 $\epsilon=1.32$	M6.5R48 $\epsilon=1.48$	M7R129 $\epsilon=1.36$
0.12	M5.5R18 $\epsilon=1.01$	M6R29 $\epsilon=1.36$	M6.5R42 $\epsilon=1.53$	M7R102 $\epsilon=1.49$
0.15	M5.5R16 $\epsilon=1.04$	M6R24 $\epsilon=1.38$	M6.5R35 $\epsilon=1.58$	M7R80 $\epsilon=1.62$

2.3 Construction of CMS

With the controlling earthquake scenarios and ground motion models available from above, the CMS can be readily computed using Eq. (2) – Eq. (4) (Baker and Cornell, 2006). The *epsilon* (ϵ) values so calculated for each combination are listed in Table 2. Demonstration of how to raise the mean response spectra to match the target spectral value at the reference period to construct CMS is illustrated in Figure 3, for the four reference periods.

$$\mu_{\ln Sa(T_2) | \ln Sa(T_1) = \ln Sa(T_1)^*} = \mu_{\ln Sa}(\bar{M}, \bar{R}, T_2) + \sigma_{\ln Sa}(\bar{M}, T_2) \rho_{\ln Sa(T_1), \ln Sa(T_2)} \bar{\epsilon}(T_1) \quad (2)$$

$$\epsilon(T^*) = (\ln Sa(T^*) - \mu_{\ln Sa}(M, R, T^*)) / \sigma_{\ln Sa}(T^*) \quad (3)$$

$$\rho_{\ln Sa(T_1), \ln Sa(T_2)} = 1 - \cos\left(\frac{\pi}{2} - (0.359 + 0.163I_{(T_{min} < 0.189)}) \ln \frac{T_{min}}{0.189} \ln \frac{T_{max}}{T_{min}}\right) \quad (4)$$

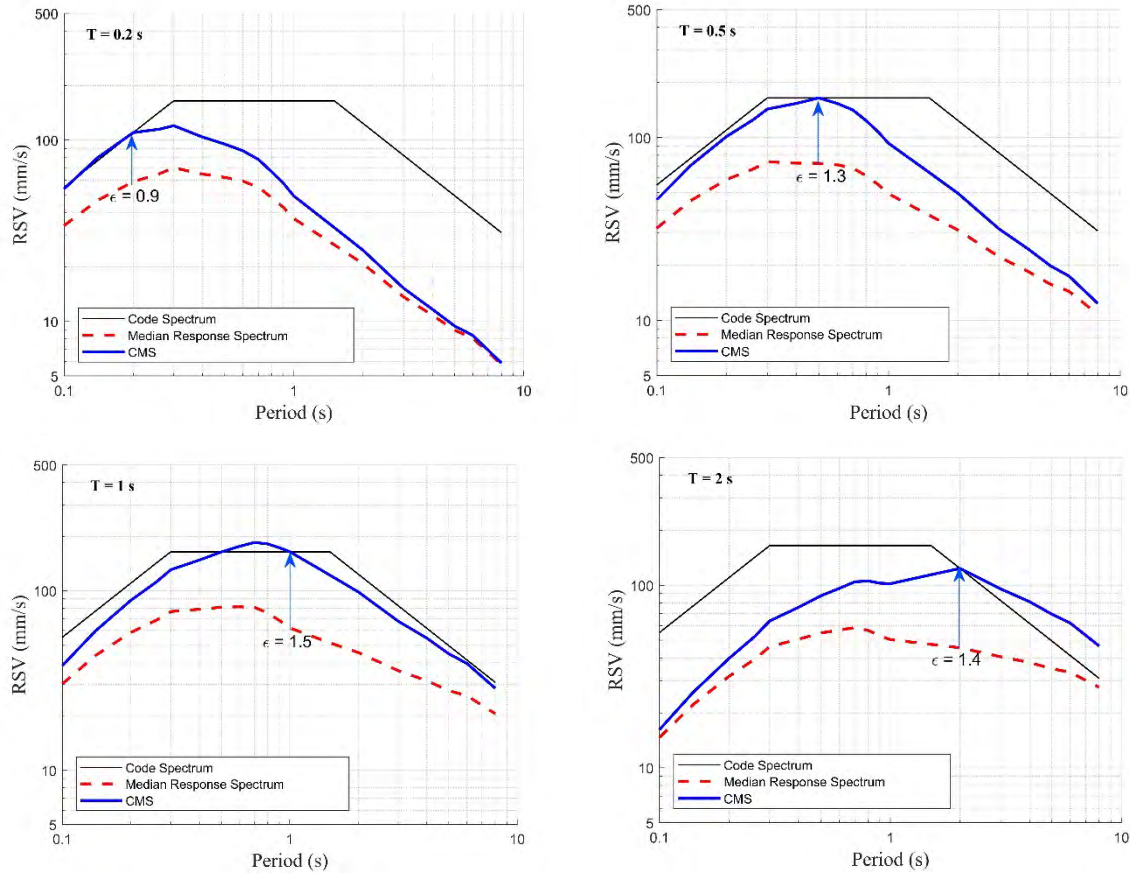


Figure 3. Demonstration of the conditional mean spectra at period 0.2, 0.5, 1 and 2 seconds

2.4 Ground Motion Selection

In order to retrieve enough accelerograms that meet the demand that each of the 24 accelerograms was recorded in different events, three strong motion databases were searched, namely the PEER NGA-West 2 database (2014), the Geo-net database of New Zealand (Kaiser et al., 2017; Van Houtte et al., 2017), and the ORFEUS database of the European-Mediterranean region (Luzy et al., 2016). Candidate ground motions were searched with the target CMS spectra and a range of criteria (Reverse/Oblique faulting type; magnitude half-bin width of $\pm 0.3 M_w$; distance half-bin width of 30 km; $V_{S,30}$ ranges from 450 m s^{-1} to 1800 m s^{-1} to represent rock conditions). The candidate accelerograms were then scaled to match with the target response spectrum in the period range of $0.2T^*$ to $2.0T^*$; those whose scale factors are outside the range of 0.7-1.5 were removed from further process.

For each reference period at each hazard level, six scaled accelerograms with minimum relative error to the target CMS were selected. Details of the earthquake events associated with the retrieved records at $T^* = 1$ seconds and hazard design factor of 0.12g are summarised in Table 3. The velocity response spectra of selected accelerograms are plotted in Figure 4, and the acceleration time histories are plotted in Figure 5. Superposed on the CMS is the ensemble average of the scaled records (represented by the solid blue line). Considering the four distinctive reference

periods (0.2, 0.5, 1 and 2 seconds) that are of structural engineering interest, an ensemble totalling 24 accelerograms were sought. Full accelerograms are available by direct communication with the authors.

Table 3. Summary of the details of the retrieved events and scaling factors at $T^* = 1s$

Earthquake	Year	Station	M_w	R_{rup} (km)	SF
Northridge-01	1994	LA - Wonderland Ave	6.7	20.3	0.76
Coalinga-01	1983	Parkfield - Stone Corral 3E	6.4	34.0	0.94
San Fernando	1971	Fairmont Dam	6.6	30.2	1.29
Niigata Japan	2004	NGNH29	6.6	46.8	1.25
Chi-Chi Taiwan-05	1999	CHY086	6.2	67.5	1.37
Georgia USSR	1991	Iri	6.2	31.5	1.12

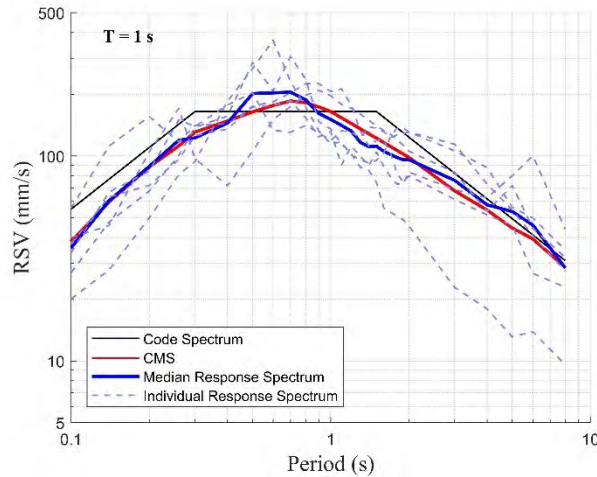


Figure 4. Demonstration of the velocity response spectra of individual selected and scaled accelerograms and the target CMS at $T^* = 1$ Seconds

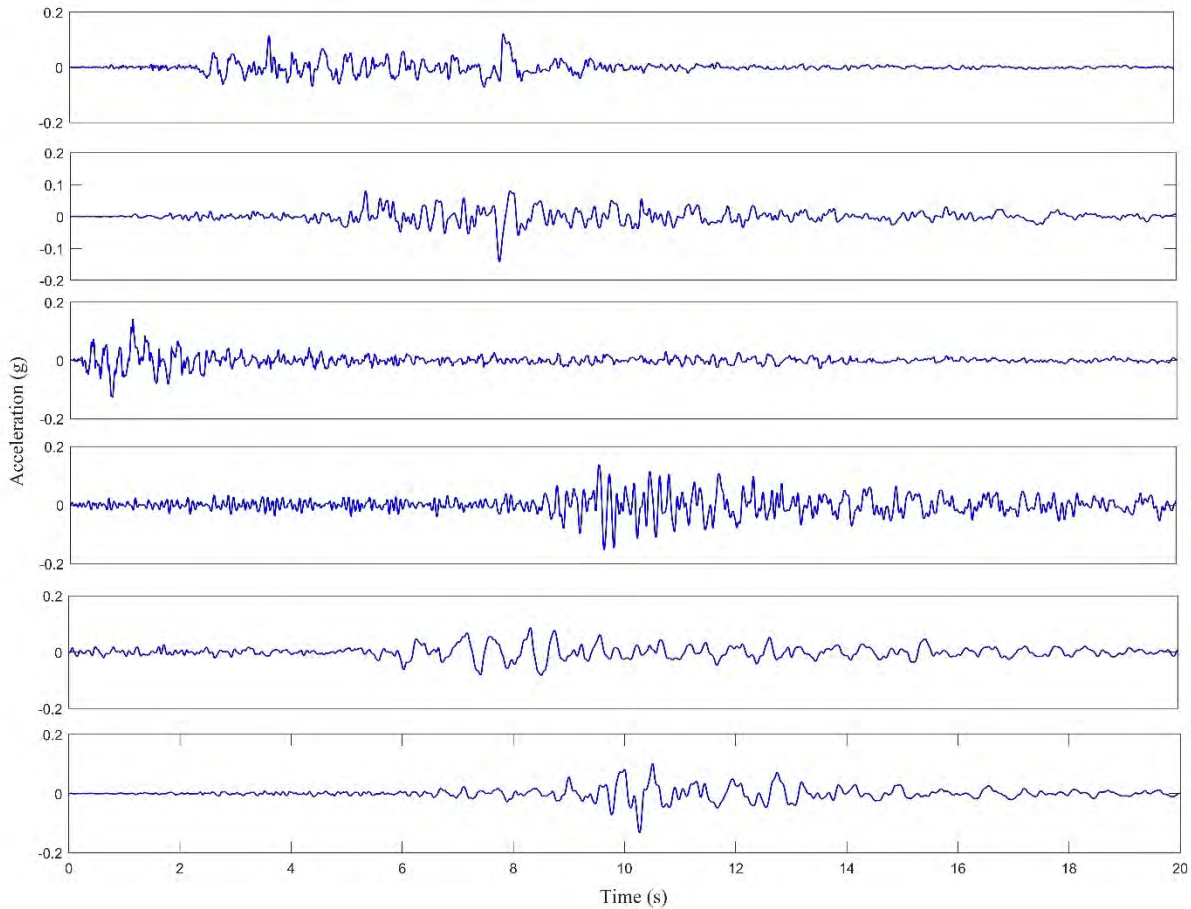


Figure 5. Selected and scaled accelerograms at $T^* = 1$ second

3. SOIL SURFACE ACCELEROGRAMS

The presence of soils and extremely weathered rocks can modify the amplitude and shape of ground motion waves. In contrast to the tightly-packed bedrock, the relatively loose surficial materials have decreasing soil density and shear wave velocity, which amplifies ground motion through an impedance. In many modern engineering design codes, the site amplification factor is accounted for by a simplified site characteristic, the average velocity of shear waves in the top 30 meters of soil ($V_{s,30}$) (e.g., AS1170.4 2018; EN 1998-1 2004; ASCE-7 2016). In this study, soil amplification effect was simulated using the equivalent linear approach to incorporate soil shear wave velocity, layer depth and geological site conditions. This approach was firstly introduced by Seed (1970), and adopted in many site-response modelling programs (e.g. SHAKE91, by Idriss and Sun, 1992; EERA, by Bardet, Ichii and Lin, 2000; and SUA, by Robinson, Dhu and Schneider, 2006). The MATLAB-based SUA program was employed in this study.

3.1 Soil Profile

This section describes how soil characteristics were retrieved from geotechnical borehole logs and processed into soil profile inputs for amplification analysis. Four parameters, i.e., soil unit weight,

shear wave velocity, soil dynamic property, and bedrock condition, are discussed herein. Among those parameters, extra care was taken in estimating soil shear wave velocity because the sediment amplification factor is more sensitive to the change of shear wave velocity values.

Soil unit weights were estimated based on soil type, water content and relative density. It is noteworthy that the void ratio for cohesive soils (silt and clay) was computed assuming over-consolidated expansive clay, which might lead to a slight overestimation of cohesive soil unit weight. The estimated unit weight values are within the typical soil unit weight range specified in Coduto et al. (1999), as shown in Table 4.

Table 4. Summary of typical soil unit weight (Coduto et al. 1999)

Soil Type	Dry Unit weight (kN/m^3)	Saturated Unit weight (kN/m^3)
Poorly graded gravel	17.28 – 20.42	19.64 – 21.99
Well graded gravel	17.28 – 21.99	19.64 – 23.56
Silty gravel	15.71 – 20.42	19.64 – 21.99
Clayey gravel	15.71 – 20.42	19.64 – 21.99
Poorly graded sand	14.92 – 19.64	18.85 – 21.21
Well graded sand	14.92 – 21.21	18.85 – 22.78
Silty sand	12.57 – 21.21	17.28 – 21.99
Clayey sand	13.35 – 20.42	17.28 – 21.21
Low plasticity silt	11.78 – 17.28	12.57 – 20.42
High plasticity silt	11.78 – 17.28	11.78 – 20.42
Low plasticity clay	12.57 – 17.28	11.78 – 20.42
High plasticity clay	12.57 – 17.28	11.00 – 19.64
Peat	4.71	11.00

Three models were considered in this study to estimate the soil shear wave velocity. The first model was proposed by Wair, DeJong and Shantz (2012) from the Pacific Earthquake Engineering Research Centre (referred to as PEER model hereafter). They reviewed many previously proposed equations, selected several equations that were developed from large-size datasets, and fitted the average values. The PEER model correlates soil shear wave velocity to soil type (silt and clay; sand; and gravel), SPT count and effective vertical stress σ_v' . The second and third models were proposed by Ohta and Goto (1978) and by Imai and Tonouchi (1982), both employing only soil type and SPT count to compute shear wave velocity. The Imai & Tonouchi model was developed from a larger dataset than the Ohta & Goto model, and subdivides soil type into Holocene soil and Pleistocene soil based on geologic age. In the comparison analysis, as geologic soil age is unknown, the average shear wave velocity of Holocene soil and Pleistocene soil was assumed.

The shear wave velocity estimated from the three models was plotted in Figure 6. Effective vertical stress of 135 kPa was assumed for the PEER model, which is typical from a 10-meter soil column (assuming groundwater level at 5 meters). It is obvious that the PEER model estimated a lower shear wave velocity for clay and sand at this stress level. As the vertical stress gradually increases over depth, the soil layers in the top 10 meters are ‘overly soft’ in the PEER model, which could result in much higher amplification effect. Also, if the overburden stress from structures and foundations were to be applied, it introduces another source of uncertainty because the stress

strongly depends on structure type and number of floors. Therefore, the PEER model was determined inappropriate for this study.

The predictions from the Ohta & Goto model and the Imai & Tonouchi model match well with each other except for gravels. Considering the SPT count range of 1- 30 blows (which is common at 10-meter soil depth), predictions from the Ohta & Goto model has a better match to that from the PEER model. Another reason that the Imai & Tonouchi model was unfavoured is that it requires the assumption that the shear wave velocity of a geologic-age-undetermined soil equals the average shear wave velocity of Holocene soil and Pleistocene soil. In conclusion, the Ohta & Goto model was selected for processing soil data.

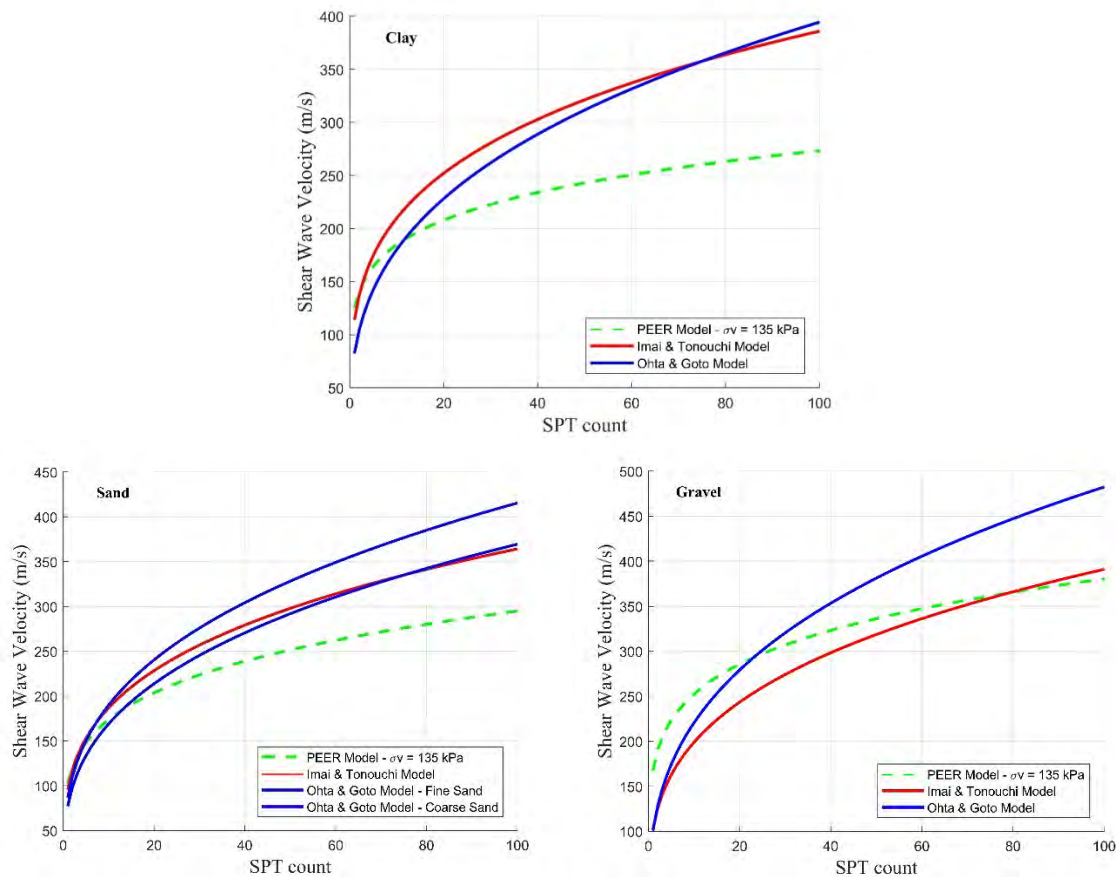


Figure 6. Comparison among soil layer shear wave velocity from 3 models

Estimation of soil dynamic properties, i.e. the modulus reduction factor and damping ratio curves, employed the Vucetic & Dobry model (1991), which parameterises soil plasticity index. The soil plasticity index was assumed from AS1276:2017 according to soil classification. The bedrock shear wave velocity was determined from geotechnical surveys across the country (Lam et al., 2006; Kayen et al., 2015; Lacey, 2016) and typical velocities for different types of rock (Wills et al., 2000).

53 soil profiles were generated based on borehole records from Melbourne, Sydney, Brisbane and Newcastle areas, and 20 profiles were selected to constitute a diverse set of site conditions. The

profile set consists of four Class E sites, four Class D sites and 12 Class C sites, according to the site classification criteria in AS1170.4-2018. The site natural period, defined as the shear-wave travel time through four times the soil thickness, ranges from 0.1 to 1.15 seconds; the soil depth ranges from 5 to 50 meters. The shear wave velocity profiles are presented in Figure 7.

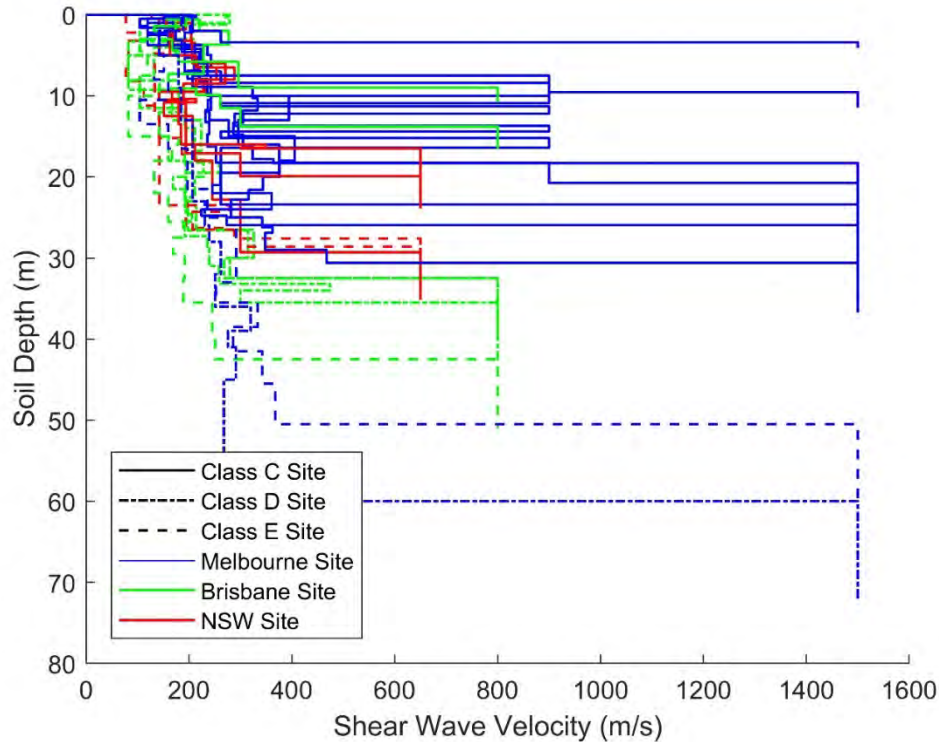


Figure 7. Demonstration of the soil shear wave velocity profile from 20 selected sites

3.2 Soil Surface Accelerograms and Baseline Correction

With the available soil profiles, soil surface accelerograms were generated using program SUA (Robinson, Dhu & Schneider, 2006). While the bedrock accelerograms were padded with zero terms at the start and end of a seismic event, those pads were removed to reduce the size of accelerograms and ease the computational effort for time history analysis. The removal of pads will not alter the frequency content, but the velocity and displacement time histories that are derived from the pad-stripped acceleration might be incompatible (i.e. the velocity and displacement do not reach zero at the end of the time history). To deal with the incompatibility issue, two proposed approaches include (1) to add the initial velocity and displacement condition; or (2) to perform baseline correction (Boore, Sisi & Akkar, 2012). In this study, baseline correction was performed to each individual soil surface accelerogram to ensure that the acceleration and velocity time histories reach zero at the end of records. Baseline correction was carried out by adding two half-sine pulses. The first pulse is applied across the entire time history, serving to reduce the final displacement to zero; and the second pulse is a short-period pulse that is added at the end of the time history to reduce the final velocity to zero. One example is given in Figure 8 & 9 to demonstrate the time history and response spectra before and after applying baseline correction.

It should be noted that the response spectra have differences less than 1% in the engineering period range of interest.

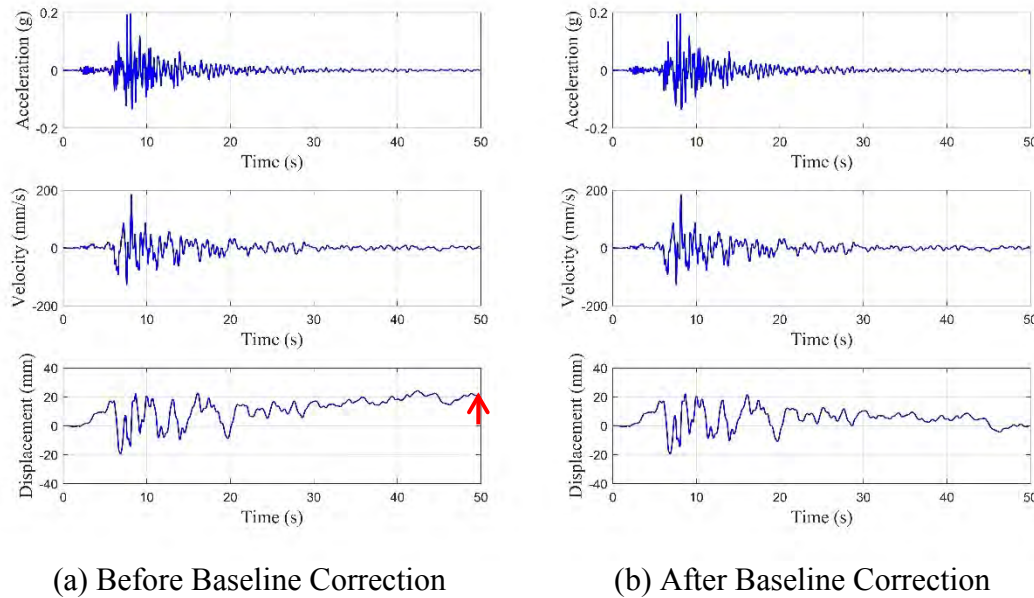


Figure 8. Example acceleration, velocity and displacement time history before and after applying baseline correction

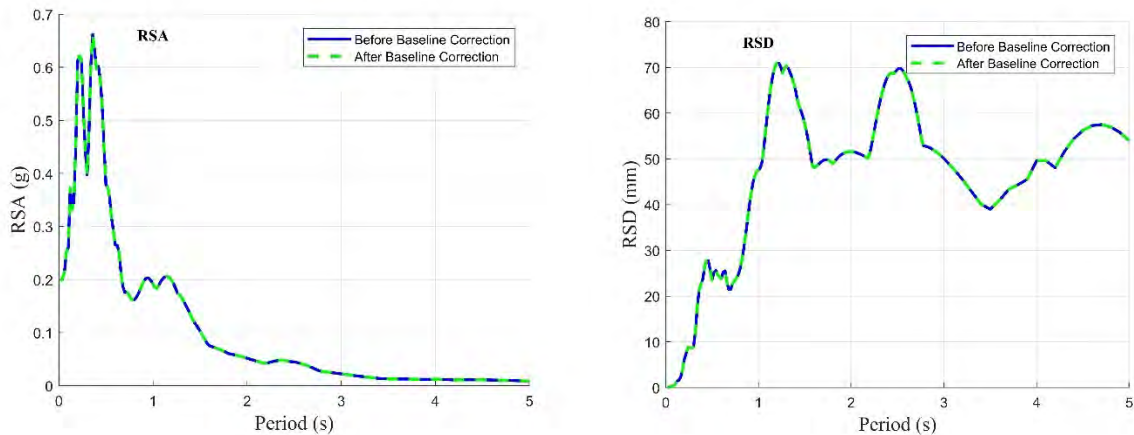


Figure 9. Example acceleration and displacement response spectra before and after applying baseline correction

4. CASE STUDY

A case study is provided in this section to demonstrate the generation of soil surface accelerograms for structural analysis, given the structural first mode period and soil site class. In the case study, accelerograms are sought for conducting seismic action analysis of a 10-storey building based on a hazard level of 0.12g on a Class C site in Melbourne. The first mode period is 0.87 second.

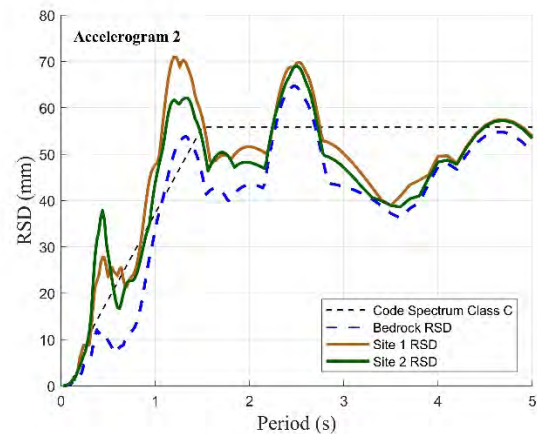
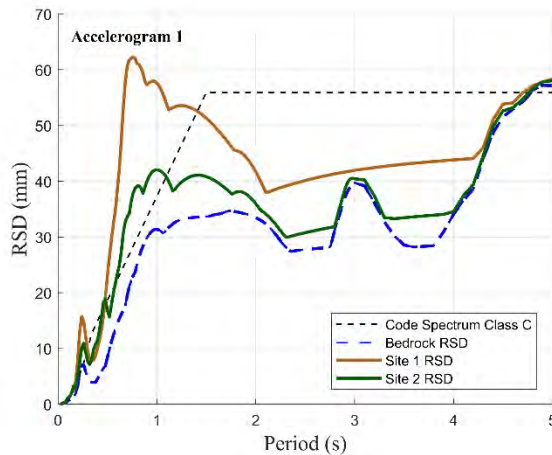
To produce eight accelerograms for nonlinear time history analysis, four bedrock accelerograms were selected and amplified by two Class C soils. The bedrock accelerograms were selected from the scaled accelerograms in Section 2 based on the first mode period of the structure. As 0.87 seconds is close to the third reference period (i.e., 1 seconds), two bedrock accelerograms were selected from the $T^* = 1$ s group. The other two bedrock accelerograms were selected from the $T^* = 0.2$ s group and the $T^* = 2$ s group to account for higher mode effect and period elongation. The information of the selected bedrock accelerograms is summarised in Table 5. Two soil profiles in Melbourne, both categorised as Class C site were employed to generate soil site accelerograms using SUA. The soil properties are listed in Table 6. The response spectra in the displacement (RSD) format are plotted in Figure 10 for both bedrock accelerograms and soil surface accelerograms.

Table 5. Summary of the details of the seismic events for the case study

Earthquake	Year	Station	M_w	R_{rup} (km)	SF
San Fernando	1971	Fairmont Dam	6.61	30.19	1.29
Coalinga-01	1983	Parkfield - Gold Hill 3W	6.36	39.12	0.73
Whittier Narrows-02	1987	Mt Wilson - CIT Seis Sta	5.27	19.78	0.99
Loma Prieta	1989	Hayward City Hall - North	6.93	55.11	1.28

Table 6. Soil properties for the case study

Property	Soil 1	Soil 2
Location	Melbourne	Melbourne
depth to rock (m)	31.5	30.6
Mean SWV (m/s)	244.5	303.8
Period (s)	0.52	0.4
Rock SWV (m/s)	1500	1500
Soil Class	C	C



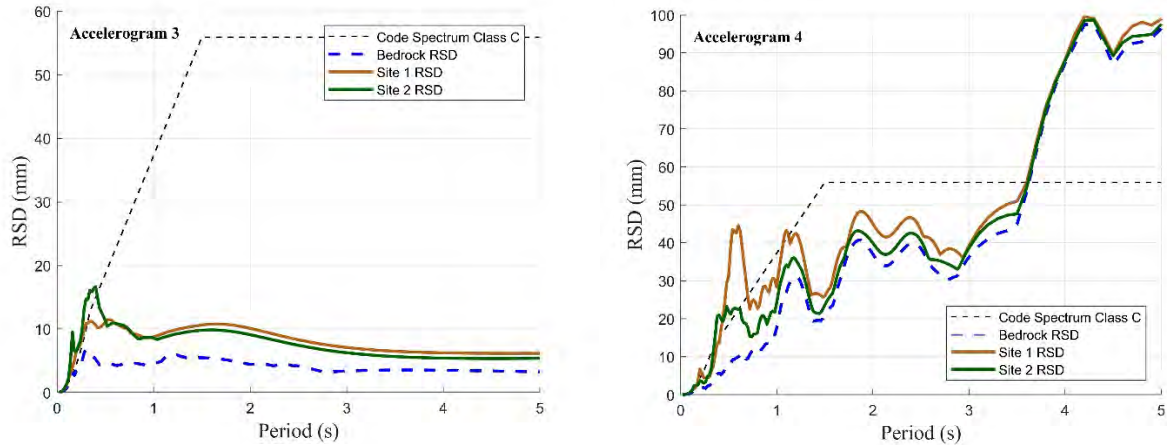


Figure 10. Response spectra of the case study soil surface accelerograms

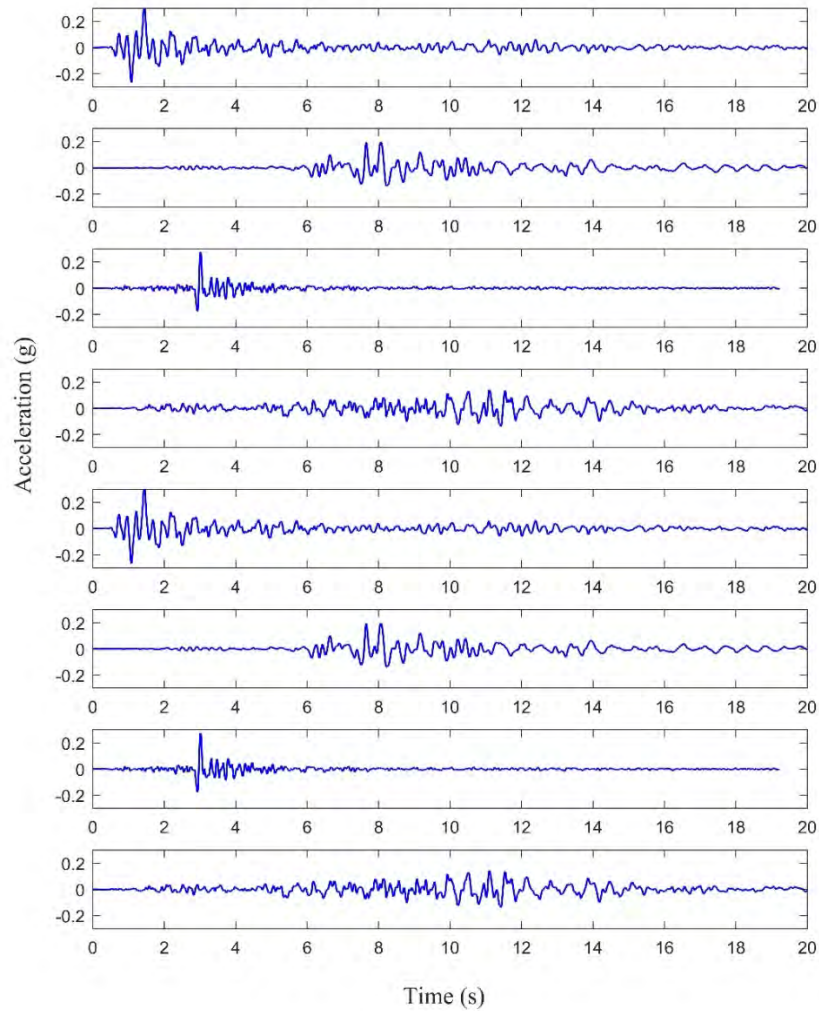


Figure 11. Case study soil surface accelerograms

It should be noted that in this case study, eight soil surface accelerograms were produced for structural analysis from four bedrock motions and two soil profiles. The soil surface acceleration time histories are plotted in Figure 11. Eurocode states when seven or more records are used in the nonlinear time history analysis, the average response can be considered for design (EN 1998 -1, 2004). However the soil accelerograms generated from this study are based on very different target response spectra and soil conditions, thus the authors recommend adopting the most adverse response for design. Also, although it meets the suggested number of accelerograms in design codes (EN 1998-1 2004; ASCE-7 2016), the diversity is limited from using four bedrock accelerograms and two soil sites. It is worthwhile to consider using six bedrock accelerograms (considering the case study structure of $T^* = 0.87$ s, the accelerograms would comprise of three accelerograms from the $T^* = 1$ s group, and one accelerogram from each of the other 3 groups) and three soil sites to cover a range of site natural periods.

5. CONCLUSION

This paper is about demonstrating the searching and scaling of accelerograms from international databases for use in the intraplate region of Southeastern Australia (SEA), and the generation of soil surface accelerograms through equivalent-linear soil amplification analysis. The Conditional Mean Spectrum (CMS) methodology was employed for the spectral scaling of the accelerograms for bedrock conditions. The primary aim of this article is to demonstrate the process of generating soil surface accelerograms for direct engineering application. The adaptation of multiple GMPEs, the uniform seismicity approach and the CMS methodology provide realistic target spectra for use in a stable region to source and scale bedrock accelerograms. Four suites of 24 pairs of bedrock accelerograms were selected from international strong motion databases to represent potential bedrock excitations consistent with the conditions of SEA. Twenty soil sites were generated from borehole records in capitals cities in SEA, and program SUA was then employed to generate accelerograms on the surface. Suites of ground motions for different soil conditions can be obtained for various levels of seismic design hazard intensities, which practitioners can adopt for the seismic design and analysis in the SCR of SEA

ACKNOWLEDGEMENT

The support of the Commonwealth Australia through the Cooperative Research Centre program and the Australian Research Council Discovery Project (DP180101593) is gratefully acknowledged.

REFERENCE

- Abrahamson, N. A., Silva, W. J., & Kamai, R. (2014). Summary of the ASK14 ground motion relation for active crustal regions. *Earthquake Spectra*, 30(3), 1025-1055.
- Allen, T. I. (2012). Stochastic ground-motion prediction equations for southeastern Australian earthquakes using updated source and attenuation parameters. *Geoscience Australia Record*, 69, 55.
- ASCE. 2016. Minimum Design Loads and Associated Criteria for Buildings and Other Structures (ASCE/SEI 7-16). *American Society of Civil Engineers*.

- Baker, Jack W. 2011. Conditional mean spectrum: Tool for ground-motion selection. *Journal of Structural Engineering* 137 (3):322-31
- Baker, J. W., & Cornell, C. A. (2006). Correlation of response spectral values for multicomponent ground motions. *Bulletin of the seismological Society of America*, 96(1), 215-227.
- Bird, Peter, Corné Kreemer, and William E Holt. 2010. A long-term forecast of shallow seismicity based on the Global Strain Rate Map. *Seismological Research Letters* 81 (2):184-94.
- Boore, D. M., Azari Sisi, A., & Akkar, S. (2012). Using pad-stripped acausally filtered strong-motion data. *Bulletin of the Seismological Society of America*, 102(2), 751-760.
- Chiou, B. S. J., & Youngs, R. R. (2014). Update of the Chiou and Youngs NGA model for the average horizontal component of peak ground motion and response spectra. *Earthquake Spectra*, 30(3), 1117-1153.
- Coduto, D. P. (1999). *Geotechnical engineering: principles and practices* (No. Sirsi) i9780135763803).
- Hu, Y., Lam, N., Menegon, S., (2019, November). Ground Motion Accelerograms for Nonlinear Time History Analysis in Low-to-Moderate Seismicity Regions. In *Proceedings of the 2019 Australian Earthquake Engineering Society Conference in Newcastle*.
- Idriss, I. M., & Sun, J. I. (1992). User's Manual for SHAKE91. *Center for Geotechnical Modeling, Department of Civil Engineering, University of California, Davis*.
- Imai, T., & Tonouchi, K. (1982). Correlation of N-value with S-wave velocity: Proc. of 2nd Europ. Sympo. on Penetration Testing, 67-72.
- Jayaram, Nirmal, Ting Lin, and Jack W Baker. 2011. A computationally efficient ground-motion selection algorithm for matching a target response spectrum mean and variance. *Earthquake Spectra* 27 (3):797-815.
- Kayen, R. E., Carkin, B. A., Allen, T., Collins, C., McPherson, A., & Minasian, D. (2015). *Shear-wave velocity and site-amplification factors for 50 Australian sites determined by the spectral analysis of surface waves method*. US Department of the Interior, US Geological Survey.
- Lacey, D. (2016). Assessment of some engineering properties and testing methods of residual soil and highly weathered rock materials in QLD, Australia.
- Lam, Nelson, John Wilson, Adrian Chandler, and Graham Hutchinson. 2000. Response spectral relationships for rock sites derived from the component attenuation model. *Earthquake Engineering & Structural Dynamics* 29 (10):1457-89.

- Lam, Nelson, Hing-Ho Tsang, Elisa Lumentarna, and John L Wilson. 2016. Minimum loading requirements for areas of low seismicity. *Earthquakes and structures* 11 (4):539-61.
- Lam, N., Venkatesan, S., Wilson, J., Asten, M., Roberts, J., Chandler, A., & Tsang, H. H. (2006). Generic approach for modelling earthquake hazard. *Advances in Structural Engineering*, 9(1), 67-82.
- Leonard, M, DR Burbidge, TI Allen, DJ Robinson, A McPherson, D Clark, and CDN Collins. 2014. The challenges of probabilistic seismic-hazard assessment in stable continental interiors: An Australian example. *Bulletin of the Seismological Society of America* 104 (6):3008-28.
- Luzi, L, R Puglia, E Russo, and WG Orfeus. 2016. Engineering strong motion database, version 1.0. *Istituto Nazionale di Geofisica e Vulcanologia, Observatories & Research Facilities for European Seismology*. doi 10:987-97.
- MS EN1998-1:2015 Eurocode 8: Design of structures for earthquake resistance—Part 1: General rules, seismic actions and rules for buildings. *European Standard NF EN 1:2005*.
- Ohta, Y., & Goto, N. (1978). Empirical shear wave velocity equations in terms of characteristic soil indexes. *Earthquake engineering & structural dynamics*, 6(2), 167-187.
- PEER. (2014). Pacific Earthquake Engineering Research (PEER) Ground Motion Database. http://peer.berkeley.edu/peer_ground_motion_database
- Robinson, D., Dhu, T., & Schneider, J. (2006). SUA: A computer program to compute regolith site-response and estimate uncertainty for probabilistic seismic hazard analyses. *Computers & geosciences*, 32(1), 109-123.
- Seed, H. B. (1970). Soil moduli and damping factors for dynamic response analysis. *EERC*.
- Bardet, J. P., Ichii, K., & Lin, C. H. (2000). User's manual for EERA: A computer program for Equivalent-linear Earthquake Site Response Analysis. *Los Angeles, California, USA: University of Southern California*.
- SS EN1998-1:2013 Eurocode 8: Design of structures for earthquake resistance—Part 1: General rules, seismic actions and rules for buildings. *European Standard NF EN 1:2005*.
- Standards Australia (2017), AS1726: 2017 Geotechnical site investigations, Standards Australia, Sydney, NSW.
- Standards Australia (2018), AS1170. 4 - 2018 Structural Design Actions, Part 4: Earthquake actions in Australia, Standards Australia, Sydney, NSW.
- Somerville, P., Graves, R., Collins, N., Song, S. G., Ni, S., & Cummins, P. (2009, December). Source and ground motion models for Australian earthquakes. In *Proc. 2009 Annual Conference of the Australian Earthquake Engineering Society* (pp. 11-13).

Tang, Yuxiang, Nelson Lam, Hing-Ho Tsang, and Elisa Lumantarna. 2020. An Adaptive Ground Motion Prediction Equation for Use in Low-to-Moderate Seismicity Regions. *Journal of Earthquake Engineering*:1-32.

Van Houtte, Chris, Stephen Bannister, Caroline Holden, Sandra Bourguignon, and Graeme McVerry. 2017. The New Zealand strong motion database. *Bulletin of the New Zealand Society for Earthquake Engineering* 50 (1):1-20.

Vucetic, M., & Dobry, R. (1991). Effect of soil plasticity on cyclic response. *Journal of geotechnical engineering*, 117(1), 89-107.

Wair, B. R., DeJong, J. T., & Shantz, T. (2012). *Guidelines for estimation of shear wave velocity profiles*. Pacific Earthquake Engineering Research Center.

Wills, C. J., Petersen, M., Bryant, W. A., Reichle, M., Saucedo, G. J., Tan, S., & Treiman, J. (2000). A site-conditions map for California based on geology and shear-wave velocity. *Bulletin of the Seismological Society of America*, 90(6B), S187-S208.

Earthquake Effects on Heritage Structures and the MCE Paradox

Doug Jenkins¹

1. Managing Director, Interactive Design Services, NSW 2077.
Email: dougjenkins@interactiveds.com.au

Abstract

It is widely recognised that structures providing essential services should be designed and maintained to withstand a more extreme event than is required for other structures. It is also widely recognised that the difference between a typical design event and the more extreme Maximum Considered Earthquake (MCE) event is greater for regions of low to moderate seismicity than it is for regions of high seismicity. In spite of this, structural design codes for regions of high seismicity such as New Zealand contain detailed specific provisions for design for the MCE event, whereas codes for regions of lower seismicity such as Australia have no or limited detailed provisions. This is what I refer to as the MCE Paradox.

This paper will focus on heritage structures, reviewing recent studies on the expected performance of the dome of the Florence Cathedral under extreme earthquakes, and the actual performance of the Christchurch Basilica in the earthquakes of 2010 and 2011. The lessons from the detailed analysis of these structures will be considered in the Australian context, with recommendations for review of heritage structures under extreme earthquake events appropriate to the Australian region.

Keywords: maximum considered earthquake, design, heritage structures, extreme events

1.0 INTRODUCTION

The intent of this paper is to discuss the appropriate level earthquake to be considered, and the appropriate level and methods of analysis to be used, when reviewing heritage structures in Australia.

Recent analysis projects are reviewed, both for prediction of the effects of possible future earthquakes (the Dome of Santa Maria del Fiore Cathedral in Florence), and review of the collapse of a structure under earthquake loading (the Christchurch Basilica). The conclusions of these studies are discussed in the context of Australian heritage structures, and current practices for review of existing structures in Australia.

2.0 THE MCE PARADOX

In regions of high seismicity such as New Zealand it is standard practice to design structures for an 'Ultimate Limit State'(ULS) event, and also to check that they will not collapse under an event with a much longer return period, known as the 'Maximum Considered Earthquake' (MCE).

In regions of lower seismicity, such as Australia and Eastern USA, the difference in intensity between a ULS and an MCE event is much greater than in higher seismic regions (see Fig. 1), and standard structural detailing practices are much less robust. In spite of this, the requirement to design for an MCE event has not been standard practice, and structural design and detailing requirements have generally been introduced later, and are less specific. For example, the Australian code for building structures (AS 3600) only introduced requirements for design for earthquake actions in the body of the code in the latest revision (2018), and this still refers to the New Zealand codes (NZS 1170.5 and NZS 3101) for detailed requirements where high a level of ductility is required.

The apparently paradoxical result of this difference in approach to design for earthquakes is that although regions of high seismicity have much more frequent damaging earthquakes, the risks arising from extreme events with a very long return period may be greater in regions of lower seismicity. This is what I refer to as the MCE Paradox.

At the CATRisk 2014 Seminar (Leonard, 2014) the risks associated with extreme earthquake events in Australia were summarised as:

- 'There is considerable uncertainty in the earthquake hazard in Australia.
- Large earthquakes ($\geq M6.3$) can occur in all Australian cities with a return period 5000-7000 years
- Catastrophic earthquakes ($> M7.0$) can occur in or near most Australian cities with a return period 15000-25000 years'

The return periods quoted above are substantially longer than the maximum of 2500 years used in the Australian and New Zealand earthquake loading codes, but consideration of these longer periods is arguably necessary to comply with the Australian Federal 'Safety in Design' legislation, that requires all risks to be removed or reduced 'so far as is reasonably practicable'.

Older structures have a higher level of risk, because there were no requirements for the design for earthquakes at the time of their construction, and the materials used

have typically low ductility and robustness. Heritage structures present an especially high risk because:

- In many cases public structures may have a high occupancy level.
- Buildings may be built close to the limit of spans and heights for the materials used.
- Collapsed structures may be irreplaceable in their original form

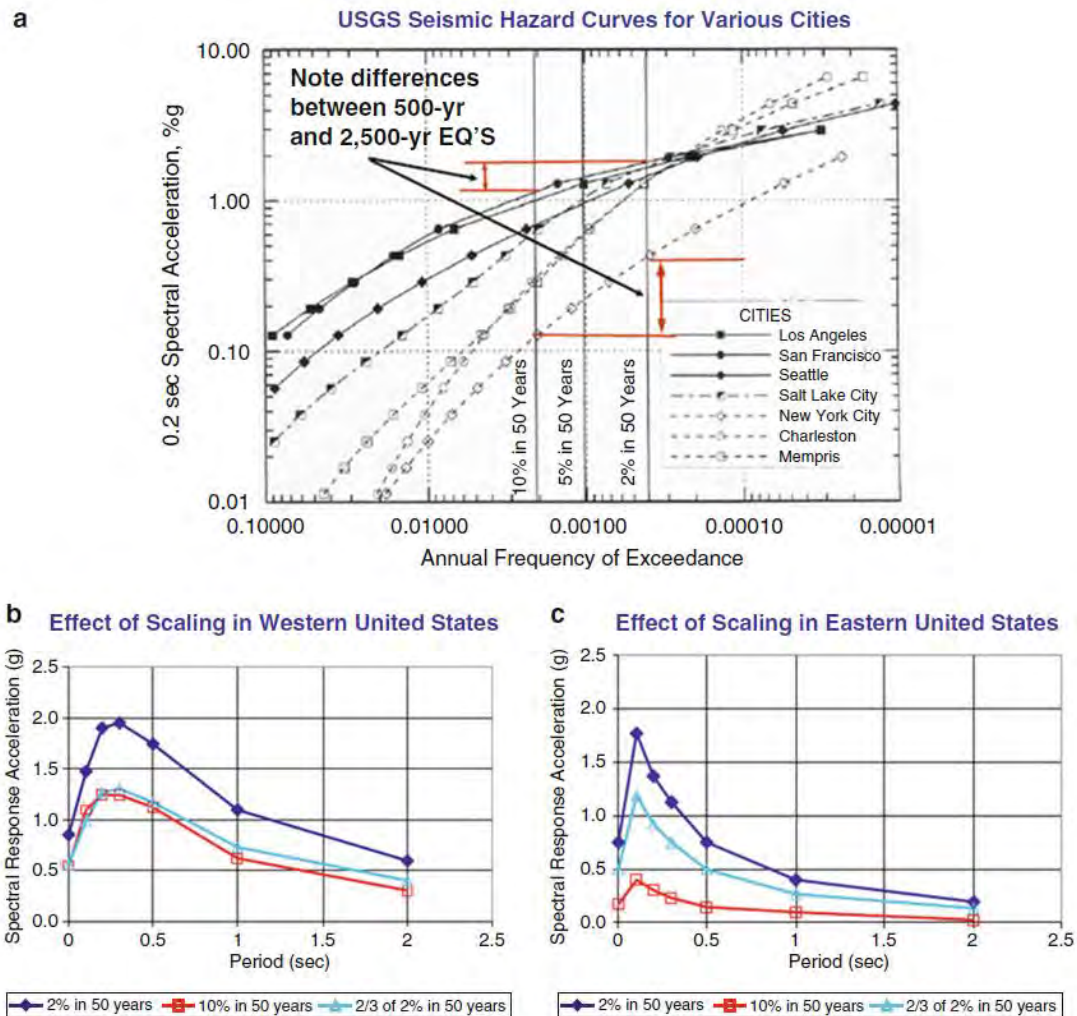


Figure 1 Comparison of hazard curves and UHS in US (Adopted from FEMA-451B (2003)); Tsompanakis (2014)

3.0 THE SANTA MARIA DEL FIORE CATHEDRAL

The dome of the Santa Maria del Fiore Cathedral in Florence, completed in 1436, was the first dome structure larger than the Pantheon in Rome (126 AD) and the Hagia Sophia in Constantinople (537 AD). The first documented cracks in the dome date back to 1639, but indirect evidence suggests that the cracks were initiated soon after the completion of construction, possibly having been caused by the strong earthquake of 1453, with further cracking probably caused by the earthquake of 1895 (Jenkins, 2013).

Investigation and monitoring of the cracks commenced in 1639, with continuous monitoring from 1955, and detailed analysis with modern techniques from the late 1980's.

The investigations of the mid-20th Century were primarily concerned with the possible adverse effects of maintenance work, but these were extended in the 1990's to include detailed computer models and investigation of differential settlement and thermal effects. These models have been further refined in recent years to analyse the effect of earthquakes (Coli, Marchetti, et al. (2013)). Analysis work by the University of Florence is reported by Bartoli, Betti and Borri (2015), with typical output from their dynamic analysis shown in Figure 2.

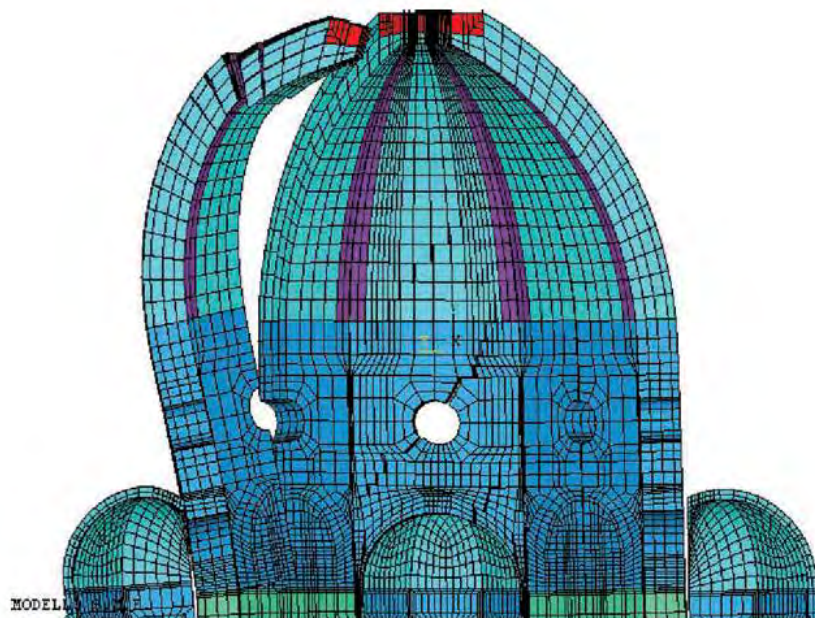


FIG. 34. Collapse configuration: global view.

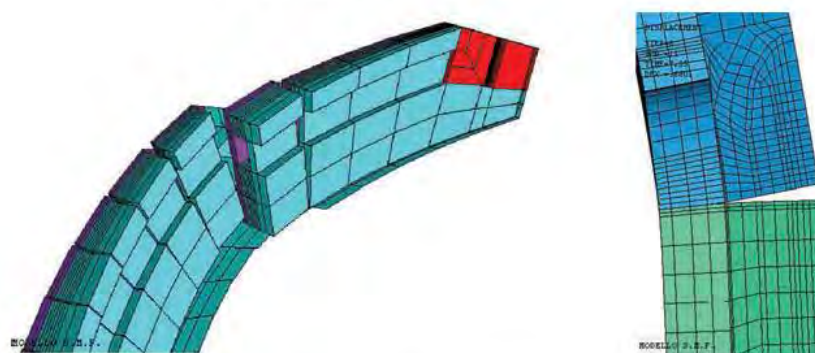


FIG. 35. Collapse configuration: details.

Figure 2 Typical dynamic analysis output (Bartoli, Betti and Borri (2015))

In the conclusion to their paper they state:

‘The study therefore represents but a first step in the evaluation of the monument’s behaviour under seismic-like forces assessing possible ultimate collapse mechanisms. Moreover the analysis of the latest data of the monitoring system will offer valuable information for both additional updating and validation of the finite element model, as well as for the seismic assessment of the monument. As a matter of fact, combination of results of numerical nonlinear models and simplified modelling strategies with the data obtained from long-term monitoring will make possible to formulate proper strategies for the structural preservation of the monument.’

4.0 THE CHRISTCHURCH CATHEDRAL OF THE BLESSED SACRAMENT

The Catholic Cathedral of the Blessed Sacrament in Christchurch was constructed between 1901 and 1905, primarily with stone used as an internal and external layer keyed into concrete poured in between.

The walls are generally 500 mm thick with 125 mm thick limestone cladding internally and externally, and no-fines concrete in-between. Some clay brick lining is used in places internally that are not visible from the main internal spaces.

The main dome drum is supported on four large arches that spring from first floor level. These arches have no-fines concrete internally with some areas of honey-comb construction to save weight. Some steel straps tie the structure together horizontally. Below this, the arches are supported by large columns with an internal spiral staircase. Typical images of failed walls are shown in Figures 3 and 4, from Lester & Brown (2012), which also provides further details of the construction and gravity and seismic load resisting systems.



Figure 3. South tower failure illustrating typical wall construction



Figure 4. Close-up of wall construction showing no-fines concrete and mesh floor reinforcing

The structure was evaluated for seismic loading in 2002, and strengthening works were carried out between 2002 and 2004. The evaluation at this time was based on simple calculations and engineering judgement, with more detailed analysis not being considered justified because the structure was thought to easily meet the low seismic loads applicable to existing structures in Christchurch at the time (Lester & Brown (2012)).

The cathedral suffered minor damage in the first of the Canterbury earthquakes on 4 September 2010, but major damage due to the M6.3 event on 22 February 2011, including total collapse of both towers and significant damage to the main dome. Following this event entry to the building was forbidden. Damage to the dome was worsened in the earthquake in July 2011, and following this event the decision was eventually made to demolish the dome.

In spite of the collapse of the towers, and the damage to the dome and subsequent demolition, Lester and Brown make the following points regarding the earlier strengthening of the structure:

- The building performed in excess of its expected capacity in an event that exceeded the design level accelerations significantly.
- The strengthening completed in 2004 undoubtedly prevented catastrophic collapse of the main part of the building.
- The strengthening of the towers finished at the 3rd floor level, ... The failure of the tower occurred where the strengthening stopped, as the accelerations exceeded the shear/sliding capacity of the walls, and the existing structure had no tensile capacity to resist overturning forces.
- The strengthening was carried out to a budget, and the intention of the strengthening was to address features of the building most at risk of failure in a seismic event. This strengthening enabled the building to perform to its expected capacity in the September 2010 earthquake, and most of the building performed better than expected in the February 2011 event.

5.0 NUMERICAL MODELLING OF THE CHRISTCHURCH CATHEDRAL

A detailed finite element analysis of the undamaged structure under earthquake loading was carried out by the University of Minho and University of Auckland (Silva, Mends, et al. (2018)). The main features of the model were:

- The structure was modelled using a combination of beam, plate/shell, and brick elements (Figure 5), to achieve an efficient compromise between reducing modelling and analysis time, and achieving an accurate and detailed model of the actual structure.
- A total-strain fixed crack model was adopted for the masonry and concrete elements, with a parabolic stress-strain relationship in compression, and exponential stress-strain in tension (Figure 6). Steel and timber were modelled as linear-elastic.
- Linear static analyses were carried out for static loads, followed by eigenvalue analyses to establish the structures dynamic behaviour, and non-linear static (pushover) analysis to model the behaviour of the structure under earthquake loading.
- Analyses were carried out to model the behaviour of the structure during the September 2010 earthquake, and the more damaging February 2011 event.
- The pushover analysis used an undamaged structural model for both considered earthquakes, on the basis that the structural damage resulting from the 2010 event was comparatively minor.
- The pushover analyses modelled only the horizontal earthquake accelerations. The authors noted that as a result the seismic capacity extracted from the analyses may be non-conservative.

Detailed results of the analysis are provided in the referenced paper. In summary, the results were in good agreement with the level of damage in the actual structure under the two earthquakes. The analyses indicated that the bell towers would become unstable at an acceleration of 0.35g for horizontal acceleration in the longitudinal direction (Figures 7 and 8).

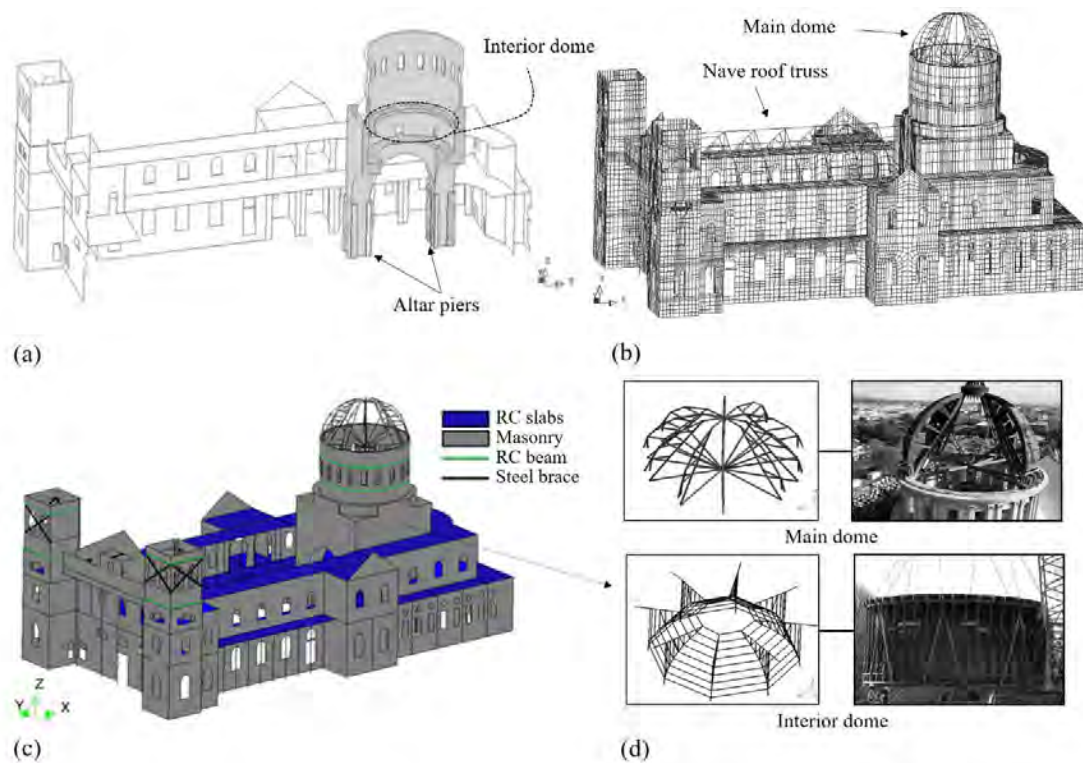


Figure 5. Three-dimensional model: (a) Shell and solid elements: west-east cut-away perspective with shell elements (coloured white) and solid elements (coloured grey); (b) Mesh discretization; (c) Description of the materials; (d) FE discretization of the main and interior dome.

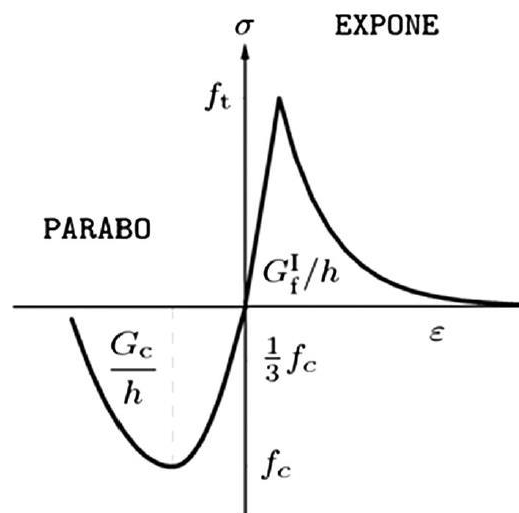


Figure 6. Stress and strain curves for the tension and compression regimes defined in the total strain fixed crack model.

Possible further strengthening of the structure was also investigated, based on addition of stainless steel tie rods and/or ring beams at the bell towers. The analyses found that both alternatives would substantially improve the structure's resistance to earthquake effects, such that it would survive an earthquake of the magnitude of the February 2011 event without collapse or major damage.

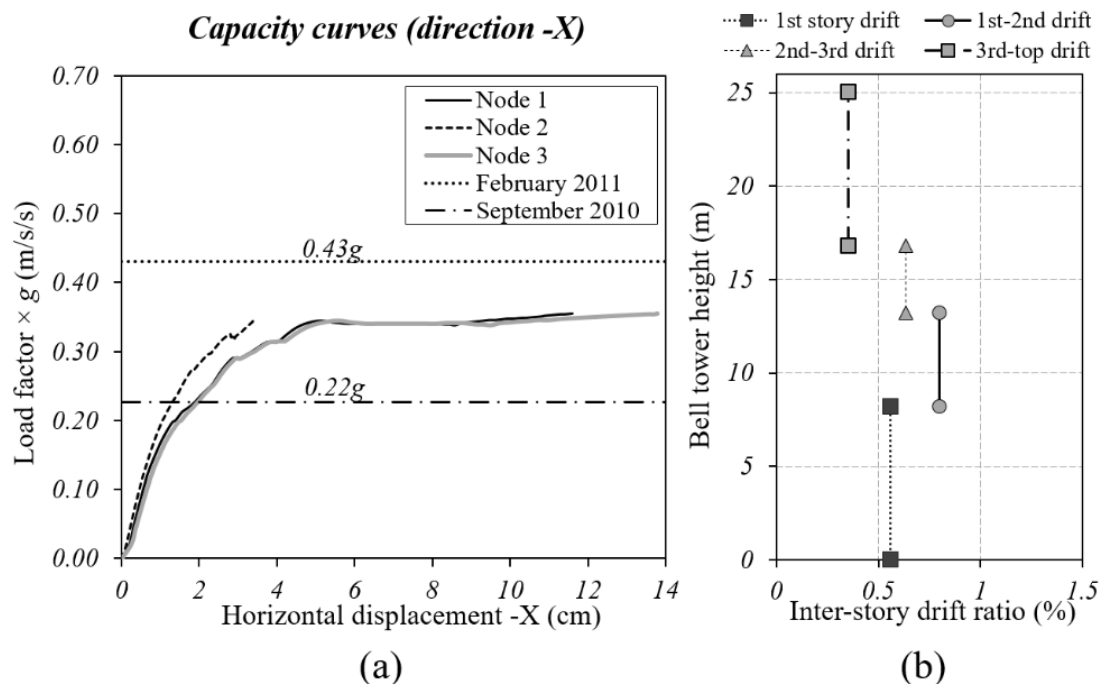


Figure 7: Pushover analysis in the longitudinal direction -X: (a) Capacity curves for control nodes 1, 2, and 3; (b) Inter-storey drifts ratio of the bell towers for an applied load factor equal to 0.35 g.

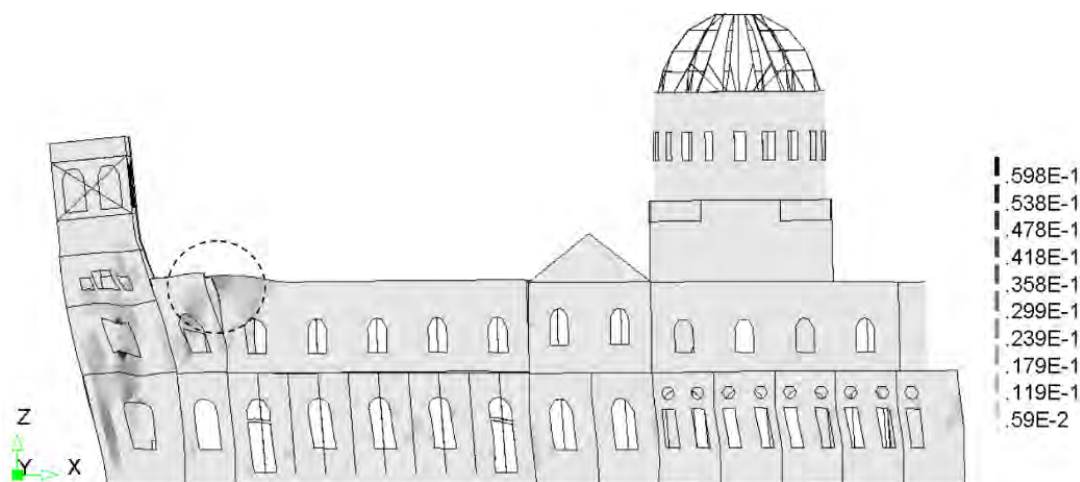


Figure 8: Principal tensile strains at the south façade walls for the pushover analysis in the longitudinal -X direction (0.35 g).

6.0 OTHER HERITAGE STRUCTURES IN CHRISTCHURCH

Two reports to the Canterbury Earthquakes Royal Commission provide comprehensive information on damage to heritage structures as well as other unreinforced masonry structures. They also discuss the history of prior work to improve the earthquake resistance of historic structures, including conflicts between preserving heritage values and reducing risk to occupants at minimum cost.

‘The Performance of Unreinforced Masonry Buildings in the 2010/2011 Canterbury Earthquake Swarm’ (Ingham & Griffith (2011)) examines the history of masonry construction and strengthening for seismic loads in New Zealand, and compares the performance of structures with and without seismic strengthening. It also

provides demolition statistics and information on the cost of seismic improvement. Recommendations are given for the identification and (where necessary) strengthening of all unreinforced masonry buildings in New Zealand, with strengthening work divided into four stages of increasing cost. It is recommended that all identified structures go through at least the first two stages as soon as possible, with further investigation for the application of Stages 3 and 4.

‘Heritage Buildings, Earthquake Strengthening and Damage’ (McClean (2012)) focusses on heritage structures in Canterbury, of which the majority are of unreinforced masonry construction, but including also significant numbers of buildings of timber-framed, steel, or reinforced concrete. It was found that the heritage buildings that were severely damaged or destroyed were largely of unreinforced masonry that had not been strengthened, or only partially strengthened. It notes that conservation plans for heritage structures do not take a uniform approach to earthquake-risk issues, with several plans developed post 2000 containing no explicit earthquake risk or strengthening policies. Whilst providing no specific recommendations for further strengthening work, the report notes that structures with existing strengthening performed significantly better than unstrengthened buildings of similar construction, but there was nonetheless a substantial proportion of strengthened structures suffering major damage or collapse under the February 2011 event.

7.0 SEISMIC RISK OF HERITAGE STRUCTURES IN AUSTRALIA

‘Characterisation of Heritage Masonry Construction in NSW’ (Howlander, Masia, et al. (2016)) reviews the risks associated with heritage masonry structures in NSW as a necessary part of the process of evaluating overall earthquake risk. Comparing earthquake risk levels in Australia and New Zealand it states ‘In terms of risk (i.e., probability times exposure), the lower seismic hazard in Australia compared to NZ is more than offset by the higher population and greater proportion of unreinforced masonry construction in Australian towns and cities. URM construction in Australia is also less likely to have been retrofitted, further increasing its vulnerability to earthquake loading. However, before these heritage buildings can be cost-effectively strengthened, their seismic capacity (or weaknesses) must be determined’.

A key point from the conclusions states that ‘The Newcastle experience serves as a reminder that assessment and mitigation of risk associated with the heritage URM buildings in NSW, and Australia more broadly, is of prominent importance for the safety of people and to preserve the buildings for their heritage importance.’

The Queensland State Earthquake Risk Assessment (Chesnais, Green et al. (2019)) provides an overview of earthquake risk in Queensland. The document provides ‘a scenario-based analysis of Queensland’s earthquake risk.’ It ‘seeks to complement and build upon existing Local and District earthquake risk assessments by providing updated and validated information relating to the changes in understanding of Queensland’s earthquake potential.’ The assessment is based on an earthquake equivalent to the 1989 Newcastle earthquake, which is considered to be ‘a credible worst-case scenario’, but was selected to have ‘a higher probability of occurrence than those previously considered catastrophic or extreme events.’ Nonetheless, the report comments ‘... a key finding of this 2019 updated assessment is that Queensland’s exposure to significant earthquake activity may have been underestimated in many previous assessments of the hazard.’

Other Australian states and the Federal Government have varying procedures and documentation for earthquake risk assessment and preparation. Examples of current public state government documents are 'Earthquakes in Victoria' (Quake Safe (2012)), 'South Australia's Earthquake Risk Assessment process' (Turner & Carr (2011)), and 'State Emergency Management Plan for Earthquake' (Department of Fire & Emergency Services, WA (2016)).

The Federal Government earthquake risk assessment, through Geoscience Australia, is focussed on the prediction of regional seismic ground acceleration, as summarised in 'The 2018 National Seismic Hazard Assessment for Australia - Model overview' (Allen, Griffin, et al. (2018)).

The recently published revision to the Australian Standard for concrete structures (AS 3600, 2018) provides significantly improved provisions for earthquake design of new buildings, but there have been no recent updates to standards for strengthening existing buildings, and the 1998 standard (AS 3826, 1998) is now withdrawn.

In summary, it is widely recognised that Australian cities may be subject to infrequent but highly damaging earthquakes, and that older buildings are most at risk, but there is limited research into the better evaluation of risks, inconsistent risk evaluation procedures between states, and no incentive for building owners to install strengthening for at-risk buildings.

8.0 CONCLUSIONS

The use of advanced computer techniques to analyse the expected performance of heritage structures under earthquake loading has only been introduced fairly recently, and the methods employed are considered to be still under development. The analysis of the Santa Maria Del Fiore however demonstrates that such analyses are practicable using established methods. The analysis of the Christchurch Basilica moreover showed that well established techniques such as push-over analysis can model the actual behaviour of a heritage structure with a reasonable level of accuracy.

In New Zealand there is a long history of strengthening of older structures, with the aim to at least achieve a specified proportion of the earthquake performance of new structures. Following the Christchurch earthquakes of 2010 and 2011 the required earthquake resistance level for older buildings has been increased, and the level of assessment of heritage and other older structures has increased.

The working of the MCE Paradox can clearly be seen in Australia, where it is recognised that whilst damaging earthquakes are much rarer than in New Zealand, when they do occur, an earthquake with a similar return period, close to an urban location, is likely to have much more severe effects, especially on older structures. The Australian Federal 'Safety in Design' legislation, requires that all risks must be removed or reduced 'so far as is reasonably practicable'. In spite of this, assessment of the resistance of older structures to earthquake loads is limited, and documented procedures for assessment have not been updated, with the applicable Australian Standard now being withdrawn.

It is clear that there is great potential for reducing the risk from damaging earthquakes with a systematic review of the likely performance of older structures, followed by strengthening work in those structures found to present the greatest risks. Implementation of such a policy presents many difficulties, including the possibility

of demolition of heritage structures where strengthening is considered to be too costly. There are however actions that can be implemented immediately that will be both a necessary part of future works, and a means to promote further action in the responsible state and federal government bodies, including:

- Update of Australian Standards for the strengthening of existing buildings, and the introduction of new standards for analysis and review of existing structures for earthquake loads.
- Review of the maximum return period of earthquakes applicable in Australia, considering the requirement of Safety in Design legislation to reduce risks ‘so far as is reasonably practicable’.
- Continuation and development of existing research into the behaviour of high-risk structures and building materials in the Australian context.
- Review of the analysis of structural behaviour of actual structures under historic earthquakes in Australia, using modern computer analysis techniques.
- Review and publication of the expected performance under earthquake loading of high-profile heritage structures in all of Australia’s major cities.
- The development of staged strengthening procedures for existing structures, as proposed in New Zealand following the Christchurch earthquakes.

REFERENCES:

Allen, T., Griffin, J., Leonard, M., Clark, D., and Ghasemi, H. (2018), The 2018 National Seismic Hazard Assessment for Australia - Model overview, Geoscience Australia, Canberra

AS 3600:2018. Concrete Structures. Standards Australia

AS 3826-1998: Strengthening existing buildings for earthquake, Standards Australia

Bartoli, G., Betti, M., and Borri, C. (2015) Numerical Modelling of the Structural Behaviour of Brunelleschi’s Dome of Santa Maria del Fiore, International Journal of Architectural Heritage: Conservation, Analysis, and Restoration, M.

Chesnais, M., Green, A., Phillips, B., Allen, T., Edwards, M., Sexton, J., Weatherley, D., Kruttschnitt, J. (2019) Queensland State Earthquake Risk Assessment 2019, Queensland Fire and Emergency Services, Brisbane

Coli, M., Marchetti E., Ripepe, M., Blasi, C., Ottoni, F., Bartoli, G., Betti, M. (2013), The Dome of Santa Maria Del Fiore in Florence: Historical, geotechnical, and structural studies for its conservation, ATC19 Work Shop on Geo Engineering for Conservation of Cultural Heritage 18th ICSMGE, Paris

Department of Fire & Emergency Services, WA (2016), State Emergency Management Plan for Earthquake, Government of Western Australia

Fanelli G., Fanelli M. (2004), ‘Brunelleschi’s Cupola, Past and Present of an Architectural Masterpiece’, Mandragora, Florence, Italy.

Howlader, M., Masia, M., Griffith, M., Ingham, J., Jordan, B., (2016) Characterisation of Heritage Masonry Construction in NSW - State Heritage Register, Australian Earthquake Engineering Society 2016 Conference, Melbourne.

Ingham, J., Griffith M.C. (2011), The Performance of Unreinforced Masonry Buildings in the 2010/2011 Canterbury Earthquake Swarm, Technical Report to The Canterbury Earthquakes Royal Commission.

Jenkins D. (2013) Structural ratchet mechanisms, ancient and modern, Concrete 2013, Concrete Institute of Australia, Gold Coast, Queensland

Leonard, M. (2014) Seismic Hazard in Australia, uncertainties and extreme event, Catastrophe Risk Seminar, Actuaries Institute, Sydney

Lester, J., Brown, A. (2012) Christchurch Cathedral of the Blessed Sacrament: Lessons learnt on the Stabilisation of a Significant Heritage Building, NZSEE Conference 2012, Christchurch, New Zealand

McClean, R. (2012), Heritage Buildings, Earthquake Strengthening and Damage, The Canterbury Earthquakes, September 2010-January 2012, Report for the Canterbury Earthquakes Royal Commission, New Zealand Historic Places Trust.

NZS 1170.5:2004. Structural Design Actions Part 5: Earthquake actions-New Zealand. Standards New Zealand.

NZS 3101:2006. Concrete Structures. Standards New Zealand.

Ottoni, F., Coisson, E. et al. (2010), The Crack Pattern in Brunelleschi's Dome in Florence: Damage Evolution from Historical to Modern Monitoring System Analysis, Advanced Materials Research, 133-134, pp 53-64.

Silva, L. C., Mendes, N., Lourenço, P. B., Ingham, J. (2018), Seismic structural assessment of the Christchurch Catholic Basilica, New Zealand, Structures, Vol 15, August 2018, pp 115-130

Tsompanakis, Y. (2014) Earthquake Return Period and Its Incorporation into Seismic Actions, Encyclopedia of Earthquake Engineering, Springer-Verlag Berlin.

Turner, S.G., Carr, J.M. (2011) South Australia's Earthquake Risk Assessment process using the National Emergency Risk Assessment Guidelines, Building Management, Department of Planning, Transport and Infrastructure, Adelaide.

Seismic Qualification and Design of Post-Installed Anchors in the Past, Present and Future

Balazs Kaknics¹

1.Codes & Approvals Manager, Hilti (Aust.) Pty Ltd, Rhodes NSW 2138. baz.kaknics@hilti.com

Abstract

Post-installed fasteners play a crucial role in tying together various structural and non-structural building components. These connections are subject to a great variety of actions and environmental conditions and must perform without failure over the entire design life of the structure. Studies conducted post-disaster have revealed the sensitiveness of post-fixed anchors to earthquake actions, such as excessive displacement or collapse under combined dynamic loads and concrete crack cycling.

Following major earthquakes, significant global research work has been conducted to improve the existing selection criteria and to develop new seismic prequalification methods for anchors. These efforts led to the advancement of relevant codes and guidelines in North America and Europe, which other countries tend to reference or adopt into their local legal frameworks. AS 1170.4, also known as the Australian earthquake design standard stipulates that all structures must transfer the seismic actions through their connections to the supporting foundation, however no further explanation or commentary is provided how to verify the adequacy of the connections.

This paper provides a global overview of the evolution of seismic anchor qualification and design guidelines through the demonstration of decades-long academic research and product development. The article demonstrates the state-of-art industry practices and highlights some of the present loopholes in the Australian standardization framework. Finally, a review is presented about the currently proposed updates to the AS 5216, the Australian anchor design standard.

1. Introduction

Despite Australia is considered as a tectonically stable continent, there are earthquakes of magnitude 6 or larger registered every couple of years in the country. The 1989 Newcastle earthquake with 13 fatalities and some significant damage demonstrated the country's exposure to seismic risk, which keeps growing with the increasing population density. Australia's building code accounts for this risk and ranks buildings according their importance, which in fact reflects the potential consequences of damage or failure. The earthquake design actions are ascertained based on the AS 1170.4 [31] and Section 8 of the same standard requires most non-structural building components and their fixings to be designed for seismic actions.

For the verification of the individual parts however, the designer has to rely on the existing standards and guidelines of various disciplines, which either entail seismic specifications or fail to address those. As for the fixings into concrete, the current national design standard, AS 5216 [30] does not set rules for the selection and verification of anchors under earthquake actions, therefore designers have no option but to apply engineering judgments to ensure the connection complies with the National Construction Code (NCC) [6] It is expected that the Australian anchor standard will be updated with seismic provisions during its next revision and in the interim, this paper seeks to provide an overview of the global engineering practices considered 'state of the art' for seismic anchor design.

The demonstrated principles equally apply for both the structural and non-structural utilization of fasteners, including mechanical and chemical types. It is also noted, that contrary to common belief, the *relative seismic demand* on non-structural fixings can be more severe compared to the structural ones due to the amplified oscillation of secondary building systems, as well as the less robustness of fasteners typically used in these applications. Following the logic of building Importance Levels in the NCC, where a greater level reflects greater consequence of failure, many non-structural applications could be ranked as 'highly important' or 'safety critical', too. *Clause 1.3.26* in the AS 5216:2018 [30] defines safety critical applications where a potential collapse could endanger human lives or result in considerable economic loss, noting that both structural and non-structural fixings may be considered safety critical.

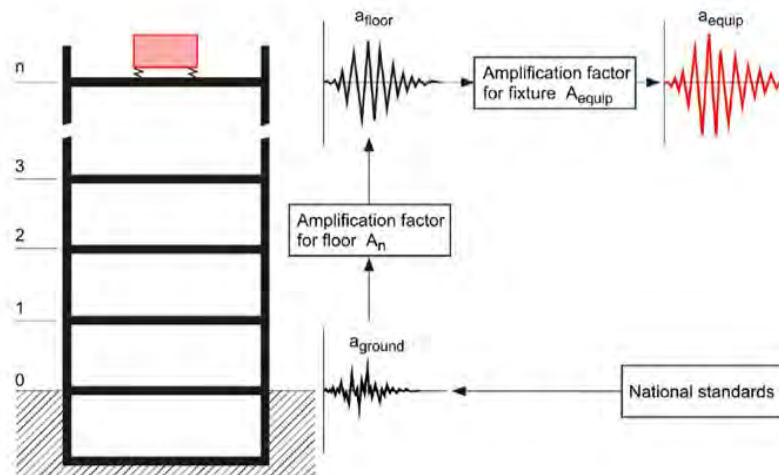


Figure 1 - Amplified seismic demand on non-structural building components

(Source: Hilti Guidelines for earthquake-resistant design of installations and non-structural elements, Schaen, Lichtenstein, 2003.)

The continued demographic growth, coupled with increased volumes of construction in Australia are calling for stronger code enforcement, so that the risks of unsafe or non-compliant buildings can be minimized. Improving the resilience of buildings against natural hazards, like earthquakes is becoming a fundamental part of engineering practices worldwide, with the focus of stakeholders gradually shifting from basic collapse prevention to minimizing damages. Numerous studies have been made to demonstrate the impacts and costs of failed non-structural components, which often make up the largest portion of the repair bill. By minimizing seismic damage and the required amount of rectification works, the downtime till full re-occupancy can be shortened, resulting in less economic loss.

The philosophy of better seismic resilience through damage mitigation is gradually finding its way into our national standards. For instance, the 2018-update of the AS 3600 [29] saw the addition of new detailing requirements in order to broadly improve the performance of concrete structures against earthquakes in Australia. Similarly, the new suspended ceiling standard, AS 2785:2020 [32] applies a wholistic approach to ensure ceilings can resist seismic, wind and fire actions, and all critical fixings into concrete must comply with the provisions of the AS 5216 [30]. To further mitigate the risks of non-compliant materials, regulators are receiving increasing power to be able to enforce code requirements on building sites. As such, the Residential Apartment Buildings Bill passed by the Parliament of NSW in 2020, commonly referred to as '*the RAB Act*' [33], enables the regulator to carry out site inspections and to withhold occupation certificates in the lack of conformity or compliance with the NCC [6]. In light of the advancements, a seismic review of safety critical anchoring applications is warranted to ensure that all structural and non-structural connections would hold up safely during a disaster event.

2. Historical overview of seismic anchors

2.1. The relevance of post-installed anchors

Traditionally, engineered concrete connections in the first half of the 20th century had been achieved by means of cast-in anchors or the early forms of anchor channels. The development of highly efficient, electropneumatic concrete drills in the 1960's was followed by the increasing popularity of post-installed anchors on construction sites, marking the beginning of a new era in fastening technology. Post-fixed mechanical anchors became widespread through the 70's, soon followed by the evolution of adhesive anchoring technologies, commonly known as chemical or bonded anchors. By the mid 1980's, both types of fastenings were specified by engineers to secure structural and non-structural connections likewise. The design of anchors was mainly achieved by utilizing manufacturer handbooks listing the allowable loads, which were typically derived from static pull-out and shear tests in uncracked concrete. For almost a quarter century, earthquake actions were not typically considered during anchor selection or design, unless the fasteners were specified for highly critical projects, such as nuclear power plants.

2.2. Seismic anchor awareness in the United States

In January 1994, the catastrophic Northridge earthquake hit the San Fernando Valley region of California, leaving over 50 fatalities and hundreds of injured people behind, with a damage bill considered one of the largest caused by natural disasters in modern US history [34]. Investigations of building failures revealed the vulnerability of the typical fixings used by the industry at that time, which resulted in a two-year ban of mechanical anchors for seismic-relevant applications. The problems identified after the Northridge event revealed the complexities of fastener selection and over the following years, two new acceptance criteria

were adopted to improve existing engineering practices. The first method was based on the CAN-CSA N287.2 [7] and involved a simulated seismic test with a cyclic load protocol, originally developed for nuclear power plants in Canada. The second, alternative method was established by the *Structural Engineers Association of Southern California* (SEAOSC) and similarly to the first one, fasteners were expected to undergo cyclic load tests [27]. As a result of the new measures, the International Code Council Evaluation Service (ICC-ES) resumed the listing of certain mechanical anchors for seismic applications in 1998. [28] It is important to note however, that neither of the new assessment methods called up tests in cracked concrete, which has a detrimental effect on the performance of anchors as demonstrated by numerous studies in the past, e.g. [11]. To address this, the first edition of the ACI 355.2 [2] (2001/2002) standard introduced a new seismic testing protocol for mechanical anchors. The assessment required the anchors to be set in a 0.5mm-wide crack during the cyclic load tests and even today, following minor adjustments, this standard forms the basis of seismic anchor qualification in the US.

2.3. Relevant anchor guidelines in Europe

During the 1990's, the member states of the European Union had been working on the harmonisation of construction products regulations, as a result of which the EOTA (*European Organization for Technical Approvals*) published the ETAG 001 series of guidelines in 1997 [12]. The documents set out requirements for the assessment of anchors in cracked and uncracked concrete in line with European design practices. In order to demonstrate the fitness of a fastener for the intended use and to acquire an ETA approval (European Technical Assessment), anchors were (and still are) required to pass a series of rigorous third-party tests. Despite the verifications in cracked concrete in the early ETAG guidelines, the framework did not include seismic assessments and for years to come, the American standards were considered as best global practice for the seismic verification of anchors.

The first seismic anchor specifications in Europe were made in relation to highly safety critical buildings, such as nuclear power plants. The KKW guidelines [9] issued by the *German Building Authority* (DIBt) in 1998 included considerations for extreme loading conditions, like earthquakes, blast load or aircraft impact. The qualification of anchors involved cyclic tension and shear tests in stationary cracks and a separate test in large opening and closing cracks, called crack-movement tests [25]. The historical significance of the KKW assessment method is the introduction of a cycling crack protocol, which became an integral part of the anchor assessment process over time. Still, for the seismic assessment of regular anchoring applications designers in Europe and other 'metric countries' had to resort to engineering judgments. To address the legislative loophole, an attempt by one of the industry associations headquartered in France emerged. CISMA, a trade association of construction manufacturers (*Construction Infrastructure Sidérurgie et Manutention*) published their general safety specifications including a reduction factor concept for the design of seismic anchors [8]. The prerequisite of utilizing the 'CISMA-method' was the availability of an ETA approval for cracked concrete. One of the shortcomings of this approach was however, that it did not require specific tests to verify fitness for the intended use, which did not align with the philosophies laid down in the harmonised Construction Product Directives (CPD) and ETAG guidelines.

2.4. Combined seismic anchor research

With the help of the growing collaboration between universities, manufacturers and government agencies, seismic research gained further momentum in the years prior to 2010. Complex shake table tests made it possible to investigate the interaction of various building components under extreme conditions. Investigations conducted in both Europe and the US

turned the attention of experts towards the changes occurring in the base material, such as the development of concrete cracks and their impact on anchor performance. During an earthquake, buildings are subject to dynamic movements and cracks are likely to develop, some of which intersect the location of the anchors. While in its elastic state, the reinforcement is capable of controlling the deflections and limit the width of the developing concrete cracks. Under repeated moment reversals the cracks start to open and close, which can reduce anchor capacity and increase displacements. Once the reinforcement yields, wider cracks and plastic hinges develop in the structure, followed by the extensive spalling of the concrete. Fixing into these zones is normally outside of the scope of anchor standards and similarly, this paper only covers anchors placed away from the high-deformation zones.

For the prequalification of anchors, in their research Mahrenholtz and Eligehausen highlighted the importance of the careful selection and phasing of load cycles with crack movements. The authors found that *'when the anchor load cycles are in-phase with the crack width cycles, the anchor displaces at a lower rate than in tests with a constant tension load because the load is only gradually becoming effective. The reduction in displacement is most pronounced when load and crack cycling are out-of-phase'* [23, pg.650]. For the purpose of the cyclic crack tests therefore, the authors recommended a constant load applied to the fastener instead of a variable load. Consequently, it was both reasonable and feasible to simplify the test setup by separating the crack movement and the cyclic load tests. Further experiments were conducted to find a representative loading protocol for a uniform qualification method [25]. Experts agreed that stepwise-increased sequences of cyclic loads and the concurrent monitoring of anchor displacement return the most accurate picture about seismic performance, such as the dynamic stiffness of the fastener. [17], [24], [28].

A significant milestone of seismic anchor research was the full-scale shake table and fire testing of a 5-storey reinforced concrete building at the University of California in San Diego in 2012. [10]. The building was outfitted with a variety of non-structural components, including MEP building services, internal and external architectural elements, a fully functional lift, as well as some critical functions, like a medical operation theatre and IT data centre. The preparation and conclusion of the BNCS project (*Building Non-Structural Components and Systems*) spanned over five years and the substantial dataset gained from the tests largely contributed to the current understanding of the seismic behaviour of various building components. From the fastenings point of view, the research verified numerous assumptions from previous simplified tests, such as the combined effect of crack cycling under and transient seismic load.

3. Overview of the present seismic anchor guidelines

3.1. The current European specifications

The learnings from both the BNCS project and broader global research had been utilized during the development of the current European seismic anchor guidelines. In 2013, the ETAG 001 Annex E [12] had been published by EOTA, introducing new requirements for the qualification and selection of metal anchors used in concrete under seismic actions. As a new element, the ETAG Annex E presented a two-level anchor qualification method designated as the seismic C1 and C2 anchor performance categories. The C2 specifications are more onerous than those of the C1, involving a greater number of assessments and more stringent requirements during the individual tests. The steps involved during the assessment of the respective performance categories are shown in *Table 1*:

Test No	Purpose	Concrete Strength (Mpa)	Crack Width (Constant)	No of Load Cycles	Loading Protocol
C1.1	Functioning under pulsating tension load	C20/25	0.5 mm	140	Stepwise-decreased pulsating tension load
C1.2	Functioning under alternating shear load	C20/25	0.5 mm	140	Stepwise-decreased alternating shear load

Test No	Purpose	Concrete Strength (Mpa)	Crack Width	No of Cycles	Loading Protocol
C2.1a	Reference tension tests in low-strength concrete	C20/25	0.8 mm (constant)	1	Static tension load
C2.1b	Tension tests in high-strength concrete	C50/60	0.8 mm (constant)	1	Static tension load
C2.2	Reference shear tests	C20/25	0.8 mm (constant)	1	Static shear load
C2.3	Functioning under pulsating tension load	C20/25	0.5mm (constant) 0.8 mm (constant)	50 25	Stepwise-increased pulsating tension load
C2.4	Functioning under alternating shear load	C20/25	0.8 mm (constant)	75	Stepwise-increased alternating shear load
C2.5	Functioning with tension load under varying crack width	C20/25	0 to 0.8 mm (varying)	59	Static tension load and stepwise-increased cycling crack

Table 1 - Required tests for seismic anchor qualification according to the *EOTA TR049* [14]

The ETAG Annex E also introduced a new selection criterion to be considered by the European member states. In this method, the assignment of the anchor performance categories is based on the level of seismicity and the importance class of the building. The seismicity level is decided as a combination of the peak ground acceleration and the soil factor relevant for the site. The building importance class is basically the same as the Australian building importance levels assigned by the NCC [6]. The minimum recommended performance categories in Europe are summarized in *Table 2*. Over its lifetime, the Annex E remained optional allowing member states to deviate from the selection criterion and to utilize national specifications instead. In 2016, the document has been superseded by the EOTA TR (Technical Report) 049 [14], which remains the primary referenced document for the seismic qualification of post-installed anchors today.

The first design provisions for seismic anchors were introduced in the EOTA TR 045 [13] guideline in 2013. The design method presented in the report followed the philosophy of limit state design similarly to other European specifications. The TR 045 served as an interim design guide until the publication of the EN 1992-4 standard in 2018, also known as the Eurocode 2 Part 4 - *Design of fastenings for use in concrete* (EC2-4) [15]. The current Eurocode supersedes multiple previous EOTA documents and contains both normative and informative provisions for the design of anchors under static, seismic, fatigue and fire loads. As for the seismic design of fasteners, EC2-4 Annex C sets out the verification requirements in a ‘normative’ fashion, however for the selection of the performance categories (C1 or C2) the member states are allowed to adopt their own national annexes. In Europe, seismic anchors can be designed as ductile or non-ductile elements, the latter intended for building systems that benefit from the dissipation of seismic energy by allowing non-recoverable displacements during the earthquake. For practical reasons, this article only covers the elastic anchor theory and does not discuss ductile testing and design requirements of fastenings.

Level of Seismicity		Importance Class			
Class	$a_g \times S^{***}$	I	II	III	IV
Very Low	$a_g \times S \leq 0.05 \text{ g}$	No seismic prequalification required			
Low	$0.05 \text{ g} < a_g \times S \leq 0.1 \text{ g}$	C1	C1* or C2**		C2
> Low	$a_g \times S > 0.1 \text{ g}$	C1	C2		
* For fixings of non-structural elements ** For fixings of structural elements *** a_g = design ground acceleration; S = soil factor					

Table 2 - Selection of the seismic anchor performance categories in Europe (*Eurocode 2-4* [15])

For elastic design, the characteristic seismic resistance against steel and pull-out failures are ascertained via physical testing following the specifications of the EOTA TR 049 [14] qualification document. The test results are summarized in the ETA report (see also in Section 2.3). The characteristic strength against concrete cone, pry-out and edge break-out failures are not product-dependant features and can be ascertained based on theoretical formulas. The design resistance (ULS) is derived from the characteristic values with the application of safety reduction factors, which account for the uncertainties of the base material (concrete or steel) and the reliability of the anchor performance based on installation and other environmental factors. In the next step, the smallest design resistance values in both tension and shear are selected as the governing failure modes, which are required to be greater than the respective seismic action effects. The final verification step is to check the combined tension and shear loads with the help of a dedicated formula adopted from a conservative, linear interaction curve.

3.2. Seismic anchor design in the United States

Anchor qualification in the United States is based on the provisions of the ACI 355.2 and ACI 355.4 standards for mechanical and chemical anchors respectively [2], [3]. The independent testing agency, ICC-ES (International Code Council Evaluation Service) reviewed and adopted the test criteria from the ACI 355.2 to develop its own acceptance criteria (AC) for both mechanical (AC193) and chemical anchors (AC308) [18], [19]. Similarly to the process in place in Europe, the ICC-ES oversees the qualification of the anchors and the test results are published in the relevant Evaluation Service Reports (ICC-ESR). Since the first introduction of the seismic tests in cracked concrete under cyclic loads in the ACI 355.2 (see also in Section 2.2), there has been no major changes in the qualification requirements in the United States. The steps of the assessment are summarized in *Table 3* and are very similar to the ones seen in the European C1 qualification method:

Test No	Purpose	Concrete Strength	Crack Width (Constant)	No of Load Cycles	Loading Protocol
12	Seismic tension	17 to 28 Mpa	0.5 mm	10 + 30 + 100	Stepwise-decreased pulsating tension load
13	Seismic shear	17 to 28 MPa	0.5 mm	10 + 30 + 100	Stepwise-decreased alternating shear load

Table 3 - Seismic anchor qualification tests in the US according to the *ACI 355.2-07* [2]

In order to decide, whether a seismically qualified fastener is required, the structure first needs to be assigned to a Seismic Design Category (SDC) as specified by the ASCE 7 standard [4]. The assignment of an SDC depends on the level of seismicity and the occupancy category of

the building, which is similar to the Australian building importance levels. The level of seismicity (or seismic demand) is ascertained by calculating the spectral acceleration response for two scenarios, one at the ‘short-period range’ and another at ‘one-second period’ utilizing the relevant amplification factors for the site soil conditions. The final SDC is then decided on whether the short-period or the one-second period yields the higher demand. Finally, the International Building Code (IBC) [21] stipulates that a seismically qualified anchor must be selected for SDC levels of C, D, E or F.

The seismic design of post-installed anchors follows the principles of Appendix D of the ACI 318 [1]. The provisions of this standard, similarly to the Eurocode 2-4, does not apply to the design of anchors in plastic hinge zones. To ascertain the seismic design strength of the anchors, the concrete-related failure modes are assessed based on static strength formulas adjusted by reduction factors, whereas the steel and pull-out failures are obtained via prequalification tests. The first option of designing the connection is to select a fastener, which is controlled by ductile steel failure. Most commonly, this can be achieved by either nominating a suitable embedment depth or diameter for the anchors, so that ductile steel failure occurs before concrete failure could develop. As a second option, the engineer can design the attachment or fixture to undergo ductile yielding before any anchor failure could occur. Alternatively, an elastic design option is provided during which the possibility of brittle failure modes, (e.g. concrete cone or edge breakout) is minimized with the application of conservative capacity reduction factors.

4. The way forward

4.1. Improvements on existing standards

In Section 3, the European seismic anchor qualification and design standards were demonstrated, which are generally viewed as the state of the art. It was also noted, that a great body of research had been undertaken in the United States, which strongly contributed to the development of the current European design guidelines. Considering the level of seismicity, particularly along the western shores of the United States, combined with the recent advancements of fastening technology, a review and update of the current specifications appear to be justified.

In June 2020, the ICC-ES approved its new acceptance criteria, AC510 - *Acceptance Criteria for Seismic Qualification of Post-Installed Anchors in Concrete* [20]. The document introduced three seismic anchor performance categories (ASPC's) coupled with detailed testing requirements. Out of the three categories, ASPC 1 and ASPC 2 follow the European C1 and C2 qualification methods, whereas ASPC 0 is only assigned to structures of SDC A and B, with no additional testing requirements. The introduction of the new acceptance criteria foreshadows the potential update of the ACI 355 standards, however at the time of writing there is no publicly available information yet about any proposed changes to the selection or design of seismic anchors.

In Europe, the individual member states may issue their own national guidelines to complement the specifications of the harmonised standards. For instance, the German national annex, DIN EN 1992-4/NA published in 2019 [16] deviates from the standard seismic anchor selection method of the Eurocode 2 by stipulating the anchor performance category based on the expected characteristic concrete crack width. Unlike the previously demonstrated methods, the DIN considers the likely seismic response of the building and provides a direct link between the expected damage (cracks) and the anchor performance requirements. For cases where this information is not available, the DIN recommends utilizing the ‘q’ (ductility) behaviour factor

to predict the extent of cracks in the structure. As an illustration of this method, for German buildings designed with a q -factor of 1.5 or smaller, the characteristic crack width is not expected to exceed 0.5mm during an earthquake and therefore, fasteners with a C1 qualification are deemed to be suitable.

4.2. Developing seismic anchor specifications for Australia

The Australian anchor design standard, AS 5216 [30] was instigated by the Australian Engineered Fasteners and Anchors Council (AEFAC) following its foundation in 2012. Since then, AEFAC has been working to develop and extend the standard to cover a broad range of safety critical applications. Over the past years, multiple studies were carried out with regard to the potential seismic update of the AS 5216. In their research, Lee et al. (2018) [22] compared the level of seismicity between Australia, Europe and the United States, and investigated the potential adoption of the global seismic anchor specifications to Australia. The study concluded that the level of seismicity in Australia was similar to the one of the east coast of the United States and that a potential adoption of the US guidelines would result in less stringent fastener requirements compared to the European approach. On the other hand, the authors called on further research to investigate whether a higher performance category, similar to the European C2 was required in Australia [22].

In a subsequent study, Pokharel et al. (2019) [26] analysed the expected crack width in typical concrete members under seismic conditions and found, that in certain cases the characteristic crack width could exceed 0.5mm outside the plastic hinge zones, set as the upper limit for the C1 category. Pokharel also pointed out that for cracks smaller than 0.5mm, the detrimental effects of crack cycling could not be fully ruled out, which is not accounted for in the C1 tests. The authors found that in some instances, fasteners with a C2 qualification could be necessary, the assessment of which covers moving cracks up to 0.8mm width [26]. Following on from the results, in 2020 Amirsardari et al. [5] modelled a series of typified concrete buildings to better understand the seismic response and expected damage of structures designed to Australian standards. The research established a link between the expected level of damage to building components, including anticipated crack width, and the extent of inter-storey drift, based on which a simple specification criterion has been proposed for the selection of the suitable anchor performance category [5]. The findings of the referenced studies form the foundation of the proposal initiated by AEFAC to update the AS 5216:2018 [30].

5. Summary

A global overview of the evolution of major seismic anchor guidelines has been provided. The paper explained the development of the qualification and selection criteria of seismic anchors over the past 25 years and covered the relevant design principles of safety-critical, post-installed connections. The European seismic anchor qualification methods are generally well accepted amongst experts and are likely to serve as a basis for future standard updates in both Australia and the United States. Further analysis is required however to adjust the local selection criteria for the two seismic performance categories, based on the region's seismicity and building characteristics. There is ongoing research to investigate the response and structural behaviour of typical Australian buildings in earthquakes, which will contribute to the seismic update of the AS 5216.

6. References

- [1] American Concrete Institute, 2014. ACI 318-14: Building Code Requirements for Structural Concrete and Commentary. American Concrete Institute.
- [2] American Concrete Institute, 2007. ACI 355.2: Qualification of Post-Installed Mechanical Anchors in Concrete. American Concrete Institute.
- [3] American Concrete Institute, 2011. ACI 355.4: Qualification of Post-Installed Adhesive Anchors in Concrete. American Concrete Institute.
- [4] American Society of Civil Engineers (ASCE), ASCE 7, 2010. "Minimum design loads for buildings and other structures", American Society of Civil Engineers.
- [5] Amirsardari, A., Pokharel, T., Lee, J., & Gad, E., 2020 Seismic performance categories for post-installed fasteners in Australia, Paper to be presented at the Australasian Earthquake Engineering Society Virtual Conference.
- [6] Australian Building Codes Board, 2019. National Construction Code. Canberra, ACT: Australian Building Codes Board.
- [7] Canadian Standards Association (CSA) CAN/CSA-N287.2-M91., 1991. Material requirements for concrete containment structures for ANDU nuclear power plants, (reaffirmed 2003)
- [8] Construction Infrastructure Sidérurgie et Manutention (CISMA), 2011. Recommandations professionnelles sur le chevilage, Section 8.2 - Tenue au séisme. www.cisma.fr
- [9] DIBt KKW Leitfaden., 1998. Use of anchors in nuclear power plants and nuclear technology installations, guideline for evaluating fastenings for granting permission in individual cases according to the state structure regulations of the federal states of Germany). Deutsches Institut für Bautechnik (DIBt), Berlin (in German)
- [10] Elide Pantoli, Michelle C. Chen, Tara C. Hutchinson, Rodrigo Astroza; Landmark Dataset from the Building Non-structural Components and Systems (BNCS) Project
- [11] Eligehausen, R. and Balogh, T., 1995. Behavior of fasteners loaded in tension in cracked reinforced concrete. Structural Journal, 92(3), pp.365-379
- [12] European Organisation for Technical Assessment, (EOTA), 2013, ETAG 001, "Guideline for European Technical Approval of metal anchors for use in concrete, Annex E: Assessment of Metal Anchors under Seismic Action", www.eota.eu
- [13] European Organisation for Technical Assessment (EOTA), 2013. TR 045: Design of Metal Anchors For Use In Concrete Under Seismic Actions, www.eota.eu
- [14] European Organisation for Technical Assessment (EOTA), 2016. EOTA TR 049 Post-installed fasteners in concrete under seismic action. European Organisation for Technical Approval, www.eota.eu
- [15] European Committee for Standardization (CEN)., 2018. EN 1992-4: Eurocode 2: Design of concrete structures - Part 4: Design of fastenings for use in concrete.
- [16] German Institute for Standardization (DIN)., 2019. DIN EN 1992-4/NA: National Annex - Nationally determined parameters - Eurocode: Design of concrete structures - Part 4; Designing of fastenings for use in concrete, English translation of DIN EN 1992-4/NA:2019-04. Berlin, Germany: Beuth Verlag GmbH
- [17] Hoehler, M.S. and Eligehausen, R., 2008. Behavior of anchors in cracked concrete under tension cycling at near-ultimate loads. ACI Structural Journal, 105(5), p.601.]
- [18] International Code Council Evaluation Service (ICC-ES), 2005. AC193: Acceptance criteria for mechanical anchors in concrete elements. International Code Council Evaluation Service, Inc. (ICC-ES), Whittier, California
- [19] International Code Council Evaluation Service (ICC-ES), 2005. AC308: Acceptance criteria for post-installed adhesive anchors in concrete elements. International Code Council Evaluation Service, Inc., Whittier, California

- [20] International Code Council Evaluation Service (ICC-ES), 2020. AC510: Acceptance Criteria for Seismic Qualification of Post-installed Anchors in Concrete. California, United States of America, <https://icc-es.org>
- [21] International Code Council (ICC), 2018. 2018 International Building Code, Section 1901.3: Anchoring Into Concrete, International Code Council, INC, California, United States of America, <https://codes.iccsafe.org/content/IBC2018P4>.
- [22] Lee, J., Pokharel, T., Tsang, H.-H., & Gad, E. F., 2018. Requirement for seismic performance of post-installed fastenings in Australia. Paper presented at the Australian Structural Engineering Conference (ASEC), Adelaide, Australia
- [23] Mahrenholtz, P., Eligehausen, R., 2016. Anchor Displacement Behavior during Simultaneous Load and Crack Cycling. ACI Materials Journal, 113(5).
- [24] Mahrenholtz, P., Eligehausen, R., Hutchinson, T.C. and Hoehler, M.S., 2016. Behavior of post-installed anchors tested by stepwise increasing cyclic load protocols. ACI structural journal, 113(5), p.997
- [25] Mahrenholtz, P., Wood, R.L., Eligehausen, R., Hutchinson, T.C. and Hoehler, M.S., 2017. Development and validation of European guidelines for seismic qualification of post-installed anchors. Engineering structures, 148, pp.497-508.
- [26] Pokharel, T., Lee, J., Amirsardari, A., Tsang, H.-H., & Gad, E., 2019. Seismic prequalification and design of fasteners in Australia. Paper presented at the Concrete 2019, Sydney, Australia
- [27] SEAOSC. 1997. Standard method of cyclic load test for anchors in concrete or grouted masonry, Structural Engineers Association of Southern California (SEAOSC), Whittier, California.
- [28] Silva, J.F., 2001, September. Test methods for seismic qualification of post-installed anchors. In International Symposium on Connections between Steel and Concrete (Vol. 1, pp. 10-12). RILEM Publications SARL.
- [29] Standards Australia, 2018., AS 3600:2018 - Concrete structures. Sydney, NSW., Standards Australia.
- [30] Standards Australia, 2018. AS 5216:2018 - Design of post-installed and cast-in fastenings in concrete. Sydney, NSW., Standards Australia.
- [31] Standards Australia, 2018. AS/NZS 1170.4 [R2018] - Structural design actions, Part 4: Earthquake actions in Australia, NSW., Standards Australia.
- [32] Standards Australia, 2020. AS/NZS 2785:2020 Suspended ceilings - Design and installation, NSW., Standards Australia.
- [33] The Parliament of New South Wales, Australia. 2020. Residential Apartment Buildings (Compliance and Enforcement Powers) Act 2020 No 9, Sydney, NSW.
<https://www.legislation.nsw.gov.au/view/html/inforce/current/act-2020-009>

Determination of Component Ductility Factors for Seismic Design of Non-structural Elements

M. E. Kusz¹, M. Sfahani²

1. Corresponding Author. Principal Structural Engineer, Director, KUSCH Consulting Engineers, VIC 3699
Email: martin@kuschgroup.com.au
2. Senior Structural Engineer, R&D Team Leader, KUSCH Consulting Engineers, QLD 4000
Email: mimo@kuschgroup.com.au

Abstract

The design of seismic bracing for suspended mechanical, electrical, hydraulic and fire services within buildings has received increased attention within Australia in recent years. Many products and systems have been developed to brace suspended services against seismic loads that are determined in accordance with AS1170.4, the Australian Standard for seismic design actions. The calculation of seismic design loads includes ductility reduction factors that are not well understood and often misused by consultants and designers of seismic bracing systems. This paper critically reviews the principles behind ductility load reduction factors, and the conditions that must be present for these factors to be valid. The ductility levels that can be expected of typical suspended services and bracing systems are explored. The relatively low ductility of common seismic cable bracing systems is discussed, highlighting how common industry practice is resulting in the design and installation of seismic braces that are significantly undersized. Appropriate ductility factors are proposed for common suspended services and bracing systems, with consideration of the expected performance under ultimate and serviceability limit states.

Keywords: seismic design, building services, non-structural component, ductility factor, seismic bracing, performance-based solution.

1. Introduction

Australia has a low seismic classification, compared to neighbouring countries such as New Zealand and Japan, with the continental mainland located a significant distance from tectonic plate boundaries. Despite this fact, destructive and rare intraplate type earthquakes have occurred within the short-documented history of the country that necessitates engineered provisions for seismic risk mitigation. The Australian Standard AS1170.4 Earthquake Actions in Australia has been developed to ensure that earthquake loads are considered in the design of buildings in Australia, as a means of addressing such risks. Since the first release of this code in the early 1990s, it has been revised several times to improve seismic resilience in structural design. In 2007, Section 8 – Design of Parts and Components was added to AS1170.4, containing specific provisions for the seismic design of non-structural components, including building services. The provisions of this section are similar to those found within the International Building Code, with some modifications to suite the Hazard Spectra and other parameters unique to AS1170.4. It is important to note that AS1170.4 is a design load standard only. While Section 8 specifies design loads for non-structural building elements, it provides no guidance on how to design such elements for these loads. Furthermore, it provides no guidance on acceptable performance levels of such elements, except to require that elements within an importance class 4 building must remain operational following a 1:500yr design event.

The standard provides three methods for the design of parts and components for earthquake actions, including the use of established principles of structural dynamics, the use of effective floor accelerations as described in Clause 8.2, or the simplified method as described in Clause 8.3. Clause 8.2 allows for the use of floor design accelerations, which would be determined by the building structural engineer during their seismic response analysis of the structure. Clause 8.3 provides a simplified, but more conservative approach, that approximates floor accelerations without any input from the structural engineer. While Clause 8.2 generally provides lower design loads, design floor accelerations are not commonly made available to non-structural trades, and therefore the simplified Clause 8.3 is more commonly used in industry.

The simplified Clause 8.3 method calculates the horizontal seismic load, F_c , used to design building parts and components, as the product of the following parameters (1)

where W_c is the component's weight and k_p , Z , $Ch(0)$, a_x , I_c , a_c , R_c are the probability, seismic hazard, spectral shape, height amplification, component importance, component amplification, and component ductility factors, respectively. These parameters are determined using AS1170.4. In Eq. (1), the product of the first three parameters, $k_p Z Ch(0)$, denotes the site response and a_x is used to reflect the building response at a certain height. As such, F_c can simply be determined by reading the corresponding values from this standard and substituting in the above equation.

This paper investigates the component ductility factor R_c , which AS1170.4 specifies as $R_c=1.0$ for rigid components with non-ductile or brittle materials or connections, and $R_c=2.5$ for all other components and parts. No further guidance on the appropriate use of this ductility factor is provided in AS1170.4, or in the AS1170.4 Commentary. A ductility factor of $R_c = 2.5$ provides a 60% reduction in seismic design loads for parts and components and is therefore often desired from a cost perspective. Conversely, the incorrect use of this factor can result in parts and components being designed for loads

that are only 40% of the actual required design load, and can result in significantly undersized outcomes that present unacceptable life-safety and performance risks.

The authors of this paper are aware of widely differing interpretations and practices within industry around the application of R_c . On the conservative end of the scale, $R_c = 2.5$ is used sparingly, and only for the design of structural members that will exhibit a good degree of ductile performance, and under ultimate limit-state (ULS) loads only. At the other end of the scale, $R_c = 2.5$ is being used frequently for design of whole systems, including elements with minimal ductility, steel and masonry connections, and with serviceability limit-state (SLS) loads for systems requiring continuous post-disaster functionality.

Urgent clarification on the appropriate use of R_c is required. In the following sections, the principles of ductility that underpin factors like R_c used will be investigated further.

2. Ductility factor or force-reduction factor? Does it matter?

Displacement or displacement ductility, commonly known as the ductility μ , has become a popular indicator to quantify structures' inelastic behaviour since initial attempts for development of performance-based structural design. Displacements are observable and can be realised publicly (visual), they are measurable with basic tools for real-world structures (residual), and they can easily be formulated for engineering application (mathematical). When it comes to force it is neither visual nor residual although it can be a mathematical indicator. Nevertheless, most structural design codes still cling to Force Based Design (FBD) methods because of appreciation of simple elastic analysis. A misleading concept herein is the equal displacement approximation which assumes that the elastic characteristics are the best indicator of inelastic performance. This simply implies that the force-reduction factor R is equal to displacement ductility μ , i.e. $R=\mu$, as shown in Figure 1.

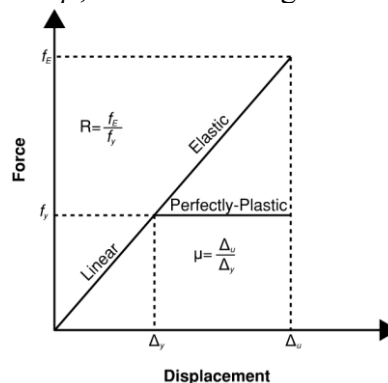


Figure 1 Equal displacement approximation

So far, it can be noted that AS1170.4 also utilises the above principle to specify R_c , as in the simplified method. There have been problems with this approach, 'in that it has long been confirmed that the equal displacement approximation is inappropriate for both very short and very long period structures, and is also of doubtful validity for medium period structures when the hysteretic character of the inelastic system deviates significantly from elastoplastic' (Priestly, 2000).

In general, the design displacement (seismic demand), i.e. Δ_d , can be expressed as

$$\Delta_d = \Delta_y + \Delta_p \leq \Delta_c \quad (2)$$

where Δ_y and Δ_p are displacement at first yield and plastic deformation, respectively, and Δ_c is capacity displacement (seismic limit-state). To use the ductility ratio AS1170.4 specifies for nonductile components, i.e. 2.5, Δ_p must be larger than 1.5 Δ_y . The reason is hysteretic energy dissipated within the nonlinear responses (e.g. $f_y \Delta_p$ for the perfectly-plastic case in Figure 1) increases damping and thus the seismic demand decreases. Note that Δ_c can also be expressed by different ductility ratios of Δ_y , to address different performance limit-states. These ductility ratios specify the seismic capacity and are different from the AS1170.4 specifications for seismic demand. When the limit-state ductility ratio (i.e. seismic capacity) is less than one (i.e. yielding threshold), Δ_d cannot be reduced since no energy dissipation occurs.

In contrast, interpretation of the above explanation with the force-reduction factor holds

$$F_c = f_y + f_E \leq F_u \quad (3)$$

where F_c is the component force in Eq (1), f_y is the yielding force, and F_u is the ultimate limit-state load capacity (i.e. the nominal load capacity reduced by a factor of safety). For steel structures, the Australian Standard AS4100 (1998) applies nominal load capacities lower than the plastic section bending moment or force, f_p . As such, f_E is by no means bigger than f_p however, with the assumption of equal displacement approximation, f_E must be bigger than 1.5 f_y for nonrigid components as per AS1170.4 specifications. This raises the question if adequate ductile performance can then be achieved for different seismic bracings. Such requirements are scrutinised for common seismic bracings, in the next section.

3. Ductility of suspended building services

Typical buildings contain a wide variety of suspended, non-structural systems and services, including ceilings, electrical, hydraulic, HVAC and fire services. These elements are typically suspended from the overhead building structure via steel threaded rod or plain rod (ceilings). While these ‘suspended rods’ provide suitable structural support for vertical gravity loads, they typically provide very little horizontal load resistance. Therefore, in order to resist horizontal seismic loads, suspended building elements typically require the addition of lateral load resisting systems at regular intervals. Often referred to as ‘seismic braces’, common systems include seismic cable braces, rigid braces using cold-formed steel (CFS) strut or threaded rod, or cantilevered steel post braces, which are discussed in further detail below. Each bracing system includes connections to the building structure and connections to the suspended service, and provides the inertial loads of the suspended service a load path back to the building structure.

When seismic design loads are determined for these bracing systems, it is essential that the ductility factor selected is appropriate for all elements within the system. As different elements within a brace will have different degrees of ductility, the design of a seismic design will inevitably result in different design loads for each element.

3.1. Threaded rods

For relatively low seismic loads, or when services are installed in close proximity to the building structure, threaded-rod support systems do provide some lateral resistance which can be relied upon. Figure 2 shows the load-displacement graph for a Grade 4.6 threaded rod under nonlinear static push-over (SPO) analysis. Both vertical (load) and

horizontal (displacement) axes were normalised by the theoretical yielding values for parametric justification purposes. As seen, the first yield happens at $\mu=1.0$ and $R=1.0$. The plastic section capacity (in terms of bending moment or force, f_p) can be also determined theoretically for circular cross section, i.e. $1.7 f_y$. This is approximated to be at $\mu=2.2$ and $R=1.7$, from the pushover curve in Figure 2. Finally, the steel hardening process can be determined by tracing the slope of the SPO curve, i.e. where the decreasing rate of change of slope becomes constant. This threshold is approximated to be at the $\mu=3.3$ and $R=1.82$. It should be noted, a quasi-dynamic (cyclic) test which captures the degrading Bauschinger effects could result in slightly varying numbers.

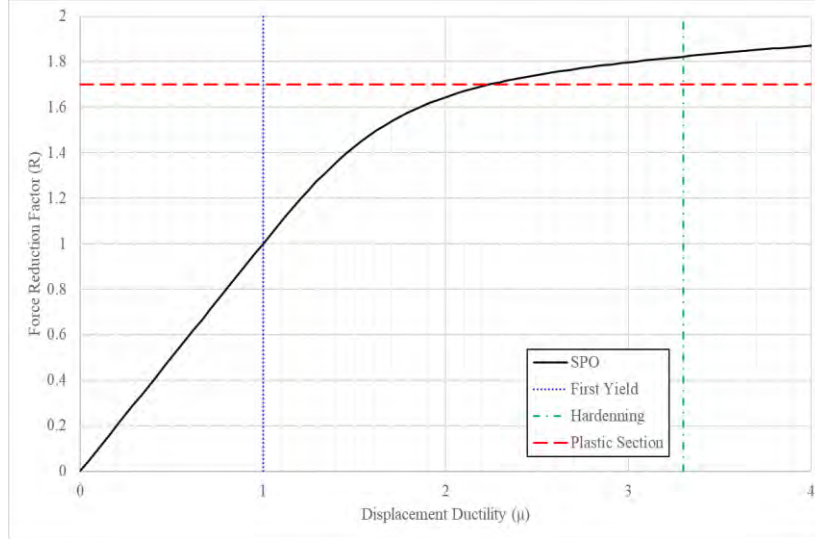


Figure 2 Inelastic response of thread rods gravity hangers

For the displacement-based design (DBD), the area under the SPO curve (i.e. work equals to force times displacement) can be interpreted as the dissipated hysteresis energy during inelastic behaviour. This increases the initial damping of the dynamic system, to a higher equivalent damping, which would diminish the cyclic responses. In other words, as a consequence of this process, the inelastic dynamic responses are less than static ones. There are some relations to establish such equivalent damping ratios (Priestly, 2000, Filiatrault et al., 2018) based on the originally proposed equation by Jacobsen (1960):

$$\xi_{eq} = \frac{E_{\Delta}}{2\pi k_{eq} \Delta^2} + \xi_i \quad (4)$$

where E_{Δ} and k_{eq} are the energy dissipated per cycle from the hysteretic behaviour and the equivalent (secant) inelastic stiffness at the target displacement Δ , respectively, and ξ_i is the nominal inherent damping ratio. Considering $\xi_i = 5\%$ for a non-structural component suspended by threaded rods, the equivalent damping, based on Eq (4) and the SPO analysis in Figure 2, is $\xi_{eq} = 32\%$. The displacement seismic demand corresponding to the equivalent viscous damping can be obtained through empirical modification factors or codified, as shown in the relationship below (CEN, 2004):

$$S_{D,i} = S_{D,eq} \sqrt{\frac{0.10}{0.05 + \xi_{eq}}} \quad (5)$$

Subsequently, for performing a linear static analysis, the total seismic demand can be reduced by about 48% (i.e. dividing by a factor of 1.92).

In an FBD, a primary question is the effect of ductile performance in the vertical load axis, similarly to that which can be observed in the horizontal displacement axis. As seen in Figure 2, this ductile performance in the vertical axis can't be achieved and it discourages using $R_c = 2.5$, as AS1170.4 advises for nonductile components can be expected. In fact, the R_c factor is applied here as substitute for the process explained above. However, to be comparable to that process, a $R_c = 2.5$ implements a $\xi_{eq} = 57\%$ or $\xi_i = 30\%$ requirement. Expecting such or higher damping factors for all non-structural components which are commonly classified as nonrigid is not realistic. In addition to this fact, the deterministic approach within AS1170.4, for choosing $R_c = 2.5$, misleads engineers without enough experience in seismic design. In the following section, the ductility of seismic bracing solutions commonly in use within the Australian building services industry are scrutinised.

3.2. Cable bracing

Seismic cable bracing is a common, versatile method for seismic bracing of suspended non-structural components. Their ideal uniaxial load performance, simplicity of installation and cost-efficiency makes them an appealing solution in many applications. Figure 3 shows some common brace configurations for suspended building services.



Figure 3 Cable braces used to seismically restrain building services

Destructive load testing of seismic cable bracing has demonstrated that these systems show negligible ductility after yielding and before reaching their nominal breaking capacity. For example, see Figure 4(a) which shows the load-displacement responses of such cable systems. As seen, the graph starts with a very low initial slope which corresponds to the take-up of play within looped cable connections. The load and displacement increase linearly to a peak, but there is no ductile behaviour after this point. The next sudden drop and increasing behaviour, which is observed repeatedly, is due to snapping of individual wires within the cable, starting from the most exterior fibres.

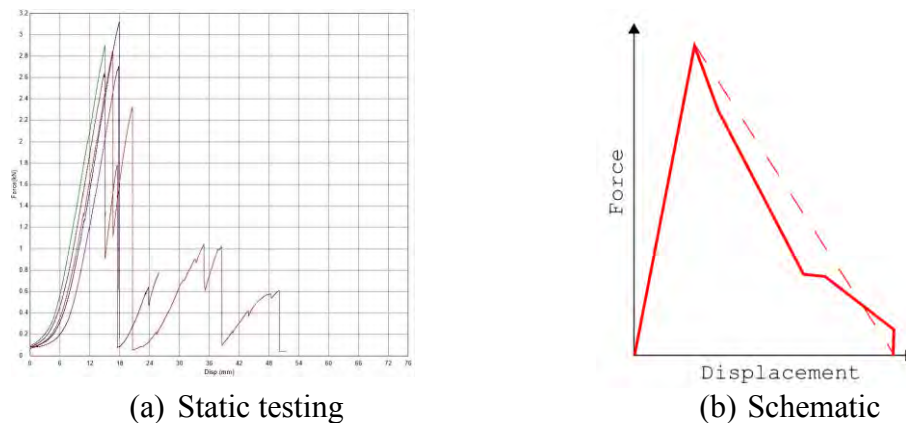


Figure 4 Force-Displacement response of a cable seismic bracing

Note the response illustrated in Figure 4(a) was recorded during a static tensile test. Therefore, under a cyclic loading regime, one or more wires would fail (breaking) in each load cycle while the remaining wires remain linear elastic. This makes the overall load-displacement response of the cable bracing triangular, as shown schematically in Figure 4(b). No softening-hardening behaviour can be seen in this response. In addition, the fact that wires are either elastic or snapped discourages consideration of any energy dissipation during the degrading response (dashed line). These observations imply that, despite using steel construction, this seismic cable bracing exhibits non-ductile behaviour and should be designed with $R_c=1.0$.

3.3. Diagonal struts

Cold-formed steel (CFS) channel or ‘strut’ is widely used in many different configurations to support building services and non-structural components. Figure 5 shows an example of struts used to seismically restrain hydraulic services. These braces are mainly fabricated to provide seismic resistance via their axial stiffness (tension and compression), but they are also used as a two-point hinge brace (longitudinal and lateral), i.e. like a simply supported beam, or less effectively as a cantilevered beam. The CFS struts’ material properties are similar to that of threaded rods. In addition, the slotted fabrication and/or thin-walled open cross-sectional properties of the struts, which trigger the necking and/or local distortions, promise a fairly ductile behaviour. This also applies to the baseplates and shear/tension bolts that are used in conjunction with the struts. However, such ductile behaviour is not guaranteed when friction resistance operated fittings such as channel nuts are used with struts. This is evidently because no extra load capacity can be expected when the friction load capacity is reached. Therefore, as a matter of load reduction for the design purposes, $R_c = 1.0$ must be used to design the friction resistant fittings but the rest of assembly can be designed with $R_c = 2.5$.



Figure 5 Diagonal CFS strut bracing

3.4. Cantilevered post

The single or multi-point cantilevered seismic posts are fabricated using a robust CFS strut or square hollow section (SHS) welded or bolted to a square baseplate, which provide resistance in all directions through their bending moment capacity. Figure 6 shows examples of cantilever strut post bracing. Due to the lower rotational (than axial) stiffness, which produces such capacity, expecting a ductile behaviour for a seismic post before absolute failure is fair and therefore using $R_c = 2.5$ is appropriate. Nevertheless, special attention needs to be paid to some welding or bolted connections (post to baseplate) types to ensure they are not brittle (e.g. poor welding or some Grade 8.6 or stainless-steel type bolted connections).



Figure 6 Cantilevered post bracing

3.5. Concrete anchors

Seismic rated concrete anchors are a fundamental element of seismic bracing. In general, any type of seismic bracing needs to be restrained via such anchors, to comply with the Australian Standard AS5216 (2018). The design process explained in this standard has yet not been validated for seismic loads and users can apply the European Standard EN 1992-4 (2018) for such purposes. Nevertheless, the extensive diversity of these anchor products and the tedious design process in these standards has led most manufacturers to develop their specific design software and technical support for the industry.

Concrete anchors are manufactured from steel and metal alloys with various material properties and they are designed to work in tension and shear. For most cases, the existing design software considers the initial combined yielding stress as the anchors'

failure threshold. In addition, the concrete cone or edge failure is a likely mechanism in seismic anchors. As a consequence of such a complex behaviour, justification for ductile performance becomes very difficult and all anchors are recommended to be designed with $R_c=1.0$.

4. Conclusion

The seismic design of non-structural components and building services is a relatively new concern within Australian building construction. The Australian Standard AS1170.4 provides the seismic design loads for such services, but minimal guidance on how to design such systems for these loads. In this paper, the principles of load reduction factor, R_c (i.e. the so-called component ductility factor in AS1170.4) have critically been discussed and reviewed. For engineers involved with the seismic design of building services, it is important to understand that a ductility factor of $R_c=2.5$ will reduce the seismic design load of a seismic brace or support, to utilise the plastic performance of that brace or support. Appropriate consideration should therefore be given to the suitability of bracing systems operating beyond their yield limit, if large ductility factors are to be used. The following recommendations for seismic design are made:

- Displacement is a more appropriate indicator of structural performance than force due to it being observable, measurable and applicable for design and analysis purposes. The validity of equal displacement approximation is doubtful, specifically when systems are designed to exhibit inelastic behaviour and for the ultimate limit-state.
- For DBD method at $\mu = 3.3$, threaded rods approximately show an extra 27% damping ratio ($\xi_i = 5\%$ and $\xi_{eq} = 32\%$) due to hysteresis energy dissipation which reduces the seismic demand by approximately 48%. Using $R_c = 2.5$ in a FBD leads to a 60% load reduction and effectively implements a $\xi_{eq} = 57\%$ or $\xi_i = 30\%$ requirement.
- Seismic cable brace systems do not perform in a ductile manner and must be designed for loads determined using $R_c = 1.0$. The use of $R_c = 2.5$ will result in design loads that are only 40% of the required demand. With break strengths of approximately 1.5 to 1.7 times typical published ULS capacities, cable systems designed to their capacity with $R_c = 2.5$ would be expected to fail under a seismic design event.
- Diagonal or horizontal struts made of CFS are relatively ductile seismic bracing systems and can be designed with $R_c = 2.5$, unless friction resistance operated fittings are used with the struts in which case seismic design must be conducted by using $R_c = 1.0$.
- Cantilevered posts with welded (or bolted) baseplates are also ductile seismic bracing systems and can be designed with $R_c = 2.5$. Special attention however needs to be paid to ensure the same level of ductility is present for the welded or high strength metal bolted connections in tension and shear.
- Seismic rated concrete anchors have a brittle failure mechanism and do not exhibit ductile behaviour. Anchors should always be designed with $R_c = 1.0$.

- While $R_c = 2.5$ may be appropriate for ductile brace systems under ULS loads, they are unlikely to be appropriate for SLS2 loads where post-disaster functionality is required. In most cases, 1:500yr loads with $R_c = 1.0$ will exceed 1:1500 loads with $R_c = 2.5$ and will likely govern the design.

REFERENCES:

Standards Australia, AS4100 - Steel structures., NSW, Australia. 1998.

ASHRAE. A Practical Guide to Seismic Restraint. 2017.

CEN. EN-1998-1: 2004: E: Eurocode 8—Design Provisions for Earthquake Resistant Structure. Comité Européen de Normalization Brussels, Belgium; 2004.

Filiatrault A, Perrone D, Merino RJ, Calvi GM. Performance-based seismic design of non-structural building elements. *Journal of Earthquake Engineering*. 2018;1-33.

Jacobsen LS. Damping in composite structures. II WCEE, Tokyo, 1960. 1960.

Perrone D, Filiatrault A, Peloso S, Brunesi E, Beiter C, Piccinin R. Experimental seismic response evaluation of suspended piping restraint installations. *Bulletin of Earthquake Engineering*. 2020;18(4):1499-524.

Priestley M. Performance based seismic design. *Bulletin of the New Zealand society for earthquake engineering*. 2000;33(3):325-46.

Standards Australia, AS1170. 4 - Structural Design Actions., NSW, Australia. 2007.

Standards Australia, AS5216 - Design of post-installed and cast-in fastenings in concrete., NSW, Australia. 2018.

European Standards, EN 1992-4 - Eurocode 2 - Design of concrete structures - Part 4: Design of fastenings for use in concrete., Ireland. 2018.

Seismic Stability of Slopes Subject to Loads from Shallow Foundation

Erin H. Y. LEUNG¹, Aslan S. HOKMABADI²

1. Senior Geotechnical Engineer (BEng, PhD, CEng, MICE, MHKIE), Arup, Hong Kong Office.
Email: erin.leung@arup.com.
2. Corresponding Author. Senior Geotechnical Engineer (BEng, MSc, PhD, MIEAust, CEng, NER), Arup, Sydney Office.
Email: aslan.s-hokmabadi@arup.com.

Abstract

Previous studies have shown that earthquake-induced landslide hazard is not significant in low-to-moderate seismicity region like Hong Kong unless the slopes are close to failure at the time of earthquake. This paper extends previous studies to assess the effect of seismic loads from shallow foundation on slope stability. The assessment is based on pseudo-static approach which allows efficient parametric study of the stability of slopes with various geometries, materials and groundwater conditions under a range of seismic foundation loads. Downward slope displacement is estimated from the yield acceleration using semi-empirical methods based on sliding block model. The seismic performance of the slopes is assessed by comparing the calculated yield acceleration and the threshold yield acceleration corresponding to slope displacement limits commonly considered in international practices. Criteria in terms of yield acceleration of slope and design seismic action under which seismic slope stability checking is required are proposed which can be incorporated in seismic design standard.

Keywords: seismic slope stability, seismic slope displacement, shallow foundation

1. Introduction

Seismic slope stability assessment is one of the important aspects in geotechnical earthquake engineering as landslides can pose serious threat to human lives and properties. The hilly terrain and dense population in Hong Kong result in urban development over sloping ground and therefore slope stability is a major engineering concern. Common methods of seismic slope stability assessment include analytical methods using the simplified pseudo-static approach based on the Newmark's method and numerical dynamic time-history analyses.

Pappin & Bowden (1998) studied the likelihood of earthquake-induced landslides for typical cut slopes and fill slopes in Hong Kong through a parametric study using pseudo-static analysis and Newmark sliding block model for seismic slope displacement calculation. The study concluded that the slopes need to be close to failure, i.e. having factor of safety marginally greater than 1, for the risk of earthquake-induced landslides to become a concern under a ground motion with a return period of 475 years. Subsequent studies including Arup (2018) and Sze et al. (2019) arrived at a similar conclusion based on the results of both numerical dynamic time-history analyses and empirical correlations. All the above studies have not considered the effect of foundation loads acting on the slopes.

This study investigates the seismic stability of slopes subject to loads from shallow foundation acting on the slope crest. The relationships between yield acceleration of slope and design seismic action in Hong Kong corresponding to seismic slope displacement limits commonly considered in engineering practice are developed, which form the criteria for assessing seismic slope stability. The range of yield acceleration of typical slopes in Hong Kong subject to foundation loads is assessed through a parametric study using pseudo-static analysis. This is compared to the established criteria to provide an indication of the performance of the slopes under seismic action.

2. Seismicity of Hong Kong

The contour of peak ground acceleration (PGA) at bedrock for a return period of 475 years from the latest seismic hazard analysis for the Hong Kong region is shown in Figure 1 (Arup, 2015). A PGA value of 1.18 m/s^2 (0.12 g) covers all the land area in Hong Kong and is adopted in the analysis.

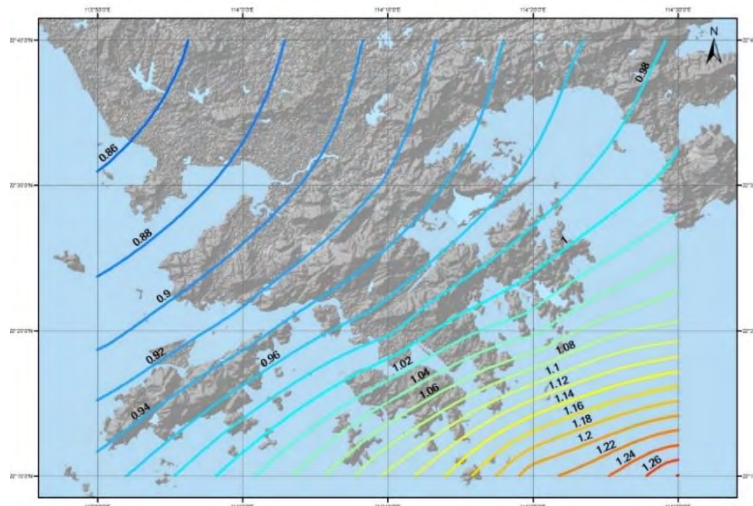


Figure 1. Contour plot for bedrock PGA (m/s^2) for a return period of 475 years in Hong Kong

3. Static factor of safety for slopes in Hong Kong

The minimum factors of safety required for new slopes in Hong Kong (BD, 1999) are shown in Table 1.

Table 1. Minimum static factors of safety for new slopes in Hong Kong (BD, 1999)			
ECONOMIC	CONSEQUENCE-TO-LIFE		
CONSEQUENCE	Category 1	Category 2	Category 3
Category A	1.4	1.4	1.4
Category B	1.4	1.2	1.2
Category C	1.4	1.2	>1.0

Slopes subject to shallow foundation loadings are expected to have a high consequence in the event of failure due to the proximity to buildings. This corresponds to a minimum static factor of safety of 1.4 as per Table 1. As such, the seismic stability of slopes with a minimum static factor of safety of 1.4 are investigated in this study.

4. Analysis approach

4.1 Pseudo-static analysis

The analysis is based on pseudo-static approach. The computer program *Oasys Slope* is used for the slope stability analysis. Static analysis is first conducted. For each case, the maximum static vertical foundation load (surcharge) that can be applied to maintain the target minimum static factor of safety of 1.4 are estimated, with values ranging from 12 kPa to 425 kPa.

For seismic analysis (see Figure 2), the seismic vertical foundation load is assumed to be the same as the static vertical foundation load and the seismic horizontal foundation load is calculated based on the seismic analysis of the superstructure. The seismic inertia forces acting on the soil mass are estimated using Equation (1) and Equation (2), with the reduction factor $\alpha = 0.5$ as per Eurocode 8.

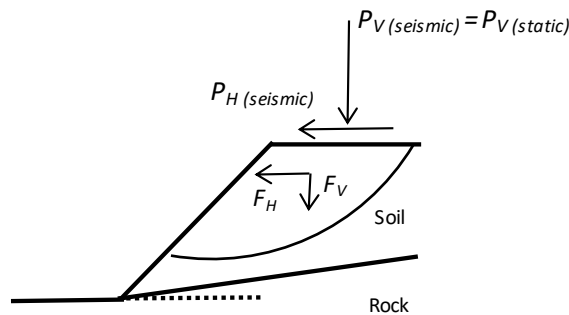


Figure 2. Schematic of seismic slope stability analysis subject to shallow foundation loads

$$F_H = k_{h(slope)} \times W; F_V = 0.5 \times F_H \quad (1)$$

$$k_{h(slope)} = \alpha \times I_E \times S_T(x) \times S \times a_{gR}/g \quad (2)$$

where F_H and F_V are soil inertial forces in horizontal and vertical directions, respectively, W is weight of the sliding soil mass, P_H and P_V are foundation loads applied on the slope as surcharge in horizontal and vertical directions, respectively,

$k_{h(slope)}$ is horizontal seismic coefficient for slope analysis, α is the reduction factor to account for soil flexibility (wave scattering), I_E (=1.0, 1.4, 1.7) is the importance factor, $S_T(x)$ (=1.0, 1.2, 1.4, 1.6) is the topographic amplification factor as a function of the distance from the crest (x), S (=1.0, 1.7, 2.0) is the soil factor, and a_{gR} (=0.12 g) is the reference horizontal peak ground acceleration on bedrock. The values in the parentheses show the variation of those parameters considered in this study. It is noted that the value of $S_T(x) \times S$ would rarely exceed 2 in practice.

Arup previous studies (Arup, 2018) showed that the effect of vertical seismic acceleration is negligible on the generated down-slope displacement in Hong Kong, and thus it has been ignored in the analysis (F_V is assumed to be zero).

4.2 Slope downward displacement calculation

Earthquake-induced sliding displacement is an index commonly used to assess the seismic stability of slopes. Various empirical correlations for seismic slope displacement calculation are proposed in the literature that differ in terms of the type and number of earthquake records considered (database), the analytical model used in calculating the seismic slope displacement, the mathematical model used in developing the predictive equation for the slope displacement, and the conditioning variables adopted in the equation, etc. Most of the current methods for predicting seismic slope displacement are largely based on the landmark works of Newmark (1965) and Makdisi & Seed (1978). Table 2 summarises the empirical correlations considered in this study.

Table 2. Empirical correlations for slope downward displacement calculation adopted in this study

Reference	Empirical Correlation
Hsieh & Lee (2011) [rigid block]	<p><u>Proposed correlation</u></p> $\log D_n = 0.847 \log I_a - 10.62 A_c + 6.587 A_c \log I_a + 1.84 \pm 0.295$ <p>Note:</p> <ul style="list-style-type: none"> Without the last term, the equation gives the median estimate of slope displacement. With the last term, it gives the value of one standard deviation below or above the median.
Jibson et al. (2000) [rigid block]	<p><u>Proposed correlation</u></p> $\log D_n = 1.521 \log I_a - 1.993 \log A_c - 1.546 \pm 0.375$ <p>Note:</p> <ul style="list-style-type: none"> Without the last term, the equation gives the median estimate of slope displacement. With the last term, it gives the value of one standard deviation below or above the median.
Saygili & Rathje (2008) [rigid block]	<p><u>Single-parameter scalar model</u></p> $\ln D_n = 5.52 - 4.43 (A_c / PGA) - 20.39 (A_c / PGA)^2 + 42.61 (A_c / PGA)^3 - 28.74 (A_c / PGA)^4 + 0.72 \ln PGA + \varepsilon \sigma_{\ln D}$ <p><u>Two-parameter vector model</u></p> $\ln D_n = -1.56 - 4.58 (A_c / PGA) - 20.84 (A_c / PGA)^2 + 44.75 (A_c / PGA)^3 - 30.5 (A_c / PGA)^4 - 0.64 \ln PGA + 1.55 \ln PGV + \varepsilon \sigma_{\ln D}$ <p><u>Three-parameter vector model</u></p> $\ln D_n = -0.74 - 4.93 (A_c / PGA) - 19.91 (A_c / PGA)^2 + 43.75 (A_c / PGA)^3 - 30.12 (A_c / PGA)^4 - 1.3 \ln PGA + 1.04 \ln PGV + 0.67 \ln I_a + \varepsilon \sigma_{\ln D}$ <p>Note:</p> <ul style="list-style-type: none"> ε is the standard normal variate with zero mean and unit standard deviation. To calculate the median estimate of the slope

displacement, ε is set to zero, whereas for 1 standard deviation above the median, ε is set to +1, etc.

- $\varepsilon\sigma_{\ln D}$ is the standard deviation in natural log units (1.13 for Single-parameter scalar model; $0.41 + 0.52 (A_c / PGA)$ for Two-parameter vector model; $0.20 + 0.79 (A_c / PGA)$ for Three-parameter vector model).

Bray & Travasarou (2007)

Rigid sliding block ($T_s < 0.05s$)

$$\ln D_n = -0.22 - 2.83 \ln k_y - 0.333 (\ln k_y)^2 + 0.566 \ln k_y \ln PGA + 3.04 \ln PGA - 0.244 (\ln PGA)^2 + 0.278 (M_w - 7) \pm \varepsilon$$

Deformable sliding block ($0.05s \leq T_s \leq 2.0s$)

$$\ln D_n = -1.10 - 2.83 \ln k_y - 0.333 (\ln k_y)^2 + 0.566 \ln k_y \ln S_a(1.5T_s) + 3.04 \ln S_a(1.5T_s) - 0.244 (\ln S_a(1.5T_s))^2 + 1.50 T_s + 0.278 (M_w - 7) \pm \varepsilon$$

Note:

- ε is the standard normal variate with zero mean and standard deviation of $\sigma = 0.66$. To calculate the median estimate of the slope displacement, ε is set to zero.

Where

D_n [cm] =	Seismic slope displacement
A_c [g] =	Yield acceleration of the slope
k_y =	Yield acceleration coefficient of the slope ($k_y = A_c/g$)
I_a [m/s] =	Arias intensity (= 0.104 m/s for $I_E = S_T = 1.0$)
PGA [m/s ²] =	Peak ground acceleration (= 0.12g for $I_E = S_T = 1.0$)
PGV [cm/s] =	Peak ground velocity (= 5.67 cm/s for $I_E = S_T = 1.0$)
M_w =	Earthquake moment magnitude (= 7.0)
T_s [s] =	Initial fundamental period of the slope ($T_s = 4H/V_s$, where H is the average height of the potential sliding mass, and V_s is the average shear wave velocity of the sliding mass)
$S_a(1.5T_s)$ [g] =	Spectral acceleration at a degraded period equal to 1.5 times the initial fundamental period of the slope

The rigid block assumption considers the sliding mass as rigid which is mainly applicable for stiff grounds (e.g. rocks) or shallow sliding failures. Referring to Bray & Travasarou (2007), the sliding mass can be assumed as rigid (or nearly rigid) if the initial fundamental period of the sliding mass (T_s) is less than 0.05 s. The initial fundamental period of the sliding mass (T_s) can be calculated using Equation (3):

$$T_s = C \times H/V_s \quad (3)$$

where H is the average height of the potential sliding mass, V_s is the average shear wave velocity of the materials within the potential sliding mass, and C is a constant depending on the shape of the potential sliding mass. Bray & Travasarou (2007) recommends $C = 4$ for the case of a relatively wide sliding mass that is either shaped like a trapezoid or segment of a circle where its response is largely 1D, and $C = 2.6$ for the case of a triangular-shaped sliding mass that largely has a 2D response.

In deformable slopes (e.g. deep sliding failure) with say $T_s > 0.05$ s, the dynamic response of the deformable earth within potential sliding mass can play considerable role in the slope downward displacement under earthquake shakings. For such cases, deformable sliding block methods are recommended over rigid block assumption being able to capture sliding mass internal deformations (Makdisi & Seed, 1978; Rathje & Bray, 2000).

4.3 Slope downward displacement limit

The Guidelines for Legislated Landslide Assessments for Proposed Residential Developments in BC, published by the Association of Professional Engineers and Geoscientists of British Columbia (APEGBC, 2010), defines the tolerable seismic slope displacement as 150 mm under a design ground motion with a 2475-year return period if the slip surface is located between the building and the slope face. The document recommends the deformable sliding block method proposed by Bray & Travarasrou (2007) for the assessment of seismic slope displacement. The performance requirement on structure under this design ground motion is ensuring “life safety”, i.e. extensive damage is allowed while resistance against collapse is retained. Blake et al. (2002) suggests tolerable seismic slope displacements of 50 mm if the slip surface intersects building and 150 mm if the slip surface does not intersect engineering structures, under a design ground motion with a 475-year return period based on the ground motion provisions in the Uniform Building Code (UBC). Arup (2018) presented a literature review on the displacement limits for landslide triggering which varies from 50 to 150 mm. The study adopted an average value of 100 mm as the displacement limit for the earthquake-induced natural terrain landslide hazard assessment in Hong Kong.

The selection of displacement limit involves engineering judgement and depends on many factors such as slope characteristics, facilities affected, design earthquake levels and the corresponding performance requirements. In this paper, threshold yield acceleration values corresponding to seismic slope displacements of 50, 100 and 150 mm under a range of design seismic action in Hong Kong are developed which provide references for seismic slope stability assessment under different performance criteria.

5. Results

5.1 Parametric study

Four typical Hong Kong slopes are selected for the parametric study. The first three cases are based on Pappin & Bowden (1998) which consist of two cut slopes in in-situ soil and a fill slope. An additional case of transported soil (Colluvium) is also considered. The typical ground material properties are based on Pappin & Bowden (1998) and medium values given in GEOGUIDE 1 (GEO, 2000) as summarised in Table 3.

Table 3. The ground materials adopted in parametric study (Pappin & Bowden, 1998)

Case	Material Type	Friction Angle [deg.]	Cohesion [kN/m ²]
Case 1	CDG	40	10
Case 2	CDV	35	7
Case 3	Fill	35	0
Case 4	Transported soil (Colluvium)	30	5

Several geometries for the typical slopes are considered in the parametric study by varying the slope angle (α_{slope}), slope height (H_{slope}), and rock angle (α_{rock}) as shown in Figure 3. It is generally assumed that the shallow foundation is located adjacent to the slope ($d = 0$) and has sufficiently large width (B) to impose a uniform surcharge over the entire failure zone. The stiffness of the foundation is ignored for simplicity.

The groundwater table is assumed to be generally at 1 m above rockhead but passing

through the toe of slope. This groundwater situation is considered to be typical for the wet season in Hong Kong between June and September (Pappin & Bowden, 1998). Cases with higher groundwater table (1 m below ground) are also investigated.

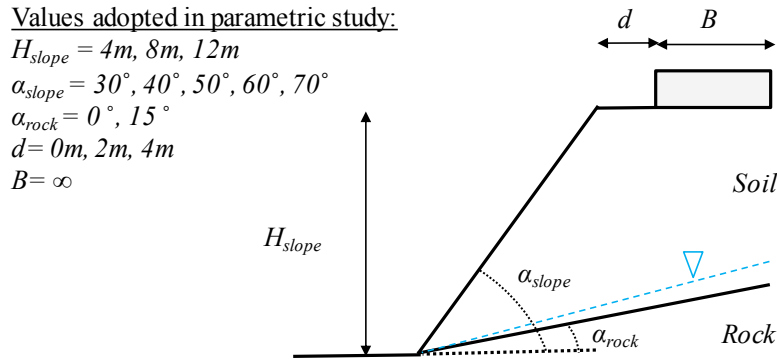


Figure 3. Slope geometry adopted in parametric study

The following main observations can be summarised from the parametric study:

- The yield acceleration coefficient for Cases 1 to 4 (as per Table 3) is in the range of 0.09 to 0.3. The yield acceleration (coefficient) (A_c or (k_y)) is the horizontal acceleration (coefficient) for slope analysis that brings the slope to a factor of safety of one in a pseudo-static analysis. This is one of the main parameters in the empirical correlations for seismic slope displacement.
- The average height of the potential sliding mass for most of the cases is less than 2.5m. This implies that most of the slopes experience shallow sliding failure. This is consistent with the previous studies on slopes in Hong Kong (e.g. Pappin & Bowden, 1998, Koo et al., 2008).
- It is noted that the predicted seismic slope displacements may be excessive in some cases, depending on the slope displacement calculation model used, particularly with high importance class and topographic and soil amplification factors.

The following section attempts to define the criteria under which seismic slope stability checking is required.

5.2 Development of a simple criteria for slope checking

Figure 4 shows the slope yield acceleration coefficient (k_y) corresponding to the slope displacement limits of 50 mm, 100 mm, and 150 mm calculated using empirical correlations. The threshold k_y for rigid sliding block model is taken as the average of four methods: (i) Hsieh & Lee (2011), (ii) Jibson et al. (2000), (iii) Saygili & Rathje (2008) three-parameter vector model, and (iv) Bray & Travasarou (2007) rigid sliding block approach (median values). It is noted that the three-parameter vector model of Saygili & Rathje (2008) gives the least variations (the most accurate) comparing with the scalar model and the two-parameter vector model and therefore the three-parameter model is considered in deriving the threshold k_y . The threshold k_y for deformable block model is estimated using Bray & Travasarou (2007) deformable sliding block approach (median values). The results are presented for practical range of $S_T(x) \times S$ as discussed in Section 4.1. The ground motion parameters for displacement calculation are currently taken as the reference ground motion parameters shown in Table 2 multiplied by the amplification factors ($I_E \times S_T(x) \times S$). Further study of the effects of topographic and soil amplification on the ground motion parameters is required in the future.

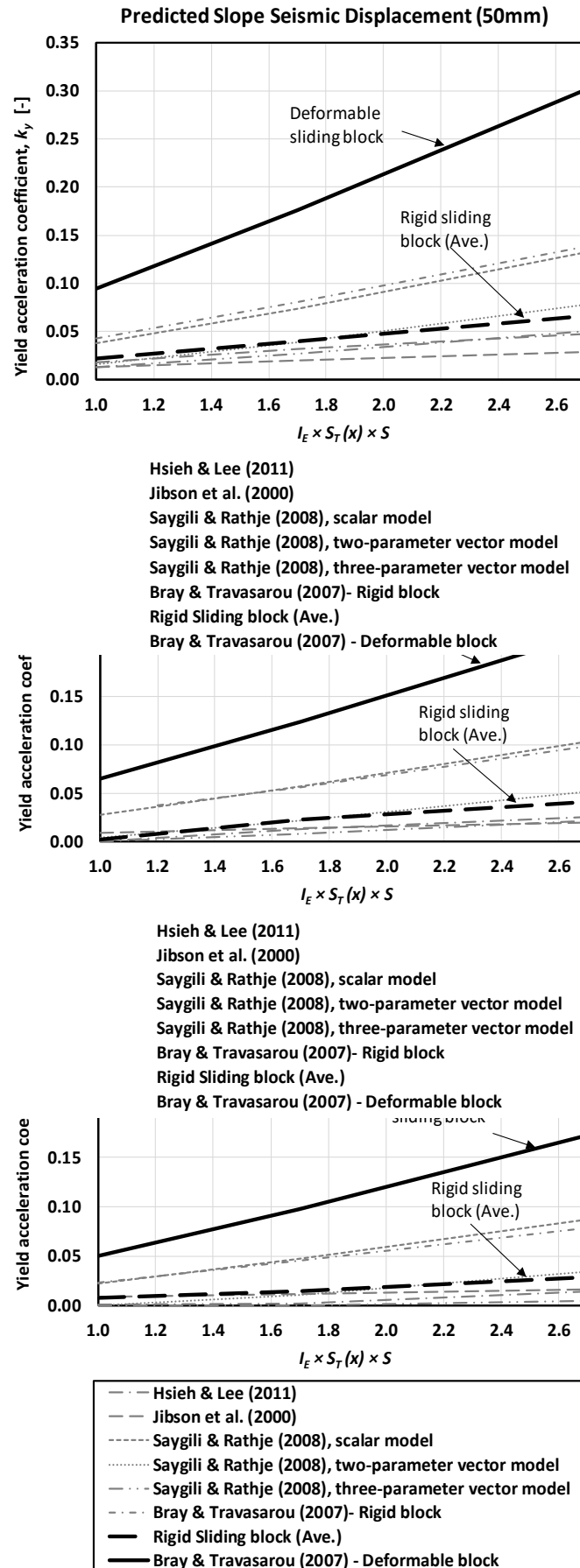


Figure 4. Predicted slope yield acceleration (k_y) corresponding to the displacement limits of 50 mm, 100 mm, and 150 mm

With reference to Figure 4, for slopes with higher k_y (above the threshold line), the predicted seismic slope displacement is expected to be less than the corresponding displacement limit. However, for cases with lower k_y (below the threshold line), the estimated seismic slope displacement exceeds the displacement limit which implies the possibility of a certain degree of slope damage. Considering that the values of k_y of typical slopes in Hong Kong subject to foundation loads lie between 0.09 and 0.3, the k_y values fall above the threshold line for rigid sliding block model for all displacement limits. Given that shallow slides are involved in typical slopes in Hong Kong, the use of the rigid sliding block model is justified, and the corresponding estimated displacement is less than all the displacement limits.

It should be noted that seismic slope displacement predictions in the field of geotechnical earthquake engineering involve many uncertainties and can only provide estimations of the likely range of displacements. This is mainly due to the complexities of the dynamic response of the earth materials involved and the variability of the earthquake ground motion (Bray & Travasarou, 2007). Therefore, the predicted values should only be treated as an index of potential seismic performance of slopes. For slopes with k_y below the threshold value shown in Figure 4, it is recommended that the designer may confirm the seismic slope stability using more advanced analysis (e.g. dynamic time-history analysis).

6. Conclusions

A parametric study using pseudo-static approach is carried out to investigate the effects of seismic foundation loadings from shallow foundation on the stability of slopes in Hong Kong. The values of slope yield acceleration coefficient k_y of typical slopes in Hong Kong subject to foundation loads lie between 0.09 and 0.3. Threshold values of k_y corresponding to seismic slope displacement limits adopted in international practices are developed using empirical correlations for slope displacement calculation and considering design seismic action in Hong Kong. Comparison of the range of k_y of typical slopes and the threshold value for rigid sliding block model suggests that the slope displacement is within the acceptable limits (i.e. satisfactory performance in seismic stability) given that the sliding mass is shallow. The developed threshold k_y lines can be used as a reference in the preliminary checking of seismic stability of slopes in Hong Kong.

7. References

- APEGBC (2010). *Guidelines for Legislated Landslide Assessments for Proposed Residential Developments in BC*. Association of Professional Engineers and Geoscientists of British Columbia, Rev. May 2010.
- Arup (2015). *Seismic Hazard Analysis of the Hong Kong Region (GEO Report No. 311)*. Geotechnical Engineering Office, Civil Engineering and Development Department, The Government of the Hong Kong Special Administrative Region, 324 p.
- Arup (2018). *Study Report on the on the Earthquake-induced Natural Terrain Landslide Hazard Assessment (GEO Report No. 343)*. Geotechnical Engineering Office, Civil Engineering and Development Department, The Government of the Hong Kong Special Administrative Region, 207 p.
- BD (1999). *Geotechnical Manual for Slopes – Guidance on Interpretation and Updating*. Practice Note for Authorized Persons and Registered Structural

Engineers, APP-109. Buildings Department, The Government of the Hong Kong Special Administrative Region.

- Blake, T. F., Hollingsworth, R. A. & Stewart, J. P. (2002). *Recommended Procedures for Implementation of DGM Special Publication 117 Guidelines for Analysing and Mitigation Landslide Hazards in California*, Southern California Earthquake Centre, Los Angeles, CA, USA.
- Bray, J. D. & Travasarou, T. (2007). Simplified procedure for estimating earthquake-induced deviatoric slope displacements. *Journal of Geotechnical and Geoenvironmental Engineering, ASCE*, 133:4, 381-392.
- BS-EN-1998-5:2004 (2004). *Eurocode 8: Design of structures for earthquake resistance – Part 5: Foundations, retaining structures and geotechnical aspects*. British Standard.
- GEO (2000). *GEOGUIDE 1 – Guide to Retaining Walls Design*. Geotechnical Engineering Office, Civil Engineering Department, The Government of the Hong Kong Special Administrative Region.
- Hsieh, S. Y. & Lee, C. T. (2011). Empirical estimation of the Newmark displacement from the Arias intensity and critical acceleration. *Special Edition of Journal of Engineering Geology, Toward the Next Generation of Research on Earthquake-induced Landslides: Current Issues and Future Challenges*, 122, 34-42.
- Jibson, R. W., Harp, E. L. & Michael, J. M. (2000). A method for producing digital probabilistic seismic landslide hazard maps. *Engineering Geology*, 58(3-4), 271-289.
- Koo, R. C. H., Kong, V., Tsang, H. H. & Pappin, J. W. (2008). Seismic slope stability assessment in a low to moderate seismicity region, Hong Kong. *The Proceedings of the 14th World Conference on Earthquake Engineering, Beijing*, Paper No. S03-027, 10 p.
- Makdisi, F. I. & Seed, H. B. (1978). Simplified procedure for estimating dam and embankment earthquake induced deformations. *Journal of Geotechnical Engineering, ASCE*, 104(GT7), 849-867.
- Newmark, N. M. (1965). Effects of earthquakes on dams and embankments. *Geotechnique*, 15, 139-159.
- Pappin, J. W. & Bowden A. J. H. (1998). The likelihood of earthquake induced landslides in Hong Kong. *Slope Engineering in Hong Kong*, 177-184.
- Rathje, E. M. & Bray, J. D. (2000). Nonlinear coupled seismic sliding analysis of earth structures. *Journal of Geotechnical and Geoenvironmental Engineering, ASCE*, 126(11), 1002-1014.
- Saygili, G. & Rathje, E. M. (2008). Empirical predictive models for earthquake-induced sliding displacements of slopes. *Journal of Geotechnical and Geoenvironmental Engineering, ASCE*, 134(6), 790-803.
- Sze, E. H. Y., Leung, E. H. Y., Koo, R. C. H., So, M. M. L. & Pappin, J. W. (2019). Geotechnical advances in development of a seismic code for Hong Kong. *Proceedings of the Institution of Civil Engineers – Geotechnical Engineering*, 172(1), 87-108.

Shake Table Studies of Precast Segmental Columns Made of Geopolymer Concrete with Basalt FRP Reinforcement

Hong Hao¹, Chao Li², Kaiming Bi³, Haoran Zuo⁴, Tin V. Do⁵

1. Hong Hao, John Curtin Distinguished Professor, School of Civil and Mechanical Engineering, Curtin University, Bentley, WA 6102, Australia. Email: hong.hao@curtin.edu.au
2. Corresponding Author, Chao Li, Lecturer, Central South University, China. Former PhD Candidate and Research Associate at Curtin University. Email: lichao@csu.edu.cn
3. Kaiming Bi, Senior Lecturer, School of Civil and Mechanical Engineering, Curtin University, Bentley, WA 6102, Australia. Email: kaiming.bi@curtin.edu.au
4. Haoran Zuo, Postdoctoral Fellow, The Hong Kong Polytechnic University, Former PhD Candidate and Research Associate at Curtin University. Email: haoran.zuo@postgrad.curtin.edu.au
5. Tin V. Do, Structural Engineer at Karagozian & Case, Former PhD Candidate and Research Associate at Curtin University. Email: tin.v.do@postgrad.curtin.edu.au

Abstract

In recent years, new construction materials and construction methods have been proposed in construction industry to develop environmentally friendly, sustainable, and resilient infrastructure systems. Geopolymer concrete is regarded as a green and sustainable construction material because it uses industry wastes as binders, therefore using geopolymer in construction leads to significant reduction of carbon emissions from cement production. On the other hand, Fibre Reinforced Polymer (FRP) has high tensile strength and is corrosion resistant, therefore using FRP as reinforcement can effectively mitigate corrosion damage to concrete structure reinforced with steel bars. Using geopolymer concrete reinforced with FRP bars in construction has been attracting increasing attentions, but most of the studies are limited to structural performances under static loading conditions. Precast construction is becoming more and more popular owing to its many advantages over the traditional on-site constructions, such as minimizing the site disruption, environmental impact, easy replacement of damaged parts and easy dissemble for end of life demolition of structures. This study investigates the seismic performances of precast segmental columns made of geopolymer concrete reinforced with basalt FRP (BFRP) bars. Segmental columns made of geopolymer concrete with BFRP bar reinforcements and BFRP posttensioning tendon were prepared and tested on shake table. For comparison, a reference segmental column made of Ordinary Portland cement concrete with steel reinforcement and steel posttensioning tendon was also made and tested. Experimental results revealed that the GPC segmental column with BFRP bars performed slightly better than the column with steel reinforced OPC under earthquake excitation; The GPC column with BFRP tendon in general performed similar to the reference column with steel tendon, but it had larger displacement responses due to the low elastic modulus of BFRP tendon and failed at a slightly lower ground excitation.

Keywords: Shake table studies; segmental column; geopolymer concrete; BFRP; tendon.

1. INTRODUCTION

On-site construction is always time consuming and often causes traffic congestions. To reduce the on-site construction time, the prefabricated construction is becoming more and more popular. The advantages of prefabricated constructions include less on-site construction time, reduced environmental impact, improved construction quality control and minimized traffic disruption. One of the prefabricated structures is the precast segmental column. It has been proposed as the substructure of bridges to accelerate the bridge construction process. Despite the many advantages as mentioned above, the applications of precast segmental column in seismic regions are limited due to the concerns of its seismic performance. Therefore, in recent years, many studies have been carried out to investigate the seismic performance of the precast segmental columns [1-3]. Previous researches revealed that the precast segmental column could undergo large displacement with small residual displacement due to the use of the prestressing tendon which provide large restoring force that could pull the column back to its original position [1]. Small residual displacement also makes the post-earthquake retrofitting feasible, therefore it is an important advantage for the precast segmental column.

It should be noted that all the studies reported in literature of the seismic performance of segmental columns considered Ordinary Portland cement (OPC) concrete reinforced with steel bars and posttensioned with steel tendons. OPC is one of the most commonly used materials in construction industry. It is reported that 5-7% of the global carbon dioxide emission is from the cement industry [4-8]. To solve this problem, geopolymers concrete (GPC) has been developed as an environmentally friendly concrete binder to replace cement in mixing concrete. The GPC consist of aluminosilicate material and alkaline liquids. The aluminosilicate material includes fly ash and slag, which are industrial byproducts. As no cement is used in the GPC, the carbon dioxide emission can be significantly reduced as compared to the OPC. Due to such advantages, a lot of researches have been carried out to investigate the mechanical properties of GPC and response of GPC structures [6, 9-11]. Most of the relevant studies reported in literature focused on the static loading conditions.

Corrosion of the steel rebars often results in cracks in the concrete and causes deterioration of the steel reinforced concrete structures. To address this problem, FRP rebars has been investigated to replace the steel rebars [12-14]. Basalt FRP (BFRP) is attracting more and more attention recently due to its low cost and good mechanical performance [15, 16]. In the present study, the BFRP rebars are used to replace the steel rebars in the concrete segments. Since unbonded posttensioned steel tendon is commonly used in the precast segmental column, corrosion of the steel tendon could result in loss of the prestressing force that clamps all the segments together. The loss the prestressing force may endanger the integrity and safety of the precast segmental column. To minimize the corrosion of the tendon, CFRP tendons has been investigated to replace the steel tendon [17-21]. Here in this study, the BFRP tendon is adopted as the prestressing tendon of the precast segmental column.

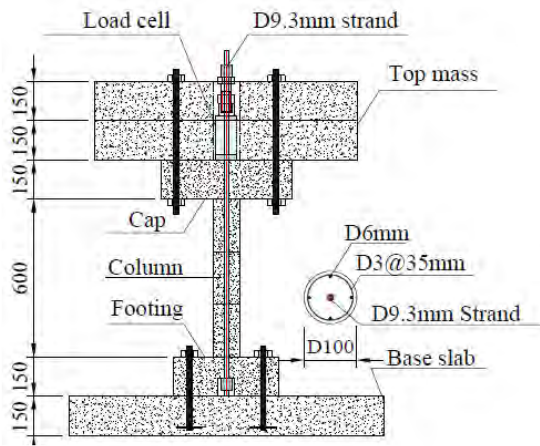
It should be noted that most of the previous studies focused on investigating the cyclic performance of the precast segmental column. To fully understand the seismic performance of the precast segmental column, shake table test should be carried out. Recently, the authors carried out shake table tests on the precast segmental column [22]. In the test, steel reinforced OPC were used to construct the segments of the precast segmental column. Also steel tendon was used to posttensioning the column. To address the concerns mentioned above, in this study, GPC is adopted to replace OPC, BFRP rebars and tendons are used to replace the steel rebars

and tendon. The combination of the corrosion resistant material (BFRP), low carbon dioxide emission concrete (GPC), and the prefabricated construction method (precast segmental column) in this study leads to the development of resilient and sustainable earthquake-resistant structures.

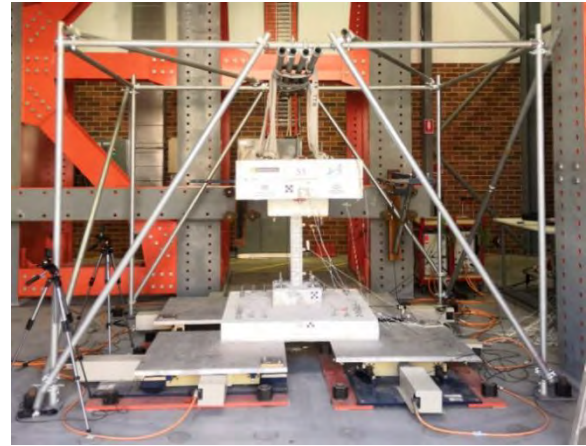
2. EXPERIMENTAL STUDY

The shake table tests were conducted in the Structural Dynamics Lab at Curtin University, Australia. A typical bridge pier with a height of 7.32m and a diameter of 1.22m was chosen as the prototype column. Considering the capacity of the shake tables, a scale factor of 12 was selected. Therefore, the height and diameter of the specimens were 600mm and 100mm, respectively. Figure 1 (a) shows the design details of the specimen. The specimen consisted of a footing, three segments and a cap. A base slab was designed as a support for the specimen to use four synchronized shake tables together. The top mass that fixed on top of the cap was used to mimic the weight of the superstructures. Each segment had a height of 200mm. Four rebars with a diameter of 6mm were used as the longitudinal reinforcement and the stirrups had the diameter of 3mm and a spacing of 35mm. The footing, segments, and cap were aligned and clamped together with a steel or BFRP tendon. Three specimens were tested in this study. The first column S1 was the steel reinforced OPC column. The second column S2 was the steel reinforce GPC column. The third column S3 was the same as column S2 except that BFRP tendon was used instead of steel tendon.

The footing, segments, cap, base slab and top mass were cast separately. After curing of the concrete, the segments, cap and footing were clamped together by the posttensioned tendon. For the anchorage of the tendon, the commonly used steel barrel and wedge anchorage systems was used for the steel tendon. For the BFRP tendon, mechanical clamping anchor was made and used [23]. The base slab was firstly installed on the shake table array. Then the posttensioned column was lifted and fixed on the base slab. After installing the column, the top mass was aligned and fixed to the cap of the column. To prevent the mass from falling onto the shake table, a catching frame was built and the mass was connected to the frame with loose cables. Figure 1 (b) shows the final setup of the specimen. The material properties of the steel and BFRP rebars and tendon are shown in Table 1. The measured compressive strength of the OPC and GPC were 37.0 MPa and 48.5 MPa, respectively. Bidirectional earthquake ground motions were used as input in the test. The original ground motion time histories were from the Niland Fire Station during the 1979 Imperial Valley Earthquake. In the test, the original records were scaled. The maximum PGA increased from 0.1g gradually till the failure of the column with an interval of 0.1g in each increment. It should be mentioned that column S1 was tested in a previous study [22] and the PGA of the inputs started from 0.2g. The time duration of the inputs was compressed by $\sqrt{12} = 3.46$ times according to the scaling law. Figure 2 shows a pair of the input with the E-W component PGA equal to 0.1g. Prior to each earthquake motion, white noise signals with the amplitude of 0.02g and duration of 40s were applied to the shake tables to get the column responses for identifying the dynamic characteristics of the column.



(a)

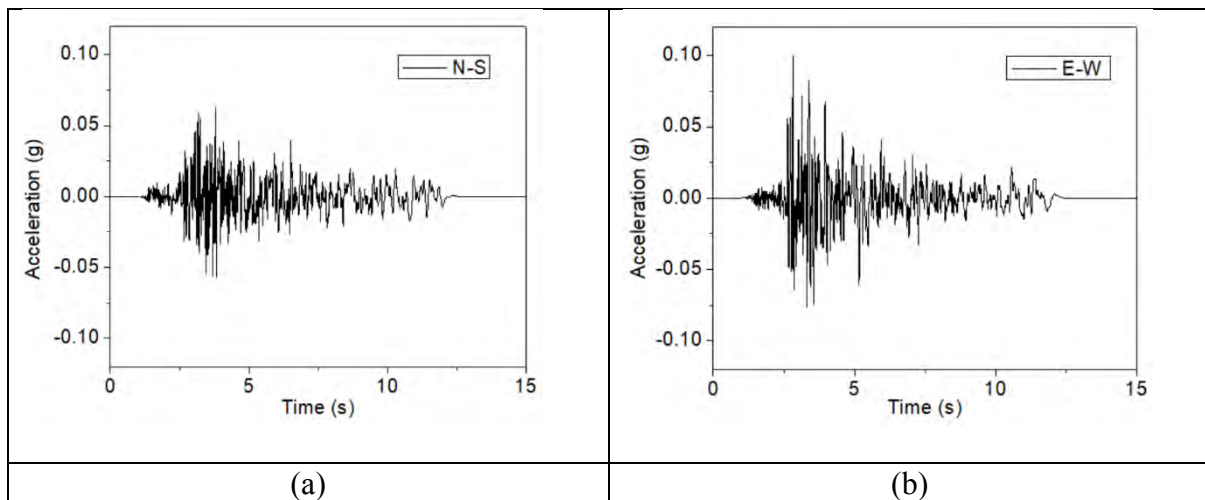


(b)

Figure 1. (a) Designs of the specimen; (b) Photo of the final setup

Table 1 Material properties

Material	Diameter	Elastic modulus	Yield strength	Ultimate strength
	(mm)	(GPa)	(MPa)	(MPa)
	Steel/BFRP	Steel/BFRP	Steel/BFRP	Steel/BFRP
Longitudinal rebar	6	200/55	555/-	616/1100
Stirrup	3	200/55	346/-	430/1100
Tendon	9.3/10	195/55	1674/-	1860/1100



(a)

(b)

Figure 2. A pair of the biaxial input motions with a maximum PGA of 0.1g: (a) N-S, (b) E-W

3. TEST RESULT

Figure 3 shows the damages of the specimens. In general, the damages of the segmental columns were mainly concentrated at the joint between the column and the footing. This is

because the rocking of the segment resulted in the small contact area between the segment and the foundation, which led to the concrete near the toes of the segments experienced large compressive stress, thus resulting in the concrete crushing and spalling damage as observed in the tests. Column S2 with BFRP reinforced GPC failed at larger PGA (0.9 g) compared to the column with steel reinforced OPC (0.8 g). The reasons could be the higher strength of the GPC (48 MPa) compared to the OPC (37.5 MPa) and the proper confinement for the GPC provided by the BFRP stirrups. Column S3 with BFRP tendon collapsed at the PGA of 0.8g, which was slightly earlier than column S2 with steel tendon (0.9g). The following two reasons might explain these results: (1) When the segmental column deformed laterally under earthquake excitation, openings occurred at the joints and thus the tendon elongated; since the elastic modulus of the BFRP tendon is lower than the steel tendon, the column S3 experienced larger displacement responses under the same excitation, which in turn caused more concrete damages in the segments and finally resulted in earlier failure of the column. (2) The large column lateral deformation resulted in the tendon experienced a shear force. It is well known that the shear resistant capacity for the FRP tendon is lower than its tensile strength and it is also normally weaker than steel tendon [24], which resulted in the fracture failure of the BFRP tendon as shown in Figure 3 (c).

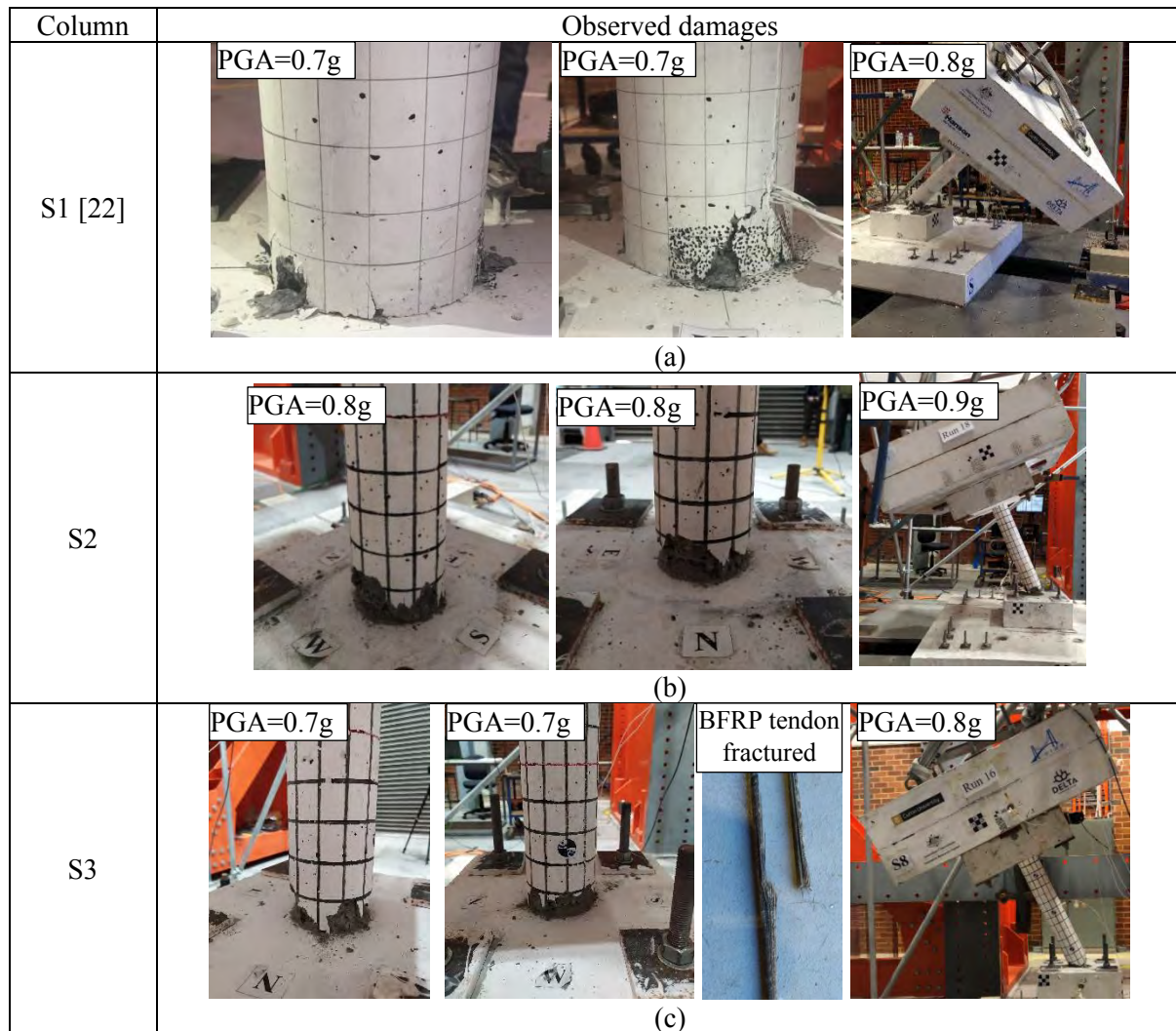


Figure 3. Damages of the specimens

As mentioned above, white noise inputs were used to identify the dynamic characteristics of the column. Figure 4 (a) shows the changes of the first vibration periods of the specimens S1 and S2. It can be observed that, before the PGA reached 0.6g, minor increase was found for both columns. This indicates that the damage of the two columns was insignificant. After 0.6g, the vibration period of column S1 started to increase obviously. In comparison, the vibration periods of column S2 started to increase obviously only at PGA of 0.7g. As explained before, this is attributed to the higher strength of the GPC as compared to the OPC and the good confinement provided by the BFRP stirrups. Therefore, the use of geopolymer concrete and BFRP reinforcement could be a good alternative to the normal steel reinforced concrete in the precast segmental column. Figure 4 (b) shows the changes of the first vibration periods of the specimens S2 and S3. The vibration period of column S3 was slightly larger than column S2. This is because the relatively smaller initial posttension force in S3 (25.8 kN) compared to S2 (28.3 kN). After the PGA reached 0.6g, the vibration period of column S3 started to increase obviously, while for column S2 it started to increase after the PGA reached 0.7g. This again indicates column S3 experienced more damage during the tests and finally failed earlier at smaller PGA in comparison with column S2.

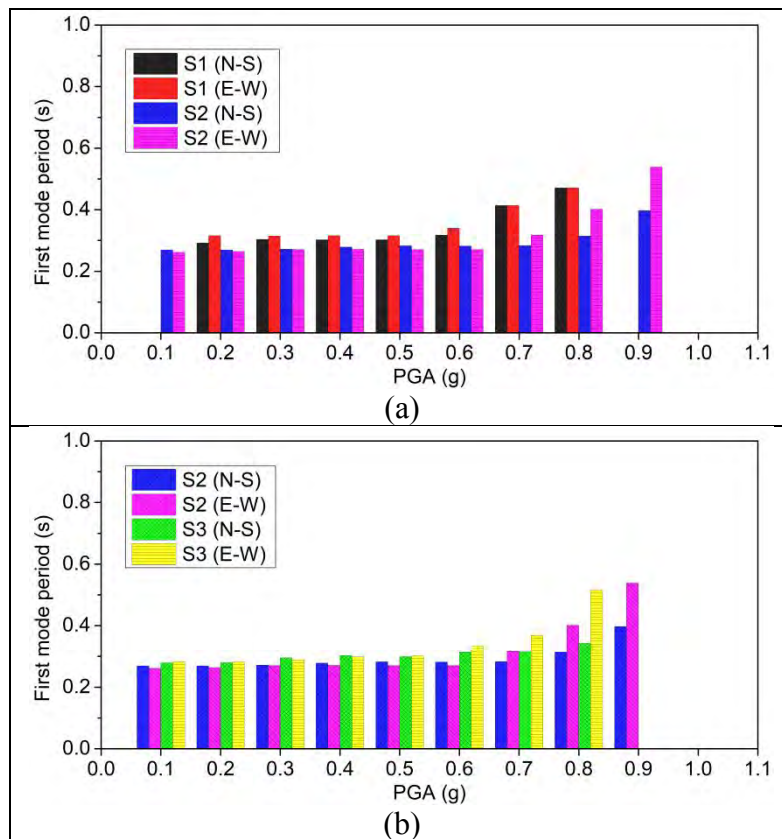
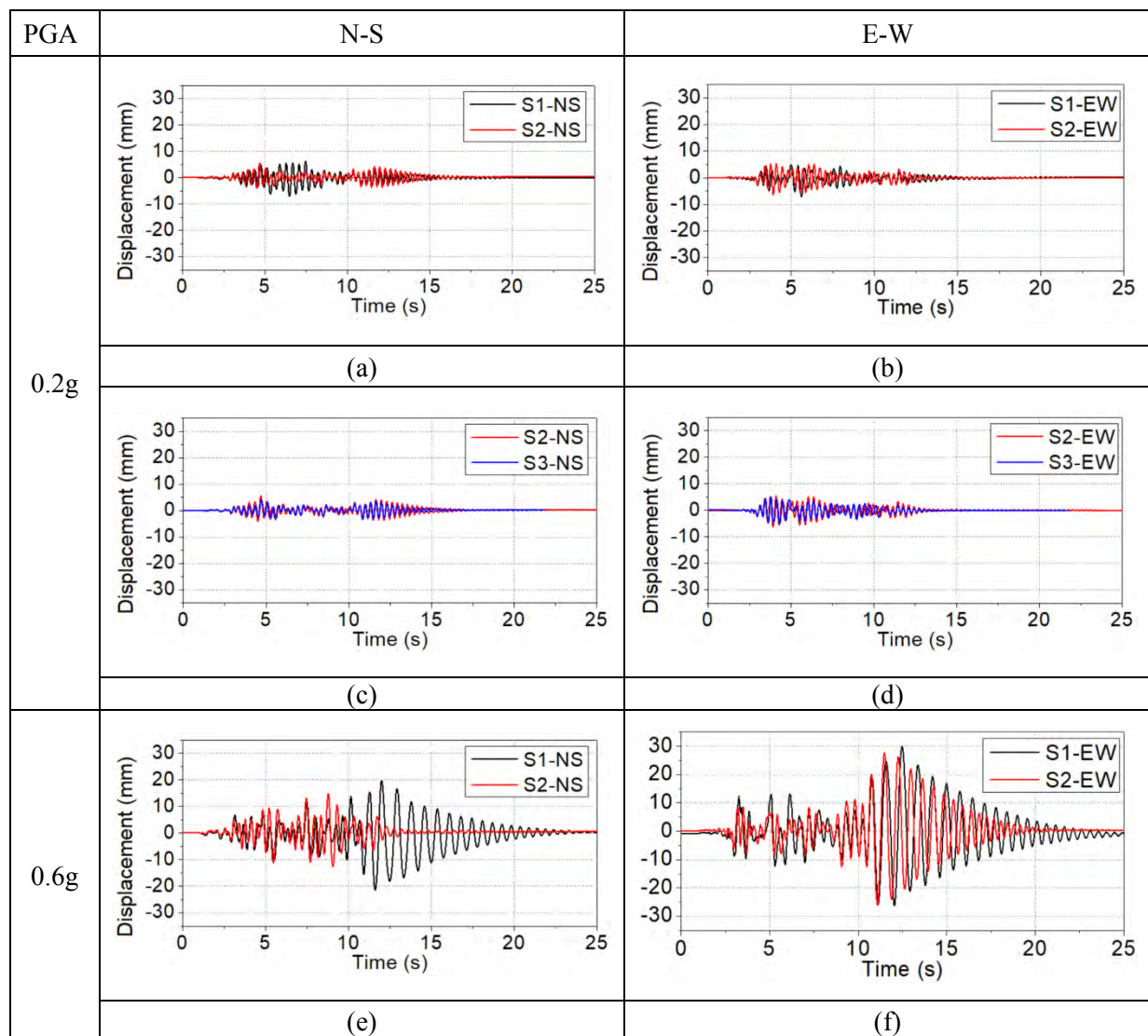


Figure 4. Fundamental periods of: (a) S1 and S2; (b) S2 and S3

Figure 5 shows the displacement responses of the columns at relatively small (0.2g) and large (0.6g) PGAs. When the PGA was 0.2g, the displacement responses of columns S1 and S2 were shown in Figure 5 (a-b). In the N-S direction, the displacement response of S1 was slightly larger than that of the column S2. This could be attributed to the different concrete materials and reinforcement used in the segments. For columns S2 and S3, as shown in Figure 5 (c) and (d), the displacement responses were similar to each other in both N-S and E-W directions, indicating that at small PGAs, the column S3 with BFRP tendon had similar performance to

the column S2 with steel tendon. When the PGA reached 0.6g, the displacement responses of columns are shown in Figure 5 (e-h). As shown in Figure 5 (e), it can be observed that in the N-S direction the displacement of S1 increased significantly after about 10s, indicating the column experienced obvious damages. However, for column S2, the displacements were still small in this direction. In the E-W direction, as shown in Figure 5 (f), both columns experienced large displacement responses, but the column S1 had slightly larger responses as compared to the column of S2. The displacement responses of these two columns demonstrated that the precast segmental column S2 with BFRP reinforcement GPC could perform better than that of column S1 with steel reinforced OPC under earthquake motions with relatively large PGAs. Figure 5 (g-h) show the displacement responses of columns S2 and S3. It can be seen column S3 with BFRP tendon experienced larger displacement responses. This could be attributed to the low elastic modulus of the BFRP tendon as compared to the steel tendon, which led to larger displacement responses and more accumulated damages in the concrete segments.



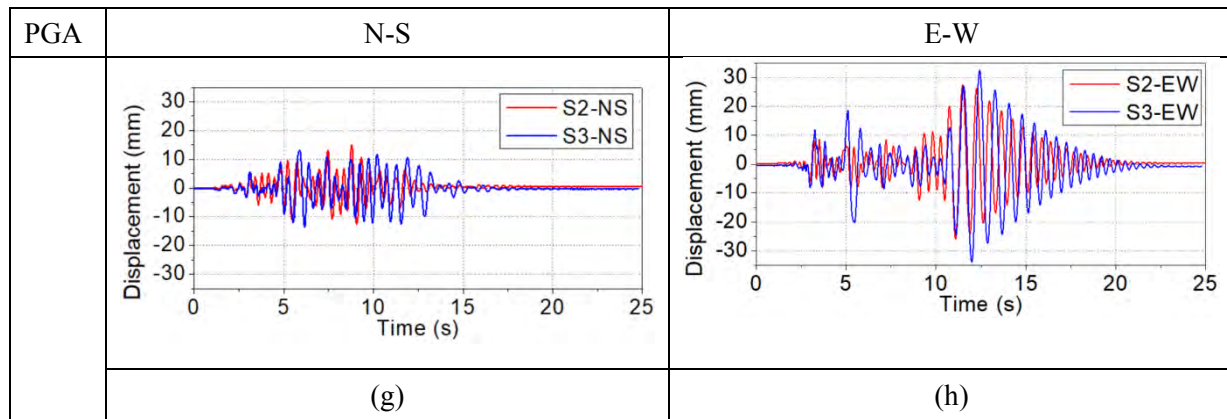


Figure 5. Displacement responses of the columns

4. CONCLUSIONS

This study experimentally investigated the seismic performance of the precast segmental column with GPC and BFRP rebars. The use of BFRP tendon was also evaluated to replace the steel tendon. According to the test results, the column with BFRP reinforced GPC segments had comparable performance under small to medium levels of excitations compared to the steel reinforced OPC column. When the PGAs reached large values, the column with BFRP reinforced geopolymer concrete segments performed slightly better owing to the higher strength of GPC and good confinement provided by the BFRP stirrups. For the column S3 with BFRP tendon, because of the lower elastic modulus of the BFRP tendon, the column experienced larger displacement responses and failed at smaller PGA as compare to the column S2 with steel tendon.

It should be noted that, the FRP was normally regarded as brittle material. Recent researches (e.g.[19, 21, 25]), however, actually indicated the structures with FRP bars or tendons could have similar ductility with the counterpart steel bars or tendons. Therefore, it is believed that, with proper design the FRP material can be used in structures and good ductility can be achieved.

REFERENCES:

- [1] Billington SL, Yoon J. Cyclic response of unbonded posttensioned precast columns with ductile fiber-reinforced concrete. *J Bridge Eng.* 2004;9:353-63.
- [2] Wang JC, Ou YC, Chang KC, Lee GC. Large - scale seismic tests of tall concrete bridge columns with precast segmental construction. *Earthquake Eng Struct Dynam.* 2008;37:1449-65.
- [3] Ou YC, Wang PH, Tsai MS, Chang KC, Lee GC. Large-scale experimental study of precast segmental unbonded posttensioned concrete bridge columns for seismic regions. *J Struct Eng.* 2009;136:255-64.
- [4] Mo KH, Alengaram UJ, Jumaat MZ. Structural performance of reinforced geopolymer concrete members: A review. *Construction and Building Materials.* 2016;120:251-64.
- [5] McLellan BC, Williams RP, Lay J, Van Riessen A, Corder GD. Costs and carbon emissions for geopolymer pastes in comparison to ordinary portland cement. *Journal of cleaner production.* 2011;19:1080-90.
- [6] Singh B, Ishwarya G, Gupta M, Bhattacharyya SK. Geopolymer concrete: A review of some recent developments. *Construction and Building Materials.* 2015;85:78-90.

- [7] Maranan GB, Manalo AC, Benmokrane B, Karunasena W, Mendis P. Behavior of concentrically loaded geopolymer-concrete circular columns reinforced longitudinally and transversely with GFRP bars. *Eng Struct.* 2016;117:422-36.
- [8] Ma C-K, Awang AZ, Omar W. Structural and material performance of geopolymer concrete: A review. *Construction and Building Materials.* 2018;186:90-102.
- [9] Khan MZN, Shaikh FuA, Hao Y, Hao H. Synthesis of high strength ambient cured geopolymer composite by using low calcium fly ash. *Construction and Building Materials.* 2016;125:809-20.
- [10] Khan MZN, Shaikh FUA, Hao Y, Hao H. Effects of Curing Conditions and Sand-to-Binder Ratios on Compressive Strength Development of Fly Ash Geopolymer. *J Mater Civil Eng.* 2018;30.
- [11] Shaikh FUA. Mechanical and durability properties of fly ash geopolymer concrete containing recycled coarse aggregates. *International Journal of Sustainable Built Environment.* 2016;5:277-87.
- [12] De Luca A, Matta F, Nanni A. Behavior of full-scale glass fiber-reinforced polymer reinforced concrete columns under axial load. *ACI Struct J.* 2010;107:589.
- [13] Hadi MNS, Karim H, Sheikh MN. Experimental Investigations on Circular Concrete Columns Reinforced with GFRP Bars and Helices under Different Loading Conditions. *J Compos Constr.* 2016;20.
- [14] Asim N, Alghoul M, Mohammad M, Amin MH, Akhtaruzzaman M, Amin N et al. Emerging sustainable solutions for depollution: Geopolymers. *Construction and Building Materials.* 2019;199:540-8.
- [15] Monaldo E, Nerilli F, Vairo G. Basalt-based fiber-reinforced materials and structural applications in civil engineering. *Composite Structures.* 2019;214:246-63.
- [16] Dal Lago B, Taylor SE, Deegan P, Ferrara L, Sonebi M, Crosset P et al. Full-scale testing and numerical analysis of a precast fibre reinforced self-compacting concrete slab pre-stressed with basalt fibre reinforced polymer bars. *Composites Part B: Engineering.* 2017;128:120-33.
- [17] Burningham CA, Pantelides CP, Reaveley LD. Repair of reinforced concrete deep beams using post-tensioned CFRP rods. *Composite Structures.* 2015;125:256-65.
- [18] Burningham CA, Pantelides CP, Reaveley LD. Repair of prestressed concrete beams with damaged steel tendons using post-tensioned carbon fiber-reinforced polymer rods. *ACI Struct J.* 2014;111:387-95.
- [19] Le TD, Pham TM, Hao H, Hao Y. Flexural behaviour of precast segmental concrete beams internally prestressed with unbonded CFRP tendons under four-point loading. *Eng Struct.* 2018;168:371-83.
- [20] Le TD, Pham TM, Hao H, Yuan C. Performance of precast segmental concrete beams posttensioned with carbon fiber-reinforced polymer (CFRP) tendons. *Composite Structures.* 2019;208:56-69.
- [21] Mohebbi A, Saiidi MS, Itani AM. Shake Table Studies and Analysis of a PT-UHPC Bridge Column with Pocket Connection. *J Struct Eng.* 2018;144:1-12.
- [22] Li C, Bi K, Hao H. Seismic performances of precast segmental column under bidirectional earthquake motions: Shake table test and numerical evaluation. *Eng Struct.* 2019;187:314-28.
- [23] Wang L, Zhang J, Xu J, Han Q. Anchorage systems of CFRP cables in cable structures—A review. *Construction and Building Materials.* 2018;160:82-99.
- [24] El-Hacha R. Prestressing concrete structures with frp tendons (ACI 440.4 R-04). *Structures Congress 2005: Metropolis and Beyond 2005.* p. 1-8.
- [25] Hadhood A, Mohamed HM, Benmokrane B. Strength of circular HSC columns reinforced internally with carbon-fiber-reinforced polymer bars under axial and eccentric loads. *Construction and Building Materials.* 2017;141:366-78.

CREATING A SOUTH AUSTRALIAN EARTHQUAKE CATALOGUE FOR 1908

Kevin McCue

Adjunct Professor Central Queensland University, Rockhampton Queensland 4700
email: k.mccue@cqu.edu.au

Abstract: Over the last 50 years various studies have been made of historical earthquakes in South Australia. This onerous task was immeasurably facilitated with the development of TROVE by the Australian National Library in December 2009. Their goal of digitising records and newspapers is a work in progress so researchers need to keep going back, not just to improve accounts of known earthquakes but to add new events. An example is given for the seismicity of South Australia in the year 1908, the year before the first seismograph was installed in South Australia, at Adelaide Observatory. Thirteen new earthquakes have been found, located and assigned magnitudes, the largest near Tarcowie caused minor damage. Its magnitude is revised up from ML 4.8 to ML5.0. The 'b' value over the magnitude range was a very low 0.50. It would be helpful if Geoscience Australia would add all these historical earthquakes to their on-line database, *dark data*, not just the larger earthquakes, to improve user assessments of earthquake hazard.

Keywords: earthquake catalogue, historical earthquakes, South Australia, hazard

INTRODUCTION

The largest earthquake in South Australia since European arrival was the 1897 earthquake offshore from Beachport in the southeast of SA, its magnitude about M6.5. What we know about this earthquake has been gleaned from contemporary newspapers, meteorological reports and lighthouse logbooks, reports of where and how strongly the earthquake was felt. Damage, liquefaction, lateral spreading, human injuries and widely felt aftershocks are all painstakingly documented. But there are hundreds of other earthquakes that have been documented, principally by Dix (2013) and her earlier thesis work as Malpas (1991, 1993) and other workers such as Burke-Gaffney (1951) and the author (McCue, 2013). Magnitude was assessed using the relationship between felt area and Richter magnitude ML (from McCue, 1980).

Ongoing document digitising by the Australian National Library has uncovered more information to review past estimates of earthquake epicentres and magnitudes and to add new events as will be demonstrated in this report of the seismicity of SA in 1908 - an interesting year. Mr George Dodwell became State government seismologist and astronomer in June, as their first seismograph was arriving in Adelaide from London, and the Commonwealth relinquished responsibility for these functions, maintaining only meteorology.

For many years the Science Museum in London displayed a seismogram of the 1906 San Francisco earthquake recorded there on the Milne instrument on test and destined for Adelaide.

The Milne seismograph was low gain, underdamped and long period making it unsuitable for recording local earthquakes. It was eventually installed in June 1909, just three months after Riverview, when space became available in a room at the Observatory with a brick pier built of 60 tons of masonry (history in Appendix 2). What a pity they hadn't chosen the same instruments as was to be used at Riverview! The first recorded earthquake, on Sunday June 27, at about 5 o'clock was located at Bougainville by the ISC but it caused damage in the New Hebrides. The seismograph's function was really a Commonwealth one, a part of Milne's worldwide network for recording large distant earthquakes, Adelaide records going to the seismological committee of the British Association for the Advancement of Science. It wasn't until 1959 that David Sutton at Adelaide University, installed a short period seismograph network in South Australia to investigate local seismicity following the destructive 1954 earthquake near Adelaide. Hence the need for this kind of intensity study to investigate the pre-1959 earthquake locations and magnitudes and the post-1959 isoseismal maps to calibrate the magnitude vs felt area relationship, and any other.

1908 SEISMICITY

Geoscience Australia's on-line catalogue lists no earthquakes in South Australia in 1908. Dix (Malpas, 1993) found 3 events, the first in April and another 2 in October. This, the latest work, using TROVE has identified 16 earthquakes in 1908, including the 3 of Dix (2013), such is the increased output of TROVE. For the isoseismal map of the largest earthquake, west of Peterborough in the mid-north on 10 April, Malpas (1993) found 19 individual town references using microfilmed newspapers and other sources. I eventually found all but three of them using TROVE, not Clare, Yunta or Kadina but 20 in all. I have added the three to the isoseismal map here, slightly different to that drawn by Malpas (1993), the epicentre 20km further west.

Following is a catalogue in chronological order, of the 16 felt earthquakes in South Australia in 1908. The actual newspaper stories are listed in Appendix 1.



Figure 1 Isoseismal Map, Tarcowie Earthquake 09 April 1908 (after Dix, 2013), my epicentre is at the centre of the generous MM5 contour, about 20km west of that shown by Malpas (1993). The earthquake may well have had a depth of about 20km because of the lack of damage and only one very small aftershock. The Arabic numbers are spot intensity on the Modified Mercalli scale. The contours, latin numbers (IV and V), delineate higher and lower intensities.

#1 A mild shock of earthquake was felt here last evening between 11 and 12. It came from the direction of the sea. There have been mild shocks annually at this time of the year since 1897

Date/time UTC	Latitude	Longitude	ML	Place
20 March 1908 at 14:00	-36.8	139.7	3.0	Kingston

#2 The largest earthquake of the twelve in the year, near Tarcowie and Peterborough (Figure 1), was assessed by Malpas (1991) to have a magnitude of ML 4.8 from its felt area but her isoseismal map shows that the magnitude is based on the MM4 isoseismal radius, not the MM3 felt radius adopted by McCue (1980), so the earthquake is larger than that. (Her tabled latitude should be 32.92°S not 33.92°S, a typo). At the approximate origin time of 2 a.m., times varied in the reports (see Appendix 1), most people were asleep so there are no assessments at MM3. There was plaster-wall damage reported at Melrose but none found that it was felt in Adelaide, limiting the magnitude to the range ML5 to ML5.2 using my formula relating magnitude ML and radius of perceptibility.

A single small aftershock was reported at Port Augusta within 15 minutes but nowhere else.

Date/time UTC	Latitude	Longitude	ML	Place
09 April 1908 at 16:25	-33.0	138.4	4.9	Mid-North, Tarcowie
09 April 1908 at 16:40	-33.0	138.4	2.5	Aftershock

#3 The next event was a much smaller earthquake in the mid-north on Sunday 24 May about 5.30pm that was reported felt only at Appila-Yarrowie about 15km from Jamestown and Laura, the magnitude not much more than about 2.5.

Date/time UTC	Latitude	Longitude	ML	Place
24 May 1908 at 08:00	-33.0	139.4	2.8	Mid-North, Appila-Yarrowie

#4 Another earthquake in the early morning hours was reported felt, quite distinctly, in the mid-north at Burra, Mount Bryan and 50km to the southeast at Gums Station, Florieton. The comment that the tremor was felt 30 miles out east at the same time as it was experienced in Burra is useful for magnitude assessment. The shaking must have been frightening, to keep people up all night at Burra. It was severely felt at Hallett causing the windows to rattle.

Date/time UTC	Latitude	Longitude	ML	Place
01 June 1908 at 14:00	-33.6	139.3	4.0	Mid-North, Gums Station

#5 HAWKER, June 5.—A slight earthquake was felt to-day at 1.34 p.m. It lasted about one and a half seconds, and the vibration was from south-west to north-east.

Date/time UTC	Latitude	Longitude	ML	Place
05 June 1908 at 04:04	-34.5	139.0	2.5	Hawker

#6 On 26 June at 23:15 UTC, lighthouse keepers at Cape Willoughby on the eastern end of Kangaroo Island phoned in a report of an earthquake felt in the lighthouse and the attendant cottages, but there are no other reports.

Date/time UTC	Latitude	Longitude	ML	Place
26 June 1908 at 23:15	-35.8	138.1	3	Cape Willoughby, KI

#7 SPALDING, July 17.—A short heavy shock of earthquake was experienced here yesterday at 5.15 p.m. The sound was unusual, reminding one of an explosion. It must have been close.

Date/time UTC	Latitude	Longitude	ML	Place
16 July 1908 at 07:45	-33.5	138.6	3.0	Spalding

#8&9 The Southern Mt Lofty Ranges, Nangkita, in the vicinity of Mt Compass is the epicentral region of the next small earthquake and aftershock on 25 August at 8:25 pm, and 26 August at 10:10 p.m. They rattled iron roofs and the first of them was also felt at Mount Compass and, slightly, at Hindmarsh Island 25-30km away on 25 August at 8:25 pm.

Date/time UTC	Latitude	Longitude	ML	Place
25 August 1908 at 10:55	-35.4	138.7	3	Southern My Lofty Ranges
26 August 1908 at 12:40	-35.4	138.7	2.5	Southern My Lofty Ranges

#10 A slight earthquake was felt at Kongal (less than 10km east of Willalooka) on Friday morning, at eight o'clock, causing the crockery to rattle.

Date/time UTC	Latitude	Longitude	ML	Place
27 August 1908 at 22:30	-36.4	140.4	2.5	Kongal, Southeast

#11 SPALDING. September 23 —A severe shock of earthquake was experienced here last night by a number of the residents.

Date/time UTC	Latitude	Longitude	ML	Place
22 September 1908	-33.5	138.6	3.0	Spalding

#12 It was Mount Mary in the Riverland where the next small earthquake was felt, on Sunday 04 October 1908 just after 5pm. It shook buildings and made iron roofs and windows rattle.

Date/time UTC	Latitude	Longitude	ML	Place
04 October 1908 at 07:40	-34.1	139.4	3.2	Riverland, Mount Mary

#13 On October 12 at 8:42 pm a slight shock of earthquake was felt at Daveyston in the Barossa Valley.

Date/time UTC	Latitude	Longitude	ML	Place
12 October 1908 at 11:12	-34.5	138.9	2.5	Barossa Valley

#14 MOUNT BRYAN, October 26.—A slight earthquake was experienced about 7.45 a.m. to-day. The roaring sound lasted for several seconds

Date/time UTC	Latitude	Longitude	ML	Place
25 October 1908 at 22:15	-33.0	138.8	2.5	Mount Bryan

#15 This earthquake was described as slight at Second Valley at 6:10 a.m., but of fair duration at 6:15 a.m., 40km to the southwest at Hog Bay (Penneshaw), on Kangaroo Island.

Date/time UTC	Latitude	Longitude	ML	Place
28 October 1908 at 20:40	-35.7	137.9	3.5	Off the northeast coast of Kangaroo Island

#16 The last reported earthquake of the year occurred on Wednesday 16 December at 9.26 p.m. in Second Valley on the Fleurieu Peninsula. It was described as severe and lasted for about half a minute. The vibrations rattled the windows and the gas lamps. It was the most severe shock since the great disturbance of 1903 (author: probably meant Warooka, 1902).

Date/time UTC	Latitude	Longitude	ML	Place
16 December 1908 at 11:56	-35.5	138.2	3.5	Fleurieu Peninsula

Epicentres of the listed earthquakes for 1908 are plotted in Figure 2 below. None were identified for either the Eyre or Yorke Peninsulas.

The cumulative number of 1908 earthquakes is plotted in Figure 3 against magnitude and superposed on the average number of annual earthquakes for the 25 year period 1965-1989 when magnitude measurements were constant. Not unsurprisingly, some of the magnitude 3 to 3.5 earthquakes went unreported. At the other end of the scale, the Tarcowie earthquake magnitude 5.0 of 9 April 1908 distorts the line of best fit which otherwise is not much different from what is expected. Study of the recurrence relation for different observation period and magnitude ranges (McCue 1975) suggests that this relationship cannot be extrapolated linearly much beyond about magnitude 5. The 'b' value, determined by least squares here, is magnitude range dependent and obviously time dependent, 0.75 for the 25 year period 1965-1989 plotted here, and a very low 0.50 for the 1908 data in the ML range 3 to 5.5.

The alternative view is that in 1908, the single largest earthquake is skewing the slope but the largest events should not be excluded as they are the ones of interest, being the most important and potentially damaging earthquakes of the year. This suggests that a single year's data is too short to conclude much about the apparent 'b' value.

The range of measured magnitudes for any particular earthquake today is about ± 0.5 regardless of magnitude with a standard deviation of about 0.2. Because of the sensitivity of magnitude with radius of perceptibility, it is considered that the computed magnitudes of these historic earthquakes derived from an isoseismal map is no worse than modern measures of magnitude. The uncertainty for those too small to be widely felt is larger, probably about 0.5. This uncertainty only gets worse when ML is converted to other scales like Mw using conversion scales developed for overseas earthquakes, especially values extrapolated from magnitude or moment scales derived for large earthquakes.

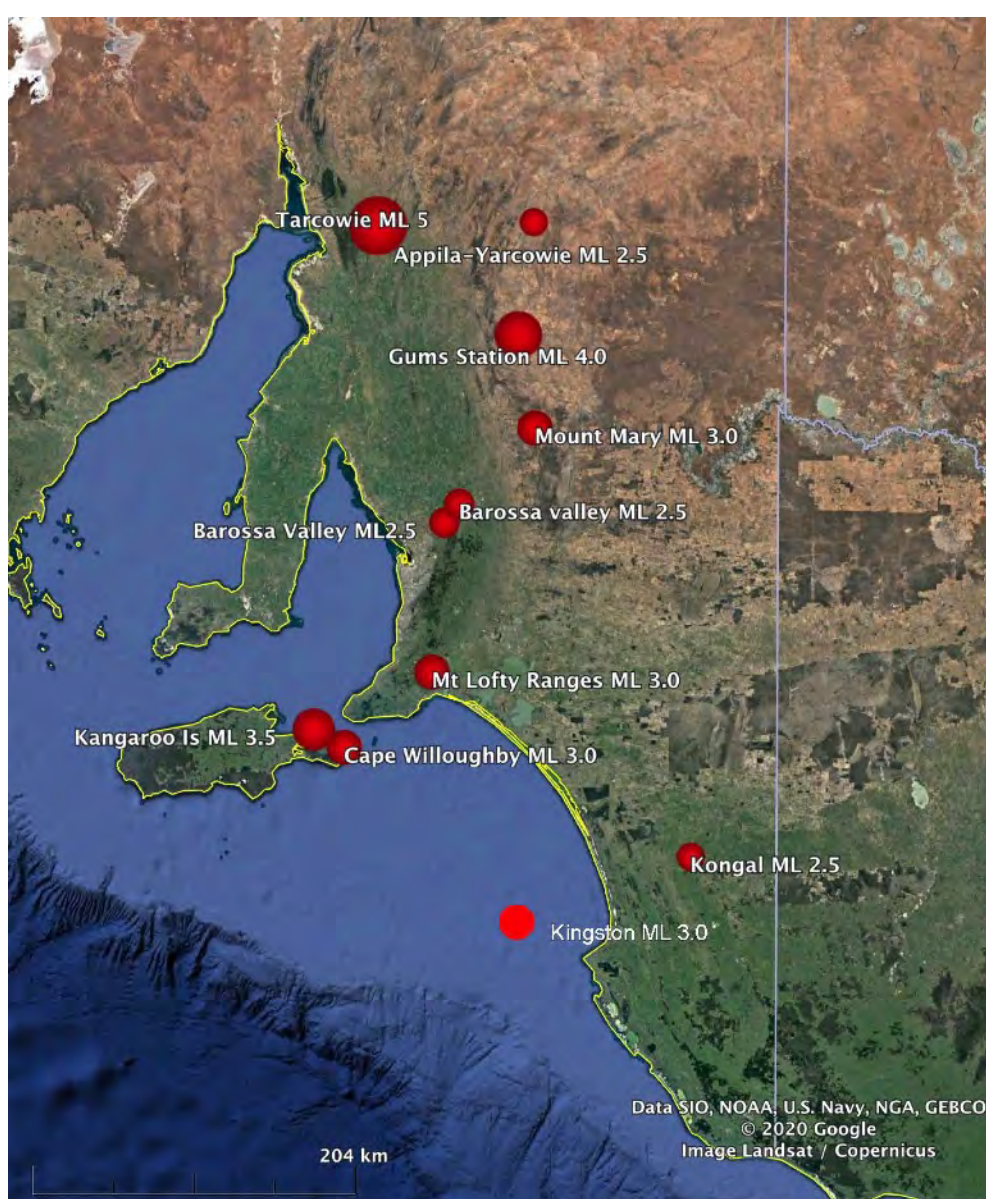


Figure 2 Epicentres of known South Australian earthquakes (red dots) in 1908, scaled for magnitude, several events are superposed..

DISCUSSION

TROVE has been used for the last decade to document earthquakes in South Australia dating back to 1836, and the number of known earthquakes has increased quickly in that time as a result. This paper was triggered, partly after reviewing a draft paper by Rubenach and others (2020) and partly serendipitously by tracing the history of the Adelaide seismograph station and its first Director George Dodwell.

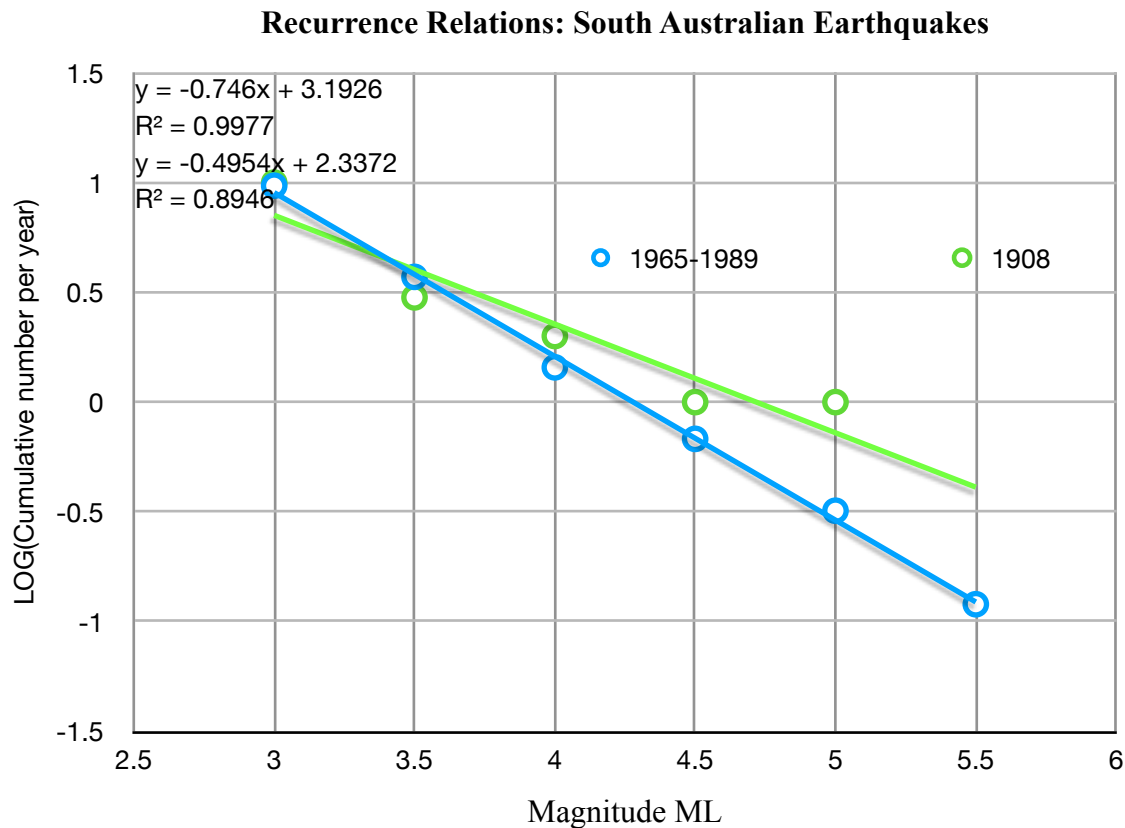


Figure 3 Recurrence relation for 1908 (green) compared with the average for 1965 to 1989 (blue). The data for the 1965-1989 period was downloaded from the Geoscience Australia on-line catalogue.

The seismicity was higher in 1908 than in an average year in South Australia thanks to the magnitude ML 5 Tarcowie (Peterborough) earthquake of 9 April. The earthquakes occurred in the usual places where they have been mapped over the last 50 years, principally along the uplifted Mt Lofty and Flinders Ranges as far as Kangaroo Island and one in the Southeast. The exception is that there were none reported on Eyre Peninsula where they were too small to be felt or weren't widely reported. This stationarity of the earthquake source over more than a century is very pertinent information for earthquake hazard assessments, as is the variability of 'b'.

The uncertainties in location are probably not much more than about 20km, especially the smaller events. Magnitudes are within ± 0.5 , about what Richter (1958) found in California when he introduced the local magnitude scale. Where an isoseismal map has been drawn then the uncertainty is more akin to the standard deviation from modern assessments using seismogram amplitudes and distance and instrumental correction factors.

Minor earthquake damage was reported at Melrose in the mid-North Tarcowie (Peterborough) earthquake where plaster was knocked off some walls but no injuries were sustained in the year. It is impossible to assign the earthquake to any fault but the earthquake is in the vicinity of the major range-front fault along the western side of the Flinders Ranges, considering the supposed focal depth.

Vacillating political patronage is damaging for science and for seismology in particular due to the need for long term monitoring and research. The Adelaide seismograph was purchased by the Federal Government of the time in ~1905 after extensive lobbying from South Australian scientists and engineers following the 1897 and 1902 earthquakes off Beachport and Adelaide. Before it could be installed this support was axed in 1908, the role picked up by the State. Ironically the reverse happened in 2016 when the State Government handed back operation of the state seismograph network to the Federal Government, a network that had grown from 1959 to cover most of the State. But what guarantee did they get from the Commonwealth Government that this function this time would continue into the future?

In South Australia in 1908 there were no seismographs, but today there are some 33 seismographs available and routinely used to locate earthquakes by SAA analysts, some are GA stations, some ANU Seismometer in Schools stations, the majority are privately owned and run by citizen scientists.

Citizen Science in South Australia

The role for citizen science in earthquake monitoring is an interesting one. English engineer John Milne set up the world's first international seismological network, 9 in the UK and about 20 overseas, from his base at Shide on the Isle of Wight, funded from a small grant from the British Association for the Advancement of Science, another from the Academy of Science, some private donations and his own money. His world earthquake database became the ISS in 1918 which morphed into the ISC in 1964.

Milne must be hailed as the first citizen-science seismologist. Todd and Howchin and the Australian Association for the Advancement of Science didn't follow suite but relied on government funding. More than 100 years later, the SA government handed responsibility for earthquakes back to the Commonwealth Government. The Seismological Association of Australia was established in 2017 and has built an impressive, professional citizen science earthquake monitoring network and database in South Australia, but succession plans for its long term viability must be developed.

A number of private networks exist in Australia; SRC has a network extending from Tasmania to central coastal NSW with a small network in WA too, the WA State Government is re-investing in a few stations after all the other states closed theirs. The ANU established an Australia wide network in schools (AuSIS) and Melbourne University has a network in SE Victoria. There are localised private company networks and several other citizen science stations, some of which, like EPSO, are very advanced.

REFERENCES

- Burke-Gaffney, T.N., 1951. *Seismicity of Australia*. Journal and proceedings of the Royal Society of New South Wales. Sydney, Royal Society of New South Wales.v.85, 47-52 pp: <http://www.biodiversitylibrary.org/item/173910> <http://www.biodiversitylibrary.org/bibliography/52324>.
- Dix, K.L., 2013. *South Australian Historical Earthquakes In the Pre-Instrumental Period 1837-1963: A Comprehensive Chronicle and Analysis of Available Intensity Data*. M.Phil. Thesis, Adelaide University September 2013.
- Malpas K. L., 1991. *Seismic Risk in South Australia*. Honours Thesis, School of Earth Sciences, Flinders University of South Australia.

- Malpas K., L., 1993. *Historical Earthquakes in South Australia. Vols 1-5*. Unpublished Record Flinders University.
- McCue K.F. 1975, Seismicity and Seismic Risk in South Australia. University of Adelaide Report ADP 137, pp88.
- McCue, K. 1980. *Magnitudes of some early earthquakes in south-eastern Australia*. Search, 11(3), pp. 78-80.
- McCue, K. 2013. Historical earthquakes in South Australia. www.aees.org.au
- Richter C.F., 1958. Elementary Seismology. Freeman Press.
- Rubenach and others, 2010 (in Press). *A review of historical earthquakes in Queensland utilising the Trove Newspaper Archive as a primary source*. Australian Journal of Earth Sciences.

APPENDIX 1

Selected newspaper reports, in chronological order

#1 Advertiser (Adelaide, SA : 1889 - 1931), Tuesday 24 March 1908, page 9

KINGSTON, March 21.—A mild shock of earthquake was felt here last evening between 11 and 12. It came from the direction of the sea. There have been mild shocks annually at this time of the year since 1897, when a severe tremor nearly wiped Kingston and Robe off the map.

#2 Register (Adelaide, SA : 1901 - 1929), Saturday 11 April 1908, page 7

A MILD EARTHQUAKE.

EXTENSIVE RANGE.

TRURO, April 10.—A distinct shock of earthquake was felt here at 1.56 this morning. Crockery and other movable things rattled for nearly half a minute. The tremor seemed to be from the west towards the east.

PETERSBURG, April 10.—A severe earth tremor was felt at 2.15 this morning. Several persons were awakened through beds moving and the rattle of crockery.

CARRIETON, April 10.—One of the severest earth tremors for some years was felt this morning at 2 o'clock. It lasted for fully a minute, shaking crockery and other articles. The direction seemed to be from west to east. It was accompanied by a loud rumbling noise.

HAWKER, April 10.—Residents were suddenly awakened by a severe earthshock at 1.56 this morning. The shock lasted seven seconds, and the vibration was from south-east to north-west.

MOUNT MARY, April 10.—A severe earthquake shock occurred at about 2 this morning. It awoke people and made windows and iron roofs rattle.

MORCHARD, April 10.—A distinct earth tremor was felt this morning at about 2 o'clock.

JAMESTOWN, April 10.—A severe earthquake was felt at 2 o'clock this morning. The vibration lasted for many seconds. Windows and doors rattled perceptibly. It appeared to go in a north-easterly direction.

ORROROO, April 10.—A rather severe earthquake was experienced this morning about 2 o'clock. It lasted a considerable time, and awoke most of the residents, who had an uncanny feeling as they were aroused from their slumbers and found the houses shaking and the windows and doors rattling.

YONGALA, April 10.—An earth tremor which lasted several seconds was felt at about 2 o'clock this morning. Windows rattled loudly, and houses shook, but not much damage was done. The rumbling sound travelled in a north-easterly direction.

Register (Adelaide, SA : 1901 - 1929), Monday 13 April 1908, page 7

THE RECENT EARTHQUAKE.

HORNSDALE, April 10.—At 2 a.m. to-day an earthshock was felt. There was a prolonged rumbling, as though heavy loads were being carted.

BOOLEROO CENTRE, April 10.—A smart earthshock occurred here at 2 this morning. It caused a shaking; beds were felt to move, and doors and windows rattled. This is the most severe shock felt here for some years.

LAURA, April 10.—This morning about 2 o'clock there was a distinct earthshock felt in Laura.

Chronicle (Adelaide, SA : 1895 - 1954), Saturday 18 April 1908, page 44

AN EARTH TREMOR.

Melrose, April 10.

An unusually severe earth shock of over 50 seconds' duration was experienced here about 2 o'clock this morning, the disturbance travelling from west to east. Plaster was knocked off some walls, and sleepers were somewhat rudely awakened. The weather at the time was sultry, with a dead calm.

Carrieton, April 10. An earth shock was experienced here, at 1.55 this morning, travelling south-west to north-east. The duration of the shock was about 30 seconds. It was the most severe felt here for many years.

Quorn, April 10. A decided earth tremor was felt about 2 o'clock this morning, awakening the residents' of the district and town. The buildings received a shaking, and crockery, &c, rattled loudly. The shock travelled, slowly from east to west, lasting about 10 to 15 sec.

It is reported to have been severe at Port Augusta, and to the north east, at Wyacca, and at Arden Vale.

Tarcowie, April 10. A severe shock of earthquake occurred here at 2 a.m. Its course was from west to east.

Petersburg, April 10. A sharp shock of earthquake was experienced here at about 2.30 a.m. It appeared to be travelling from south-west to north-east.

Laura, April 10. A slight earth-shock was felt here by a number of residents at 3.10 a.m., travelling south to north.

Hammond, April 10. A severe earthquake shock was felt here early this morning. Its duration was about 10 sec., and it was apparently travelling from a north-westerly direction.

Mannanarie, April 10. A sharp shock of earthquake was felt about 2.10 a.m. Houses were much shaken.

Hawker, April 10.— A severe earth shock was experienced here about 8 minutes to 2 this morning, and caused things to rattle and houses to shake considerably. Many people were awakened and rushed out of doors. The shock lasted fully 60 seconds. It appeared to be travelling from north to south.

Port Augusta Dispatch, Newcastle and Flinders Chronicle (SA : 1885 - 1916), Friday 10 April 1908, page 2

EARTH TREMOR.—At three minutes to 2 we were awakened by the ominous rattling of the windows, combined with a rumbling sound which continued for fully half-a-minute. The weather was calm, close and sultry. The tremor appeared to be from east to west. There was a kind of rumbling noise, at the time, a vibration and continuous shaking and rattling of the window-sashes. In a quarter-of-an hour after, whilst lying in bed, we again felt distinctly a slight quivering, which seemed to be prolonged for about, another half-minute. Many Port Augusta residents also felt the shock, more or less.

#3 Chronicle (Adelaide, SA : 1895 - 1954), Saturday 30 May 1908, page 13

AN EARTHQUAKE SHOCK.

APPILA-YARROWIE, May 25.—On Sunday at 5.30 p.m. an earth tremor was felt here, which lasted seven seconds. It seemed to be travelling from south-east to north-west.

#4 Register (Adelaide, SA : 1901 - 1929), Friday 5 June 1908, page 3

EARTHQUAKE SHOCK.

GUMS STATION, FLORIETON.—June 2.— A distinct earthquake shock was felt here at 1 1.30 last night. It lasted 10 or 15 seconds.

Chronicle (Adelaide, SA : 1895 - 1954), Saturday 13 June 1908, page 13

AN EARTHQUAKE SHOCK.

MOUNT BRYAN, June 2.— Very early this morning an earthquake shock passed over the district, lasting for many seconds. Doors and windows rattled noisily and houses received a good shaking. In one instance a door opened with the force of the shock.

Burra Record (SA : 1878 - 1954), Wednesday 3 June 1908, page 3

At about 12 o'clock on Monday night a rather severe earth tremor was felt in Burra. It was of several seconds duration, and travelled in an easterly direction. Crockery rattled, doors shook and the buildings trembled. It was the cause of many persons either remaining up all night or preventing them from sleeping. It is interesting to know that the tremor was felt 30 miles out east at the same time as it was experienced in the town.

#5 Observer (Adelaide, SA : 1905 - 1931), Saturday 13 June 1908, page 15

HAWKER, June 5.—A slight earthquake was felt to-day at 1.34 p.m. It lasted about one and a half seconds, and the vibration was from south-west to north-east.

#6 Observer (Adelaide, SA : 1905 - 1931), Saturday 4 July 1908, page 15

A report came through by telephone from Cape Willoughby Lighthouse that an earthquake shock was felt there at 8.45 on Saturday morning. The shock was also felt at the cottages several hundred yards away. It appeared to be travelling in a north easterly direction.

#7 Advertiser (Adelaide, SA : 1889 - 1931), Monday 20 July 1908, page 5

SPALDING, July 17.—A short heavy shock of earthquake was experienced here yesterday at 5.15 p.m. The sound was unusual, reminding one of an explosion.

#8&9 Chronicle (Adelaide, SA : 1895 - 1954), Saturday 5 September 1908, page 13

EARTHQUAKE SHOCKS.

NANGKITA, August 27.—A slight shock of earthquake was felt on Tuesday at 8.25 p.m., and another on Wednesday at 10.10 p.m. Both shocks were heavy enough to make iron roofs rattle.

HINDMARSH ISLAND, August 26.— A slight shock of earthquake was felt last evening about 8.25 o'clock.

Register (Adelaide, SA : 1901 - 1929), Monday 31 August 1908, page 6

EARTH TREMOR.

MOUNT COMPASS, August 28.—On Tuesday evening, at about 8.30, an earth tremor was experienced, accompanied by a great rumbling noise.

#10 Border Chronicle (Bordertown, SA : 1908 - 1950), Friday 4 September 1908, page 3

EARTH TREMOR

Kongal. A slight earth-quake was felt out this way on Friday morning last, eight o'clock, causing the crockery to rattle.

#11 Chronicle (Adelaide, SA : 1895 - 1954), Saturday 3 October 1908, page 14

SPALDING. September 23 —A severe shock of earthquake was experienced here last night by a number of the residents.

12 Chronicle (Adelaide, SA : 1895 - 1954), Saturday 10 October 1908, page 14

EARTHQUAKE SHOCKS.

EUDUNDA, October 6.— A sharp earthquake shock was felt here on Sunday about 5.10 p.m. It was accompanied by a loud, rumbling noise, like a heavy waggon passing over hollow ground. It lasted about 20 seconds.

SUTHERLANDS, October 6.— On Sunday, about 5 p.m., a severe earthquake shock was felt. The vibration caused windows, crockery, and furniture to rattle. It was accompanied with a loud rumbling noise like thunder.

MOUNT MARY, October 5.— A sharp shock of earthquake occurred here about 5.10 p.m. yesterday. It shook buildings and made iron roofs and windows rattle. The vibration seemed to travel from east to west.

#13 Evening Journal (Adelaide, SA : 1869 - 1912), Tuesday 13 October 1908, page 2.

EARTHQUAKE SHOCK.

DAVEYSTON, October 12.—A slight shock of earthquake, lasting a few seconds, occurred at 8.42 tonight. It was travelling from south-west to north-east.

14 MOUNT BRYAN, October 26.—A slight earthquake was experienced about 7.45 a.m. to-day . The roaring sound lasted for several seconds.

#15 Register (Adelaide, SA : 1901 - 1929), Saturday 31 October 1908, page 1

EARTHQUAKE SHOCK.

HOG BAY, K.I. October 29.—An earthquake shock of fair duration was felt here this morning at about quarter past 6. The vibration appeared to be travelling from the south-east towards the north-west.

SECOND VALLEY, October 29.— At about 6.10 this morning a slight earthquake was felt. It appeared to be travelling from south-west to north-east.

#16 Chronicle (Adelaide, SA : 1895 - 1954), Saturday 26 December 1908, page 12.

AN EARTHQUAKE SHOCK

Second Valley, December 17. — On Wednesday at 9.26 p.m. a severe shock of earthquake was experienced, its direction being from south-east to north-west. It lasted for about half a minute. The

vibrations rattled the windows and the gas lamps. It was the most severe shock since the great disturbance of 1903.

Appendix 2 The Adelaide Seismograph

Express and Telegraph (Adelaide, SA : 1867 - 1922), Saturday 23 January 1904, page 1

At a meeting of the astronomy, mathematics, physics, and mechanics' section of the Australasian Association for the Advancement of Science, held in Dunedin in January 1904, the Seismological Committee recommended that the Government of South Australia be asked by the Council of the Association to enable Sir Charles Todd to procure and install a Milne seismograph at the Adelaide Observatory (author: Todd had been lobbying since the 1897 earthquake for a local seismograph).

Register (Adelaide, SA : 1901 - 1929), Tuesday 1 October 1907, page 4

A slight earth tremor was experienced in Adelaide and suburbs on Monday morning. It occurred at 8.45, and lasted about a second and a half. Two reports were received at the Observatory from the suburbs regarding the tremor. The Government has authorized the construction of a seismograph at West terrace to record earthquakes, and the necessary buildings are now being put up.

Express and Telegraph (Adelaide, SA : 1867 - 1922), Friday 3 January 1908, page 3

THE SEISMOGRAPH.

A seismograph, an instrument for recording earth tremors, which has so long been needed in South Australia, is now on its way out from England, and is expected to arrive at Port Adelaide early next month. The construction of the building for its reception at the Observatory, which necessitated an excavation to the solid rock is now nearly completed. All those portions of the plant that could be procured in Australia are in readiness, and Mr. Dodwell, the divisional officer, anticipates that the seismograph will be installed at the Observatory within a couple of months.

Evening Journal (Adelaide, SA : 1869 - 1912), Wednesday 15 April 1908, page 2

THE SEISMOGRAPH HUNG UP

South Australia is in the foolish position of possessing the finest seismograph south of the line, and yet the instrument cannot be brought into operation because of clashing Commonwealth and State interests. The Observatory staff is undermanned, the vacancy created by the death of Mr. Chettle not having been filled. Further, the authorities have not yet been able to determine whether the astronomical staff is part of the meteorological staff, and in the meantime astronomical affairs are between the devil and the Grand Canal, as they say in Venice. The members of the Astronomical Society inspected the seismograph at the Adelaide Observatory on Tuesday night. It is mounted on brick and concrete piers let into mother earth, and the "boom" is so delicately balanced that mere hand pressure on the masonry causes it to vibrate.

Register (Adelaide, SA : 1901 - 1929), Tuesday 5 January 1909, page 6

ADELAIDE'S SEISMOGRAPH.

Most of the capitals of the world have seismographs—the instrument which registers earth tremors. They are of decided value to scientists in assisting them to detect the far-reaching influence of any upheaval or subterranean disturbance. The recent disaster in southern Italy and Sicily was recorded on those in operation in Australia, and probably would have been marked on the plan had the apparatus in Adelaide been in working order. South Australia has had one in stock or in process of being fitted up for some considerable time, but when it will be completed nobody knows. The instrument was purchased long ago, the contract for the erection of the building to house it was let in August, 1907, and this work was finished months ago. The recording appliance is in position, but there remain certain finishing touches to be added before the seismograph will work properly. An explanation of the delay is that all the money voted for the work has been spent, and there is no grant for further expenditure.

note: Adelaidians had to wait another 6 months before the seismograph was inaugurated.

COLLAPSE BEHAVIOUR OF A MODULAR BUILDING IN SEISMIC CONDITIONS

Mohamed Mafas M.M¹, Nelson T.K. Lam², Siddhesh Godbole³, Pat Rajeev⁴

1. Corresponding Author. PhD student, Department of Infrastructure Engineering, The University of Melbourne, Parkville, VIC 3010, Australia.
Email: mmohamed7@student.unimelb.edu.au
2. Professor, Department of Infrastructure Engineering, The University of Melbourne, Parkville, VIC 3010, Australia. Email: ntkl@unimelb.edu.au
3. PhD student, Department of Infrastructure Engineering, The University of Melbourne, Parkville, VIC 3010, Australia. Email: godboles@student.unimelb.edu.au
4. Associate Professor, Faculty of Science, Engineering & Technology, Swinburne University of technology, Hawthorn VIC 3122. Email: prajeev@swin.edu.au

Abstract

In severe seismic conditions, a modular building may behave very differently to a building of the conventional form of construction. As the relative load bearing capacity of the module is expected to be higher than the intra-modular connections, failure is expected to occur at the connections, which may be limited to a single storey (unzipped) when the rest of the building may remain in the elastic state. The superstructure above the failure plane could experience a combination of sliding and overturning motions. This study is aimed at modelling the ultimate performance behaviour of the inter-modular connections between adjacent storeys as well as the near-collapse response behaviour of the building as a whole using numerical and experimental analysis. Shaker table experiments conducted on a scaled down model of a modular building revealed that what caused collapse of the building tower was precisely the bolted connections. The sudden release of strain energy caused by the fracturing of the bolts can topple a building tower. Overturning ensued as the bolts became unzipped. As that happened the shaker table only moved by 45 mm. This amount of movement was less than 20% of the width of the scaled down model of the tower which would not have overturned had it been free standing as opposed to being secured by bolts in the first place. Ironically, it is the intention of the structural designer to use holding down bolts to secure the modular units in place.

1 Introduction

The concept of Modular building construction (MBC) has been gaining popularity over the last two decades due to increased productivity, reduced material wastage, reduced costs and construction time, and more sustainable scalable approach [1]. Starting from prefabrication of single components such as slab elements or any other small component of a building, Modular construction gradually transformed to prefabrication of volumetric cubicle components manufactured at controlled factory environments. These volumetric components slowly incorporated all the necessary equipment's and fittings necessary for the place in the building where the volumetric component belong to [2, 3].

Despite many advantages, current modular buildings still depend on in situ core wall constructed to provide lateral force resistance. Requirement of the in situ concrete core inhibits the productivity of the modular construction. Modular constructions which eliminates these requirements, totally eliminating any work at site other than assembly of modules are considered as pure (fully) modular construction [3, 4]. Pure modular structures are not fully realised in the current practise. However, current building codes do not restrict a purely modular building as long as the design meet the performance requirements in standards. There are no rules or regulations in the current practise requiring external lateral force resisting systems (LFRS) for structures built in low to moderate seismic regions. Given the enormous time and cost savings from eliminating any external LFRS, designers might soon opt to move towards pure modular structures while still designing the structure as per conventional design standards.

Regardless of the construction type, a structure behaves elastically and adequately against the loads under the design performance limit. Nevertheless, if a rare seismic event exceeding the design limit occurs, a modular building might behave differently than a conventional building. In this scenario, the discontinuous nature of the building due to the alternate arrangement of connections and modules may render comparatively weaker connections (compared to modules) more susceptible to failure. This failure may result in a discontinuity in the lateral and gravity load-flowing path between modules.

Bolted connections are more commonly used in current modular construction practise. Bolted connections show brittle fracture post limit conditions. Failure of one connection may increase the stress concentration in other connections in the same storey triggering series of connection

failures in an unzipping fashion. This may result in a plunge in the damage variation of the structure, resulting in adverse effects on the serviceability of the structure. Furthermore, an unzipping of connections across one storey may leave a colossal mass of structural component comprising a stack of modules to stand freely and overturn and collapse if the ground motion intensity continued to increase further. Analysis of collapse of this nature may include the rigid body motion of free-standing blocks of modules or free-falling single modules. This sort of potential destructive collapse behaviour in modular construction has not been studied yet.

The aim of this study is to highlight the aforementioned potential risk involved in pure modular buildings that are built using conventionally available bolted connections when they undergo dynamic events exceeding their design intensity. A mid-rise (ten storey) pure modular structure designed as per Australian design standards for Melbourne conditions was chosen as a prototype building in this study.

2 Highlights of Findings

This section briefly presents the main finding of the research. However, further details on these findings are presented under subsequent sections.

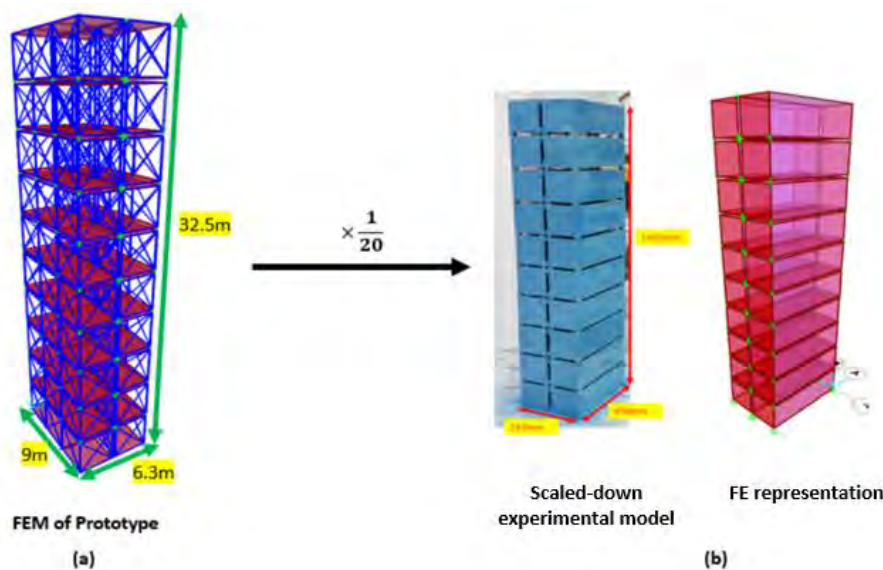


Figure 1 (a) FEM of prototype (b) Scaled down model on the shaker table (FE & Physical models)

Shaker table experiments on the scaled down modular building revealed that a free-standing superstructure component could be formed due to failure of all the connections in the first

storey. The superstructure thus formed experienced sliding while rocking and finally overturning (Figure 2 (a)).

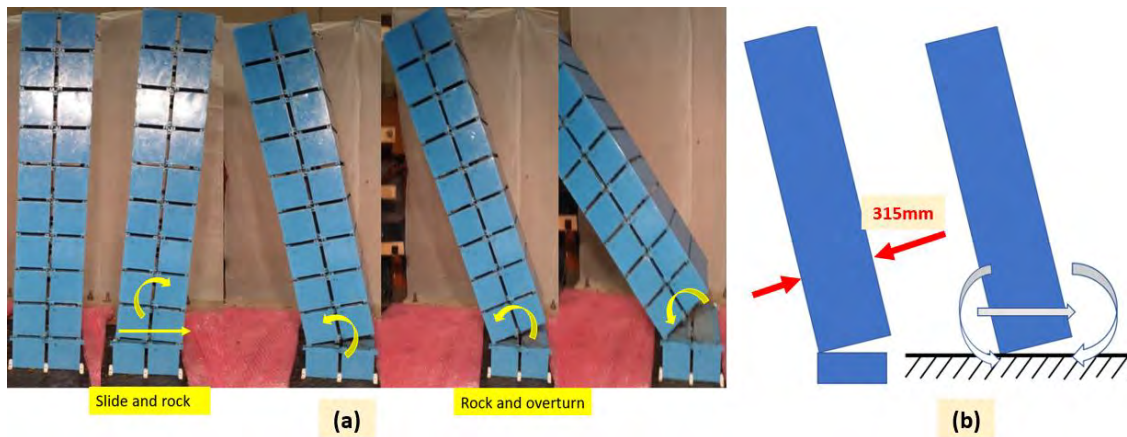


Figure 2 (a) Free-standing motion phase of the modular building superstructure (b) Rigid body assumption of the modular building superstructure

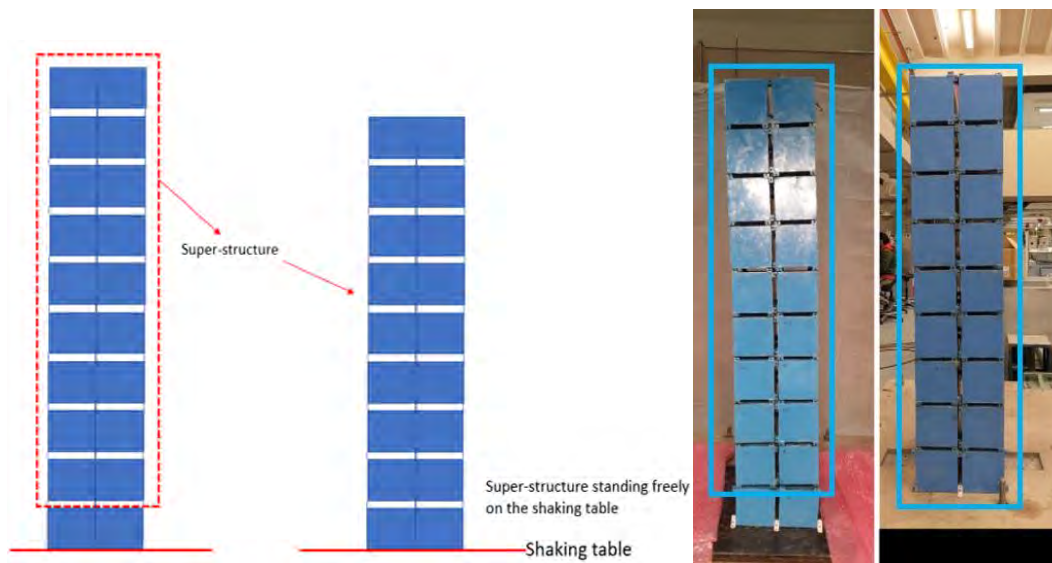


Figure 3 Representation of the free-standing superstructure component analysed on the shaking table

The free-standing superstructure formed was set to stand free on the shaking table (Figure 3) and subjected to the same ground motion stretch corresponding to the rocking, sliding, and overturning of the modular building (Same analysis was repeated numerically). The experimental and numerical results revealed that the superstructure starting from rest, free-standing, did not overturn. This concludes that the cause of overturning is the failure of bolted connections. The sudden strain energy released from the failure of these connections resulted

in sufficient energy in the free-standing superstructure to overturn. The amount of ground movement was less than 20% of the width of the scaled down model of the tower (Figure 5) which would not have overturned had it been free standing as opposed to being secured by bolts in the first place (Figure 4).

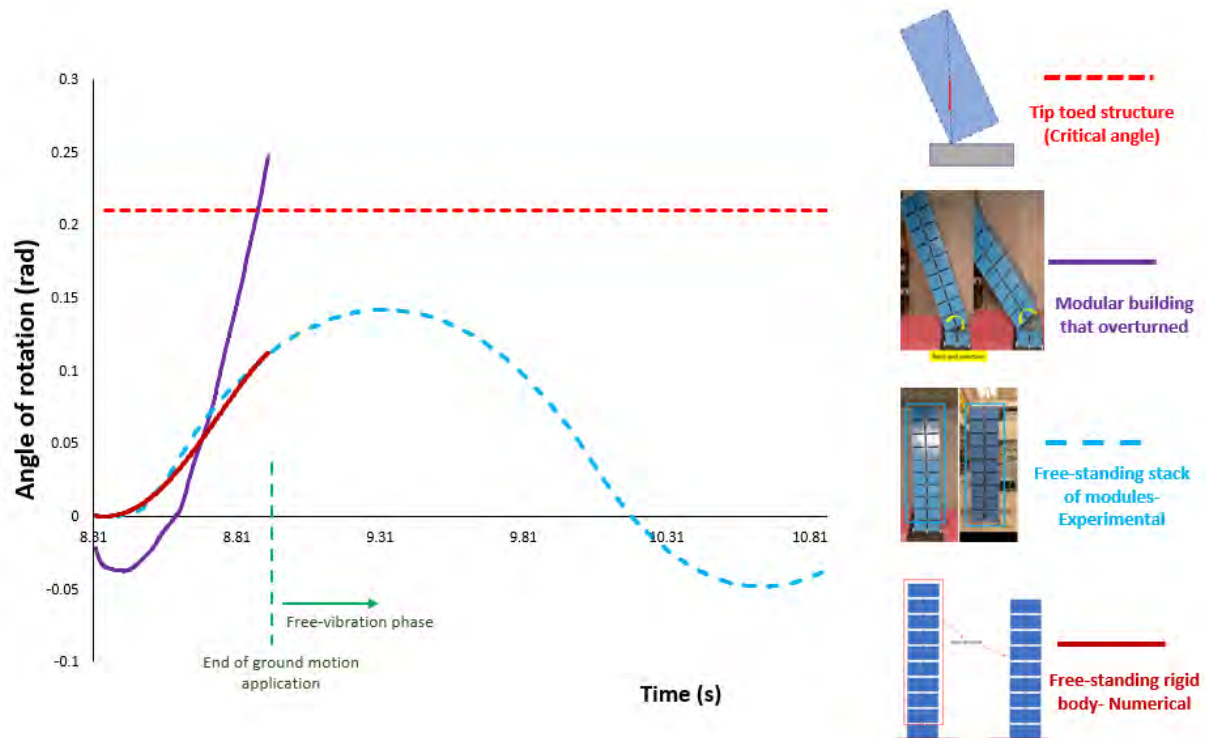


Figure 4 Angle of rotation of a free-standing body with and without initial conditions.

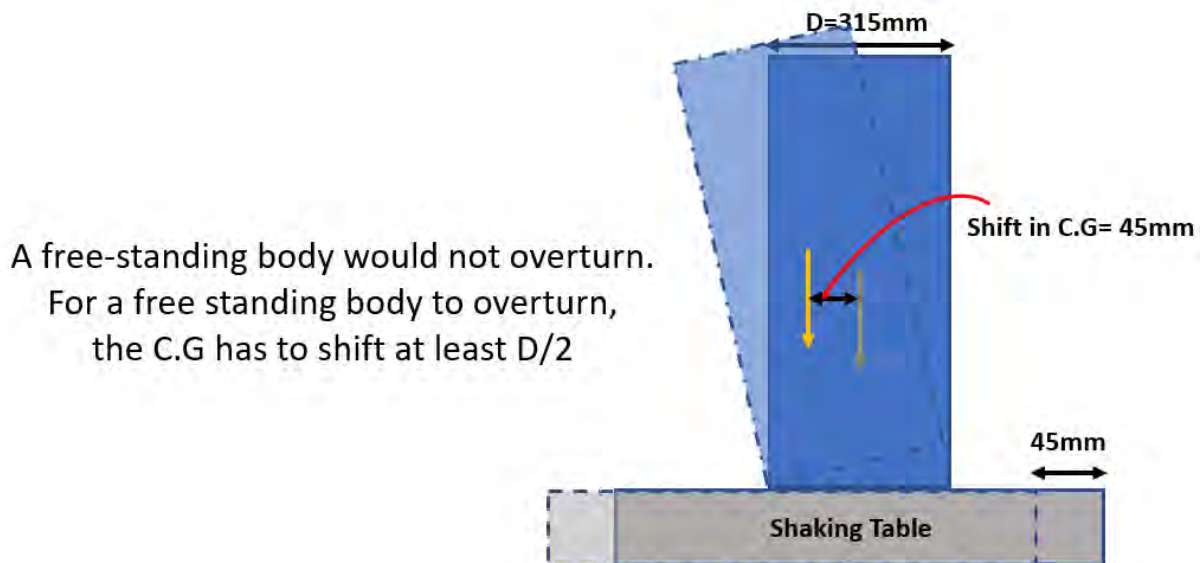


Figure 5 Response of a free-standing body under the considered ground motion.

3 Dynamic Time History Analysis

3.1 Incremental Dynamic Analysis (IDA).

The most common method used in performing a comprehensive assessment of the behaviour of structures under seismic loads is Incremental Dynamic Analysis (IDA) [5]. Conducting an IDA could get computationally expensive. Experimental IDA of structures on shaking table can get cumbersome and expensive owing to the number of different intensity trials one might need to perform to evaluate the trend of the damage extent with increasing loading intensity [6]. To overcome these challenges in practise, researchers such as Estekanchi et al. [7] proposed a concept of Endurance Time History Analysis (ETHA). Since the introduction of the concept, there have been significant improvements in this method over the past decade.

3.2 Endurance Time History Analysis (ETHA)

Endurance time method is a seismic structural analysis method using intensifying dynamic loads. The structural response is monitored as the intensity of excitation is increased. Structural performance is assessed based on the response of the building as function of the excitation intensity [8]. As the applied excitation progressively intensifies, the “time” taken to reach a certain limit state since the commencement of excitation can be taken as the measure of the ground shaking intensity, and can be mapped to a more commonly used intensity measure such as Peak Ground Acceleration (PGA). The response parameter can be any measure of structural response such as top displacement, drift, and the like. This is very much similar to an IDA in terms of output obtained but the load application process is simpler compared to an IDA [8].

Generating meaningful Endurance Time Excitation Functions (ETEFs) is essential in obtaining more realistic results that are compatible with time history analysis results. The response spectrum well represents the important characteristics of earthquake ground shaking and has therefore been adopted as the concept in developing ETEF. ETEFs are produced by considering a seismic code-based design spectrum as a template (target spectrum). A progressively intensifying excitation time-history which has the feature of producing a response spectrum that always remains to be proportional to a target spectrum at all times has been generated [9-12].

At the time stretch: $t = 0$ to $t = T_{target}$, the response spectrum would match with the target response spectrum that had been used to generate the ETEF. In this study, ETA40lc01, being one of the ETEF's available on the Endurance time method website [7] was adopted. The

FEMA P-695 far field ground motions average spectra has been used as the target spectra for generating this ETEF [13].

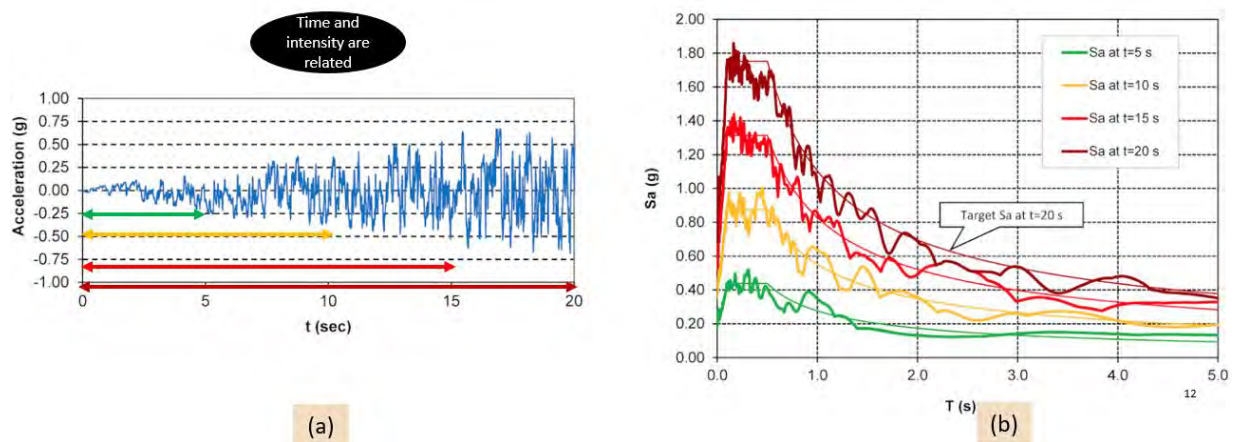


Figure 6 (a) An ETEF (b) Response spectra corresponding to different time stretches [8]

4 Experimental and Numerical Analysis

4.1 FE Analysis of the Prototype

Since the structure considered in this study is a pure modular structure, prior to proceeding to analyses on scaled-down models, analyses were conducted on the prototype model of the modular building (Figure 1 (a)) to study its feasibility in terms code requirements. Accordingly, the structure performance was deemed satisfactory in terms of modal analysis, Capacity spectrum analysis and non-linear dynamic analysis within the design limits. However, it was noticed under the ETEF that the structure failed in a catastrophic manner under dynamic loadings beyond the design limit. Although most of the structural deformation was mapped to the deformation in the modules, the failure was observed to be initiating and progressing through first storey edge connections. Failure in the peripheral connections was observed to progress to interior connections of the same storey leading to catastrophic failure of the entire structure in an unzipping manner. These observations can be viewed at: <https://youtu.be/clBrX40jUY0>. These observations aligned very well with the hypothesis formed during this study.

Based on the observations on the FE model of prototype and considering constraints in terms replicating the exact prototype model response in the experimental model, rigid boxes were employed to represent the modules in the experimental model. Accordingly, the developed experimental and numerical model of the scaled-down building are presented in Figure 1 (b).

4.2 Scaled-down Models for Shaker Table Testing

Repeating the analyses conducted on the FE model of the prototype, modal analysis and pushover analysis were conducted on the scaled down FE and experimental models of the building. Modal analysis and pushover analysis results obtained using numerical and experimental methods showed a good agreement and correlated well with the scaled down results of the same obtained using the prototype.

Following the static analyses (modal and pushover), the experimental model was subjected to the ETEF on the shaking table while the corresponding FE model was also subjected to the same ETEF. Since the global structural response under increasing seismic intensity was of concern, the roof displacement was recorded during both experimental and numerical analyses. An important advantage of employing ETHA is that the damage parameter recorded with time can be easily converted to the corresponding IDA curve by replacing the time axis with seismic intensity. The IDA curves thus obtained using experimental and numerical methods are depicted in Figure 7.

With the gradual increase in applied acceleration under the ETEF, the structure began showing signs of excessive flexing around the first-storey edge connections. This was also an important observation in the pushover analysis. Gradually, when the acceleration time history intensified further, initiation of failure was observed along the connections along one edge of the first storey. This was immediately followed by the failure of peripheral connections in the opposite edge of the building. Sudden drop in lateral restraints marked by failure of peripheral connections put interior connection under much higher forces leading to their brittle failure. These observations were verified through the FE model simulations as well. A comparison of the response obtained using numerical and experimental methods can be viewed at: <https://youtu.be/WasqvdQvY18>.

It is evident from Figure 7 that there is a sudden increase in the damage variation of the structure around a seismic intensity of 2500-year hazard return period while it managed to perform adequately under seismic intensity of 500-year hazard return period (that corresponded to the design limit). Once all the connections of the first storey had failed, a slip of the free-standing superstructure (stack of modules above the first storey) was observed, followed by overturning and collapse (Figure 2(a)). Even though the FE model indicated the separation of the superstructure due to failure of connections, the slide, rock, and overturning observed was something not captured in the FE models. In order to simulate the free-standing motion phase

observations, a numerical model was developed assuming the superstructure component as a rigid body (as shown in Figure 2(b)). The numerical model thus developed was subjected to the ground motion corresponding to the free-standing motion phase of the structure and it was observed that the numerical model could very well represent the sliding, rocking and overturning observed in the modular building superstructure. The response of the superstructure predicted by the numerical model agreed very well with the response observed during the shaking table experiment.

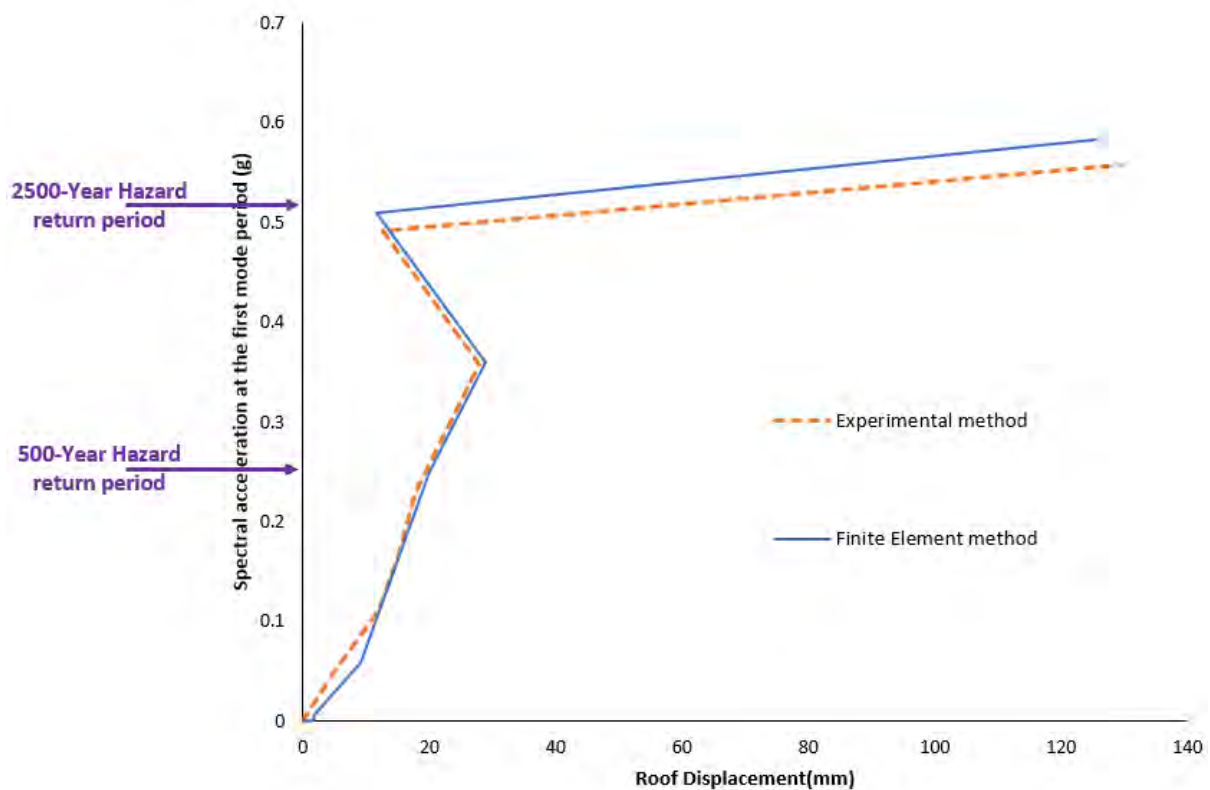


Figure 7 Comparison of IDA curves for the modular building obtained using experimental and FE analyses

According to Ref [14] a free-standing rectangular block is safe from overturning if the peak displacement demand is within half of the base dimension of the block. In this study, the peak displacement demand of the earthquake ground shaking was calculated to be 45 mm whereas the base dimension of the scaled experimental model in the direction of ground movement was 315mm (Figure 5). Hence, the structure is much wider than the input ground motion displacement. This is an alarming result on the collapse of modular structure, where the overturning of the superstructure was triggered without the necessity to satisfy one of the main requirements outlined as per Ref [14].

However, the rule of the thumb as stated only applies to a free-standing object which is free to rock (rotate in the vertical plane throughout the event) (starting from rest). For a bolt connected modular building, rocking only occurs as the connections become unzipped. In this sudden switch from a cantilever system to a free standing block, overturning would be possible if the response spectral velocity (V) of the building at the level of centre of inertia exceeds the critical velocity ($V_{critical}$) needed to overturn, regardless of the peak displacement demand. A preliminary energy balance considering the kinetic energy of the free-standing superstructure just after failure of all the connections and the potential energy required to overturn revealed that the critical velocity required for overturning exceeded the response spectral velocity of the superstructure just after failing all the connections. Although this is an indication that the initial velocity gained by the free-standing superstructure at the beginning of the free-standing motion is the cause of overturning, energy approach did not account for any energy loss due to friction and energy input due to the ground motion. Hence, experimental analysis accompanied by analyses on the developed numerical model of the free-standing superstructure were conducted to study the effect of the initial velocity.

The superstructure component that experienced the free-standing motion was set to stand freely on the shaking table (as illustrated in Figure 3) and subjected to the same ground motion stretch corresponding to the free-standing motion (i.e. rocking, sliding and overturning). However, in this section of the analysis, the superstructure component started from rest in contrast to starting the free-standing motion with an initial velocity (strain energy released from the failure of connections elevating the kinetic energy of the free-standing superstructure) in the case of original modular building that overturned.

The same analysis was also repeated on the numerical model of the free-standing superstructure. Both the numerical and experimental analyses revealed that the free-standing body did not overturn. It was observed that the free-standing body experienced pure rocking under the ground motion and came to rest after few oscillations under the free vibration. This observation compared with the observation for the original modular building which overturned can be viewed at: https://youtu.be/uc-XLpri1_0. The roof displacement recorded during the analysis were converted to the corresponding angle of rotation of the superstructure.

Figure 4 compares the angle of rotation of the original modular building superstructure which overturned due to the initial conditions, together with the angle of rotations of the free-standing

superstructures that started from rest and experienced the same stretch of ground motion, obtained using numerical and experimental methods.

Observations on the experimental models together with the plots in Figure 4 can be used to conclude that there is a substantial effect on overturning from the initial conditions gained by the superstructure component at the beginning of free-standing motion. These initial conditions which came into the free-standing body in the form of initial velocity, were gained from the strain energy released from the failure of the connections. Further, it was highlighted under previous paragraphs that all these connections failed in a matter of no time, which is a lot of strain energy released in a very small time. This sudden release of energy can be related to the overturning of the free-standing superstructure.

The energy released due to the failure of connections can be related to the strength of the connections. To study this effect, the entire study was repeated on a modular building with half the strength of the original connection. It was revealed that the free-standing superstructure block thus formed did not overturn under the rest of the ground motion but managed to rock and come to rest. This is due to the insufficient energy released (due to the lesser connection strength) from the failure of the connections, imparting lesser kinetic energy gain on the free-standing superstructure and hence no overturning.

It can be seen that there is a great agreement between the results obtained using numerical and experimental methods of the free-standing superstructure. This also served as a validation of the numerical model developed to simulate the rock, slide, and overturning motion of the superstructure component.

5 Intensity of Ground Shaking to Cause Collapse

The catastrophic nature of the collapse observed and discussed in the previous sections raises significant concerns over the seismic intensity that would lead to a collapse of this nature. A ground motion modelling tool called the Component Attenuation Model (CAM) [15] is employed to convert the seismic intensity responsible for collapse to generate a corresponding earthquake scenario.

Accordingly, the intensity that causes the sudden increase in damage is computed to be equivalent to that for a structure experiencing an M5.5 earthquake 10 km away, anywhere in south-east Australia. This implies that any modular structure within the 300-km² area with the

seismic source at its centre is likely to collapse in a manner similar to that observed during the shaking table experiment (Figure 7 (a)).

This intensity of ground shaking that causes the collapse of the building is consistent with an MMI value of VII-IX, as shown in (Figure 7 (b)). An MMI of IX was observed during both the 1968 Meckering (Western Australia, Australia) earthquake and the 1989 Newcastle (New South Wales, Australia) earthquake. Both these earthquakes resulted in massive damage in urban areas. Hence, if a modular building similar to that studied here was standing in one of these areas at the time of the earthquakes, it would have collapsed in a manner demonstrated through the shaking table experiments.

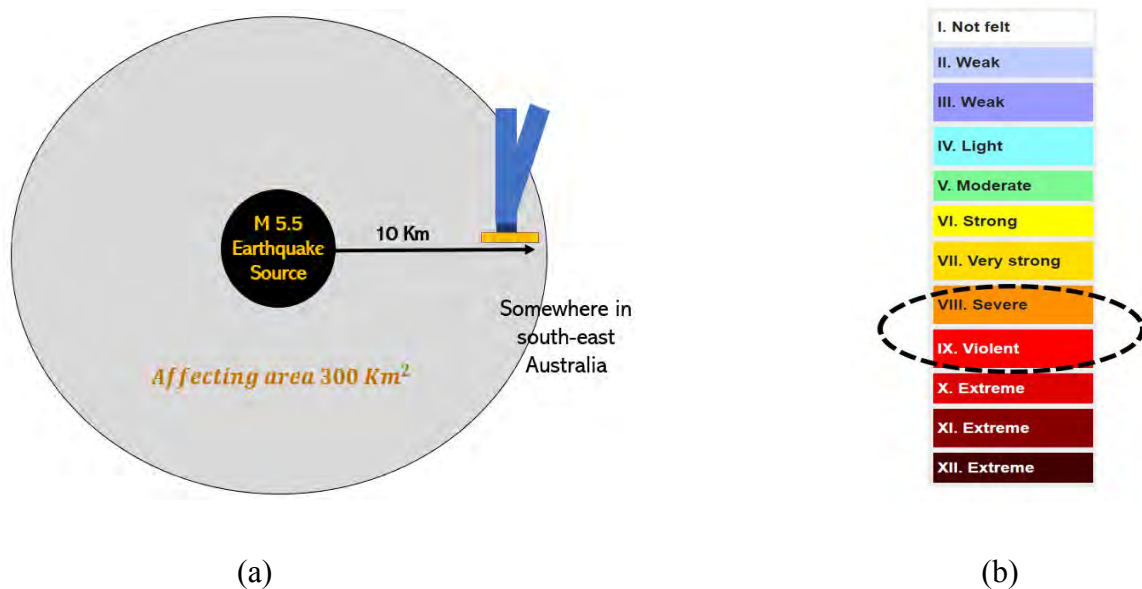


Figure 7 (a) Graphical interpretation of the potential risk area (b) Locating the corresponding intensity on the MMI scale

6 Conclusions and Recommendations

- Modular buildings have a discrete construction nature throughout the height where stronger module and less stronger connections are arranged in an alternate manner.
- The failure in pure modular structures is more concentrated at the connections despite the deformations in modules being the most contributing factor for the total deformation of the structure.
- First storey edge connections are the most critical connections. Failure of a single connection is sufficient to cause a catastrophe by resulting in a sudden increase in damage and resulting in other connections of the same storey vulnerable and fail.

- Even though pure modular structures are feasible in terms of design code requirements, the structures fail in a hazardous manner under dynamic events exceeding design limits.
- Damage progression in pure modular structures is restricted to a single storey as opposed to being distributed throughout the structure in conventional structures.
- Nature of failure involved in modular structures results in the possibility of a large, colossal mass to undergo rocking, sliding, and overturning as demonstrated through this study. This nature of collapse is unique to modular structures whereas in conventional structures the collapse involves failure of elements distributed throughout the structure in a progressive manner.
- The cause of overturning of the free-standing superstructure formed as a result of failure of connections can be entirely related to the energy released from the failure of connections.
- As recommendations for pure safer modular structures, allowing the structure to rock about the foundation is recommended. This will eliminate the higher inelasticity concentrations in the structure and hence the failure of the connections.
- Further, it is recommended to allow the failure to be incorporated in to the modules rather than allowing them to be focussed in the connections, so that the failure will be more distributed and there will be many ductile components which can undergo failure and result in a ductile, progressive collapse response of the entire structure.

7 Acknowledgements

The authors would like to thank The Department of Infrastructure Engineering of The University of Melbourne for the research funding and supports.

8 References

1. Lawson, M., R. Ogden, and C. Goodier, *Design in modular construction*. 2014: CRC Press.
2. Mohamed Mafas M.M, N.T.K.L., Siddhesh Godbole, Pat Rajeev, *Safety of Modular Buildings in Seismic conditions*, in *Australian Earthquake Engineering Society 2019 Conference*. 2019: Newcastle, NSW.
3. Gunawardena, T., *Behaviour of Prefabricated Modular Buildings Subjected to Lateral Loads*. 2016, The University of Melbourne.
4. Sendanayake, S.V., *Seismic mitigation of steel modular buildings using novel inter-modular connections*. 2020, Queensland University of Technology.
5. Asgarian, B., A. Fiouz, and A. Shakeri Talarposhti. *Incremental Dynamic Analysis Considering Pile-Soil-Structure Interaction for the Jacket Type Offshore Platforms*. in *International Conference on Offshore Mechanics and Arctic Engineering*. 2008.

6. Vamvatsikos, D. and C.A. Cornell. *The incremental dynamic analysis and its application to performance-based earthquake engineering*. in *Proceedings of the 12th European Conference on Earthquake Engineering*. 2002.
7. Estekanchi, H.E. *Endurance Time Method*. 2007; Available from: <https://sites.google.com/site/etmethod/home?authuser=0>.
8. Estekanchi, H. and H. Vafai, *Seismic Analysis and Design Using the Endurance Time Method, Volume II: Advanced Topics and Application*. 2018: Momentum Press.
9. Chiniforush, A.A., H. Estekanchi, and K.M. Dolatshahi, *Application of endurance time analysis in seismic evaluation of an unreinforced masonry monument*. *Journal of Earthquake Engineering*, 2017. **21**(2): p. 181-202.
10. Estekanchi, H., H. Riahi, and A. Vafai. *Endurance time method: exercise test for seismic assessment of structures*. in *Proceedings of the 14th world conference on earthquake engineering, Beijing*. 2008.
11. Estekanchi, H., H. Riahi, and A. Vafai, *Application of endurance time method in seismic assessment of steel frames*. *Engineering Structures*, 2011. **33**(9): p. 2535-2546.
12. Maleki-Amin, M.J. and H.E. Estekanchi, *Damage Estimation of Steel Moment-Resisting Frames by Endurance Time Method Using Damage-Based Target Time*. *Journal of Earthquake Engineering*, 2018. **22**(10): p. 1806-1835.
13. Mashayekhi, M., et al., *Simulation of cumulative absolute velocity consistent endurance time excitations*. *Journal of Earthquake Engineering*, 2018: p. 1-26.
14. Kafle, B., et al., *Displacement controlled rocking behaviour of rigid objects*. *Earthquake engineering & structural dynamics*, 2011. **40**(15): p. 1653-1669.
15. Lam, N. and J. Wilson. *The component attenuation model for low and moderate seismic regions*. in *Procs. of the Sixth Pacific Conference of Earthquake Engineering, University of Canterbury, Christchurch, New Zealand*. 2003.

Construction Monitoring Report for Seismic Bracing of Non-structural components

Arash Nazari Rad¹ and Peyman Sharifi²

1. Principal Structural/Seismic Engineer, MIEAust, NER, RPEQ, CPEng, Eurofast Pty Ltd, Sydney, NSW 2128, Australia. Email: Arash.n@eurofast.com.au
2. Structural Engineer, MIEAust, Eurofast Pty Ltd, Sydney, NSW 2128, Australia. Email: Peyman.sharifi@eurofast.com.au

Abstract

There has been a rising debate about seismic restraint compliance of non-structural components (NSCs) with AS1170.4:2007- earthquake actions standard in Australia. To achieve seismic code compliance, building services contractors usually would engage a seismic specialist to conduct design and construction monitoring for their scope of work. Seismic specialist will provide seismic restraint drawings which illustrate the requirement needed for compliance with relative standards and consequently certifies the design. Another scope of work which is a bit vague in the industry is construction monitoring report. This requirement would ensure on reasonable grounds that installation follows drawings. The required level of construction monitoring would vary depending on size, importance and complexity of the project, demonstrated experience and skills of the installer and also requested monitoring level at the initial stage of a project. One of the common issues regarding construction monitoring is ceiling closure before inspection. That is why having a scheduled plan for construction monitoring is vital for seismic specialist. In this paper, importance, different types and applications of construction monitoring will be discussed. Clients' responsibilities, liabilities and expectations will be explained and finally some suggestions for construction monitoring for seismic bracing on NSCs in Australia will be made.

Keywords: Non-Structural Components (NSCs), seismic restraint design, seismic bracing, inspection, construction monitoring report, Australian Standards, building services, MEPF (mechanical, electrical, plumbing, fire services)

1. Introduction

The behaviour of non-structural components (NSCs) in seismic events depends on design and installation of seismic restraints. Non-structural components within a building are included but not limited to architectural elements such as ceiling and partitions, mechanical services such as ducts, pipes and equipment and also electrical systems such as cable tray and devices. Linear components and floor mounted components in plumbing services, fire and medical gas systems are included in NSCs as well.

Any damage to NSCs during and after an earthquake event can affect operationality of NSCs that maybe vital for important buildings. Damages to NSCs not only interfere with immediate occupancy of the building, but also continuous operation of the building would be compromised during the repair work period and this in turn leads to significant economic losses and downtime.

Post Meckering earthquake in October 1968, the first earthquake code AS 2121 published in 1979. AS 1170.4 earthquake loads was published in 1993 and referenced in the BCA 1995 that contained a section “requirement for non-structural components”. In 2007 reissued as “earthquake actions in Australia” and section 8 covers “design for parts and components”. (Development of the new Australian earthquake loading standard, EJSE, 2008)

The process of seismic restraint design starts with extracting parameters of earthquake from structural reports, reviewing the seismic requirement of the NSCs’ specification and drawings, calculating suitable seismic restraints, followed by installation of bracing. In the following, construction monitoring of seismic restraint installations is being reviewed.

2. Seismic bracing design

According to the project design parameters, a seismic engineer will specify the seismic requirements. Seismic restraint design requirements and relevant exemptions have been mentioned in clause 8.1.4 and clause xviii of AS 1170.4, respectively. Depending on primary supports’ type and spacing, capacity of base-build structure, site access and clashes to other services the location of bracing and type of restraints is determined. Clash detection is very important to prevent collision between seismic braces with other nearby services. Appropriate clearances to minimise the chance of collision between services and subsequent damages in a seismic event, for both braced and unbraced components, have been recommended in G-172 (Seismic restraint of Engineering services-Government of South Australia – April 2019) and AS-2785: suspended ceiling design standard. Figure 1 shows an example of real site conditions of NSCs on construction sites.

In section 8 of AS 1170.4 two methods of load calculations have been mentioned, that is the acceleration method and the simple method. In both methods, seismic restraint design is to be carried out for horizontal and vertical earthquake actions in combination with gravity loadings. Moreover, NSCs shall accommodate inter-story drift caused by earthquake. After design completion by the seismic engineer, detailed drawings and plans are to be issued and sent to the client. These documents show type, size and location of the restraints. Finally, the seismic designer will provide full detailed design documentation (drawings, calculations, specifications and technical reports). In design certification, the following points are required to be addressed:

- Compliance with the building code should be clearly demonstrated.
- Any alternative solution based on site situation should be identified.

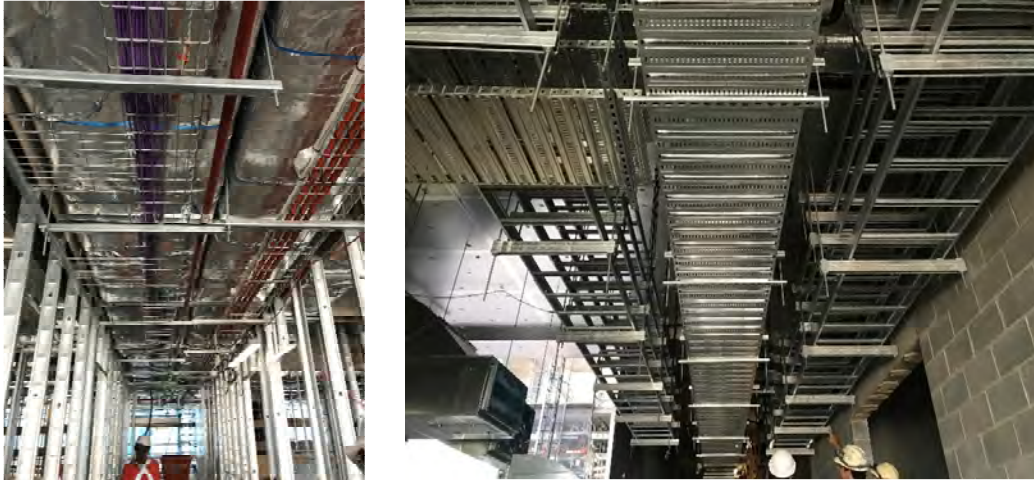


Figure 1: Real site conditions – Non-structural components

3. Construction/Installation Review

Seismic bracing installation needs to be carried out according to detailed drawings and documentations. A skilled/experienced engineer should audit the work to ensure compliance of installations with the designed drawings. This will give authorities more confidence that construction/installations comply with the building code and approved design methods.

A construction monitoring report certifies that installations carried out follow the seismic design, however this will not relieve any other party from their liabilities, responsibilities and contractual obligations, meaning the installer needs to put in place appropriate supervision and quality control procedures to ensure that installation carried out is based on the design documentation. For further guidance, we refer the reader to “Guideline for procedure statement” for “Construction review” (ACENZ)

For construction monitoring to be effective, the following points need to be considered by relevant authorities (Guidelines on procedure statements-ACENZ):

- The magnitude and complexity of project
- The possible consequences of failure (economic, environmental, health and safety)
- Confirmation of the competence of the author of the producer statement and any record of disciplinary action (from the Statutory Registers)
- Extent and quality of documentation provided
- Completeness of supporting documentation
- Demonstration of compliance with the Building Code
- Author’s legal/contractual entity information (e.g. professional indemnity insurance)
- Known quality assurance systems
- Any of the producer statement’s qualifications and/or limitations
- The peer reviewer’s independence from the designer and/or owner
- The nature and frequency of periodic audits of works for which producer statements are accepted (detailed review, peer review etc).

Construction monitoring is a service which is provided by the design professional, and provides the councils and owners independent verification that the work has been completed in accordance with the approved consented plans and building codes (AC2301-producer statement policy-V.6-July 2015)

The statements are issued by contractors or design professionals stating in their view that part, or all of the project as described on the consented plans and specifications has been constructed and meets certain performance requirements of the building codes and or conditions of building consent. There are two types of statement issued in construction category:

- Producer statement construction: this statement is issued by the contractor
- Producer statement construction review: this statement is issued by the design professional who has designed and reviewed the project

There are five construction monitoring levels defined by the Institute of Professional Engineers of NZ (IPENZ) that we recommend being used for seismic bracing of NSCs as well in Australia. The appropriate level of construction monitoring will be project-dependent and identified by the design professional.

Construction monitoring levels as categorized in IPENZ are as follow:

Level	Review
CM1	Monitor the outputs from another party's quality assurance program against the requirements of the plans and specifications. Visit the works at a frequency agreed with the client to review important materials of construction critical work procedures and/or completed plant or components. Be available to advise the constructor on the technical interpretation of the plans and specifications
CM2	Review, preferable at the earliest opportunity, a sample of each important work procedure, material of construction and component for compliance with the requirements of the plans and specifications and review a representative sample of each important completed work prior to enclosure or completion is appropriate. Be available to provide the constructor with technical interpretation of the plans and specification.
CM3	Review, to an extent agreed with the client, random samples of important work procedures, for compliance with the requirements of the plans and specifications and review important completed work prior to enclosure or on completion as appropriate. Be available to provide the constructor with technical interpretation of the plans and specifications.
CM4	Review, at a frequency agreed with the client, regular samples of work procedures, materials of construction and components for compliance with the requirements of the plans and specifications and review the majority of completed work prior to the enclosure or on completion as appropriate.
CM5	Maintain personnel on site to constantly review work procedures, materials of construction and components for compliance with the requirements of the plans and specifications and review completed work prior to enclosure or on completion as appropriate.

If construction monitoring is required, the author must provide a site inspection record. The record must accurately report the nature and detail of the inspection including any instructions given to the contractor on site.

Design changes must be documented and supported by either a formal amendment or a minor variation where on-site or client-driven changes are required, these should be communicated to the seismic specialist, and other affected subcontractors. The seismic specialist is to provide an amendment to the design documents.

4. Common issues and solutions

Clear definition of design and construction responsibilities for all stakeholder forms a significant proportion of NSCs project. Therefore, it is the authors' recommendation to identify where the responsibilities of each party starts and ends. It is recommended that construction monitoring be carried out by the designer or their representative (IPENZ/ACENZ practice note). Moreover, clients and contractors understand the important task the designers perform during the construction phase, including (Structural engineering design office practice, IPENZ, version 1, AUG 2009):

- Answering queries and providing interpretation of the construction documentation
- Addressing contingent design issues that arise during construction
- Monitoring construction quality and correct implementation of design intent
- Reviewing proprietary design and construction phase documentation.

The scope and intensity of construction monitoring should be determined by a review of the following factors:

- The size and complexity of the work
- The experience of the contractor
- The consequences of non-compliance.

The complexity and importance of the construction work should also have a bearing on the experience of the engineer who is selected to carry out the construction monitoring.

It is useful for the designer to advise the BCA on the extent of the proposed construction monitoring, particularly when providing a producer statement.

In design certificate, the seismic engineer recommends the level of construction monitoring/observation then an inspection schedule would also be suggested. In construction monitoring review schedule, type of braces (installed services or bracing elements), stage of construction (prior to ordering brace installation) and who authorised the inspection (site engineer or seismic designer) is to be specified.

Furthermore, amount of random sampling (percentage of visual scan and visual inspection) is recommended to be clarified in design documentation. Where visual scan/inspection required, it is important that contractor understand their responsibility is to provide access for inspection when seismic restraints are visible. The contractor also needs to ensure all required inspection points are reviewed and approved by seismic engineer before ceiling closure.



Figure 2: Inspection to be carried out before ceiling closure.

5. Conclusion

Behavior of NSCs in an earthquake event depends on design and installation quality, that is why, the monitoring construction process is vital for code compliance. Seismic engineers specify/suggest the level of construction monitoring required. This can be used to prepare a comprehensive schedule table to clarify the liabilities and responsibilities of each stakeholder/contractor.

Types, frequency, and priority of inspection is to be described in the schedule table. Contractor is to ensure access is available for an inspector to check/review the installation before ceiling elements block the view of seismic restraints.

Construction monitoring report can maximise the quality of installation, on the condition of being done by the right person, according to the plan and on time.

It is authors' suggestion that more real case studies are carried out to adopt the best practice of construction monitoring for seismic bracing of non-structural components.

6. References

- AC 2301: Producer statement policy-V.6-July 2015
- AS 1170.0: 2002 Structural design actions, Part 0, General Principles.
- AS 1170.4: 2007 Structural design actions, Part 4, Earthquake action in Australia.
- AS 2121: 1979 The design of earthquake-resistant building (earthquake code)
- AS 2785: Suspended ceiling design standard.
- BCA: 2019 Building Code of Australia
- IPENZ/ACENZ: Engineering New Zealand practice note 1 "Guidelines on Producer Statement" – Version 3, January 2014

- NCC: 2019 National Construction Code
- Seismic restraint of engineering services – South Australia government - G172 (April 2019)
- Structural engineering design office practice, IPENZ, version 1, AUG 2009
- Wilson, J., Lam, N.T.K. and Pham, L. (2008) Development of the New Australian Earthquake Loading Standard, EJSE special issue, 2008, pp 25-31
- Woodside, J. and McCue, K. (2016) ASEC, pp 194-207

Development of Seismic Test Set-up for Fasteners in Australia

Chandani C. Neupane¹, Jessey Lee², Tilak Pokharel³, Hing-Ho Tsang⁴ and Emad F. Gad⁵

1. Corresponding Author. Ph.D. Candidate, Department of Civil and Construction Engineering, Swinburne University of Technology. Email: cneupane@swin.edu.au
2. Training and Development Manager, Australian Engineered Fasteners and Anchors Council (AEFAC); Lecturer, Department of Civil and Construction Engineering, Swinburne University of Technology. Email: jesseylee@swin.edu.au
3. National Technical Manager, Australian Engineered Fasteners and Anchors Council (AEFAC). Email: tilakpokharel@swin.edu.au
4. Associate Professor, Department of Civil and Construction Engineering, Swinburne University of Technology. Email: htsang@swin.edu.au
5. Professor & Dean, School of Engineering, Faculty of Science, Engineering and Technology, Swinburne University of Technology. Email: egad@swin.edu.au

Abstract

Fasteners are important for the safety and reliability of buildings and infrastructure as they are used for structural and non-structural connections in concrete. In Australia, the prequalification and design of fasteners are covered by AS 5216. The National Construction Code (NCC) requires seismic design and verification of fasteners, however, the design provision of AS 5216: 2018 does not cover exposure to seismic actions. Thus, prequalification and design of fasteners are currently being carried out using European/American guidelines. European Technical Assessment (ETA) prequalified fasteners are commonly accepted and used in Australia. Work is currently undertaken by the authors to develop recommendations for selecting seismic categories for post-installed fasteners in Australia, which is presented in a parallel paper at this conference. This paper presents the first seismic test set-up for fastenings in Australia which is currently under development to support testing of fastenings with crack cycling under different crack widths.

Keywords: Fasteners, prequalification, testing set-up, cracked concrete, seismic actions

1. INTRODUCTION

Fasteners are used globally to connect non-structural and structural elements to structure. Hence, its performance is crucial for the safety and reliability of the structure. Application of fasteners is very common to connect facades, ceilings, mechanical, electrical and pipeline systems, etc. in buildings. Inadequate anchorage to concrete, particularly poor non-structural connection, is the major and substantial contributor to damages and losses that happened during past earthquakes (P. Mahrenholtz *et al.*, 2017).

Qualification of fasteners has been practised for more than 40 years in Europe and the US, with these regions driving the development of anchor technology based on standards and guidelines (P. Mahrenholtz & Pregartner, 2016). Particularly, the seismic qualification of fasteners is gaining increased attention. For example, the European prequalification guideline was upgraded to TR-049 in 2016 (EOTA, 2016b). However, the Australian anchor industry is still new. After the establishment of the Australian Engineered Fasteners and Anchors Council (AEFAC) in 2012, it has been working on improving the quality and safety of the anchor industry. AEFAC instigated SA TS 101 as deemed-to-satisfy design provisions of fastenings to concrete for safety-critical applications (Standards Australia, 2015). The standard was later upgraded to Australian Standard AS 5216 (Standards Australia, 2018) and referenced in National Construction Code (NCC) in 2019.

The NCC requires the design and verification of fasteners under all reasonably expected action, including seismic actions (ABCB, 2019). However, the seismic provisions are not covered by the scope of AS 5216 (Standards Australia, 2018). On the other hand, there is no seismic prequalification guideline for fasteners in Australia. Thus, either European or US guidelines are generally used in Australia. AEFAC has been working on seismic design and qualification requirements of fasteners in Australia (Heath *et al.*, 2016; Lee *et al.*, 2018; Pokharel *et al.*, 2019; Amirsardari *et al.*, 2020) and seismic provisions are expected to be included in the next revision of AS 5216.

The European and American seismic prequalification, performance and design requirements have been compared in previous studies (Heath *et al.*, 2016; Lee *et al.*, 2018) and evaluated for adaptation based on suitability and relevancy. These studies concluded that the European seismic requirements for fastenings are more stringent compared to the US requirements based on direct adaption.

TR-049 is the current seismic prequalification guideline for fasteners in Europe, which lists out two performance categories – C1 & C2: C2 performance category being more stringent than C1 (EOTA, 2016b). Hence, European qualified fasteners hold European Technical Assessment (ETA) document with approval for seismic performance category C1 and/or C2 based on the fastener's intended application. In the US, ACI 355.2 (ACI, 2007) and ACI 355.4 (ACI, 2011) provide provisions for the qualification of post-installed mechanical anchors and adhesive anchors respectively. The seismic prequalification requirements for fasteners in the US are equivalent to performance category C1 of European guidelines (Heath *et al.*, 2016). For Australian practice, Amirsardari *et al.* (2020) have recommended criteria for selecting suitable seismic performance categories (C1 or C2) for post-installed anchors by determining the expected extent of damage to building components.

As per the seismic prequalification requirements in Europe and the US, cyclic tests in cracked concrete are required with specific maximum crack width. Additional crack cycling test (crack

opening and closing test) is required for performance category C2. However, no experimental seismic testing on fasteners has been carried out in Australia as per our knowledge, as the required testing facility is not available locally. Hence, a seismic test set-up for fasteners on cracked concrete has been developed, mainly focusing on the crack cycling test.

2. PERFORMANCE CATEGORIES (AS PER TR-049)

Australia does not have its own seismic prequalification guideline for fasteners. Hence, fasteners are currently tested and assessed either using European TR-049 (EOTA, 2016b) or American ACI 355.2 (ACI, 2007) and ACI 355.4 (ACI, 2011) guidelines. There are two performance categories – C1 performance category and C2 performance category, for seismic prequalification of fasteners as per TR-049 (EOTA, 2016b), whereas American guidelines have a single category and equivalent to the C1 performance category. C2 performance category is stringent as compared to C1. Recently, the US has proposed a second seismic performance category (ASPC 2), which will require more rigorous test and assessment criteria and will be similar to the C2 performance category (ICC-ES, 2020). Requirements of two seismic performance categories as per TR-049 (EOTA, 2016b) are compared and presented in Table 1.

Table 1: Comparison between seismic performance categories as per TR-049 (EOTA, 2016b)

No.	Criteria	C1 Performance Category	C2 Performance Category
1	Maximum crack width (Δw) *	0.5 mm	0.8 mm
2	Anchor capacity/ Design information	Strengths (force) at ultimate limit state <ul style="list-style-type: none"> • Tension resistance • Shear resistance 	Strengths at ultimate limit state <ul style="list-style-type: none"> • Tension resistance • Shear resistance Displacement at the damage and ultimate limit state <ul style="list-style-type: none"> • Fasteners displacement
3	Tests	C1.1 Functioning under pulsating tension load C1.2 Functioning under alternating shear load	C2.1a Reference tension in low strength concrete C2.1b Tension tests in high strength concrete C2.2 Reference shear tests C2.3 Functioning under pulsating tension load C2.4 Functioning under alternating shear load C2.5 Functioning with tension load under varying crack width
4	Assessment	Completion of cycling history & mean residual capacity ≥ 160 % of peak load during tension and shear cycling (N_{eq}^{**} , V_{eq}^{***})	Completion of cycling history, load-displacement characteristics, displacement limits, coefficient of variation in capacity and displacement, failure mode, etc.

* Δw = additive crack width to hairline crack after anchor installation but before loading

** N_{eq} = maximum tension load in test series C1.1

*** V_{eq} = maximum shear load in test series C1.2

3. SEISMIC TEST SET-UP DEVELOPMENT

Experimental set-ups for seismic tests are provided in TR-048 (EOTA, 2016a) and TR-049 (EOTA, 2016b). These guidelines provide information about a set-up for tension tests (confined and unconfined) and shear tests. However, they do not cover much on crack forming methods for test specimen and test set-up for crack cycling, which is the most complex test. Hence, the set-up is developed based on qualification guidelines (ACI, 2007; ACI, 2011; EOTA, 2016a; EOTA, 2016b) and past research (Hoehler, 2006; P. Mahrenholtz, 2013; C. Mahrenholtz & Sharma, 2017) (of similar kind), focusing mainly on crack cycling test. This set up can be used for carrying out tests for fasteners in both low strength and high strength concrete.

3.1. Concrete Test Specimen

Prequalification guidelines (ACI, 2007; ACI, 2011; EOTA, 2016a; EOTA, 2016b) for fasteners on concrete provide information on requirements of specimen, size and configuration. The thickness of the test specimen shall be at least 1.5 times of embedment depth (h_{ef}) of anchor and width shall be adequate to avoid edge influence. Reinforcement shall be of equal size and placed symmetrically with spacing between them being less than 400 mm. Reinforcement shall not influence the capacity of fasteners. Also, reinforcement shall be kept within the elastic range during a test and reinforcement buckling shall be avoided.

Bond breakers can be used in a reinforcement bar at both sides of the expected crack plane to aid the crack opening. TR-049 (EOTA, 2016b) recommends de-bonding length of up to 5 times the reinforcement bar diameter using a bond breaker (*e.g.* plastic pipe, foam tape). Also, ‘crack-formers’, commonly known as crack inducers, may be built into the test specimen in the expected crack plane to facilitate the initiation and control of crack. However, they must not be placed near the anchorage zone and should not affect the failure of an anchor. Thin steel plates can be used as crack inducers.

With a focus on crack cycling test, C. Mahrenholtz and Sharma (2017) provided some recommendations which are listed below:

- Test specimens with only one crack plane as criteria for acceptable scatter in ultimate load and the corresponding displacement during testing are very demanding as per TR-049 (EOTA, 2016b), ACI 355.2 (ACI, 2007) and ACI 355.4 (ACI, 2011).
- Depending on the thickness of the test member, two fasteners may be tested in a single concrete member at the top and bottom.
- When the concrete member is compressed for full crack closure, local transverse tensile stresses develop. Thus, at least one stirrups should be placed on both edges to take over these stresses.
- The distance between ends of the test specimen and the crack plane needs to be long enough to form sufficient strain for crack width requirement, but short enough to avoid the formation of intermediate cracks. These two criteria govern the length of the test specimen.

3.2. Crack Forming Methods for Test Specimen

Forming approximately constant crack width throughout the member is an important prerequisite for test specimen, which is also a challenge for the test. The so formed crack line

will be the position for installing the testing anchor and its location in a crack over the load transfer zone shall be verified. This can be done by using a borescope.

There are two different methods for crack formation in the concrete test specimen by introducing tension force (Figure 1). The two methods are a) Splitting wedge method, and b) Tensioning reinforcement method. In the splitting wedge method, the wedge is hammered into expansion sleeves set in a drilled/pre-formed hole, whereas the reinforcement of the slab is pulled to form a crack in the tensioning reinforcement method.

The splitting wedge method is commonly used and works well for static crack widths. This method is capable of precise crack control and has a comparatively lower cost as compared to the tensioning reinforcement method. The tensioning reinforcing method requires an electronic servo-controlled system and is used for precise control of crack width, mainly for crack cycling test. Furthermore, a combination of both methods can also be used by using a splitting wedge method for forming the crack and tensioning reinforcement method for controlling crack width by precisely opening and closing the crack during the test. In Eligehausen *et al.* (2004), two different set-ups are mentioned for tensioning reinforcement based on the application of load to the frame or directly to reinforcement.

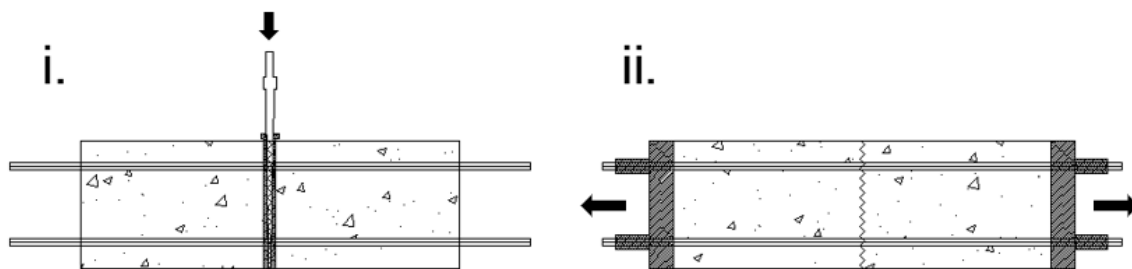


Figure 1: Crack forming methods (i) Splitting wedge method (ii) Tensioning reinforcing method

After crack formation, the test anchor is installed in the 'hairline crack'. A crack width in the order of 0.1 mm is considered as 'hairline crack'. Requirements and process for crack measurement throughout the test are explained in TR-049 (EOTA, 2016b). Crack width shall be greater than or equal to the specified crack width in the test series.

3.3. Actuator Capacity for Crack Opening and Closing

The crack cycling test requires precise control of crack width. Hence, a computer-controlled servo-valve system with an actuator is a common and suitable method for applying external centric tensile loading on reinforcement bars to generate and open the crack. Application of centric compression force is required to close crack planes during crack initiation, stabilisation and in each cycle of the test (EOTA, 2016b). Thus, estimation of actuator capacity is crucial to ensure that actuator capacity is sufficient for generation and control of required crack width during the testing.

C. Mahrenholtz & Sharma (2017) derived an equation for conservative determination of actuator capacity (F_{act}) to achieve the expected crack width for test member with four rebars (Equation 1).

$$w \approx s \left(\frac{F_{act}}{\pi d^2} - 0.18 f_c^{\frac{2}{3}} \left(\frac{HW}{\pi d^2} + 7 \right) \right) / E_s \quad (1)$$

where w is expected crack width (mm), s is crack spacing = $L/2$ (mm), d is reinforcement diameter (mm), L , H and W are dimensions of the test specimen in mm (length, height and width), f_c is the compressive strength of concrete cylinder specimen (MPa) and E_s is the modulus of elasticity of reinforcement steel (MPa).

According to TR-049 (2016), a centric compressive force for closing initiated crack (C_{ini}) and crack in each cycle of the test (C_{test}) shall be obtained as per Equation 2. Furthermore, the compressive force can be increased up to $C_{test,max}$ if the crack is not closed to satisfy $\Delta w \leq 0.1$ mm.

$$C_{ini} = C_{test} = 0.1 f_{cube} A_g \quad (2)$$

$$C_{test,max} = 0.15 f_{cube} A_g \quad (3)$$

where f_{cube} is the mean compressive strength of concrete cube specimen and A_g is the cross-sectional area of test member ($H \times W$).

As per TR-048 (EOTA, 2016a), concrete compressive strength can be converted from cube to cylinder using Equation 4 for low strength concrete (C20/25).

$$f_c = \frac{1}{1.25} f_{cube} \quad (4)$$

After re-arranging and combining the above equations (1-4), Equation 5 & 6 can be used to estimate approximate tension and compression capacity of the actuator ($F_{act,t}$ & $F_{act,c}$) for opening and closing of crack respectively, during the crack cycling test.

$$F_{act,t} \approx 2 w E_s \pi \frac{d^2}{L} + 0.18 f_c^{\frac{2}{3}} (H W + 7 \pi d^2) \quad (N) \quad (5)$$

$$F_{act,c} \approx 0.19 f_c H W \quad (N) \quad (6)$$

3.4. Seismic Test Set-up

Crack cycling test procedure was first introduced by Hoehler (2006). The author considered 10 equal cycles of crack opening and closing with maximum crack width 0.8 mm, to consider the effect of seismic actions. For his seismic test, four-line cracks were generated using a servo-controlled hydraulic actuator in a single concrete specimen and closed by applying compressive stress on the face of the specimen. In recent years, test set-up was improved and used for crack cycling tests in studies (C. Mahrenholtz *et al.*, 2017; P. Mahrenholtz, 2013; P. Mahrenholtz *et al.*, 2017) with a single crack plane. The crack protocol was also improved to 'stepwise increasing crack protocol' and has been included as test series C2.5 in the current European guideline (EOTA, 2016b) for seismic actions.

This research has developed a seismic test-setup for testing of fasteners on cracked concrete, which is presented here as an example set-up. The set-up is developed to ensure that it will be capable to perform different test series as required for C1 and C2 performance categories, including the crack cycling test.

In this set-up, the servo-controlled actuator system is used as a horizontal actuator (500 kN, 150 mm stroke) to control the crack width as required in the specific test series. Achieving the allowance criteria of crack width tolerance (*i.e.* $\pm 10\%$ and $\pm 15\%$ in TR-049 (EOTA, 2016b) and ACI 355.2 & ACI 355.4 (ACI, 2007; ACI, 2011) respectively) is very challenging. In addition, crack width control during crack cycling test is complex. Thus, the servo-control actuator system is selected for developing the set-up as it allows precise control of crack width. Support systems are designed in such a way that test specimen and actuator can be mounted as shown in Figure 2 & Figure 3. The specimen is connected with a fixed support system on one side and actuator on another (with the help of a connector) so that it can be pulled and pushed to open and close the crack during testing. Since we are conducting tests on the post-installed anchor, ‘hairline crack’ in concrete test specimens will be generated using splitting wedges before mounting it on the set-up. Then, the anchor selected for investigation will be installed in the generated ‘hairline crack’.

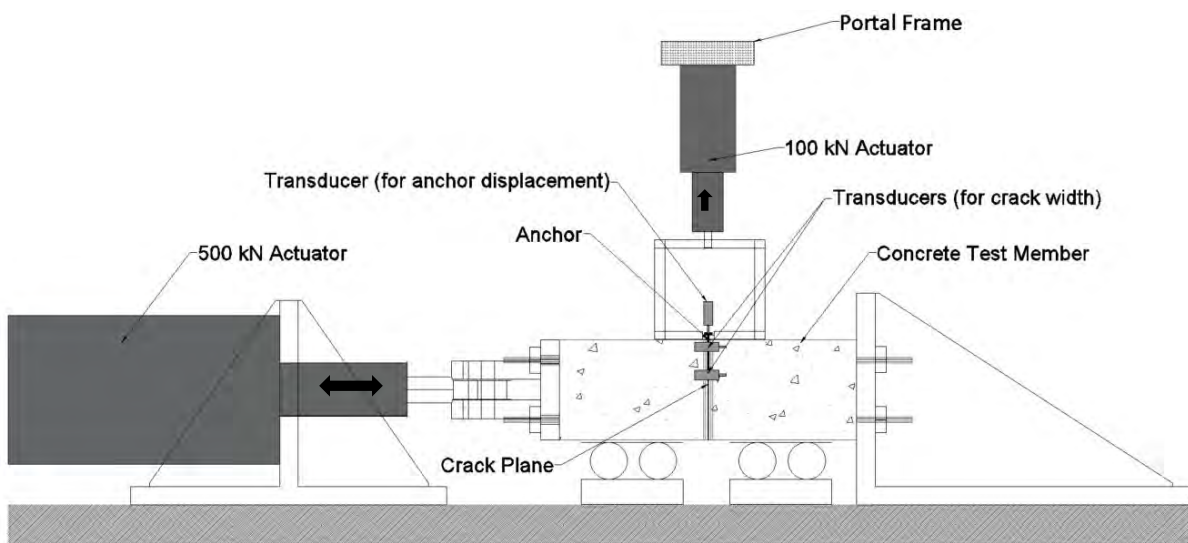


Figure 2: Schematic view of the tension test set-up

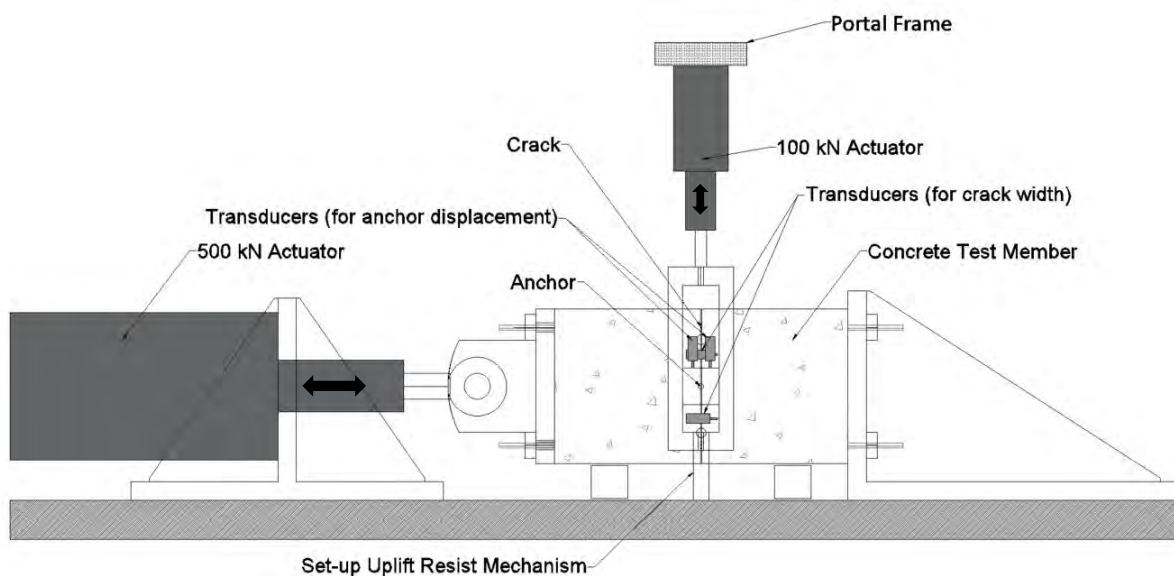


Figure 3: Schematic view of the shear test set-up

Another 100 kN servo-controlled actuator is used as a vertical actuator for loading (shear and tension) the anchor during testing. This actuator is supported by a portal frame which has the flexibility of movement in both horizontal and vertical direction. Tension loading device or shear loading device will be connected as required by specific test series as per TR-048 (EOTA, 2016a) and TR-049 (EOTA, 2016b). Our target, in this set-up, is to synchronize both actuators so that load can be applied and controlled for concrete test specimen and anchor simultaneously.

As per provisions in TR-049 (EOTA, 2016b), displacement transducers need to be installed in the test specimen and at the location of the fastener. Displacement transducers are placed in the test specimen to control and measure crack width, whereas the transducer is placed on top of the fastener or at the location of the fastener to measure the displacement of the fastener during testing.

After installing the fastener, the test specimen will be rotated by 90-degree for the shear loading test (Figure 3). Also, the shear loading plate is restrained from uplifting to avoid the generation of the significant frictional force.

4. CONCLUSIONS

Although NCC has provisions of seismic requirements, the current version of AS 5216 (2018) does not cover seismic prequalification and design of fasteners. In absence of Australian qualification guidelines/ requirements, fasteners approved as per European or American guidelines are currently used in Australia. As per European guidelines, there are two seismic performance categories - C1 and C2, which requires testing of fasteners in cracked concrete. This paper reviews state-of-the-art testing of fastening in cracked concrete and proposes the first Australian test set-up for fasteners in cracked concrete to investigate the seismic performance of fastenings in different crack widths, including crack cycling conditions.

The developed set-up is also capable to conduct testing of reinforcement bars under the crack opening and closing condition. The set-up is not only limited to seismic tests but can also be used for non-seismic assessments requiring a crack cycling test. Also, it can be used to fulfil requirements of infrastructure projects requiring a crack cycling test and is flexible to be used for tests involving different types of concrete (*e.g.* steel-fibre reinforced concrete).

ACKNOWLEDGEMENTS

The research is financially supported by the Swinburne University of Technology (Swinburne University Postgraduate Research Award, 2019). The authors would also like to acknowledge the technical support and guidance from AEFAC and AEFAC founding members: Ancon Building Products, Hilti (Australia), Hobson Engineering, ramsetreid, Stanley Black and Decker (Powers) and Würth Australia and Supporting members: Allthread Industries, Icons, Simpson Strong-Tie (Australia) and United Fasteners.

REFERENCES

American Concrete Institute, (2007) ACI 355.2-07: Qualification of post-installed mechanical anchors in concrete and commentary, In. Farmington Hills, MI 48331, USA: American Concrete Institute.

American Concrete Institute, (2011) ACI 355.4M-11: Qualification of post-installed adhesive anchors in concrete and commentary, In. Farmington Hills, MI 48331, USA: American Concrete Institute.

Amirsardari, A., Pokharel, T., Lee, J., & Gad, E. (2020) Seismic performance categories for post-installed fasteners in Australia, Paper to be presented at the Australian Earthquake Engineering Society Virtual Conference: AEES 2020.

Australian Building Codes Board, (2019) NCC: National Construction Code, In. Canberra: ACT: Australian Building Codes Board.

Eligehausen, R., Mattis, L., Wollmershauser, R., & Hoehler, M. S. (2004) Testing anchors in cracked concrete, *Concrete international*, 26(7), 66-71.

European Organisation for Technical Assessment, (2016a) TR-048: Details of tests for post-installed fasteners in concrete, In EOTA Technical Report.

European Organisation for Technical Assessment, (2016b) TR-049: Post-installed fasteners in concrete under seismic action, In EOTA Technical Report.

Heath, D. J., Tsang, H.-H., Lee, J., & Gad, E. F. (2016) Seismic design provisions for fastenings to concrete in Australia, Paper presented at the Australasian Structural Engineering Conference: ASEC 2016.

Hoehler, M. S. (2006) Behavior and testing of fastenings to concrete for use in seismic applications.

International Code Council Evaluation Service, (2020) AC510-0620-R2: Proposed New Acceptance Criteria for Steel Seismic Qualification of Post-installed Anchors in Concrete, California, United States of America

Lee, J., Pokharel, T., Tsang, H.-H., & Gad, E. F. (2018) Requirements for seismic performance of post-installed fastenings in Australia, Paper presented at the Australian Structural Engineering Conference: ASEC 2018.

Mahrenholtz, C., Eligehausen, R., Hutchinson, T. C., & Hoehler, M. S. (2017) Behavior of post-installed anchors tested by stepwise increasing cyclic crack protocols, *ACI Structural Journal*, 114(3), 621.

Mahrenholtz, C., & Sharma, A. (2017) Testing of Anchors and Reinforcing Bars in Concrete under Cyclic Crack Movements, *Journal of Testing and Evaluation*, 45(4), 1326-1337.

Mahrenholtz, P. (2013) Experimental performance and recommendations for qualification of post-installed anchors for seismic applications.

Mahrenholtz, P., & Pregartner, T. (2016) Qualification and design of seismic anchors—Requirements in New Zealand and Australia, Paper presented at the NZSEE 2016.

Mahrenholtz, P., Wood, R. L., Eligehausen, R., Hutchinson, T. C., & Hoehler, M. S. (2017). Development and validation of European guidelines for seismic qualification of post-installed anchors, *Engineering structures*, 148, 497-508.

Pokharel, T., Lee, J., Amirsardari, A., Tsang, H.-H., & Gad, E. (2019) Seismic prequalification and design of fasteners in Australia, Paper presented at the Concrete 2019.

Standards Australia, (2018) AS 5216: Design of post-installed and cast-in fastenings in concrete, In (pp. 109): Standards Australia.

Standards Australia, (2015) SA TS 101: Design of post-installed and cast-in fastenings for use in concrete, In. Sydney, NSW: Standards Australia.

An interface constitutive model for predicting masonry structural failure by finite element method

Nie, Y¹, Sheikh, A.², Griffith, M.³, Visintin, P.⁴ and Vaculik, J.⁵

1. Corresponding Author. PhD student, School of Civil, Environmental and Mining Engineering, University of Adelaide, SA 5000, Australia. Email: yu.nie@adelaide.edu.au
2. Associate Professor, School of Civil, Environmental and Mining Engineering, University of Adelaide, SA 5000, Australia. Email: abdul.sheikh@adelaide.edu.au
3. Professor, School of Civil, Environmental and Mining Engineering, University of Adelaide, SA 5000, Australia. Email: michael.griffith@adelaide.edu.au
4. Associate Professor, School of Civil, Environmental and Mining Engineering, University of Adelaide, SA 5000, Australia. Email: phillip.visintin@adelaide.edu.au
5. Research Fellow, School of Civil, Environmental and Mining Engineering, University of Adelaide, SA 5000, Australia. Email: jaroslav.vaculik@adelaide.edu.au

Abstract

This paper introduces an interface model which can be used to predict the failure modes of masonry walls under in-plane loads. The interface constitutive model is developed for a cohesive element that simulates the cracking behaviour in mortar joints and brick potential cracking area based on a 2D traction-separation law in the framework of plasticity. Interfacial characteristics, including dilation, friction and mixed mode cohesive failure, are considered in the interface model which can simulate the tensile-shear failure of masonry interface. A concrete damage plasticity model is applied to simulate the compressive crushing behaviour of bricks. A fully backward Euler method with consistent tangent operator is adopted for the implementation of the zero thickness interface model, while an adaptive sub-stepping scheme is adopted for the algorithm to improve the robustness of numerical models. Performance of the interface constitutive model is evaluated by comparing modelling results with experimental results. The comparisons show that the proposed model can effectively predict the load capacity and nonlinear response of masonry walls under in-plane loading. In the further work, the interface elastoplastic model would be extended to damage-plasticity model which has a wider application in simulating masonry walls under cyclic and seismic loads.

Keywords: Masonry simulation, finite element modelling, cohesive element, interface constitutive model, adaptive sub-stepping

1. Introduction

Masonry structures and materials were widely used in historical buildings (eg. construction age over 100 years) which are sensitive to the external loads, such as earthquake and foundation settlement. To protect these buildings from external dangers and reduce potential loss, predicting the failure modes for masonry is necessary as it can provide useful information for

reinforcement and repairing work. The analysis of masonry structure is relatively complex compared with steel or concrete buildings due to its composite material characteristics and the different mechanics of brick and mortar. Thus, predicting the cracking propagation and crushing failure in masonry structures is a challenging task. To analyse masonry structures the use of empirical formula is a common methodology which can provide necessary engineering information including load capacity, deformation in certain position and stiffness degradation (Griffith et.al, 2007; Vaculik & Griffith, 2017). While analytical methods are concise and practical in masonry construction, its performance in detecting the post-failure modes of aging masonry buildings is limited. In the early stage of repairing historical architectures, determining potential cracking or crushing regions in the masonry structure is a key step for further reinforcement work (Vaculik et.al 2018). Compared with traditional analytical methods, numerical modelling can offer more comprehensive details on the post-failure response of masonry structures by presenting the cracking contours in mortar joints and compression failure contours in bricks. Clear identification of failure modes is helpful in reducing reinforcement cost and improving repairing efficiency (Su et.al, 2011).

Plasticity theory and damage mechanics are two popular frameworks for creating the constitutive criterion for the interface of masonry and other quasi-brittle materials (D'Altri et.al 2019). Both frameworks establish the fracture criteria of interface in tension (Mode I) and shear (Mode II) by using a traction-separation law in the cohesive element (Camanho & Dávila, 2002).

Damage mechanics simulate the nonlinear behaviour of material using a stiffness degradation assumption which has a specified advantage in cyclic loading simulations (Smoljanović et.al, 2015). However, two critical characteristics of quasi-brittle materials, frictional and dilation effects, are not considered in the damage constituents. Thus, plasticity theory including Coulomb frictional criterion with non-associated flow rule is a more proper framework for masonry structure modelling. The idea of applying plasticity theory in cohesive element for cracking modes simulation is not only using in masonry structures (Macorini & Izzuddin, 2011; Giambanco et.al, 2001), but also widely accepted in rock (Linh et.al 2017), concrete (Linh et.al 2019) and geotechnical material modelling (DeBorst et.al, 2012). Although plasticity theory includes comprehensive characteristics of masonry nonlinear behaviour, its accuracy and robustness meets difficulties during implementation stage. To ensure the accuracy, backward Euler integration method with Newton-Raphson iteration (Trapp & Öchsner, 2018) is adopted as the stress return mapping strategy but it may lead to diverging problem, thus adaptive sub-stepping scheme (Pérez et.al, 2001; Abbo 1997) is considered in the implementation algorithm for enhancing the modelling robustness.

In this paper, a hyperbolic yield surface (Caballero et.al, 2008) considering a tension-shear mixed mode failure is proposed for simulation of masonry joint cracking while a concrete damage plasticity model is used to predict brick compressive crushing. This modelling combination provide a comprehensive and detailed failure model for masonry structures and avoids the convex problem in multi-surface constitutive models. Implicit integration approach and sub-stepping scheme at the material level ensure both accuracy and robustness of modelling results.

2. Finite element modelling

There are three main categories for finite element modelling and each of them have pros and cons regarding their computing costs and accuracy, there are: (1) detailed micro-modelling

which contains all detailed instances including brick element, mortar element and brick-mortar interface; (2) simplified micro-modelling where mortar layers are simplified as zero-thickness interface connecting bricks and (3) macro-modelling where the brick and mortar are combined and regarded as one material.

The simplified modelling strategy is a common approach assumes the masonry structure is mainly composed of extended bricks, while the mortar joints are lumped into a series of horizontal and vertical zero-thickness interfaces between the extended bricks, as shown in the Figure 1.

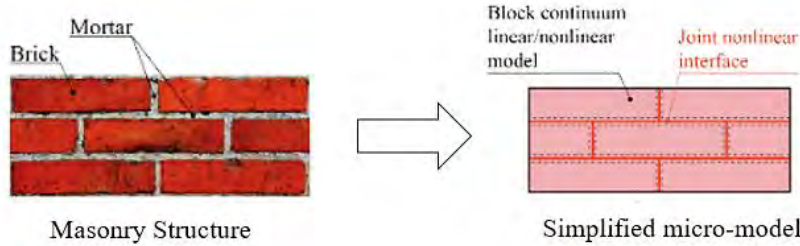


Figure 1. Simplified micro-modelling strategies (D'Altri et.al 2018)

3. Interface constitutive model

The current interface constitutive model mimics the nonlinear material behaviour in 2D stress space ($\sigma - \tau$) based on a plasticity framework. A typical cohesive element having two parallel surfaces with zero thickness between them is shown in Figure 2 that has normal (n) and shear (s) displacements or rather relative displacements (u_n , u_s) and corresponding stresses components (σ , τ). The elastic stiffness of the interface in the normal and shear directions can be represented by two springs having stiffness of K_n and K_s with no coupling between them. With these quantities, the elastic stiffness matrix $[K]$, stress vector $\{\sigma\}$ and displacement vector $\{u\}$ are as follows:

$$[K] = \begin{bmatrix} K_n & 0 \\ 0 & K_s \end{bmatrix} \quad \{\sigma\} = \begin{Bmatrix} \sigma \\ \tau \end{Bmatrix} \quad \{u\} = \begin{Bmatrix} u_n \\ u_s \end{Bmatrix} \quad (3.1)$$

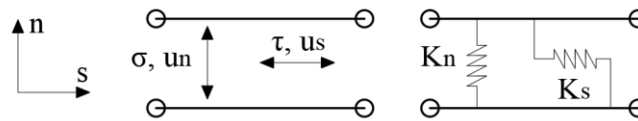


Figure 2. Elastic behaviour

Figure 3 shows the interfacial stress-displacement response with softening, modelled as plastic deformations, where the displacement increment $\{du\} = [du_n \quad du_s]^T$ can be decomposed in its elastic $\{du^e\} = \{du_n^e, du_s^e\}^T$ and plastic $\{du^p\} = \{du_n^p, du_s^p\}^T$ components i.e. $\{du\} = \{du^e\} + \{du^p\}$. Figure 3 also helps to write the increment stress-strain relationship as:

$$\{d\sigma\} = [K]\{du^e\} = [K](\{du\} - \{du^p\}) \quad (3.2)$$

It shown the determination of plastic displacement increment $\{du^p\}$ is vital and it can be obtained using the flow rule of plasticity as:

$$\{du^p\} = \lambda \frac{\partial Q}{\partial \{\sigma\}} \quad (3.3)$$

where Q is the plastic potential which is similar to yield or failure surface F as shown in Figure 4.

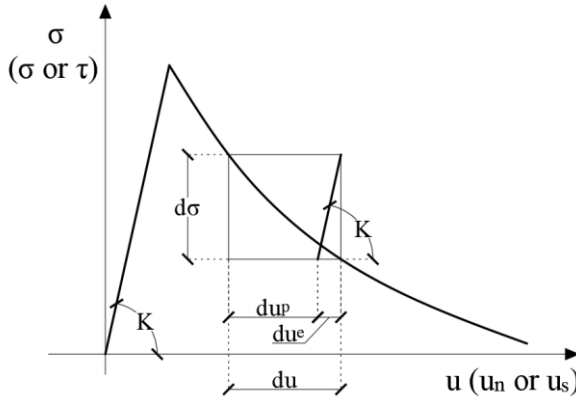


Figure 3: Stress-displacement response

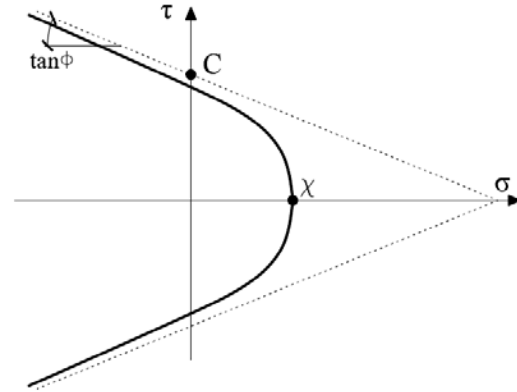


Figure 4: Yield surface of the interface

3.1 Plastic potential and failure surfaces

The failure surface (Figure 4) is having a hyperbolic shape that can be enveloped considering normal-shear mixed yield behaviour. The hyperbolic failure surface F is defined by three hardening parameters: 1) tensile strength χ , 2) cohesive strength in shear C (asymptotic cohesion in this case), and 3) friction angle ϕ or friction coefficient $\tan\phi$ as follows.

$$F(\{\sigma\}, \{\Phi\}) = -(C - \sigma \tan\phi) + \sqrt{\tau^2 + (C - \chi \tan\phi)^2} = 0 \quad (3.4a)$$

$$\{\Phi\} = \{\tan\phi, C, \chi\} \quad (3.4b)$$

Since masonry joints have a quasi-brittle material behaviour, a non-associate flow rule is adopted by taking a plastic potential Q which is different with the yield surface F . The expression of Q can be obtained from that of F (Equation 3.4) by replacing friction angle ϕ with dilation angle ϕ_Q and cohesion C with C_Q as follows.

$$Q(\{\sigma\}, \{\Phi_Q\}) = -(C_Q - \sigma \tan\phi_Q) + \sqrt{\tau^2 + (C_Q - \chi \tan\phi_Q)^2} = 0 \quad (3.5a)$$

$$\{\Phi_Q\} = \{\tan\phi_Q, C_Q, \chi\} \quad (3.5b)$$

3.2 Plastic work and its evolution

Plastic work is taken as the internal variable that is utilised to characterising the evolution of cracking in the plastic stage. With the growth of cracks, the hardening parameters ($\tan\phi, C, \chi$) show a softening behaviour leading to shrinking of the yield surface. The plastic work increment due to crack growth is defined as:

$$dW = \begin{cases} \sigma du_n^p + \tau du_s^p, & \sigma \geq 0 \text{ (Tension)} \\ (|\tau| + \sigma \tan\phi) |du_s^p|, & \sigma < 0 \text{ (Compression)} \end{cases} \quad (3.6)$$

The effect of σ in the second part of the above equation ($\sigma < 0$) follows the recommendation of Willam et al. (1984). Figure 5 shows the evolution of hardening parameters ($\tan\phi, C, \chi$) where all of them are having a softening behaviour which are defined as follows.

$$\chi = \begin{cases} \chi_0 \left(\frac{1}{2} + \frac{1}{2} \cos \left(\frac{\pi W}{G_f^I} \right) \right), & 0 < W \leq G_f^I \\ 0, & W > G_f^I \end{cases} \quad (3.7)$$

$$C = \begin{cases} C_0 \left(\frac{1}{2} + \frac{1}{2} \cos \left(\frac{\pi W}{G_f^{II}} \right) \right), & 0 < W \leq G_f^{II} \\ 0, & W > G_f^{II} \end{cases} \quad (3.8)$$

$$\tan\phi = \begin{cases} \tan\phi_0 - (\tan\phi_0 - \tan\phi_r) \left(\frac{1}{2} - \frac{1}{2} \cos \left(\frac{\pi W}{G_f^{II}} \right) \right), & 0 < W \leq G_f^{II} \\ \tan\phi_r, & W > G_f^{II} \end{cases} \quad (3.9)$$

It is to be noted that cosine functions are used in the above equations which helps to ensure continuity in the derivatives needed in future calculations. Figure 5 shows that the hardening parameters varied from their initial values $\chi_0, C_0, \tan\phi_0$ to zero except for $\tan\phi_0$ which is having a residual frictional coefficient $\tan\phi_r$. The above equations also need G_f^I and G_f^{II} which are fracture energies in normal (tension) mode (Mode I) and shear mode (Mode II) respectively.

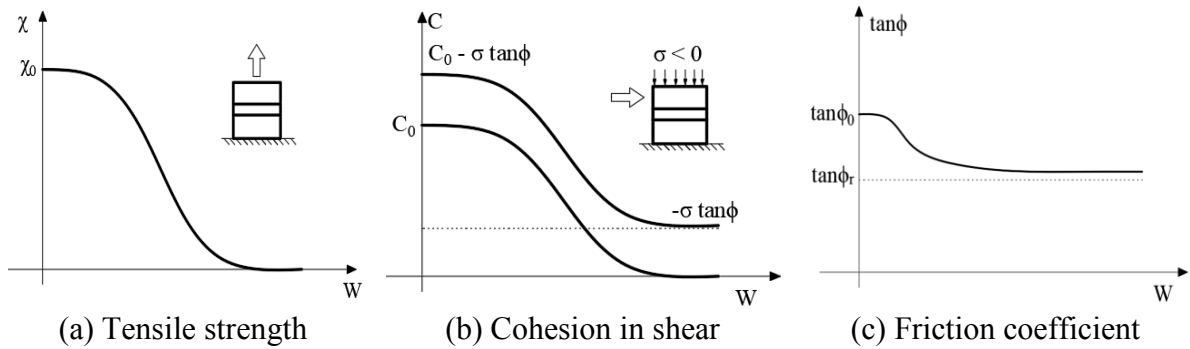


Figure 5 Evolution of hardening parameters

4. Numerical implementation and adaptive sub-stepping scheme

The above formulation for the interface constitutive model is implemented by using an elastic predictor-plastic corrector strategy in a monolithic framework. A system of nonlinear equations

containing of stress $\{\sigma\}_{n+1}$, plastic work W_{n+1} and plastic multiplier $d\lambda$ is solved together using a full implicit backward Euler stress updating scheme with the help of Newton-Raphson iteration technique applied at each Gauss point (local level). Moreover, consistent tangent stiffness matrix is derived to support the full Newton-Raphson iteration at the element or global level. Even though the backward Euler technique provides accurate results, convergence is a common issue in many situations for solving complex numerical problems. To improve the robustness of the FE model, an adaptive sub-stepping scheme is adopted in this study.

4.1 Stress return mapping

The objective of the time integration technique (backward Euler) for stress return at a local level (Gauss point) is to determine its stress $\{\sigma\}_{n+1}$ and plastic work W_{n+1} corresponding to load step $n+1$ using their known converged values in the previous load step n and the known displacement increment $\{du\}_{n+1}$ coming from the global analysis. This will be solved iteratively using Newton-Raphson technique due to nonlinearity if yielding occurs.

The first step is to determine the trial stress (elastic predictor) that can be expressed as:

$$\{\sigma^{trial}\}_{n+1} = \{\sigma\}_n + [K]\{du\}_{n+1} \quad (4.1)$$

If the substitution of above trial stress and known plastic work (W_n) in Eq. (3.4) gives a negative value of F , there is no yielding occurs and it will lead to $\{\sigma\}_{n+1} = \{\sigma^{trial}\}_{n+1}$ and $W_{n+1} = W_n$. Otherwise, the stress and internal variable need to be updated as follows:

$$\{\sigma\}_{n+1} = \{\sigma^{trial}\}_{n+1} - \dot{\lambda} [K] \{m(\{\sigma\}_{n+1}, W_{n+1})\} \quad (4.2)$$

$$W_{n+1} = W_n + dW_{n+1}(\{\sigma\}_{n+1}, W_{n+1}, \dot{\lambda}) \quad (4.3)$$

where $m(\{\sigma\}_{n+1}, W_{n+1}) = \{m\}_{n+1} = \partial Q / \partial \{\sigma\}$ is the direction of the flow vector which is function of $\{\sigma\}_{n+1}$ and W_{n+1} . As both Eqs. (4.2) and (4.3) are having implicit forms in terms of $\{\sigma\}_{n+1}$ and W_{n+1} , the problem is solved by NR iterative technique but it needs one more extra equation due to occurrence of the incremental plastic multiplier $\dot{\lambda}$ as an additional unknown variables. The full consistency condition of the yield function (3.4) i.e. $F(\{\sigma\}_{n+1}, W_{n+1}) = 0$ is for that purpose. In order to solve these equations iteratively in a combined or monolithic form, they are rearranged to express their residuals $\{r\}_{n+1} = \{r\} = [\{r_\sigma\}^T \quad r_W \quad r_F]^T$ (the subscript for the current load step $n+1$ is omitted for simplification of the presentation) as follows:

$$\begin{cases} \{r_\sigma\} = \{\sigma\}_{n+1} - \{\sigma^{trial}\}_{n+1} + \dot{\lambda} [K] \{m\}_{n+1} \\ r_W = W_{n+1} - W_n - dW_{n+1} \\ r_F = F(\{\sigma\}_{n+1}, W_{n+1}) \end{cases} \quad (4.4)$$

For solution of the set of above equations, $\{\sigma\} = \{\sigma\}_{n+1}$, $W = W_{n+1}$ and $\dot{\lambda}$ are taken as the independent unknowns which are expressed in a compact form as $\{\psi\} = [\{\sigma\}^T \quad W \quad \dot{\lambda}]^T$ for the convenience. Now the residual is linearized using Taylors series for the NR iterative solution as follows:

$$r(\{\psi\}^{j+1}) = r(\{\psi\}^j + \{\delta\psi\}^{j+1}) = r(\{\psi\}^j) + \frac{\partial r(\{\psi\}^j)}{\partial \{\psi\}^j} \{\delta\psi\}^{j+1} + O[\delta^2] \quad (4.5)$$

where j is the iteration number. The gradient expression $\frac{\partial r(\{\psi\})}{\partial \{\psi\}} = \frac{\partial r(\{\sigma\}, W, \lambda)}{\partial (\{\sigma\}, W, \lambda)}$ is the Jacobian matrix $[J] = [J](\{\psi\}^j)$ which can be expressed as:

$$[J](\{\psi\}^j) = \frac{\partial r(\{\psi\}^j)}{\partial \{\psi\}^j} = \frac{\partial r(\{\sigma\}, W, \lambda)}{\partial (\{\sigma\}, W, \lambda)} = \begin{bmatrix} [I] + \lambda [K] \frac{\partial \{m\}}{\partial \{\sigma\}} & \lambda [K] \frac{\partial \{m\}}{\partial \{\kappa\}} & [K]\{m\} \\ -\frac{\partial dW}{\partial \{\sigma\}} & 1 - \frac{\partial dW}{\partial W} & -\frac{\partial dW}{\partial \lambda} \\ \left\{ \frac{\partial F}{\partial \{\sigma\}} \right\}^T & \left\{ \frac{\partial F}{\partial W} \right\}^T & 0 \end{bmatrix} \quad (4.6)$$

Assuming a correct solution of Eq (4.5) at iteration number $j+1$ i.e. $r(\{\psi\}^{j+1}) = 0$ and truncation of the equation after its first order terms i.e. $O[\delta^2] \cong 0$, Eq (4.5) can be rewritten as:

$$[0] = r(\{\psi\}^j) + \frac{\partial r(\{\psi\}^j)}{\partial \{\psi\}^j} \{\delta\psi\}^{j+1} = r \begin{pmatrix} \{\sigma\}^j \\ W^j \\ d\lambda^j \end{pmatrix} + [J](\{\psi\}^j) \begin{Bmatrix} \{\delta\sigma\}^{j+1} \\ \delta W^{j+1} \\ \delta \lambda^{j+1} \end{Bmatrix} \quad (4.7)$$

With this equation, the unknown variables can be updated iteratively as:

$$\{\psi\}^{j+1} = \{\psi\}^j + \{\delta\psi\}^{j+1} \quad (4.8)$$

$$\{\delta\psi\}^{j+1} = \begin{Bmatrix} \{\delta\sigma\}^{j+1} \\ \delta W^{j+1} \\ \delta \lambda^{j+1} \end{Bmatrix} = -[J]^{-1}(\{\psi\}^j) r \begin{pmatrix} \{\sigma\}^j \\ W^j \\ d\lambda^j \end{pmatrix} \quad (4.9)$$

The iteration will continue till the norm of the residual meets the convergence tolerance i.e. $\|r(\{\psi\}^{j+1})\| < TOL$ (a small number that is taken as 10^{-6} in this study). Once the convergence is obtained, the latest updated values of these variables $\{\psi\}^{j+1}$ will be their final results for the load step $n+1$ i.e. $\{\psi\}^{j+1} = \{\psi\}_{n+1}$, which can be used as their initial values for the next load step ($n+2$). The initial values of these variables for the load step $n+1$ are taken as: $\{\sigma\}^{j=0} = \{\sigma^{trial}\}_{n+1}$, $W^{j=0} = W_n$, and $\lambda^{j=0} = 0$.

4.2 Consistent tangent stiffness

For the FE solution at the global (structural) level, the formulation of elements needs a consistent tangent stiffness matrix at Gauss points if full Newton iteration technique is used for the global level solution to minimise the unbalanced load vector of the whole structure. For this purpose, derivative of Eq. (4.4) with respect to displacement increment $\{du\}$ and a rearrangement of the equation can be made as follows:

$$\frac{\partial}{\partial \{du\}} \begin{bmatrix} \{\sigma\}_{n+1} + \lambda [K]\{m\}_{n+1} \\ W_{n+1} - dW_{n+1} \\ F(\{\sigma\}_{n+1}, W_{n+1}) \end{bmatrix} = \frac{\partial}{\partial \{du\}} \begin{bmatrix} \{\sigma\}_n + [K]\{du\}_{n+1} \\ W_n \\ 0 \end{bmatrix} \quad (4.10)$$

By using chain rule for the left hand side of Eq (4.10) consisting of unknown variables at the current load step ($n+1$) along with initial knowns values of these variables ($\{\sigma\}_n, W_n$) from previous load step on the right hand side of the equation, it can be expressed in terms of Jacobian (see Eq. 4.6) as:

$$[J](\{\psi\}_{n+1}) \begin{bmatrix} \frac{\partial\{\sigma\}_{n+1}}{\partial\{du\}} \\ \frac{\partial W_{n+1}}{\partial\{du\}} \\ \frac{\partial d\lambda_{n+1}}{\partial\{du\}} \end{bmatrix} = \begin{bmatrix} [K] \\ 0 \\ 0 \end{bmatrix} \quad (4.11)$$

The above equation is rewritten by inverting the Jacobian as:

$$\begin{bmatrix} \frac{\partial\{\sigma\}_{n+1}}{\partial\{du\}} \\ \frac{\partial W_{n+1}}{\partial\{du\}} \\ \frac{\partial d\lambda_{n+1}}{\partial\{du\}} \end{bmatrix} = [J]^{-1}(\{\psi\}_{n+1}) \begin{bmatrix} [K] \\ 0 \\ 0 \end{bmatrix} \quad (4.12)$$

where the portion of the right hand side of Eq. (4.12) correspond to $\begin{bmatrix} \frac{\partial\{\sigma\}_{n+1}}{\partial\{du\}} \end{bmatrix}$ is the consistent tangent stiffness matrix.

4.3 Adaptive sub-stepping scheme

The iterative solution of nonlinear equations using NR technique often encounters convergence problem in both local and global level if the load or displacement increment are not small. The global level problem can usually be controlled automatically by adjusting the size of global load increment in commercial FE codes (such as ABAQUS) with in-built options, but the local level problem need be addressed specifically by using our own material model UMAT. For this purpose, the sub-stepping scheme is adopted in the present study (Perez-Foguet et al. 2001) which divides a larger displacement increment in small sub-increments as $\{du\} = \sum_{i=1}^{ns} \{du\}_i = \sum_{i=1}^{ns} \alpha_i \{du\}$ where ns is the number of sub-steps and α_i is the scaling parameter of i th sub-step.

Figure 6 illustrates the general concept used in the sub-stepping strategy where a typical displacement increment is divided into six small sub-increments. The initial value of the stress for the 1st sub-step is defined as $\{\sigma\}_{i=0}$ which is equal to the known converged stress values obtained at the end of previous load step $\{\sigma\}_n$. In this case, the trial stress for the first sub-step $\{\sigma^{trial}\}_{i=1} = \{\sigma\}_{i=0} + [K]\{du\}_1$ is the final stress at the end of this sub-step i.e. $\{\sigma^{trial}\}_{i=1} = \{\sigma\}_{i=1}$ as it is located within the yield surface $F(\{\sigma\}_n, \chi_n, C_n, \tan\phi_n)$. This is similarly applicable for next two sub-steps ($i = 2$ and 3) to get $\{\sigma\}_{i=2}$ and $\{\sigma\}_{i=3}$. However, the trial stress for the 4th sub-step $\{\sigma^{trial}\}_{i=4}$ is outside the yield surface, which will require NR iteration to return back to the correct yield surface $F(\{\sigma\}_{i=4}, \chi_{i=4}, C_{i=4}, \tan\phi_{i=4})$ from

$\{\sigma^{trial}\}_{i=4}$ using the procedure stated in section 4.1 for this sub-step. It should be noted that the value of plastic work $W_{i=4}$ will be updated in this sub-step along with the stress $\{\sigma\}_{i=4}$ while $W_{i=1} = W_{i=2} = W_{i=3} = W_{i=0} = W_n$. This process will be repeated up to last sub-step ($i = 6$ in this case) to get $\{\sigma\}_{i=6}$ and $W_{i=6}$, which are the final values of stress and plastic work at the end of this load increment ($n+1$) i.e. $\{\sigma\}_{n+1} = \{\sigma\}_{i=6}$ and $W_{n+1} = W_{i=6}$. The hardening parameters can be determined using the value of W_{n+1} which will help to get the new yield surface $F(\{\sigma\}_{n+1}, \chi_{n+1}, C_{n+1}, \tan\phi_{n+1})$.

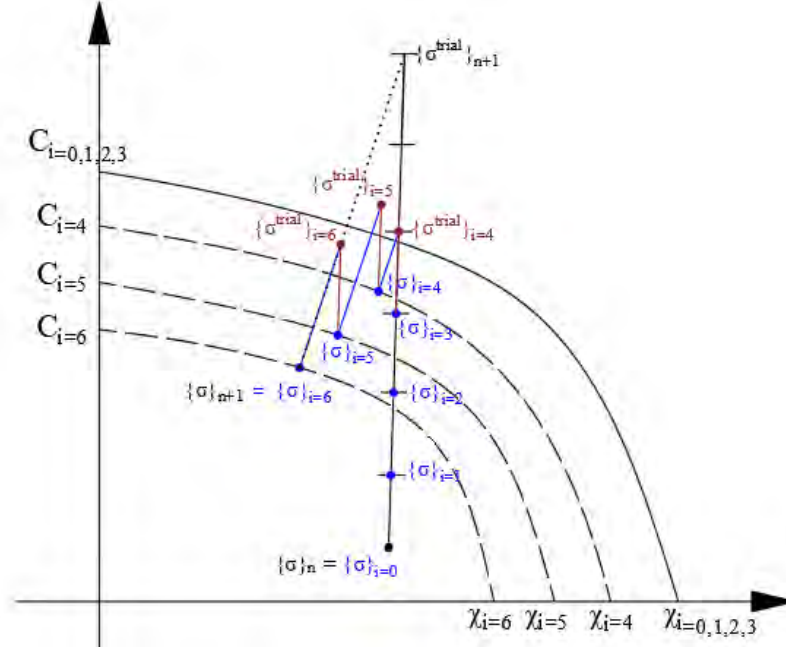


Figure 6. Sub-stepping iteration scheme for stress return mapping

The procedure for getting the consistent tangent stiffness in this scheme is more complex than that illustrated in Eq 4.10 as it should be updated in every sub-step. For a sub-step (say i th sub-step), Eq (4.10) can be expressed as:

$$\frac{\partial}{\partial \{du\}} \begin{bmatrix} \{\sigma\}_{i+1} + d\lambda [K] \{m\}_{i+1} \\ W_{i+1} - dW_{i+1} \\ F(\{\sigma\}_{i+1}, W_{i+1}) \end{bmatrix} = \frac{\partial}{\partial \{du\}} \begin{bmatrix} \{\sigma\}_i + [K] \{du\}_{i+1} \\ W_i \\ 0 \end{bmatrix} \quad (4.13)$$

Using $\{du\}_i = \alpha_i \{du\}$, the procedure used for deriving the left hand side of Eq (4.11) is applied to both sides of Eq. (4.13) to expressed the equation in the following form.

$$[J](\{\psi\}_{i+1}) \begin{bmatrix} \frac{\partial \{\sigma\}_{i+1}}{\partial \{du\}} \\ \frac{\partial W_{i+1}}{\partial \{du\}} \\ \frac{\partial d\lambda_{i+1}}{\partial \{du\}} \end{bmatrix} = \begin{bmatrix} \frac{\partial \{\sigma\}_i}{\partial \{du\}} + \alpha_{i+1} [K] \\ \frac{\partial W_i}{\partial \{du\}} \\ 0 \end{bmatrix} \quad (4.14)$$

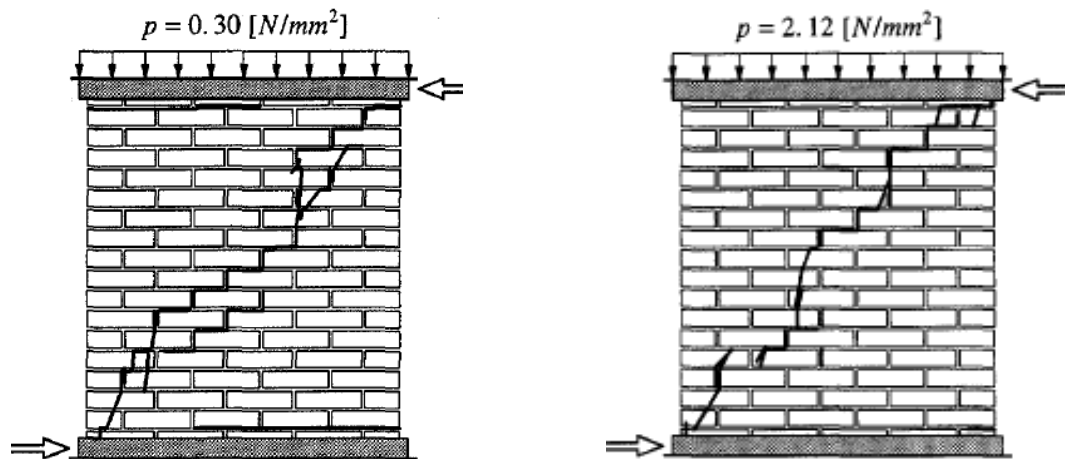
The above equation can be rearranged in a similar manner as of Eq. (4.12) as follows to get the consistent tangent stiffness matrix.

$$\begin{bmatrix} \frac{\partial \{\sigma\}_{i+1}}{\partial \{du\}} \\ \frac{\partial W_{i+1}}{\partial \{du\}} \\ \frac{\partial d\lambda_{i+1}}{\partial \{du\}} \end{bmatrix} = [J]^{-1}(\{\psi\}_{i+1}) \begin{bmatrix} \frac{\partial \{\sigma\}_i}{\partial \{du\}} + \alpha[K] \\ \frac{\partial W_i}{\partial \{du\}} \\ 0 \end{bmatrix} \quad (4.15)$$

5. Numerical examples

In this section, the response of two unreinforced masonry walls under in-plane loads has been simulated using a well-regarded FE code ABAQUS. For an accurate prediction of the response of the masonry walls, a new interface model developed in this study is implemented with ABAQUS using a user defined material model (UMAT) in the form a subroutine developed in FORTRAN. Both walls have the same geometry but different pre-pressures (p) as shown in Figure 7. The dimension of the shear wall is 1000mm (height) \times 990mm (width) \times 100 mm (thick) made of 18 courses (layers) of solid clay bricks each having a size of 210mm (length) \times 52mm (height) \times 100mm (thick). The top course of bricks is connected to a steel beam which provide lateral shear displacement while another steel beam is connected to the bottom course of bricks to provide a fixed boundary condition (Rajmakers, 1992).

The simplified micro-modelling strategy (Lourenco and Rots 1996) that lumps mortar joints as zero thickness interfaces is adopted in the present study for improving the computational efficiency and obtaining a reasonable cracking pattern. The bricks are modelled using plane stress rectangular elements (CPS4R) while cohesive elements (COH2D4) are used for mortar joints. As the vertical mid-plane of brick units is one of the potential failure plane, cohesive elements (COH2D4) are also used for that by treating this plane as an artificial (fake) joint for all brick units. The damage-plasticity model (CDP) is used for simulating the material behaviour of bricks which can also simulate cracking and crushing of bricks indirectly. The parameters used in the nonlinear modelling of bricks and interfaces are listed in the Table 1 and Table 2.



(a) shear wall under 0.3MPa pressure

(b) shear wall under 2.12MPa pressure

Figure 7. Loading conditions and failure modes of experimental walls

Table 1. Brick properties

Elastic modulus (MPa)		Poisson's ratio		Density Ns^2/mm^4	
16700		0.18		19×10^{-9}	
Tensile nonlinear uniaxial behaviour		Compressive nonlinear uniaxial behaviour		Dilation angle	10
Stress (MPa)	Inelastic strain	Stress (MPa)	Inelastic strain	Eccentricity	0.1
3.5	0	11	0	f_{b0}/f_{c0}	1.12
0.3	0.002	11.5	0.001	K	0.667
		0.6	0.007	Viscosity parameter	0.0002

Table 2. Interface properties

Mortar interface (0.3MPa ; 2.12MPa)			
Normal stiffness Kn (N/mm ³)	Shear stiffness Ks (N/mm ³)	Tensile strength χ (N/mm ²)	Shear strength C (N/mm ²)
82; 82	36; 36	0.25; 0.16	0.375; 0.224
Tensile fracture energy G_f^i (N/mm ²)	Shear fracture energy G_f^{ii} (N/mm ²)	Friction coefficient $\tan\phi$	Dilation coefficient $\tan\phi_Q$
0.018; 0.018	0.125; 0.05	0.75	0.001
Fake joint for brick (0.3MPa and 2.12MPa)			
Normal stiffness Kn (N/mm ³)	Shear stiffness Ks (N/mm ³)	Tensile strength χ (N/mm ²)	Shear strength C (N/mm ²)
500	500	2	2.8
Tensile fracture energy G_f^i (N/mm ²)	Shear fracture energy G_f^{ii} (N/mm ²)	Friction coefficient $\tan\phi$	Dilation coefficient $\tan\phi_Q$
0.08	0.5	1	1

Load-displacement relations shown in Figure 8 compares the numerical results and experimental results. The wall under 0.3MPa pre-pressure has in-plane loading capacity around 50kN and it shows a long plateau in the nonlinear response, while the wall under 2.12MPa pre-pressure has approximated 100kN peak load capacity followed by a softening response until the load capacity reduces to 60kN. Besides the experimental data, the ABAQUS built-in damage model (Camanho, P.P. and Dávila, C.G., 2002) is utilized by the authors (2019) and its modelling results of in-plane walls are also presented in the Figure 8.

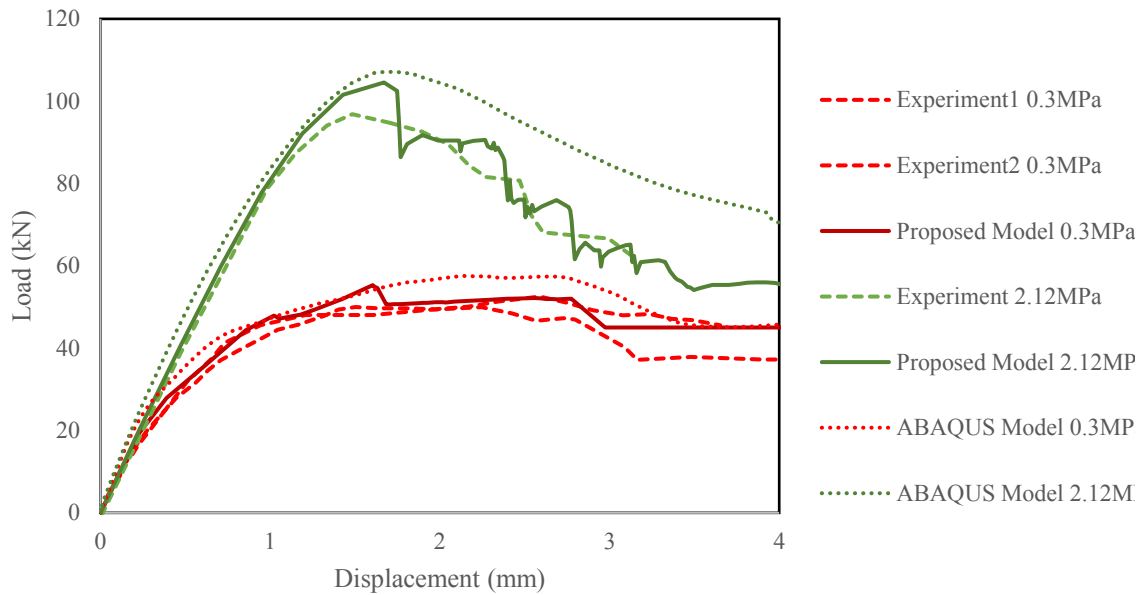
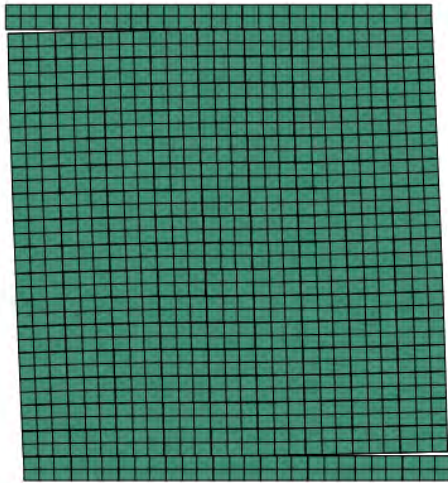


Figure 8. Load-displacement relations

Experimental results indicate that the pre-pressure can influence the cracking patterns in corners of the walls. In Figure 7(a), the wall under 0.3MPa pressure has two significant horizontal cracks in the top left corner and bottom right corner, while in Figure 7(b) there is no similar cracks occur in the corner. The reason resulting in different cracking patterns is that higher pressure (2.12MPa) provides more compression on the horizontal bed interfaces thus the opening cracks in wall left top and right bottom corners would be restrained. The difference of carking growth is captured by FE models clearly from Figure 9(a) to 9(c).

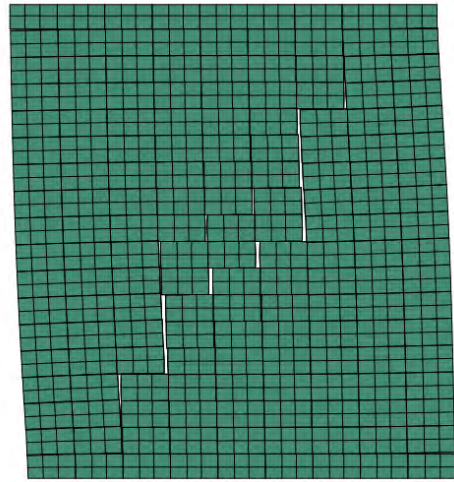
The initial cracks (in Figure 9a) for 0.3MPa wall are firstly found in top and bottom corners as horizontal opening, while that for 2.12MPa wall are found in the wall central area as vertical opening. After that, cracks continue developing (in Figure 9b) in the 0.3MPa Wall and 2.12MPa wall. For the former, corner cracks keep growing and meanwhile cracks in the wall centre begin to form, while for the latter the initial central cracks gradually extend to the corner along the dialog path and some vertical opening become more obvious. Figure 9(c) shows the final failure modes of both walls, the 0.3MPa wall has a continued jogged pattern dialog cracks and two horizontal cracks in the top and bottom corners, while the 2.12MPa wall presents a dialog cracking pattern with several vertical cracks. The applied horizontal displacements corresponding to different cracking stages are also commented in the Figure 9(a)-(c).

Figure 9(d) use ABAQUS built in concrete damage plasticity (CDP) model to detect the compressive failure of bricks during the in-plane loading process, and the crushing failures are determined by the material yield contour in the wall toes.

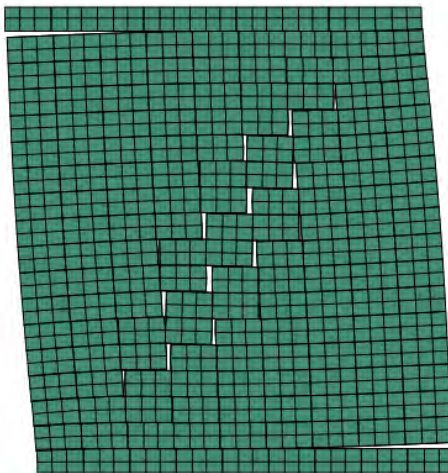


Wall under 0.3MPa pressure

(a) Deformation & failure patterns (initial cracking, around 1.5mm)

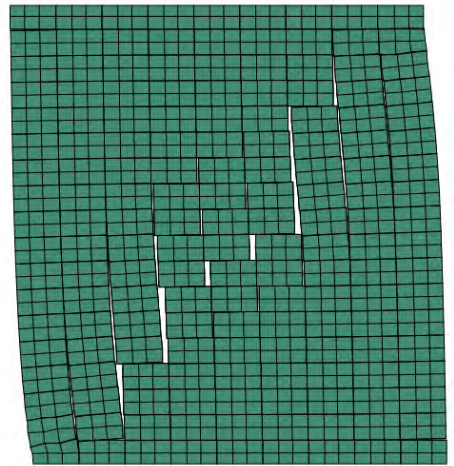


Wall under 2.12MPa pressure

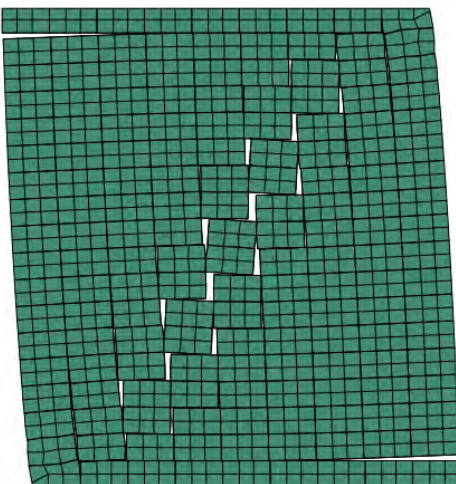


Wall under 0.3MPa pressure

(b) Deformation & failure patterns (cracking growth, around 2mm)

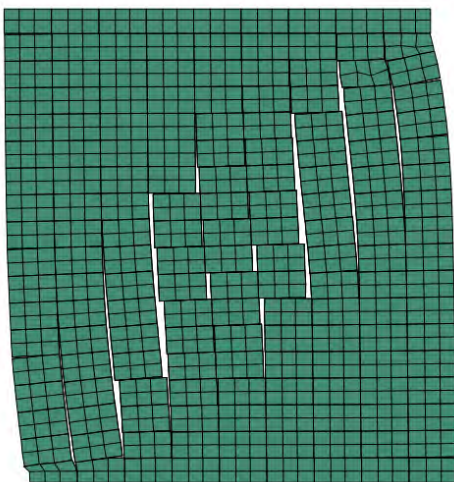


Wall under 2.12MPa pressure



Wall under 0.3MPa pressure

(c) Deformation & failure patterns (fully cracking, around 3.5mm)



Wall under 2.12MPa pressure

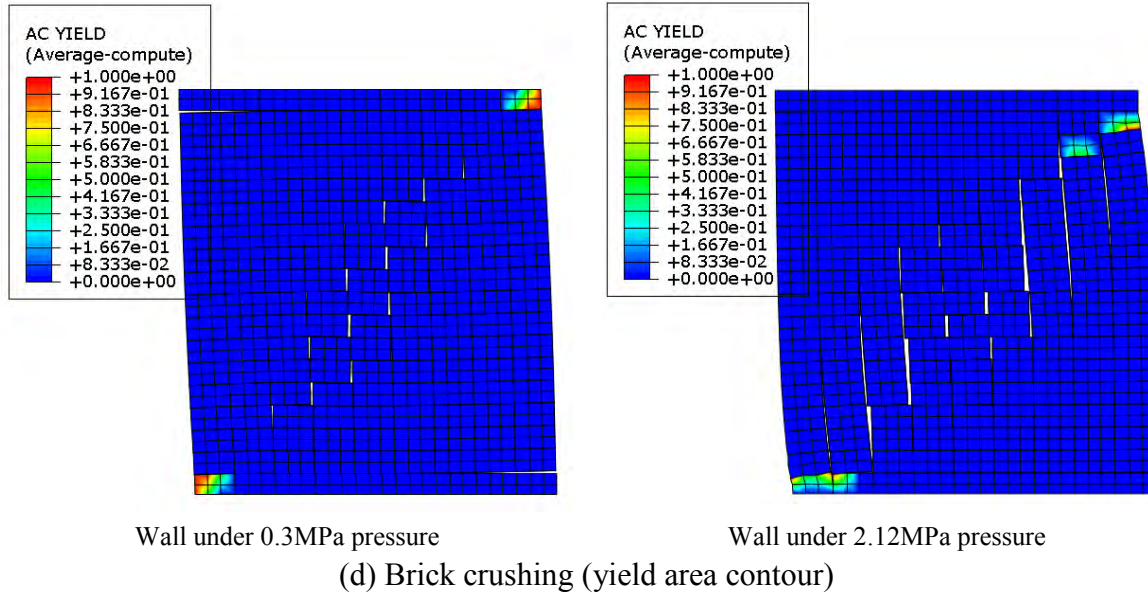


Figure 9. Masonry wall cracking and crushing failure modes

6. Conclusion

This paper proposes an interface model which is applied in predicting the nonlinear response and cracking patterns of unreinforced masonry walls under in-plane loads. Simplified micro-modelling strategy with extended brick and zero-thickness mortar is adopted for running finite element models considering is computational efficiency and proper failure modes visualization. An interface model is proposed in 2D stress space based on the plasticity theory, and an adaptive sub-stepping approach is adopted for improving the convergence performance of FE model in local level. The backward Euler integration method with consistent tangent operator ensures the accuracy of modelling results. Softening evolution laws define the softening process of strength variables with the energy dissipation in interface area. Comparison between experimental and numerical results demonstrated that the proposed interface model performs well in simulating the nonlinear behaviour and cracking failure of masonry walls under in-plane loading conditions. Load-displacement relations have a satisfied agreement in both experimental and numerical results. Diagonal cracking are cleared captured by FE models and the influence of pre-pressure on the failure modes are well reflected in the modelling progress.

Table 3 compared the key mechanisms and characteristics of proposed interface model with other existing models. In the further work, damage mechanism would be combined with the existing plasticity criterion forming plasticity-damage model for predicting the failure modes of masonry walls under seismic loads.

Table 3. Comparison the proposed model with existing models

Existing models	Interface model type	Characterises	Disadvantages
D'Altri et.al (2019)	Damage model	High computational efficiency for large scale models; Suitable for simulating models under cyclic models.	No dilation effect are considered; Trivial parameter calibration works are needed for ensuring accuracy.
Caballero et.al (2008)	Plasticity model	High accuracy and robustness for interface models subjected to shear-tension mixed modes loading.	The failure of masonry caused by compression is not included in the model; Cannot simulate the cyclic response of the interface.
Proposed model	Plasticity model	Both accuracy and robustness performs properly; The compressive failure of masonry is captured by using CDP model	Stiffness degradation and cyclic response of the interface cannot be captured.

Reference

- Abbo, A.J., (1997). Finite element algorithms for elastoplasticity and consolidation (Doctoral dissertation, University of Newcastle).
- Caballero, A., Willam, K.J. and Carol, I., (2008). Consistent tangent formulation for 3D interface modeling of cracking/fracture in quasi-brittle materials. *Computer Methods in Applied Mechanics and Engineering*, Vol 197(33-40), pp.2804-2822
- Camanho, P.P. and Dávila, C.G., (2002). Mixed-mode decohesion finite elements for the simulation of delamination in composite materials. NASA report.
- D'Altri, A.M., Sarhosis, V., Milani, G., Rots, J., Cattari, S., Lagomarsino, S., Sacco, E., Tralli, A., Castellazzi, G. and de Miranda, S., (2019). Modeling strategies for the computational analysis of unreinforced masonry structures: review and classification. *Archives of Computational Methods in Engineering*, pp.1-33.
- De Borst, R., Crisfield, M.A., Remmers, J.J. and Verhoosel, C.V., (2012). *Nonlinear finite element analysis of solids and structures*. John Wiley & Sons.
- Giambanco, G., Rizzo, S. and Spallino, R., (2001). Numerical analysis of masonry structures via interface models. *Computer methods in applied mechanics and engineering*, Vol 190(49-50), pp.6493-6511.
- Griffith, M.C., Vaculik, J., Lam, N.T.K., Wilson, J. and Lumantarna, E., (2007). Cyclic testing of unreinforced masonry walls in two-way bending. *Earthquake Engineering & Structural Dynamics*, Vol 36(6), pp.801-821.

Le, L.A., Nguyen, G.D., Bui, H.H., Sheikh, A.H. and Kotousov, A., (2019). Incorporation of micro-cracking and fibre bridging mechanisms in constitutive modelling of fibre reinforced concrete. *Journal of the Mechanics and Physics of Solids*, Vol 133, p.103732.

Le, L.A., Nguyen, G.D., Bui, H.H., Sheikh, A.H., Kotousov, A. and Khanna, A., (2017). Modelling jointed rock mass as a continuum with an embedded cohesive-frictional model. *Engineering Geology*, Vol 228, pp.107-120.

Nie, Y, Sheikh, A., Griffith, M., Visintin, P. and Vaculik, J. (2019). The application of mixed-mode de-cohesion criteria in masonry finite element analysis, Australian Earthquake Engineering Society 2019 Conference, Nov 29- Dec 1, Newcastle City Hall, New South Wales

Pérez-Foguet, A., Rodríguez-Ferran, A. and Huerta, A., (2001). Consistent tangent matrices for substepping schemes. *Computer methods in applied mechanics and engineering*, Vol 190(35-36), pp.4627-4647.

Raijmakers, T.M.J. and Vermeltfoort, A.T., (1992). Deformation controlled tests in masonry shear walls. (holandés), Report B-92-1156, TNO-Bouw, Delft, Países Bajos.

Smoljanović, H., Nikolić, Ž. and Živaljić, N., (2015). A combined finite–discrete numerical model for analysis of masonry structures. *Engineering fracture mechanics*, Vol 136, pp.1-14.

Su, Y., Wu, C. and Griffith, M.C., (2011). Modelling of the bond–slip behavior in FRP reinforced masonry. *Construction and Building Materials*, Vol 25(1), pp.328-334.

Vaculik, J. and Griffith, M.C., (2017). Probabilistic analysis of unreinforced brick masonry walls subjected to horizontal bending. *Journal of Engineering Mechanics*, Vol 143(8), p.04017056.

Vaculik, J., Visintin, P., Burton, N.G., Griffith, M.C. and Seracino, R., (2018). State-of-the-art review and future research directions for FRP-to-masonry bond research: Test methods and techniques for extraction of bond-slip behaviour. *Construction and Building Materials*, Vol 183, pp.325-345.

Seismic restraints for floor-mounted components

Peyman Sharifi¹ and Arash Nazari Rad²

1. Structural Engineer, MIEAust, Eurofast Pty Ltd, Sydney, NSW 2128, Australia. Email: peyman.sharifi@eurofast.com.au
2. Head of Engineering Department, MIEAust NER RPEQ Eurofast Pty Ltd, Sydney, NSW 2128, Australia. Email: Arash.n@eurofast.com.au

Abstract

Recently, design of seismic restraints for non-structural components has grabbed a great amount of attention across Australia. There is a heated debate in industry regarding code compliance of non-structural components with AS1170.4:2007: Earthquake Actions in Australia. According to section 8 of AS1170.4, seismic design needs to be carried out for variety of component types including but not limited to suspended, recessed, surface-mounted, wall-mounted and floor-mounted components. In some occasions, seismic restraints for floor-mounted components are being neglected in the design and construction process. In this paper, seismic restraint design for floor-mounted components such as UPS, switchboards, cooling tower, battery racks, tanks and other equipment will be described, and issues that are typically arising at construction sites due to vibration and radiation isolation requirements will be mentioned. In addition, adequacy of the components' body, component's seismic certification and liability issues will be discussed. Finally, some suggestions will be made to address these issues accordingly.

Keywords: seismic restraint design, non-structural components, floor-mounted, building services, seismic bracing

1. Introduction

Non-structural components of a building classify as those permanent elements supported by and fixed to base build structure, that are not part of building's structural system. Mechanical, electrical, plumbing, fire, medical gas, ceiling and walls components are some example of non-structural components. Historically, non-structural components of buildings have suffered extensive damage in earthquakes events, which in turn not only did cause huge economic losses, but also threatened the life safety of building's occupants.

Although Australia has been located in the middle of a large tectonic plates implying lower seismic risk, this country have been subjected to 17 earthquakes registering 6 or more on the Richter Scale in the last 80 years.(Seismic Restraint of Engineering Services: 2019- Government of South Australia). Figure 1 shows Newcastle after ML 5.6 Richter earthquake, December 1989 (Newcastle Earthquake Database Website).



Figure 1-Newcastle after ML 5.6 Richter earthquake, December 1989 (Newcastle Earthquake Database Website)

Seismic design for non-structural components needs to be carried out so that they can withstand the seismic loadings calculated based on section 8 of AS1170.4-2007: Structural design actions-Part 4: Earthquake actions in Australia. This standard requires all non-structural components within a building to be designed to resist earthquake forces. Domestic structures with height of less than 8.5m and importance “level one” structures are exempted from this requirement.

2. Floor-mounted components

One type of non-structural components are those freestanding components mounted on the surface floor. These items can slide and/or overturn during a seismic motion due to lack adequate anchorage to the floor, and subsequently cause economical damage, threaten safety of people. These components can also lose their function due to internal mechanism failure and interfere with operability of the systems that are essential to post earthquake operation such as emergency generators. Failure of these items can contribute to catastrophic events even after earthquake excitation. Not to mention damages to electrical equipment can lead to electrical and fire hazards. Figure 2 shows unanchored electrical cabinets overturned during earthquake (FEMA E-74:2011)

Some examples of floor-mounted components that are typically included in MEP-F engineering systems are included but not limited to boilers, furnaces, pumps, water heaters, chimneys, flues, smokestacks, vents and pressure vessels chillers, compressors, cooling towers, air handling units, cylinders, control panels, motor control centres, switchgear, emergency generator, transformers, batteries and battery rack, communications Antennae, elevator and escalators, electrical boards.



Figure 2-unanchored electrical cabinets overturned during earthquake (FEMA E-74:2011)

4. Design Parameters

Floor-mounted components can slide, tilt overturn, or fall during seismic event. Failure mechanism would depend on dimension and weight, and centre of gravity of component. Figure 3 shows the concept of seismic load calculation for each support. Imposed seismic force (F) to the centre of gravity of the component would be calculated from multiplying operational weight of the component by seismic coefficient. Value of this coefficient depends on structure parameters and components' mounting type, importance factor and ductility factor. Horizontal force generated on the component can be maximum half of the operational weight of the components. Moreover, vertical earthquake forces to centre of gravity of components are half of the horizontal earthquake forces. (AS1170.4:2007-section 8).

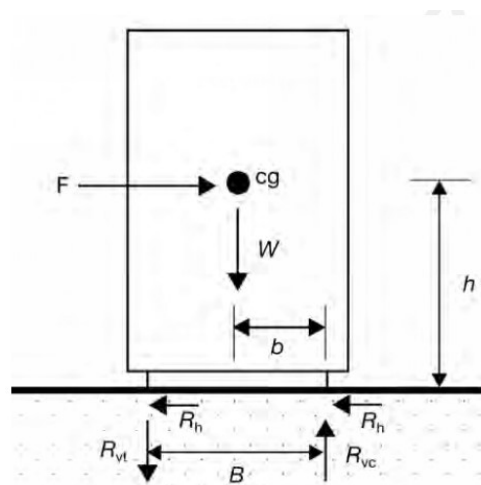


Figure 3- Forces on Floor-mounted components (Seismic Performance of engineering systems in buildings - NZS4219:2009)

Non-structural parts and components and their attachments are to be designed for forces calculated from either acceleration or simple method. Simple method although conservative, is usually more practical in non-structural design. This is because seismic designer often does not have access to the values of acceleration for each floor, as this is calculated based on computer analysis of the building by base-build consultant. Clause 8.3 of AS1170.4 set forth the horizontal earthquake force to non-structural components as follow:

$$F_c = [K_p Z C_h(0)] a_x \left[\frac{I_c a_c}{R_c} \right] W_c \quad \text{Equation 4.1}$$

Where K_p , Z , $C_h(0)$ are probability factor, hazard factor and spectral shape factor for the period of zero seconds, respectively. Unlike the later parameters, a_x , I_c , a_c and R_c are related to part and components and describe the component height amplification factor, importance factor and amplification factor and ductility factor, respectively. In the following, some interpretation of authors about determining value of these parameters would be mentioned.

When determining the value of I_c for each component, it is of great importance that components that are essential to function immediately after earthquake are to be given value of $I_c = 1.5$, even though they are not in an important level 4 structure. All other non-essential components have importance factor of $I_c = 1$.

Amplification factor(a_c) is to be chosen $a_c = 2.5$ for flexible spring type mounting systems, whereas for all other mounting systems it would be equal to $a_c = 1$. There is different interpretation about how ductility factor is to be chosen for floor mounted components. It is authors' opinion, that unless floor-mounted components are constructed from high-deformability ductile materials, the value of R_c is safe to be considered as $R_c = 1$.

After earthquake forces have been calculated from AS1170.4, the performance of component and its connection under this seismic force is to be calculated. Until further development of the section 8 of the AS1170.4, one may refer to NZS4219, seismic performance of engineering systems in buildings in New Zealand, to design the required fixings of floor-mounted components based on calculated forces from AS1170.4. Herein is summary of authors' suggestion of parts which may be utilised to achieve code compliance with AS1170.4 section 8.

Horizontal seismic force to centre of gravity of component will cause overturning and this will be transmitted as tension (R_{vt}) and compression (R_{vc}) in the base of the component. Weight and dimension of the component will dictate whether overturning will be a governing failure or not. Sliding will happen at the base due to horizontal seismic forces. Both overturning and sliding can be prevented by providing appropriate fixings at the base using seismic springs and/or snubbers and seismic anchors. Horizontal braces may be used in combination with fixings at the base. Equations 4.2 and 4.3 may be used to calculate horizontal and vertical earthquake force on each support when components are fixed from the base only. (Seismic performance of engineering systems in buildings -NZS4219:2009)

$$R_h = \frac{CW}{N} \quad \text{Equation 4.2}$$

$$R_{Vc} \text{ or } R_{Vt} = \pm \frac{CWh}{nB} + \frac{W}{N} \quad \text{Equation 4.3}$$

Where:

N denotes total number of supports

n denotes total number of supports acting on tension in the direction being considered

B denotes spacing of supports in the direction being considered

h denotes operational height of central of gravity

C denotes earthquake force coefficient

Depending on whether floor-mounted components are rigidly mounted or resiliently mounted, above formulas may differ, and correction coefficient is to be applied to formulas to take account for impact of mounting type. Resilient mounts have two types, one type is a system that the mountings or vibration isolation system have enough capacity to withstand the seismic actions without the need for adding extra snubbers. Equation 4.4 may be used to calculate vertical earthquake force on each support when components are fixed from the base only. (Seismic Performance of engineering systems in buildings -NZS4219:2009)

$$R_{Vc} \text{ or } R_{Vt} = \pm 1.3 \times \frac{CWh}{nB} + \frac{W}{N} \quad \text{Equation 4.4}$$

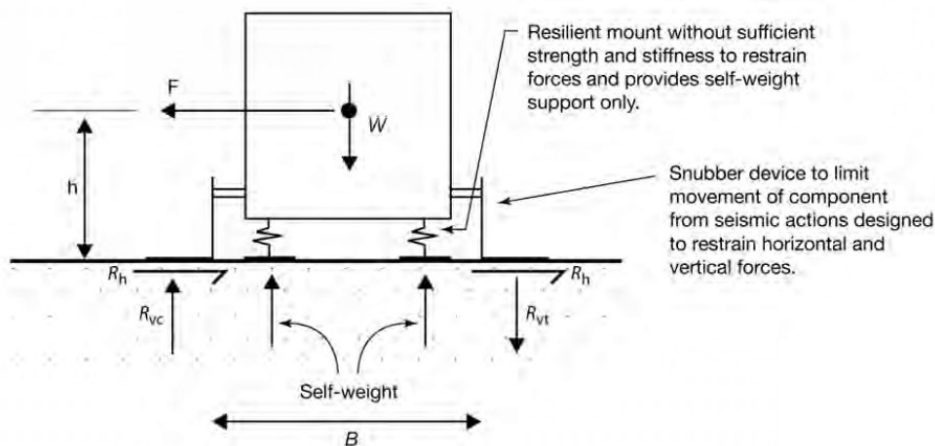


Figure 4-Forces on floor-mounted components using vibration isolation with additional snubbers (Seismic Performance of engineering systems in buildings -NZS4219:2009)

Figure 4 shows another type which are those mountings or vibration isolators that do not have the capability to withstand the seismic loadings and additional seismic snubbers are to be installed. Equation 4.5 and Equation 4.6 may be used to calculate horizontal and vertical earthquake force on each support when components are fixed from the base only. (Seismic Performance of engineering systems in buildings - NZS4219:2009)

$$R_h = \frac{CW}{N} \times i \quad \text{Equation 4.5}$$

$$R_{Vc} \text{ or } R_{Vt} = \pm 1.3 \times \frac{CWh}{nB} \times i \quad \text{Equation 4.6}$$

Where

i = impact factor:

- 1** for snubbers with resilient pads and less than 6 mm clearance between the component support frame and the snubber device in the direction being considered.
- 1.5** for snubbers with less than 6 mm clearance and no resilient pads (metal on metal contact) between the component support frame and the snubber device in the direction being considered
- 2** for snubbers with more than 6 mm clearance and resilient pads between the component frame and the snubber device in the direction being considered
- 3** for snubbers with more than 6 mm clearance and without resilient pads (metal on metal contact) between the component support frame and the snubber device

5. Industry Code Compliance Review

In this section, common problems in achieving compliance with AS1170.4: section 8 for floor-mounted seismic requirement would be reviewed. Below are summary of key points needed to be considered for floor-mounted component compliance:

- 5.1. Usually, plinths and piers are supports for many freestanding elements. It is essential for contractor to engage with structural engineer and seismic specialist at the early design stages to ensure plinths and piers have been designed to withstand seismic loadings. This is important because integrating seismic requirement to piers and plinths can be straightforward in the design stage, however, once constructed, retrofitting might be very difficult and costly. Figures 5-1 to 5-3 shows some options how floor-mounted components/plinth can be anchored down to plinth. In all methods, contractor needs to ensure plinth reinforcement, concrete strength and plinth's anchorage to slab and component's anchorage to plinth/slab has been designed to transfer the imposed loads from component to base build structure.

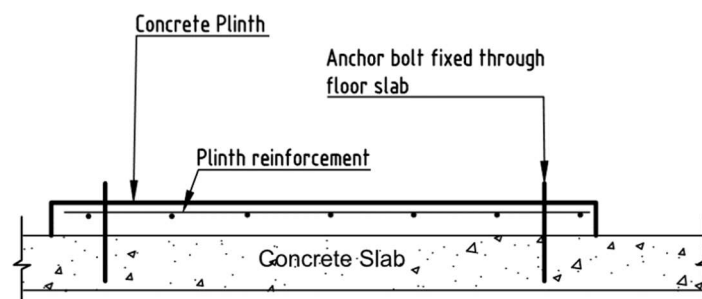


Figure 5-1-Plinth/component fixing options to slab-option 1

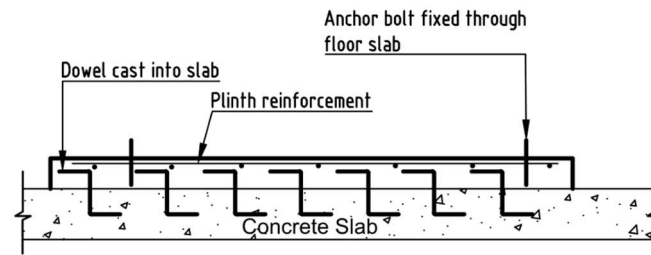


Figure 6-2-Plinth/component fixing options to slab-option 2-Dowel cast into slab

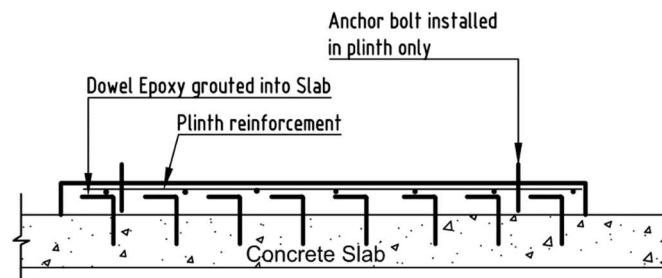


Figure 7-3-Plinth/component fixing options to slab-option 3-Dowel epoxy-grouted into slab

- 5.2. Loads from components with significant weight are to be checked with structural consultant of the base build structure to ensure they have allowed for this imposed load in design stages. These loading schedule might be provided by seismic specialist.
- 5.3. Where vibration and radiation shielding are required an extra degree of care needs to be taken to ensure a system would be selected that can be certified for seismic requirement without compromising noise cancelling and/or anti-radiation performance. These systems usually have been placed as a mat underneath topping slab and/or concrete screed and cannot be penetrated in most of the cases .That is why connection of the component to topping slab and/or base build structure to be designed before installation takes place. After the components are in place, it would be very difficult or not practical to amend the existing systems installed on site. Moreover, topping slab and/or concrete screed is to be designed and constructed strong enough to withstand the imposed seismic loads.
- 5.4. Where spring is needed to fix an element to primary structure/plinth, contractor is to ask spring suppliers for seismically rated springs that are strong enough to withstand lateral seismic forces. This is to avoid the need for adding extra braces/snubbers.
- 5.5. Anchors used to fix the components to primary structure/plinth to withstand seismic actions are to have seismic certification C1/C2 based on building importance level and importance of the component itself. In lieu of seismic technical assessment for anchors to concrete in AS5216:2018: design of post-installed and cast-in fastenings in concrete, European anchoring technical assessment for seismic loadings, C1/C2 certification may be used.
- 5.6. Body of components needs to be strong enough to withstand seismic imposed forces and to work as a solid object. Therefore, contractor should advise supplier

that the component will be used in seismically active area to get the most suitable products. Components are to be braced horizontally on top or mid-height as well if their body is not strong enough to transfer the imposed loads to the base.

- 5.7. Many of the components can be supplied with welded brackets and/or pre-manufactured holes, so it is important that contractor orders components that seismic anchorage details have been considered by supplier. Switchboards with low height PFC channels underneath can be challenging to be anchored down to floor slab, it is recommended that appropriately sized welded tags and brackets to PFC channels to be provided to make anchorage process easy.
- 5.8. Floor-mounted components such as switchboard sitting on raised floors are to be positively fixed to raised floor framing. In addition, a compliance certificate with AS1170.4 needs to be provided by raised-floor contractor.
- 5.9. Battery racks which are one of the essential components for continuity of operation of the important buildings such as hospitals are vulnerable to seismic excitation. Not only do racks need to be strong enough, but also batteries themselves need to be restrain in place to avoid being dislodged and fell over racking.

6. Conclusion

Non-structural floor-mounted components, if not anchored down properly, not only do impose great safety risk to building occupants but also usually account for huge economical and financial losses in the event of seismic excitation. This paper reviews current industry standard practice for floor-mounted components design and installation and presents points that needed to be considered to satisfy seismic design requirements of this free-standing components.

From the industry experience, in order to make the freestanding components seismically compliant with AS1170.4, following points needs to be considered. Body of components, plinth/piers, fixing point of component to plinth and fixing point of plinth to structure need to be designed for imposed seismic loads. Moreover, spring and anchors are to be certified and rated for seismic loadings. While selecting floor-mounted components, contractors should inform supplier about seismic requirements to avoid further complications. It is also recommended that contractors involve seismic specialist from the design stage. This is to reduce the total cost of making floor-mounted components seismically compliant.

References

- AS1170.4:2007, Structural design actions- Part 4 Earthquake actions in Australia
- Seismic Restraint of Engineering Services:2019-Government of South Australia
- FEMA E-74,2011, Reducing the risk of non-structural Earthquake Damage
- Seismic Performance of engineering systems in buildings-NZS4219:2009
- ASHRAE: Practical guide to seismic restraint- American society of heating, refrigerating and air-conditioning engineers
- Newcastle Earthquake Database Website

Seismic Tomography Experiments: case study of the Southern Highlands of PNG

Cvetan Sinadinovski¹, Agus Abdullah², Kevin F. McCue³ and Dicky Ahmad Zaky²

1. Corresponding Author. Director, Global SeismiCS, Canberra ACT, Australia.
Email: cvetansin@hotmail.com
2. Geophysical Engineering Department, Pertamina University, Indonesia.
agusabdullah@gmail.com
3. Adjunct Professor, Central Queensland University, Rockhampton, Qld, Australia. mccue.kevin@gmail.com

Abstract

Our aim is to investigate the effectiveness of new seismic tomography software to determine three-dimensional crustal structures and better earthquake locations in active tectonic regions. We invert near-field P and S arrival times from an updated dataset comprising aftershocks recorded in Papua New Guinea on 6 accelerographs deployed in the near field of the magnitude M7.5 earthquake on 26 February 2018.

The cross-sections of the crust produced by this new methodology show the potential of the geotomography application in revealing velocity perturbations in the lithosphere. The images can constrain the velocity versus depth relationship and help relocation of the earthquakes through 3-D models. Our results will contribute towards a better understanding of the seismicity and tectonic processes in the Southern Highlands and will lead to an overall improvement of the regional earthquake hazard assessment across Papua New Guinea.

Keywords: earthquakes, velocity modelling, inversion, seismic tomography

1 INTRODUCTION

We wanted to test new geotomographic software to investigate the seismotectonic features and crustal structure in an active tectonic region such as the Highlands of Papua New Guinea. The 3-D models and the cross-sections of the crust produced by this methodology show the potential of the geotomography application in revealing velocity perturbation in the lithosphere. These images will help constrain the velocity versus depth relationship and ultimately contribute towards better relocation of earthquakes.

A recently compiled and updated dataset of aftershocks recorded in Papua New Guinea on 6 accelerographs deployed in the near field of the magnitude M7.5 earthquake on 26 February 2018 (Gibson *et al.*, 2018) were used as input into the tomography program. The Australian Earthquake Engineering Society and Oil Search funded seismologists to deploy instruments and monitor the aftershocks a month after the main event (M^cCue *et al.*, 2018). Many events were recorded including the aftershock on 7th of April with magnitude M6.3, which caused further casualties and damage. After inspection, some 125 earthquakes were selected for our tomography experiment. The selected events satisfied the criteria to be recorded on at least three stations and to have clear P- and S-arrival times.

In our method, we first inverted the travel-times from all the source-receiver combinations to calculate the propagation times of seismic rays and then compared the results with the theoretical forward modelling. The difference between the theoretical arrival times and the observed times was minimised and at the end, we performed a series of tests with various 3-D velocity models in order to monitor their effect on the location accuracies.

With the new tomography suite, we can display a variety of images; the velocity or slowness perturbations in respect to a reference velocity model, horizontal or vertical slices through the volume, seismic ray density through the grid mesh, refinement of discretization and so on.

2 METHODOLOGY

In seismic tomography, the time of the seismic waves travelling between the focus of the earthquake and the station is measured and used in an inversion process, referred to as travel-time inversion. The surveyed volume, the cuboid, is discretised into cells of a certain grid size on the surface and depth ranges in chosen intervals. Within the cuboid, for each source-receiver i.e. earthquake-station combination, the travel-time is calculated based on the initial velocity model. Then the calculated arrivals are compared with the observed arrivals on the seismograms, commonly for the P and S-phases (Kennett and Abdullah, 2011, Sinadinovski *et al.*, 2019b).

Here, the tomographic inversion is performed using irregular grid parametrization; tetrahedron cell discretization (Fig. 1a) of complex geological models is especially useful in situations of rough topography and high-contrast anomalies. Tetrahedron ribs are utilized for ray tracing that are finer at shallow depths and coarser at greater depth (Fig. 1b). Source and receiver locations are embedded into the ribs to enable ray tracing between each source and receiver pair. Our approach allows fast iterations for geometry with narrow offset (local earthquakes) as well as inclusion of the more distant earthquakes in reduced computation time.

Furthermore, the search for finding the nearest neighbours of a specific number of points is used to optimize the algorithm during searching for the fastest path that fulfills the Fermat principle. Therefore, forward models are more realistic and the resulting images of the sub-structures can indicate variations in the velocity with a higher degree of resolution.

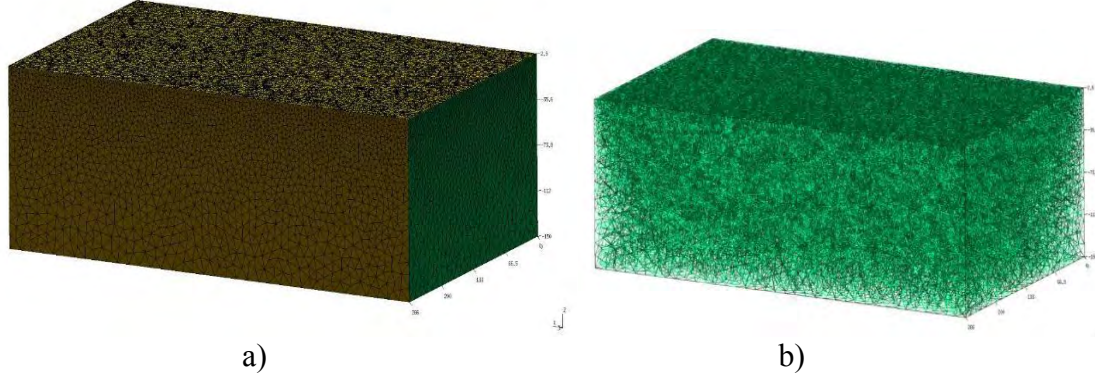


Figure 1 Schematic representation of a) grid parametrization and b) tetrahedron ribs used for ray tracing. (Model size is relative and numbers can be scaled up or down).

The tomography calculations are stored as a matrix of velocity values and slowness perturbations in respect to the initial model. The images can be graphically shown at various slices through the cuboid, typically horizontally (depth) and vertically (longitude and latitude). The novelty of our approach over the previous tools is its ability to be applied simultaneously in forward modelling and inversion, thus allowing the user to monitor in 3-D space the effects of the re-location of seismic events by the model composition.

The inverse problem of earthquake relocation can be described using relationship of data \mathbf{d} and model parameter \mathbf{m} :

$$\mathbf{d} = \mathbf{g}(\mathbf{m}) \quad (\text{Eq. 1})$$

where \mathbf{d} matrix is travel time, \mathbf{m} is the hypocenter location (x_0, y_0, z_0) and \mathbf{g} is the velocity model. The calculated travel time \mathbf{d} could be modified by adjusting the hypocenter location for given velocity models. The solution will converge as the travel time in the model (\mathbf{d}_m) comes close to the travel time of observation (\mathbf{d}_{obs}).

Since the inverse problem is a non-linear by nature, to reach convergence we adopted non-linear approximation of a Fast Marching Method – FMM, to predict the travel time in 3-D grid volume with inhomogeneous medium velocity (Abdullah A. and Zaky D.A., *personal communications*, 2020). The new hypocenter location is obtained by minimizing the objective function $S(\mathbf{m})$ defined by Eq.2:

$$S(\mathbf{m}) = (\mathbf{d}_{obs}^r - \mathbf{d}_m^r)^T (\mathbf{d}_{obs}^r - \mathbf{d}_m^r) \quad (\text{Eq. 2})$$

where \mathbf{d}_{obs}^r is a vector $(N \times 1)$ matrix containing observed arrival times of N stations with the mean subtracted, and \mathbf{d}_m^r is a same size vector matrix containing predicted travel times from FMM, also with the mean subtracted (Rawlinson, 2008). Thus, the result of Eq.2 matrix multiplication should be a single value of the scalar objective function for one grid point.

The reciprocity principle is used to build the travel time model (\mathbf{d}_m), where the station is considered a source and then predict the travel time for every grid point using FMM for given velocity models. In this case we used the output from velocity tomography.

In resolving Eq.2, for every grid points we performed the multi-dimension matrix multiplication (vectorization) instead of looping. A 3-D medium matrix was considered with size $(I \times J \times K)$ corresponding to (x, y, z) coordinates. Regarding the reciprocity principle, the travel time model was built for every station, for instance (M) the number of stations and a 4-D matrix $(I \times J \times K \times M)$ was formed of the travel time model (\mathbf{d}_m). By taking the travel time observation (\mathbf{d}_{obs}) into account, the residual travel time of observed and model ($\mathbf{d}_{obs} - \mathbf{d}_m$) matrix can be obtained with size $(I \times J \times K \times M)$. Finally, by adapting Eq.2, we calculated the objective function $S(\mathbf{m})$ as a 4-D matrix multiplication resulting of 3-D matrices $(I \times J \times K)$ of the objective functions.

In order to obtain more accuracy when the station coordinates fall between the grid points, we performed a 3-D interpolation of the FMM results to build the travel time model. First, we specified a voxel proportional to the grid spacing around the station location and then interpolated the travel times between its 8 points until the actual position of the station is covered.

The last step was to find the minimum value of the objective function. We assumed that the minimum value is located within the grid. Therefore, to have more accurate locations, we applied gradient descent and damping to minimize the misfit function for every voxel.

In tomography, there is always a trade-off between the grid size or refinement and the misfit function which depends on many input parameters during the iterations. *A priori* assumptions in geology can help in constraining the velocity model, so researchers need to find the best combination of parameters to best fit the geology.

3 SYNTHETIC TESTS

We designed a few synthetic datasets to test the sensitivity of the input parameters and to fine-tune them for cases similar to PNG area in search of optimal results. One simple case of a discretized volume $2.5^\circ \times 2.5^\circ$ with five layers containing 11 events (red dots) recorded on 5 stations (green dots) is presented on Figure 2.

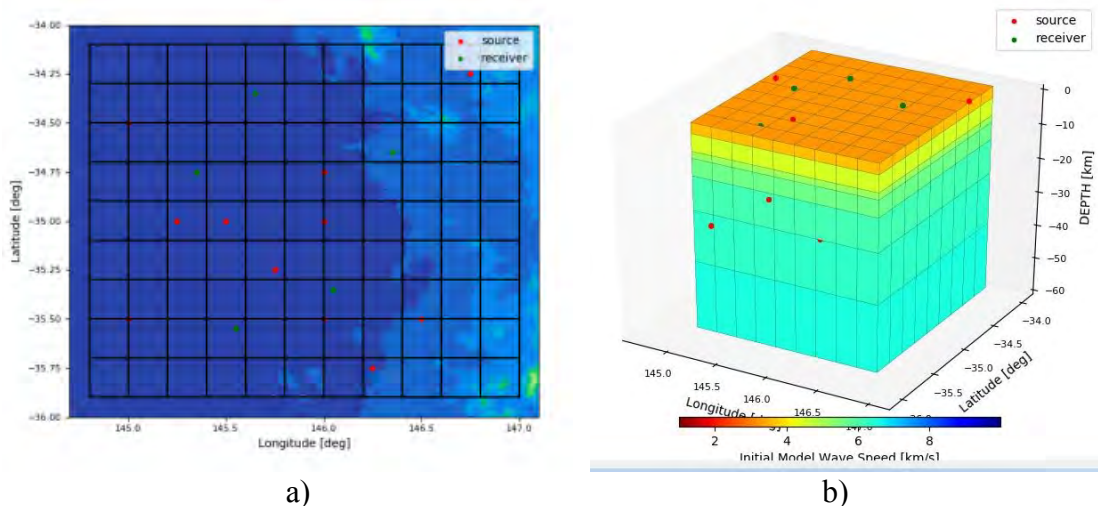


Figure 2 Synthetic model for testing: a) topography and b) 3-D V_p model.

The so-called checkerboard test was performed first, in which the cells of alternating high- and low-velocity values were placed in each layer. The recovered image for the rays from all the source-receiver pairs gave an indication of the ability of the program to detect velocity variations. A Quality Control is run automatically in parallel and the results can be monitored for each stage of the calculation. Figure 3 displays the ray coverage and recovered checkerboard for one chosen cross-section in vertical direction

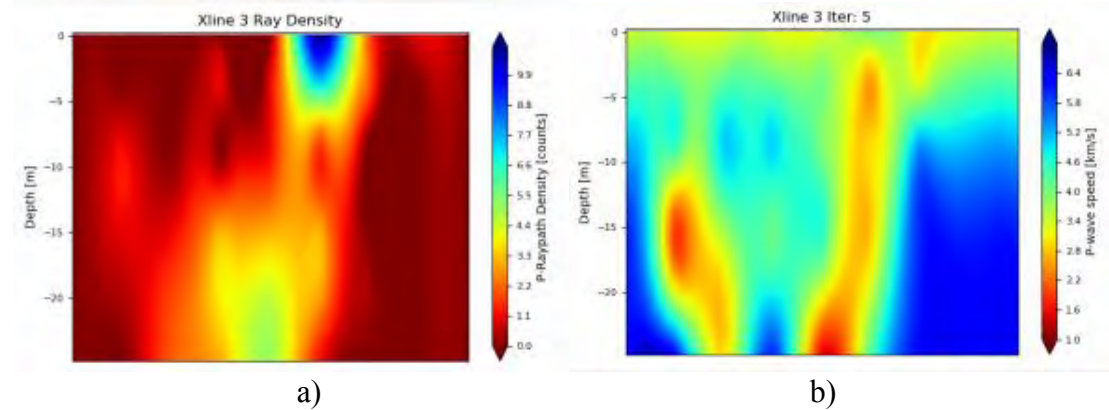


Figure 3 Visualization of: a) the ray coverage and b) the recovered checkerboard image for one latitudinal slice through the synthetic model.

The P- and S-arrival data were created with forward modelling. An assumed random error of ± 0.1 s was introduced to the calculated times, which is about the reading error of phases from seismograms. We did multiple runs with the tomography program to monitor the influence of the parametrization on the output images. Figure 4 shows the ray coverage and recovered field data image for a horizontal cross-section at a depth of 4km.

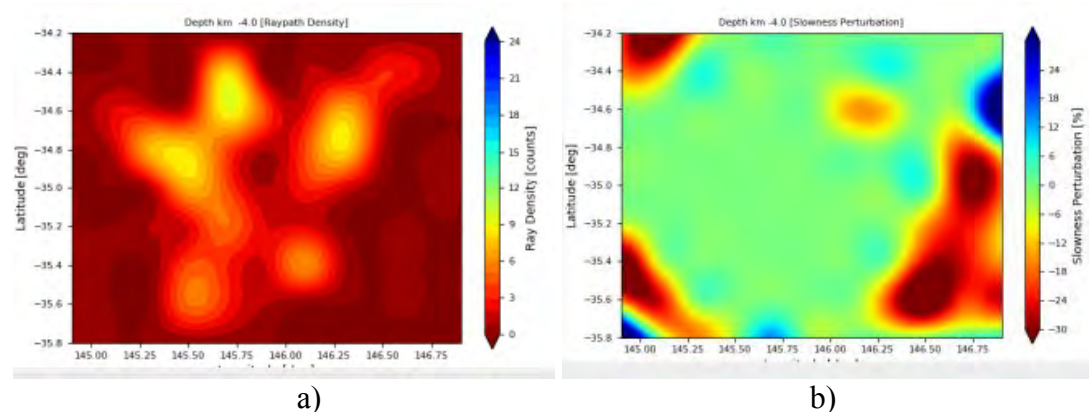


Figure 4 Visualization of: a) the ray coverage and b) the recovered image with field data, for one horizontal slice through the synthetic model.

The results of the tomography inversion are reliable only in areas with good ray coverage. For example, in Fig. 4, just the part within the star-shaped area is sufficiently well covered by rays, outside the star ray paths are influenced by artefacts. Voxels which were not criss-crossed by rays were set to their initial values in the velocity model, because no extra information was available.

In general, the tomographic images are better resolved under the network of stations, while the uncertainty increases with the distance from the closest station. Also, a good azimuthal coverage is important, since the station configuration aligned at one side of the zone where events occur may cause spurious effects in calculation of their spatial location.

We tried to test the relocation of events within the 3-D synthetic model with the procedure described in the earlier section 2. The grid size and the nodes refinement were varied from cases with large spacing down to just ± 1 km, which consumed a lot of computer CPU memory. The coordinates of the original events were compared with the relocated events and differences saved in the associated output directory. Figure 5 shows the distribution of the original (orange points) versus the relocated events (blue points).

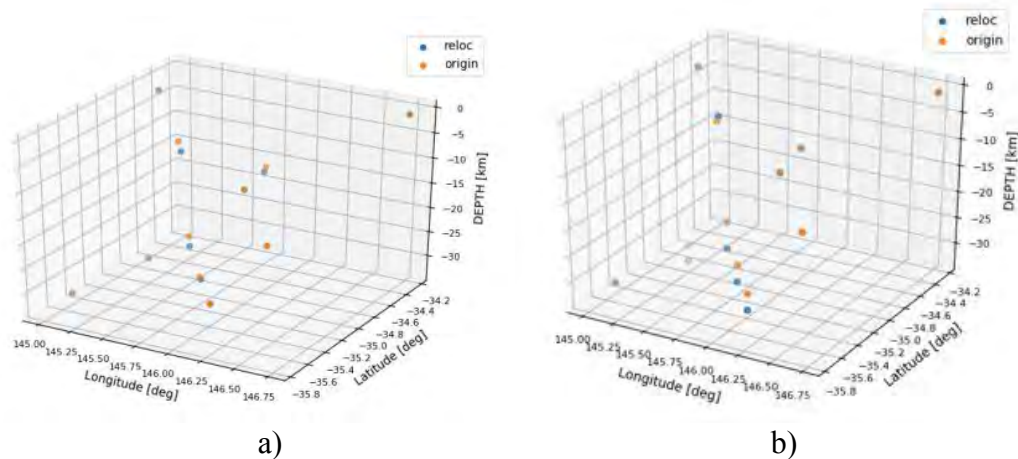


Figure 5 Distribution of the original versus relocated events when: a) the maximum difference was limited to ± 6 km and b) the maximum difference was not limited.

The results of the relocation are strongly dependent on the 3-D velocity model, especially on its near surface layers. If the tomography model is too far from the initial model used to generate the arrival times, then the calculation of the objective function is stacked in the local minima and gives unrealistic solutions.

4 FIELD DATA TESTS FOR PNG

The acquired data consisted of picked P- and S-arrivals from the seismograms collected from 6 accelerographs deployed to record the aftershocks in the Southern Highlands of Papua New Guinea after the magnitude M7.5 earthquake on 26 February 2018. We selected around 125 earthquakes for our tomography experiment, which satisfied the criteria to be recorded on at least three stations and to have clear arrival times readings on the seismograms. Between 600 and 700 P-arrival times and a corresponding number of S-arrival times were used in the tomographic analysis.

To explore the crust under the Southern Highlands of PNG, the events that occurred in a cuboid of $2.5^\circ \times 2^\circ$ centred on the temporary network and down to 60km deep were processed. The volume was discretised into cells of a $20\text{km} \times 20\text{km}$ grid in the surface area and depth ranges in the intervals from 3, 8, 15, 20, 25, 35, 45 to 60km (Figure 6). To investigate the 3-D structure underneath the area, the modified Gippsland velocity model (Gibson G., *pers. communications*, 2018) was utilised, values shown in Table 1.

Table 1 Velocity model used for aftershock locations.

Depth (km)	V _p (km/s)	V _s (km/s)
0-3	3.802	2.398
3-8	5.521	3.413
8-20	6.052	3.572
20-45	6.240	3.661
45-60	7.812	4.460

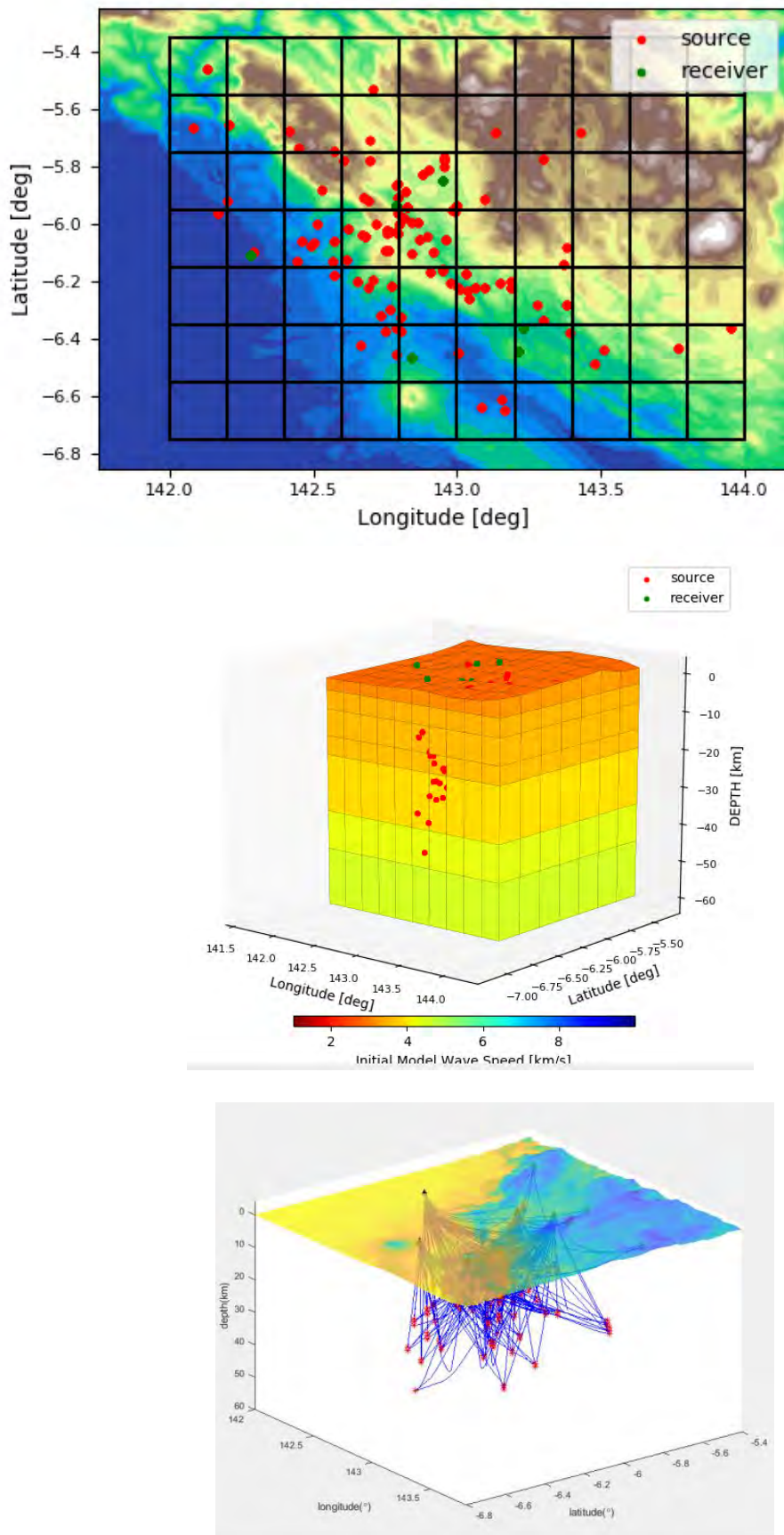


Figure 6 Field data model for PNG: top – topography, middle – the 3-D V_s model, and bottom – ray paths between sources and receivers; (Red dots denote the earthquake locations).

The results for each stage are done in windows with dynamic resizing, so the discretized volume, the events, the cross-sections and the rays can be displayed in a user-defined frame. The model misfit function was monitored for each inversion (Fig. 7), and was found that for this PNG dataset converges to a minimum after a few

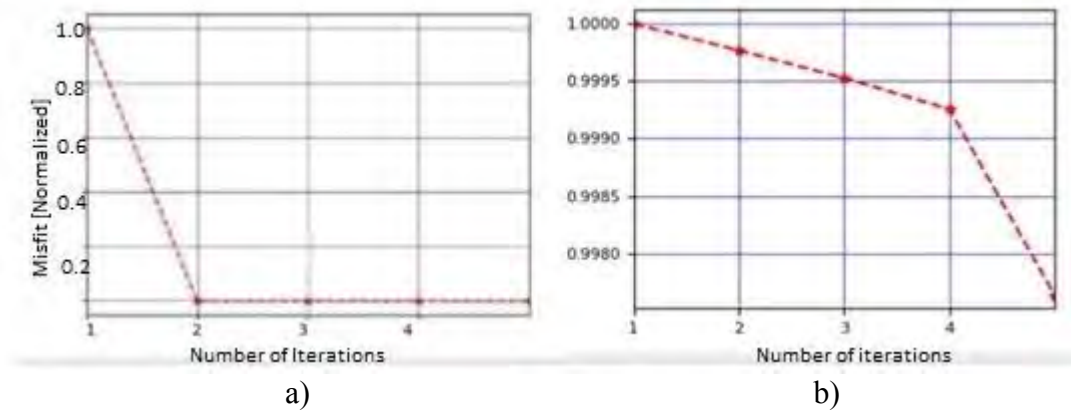


Figure 7 Misfit function vs number of iterations for: a) checkerboard test and b) field PNG data

At first instance, we reproduced the previous results from Sinadinovski *et al.*, (2019a) with the new version of the tomography package. For example, Figure 8 shows the images of the checkerboard tests and the latitudinal slices of relative slowness perturbation in respect to the initial velocity model.

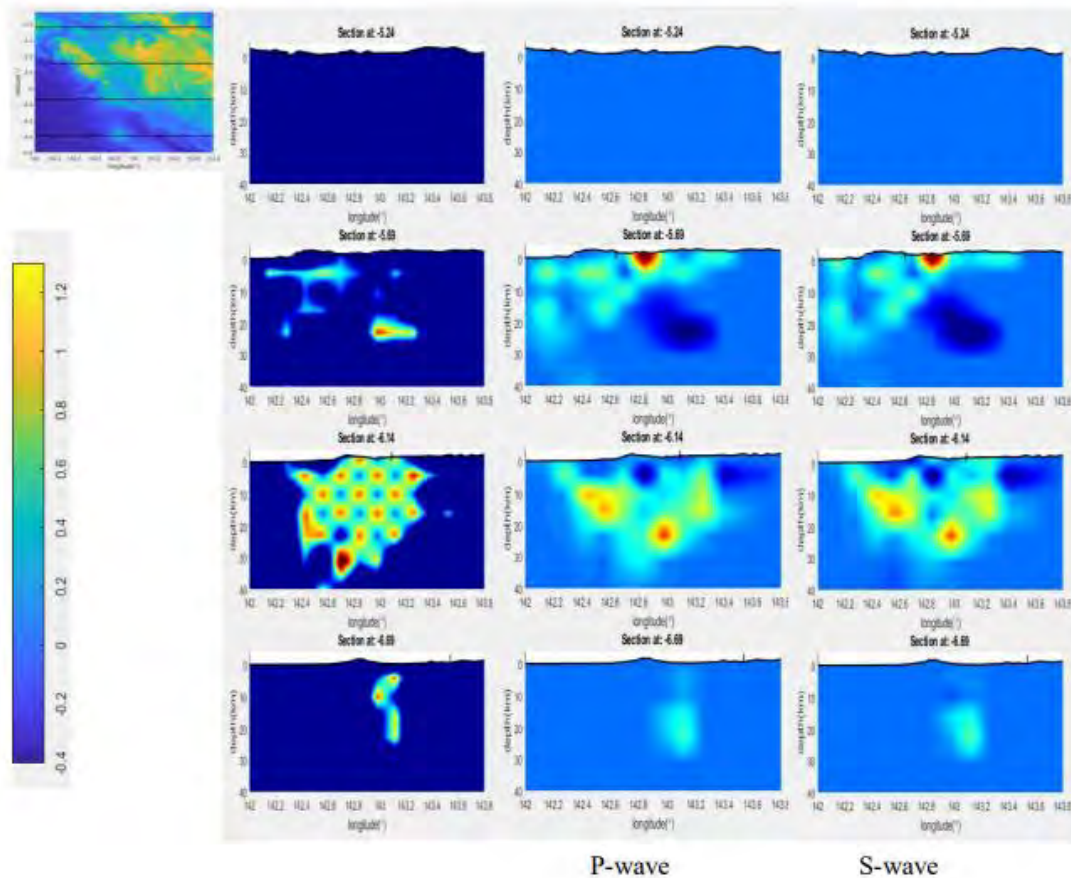


Figure 8 Checkerboard tests (left column) and latitudinal slices of relative slowness perturbation in respect to the initial velocity model; (Blue-fast, Red-Slow).

The W-E slices through the cuboid on Figure 8 are shown from north to south, and on the colour bar the blue end represents fast, while the red end of the spectrum represents slow velocities. The most northerly slice in the cuboid has insufficient data to change the background velocity. The images produced using the P- and S-arrivals look very similar, due to the fact that the number of readings used in the inversion was very close in both cases. The results in the second and the third vertical slice of the cuboid can be viewed with higher confidence. A slow velocity zone coinciding with the known volcano Mt. Bosavi is noticeable on the southern side, with its imprint extending down to 20km. However, since that part of the area is not well covered by the rays, the deeper section may be an artefact of the tomography.

Next, Figure 9 shows the images of the checkerboard tests and the longitudinal slices of relative slowness perturbation in respect to the initial velocity model. The N-S slices through the cuboid are ordered from west to east, and on the colour bar the blue end represents fast, while the red end of the spectrum represents slow velocities. The images produced using the P- and S-arrivals look very similar too, because the number of readings used in the inversion was nearly the same in both cases. The results in the second and the third vertical slice of the cuboid can be viewed with higher confidence because of better ray coverage.

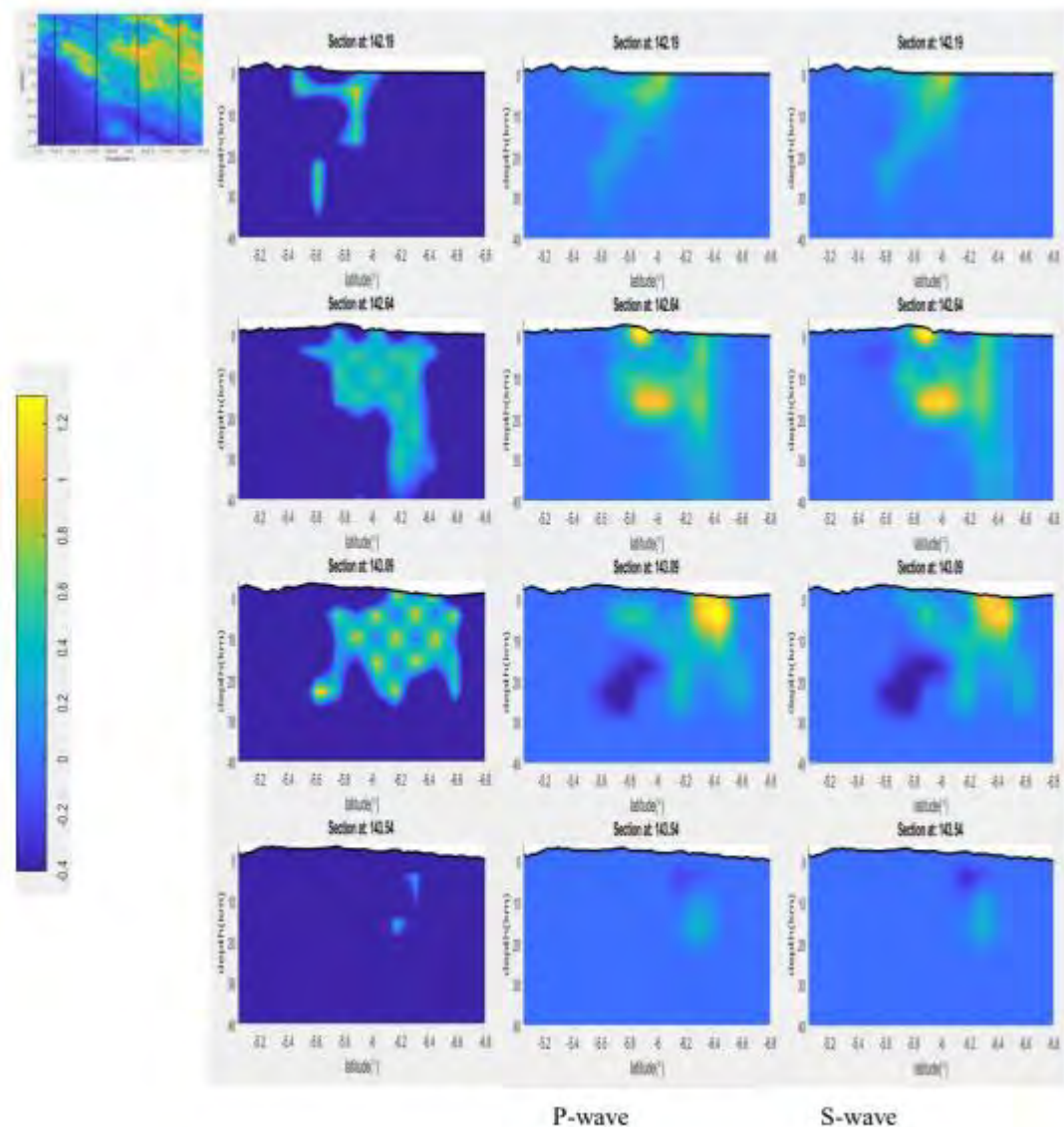


Figure 9 Checkerboard tests (left column) and longitudinal slices of relative slowness perturbation in respect to the initial velocity model; (Blue-fast, Red-Slow).

The shape of the velocity anomalies on the images is consistent with the existing geological maps for the Papuan Belt area. The slices can be chosen parallel to the orientation of the PNG highlands, to allow viewing of the geological sections in comparison with the existing maps (Sinadinovski *et al.*, 2019a).

So far, with tomography we have used the data to image the volume in 3-D, detect layers in the crust and evaluate the Moho discontinuity. In the following step, the output velocity model from tomography was employed to relocate the seismic events.

Multiple combinations of initial models and arrival times types were used in the relocation process. The first series of computer runs was completed using the extended 1-D model of Table 1 into layers of constant velocity. The second series of runs was done with a computer generated 3-D model consisting of interpolated velocity values from the initial model, used at the start of iterations. Both series were performed with the selected P- and S-arrival times. A sample distribution of the original versus relocated events for variety of search spacing and seismogram readings is presented on Fig. 10.

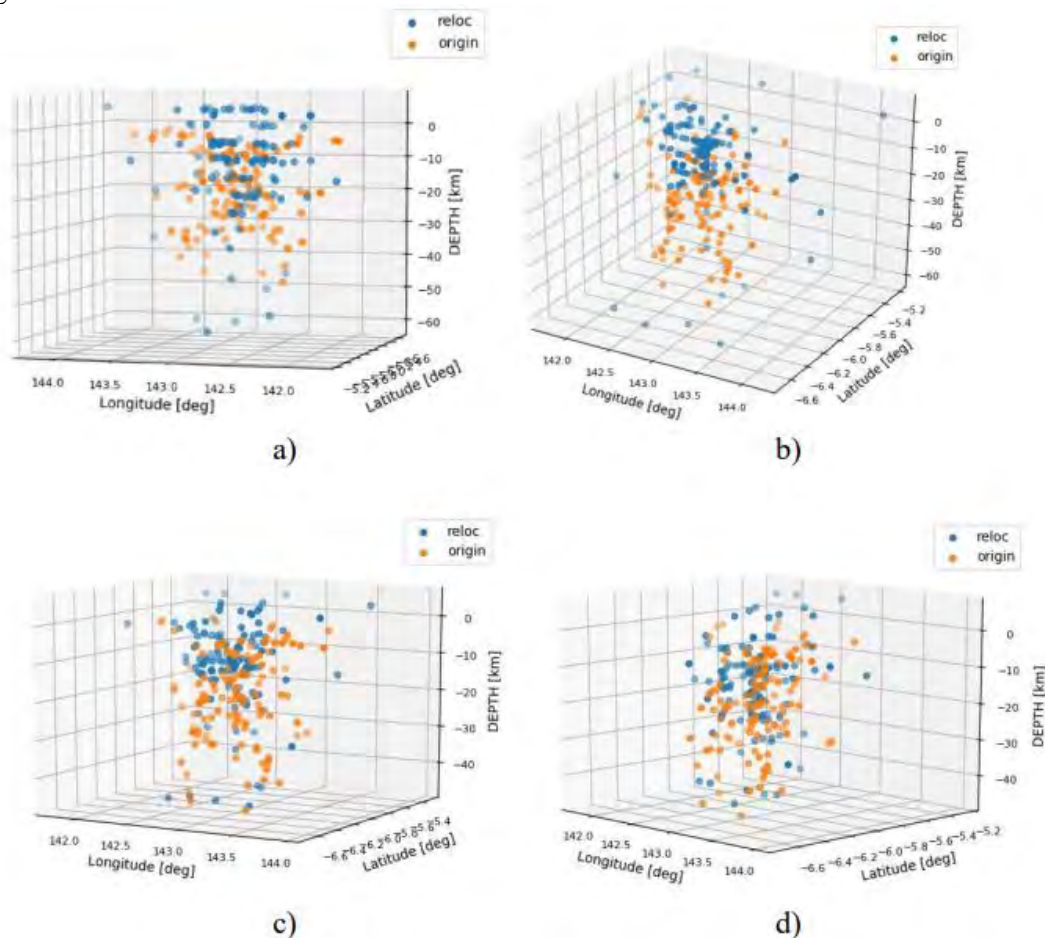


Figure 10 Distribution of the original versus relocated events: a) for spacing of 5km and extended 1-D model with P-arrivals; b) for spacing of 5km and 3-D model with P-arrivals; c) for spacing of 1km and 3-D model with P-arrivals; and d) for spacing of 5km and 3-D model with S-arrivals.

An overall impression from our location calculation was an upwards trend of the relocated events in respect to their originally calculated position, which was based on the extended 1-D model or proxy 3-D model. That is in line with the previously stated

observation that the results are strongly influenced by the velocity values in the top layers. Events outside the network area cannot be uniquely located if only the travel-time is used. An improved approach to constrain the tomography images would be consideration of the 3-component records and polarization test to narrow the azimuth of the incoming waves at the stations, which in terms of computing may speed up the search algorithm of the location objective function.

The tomography and relocation results are comparatively stable and reflect the limitation of the source-receiver geometry and discretisation of the velocity model. It has to be mentioned that more intermediate interventions are possible, such as seismic zoning, which could introduce the *a priori* assumptions from geology and help in constraining the velocity model.

A full set of trials with the tomography program has been run over a period of a few months. Given the enormity of the output results and the limitation for printed pages, the authors plan to upload them as a separate project and link them within the aees.org.au website.

5 SUMMARY AND DISCUSSION

This study is a continuation on the work done in the aftermath of the major magnitude 7.5 earthquake in February 2018 which occurred in the Southern Highlands of PNG. We reproduced the previous tomographic images and expand the analysis with an updated dataset.

In the beginning, an extended 1-D model or proxy crustal model was used to locate the aftershocks that occurred a month after the main event and were recorded on 6 temporary stations. Thousands of seismic events were recorded, but after inspection, just 125 earthquakes were selected for our tomography experiment. They satisfied the criteria to be recorded on at least three stations and to have clear P- and S-arrival times.

We had a series of runs with the proxy model and the computer generated 3-D model consisting of smoothed velocity values. Still, no characteristic pattern of aftershocks that might indicate a distinctive fault system could be discerned, rather than the whole region is being sheared, thickened and uplifted by crustal compression. The shapes of the anomalies on our tomography images are consistent with the existing geological and tectonic maps for the region (e.g. <https://pubs.usgs.gov/of/2010/1083/h/>).

The results of the tomography inversion are reliable merely in the areas with good ray coverage. Only the parts criss-crossed by dense ray paths should be considered for interpretation, while the edges are probably influenced by artefacts. Voxels which were not covered by rays were set to keep their values as in the initial velocity model, because no additional information was available for them. In general, the tomographic images are always better resolved under the network of stations, while the uncertainty increases with the distance from the closest station.

It should be emphasised that besides the velocity model, the focal depth is an important parameter for seismic hazard assessment and consequently can influence the recommended design spectra for the regions. Focal depth is the parameter with the highest uncertainty in locations using whole Earth models used by international seismological centres. In exploration geophysics, the positions of the sources and the

receivers are known with certainty, thus the task of checking the inversion results is relatively easier.

We started to test the relocation of events with a 3-D synthetic model, then with the proxy model and lastly with the computer generated 3-D model, following the method described earlier in section 2. The grid size and the nodes refinement were varied from large spacing down to very small of ± 1 km. An overall impression from our location calculation was an upwards trend of the relocated events in respect to their originally calculated position, which is in line with the previously stated observation that the results are strongly influenced by the velocity values in the top layers.

Our geotomography images are in agreement with other authors for areas underneath the Southern Highlands of PNG, where its estimated depth from the surface is approximately 40km. McCue *et al.*, (2018), pointed out that the records of the many examined aftershocks look alike, and are quite different from Australian earthquakes at the same distance. It was noticed from the isoseismal maps of past earthquakes and the studies of the quality factor Q , that the ground motion attenuation is much higher in PNG, the felt area being much smaller than for a similar sized earthquake in Australia.

Therefore, based on this and other studies, we conclude that the application of the Australian velocity model in the Southern Highlands of PNG should be modified to around 10-20% for the relatively lower velocities in the top layers. More certain interpretations can be achieved with longer term deployment of seismic instruments and increased number of recorded earthquakes. Access to the PNG network data would have been useful. With this new tomography tool, we are able to run the program from various aspects and display the resulting images in forms suitable for further research such as the regional earthquake hazard and risk assessment studies.

6 REFERENCES

Gibson G., McCue K.F. and Love D., (2018) Aftershocks, Crustal Structure and Faulting along the Southern Side of the Central Highlands, Papua New Guinea. AEES Earthquake Engineering Society Conference, WA, paper 43.

Kennett, B.L.N., and Abdullah, A. (2011) Seismic wave attenuation beneath the Australasian region, Australian Journal of Earth Sciences, 58, pp. 285-295.

McCue K.F., Gibson G., and Love D., (2018) Monitoring Aftershocks in the Southern Highlands, Papua New Guinea. AEES Earthquake Engineering Society Conference, WA, paper 45.

Rawlinson, N., (2008) Seismology Lecture Notes: Earthquake relocation. Research School of Earth Sciences, Australian National University, Canberra, ACT.

Sinadinovski C., McCue K.F., Gibson G., Abdullah A. and Love D., (2019a) AEES Reconnaissance Mission to Papua New Guinea, Pacific Conference on Earthquake Engineering PCEE, Auckland, New Zealand, paper 385.

Sinadinovski C., McCue K.F., Abdullah A. and Pekevski L., (2019b) Geotomography Trials on the Edge of the Australian and European Plates. AEES Conference, Newcastle, NSW, paper 12.

What do earthquakes at Zagreb 2020, Newcastle 1989 and Rabaul 1978 have in common?

Cvetan Sinadinovski¹, Kevin F. McCue², Snjezana Markusic³, Lazo Pekevski⁴
and Ines Ivancic³

1. Corresponding Author. Director, Global SeismiCS, Canberra ACT, Australia.
Email: cvetansin@hotmail.com
2. Adjunct Professor, CQ University, Rockhampton, Qld, Australia.
mccue.kevin@gmail.com
3. Department of Geophysics, Faculty of Science, University of Zagreb, Croatia.
markusic@gfz.hr
4. Associate Professor, Seismological Observatory, PMF, University “Ss. Cyril and Methodius” (UKIM), Skopje, Macedonia. lazopekovski@yahoo.com

Abstract

Strong motion records of moderate magnitude, shallow, thrust-type earthquakes, our ‘type earthquake’, recorded at similar distances in three different tectonic regions have been analysed and found to have similar frequency and peak amplitudes. This opens up the possibility of using these recordings interchangeably for design purposes where such earthquakes are expected, such as in Australia.

The March 2020 Zagreb earthquake Mw 5.3 matched our ‘type earthquake’. Data and tectonic information were provided by seismologists at the Department of Geophysics, University of Zagreb who manage the Croatian national seismological network and regional seismic stations. We used strong motion records from their three closest stations to deduce their spectral characteristics.

One of the few Papua New Guinea accelerograms of our ‘type earthquake’ was recorded near Rabaul Papua New Guinea in 1978 on an analogue SMA-1 instrument. We have digitised the record to analyse the spectral content of the recording.

In Australia the third earthquake occurred near Newcastle in 1994, not quite 5 years after the destructive Newcastle earthquake, a moderate magnitude ML 5.6 (Mw 5.3) earthquake which caused more than \$1B damage and killed 13 people. No near-field ground motion record of the Newcastle earthquake exists, but a digital accelerograph was sited there in time to record an aftershock and subsequently the 1994 earthquake.

The response spectra of these earthquakes are compared with the Design Spectra from the respective countries' Building Codes and Loading Standards.

Keywords: earthquakes, strong motion records, response spectra, building codes

Seismic Performance of Earth Retaining Structures Considering Different Support Conditions

Rohit Tiwari^{1*}, Nelson Lam²

- 1* Corresponding Author, The Department of Infrastructure Engineering, The University of Melbourne, Parkville, VIC 3010, Australia.
E-mail: rohitt@unimelb.edu.au.
2. Professor, The Department of Infrastructure Engineering, The University of Melbourne, Parkville, VIC 3010, Australia.
Email: ntkl@unimelb.edu.au

Extended Abstract

Present work evaluates the seismic performance of retaining walls considering different support conditions. A detailed and rigorous Finite element (FE) investigation has been performed on two dimensional (2D) models of earth retaining structures to understand the seismic behaviour of base restrained, free-standing and pile-supported retaining walls (RW). A detailed shaking table investigation has also been performed in order to understand the seismic performance of RW's with different support conditions. The backfill has been characterised by performing several geotechnical testings for understanding its role into the seismic performance of earth retaining structures. Different dynamic properties of the RW and the backfill have also been estimated during the shaking table experiment. Shaking table experiment results have also been used for calibrating the FE RW models. The FE models of RW with different support conditions have been analysed against different base excitations. The hardening and softening behaviour of backfill has been simulated by calibration of backfill material model with consolidated drained (CD) triaxial test. Seismic performance of the earth retaining structures (with different support conditions) has also been studied for different backfill type. Three different backfill type have been considered for FE investigations, (i)

Crushed rock (characterized at The University of Melbourne), (ii) Fontainebleau sand (Dano et al. 2004), and (iii) Dune sand (Daheur et al. 2019) respectively.

It was observed that the backfill plays an essential role in the seismic performance of earth retaining structures. In the case of base restrained RW increasing displacement of RW has been observed with increasing peak ground acceleration. It was also observed from the FE investigations that the backfill type does not have a high influence on the seismic displacement of base restrained RW. In the case of free-standing RW, it was observed that the RW with granular backfill shows better seismic performance than the RW with sands as backfill soil. The RW supported by rock socketed piled foundation also shows better seismic performance when subjected to granular backfill. High displacement of rock socketed piles has also been observed in all cases. Nonlinear dynamic soil pressure and residual soil pressure behind the RW's has also been observed, irrespective of RW support condition.

Keywords: Retaining wall, seismic design, displacement based design, shaking table test, rock socketed piles, earthquake.

REFERENCES

- Dano, C., Hicher, P. Y., & Tailliez, S. (2004). Engineering properties of grouted sands. *Journal of Geotechnical and Geoenvironmental engineering*, 130(3), 328-338.
- Daheur, E. G., Goual, I., Taibi, S., & Mitiche-Kettab, R. (2019). Effect of dune sand incorporation on the physical & mechanical behaviour of tuff: (experimental investigation). *Geotechnical & Geological Engineering*, 37(3), 1687-1701.

Recent Research on Geotechnical Seismic Isolation System based on Rubber-Soil Mixtures

Hing-Ho Tsang¹, Kyriazis Pitilakis², Duc-Phu Tran³,
Sheng Li⁴, Wen-Yi Hung⁵, Emad F. Gad⁶

1. Associate Professor, Swinburne University of Technology, Melbourne, Australia; Bushfire and Natural Hazards Cooperative Research Centre, Melbourne, Australia. (Corresponding Author, Email: htsang@swin.edu.au)
2. Professor, Aristotle University, Thessaloniki, Greece. (2018-2022 President of European Association of Earthquake Engineering)
3. PhD Candidate, Swinburne University of Technology, Melbourne, Australia.
4. Senior Research Engineer, China Electric Power Research Institute, Beijing, China; PhD Candidate, The University of Melbourne, Parkville, Australia.
5. Associate Professor, National Central University, Taoyuan, Taiwan.
6. Dean of Engineering, Swinburne University of Technology, Melbourne, Australia; Bushfire and Natural Hazards Cooperative Research Centre, Melbourne, Australia.

Abstract

The innovative concept of geotechnical seismic isolation (GSI) with the use of a continuous layer of low-modulus rubber-soil mixtures (RSM) surrounding the foundation of structure has attracted considerable research interest globally in the past decade. This paper presents a brief review of the recent works completed by the authors. This includes an equivalent-linear lumped-parameter analytical model, which has been verified based on a 2-D finite element model, for dynamic soil-foundation-structure interaction (SFSI) analysis and for explaining the isolation mechanism of the GSI system. On the other hand, the effectiveness of the isolation system has been validated by geotechnical centrifuge modelling. It has been confirmed that the GSI-RSM foundation layer can reduce the rocking stiffness, that enhances the seismic isolation capability, whilst without having large permanent deformations due to the higher elasticity of RSM. Finally, a series of shaking table tests has also been conducted to examine the effectiveness of GSI-RSM system on isolating electrical transformer. Generally, it was found in these studies that 30% to 60% reduction of structural demand can be achieved.

Keywords: geotechnical seismic isolation, rubber-soil mixtures, waste tyre, lumped-parameter model, centrifuge, shaking table, augmented rocking mechanism

INTRODUCTION

Geotechnical seismic isolation (GSI) takes advantages of the dynamic interaction between structure and low-modulus foundation material (Tsang and Pitilakis 2019). The foundation natural soil material is replaced or modified down to a certain depth (e.g. 2–3 m) by well-controlled low-modulus materials such as rubber-soil mixtures (RSM) (initially proposed in Tsang 2008), in order that the soil-foundation-structure interaction (SFSI) favourably affects the overall structural response. The key advantage of the GSI system is that seismic energy is dissipated before it transmits into the structure, which is fundamentally different from conventional seismic isolation systems or other earthquake protection techniques (Tsang 2009, Karatzia and Mylonakis 2017). This is a paradigm shift.

Whilst the concept of GSI is not limited to a particular choice of materials, RSM were chosen because (i) rubber has been widely used in vibration damping and isolation and both the static and dynamic properties of RSM were available in the literature, and (ii) waste tyres are available in abundance with an urgent need of recycling, which also provides a green and economical source for RSM (Tsang 2012, Xiong and Li 2013, Tsiavos et al. 2019, Chiaro et al. 2019). Granulated RSM are characterised by nonlinearity and high damping in the medium-to-high strain range, with properties that can be adjusted via rubber content (Senetakis et al. 2012). With high shear resistance, low shear modulus (Anastasiadis et al. 2012), controllable stress-strain behaviour and increased damping, RSM is a desirable candidate for use in GSI system.

Significant amount of research works has been carried out to demonstrate the potential of GSI-RSM system (e.g. Tsang et al. 2009, Shimamura 2012, Tsang et al. 2012, Kaneko et al. 2013, Pitilakis et al. 2015, Brunet et al. 2016, Forcellini 2017, Nanda et al. 2018, Dhanya et al. 2020), however the isolation mechanism has not been thoroughly investigated. Hence, an equivalent-linear lumped-parameter model was recently developed for dynamic SFSI analysis of the GSI system and for characterising its isolation mechanism (Tsang and Pitilakis 2019). On the other hand, experimental research is indispensable for confirming its effectiveness in reducing structural response. To this end, centrifuge modelling with an earthquake shaker under an acceleration field of 50 g was conducted (Tsang et al. under review) such that the actual nonlinear response characteristics of RSM and subsoil can be mimicked in scaled models. Also, shake table tests (in a 1-g environment) on scaled models of a coupled soil-structure system of electrical transformer were also performed as a case study (Li et al. under review). This article briefly reports these recent works.

ANALYTICAL MODELLING

The performance of the GSI system has been studied through various numerical, physical and hybrid modelling techniques; but due to the complexity of the problem, the isolation mechanism has not been thoroughly investigated. Hence, Tsang and Pitilakis (2019) aimed at initiating this aspect of development. A simple and efficient lumped-parameter model has been developed for analysing the dynamic SFSI of the GSI system (Figure 1). Considering the importance of various nonlinearities involved, a theoretical approach for estimating effective shear strain has been derived for capturing the nonlinearity of subsurface materials by the equivalent-linear method, which is widely used in practical geotechnical seismic analysis. The analytical model has then been verified based on numerical modelling of a coupled soil-structure system using a 2D finite element model. The effectiveness of the equivalent-linear lumped-parameter model has also been demonstrated through a representative case study, based on which the main features of the isolation mechanism are investigated.

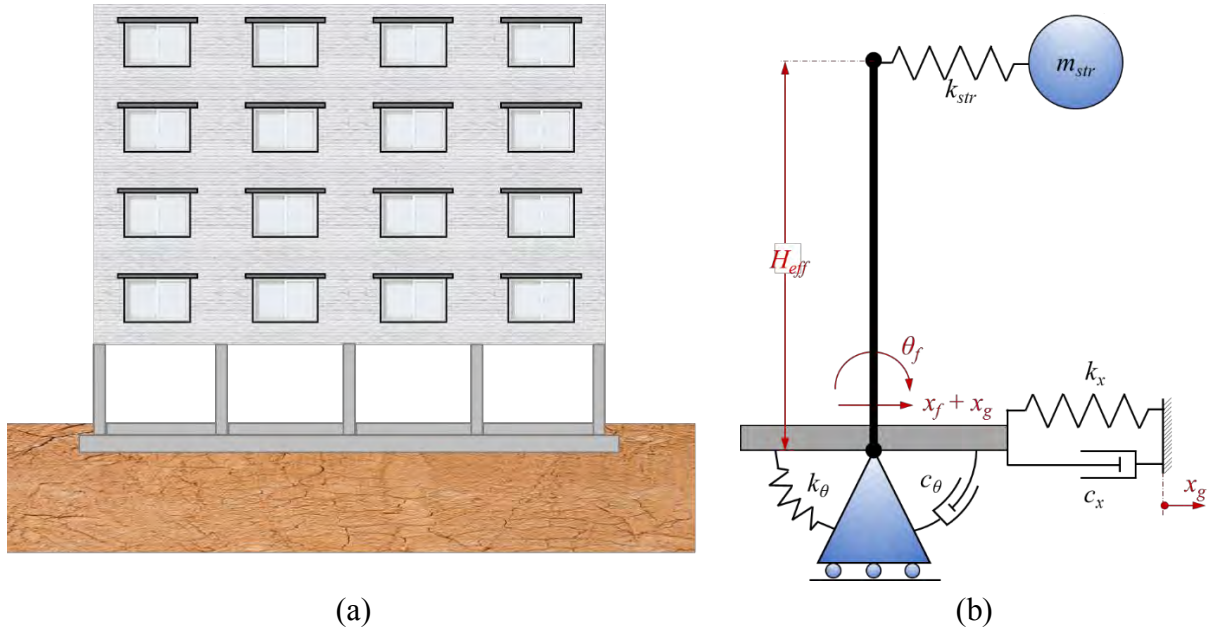


Figure 1. (a) Schematic diagram of a five-storey building, sitting on a shallow foundation in a viscoelastic half-space, and (b) the mass-spring-dashpot model of a soil-shallow foundation-structure system adopted in the equivalent-linear analytical model (Tsang and Pitilakis 2019).

Figure 2(a) shows the reduction of structural displacement demand of GSI system with RSM layer of 2 m thick and 30% rubber by weight. It was concluded that the seismic isolation capability of the GSI system is founded on the reduced lateral stiffness of the RSM layer and the lower modulus of RSM that reduces the rocking stiffness, which leads to the amplification of foundation rotation as shown in Figure 2(b). This might be considered, to a certain degree, as analogous to the traditional seismic isolation with the use of rubber bearings, which is further augmented by rocking foundation isolation. GSI system aims to redistribute seismic demand on the whole SSFS system to a well-controlled low-modulus foundation material, such that the demand on the superstructure can be reduced and the associated damage can be minimised.

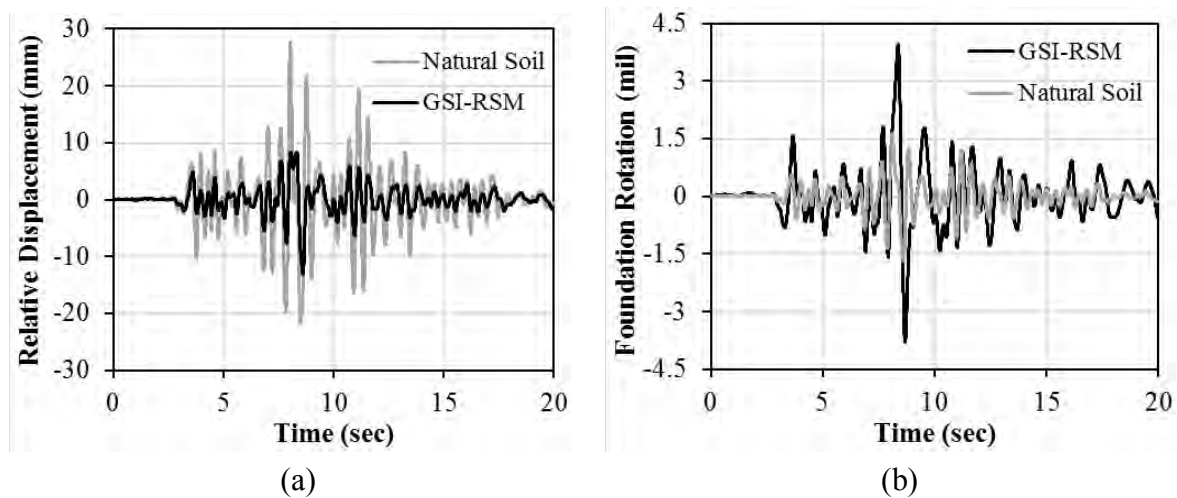


Figure 2. Time histories of (a) the displacement response of the SDOF superstructure relative to the foundation, and (b) the rotation response of the foundation (in unit of milliradian, i.e. mil) under the 1994 Northridge earthquake ground shaking (Tsang and Pitilakis 2019).

GEOTECHNICAL CENTRIFUGE TESTING

Centrifuge modelling with an earthquake shaker under an acceleration field of 50 g was conducted at National Central University in Taiwan (Figure 3) in order to mimic the actual nonlinear dynamic response characteristics of RSM and subsoil in a coupled soil-foundation-structure system (Tsang et al. under review). RSM with 30% and 40% rubber by weight were used in the tests. It was found in previous studies (Sheikh et al. 2013; Mashiri et al. 2015; Disfani et al. 2017) that the skeleton of RSM is formed by both soil and rubber particles when rubber content is between 10–18% and 30–35% by weight. Hence, RSM-30% would behave as a true mixture, whilst RSM-40% is expected to exhibit rubber-like behaviour.

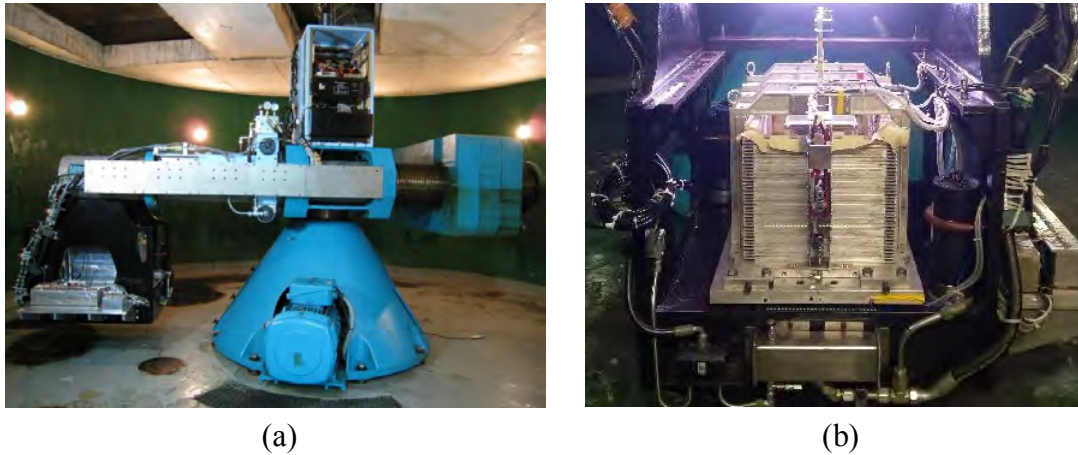


Figure 3. (a) Overview of the geotechnical centrifuge facility at National Central University in Taiwan (Hung and Liao 2020), and (b) the laminar box mounted in the swing basket.

It is evidenced from the test results as shown in Figure 4(a) that the structural demand can be reduced by as much as 40–60%. The increase in both the horizontal and rotation responses of the foundation was also evidenced. The increase in horizontal response of the foundation is analogous to the large shear displacement that is experienced by rubber bearings during an earthquake, whereas the increased yet reversible rotation response of the foundation due to reduced rocking stiffness as observed in Figure 4(b) leads to an augmented rocking mechanism. Importantly, the elasticity of the properly designed RSM layer can avoid soil failure/yielding and minimise the undesirable residual ground deformation due to rotation and sliding.

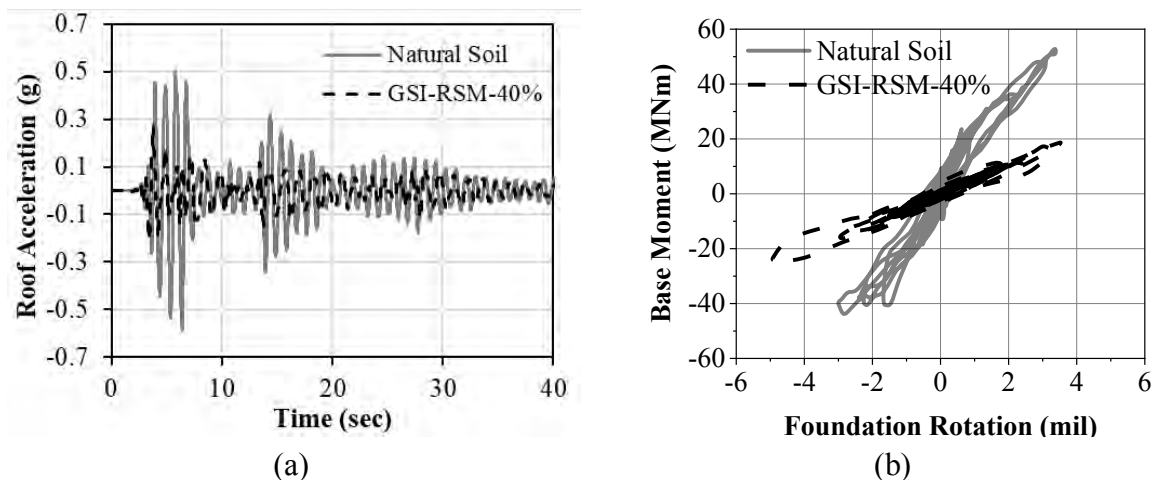


Figure 4. (a) Time histories of the total acceleration response recorded at the roof, and (b) the foundation moment-rotation response under the 1940 El Centro earthquake ground shaking.

SHAKING TABLE TESTING

Electrical transformers were repeatedly damaged in recent earthquakes, causing great loss to power infrastructure (Li et al. 2017, 2018). GSI-RSM system can be a promising candidate for mitigating structural responses caused by both horizontal and vertical ground motions. Shaking table test was carried out by Li et al. (under review) to investigate the performance of GSI-RSM system for protecting electrical transformers on shallow foundation. A prototype 1000 kV electrical transformer is shown in Figure 5(a), whilst the 1:5 scaled transformer model sitting on RSM is shown in Figure 5(b). Steel was used for fabricating the scaled bushings of the transformer model.

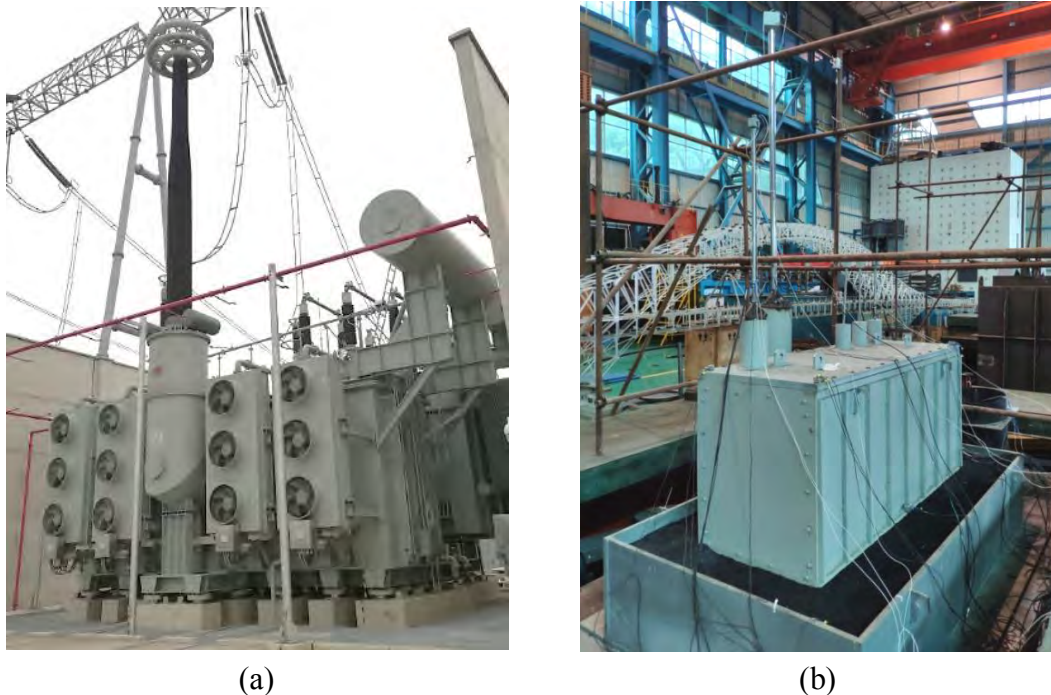


Figure 5. (a) A prototype 1000 kV electrical transformer selected for the case study, and (b) the shaking table test set-up for the isolated case where prototype transformer is placed on RSM with 35% rubber by weight (Li et al. under review) (55% in 1:5 scaled model in order to achieve the target elastic modulus that satisfies Cauchy condition as recommended in Moncarz and Krawinkler 1981 and Meymand 1998).

The bushings on the transformer model had different fundamental frequencies, which provided a chance to investigate the performance of GSI-RSM system on a wide range of natural frequency. It was observed in the shake table test that the reduced horizontal and rotational stiffnesses of the RSM foundation layer are the key attributes to the isolation effectiveness. The results show that the GSI-RSM system could effectively reduce the seismic responses of all three sizes of bushings on the transformer model by an average of 35-40% when it was subjected to either horizontal-only or combined horizontal-and-vertical ground motions. The vertical acceleration response of various components could also be reduced when the transformer model was subjected to the combined horizontal-and-vertical actions. Figure 6(a) shows the reduction of strain response, which is the most important performance indicator for the bushings of the transformer. The Fourier amplitude spectra of the acceleration response of the non-isolated and the GSI-isolated cases are shown in Figure 6(b).

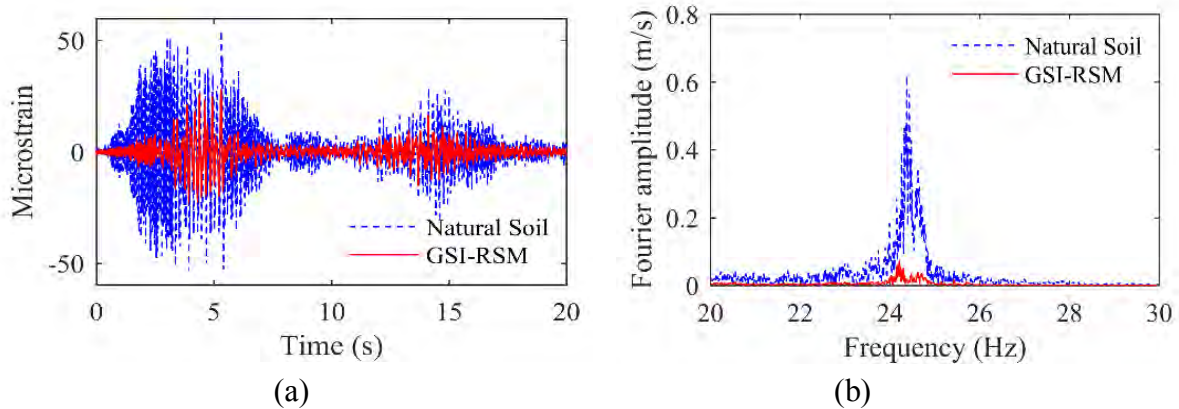


Figure 6. (a) Flexural strain response recorded at the bottom of the low voltage bushing, and (b) the Fourier amplitude spectra of acceleration response at the top of the bushing under the 2008 Wenchuan earthquake ground shaking with PGA of 0.4 g (Li et al. under review).

CONCLUSIONS

Geotechnical seismic isolation (GSI) is an emerging technology for protecting structures from earthquake ground shaking by exploiting the beneficial effects of soil-foundation-structure interaction (SFSI). GSI system aims to redistribute seismic demand on the whole soil-foundation-structure system to a well-controlled low-modulus foundation material, such that the demand on the superstructure can be reduced and the associated damage can be minimised.

A lumped-parameter analytical model has been developed for GSI system, which has taken into account the nonlinearity of subsurface materials in the soil-foundation-structure model. A new theoretical approach for estimating effective shear strain as part of the equivalent-linear method has been proposed whilst detailed derivation can be found in Tsang and Pitilakis (2019). The isolation mechanism of GSI system has been demonstrated and explained through a case study of which some results are presented in the first part of this paper.

The second part of this paper briefly presents a dynamic centrifuge test on the performance of GSI system that is founded on the use of rubber-soil mixtures (RSM) as a well-controlled low-modulus foundation material. An average of 40–60% reduction of structural demand in terms of roof acceleration, inter-storey drift and base moment was achieved. The increased yet reversible horizontal and rotation responses of the foundation were evidenced which also highlights the unique “augmented rocking mechanism”. The observed elasticity of GSI-RSM foundation layer can avoid soil failure/yielding and minimise the undesirable residual ground deformation due to rotation and sliding.

Finally, a shaking table test has been conducted on GSI-RSM system for protecting electrical transformer. An average of 35-40% reduction of bushing responses has been achieved. It has further been confirmed that the reduced stiffness of RSM layer is the key attribute to isolation effectiveness. The performance was comparable when vertical excitation was jointly applied.

GSI is aligned perfectly with the low-damage seismic design strategy, which is increasingly being used to enhance public safety and to build a more resilient society. Further experimental and theoretical investigation is required to improve and optimise the GSI system for different structural typologies and soil conditions.

ACKNOWLEDGEMENTS

The geotechnical centrifuge test was partially supported by the Bushfire and Natural Hazards Cooperative Research Centre [Project A9] of the Australian Government. The shake table test was supported by the National Key R&D Program of China [2018YFC0809400] and Scientific Research Program of State Grid Corporation of China [SGSD0000JJJS1800508]. The assistance provided by the research students in the Centrifuge Modelling Laboratory at National Central University in Taiwan is gratefully appreciated.

REFERENCES

- Anastasiadis A, Senetakis K, Pitilakis K. Small-strain shear modulus and damping ratio of sand-rubber and gravel-rubber mixtures. *Geotech Geol Eng* 2012;30(2):363–382.
- Brunet S, de la Llera JC, Kausel E. Non-linear modeling of seismic isolation systems made of recycled tire-rubber. *Soil Dynamics and Earthquake Engineering* 2016;85:134–145.
- Chiaro G, Palermo A, Granello G, Tasalloti A, Stratford C, Banasiak LJ. (2019). Eco-rubber seismic-isolation foundation systems: a cost-effective way to build resilience. *Proceedings of the 2019 Pacific Conference on Earthquake Engineering*, Auckland, New Zealand, 4-6 April 2019.
- Dhanya JS, Boominathan A, Banerjee S. Response of low-rise building with geotechnical seismic isolation system. *Soil Dynamics and Earthquake Engineering* 2020;136, Article no. 106187.
- Disfani MM, Tsang HH, Arulrajah A, Yaghoubi E. Shear and Compression Characteristics of Recycled Glass-Tire Mixtures. *ASCE Journal of Materials in Civil Engineering* 2017;29(6), Article no. 06017003.
- Forcellini D. Assessment on geotechnical seismic isolation (GSI) on bridge configurations. *Innovative Infrastructure Solutions* 2017;2:9. DOI: 10.1007/s41062-017-0057-8
- Hung WY., Liao TW. (2020) LEAP-UCD-2017 Centrifuge Tests at NCU. In: Kutter B., Manzari M., Zeghal M. (eds) *Model Tests and Numerical Simulations of Liquefaction and Lateral Spreading*. Springer, Cham.
- Kaneko T, Orense RP, Hyodo M, Yoshimoto N. Seismic response characteristics of saturated sand deposits mixed with tire chips. *Journal of Geotechnical and Geoenvironmental Engineering*, ASCE 2013;139(4):633-643.
- Karatzia X, Mylonakis G. Geotechnical isolation of pile-supported bridge piers using EPS geofoam. *Proceedings of the 16th World Conference on Earthquake Engineering*, Santiago, Chile, January 9-13, 2017.
- Li S, Tsang HH, Cheng Y, Lu Z. Effects of sheds and cemented joints on seismic modelling of cylindrical porcelain electrical equipment in substations. *Earthquakes Struct* 2017;12:55–65.
- Li S, Tsang H-H, Cheng Y, Lu Z. Seismic testing and modeling of cylindrical electrical equipment with GFRP composite insulators. *Compos Struct* 2018;194:454–67.
- Li S, Cheng Y, Tsang HH, Lu Z, Liu Z, Pitilakis K. Shaking table test on geotechnical seismic isolation of electrical transformer on shallow foundation. *Soil Dynamics and Earthquake Engineering* (under review).
- Mashiri MS, Vinod JS, Sheikh MN, Tsang HH. Shear Strength and Dilatancy Behaviour of Sand-Tire Chip Mixtures. *Soils and Foundations* 2015;55(3):517-528.
- Meymand P. Shaking Table Scale Model Tests of Nonlinear Soil-Pile-Superstructure Interaction in Soft Clay, Ph.D. Dissertation, University of California, Berkeley. 1998.

- Moncarz P, Krawinkler H. Theory and Application of Experimental Model Analysis in Earthquake Engineering. Rpt. No. 50, John Blume Earthquake Eng. Ctr., Stanford Univ. 1981.
- Nanda RP, Dutta S, Khan HA, Majumder S. Seismic Protection of Buildings by Rubber-Soil Mixture as Foundation Isolation. *International Journal of Geotechnical Earthquake Engineering* 2018;9(1):99-109. DOI: 10.4018/IJGEE.2018010106
- Pitilakis K, Karapetrou S, Tsagdi K. Numerical investigation of the seismic response of RC buildings on soil replaced with rubber–sand mixtures. *Soil Dynamics and Earthquake Engineering* 2015;79:237–252.
- Senetakis K, Anastasiadis A, Pitilakis K (2012) Dynamic properties of dry sand/rubber (SRM) and gravel/rubber (GRM) mixtures in a wide range of shearing strain amplitudes. *Soil Dynamics and Earthquake Engineering* 33:38–53.
- Sheikh MN, Mashiri MS, Vinod JS, Tsang HH. Shear and Compressibility Behaviors of Sand-Tire Crumb Mixtures. *ASCE Journal of Materials in Civil Engineering* 2013;25(10):1366-1374.
- Shimamura A. Study on Earthquake Response Reduction by Improved Composite Geomaterial using Rubber Chips and Fibrous materials (translated from Japanese). PhD Thesis, Osaka University, Japan, 2012. (in Japanese)
- Tsang HH. Seismic isolation by rubber–soil mixtures for developing countries. *Earthquake Engineering and Structural Dynamics* 2008;37(2):283–303.
- Tsang HH. Geotechnical seismic isolation. In: *Earthquake Engineering: New Research*, New York, U.S.: Nova Science Publishers Inc; 2009, p. 55–87.
- Tsang HH. Uses of scrap rubber tires. In: *Rubber: Types, Properties and Uses*, New York, U.S.: Nova Science Publishers Inc; 2012, p. 477-492.
- Tsang HH, Pitilakis K. Mechanism of geotechnical seismic isolation system: Analytical modeling. *Soil Dynamics and Earthquake Engineering* 2019;122:171–184.
- Tsang HH, Lo SH, Xu X, Sheikh MN. Seismic isolation for low-to-medium-rise buildings using granulated rubber–soil mixtures: numerical study. *Earthquake Engineering and Structural Dynamics* 2012;41:2009–2024.
- Tsang HH, Lam JYK, Yaghmaei-Sabegh S, Lo SH. Protecting underground tunnel by rubber–soil mixtures. *Proceedings of the 7th International Conference on Lifeline Earthquake Engineering*, ASCE-TCLEE, Oakland, California, U.S., June 28 – July 1, 2009.
- Tsang HH, Tran DP, Hung WY, Pitilakis K, Gad EF. Performance of Geotechnical Seismic Isolation System using Rubber-Soil Mixtures in Centrifuge Testing. *Earthquake Engineering and Structural Dynamics* (revised manuscript submitted on 10 Oct 2020).
- Tsiavos, A., Alexander, N.A., Diambra, A., Ibraim, E., Vardanega, P.J., Gonzalez-Buelga, A., Sextos, A. A sand-rubber deformable granular layer as a low-cost seismic isolation strategy in developing countries: Experimental investigation. *Soil Dynamics and Earthquake Engineering* 2019;125, Article no. 105731.
- Xiong W, Li Y. Seismic isolation using granulated tire–soil mixtures for less-developed regions: experimental validation. *Earthquake Engineering and Structural Dynamics* 2013;42:2187–2193.

Response of Mortar-Free Interlocking Brick Wall under Seismic Excitation

Guanyu Xie¹, Xihong Zhang², Hong Hao³ and Joyis Thomas⁴

1. PhD candidate, Centre for Infrastructural Monitoring and Protection, School of Civil and Mechanical Engineering, Curtin University, Bentley, WA 6102, Australia.
Email: guanyu.xie@postgrad.curtin.edu.au
2. Senior Research Fellow, Centre for Infrastructural Monitoring and Protection, School of Civil and Mechanical Engineering, Curtin University, Bentley, WA 6102, Australia.
Email: xihong.zhang@curtin.edu.au
3. Professor, Centre for Infrastructural Monitoring and Protection, School of Civil and Mechanical Engineering, Curtin University, Bentley, WA 6102, Australia.
Email: hong.hao@curtin.edu.au
4. Managing director, Tetraloc Pty Ltd, Bellevue, WA 6056, Australia.
Email: joyis.thomas@tetraloc.com

Abstract

Mortar-free construction using interlocking bricks for masonry structure is an attractive technology which offers many advantages such as improved construction efficiency. In this paper both laboratory and numerical studies were carried out to investigate the seismic responses of interlocking brick walls. Laboratory shaking table tests were performed on an interlocking brick wall constructed using the mortar-free method. The responses and damage/failure mode of the interlocking brick wall under the in-plane seismic loading were studied. A detailed numerical model was then built and validated with the laboratory test results and used to analyse the seismic performance of the interlocking brick wall. Comparison was made with a conventional masonry wall bonded with mortar. It is found that comparing with the conventional mortar bonded masonry wall, the interlocking brick wall exhibits rocking damage instead of diagonal shear cracking usually found in masonry wall. Larger lateral drift is also observed on the interlocking brick wall under the same loading condition than that on the conventional masonry wall. The results demonstrate the good seismic performance of the mortar-free masonry wall made of interlocking bricks.

Keywords: seismic response, interlocking brick, masonry structure, mortar-free

1. INTRODUCTION

Masonry structures are widely constructed all over the world because of their low cost. Due to its low ductility, high specific weight, and weak connection between bricks, masonry structures normally have low seismic resistance (Tomažević 1999, Lourenço et al. 2013). Many studies have therefore been carried out by researchers and engineers to improve the performance of masonry structures, among which interlocking brick is one category of the developments.

Being different from conventional bricks, interlocking bricks are bonded together through tenons and mortises where mortar-free construction method is commonly employed. It leads to two distinct advantages of interlocking bricks that require none skilful brick layer for construction and offer high construction efficiency compared to conventional masonry (Ramamurthy and Kunhanandan Nambiar 2004, Wang et al. 2017, Al-Fakih et al. 2018), as the interlocking bricks can be simply stacked on one another being self-aligned without worrying about flatness or waiting for the mortar to solidify.

Despite many studies on the seismic responses of conventional brick walls, the current understandings cannot be simply applied to mortar-free interlocking brick walls because of the differences in the connection between adjacent bricks. For example, for conventional masonry walls shear cracking usually occurs at mortar joints, while in interlocking brick system, shear force is transferred through the interlocking tenons and mortises. As reported by Qu et al. (2015) who investigated the dynamic response of interlocking brick wall with two shallow truncated cones, damage to the tenons was widely observed indicating the influence of the interlocking mechanism. Further, for an interlocking brick wall, gap opening and closure between adjacent bricks could be the predominant response mode; and rocking and sliding between interlocking bricks would also occur. Elvin and Uzoegbo (2011) carried out shaking table tests on a full-scale dry-stack masonry structure and observed significant gap opening during the test. Ali et al. (2013) also conducted shaking table tests on two interlocking brick piers observing uplifts of blocks during the test. Research on interlocking brick structures are still limited, and systematic studies on the seismic performance of interlocking brick structures are needed before its wide and reliable applications.

This study examines the seismic behaviour of interlocking brick walls. Shaking table tests and numerical simulations were conducted, and comparison was made between the interlocking brick wall and a conventional masonry wall on their damage and failure modes, energy dissipation mechanisms, and drift ratios.

2. TEST SETUP AND NUMERICAL MODELLING

2.1 BRICK DETAILS AND TEST SETUP

Figure 1 shows the dimension of the interlocking bricks used in this study, which was a half-scale of the prototype brick. The mortar used to make the bricks had a compressive strength of 7.5MPa, which also followed the physical modelling law.

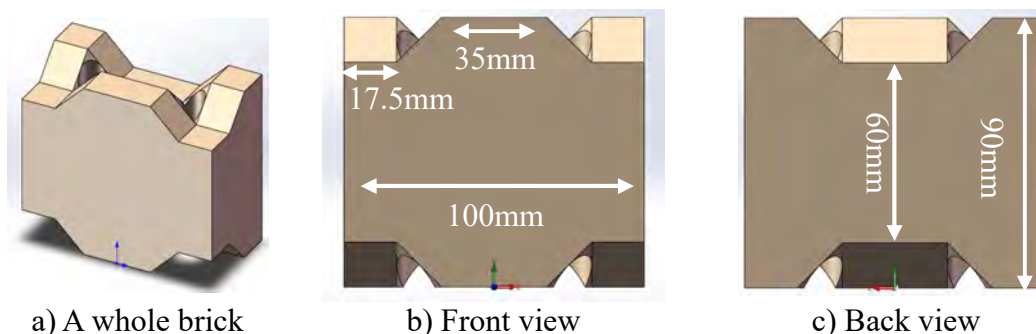


Figure 1 Illustration of the interlocking brick with dimensions

The scaled wall model was 825mm height and 800mm wide, with a concrete slab weighting 375kg connected to the top of the wall through a steel adapter, leading to an axial compression ratio of 3.2%. Also, 4 rebars with a diameter of 6mm were inserted into the wall through vertical holes in the brick at equal spacing, after which fast-set grout was applied to fill in these holes. To record the in-plane dynamic response of the interlocking brick wall, four accelerometers and two LVDTs (Linear variable differential transducers) were installed on the wall for acceleration and displacement measurements. The four accelerometers were installed on the top added mass, the top, middle and the bottom of the wall. The LVDTs were installed at the top and bottom parts of the wall. A synthetic ground acceleration time history complying with AS1170.4 (2007) was generated and used as the seismic input in this test. The seismic inputs with a PGA of 0.05g were applied at first, which gradually increased until the wall experienced substantial damages and lost its load bearing capacity at PGA of 0.6g.

2.2 NUMERICAL MODEL

Abaqus was used to build the finite element model of the interlocking brick wall. Concrete damaged plasticity model (CDP) was adopted for the brick material. For rebars, an elastic-plastic material model was used with a yield stress of 500MPa and Young's modulus of 200GPa. The concrete in the footing, top mass, etc., is modelled using an elastic material model because no damage was observed to these components in the tests. Automatic surface contact algorithm was used for the brick contact modelling with a friction coefficient of 0.5. For loading sequence, gravity was firstly applied to each part of the model, after which the ground acceleration time history was applied to the model. Explicit analysis was conducted.

3. EXPERIMENTAL AND NUMERICAL RESULTS

In the laboratory test, as the input ground excitation gradually increased, the wall did not show any visible damage when the input PGA was lower than 0.3g. Cracks began to initiate in bricks under excitations with PGA=0.3g, which gradually extended and widened under subsequent excitation with higher PGAs. Under 0.6g ground excitation, the interlocking brick wall displayed significant rocking response after which the load bearing capacity appeared to be significantly degraded and the test was therefore stopped.

3.1 DISPLACEMENT TIME HISTORIES

The displacement time histories recorded at the top of the wall under 0.2g, 0.3g, 0.4g and 0.5g excitation are shown and compared with those simulated by the numerical model in Figure 2. Overall, the numerically modelled displacement time histories agree well with those measured from the laboratory tests.

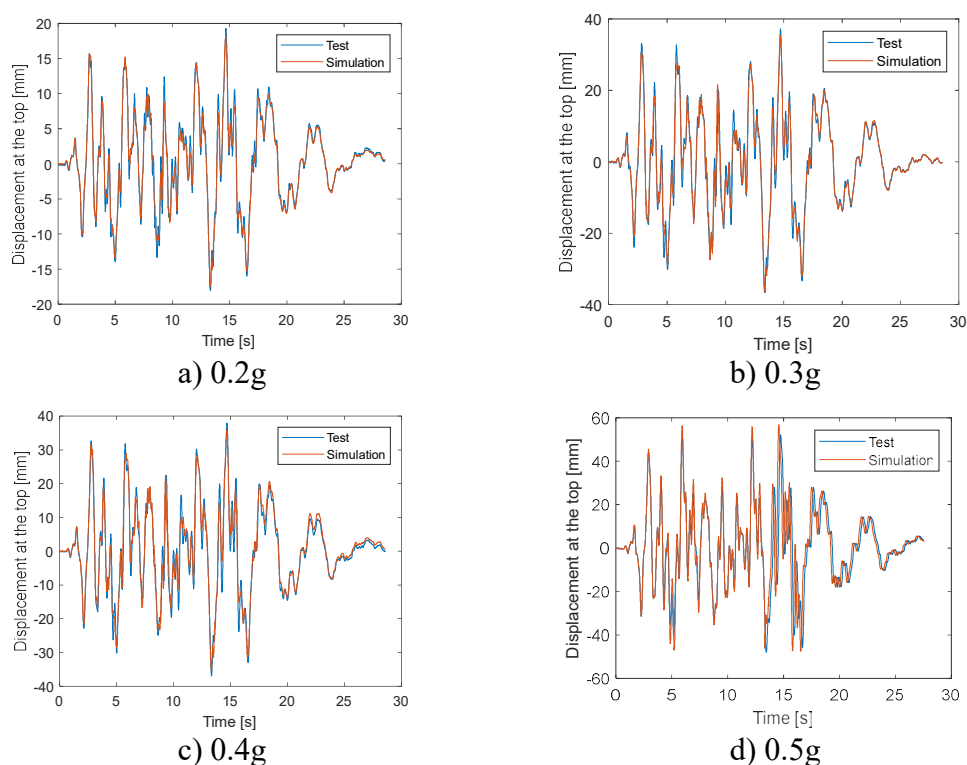


Figure 2 Comparisons between the laboratory measured and numerically modelled wall top displacement time histories

3.2 RESPONSE MODE

Under 0.6g seismic excitation, severe and repetitious rocking were observed on the interlocking brick wall, as seen in Figure 3 a). It is evident that the two bottom corners of the interlocking wall both experienced severe damages with the stacked bricks falling off. As highlighted in Figure 3 b), bricks in the middle and upper sections of the wall also experienced some damages. Similar rocking response mode and brick damages were simulated by the numerical model, which demonstrated the numerical model could reasonably predict the responses of the mortar-free interlocking brick wall subjected to seismic loading.

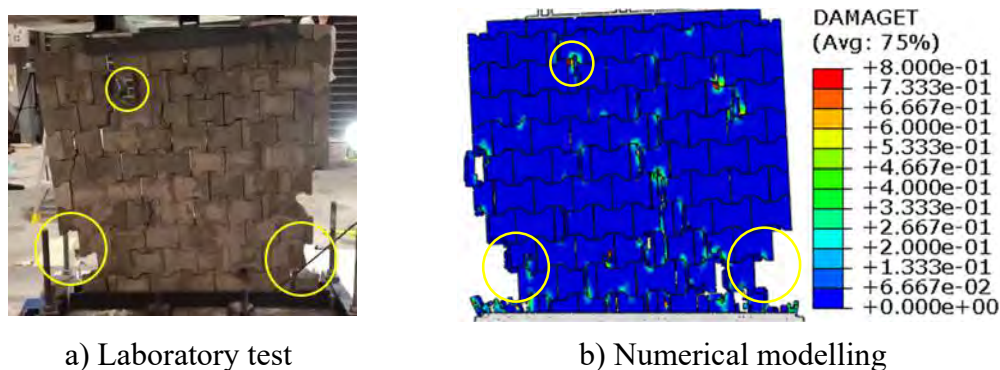


Figure 3 Damage mode of the wall under 0.6g ground excitation

4. COMPARISON WITH CONVENTIONAL MASONRY WALL

To better understand and evaluate the behaviour and damage/failure mode of the interlocking brick wall as compared to the conventional masonry wall subjected to

seismic load, a finite element model of a conventional masonry wall of the same dimension as the above tested interlocking brick wall made of concrete masonry units (CMU) and bonded by mortar of the same material strength was generated and loaded with the same seismic excitation. The conventional CMU wall model was developed with reference to Turek et al.'s work (Turek 2002, Turek et al. 2007). Comparisons are made with respect to wall damage mode, energy dissipation, and drift ratio.

4.1 DAMAGE AND FAILURE MODE

As shown in Figure 4, under 0.6g ground excitation the interlocking brick wall displayed a significant rocking response but managed to survive the applied seismic load, while the conventional CMU wall collapsed at an early stage under the same level of ground excitation. Figure 4 shows the different damage and failure modes of the interlocking brick wall and the conventional CMU wall under the 0.6g ground excitation. Typical diagonal shear failure with X-shaped cracks can be observed for the conventional CMU wall. In comparison, a completely different rocking damage mode was observed for the interlocking brick wall. The damages mainly concentrated on the two corners where bricks collided with each other in the process of repetitive uplifting and falling, while only limited brick damages in the upper part of the wall were developed.

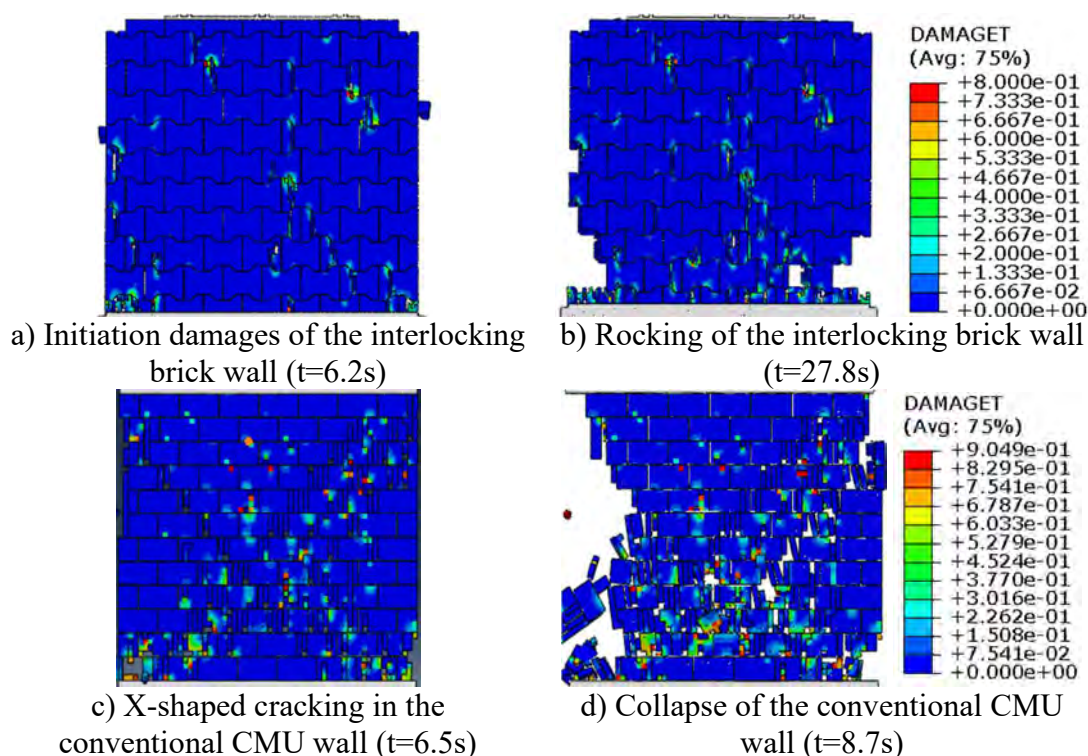


Figure 4 Different damage and failure modes of the interlocking brick wall and the conventional CMU wall

As compared to the conventional CMU wall, the different damage mode observed in the interlocking brick wall could be attributed to the following reasons: 1) because of the tenon and mortise in each block, the interlocking brick wall has higher shear strength in comparison to the conventional CMU wall that is bonded by mortar between each block. The higher shear resistance of the interlocking brick wall mitigates the commonly observed shear damage in the conventional masonry wall under earthquake excitations. 2) the mortar-free construction method for the interlocking brick wall leads to low tensile strength for the interlocking brick assembly. When the tensile stress

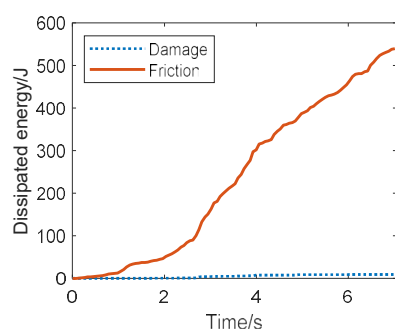
induced by rocking response at the two corners of the wall overcomes the axial compressive stress from self-weight and added mass in the brick, uplifting and detachment of the corner bricks are resulted. In comparison, because of the lower shear resistance in the conventional CMU wall, shear failure is developed with the formation of X-shaped cracking across the wall, which subsequently caused the wall to collapse. 3) relative movement and friction between mortarless interface of the adjacent bricks dissipate seismic energy and hence mitigate the damage to the wall. The above comparison also demonstrates that the interlocking wall is prone to rocking when subjected to seismic excitation. To enhance the seismic capacity of the interlocking wall, a larger prestressing force or larger reinforcing bar is needed to minimize rocking damage of the wall.

4.2 ENERGY DISSIPATION MECHANISM

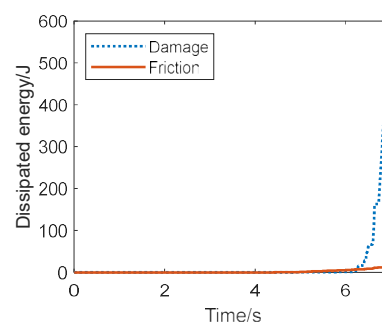
Additionally, with the dry-stacking construction method, no mortar is used to bond the interlocking bricks. Small gap opening could develop and widen while the wall is subjected to seismic loading. It therefore results in friction between adjacent interlocking brick surfaces, leading to a relatively large energy dissipation. As for the conventional masonry wall, the CMU blocks are bonded by the brittle mortar, in which relative movements between blocks will lead to the damage and eventually collapse of the wall.

To prove the assumption above, the energy dissipation time histories of the interlocking brick wall and the conventional CMU wall under the aforementioned 0.6g ground excitation were obtained from the numerical simulations, which include the energies dissipated by inter-brick friction and plastic strain energy reflecting brick and mortar plasticity and damage. It is to note that only first 7 seconds are displayed as the CMU wall began to collapse at 7-second under the excitation of the 0.6g seismic motion.

From Figure 5, a distinct difference in the energy dissipation mechanisms for the walls can be found. For the interlocking brick wall, friction was the predominant energy dissipation mechanism, which gradually increased as the imposed seismic energy to the wall increased. It indicates that friction between the dry-stacking interlocking bricks contributes largely to the dissipation of earthquake energy, while those consumed by brick damage and material plasticity are much smaller. In contrast, for the conventional CMU wall, during the initial 6.3s the values of dissipated energy was low, followed by a sudden increase of energy dissipated due to material plasticity and damage afterwards, which came from the decohesion of mortar layers between the CMU blocks and block/mortar damages. Hence, compared to the interlocking brick wall the failure of the conventional wall was brittle. The above comparison of energy dissipation shows that the interlocking brick wall has a better energy dissipation capacity as compared to the conventional masonry wall with the same dimension and material properties due to their different energy dissipation mechanisms, which also explains the relatively low brick damages observed in the upper part of the interlocking brick wall.



a) The interlocking brick wall



b) The conventional CMU wall

Figure 5 Comparison of energy dissipations by different mechanisms

4.3 DRIFT RATIOS

Table 1 tabulates the maximum drift ratios of the interlocking brick wall and the conventional CMU wall under different levels of ground excitations. It is noted that the drift ratios under the 0.1g and 0.6g excitations are not included, as neither walls experienced any damages under 0.1g, and the interlocking brick wall rocked significantly while the conventional CMU wall collapsed under 0.6g ground excitation. From the table, it can be seen that under the same level of seismic loading, the peak drift ratios of the interlocking brick wall are always larger than those of the conventional CMU wall. This is because the pre-existing gaps between the interlocking bricks as well as the inter-brick sliding under the ground excitation greatly enhance the deformation capacity of the interlocking masonry wall. It also indicates that comparing with the conventional mortar bonded CMU wall, the interlocking brick wall could tolerate much higher drift ratio under the same seismic loading conditions. Therefore, current design criteria for earthquake design of masonry structures may not be applicable to interlocking brick structures.

Table 1 Maximum drift ratios under different levels of seismic loading

PGA	The interlocking brick wall	The conventional CMU wall
0.2g	0.69%	0.11%
0.3g	1.64%	0.19%
0.4g	1.62%	0.36%
0.5g	3.40%	0.63%

5. CONCLUSIONS

This paper carried out laboratory shaking table tests and numerical simulations to investigate the behaviour of a mortar-free interlocking brick wall under seismic excitation. Through comparison with a conventional CMU wall, it was found that the interlocking brick wall has much larger deformation capacity than the conventional masonry wall under the same seismic excitation as a result of the inter-brick gap opening and closure and inter-brick sliding. Subsequently, compared with the conventional mortar-bonded masonry wall which failed with diagonal shear cracking, the mortar-free interlocking brick wall exhibited a rocking damage mode under strong seismic excitation. More energy was dissipated by inter-brick friction in the interlocking brick wall as compared to the conventional masonry wall. Further improvement such as adopting a larger prestressing force or larger reinforcing bar could be introduced for interlocking brick wall against earthquake load to prevent rocking damage of the wall.

6. ACKNOWLEDGEMENT

The authors would like to acknowledge the financial support from Australian Research Council and Tetraloc Pty Ltd under ARC Linkage project LP170100846 for carrying out this research.

REFERENCES

- Al-Fakih, A., Mohammed, B.S., Nuruddin, F., Nikbakht, E. (2018) Development of interlocking masonry bricks and its structural behaviour: a review paper. IOP Conf. Ser.: Earth Environ. Sci., Vol 140, pp 1–9.
- Ali, M., Briet, R., Chouw, N. (2013) Dynamic response of mortar-free interlocking structures. *Construction and Building Materials*, Vol 42, pp 168–189.
- Australian Standards, AS 1170.4 (2007), Structural design actions, Part 4: Earthquake actions in Australia.
- Elvin, A., Uzoegbo, H.C. (2011) Response of a full-scale dry-stack masonry structure subject to experimentally applied earthquake loading. *Journal of the South African Institution of Civil Engineering*, Vol 53, No1, pp 22–32.
- Lourenço, P.B., Avila, L., Vasconcelos, G., Alves, J.P.P., Mendes, N., Costa, A.C. (2013) Experimental investigation on the seismic performance of masonry buildings using shaking table testing. *Bull Earthquake Eng*, Vol 11, No 4, pp 1157–1190.
- Qu, B., Stirling, B.J., Jansen, D.C., Bland, D.W., Laursen, P.T. (2015) Testing of flexure-dominated interlocking compressed earth block walls. *Construction and Building Materials*, Vol 83, pp 34–43.
- Ramamurthy, K., Kunhanandan Nambiar, E.K. (2004) Accelerated masonry construction review and future prospects. *Prog. Struct. Engng Mater.*, Vol 6, No 1, pp 1–9.
- Tomaževič, M. (1999) Earthquake-resistant design of masonry buildings. Series in innovations in structures and construction, Vol 1. Imperial College Press, London.
- Turek, M., Ventura, C.E., Kuan, S. (2007) In-plane shake-table testing of GFRP-strengthened concrete masonry walls. *Earthquake Spectra*. Vol 23, No 1, pp 223–237.
- Wang, G., Li, Y., Zheng, N., Ingham, J.M. (2017) Testing and modelling the in-plane seismic response of clay brick masonry walls with boundary columns made of precast concrete interlocking blocks. *Engineering Structures*, Vol 131, pp 513–529.

Evaluation of torsional effects on reinforced concrete buildings due to the excitation of an earthquake

B. Xing^{1,5}, E. Lumantarna^{2,5}, Nelson T. K. Lam^{3,5} and Scott Menegon^{4,5}

1. Corresponding Author. PhD candidate, Department of Infrastructural Engineering, The University of Melbourne, Parkville, VIC 3010, Australia.
Email: bxxi@student.unimelb.edu.au
2. Lecturer, Department of Infrastructure Engineering, The University of Melbourne, Parkville, VIC 3010, Australia.
Email: elu@unimelb.edu.au
- +
3. Professor and Reader, Department of Infrastructural Engineering, The University of Melbourne, Parkville, VIC 3010, Australia.
Email: ntkl@unimelb.edu.au
4. Research Fellow, Centre for Sustainable Infrastructure, Swinburne University of Technology, Melbourne, Australia.
Email: smenegon@swin.edu.au
5. Bushfire and Natural Hazard Cooperative Research Centre, Melbourne, Australia

ABSTRACT

Most reinforced concrete (RC) buildings in Australia feature plan or vertical irregularities, which may be caused by core or shear walls that are eccentrically located, structural setback, and requirements of architectural design. Torsional effects caused by the plan irregularities could amplify the structural response under the excitation of an earthquake. The paper introduces an approach to identify the elastic radius ratio (b_r), which indicate the torsional rigidity of the buildings, and predict the displacement demand induced by an earthquake. A three-tiered approach is created based on the assumption of a single storey building model idealisation and adopted for multi-storey buildings to evaluate their torsional effects. It is expected that the methodology will significantly reduce the computational cost of seismic assessments and provide a significant contribution to the seismic resistance design of RC buildings.

Keywords: reinforced concrete building, asymmetrical buildings; torsional effect; three-tiered approach

1. INTRODUCTION

The torsional effect on reinforced concrete buildings due to the excitation of an earthquake is still an open area of research, although it has been extensively investigated in the past decades (Anagnostopoulos et al., 2015). The common practice to design RC buildings is to provide a concrete core or shear wall system, moment frame, coupled shear wall system, or a combination of any two or more of the above lateral load resisting systems to resist lateral loads (Manohar & Madhekar, 2015). The core walls (and shear walls) are commonly asymmetrically designed within the buildings to satisfy the aesthetics requirements of architecture. The structural design and assessment of asymmetric structures are more complex as the torsional effects on the irregular structural plans will create additional displacements on the structural elements located at the edges of the RC structures (Anagnostopoulos et al., 2015; Xing et al., 2019).

There are many approaches, such as equivalent static analysis, spectral analysis and time-history analysis, to determine torsional response of buildings in an earthquake. Many standard codes of practice (such as NZS1170.5 (2004), BSI (2004), IBC (2012), MOC (2008), and ASCE/SEI(7-10) (2010)) requires a three-dimensional dynamic analysis of the buildings. The assessment of the torsional response behaviour of structures are complicated and time-consuming (Anagnostopoulos et al., 2015).

Despite extensive studies such as Bosco et al. (2015), Lam et al. (1997), Lee and Hwang (2015), Humar and Kumar (1998), Birzhandi and Halabian (2014), Beka Hailu and Jong Seh (2019), Mehana et al. (2019), Tso (1990), Anastassiadis et al. (1998) and Tabatabaei and Saffari (2011) on the torsional behaviour, there is no systematic methodology to evaluate the torsional effects of seismic evaluation that can be easily applied to quickly assess RC buildings' torsional effects. A simple and accurate method referred to as Generalised Force Method (GFM) has been developed to evaluate torsional effects of multi-storey buildings (Lam et al., 2016; Lumantarna et al., 2018). The method also introduces a procedure that can be applied to evaluate the torsional rigidity of buildings through the value of b_r (referred as elastic radius ratio) (Lam et al., 1997; Lumantarna et al., 2018). A building with b_r value larger than one is deemed to have sufficient torsional rigidity and will have the edge displacement that is less sensitive to the change in the eccentricity of the building (Lumantarna et al., 2018; Lumantarna et al., 2019; Mehana et al., 2019; Xing et al., 2019). The building's damages are mainly translational rather than the torsion (Mehana et al., 2019). Parametric studies conducted by the authors showed that RC buildings with the value of b_r less than one would result in an erratic behavioural trend and should be discouraged in practice (Lam et al., 2016; Lumantarna et al., 2019; Xing et al., 2019).

The study presented in this paper extends the previous studies of Xing et al. (2019), Lumantarna et al. (2019), and Lumantarna et al. (2018). It addresses three critical issues regarding the torsional effects of RC building: (i) the use of design charts to estimate the edge displacement ratio, (ii) a three-tiered approach to evaluate torsional effects and predict maximum deflection; and (iii) validation of a three-tiered approach to estimate the peak edge displacement ratios by comparison with results of dynamic analysis of multi-storey buildings. The study presented in this paper is based on rectangular buildings. However, the method proposed is applicable to buildings with non-rectangular plans. Future studies involve testing the proposed method on non-rectangular buildings.

2. EDGE DISPLACEMENT RATIOS OF ASYMMETRICAL BUILDINGS

Expressions (1) – (7) providing estimates of the maximum displacement demand of asymmetrical buildings have been previously developed by Lumantarna et al. (2018)

based on a single-storey building idealisation (Fig. 1). The building model shown in Figure 1 is classified as a uni-axial asymmetric building model and has two degrees of freedoms (2DOFs, $n=2$): translation in the direction of motion y and rotation θ . Parametric studies conducted by Lumantarna et al. (2018) have found that buildings with uni-axial asymmetry can provide conservative estimates of displacement demands of structures with bi-axial asymmetry.

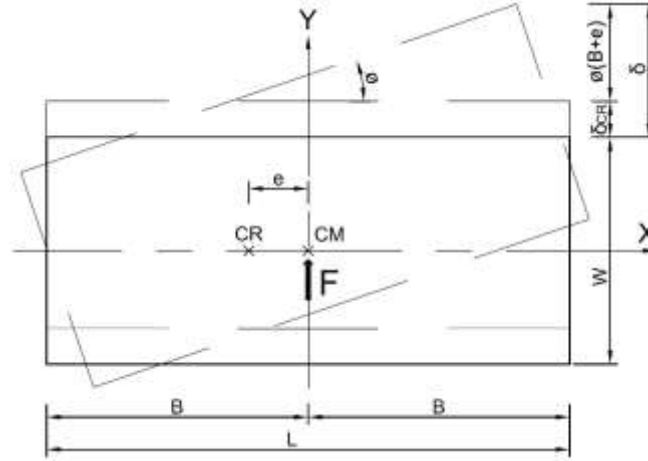


Figure 1 Uni-axial asymmetry single-storey building model

θ_j is the rotational component of the eigenvector solutions to the dynamic equations of equilibrium uni-axial asymmetric buildings defined by equation (1).

$$\theta_j = \frac{\lambda_j^2 - 1}{e_r} \quad (1)$$

where, λ_j^2 is the solution of the eigenvalue. For a building with uni-axial asymmetry, the eigenvalue solutions are given by equation (2).

$$\lambda_j^2 = \frac{1 + (b_r^2 + e_r^2)}{2} \pm \sqrt{\left[\frac{1 - (b_r^2 + e_r^2)}{2} \right]^2 + e_r^2} \quad (2)$$

The maximum displacement demand at the edge of the building normalised with respect to 2D displacement (δ/δ_0) can be defined by the following equations of (3)-(5):

$$\frac{\delta}{\delta_0} = \frac{x_{\pm B}(\max)}{RSD(T, \xi)} = \sqrt{\sum_{j=1}^2 \left[\frac{1 + \theta_j(\pm B_r)}{1 + \theta_j^2} \times \frac{1}{\lambda_j^2} \right]^2} \quad (3)$$

for the acceleration-controlled condition (Fig. 2).

$$\frac{\delta}{\delta_0} = \frac{x_{\pm B}(\max)}{RSD(T, \xi)} = \sqrt{\sum_{j=1}^2 \left[\frac{1 + \theta_j(\pm B_r)}{1 + \theta_j^2} \times \frac{1}{\lambda_j} \right]^2} \quad (4)$$

for the velocity-controlled condition (Fig. 2).

$$\frac{\delta}{\delta_0} = \frac{x_{\pm B}(\max)}{RSD(T, \xi)} = \sqrt{\sum_{j=1}^2 \left[\frac{1 + \theta_j(\pm B_r)}{1 + \theta_j^2} \right]^2} \quad (5)$$

for the displacement-controlled condition (Fig. 2).

The torsional stiffness parameters of the structure can be defined by the following equations of (6) - (7).

$$b_r = \frac{b}{r} = \frac{\sqrt{\frac{K_\theta}{K_y}}}{r} \quad (6)$$

$$r = \sqrt{\frac{J}{M}} = \sqrt{\frac{L^2 + W^2}{12}} \quad (7)$$

where, M is the building's mass, J is the torsional moment of inertia, L is the building's width in the direction perpendicular to the direction of earthquake excitation, W is the building's depth in the direction parallel to the direction of earthquake excitation, r is the mass radius of gyration, K_θ is torsional stiffness of the building, K_y is translational stiffness of the structure, b_r is the elastic radius ratio, e is the eccentricity perpendicular to the direction of motion, e_r is e normalised with respect to r and B_r is the distance from the CM to the edge of the building, normalised with respect to r .

Equations (3) - (5) were used to construct the charts of edge displacement ratio in Figures 3 to 6. The edge displacement ratios were computed for a range of building parameters e_r and b_r representative of the eccentricity and torsional rigidity of multi-storey buildings (Lumantarna et al., 2018).

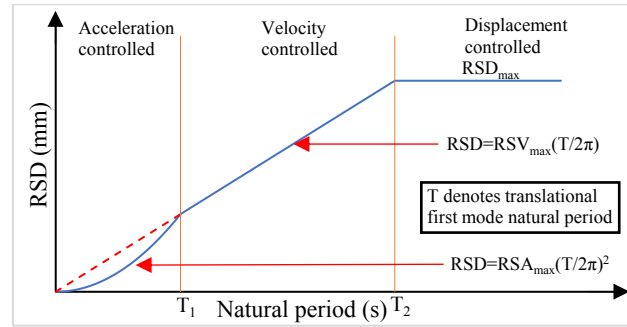
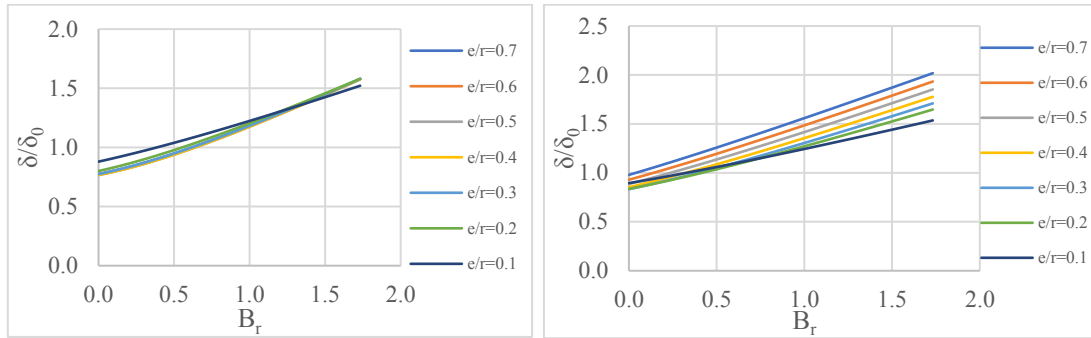
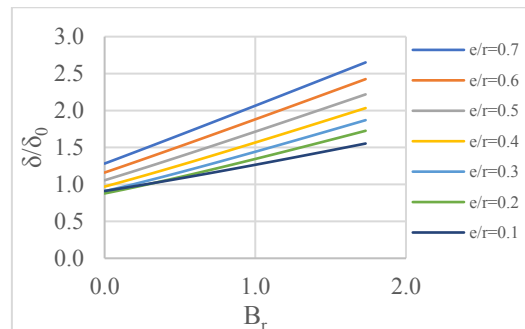


Figure 2 Displacement response spectrum featuring acceleration-, velocity-, and displacement-controlled region



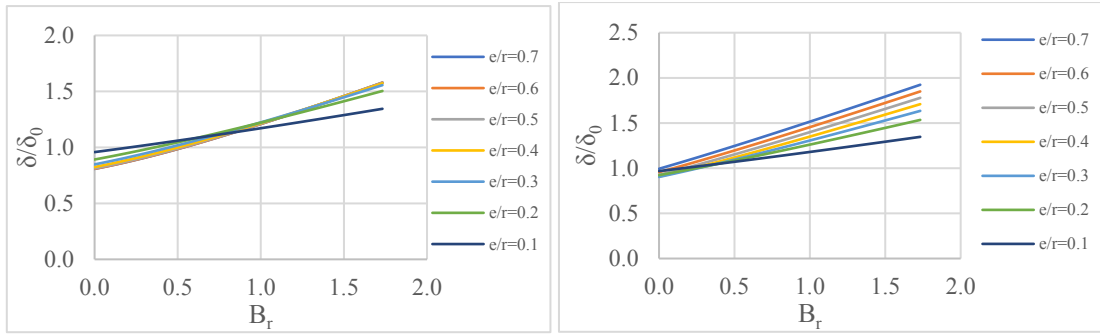
(a) Displacement-controlled ($b_r=1.1$)

(b) Velocity-controlled ($b_r=1.1$)



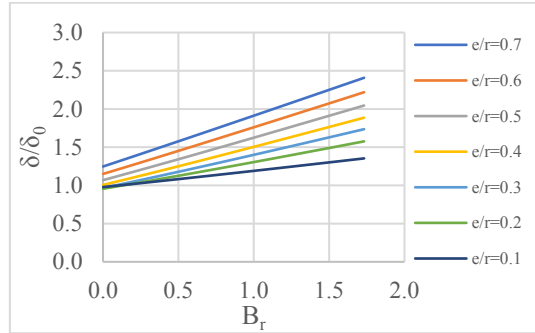
(c) Acceleration-controlled ($b_r=1.1$)

Figure 3 Displacement amplification factors for $b_r = 1.1$



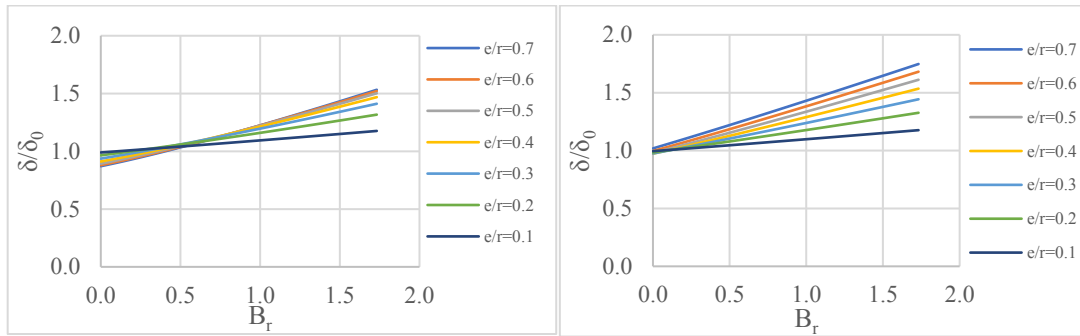
(a) Displacement-controlled ($b_r=1.2$)

(b) Velocity-controlled ($b_r=1.2$)



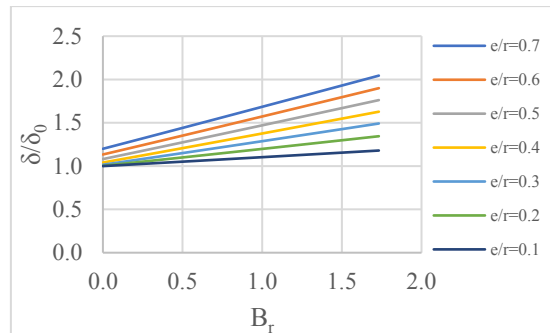
(c) Acceleration-controlled ($b_r=1.2$)

Figure 4 Displacement amplification factors for $b_r = 1.2$



(a) Displacement-controlled ($b_r=1.4$)

(b) Velocity-controlled ($b_r=1.4$)



(c) Acceleration-controlled ($b_r=1.4$)

Figure 5 Displacement amplification factors for $b_r = 1.4$

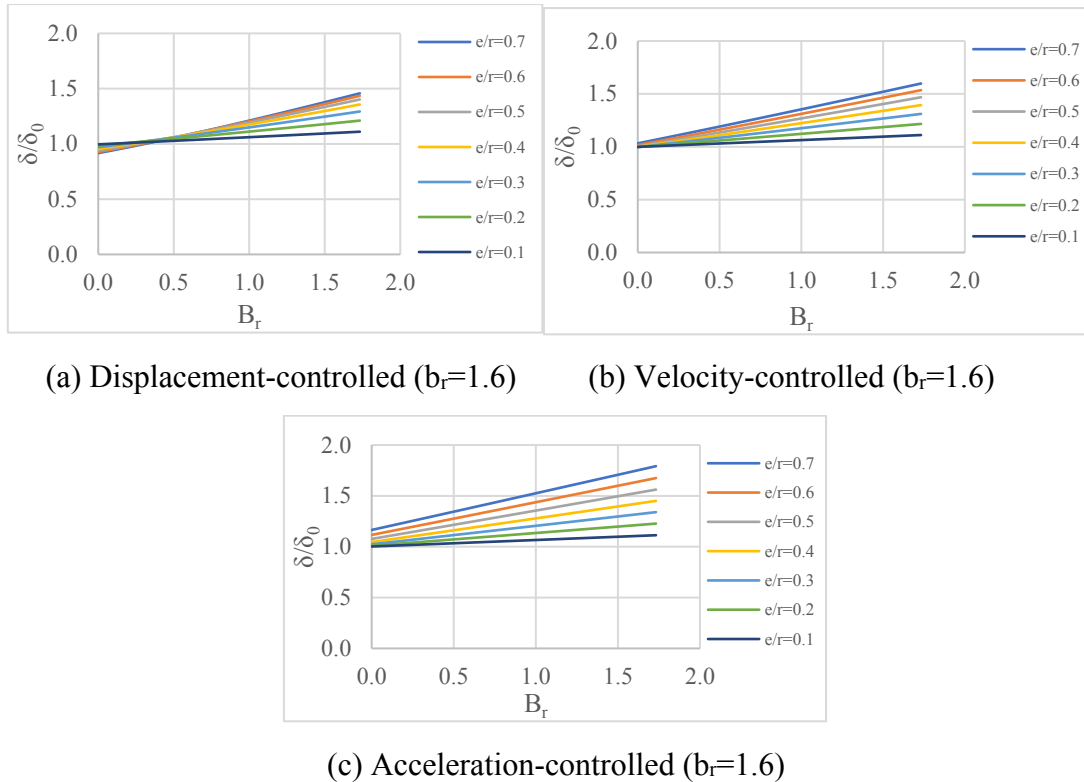


Figure 6 Displacement amplification factors for $b_r = 1.6$

3. THREE-TIERED APPROACH TO PREDICT MAXIMUM DISPLACEMENT

A three-tiered approach is presented in this section to estimate the maximum displacement of asymmetrical buildings in an earthquake. The three-tiered approach was developed to satisfy the requirement of the different design stages. Tier 1 allows the torsional effect can be estimated conservatively without very detailed structural information. A more accurate prediction can be obtained using Tiers 2 and 3 when more structural information are available.

3.1 TIER ONE

Tiered one is subdivided into two tiers. Tiered 1.1 can be used to identify if the b_r value of a building is larger than 1.0 without the need to do any calculation. It is based on a few criteria, including mass-radius gyration, core wall numbers, and the separation distance between core wall systems. When $b_r > 1.0$ cannot be established using tier 1.1, tier 1.2 can be used, which involves applying static loading on the multi-storey building.

If the building has a b_r value greater than 1.0, the peak edge displacement ratios provided by Equations (12) – (17) can be used to provide conservative estimates of the maximum displacement demand of the building. Tier 1 can be used without the knowledge of eccentricity (hence the location of the building's CM), which can be difficult to determine in multi-storey buildings.

3.1.1 Tier 1.1 - proposed method to quickly identify if the value of b_r is larger than 1.0

The b_r value can be evaluated through the structural floor plan and the location of cores or shear walls. The example case studies shown in Figure 7 illustrate how buildings' b_r value can be assessed. The b_r value of a building is considered to be greater than 1.0 if the following conditions are met:

- For three core wall systems

A separation distance between the external two core wall systems should be approximately equal to the building width, which is shown in Figure 7 (a). If two core of the three core wall systems are located close to each other (as illustrated in Figure 7(b), the three core systems can be classified into two core systems. Buildings with the separation distance between the two external core walls more than $2r$ can be deemed to have the value of b_r is more than one for the building in Figure 7 (b).

- Two core wall systems

The minimum separation distance between the two core wall systems must be larger than $2r$ (where r is mass-radius gyration). The typical example of a two core wall system building is shown in Figure 7 (c). The value of b_r for the building is identified to be more than one because the separation distance between the two core walls is more than $2r$.

- One core wall system or closely spaced two core wall systems

Parametric studies conducted by the authors show that the building with only one core wall system or closely spaced two core wall systems will have the value of b_r that is less than one (Xing et al., 2019). The example building with one core wall system is shown in Figure 7 (d).

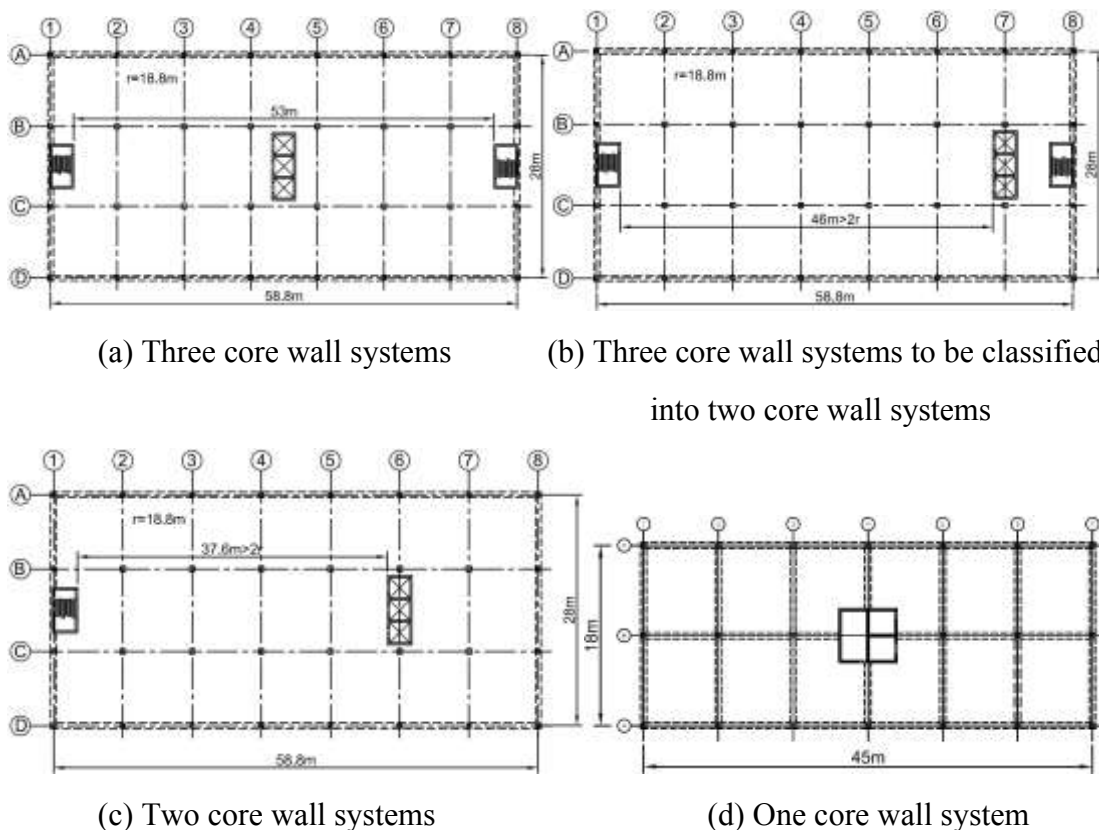


Figure 7 Identification of the value of b_r for the buildings with three, two, and one core wall systems

3.1.2 Tier 1.2 - proposed method to calculate the value of b_r using static analysis

If a building has not met the criteria outlined in tier 1.1, tier 1.2 can be used to compute the value of b_r . The method involves applying static loading on multi-storey buildings. The static load can be applied in accordance with the standard code procedures. In this paper, AS1170.4-2007 was adopted, where a set of point loads are applied at a distance

equals to 10% of the building width away from the building's centre of mass (as shown in Fig. 8). The application of this eccentric set of point loads is to estimate the location of the centre of rigidity of the building (CR).

The location of CR and the value of b_r can be estimated from the deflection at the flexible edge ($\delta_{\text{eff,flex}}$), the deflection at the stiff edge ($\delta_{\text{eff,stiff}}$) and the deflection at the CR ($\delta_{\text{eff,CR}}$). To obtain the values representing the multi-storey building, the effective displacements at different locations on a building plan can be calculated based on the storey displacements by the equation (8).

$$\delta_{eff} = \frac{\sum(m_i \delta_i^2)}{\sum(m_i \delta_i)} \quad (8)$$

Where, m_i and δ_i are respectively the mass and displacement of each floor i .

The effective displacement at the building's CR ($\delta_{\text{eff,CR}}$) is equal to the two-dimensional (2D) displacement (as illustrated in Fig. 8) of the building, which can be obtained by performing static analysis while restraining the rotational degree of freedom of the building. The effective displacements at the flexible and stiff edge ($\delta_{\text{eff,flex}}$ and $\delta_{\text{eff,stiff}}$) can be obtained by performing a three-dimensional analysis of the building.

Based on the displacement values ($\delta_{\text{eff, CR}}$, $\delta_{\text{eff, flex}}$ and $\delta_{\text{eff, stiff}}$), the location of the CR (x_2) can be estimated by using linear interpolation between $\delta_{\text{eff, stiff}}$ and $\delta_{\text{eff, flexible}}$ as illustrated in the lower graph of Figure 8.

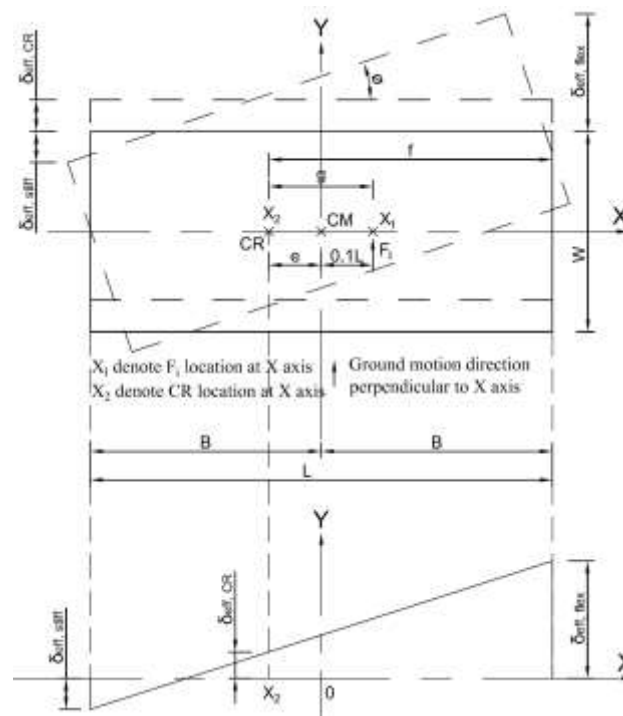


Figure 8 Identification of the location of CR of the structure

The value of b_r can be calculated from the equations of (9)-(11) after the location of CR of the building has been identified.

$$g = |x_1 - x_2| \quad (9)$$

$$f = |B - x_2| \quad (10)$$

$$b_r = \sqrt{\frac{\frac{g}{r} \times \frac{f}{r}}{\frac{\delta_{eff,flex}}{\delta_{eff,CR}} - 1}} \quad (11)$$

Where, $\delta_{\text{eff,flex}}$ is the effective displacement at the flexible edge of the building under the lateral loads; $\delta_{\text{eff,CR}}$ is the effective displacement of the building at the location of the CR.

If the building of b_r value is greater than 1.0, the maximum displacement demand of asymmetrical buildings can be estimated. Studies previously undertaken by the authors have shown that the maximum displacement demand can be conservatively estimated by Equations (12) – (14) and illustrated in Figure 9:

$$RSD_{\text{peak}} = \min \left(RSA_{\text{max}} \left(\frac{T}{2\pi} \right)^2 \times 2.7, RSV_{\text{max}} \left(\frac{T}{2\pi} \right) \times 2.1 \right) \quad \text{for acceleration-controlled condition} \quad (12)$$

$$RSD_{\text{peak}} = \min \left(RSV_{\text{max}} \left(\frac{T}{2\pi} \right) \times 2.1, RSD_{\text{max}} \times 1.6 \right) \quad \text{for velocity-controlled condition} \quad (13)$$

$$RSD_{\text{peak}} = RSD_{\text{max}} \times 1.6 \quad \text{for displacement-controlled condition} \quad (14)$$

As $RSV_{\text{max}} = RSA_{\text{max}} \left(\frac{T_1}{2\pi} \right)$ and $RSD_{\text{max}} = RSV_{\text{max}} \left(\frac{T_2}{2\pi} \right)$, Equations (12) to (14) can be re-arranged to form expressions for the peak edge displacement ratio:

$$\left(\frac{\delta}{\delta_0} \right)_{\text{Peak}} = 2.7 \text{ or } 2.1 \left(\frac{T_1}{T} \right) \text{ whichever is less in acceleration-controlled condition} \quad (15)$$

$$\left(\frac{\delta}{\delta_0} \right)_{\text{Peak}} = 2.1 \text{ or } 1.6 \left(\frac{T_2}{T} \right) \text{ whichever is less in velocity-controlled condition} \quad (16)$$

$$\left(\frac{\delta}{\delta_0} \right)_{\text{Peak}} = 1.6 \text{ in displacement-controlled condition} \quad (17)$$

where, T is the fundamental period of the equivalent 2D building natural period (obtained from 2D analysis). T_1 is the first corner period, T_2 is the second corner period, RSD_{max} , RSV_{max} , and RSA_{max} are respectively the maximum response spectrum displacement, velocity, and acceleration in displacement-, velocity- and acceleration-controlled conditions as shown in Figure 9. The maximum displacement demand can be obtained by multiplying Equations (15) to (17) with the displacement values of the building obtained from two-dimensional analyses.

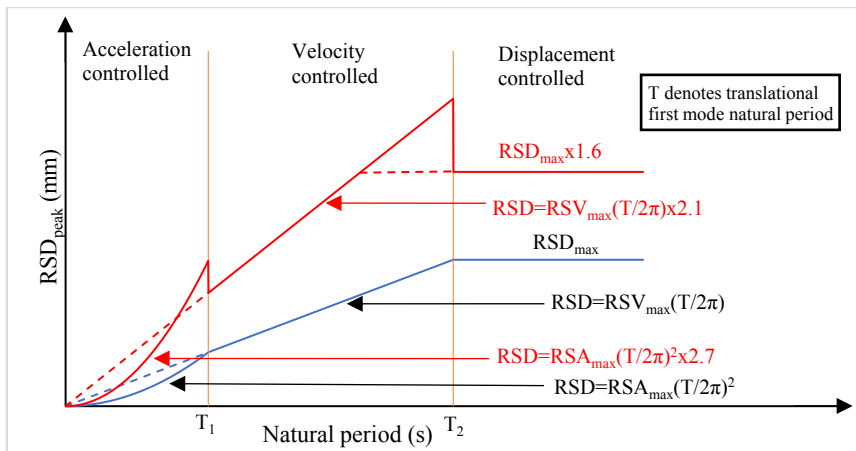


Figure 9 Displacement response spectrum with and without caps of edge displacement ratio featuring acceleration-, velocity-, and displacement-controlled region

3.2 TIER TWO

Tier 2 involves the use of the edge displacement ratio presented in Figures 3 to 6. Tier 2 requires the eccentricity and elastic radius ratio (b_r) of multi-storey buildings to be determined. The process outlined in Section 3.1.2 can be used to compute the b_r value.

3.3 TIER THREE

Tier three is a more rigorous analysis based on equations of edge displacement ratio introduced in Section 2 (equations of (3)-(5)). Similar to Tier 2, Tier 3 requires the knowledge of the eccentricity and elastic radius ratio (b_r) of multi-storey buildings. The maximum deflection of the structure can be calculated by multiplying the displacement from 2D analysis by the edge displacement ratio. Tier 3 can also be used when the parameters of the buildings (e_r , b_r and B_r) are outside the range presented in Figures 3 to 6.

4. VALIDATION OF THE THREE-TIERED APPROACH METHOD

This section presents dynamic analyses of multi-storey buildings to verify the three-tiered method and the peak edge displacement ratio for displacement-, velocity- and acceleration-controlled conditions. Twenty six-building models were created based on eight-building layouts presented in Figure 10. Each case study of 1a, 1b, and 1d involve 4- to 9-storey building models (building height of 16m to 36.8m) as listed in Table 1. The case study of 1c includes 4- to 7-storey building models (building height of 16m to 28m), as detailed in Table 1. Each case study of 2a, 3a, 3b, and 3c is 4-storey building models (building height of 14m to 15 m), as shown in Table 1.

For case study building 2a, the superimposed dead load and live load are respectively 1.5kPa and 2kPa for a typical floor, and 2.5kPa and 0.25kPa for the roof. For the rest of the case study buildings, the superimposed dead load and live load are respectively 1.5kPa and 4kPa for a typical floor, and 1.5kPa and 0.25kPa for the roof. The buildings were assumed to be located on a site class D with a design return period of 500 years for earthquake actions in Melbourne ($Z = 0.08g$). The critical dimensions of the structural elements are presented in Table 1. The base connections for columns and walls were assumed to be fixed. Dynamic response spectral analyses with the consideration of higher modes were conducted using the program ETABS (CSI, 2015).

Based on tier 1.1, the case study buildings in Figure 10 all have the values of b_r larger than one when ground motion is along the y-axis of the buildings, which are the critical direction of the buildings. According to the criteria of tier 1.1 in Section 3.1.1, the case studies 1a, 1b, 1c, 1d, 3a, 3b, and 3c can be classified as three core wall systems with external cores or shear walls separated by a distance approximately equals to the building's width. Moreover, the case study buildings 1c and 1d can be classified as two core wall systems with a separation distance that is larger than $2r$ (where, r is the mass radius of gyration of the buildings' plan). For case study building 2a, the value of b_r cannot be identified through the criteria of tier 1.1.

The b_r values of all of the case study buildings were also computed using the method outlined in Tier 1.2 (Section 3.1.2). The values of b_r were found to be greater than 1.0 (Table 2), demonstrating the robustness of Tier 1.1.

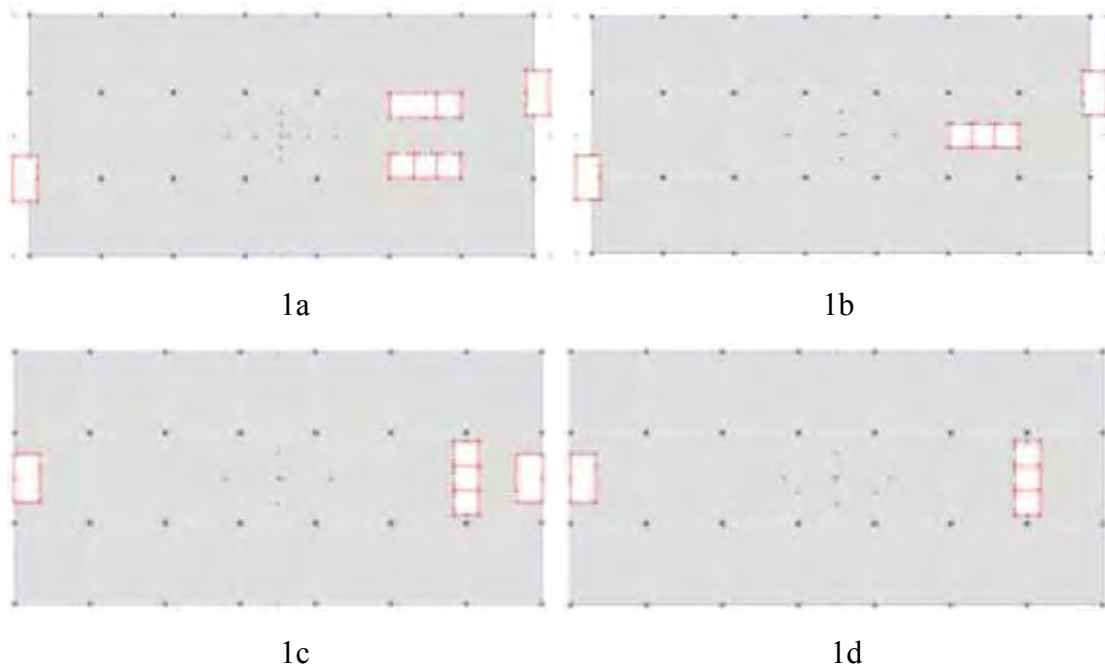
The proposed method to estimate the maximum displacement demand of buildings in the displacement-controlled condition was verified by comparison with results from the dynamic analysis of case study buildings 1a-L9, 1a-L8, 1b-L9, 1b-L8, 1b-L7, 1d-L9, and 1d-L8. L9, L8, and L7 represent that the number of stories of the building models. Table 2 presents the fundamental period of the buildings from 2D and 3D analyses. It is shown that the values of b_r of the case study buildings are all larger than one. The

peak edge displacement ratio of 1.6 in displacement-controlled condition can be applied to predict the building's maximum deflection.

Table 1 Summary of the building geometries of case studies

Case study	Length (m)	Width (m)	Height (m)	Ext./Int column (m)	Beam	Slab thickness (mm)	No. of core wall	The thickness of wall (m)
1a	62.55	28	36.8/32.8/28/24/20/16	0.5x0.5/0.6x0.6	0.7Wx0.7D	0.25	4	0.25
1b	62.55	28	36.8/32.8/28/24/20/16	0.5x0.5/0.6x0.6	0.7Wx0.7D	0.25	3	0.25
1c	58.8	28	28/24/20/16	0.5x0.5/0.6x0.6	0.7Wx0.7D	0.25	3	0.25
1d	58.8	28	36.8/32.8/28/24/20/16	0.5x0.5/0.6x0.6	0.7Wx0.7D	0.25	2	0.25
2a	25	42.45	14	0.4x0.6 0.2x1/1.2	2.4/1.8Wx0.6D	0.2	1	0.2/0.25
3a	45	18	15	0.5x0.5	0.6Wx0.7D	0.22	1	0.2
3b	45	18	15	0.5x0.5	0.6Wx0.7D	0.22	1	0.2
3c	45	18	15	0.5x0.5	0.6Wx0.7D	0.22	1	0.2

Figure 11 compares the maximum displacement profiles of the buildings from dynamic analysis with those estimated by the proposed method. It is shown that tier 1 is able to provide conservative estimates of the maximum displacement demand of the buildings. Tier 2 is shown to be able to provide predictions of the displacement demand with reasonable accuracy.



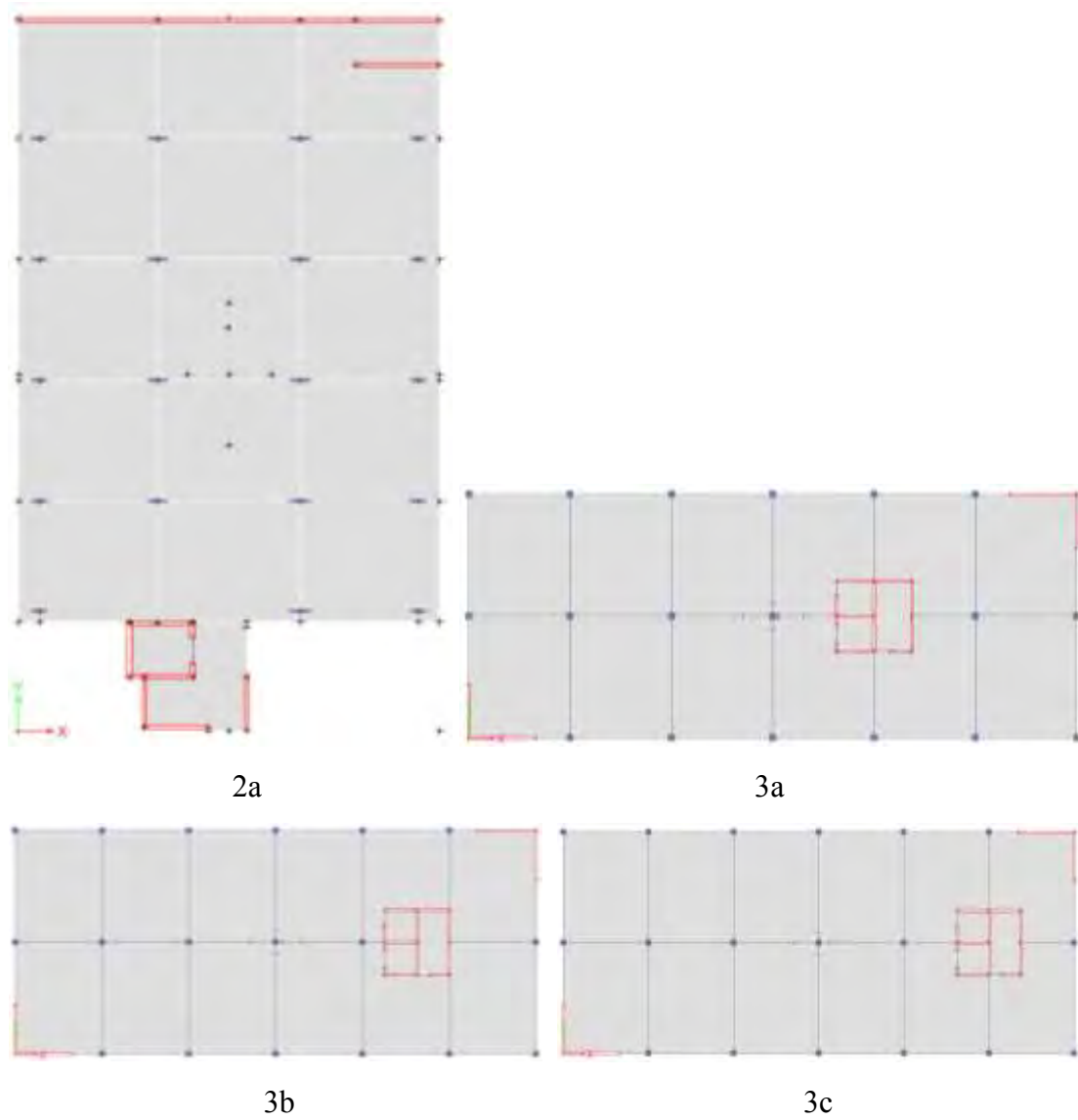
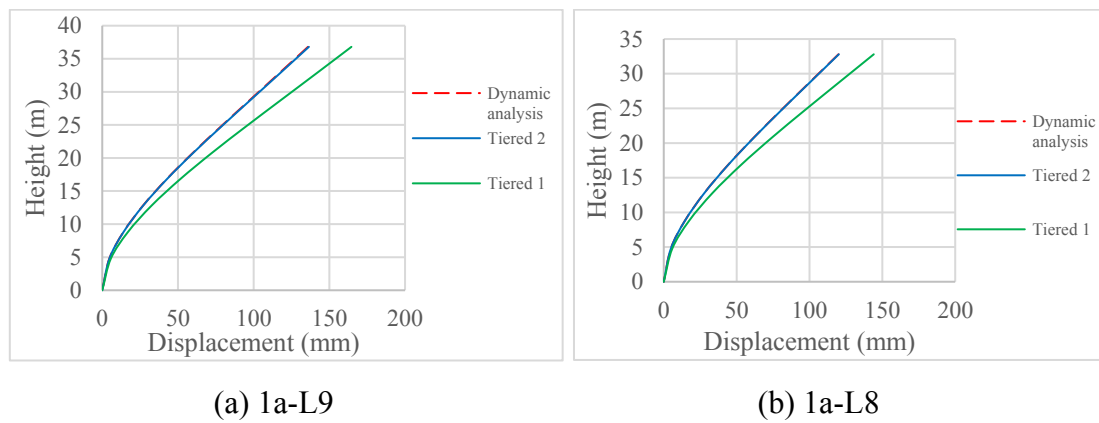


Figure 10 Layout of buildings used to investigate the torsional effect of case studies



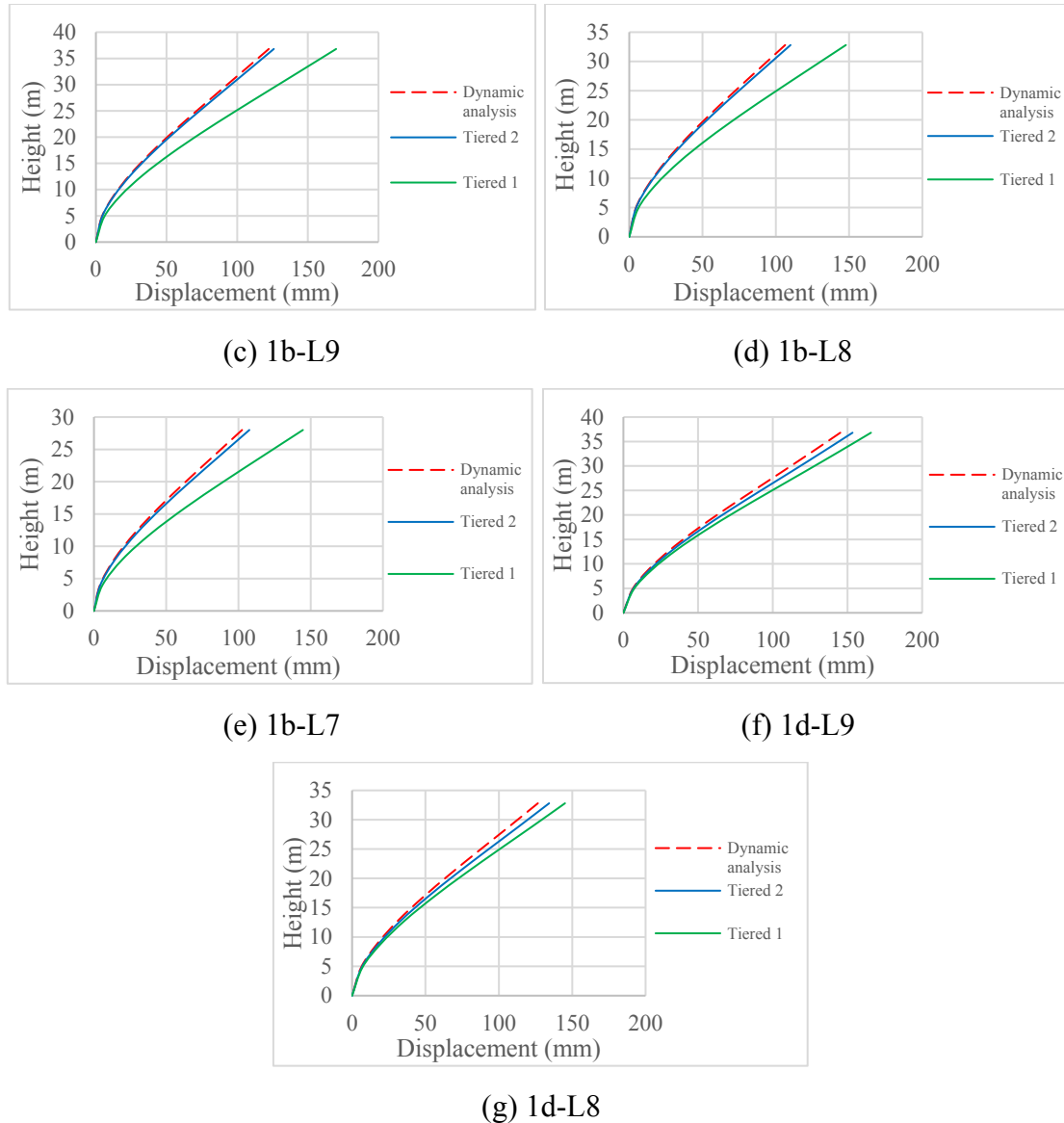
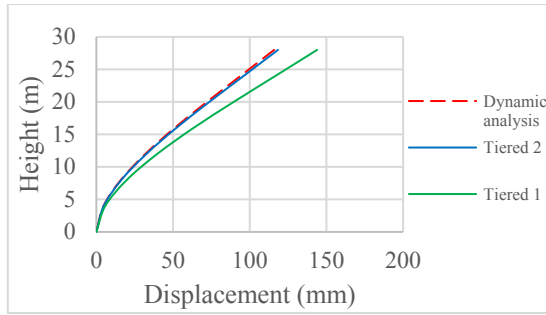


Figure 11 Comparison between edge displacement ratio of caps, GFM, and dynamic analysis in displacement-controlled condition

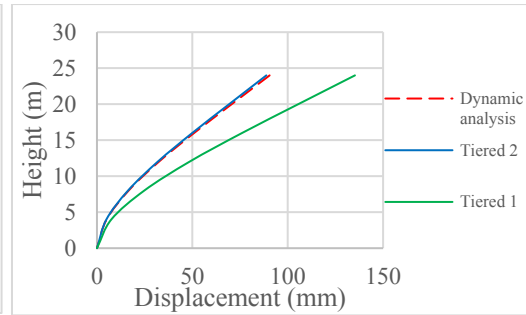
Table 3 presents the case study buildings in the velocity-controlled condition. L9, L8, L7, L6, L5, and L4 denote that the number of stories in the buildings. The maximum deflection profiles of the buildings from dynamic analysis and the proposed method (tier 1 and tier 2) are shown in Figure 12. The figures demonstrate that the proposed method can provide reasonable predictions of the buildings' maximum displacement demand.

Table 2 Summary of elastic radius ratio (b_r), the fundamental period from 2D analyses and 3D analyses – case study buildings in the displacement-controlled condition

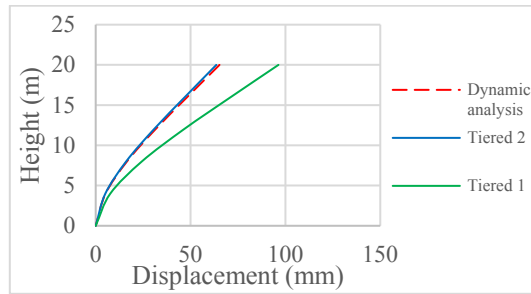
Building model	$T_{1,y, 2D}$	$T_{1, 3D}$	b_r
1a-L9	2.082	2.165	1.515
1a-L8	2.028	2.12	1.489
1b-L9	2.277	2.315	1.642
1b-L8	2.234	2.275	1.624
1b-L7	1.657	1.689	1.624
1d-L9	1.8	4	1.276
1d-L8	1.8	3.882	1.276



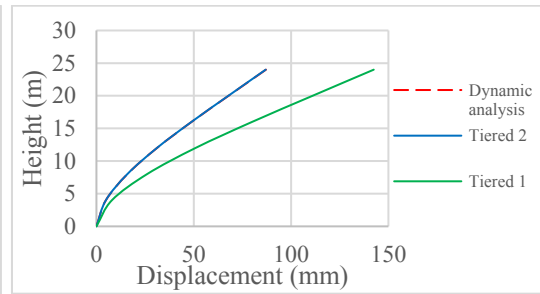
(a)1a-L7



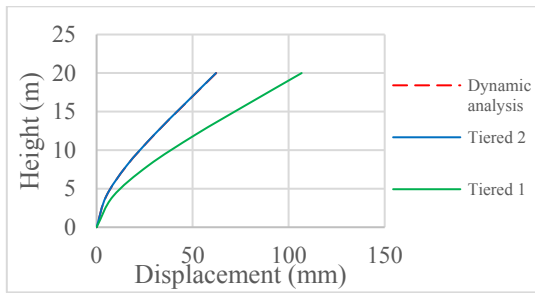
(b)1a-L6



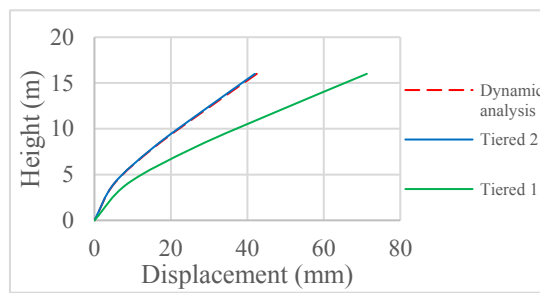
(c)1a-L5



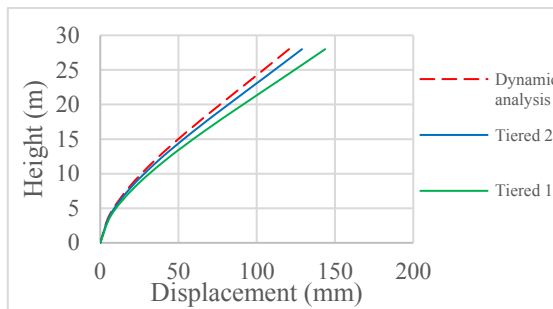
(d)1b-L6



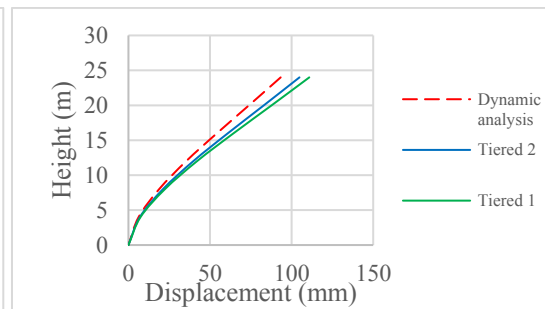
(e)1b-L5



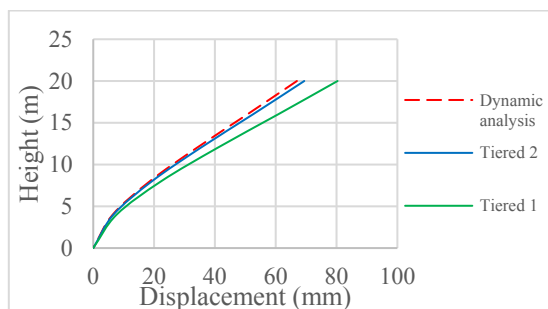
(f)1b-L4



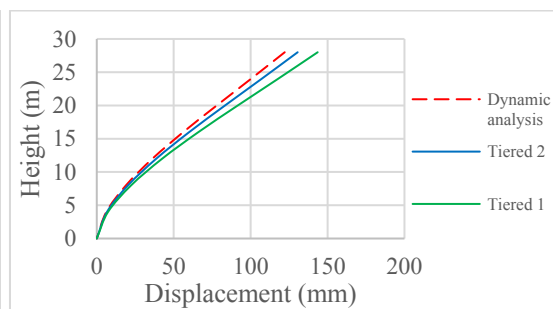
(g)1c-L7



(h)1c-L6



(i)1c-L5



(j)1d-L7

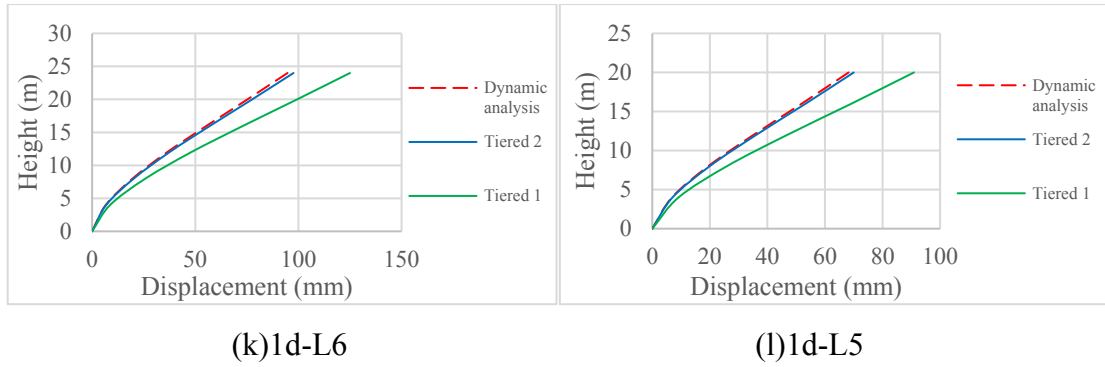
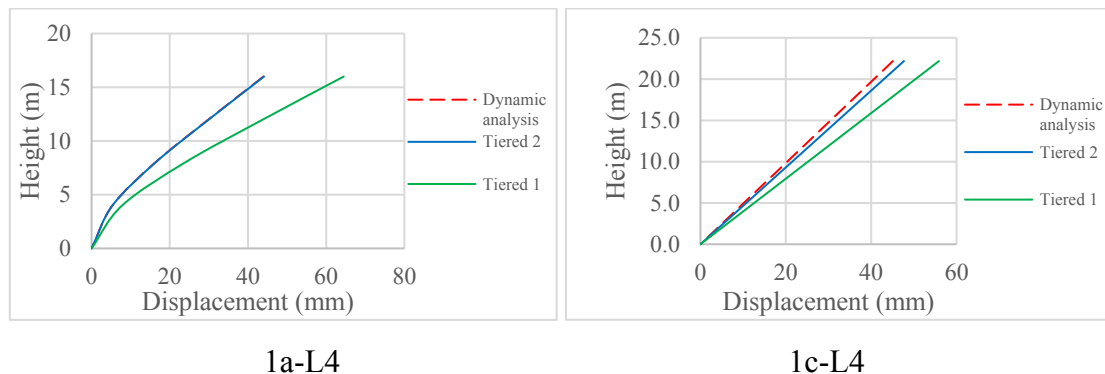


Figure 12 Comparison between edge displacement ratio of caps, GFM, and dynamic analysis in velocity-controlled condition

Table 3 Summary of elastic radius ratio (b_r), the fundamental period from 2D analyses and 3D analyses – case study buildings in the velocity-controlled condition

Building model	$T_{1,y, 2D}$	$T_{1, 3D}$	b_r
1a-L7	1.444	1.578	1.49
1a-L6	1.136	1.193	1.50
1a-L5	0.823	0.867	1.51
1b-L6	1.249	1.275	1.63
1b-L5	0.904	0.925	1.64
1b-L4	0.62	0.637	1.64
1c-L7	1.205	2.356	1.22
1c-L6	0.921	1.761	1.23
1c-L5	0.679	1.264	1.24
1d-L7	1.4	2.8	1.29
1d-L6	1.038	2.1	1.30
1d-L5	0.768	1.496	1.32

The proposed method was verified for buildings in the acceleration-controlled condition (Table 4). L4 here denotes that the building models have four storeys. The results from the dynamic analysis are compared with the predictions from tier 1 and tier 2 of the proposed method in Figure 13. It is shown that the method is able to provide reasonable predictions of the maximum displacement demands. The robustness of the proposed method has been demonstrated for the three different conditions.



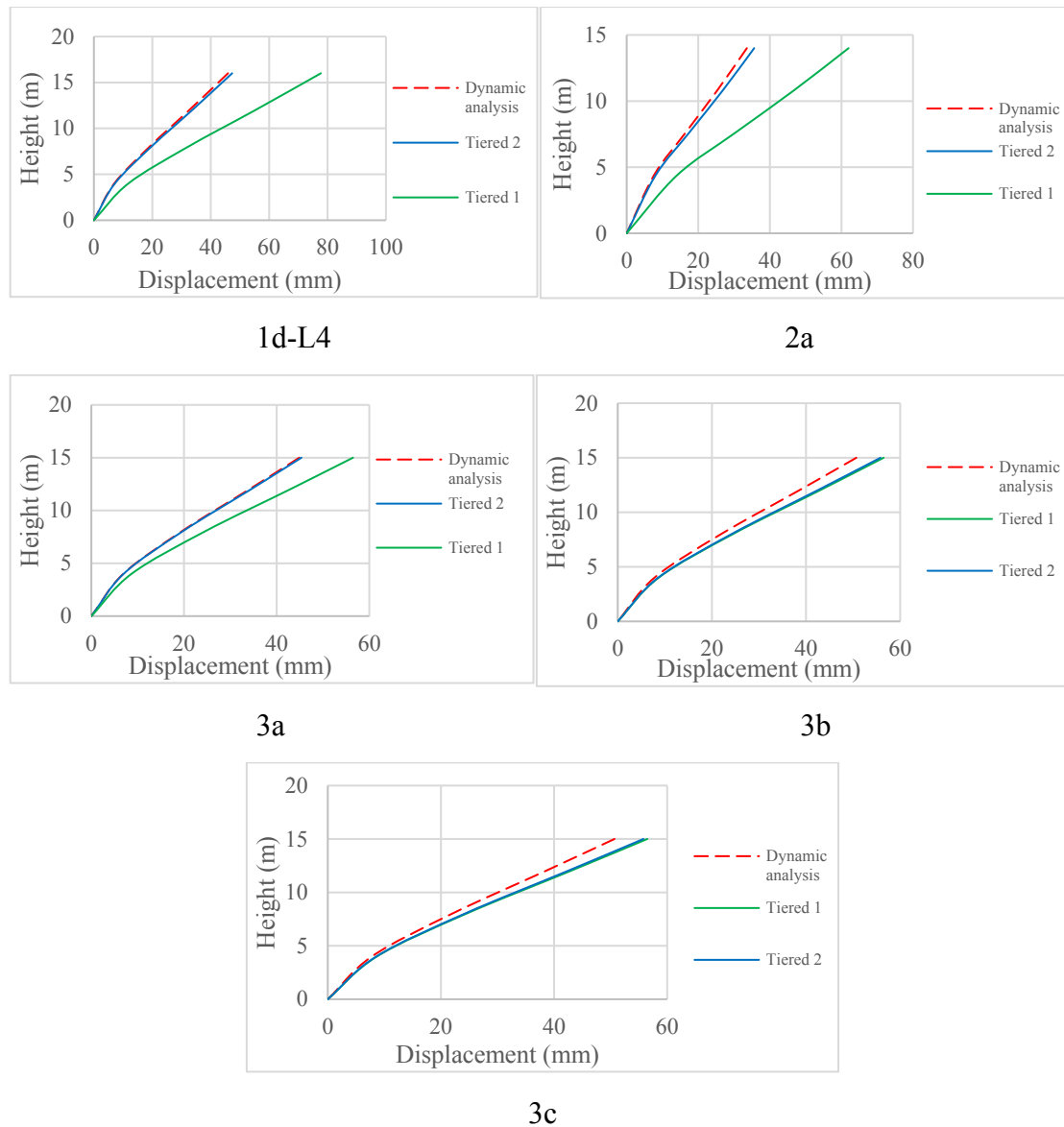


Figure 13 Comparison between edge displacement ratio of caps, GFM, and dynamic analysis in acceleration-controlled condition

Table 4 Summary of elastic radius ratio (b_r), the fundamental period from 2D analyses and 3D analyses – case study buildings in the acceleration-controlled condition

Building model	$T_{1,y, 2D}$	$T_{1, 3D}$	b_r
1a-L4	0.54	0.599	1.53
1c-L4	0.478	0.859	1.253
1d-L4	0.544	1.012	1.35
2a	0.524	0.597	1.963
3a	0.483	0.615	1.21
3b	0.483	0.67	1.24
3c	0.479	0.703	1.26

5. CONCLUDING REMARKS

This paper presents a simple and accurate method to provide estimates of maximum deflection due to the torsional effects on RC structures. The technique involves a three-tiered approach based on static analysis, which is an extension of a method (referred to as Generalised Force Method of analysis) previously developed by the authors. Charts

of edge displacement ratios in displacement-, velocity- and acceleration-controlled conditions have been developed based on the previously developed equations.

The tiered method introduced includes: i) Tier 1, which is based on visual assessment (tier 1.1) or calculation (tier 1.2) to establish b_r , and the use of the peak edge displacement ratio to predict the maximum displacement demand of asymmetrical buildings; ii) Tier 2, which is based on the charts of edge displacement ratios (Figs. 3-6), and iii) Tier 3, which is based on the equations (Eqs. (3) to (5)) for the edge displacement ratios.

The proposed method has been validated by comparison with results from the dynamic analysis of case study buildings. The comparison demonstrates the robustness of the proposed method.

ACKNOWLEDGMENTS

The support of the Commonwealth of Australia through the Cooperative Research Centre (CRC) program is acknowledged.

REFERENCES:

- Anagnostopoulos, S., Kyrkos, M., & Stathopoulos, K. (2015). Earthquake induced torsion in buildings: critical review and state of the art. *Earthquakes and Structures*, 8(2), 305-377.
- Anastassiadis, K., Athanatopoulou, A., & Makarios, T. (1998). Equivalent static eccentricities in the simplified methods of seismic analysis of buildings. *Earthquake spectra*, 14(1), 1-34.
- ASCE/SEI(7-10). (2010). Minimum Design Loads for Buildings and Other Structures. *ASCE/SEI 7-10*, xxxix+593.
- Beka Hailu, A., & Jong Seh, L. (2019). Incorporation of Torsional & Higher-Mode Responses in Displacement-Based Seismic Design of Asymmetric RC Frame Buildings. *Applied Sciences*, 9(6), 1095-1095. doi:10.3390/app9061095
- Birzhandi, M. S., & Halabian, A. M. (2014). Inelastic response of bi-eccentric-plan asymmetric reinforced concrete buildings. *Structures & Buildings*, 167(8), 469.
- Bosco, M., Ferrara, G. A. F., Ghersi, A., Marino, E. M., & Rossi, P. P. (2015). Predicting displacement demand of multi-storey asymmetric buildings by nonlinear static analysis and corrective eccentricities. *Engineering Structures*, 99, 373-387. doi:10.1016/j.engstruct.2015.05.006
- BSI. (2004). BS EN 1998-1:2004 Eurocode 8: Design of structures for earthquake resistance - Part 1: General rules, seismic actions and rules for building (pp. 229): British Standards Institution (BSI) London, UK.
- CSI. (2015). Etabs (version 2015) Retrieved from www.csiamerica.com/support/downloads.
- Humar, J., & Kumar, P. (1998). Torsional motion of buildings during earthquakes. I. Elastic response. *Canadian Journal of Civil Engineering*, 25(5), 898-916.
- IBC. (2012). International Building Code (pp. 728). 4051 West Flossmoor Road, Country Club Hills: International Code Council.
- Lam, N. T., Wilson, J. L., & Hutchinson, G. L. (1997). Review of the torsional coupling of asymmetrical wall-frame buildings. *Engineering Structures*, 19(3), 233-246.
- Lam, N. T. K., Wilson, J. L., & Lumantarna, E. (2016). Simplified elastic design checks for torsionally balanced and unbalanced low-medium rise buildings in lower seismicity regions. *Earthquakes and Structures*, 11(5), 741-777.
- Lee, H. S., & Hwang, K. R. (2015). *A new methodology in seismic torsion design of building structures*. Paper presented at the The 2015 World Congress on Advances in Structural Engineering and Mechanics (ASEM15), Incheon, Korea.

- Lumantarna, E., Lam, N., & Wilson, J. (2018). Methods of analysis for buildings with uni-axial and bi-axial asymmetry in regions of lower seismicity. *Earthquake and Structures*, 15(1), 81.
- Lumantarna, E., Lam, N., & Wilson, J. (2019). *Predicting Maximum Displacement Demand of Asymmetric Reinforced Concrete Buildings*. Paper presented at the AEES national conference, Newcastle City Hall.
- Manohar, S., & Madhekar, S. (2015). *Seismic design of RC buildings : theory and practice*: Springer.
- Mehana, M. S., Mohamed, O., & Isam, F. (2019). *Torsional Behaviour of Irregular Buildings with Single Eccentricity*. Paper presented at the IOP Conference Series: Materials Science and Engineering.
- MOC. (2008). Manual of Civil Structures. Mexico.
- NZS1170.5. (2004). NZS 1170.5: 2004 earthquake Actions - New Zealand (pp. 76). New Zealand: Standards New Zealand.
- Tabatabaei, R., & Saffari, H. (2011). Evaluation of the Torsional Response of Multistory Buildings Using Equivalent Static Eccentricity. *Journal of Structural Engineering*, 137(8), 862-868. doi:10.1061/(ASCE)ST.1943-541X.0000324
- Tso, W. K. (1990). Static eccentricity concept for torsional moment estimations. *Journal of Structural Engineering*, 116(5), 1199-1212.
- Xing, B., Lumantarna, E., Lam, N. T., & Menegon, S. (2019). *Prioritisation strategy for seismic retrofitting of reinforced concrete buildings in Australia*. Paper presented at the Australian Earthquake Engineering Society 2019 Conference, Newcastle, NSW.